Unveiling the Progenitors of Short-duration Gamma-ray Bursts

Dissertation Advisor: Professor Edo Berger Wen-fai Fong

Unveiling the Progenitors of Short-duration Gamma-ray Bursts

Abstract

Gamma-ray bursts (GRBs) are relativistic explosions which originate at cosmological distances, and are among the most luminous transients in the universe. Following the prompt γ-ray emission, a fading synchrotron "afterglow" is detectable at lower energies. While long-duration GRBs (duration > 2 sec) are linked to the deaths of massive stars, the progenitors of short-duration GRBs (duration < 2 sec) have remained elusive. Theoretical predictions formulated over the past two decades have suggested that they are the mergers of two compact objects, involving either two neutron stars (NS-NS) or a neutron star and a black hole (NS-BH). Such merging systems are also important to understand because they are premier candidates for gravitational wave detections with upcoming facilities and are considered likely sites of heavy element nucleosynthesis. The launch of the *Swift* satellite in 2004, with its rapid multi-wavelength monitoring and localization capabilities, led to the first discoveries of short GRB afterglows and therefore robust associations to host galaxies. At a *Swift* detection rate of ≈ 8 events per year, the growing number of well-localized short GRBs enables comprehensive population studies of their afterglows and environments for the first time. In this thesis, I undertake a multi-wavelength observational campaign to address testable predictions for the progenitors of short GRBs. From their local environments, I show that short GRBs explode in diffuse regions of their host galaxies and are weakly correlated with the distribution of stellar mass and star formation in their host galaxies. I study the host galaxy demographics for the entire population and find that $\approx 20 - 40\%$ of short GRBs originate from elliptical

galaxies, implying an older stellar progenitor. From their afterglows, I present evidence that some short GRBs are collimated in narrow jets of $\approx 5 - 10^{\circ}$, directly affecting the true energy scale and event rate. Finally, taking advantage of a decade of broad-band afterglow observations at radio through X-ray wavelengths, I find that short GRBs have median isotropic-equivalent energies of $\approx 10^{51}$ erg and that their local environments have low densities, $\approx 10^{-3} - 10^{-2}$ cm^{-3}. Taken together, this thesis comprises several lines of independent evidence to demonstrate that short GRBs originate from the mergers of two compact objects, and also provides the first constraints on the explosion properties for a large sample of events. With the direct detection of gravitational waves from compact object mergers on the horizon, these studies provide necessary inputs to inform the next decade of joint electromagnetic-gravitational wave search strategies.

Contents

Acknowledgments

When I reflect on the story of my life, I find that graduate school has been the most fulfilling chapter to date. This chapter has tested me both intellectually and emotionally, but I have reached the finish line with a small army of faithful supporters that I have accreted along the way. The completion of this thesis is special to me because I can now share it with those who have played a role.

I ultimately decided to pursue astronomy because I had exceptional early mentors in the field, and throughout graduate school, my network of mentors has grown significantly. I thank the three professors who wrote reference letters that made my graduate school dream possible, and went above and beyond to advocate for me: Eric Blackman, Jim Elliot, and Julia Lee. My discussions with them were crucial in my decision to attend Harvard. There have been ephemeral moments when I have lost sight of my purpose as a graduate student. I thank Alicia Soderberg, Jim Moran, and John Johnson, for their insight during these times and for always providing a light at the end of the tunnel. I have truly grown as a scientist through discussions with my thesis committee, Rosanne DiStefano, Josh Grindlay, Neil Gehrels, and Ramesh Narayan, who kept in touch with my research and provided invaluable input which ultimately served to improve my thesis. I was able to develop my teaching skills by serving as a Teaching Fellow under Bob Kirshner, Rosanne DiStefano, and Daniel Eisenstein, who provided premier examples as lecturers. I thank Irwin Shapiro for countless impromptu hallway conversations, and I only hope I can achieve his infectious love of life and astronomy throughout my career. I thank Rachel Bezanson, Nathan Smith, and Dan Stark for their guidance in the final year of my PhD, and for their infinite patience in answering my questions about the

University of Arizona. They have given me just a few of many reasons to be excited about my life's next chapter in Tucson.

Over the years, I have built many memories through social interactions with my fellow Harvard Astrograds. I have cherished every day among this unique population of graduate students, who have made me feel like every day is my birthday. I thank my officemates: Lauranne Lanz, for providing much support over the years in the form of Swiss chocolate and beautiful hand-knit scarves, and Paul Torrey for putting up with me and for all of the Cadbury eggs. My first friends at Harvard were the members of my incoming class, Zach Berta-Thompson, Maggie McLean, Bob Penna, Sarah Rugheimer, Greg Snyder, Nick Stone and Paul Torrey. I am so proud to be part of this cohesive unit, and I will continue to root for them through all of their future accomplishments. In particular, I thank Zach Berta-Thompson for his unique sense of humor, and Nick Stone for his hauntingly high-pitched laugh and his penchant for engaging, albeit repetitive, story-telling. I have enjoyed many conversations over coffee, cocktails, and craft beers with Sarah Wellons, Maria Drout, Dylan Nelson, Ellie Newton, Katherine Rosenfeld, Ian Czekala, Jason Dittmann, Courtney Dressing, Chris Faesi, Phil Cowperthwaite and Peter Blanchard. For providing unwavering guidance especially as I went through the job application process, I thank Laura Blecha, Sarah Ballard, Gurtina Besla, Ann Mao, Diego Munoz, Joey Neilsen, and Jack Steiner. I strongly value mentoring, and created a dedicated program for graduate students within the department. For being a co-pilot in this effort and sharing my passion for mentoring, I heartily thank Anjali Tripathi. Although I will miss being a part of this eclectic group of graduate students, I rest assured that I have made life-long friends out of many.

I thank my non-astronomer friends, Julia, Jessie, and Buddy for exploring New

England with me and for letting me cancel engagements at the last minute for gamma-ray bursts; my housemates Yelee, Kristin, Lindsay and Helen for providing a welcoming environment in which to live; and my long-distance friends Amy, Cong, Melissa, Rachel and Dan for cheering me on from hundreds of miles away.

The CfA has been a wonderful place to work, in large part due to the invaluable administrative staff who have kept everything running smoothly. I thank Lisa Catella, Robb Scholten, and Nina Zonnevylle for the tremendous amount of work they put in to ensure that we are happy as graduate students. Over the years, I would often enter the office of department administrator Peg Herlihy with a seemingly insurmountable problem, and would always walk away with a solution. I am greatly indebted to Peg for having a genuine love of students, and for playing the roles of confidante, therapist, or cheerleader whenever the situation called for it.

Although the field of gamma-ray bursts is competitive, a few people outside of the CfA made me feel welcome in the field from the start: Brad Cenko, Judy Racusin, Enrico Ramirez-Ruiz and Brian Metzger. Within the CfA, there is a vibrant community of people working in transient astrophysics and it has been the utmost pleasure to be part of this team. I have learned much about academic life, observing, and data reduction from Ryan Foley, Giulia Migliori, Dan Milisavljevic, and Peter Williams. The Berger Time-Domain Research Group at the CfA has become akin to a family unit for me. I consider myself exceptionally lucky to be part of a group of people who are superlative in their dedication, knowledge, work ethic, and support for one another. Like a puzzle, every piece is unique in its own way, but the whole comes together beautifully. I thank my "academic little brother and sister" of the group, Tanmoy Laskar and Ragnhild Lunnan, for their company on observing runs and conference trips, for always being

there for me, and for providing encouragement every step of the way. How wonderful it has been to go to work every day with three outstanding collaborators and role models, Raffaella Margutti, Ashley Zauderer and Ryan Chornock. I thank them for teaching me countless astronomy skills, for having unique personalities, for their invaluable advice, and for listening when I needed it most. Their combined efforts have elevated my overall happiness and productivity as a graduate student, and I only hope that I can have such a significant impact on a student's life in the future as they have had on mine.

The choice to work with my PhD advisor, Edo Berger, is the single best decision that I have made during graduate school. I thank Edo for introducing me to the wonderful world of gamma-ray bursts and for leading by example every single day. I thank him for his contagious love of astrophysics, ceaseless mentorship, frequent promotion of my work, training in scientific writing and data reduction, and for being a never-ending fountain of corny jokes. Above all else, I thank Edo for believing in me more than I could ever believe in myself. I could not have asked for a better and more inspiring PhD advisor.

I owe my general happiness to my incredibly close relationship with my family. I thank my brother-in-law, Danny, for being the older brother figure that I never had. I thank my sisters and my two best friends in life, Hiu-fai and Ming-fai, for providing comic relief and unconditional support since the day I was born. I could not imagine my life without them. Finally, I dedicate this thesis to my parents, Chin-To and Helen Fong, who have overcome so many obstacles in their own lives so that I could lead a life of privilege. I thank them for their selflessness, for insisting that I follow my dreams, and for always encouraging me to read my own books.

For my parents,

two unending sources of energy, inspiration, and love

Chapter 1

Introduction

1.1 Gamma-ray Bursts in the pre-*Swift* Era

In 1967, the *Vela* satellites serendipitously discovered an unprecedented flash of emission of unknown origin at γ-ray energies. The next generation of *Vela* satellites discovered 16 additional such events over the next few years (Klebesadel et al. 1973). The energy range at which these bursts were detected, coupled with their fast timescales of $\lesssim 100$ seconds, led to a suitable name: γ-ray bursts (GRBs). Over the subsequent three decades, the launch of missions optimized to detect GRBs, including the Compton Gamma Ray Observatory (CGRO; 1991-2000), *Beppo-SAX* (1996-2003; Boella et al. 1997), and HETE-2 (2000-present; Ricker et al. 2003) discovered thousands of GRBs, providing a wealth of information regarding their γ-ray properties and clues to their origin. In particular, their isotropic distribution on the sky (Meegan et al. 1992; Schmidt 2001), along with their fluence distribution, strongly suggested that GRBs are extragalactic (Paczynski 1995). A cosmological origin would imply enormous isotropic-equivalent

γ-ray energy releases of $\approx 10^{50} - 10^{54}$ erg in less than a matter of minutes.

Studies of the γ-ray emission for the rapidly growing sample of GRBs uncovered bimodality in two key properties: duration and spectral hardness. The distribution of durations over which 90% of the photons are detected, T_{90}, has a separation at ≈ 2 sec, based on the BATSE sample of GRBs (e.g., Norris et al. 1984; Klebesadel 1992; Kouveliotou et al. 1993). Analysis of the γ-ray spectra also showed that short-duration GRBs ($T_{90} \lesssim 2$ sec) generally have harder spectra than long-duration events ($T_{90} \gtrsim 2$ sec; Dezalay et al. 1992; Kouveliotou et al. 1993; Dezalay et al. 1996). Thus, two populations of GRBs emerged: long-soft and short-hard GRBs.

Since the discovery of the first GRBs, dozens of theories arose to explain these catastrophic events. Over time, two progenitor models which have garnered support are the mergers of two compact objects, involving either two neutron stars or a neutron star and a black hole (NS-NS/NS-BH; Eichler et al. 1989; Narayan et al. 1992; Mochkovitch et al. 1993), or the collapse of massive stars, in a "collapsar" (MacFadyen & Woosley 1999). By the late 1990s, observations were needed to unambiguously establish the distance scale, test these progenitor models, and understand their connection to the two classes of GRBs.

1.2 The Importance of Afterglows and Host Galaxies

An understanding of the origin of GRBs requires precise localization of these events to place these bursts in their astrophysical contexts. CGRO was able to detect GRBs at a rapid rate of ≈ 1 per day due to all-sky coverage. However, most events had typical

localization uncertainties of tens of square degrees, making fruitful follow-up observations at other wavelengths challenging for the large majority of bursts. Thus, the detection of γ-rays alone did not enable precise localization.

Following the prompt γ-ray emission, the blastwave interacts with the circumburst medium. This interaction is predicted to produce longer-lived synchrotron emission, termed the "afterglow", which is in principle detectable at X-ray through radio wavelengths (Paczynski & Rhoads 1993; Katz 1994; Meszaros & Rees 1997; Sari et al. 1998). In the afterglow model, the spectral energy distribution provides a direct mapping to the burst basic explosion properties; in particular, the blast-wave kinetic energy and density of the sub-parsec-scale circumburst environment (Sari et al. 1998; Granot & Sari 2002). Thus, afterglows offer a unique opportunity to localize GRBs to substantially higher precision and to study their basic properties.

Therefore, in 1997, the discovery of long-wavelength emission following the long-duration GRB 970228 was a watershed event (Galama et al. 1997). The fading afterglow was detected at X-ray and optical wavelengths (Costa et al. 1997; van Paradijs et al. 1997; Wijers et al. 1997), which localized the burst to sub-arcsecond precision. This enabled the robust association with a star-forming host galaxy (Lamb et al. 1999) and confirmed an extragalactic origin from the host galaxy redshift of $z = 0.695$ (Bloom et al. 2001). Importantly, this set an isotropic-equivalent γ-ray energy scale of $\approx 10^{52}$ erg for this event. Furthermore, the star-forming host galaxy was suggestive of an origin from a massive star progenitor (Bloom et al. 2001). Another major discovery occurred the next year in 1998, when the joint detection of a long GRB associated with a spectroscopically-confirmed Type Ic supernova provided a "smoking gun" which linked this event to a massive star progenitor (Galama et al. 1998). This GRB-supernova event,

GRB 980425/SN 1998bw, was also associated with a star-forming galaxy at $z = 0.0085$ (Fynbo et al. 2000). Thus, the discovery of afterglows had a significant impact on the long GRB field by confirming their cosmological origin, setting the energy scale, and providing precise localization, the latter of which paved the way for host galaxy studies.

To date, the number of long GRBs with associated SNe continues to climb (e.g., Hjorth et al. 2003; Malesani et al. 2004; Campana et al. 2006; Chornock et al. 2010; Cobb et al. 2010), further establishing long GRBs to massive star origins. The massive star progenitor is well supported by observations of long GRB local and galactic environments. Over fifteen years of host galaxy observations have led to the finding that long GRBs are exclusively associated with star-forming host galaxies (Le Floc'h et al. 2003; Fruchter et al. 2006; Wainwright et al. 2007a). Furthermore, a decade of concerted efforts to characterize the stellar populations of long GRB hosts revealed young stellar population ages of $\lesssim 0.2$ Gyr, a mean stellar mass of $\approx 2 \times 10^9\,M_\odot$, and inferred UV/optical star formation rates (SFR) of $\approx 1 - 50\,M_\odot\ \mathrm{yr}^{-1}$ (Christensen et al. 2004; Savaglio et al. 2009; Leibler & Berger 2010; Laskar et al. 2011). Finally, the spatial locations of long GRBs with respect to their host galaxy centers (with a mean of ~ 1 half-light radius; Bloom et al. 2002) and their concentration in bright UV regions of their hosts (Fruchter et al. 2006) provided a direct association between long GRBs and ongoing star formation.

1.3 Short GRBs: A Distinct Progenitor?

1.3.1 The Discovery of Short GRB Afterglows and Host Galaxies

By the early 2000s, a cohesive picture was emerging for the progenitors and explosion properties of the long GRB class. However, despite multi-wavelength searches, there were no detected short GRB afterglows, demonstrating that their afterglows are fainter than those of long GRBs (Kehoe et al. 2001; Hurley et al. 2002).

With its novel rapid slewing and localization capabilities, the *Swift* satellite significantly changed the landscape of the GRB field when it was launched in 2004 (Gehrels et al. 2004). *Swift* carries a multi-wavelength suite of instruments: the Burst Alert Telescope (BAT; Barthelmy et al. 2005), the X-ray Telescope (XRT; Burrows et al. 2005) and the UV-Optical Telescope (UVOT; Roming et al. 2005). In particular, XRT and UVOT enabled multi-wavelength searches starting on minute timescales after the bursts. In addition, the localization is significantly improved compared to previous generations of detectors, with γ-ray, X-ray, and UV/optical uncertainties of $\approx 2 - 5'$, $\approx 1 - 10''$, and $\lesssim 1''$, respectively.

Shortly after the launch of *Swift* a series of watershed events in the study of short GRBs occurred in 2005. The short GRB 050509B ($T_{90} = 0.04$ sec) had the first X-ray afterglow detected by *Swift*/XRT (Gehrels et al. 2005), and dedicated searches for an optical counterpart placed stringent limits of $R \gtrsim 25$ mag at ≈ 25 hr after the burst (Gehrels et al. 2005; Bloom et al. 2006). Thus, the most precise position for this burst is $\approx 10''$ in radius, allowing for the likely association of GRB 050509B with

an elliptical host galaxy at $z = 0.225$ (Gehrels et al. 2005; Bloom et al. 2006). The discovery of the first optical afterglow of a short GRB occurred a few months later, for GRB 050709 (Hjorth et al. 2005b; Fox et al. 2005). The sub-arcsecond localization from the optical afterglow enabled an unambiguous association of this event with a star-forming host galaxy at $z = 0.160$ (probability of chance association $\approx 10^{-3}$; Fox et al. 2005; Hjorth et al. 2005b; Covino et al. 2006). Furthermore, late-time optical observations ruled out an accompanying supernova event (Fox et al. 2005). The first radio afterglow was detected in the short GRB 050724A (Berger et al. 2005), spatially coincident with the near-infrared (NIR), optical and X-ray afterglows (Panaitescu 2006; Malesani et al. 2007b). This burst has a robust association to an elliptical host galaxy at $z = 0.257$ (Berger et al. 2005). Applying a synchrotron broad-band afterglow model to GRB 050724A, the inferred isotropic-equivalent kinetic energy is $\approx 10^{51}$ erg and the circumburst density is $\approx 0.01 - 1$ cm^{-3} (Berger et al. 2005; Panaitescu 2006).

1.3.2 Early Studies and Key Predictions for the Progenitors

The first three well-localized short GRBs led to associations with both elliptical and star-forming host galaxies, indicating that a significant fraction of short GRBs arise from older stellar populations, in stark contrast to the long GRB host population. Despite numerous optical and NIR searches after the launch of *Swift*there are no detected SNe following short GRBs (Covino et al. 2006; Soderberg et al. 2006b; Kocevski et al. 2010; Rowlinson et al. 2010a), suggesting that they are not from massive star progenitors. However, there lacked a comprehensive body of observational evidence in favor of another progenitor model.

Prior to the definitive association of long GRBs with massive star progenitors, one of the leading progenitor models for all GRBs was compact object mergers, involving two neutron stars (NS-NS) or a neutron star and a black hole (NS-BH), and still remains viable for short GRBs. It has also been proposed that a fraction of mergers are formed in dense stellar environments such as globular clusters, which may merge and produce a GRB (Grindlay et al. 2006; Lee et al. 2010). Other proposed progenitors, albeit less well-understood, include the accretion-induced-collapse of a white dwarf or neutron star (WD/NS-AIC; Qin et al. 1998; Levan et al. 2006a; Metzger et al. 2008a), or flares from young magnetars (Chapman et al. 2008).

Motivated by the fundamental question of the origin of short GRBs, in this thesis, I use the past decade of short GRB observations in the *Swift* era to *place constraints on the progenitors and explosion properties of short GRBs*. To provide context for my work, I address each of the key predictions for the progenitor models, and also draw upon known results from the Galactic population of NS-NS binaries for the compact object merger hypothesis. I then briefly describe the type of analysis needed to constrain each of these predictions, and any progress that was made prior to my thesis. A summary of the expectations for the progenitor models is displayed in Table 7.1.

Supernova kicks

Compact objects are expected to receive kicks at birth, achieving space velocities in excess of several hundred km s^{-1} (Fryer et al. 1998; Scheck et al. 2006; Wongwathanarat et al. 2013). These kicks are evident from the observed population of single pulsars (e.g., Hansen & Phinney 1997; Arzoumanian et al. 2002), and offsets of central compact

Table 1.1. Testable Predictions and Expectations for Short GRB Progenitor Models

Testable Prediction	NS-NS/NS-BH	Massive Stars	WD-WD/WD-AIC
Associated SN?	No	Yes	No
Spatial offsets	Substantial	Small	Small
Correlation with SF regions	Weak	Strong	Weak
Correlation with stellar mass	Weak	Strong	Strong
Host Demographics	Mix of elliptical and SF	SF only	Mix of elliptical and SF
Parsec-scale environments	Low densities (ISM/IGM)	High densities	Average densities (ISM)

objects from SN remnant centers (Fesen et al. 2006; Becker et al. 2012; Milisavljevic & Fesen 2013). For compact object binaries, the total velocity of the system is not as extreme: $\lesssim 400$ km s^{-1} for NS-NS systems and $\lesssim 300$ km s^{-1} for NS-BH, since more extreme kicks would disrupt the binary (Eldridge et al. 2011). Compact object binaries involving a white dwarf are less likely to survive a supernova kick due to the smaller mass of the system; thus, any surviving WD-NS/WD-BH systems will have $\lesssim 200$ km s^{-1}. In comparison, the Galactic population of NS-NS binaries have inferred kick velocities of $\approx 5 - 400$ km s^{-1} (Wang et al. 2006; Wong et al. 2010), which are consistent with the predictions, albeit still uncertain. In the WD-AIC or magnetar models, kicks would not be expected to play a significant role. Thus, if short GRBs arise from NS-NS/NS-BH binary mergers, the migration from their birth sites to their eventual explosion sites would be evident in the distributions within their host galaxies. Thus, *it is crucial to test the presence of supernova kicks by exploring the locations of short GRBs with respect to their host galaxy centers.*

Ages and merger timescales

Compact object binaries have a wide range of predicted merger timescales, due to the range of eccentricities and orbital separations (Fryer et al. 1999; Belczynski et al. 2006; Eldridge et al. 2011). For instance, of the eight known NS-NS systems in the Milky Way, four are predicted to merge in $\lesssim 10$ Gyr while the remainder have predicted merger timescales which exceed a Hubble time (Kalogera et al. 2004; O'Shaughnessy et al. 2005). Assuming that the compact objects formed in the most recent episode of star formation, the range of merger timescales should map to the stellar population ages of the host galaxies, and will lead to a diversity in host galaxy types (O'Shaughnessy et al. 2008;

Zheng & Ramirez-Ruiz 2007). For instance, if most mergers have delay times of $\gtrsim$ few Gyr, the galaxies in which we observe short GRBs would have predominantly old stellar populations and would be pushed to low redshifts (Zheng & Ramirez-Ruiz 2007). If they primarily form in globular clusters, the delay time would depend on the time needed for the cluster to undergo core-collapse, and the host galaxy demographics would tend toward massive, elliptical galaxies (Grindlay et al. 2006; Lee et al. 2010). Expectations for the WD/NS-AIC model are similar to those for the primordial NS-NS population, while a population of young magnetar flares or massive stars would primarily occur in younger, star-forming galaxies.

Berger (2009) focused on a sample of $\approx$ 20 short GRBs with sub-arcsecond localization and found that the population of hosts is dominated by late-type galaxies, albeit with lower specific SFRs, higher luminosities, and higher metallicities than the star-forming hosts of long GRBs. Leibler & Berger (2010) studied a sample of 19 short GRB host galaxies and found a range of stellar population ages, $\approx 0.3 - 3$ Gyr, indicating a range of delay times, although not as broad as the allowed range of merger timescales (e.g., Fryer et al. 1999; Belczynski et al. 2006). These studies also relied on sub-arcsecond localized bursts, which are primarily selected by the detection of optical afterglows. If there exist correlations between the detectability of an optical afterglow and host galaxy properties, the study of hosts selected by optical afterglows will not be a fair representation of the short GRB population.

The redshift distribution can also give information on the delay times (and merger timescales, if applicable) of the short GRB progenitor population. While the majority of long GRBs are detected at redshifts of $z > 1$, the large majority of short GRBs detected by 2008 were at $z < 1$ (Berger et al. 2007b). Thus, *it is necessary to study the*

demographics and redshift distribution of short GRB host galaxies for the entire sample, including bursts with no detected optical afterglows. The ratio of bursts detected in each host galaxy type will also constrain whether the short GRB rate traces stellar mass or star formation. Such a comprehensive study is imperative in understanding the link to the progenitors.

Another outcome of merger timescales is an offset distribution that depends both on the distribution of supernova kick velocities and the delay time distribution. Population synthesis models which take these effects into account have shown that NS-NS mergers occur at a median offset of $\approx 5 - 7$ kpc (Bloom et al. 1999; Fryer et al. 1999; Belczynski et al. 2006; Zemp et al. 2009), and a small fraction may make it to distances of a few Mpc (Kelley et al. 2010). As with the supernova kicks, this scenario can be tested using the distribution of short GRBs in their host galaxies.

Local environments

While the sub-parsec-scale environments of long GRBs reflect those expected for massive stars (Chevalier & Li 2000; Yost et al. 2003; Laskar et al. 2014), the circumburst densities of short GRBs are less clear. The relative difficulty of detecting short GRB afterglows compared to those for long GRBs suggests that the explosion environments have comparatively low densities (Panaitescu et al. 2001; Perna & Belczynski 2002). If short GRBs originate from compact object binary mergers, the burst explosion environment will depend on the nature of the supernova kick, merger timescale, and to some extent on the average ISM density of the host galaxy. Population synthesis of compact object mergers show that NS-NS mergers have a median density of ≈ 0.1 cm^{-3}, while the

gas densities of NS-BH mergers are more uniformly distributed over several orders of magnitude (Perna & Belczynski 2002). However, the exact distribution of densities depends sensitively on the host galaxy type (Belczynski et al. 2006), as ellipticals generally have lower ISM densities than star-forming galaxies (e.g., Fukazawa et al. 2006). Short GRBs would thus offer a unique way to study the sub-parsec environments of compact object mergers, and offer another clue to their progenitors. In particular, for systems which have substantial kicks and may escape their host galaxies, the expected circumburst densities would be more typical of the IGM ($\lesssim 10^{-4}$ cm^{-3}). Such low densities would not be expected for other progenitor models.

The circumburst densities can be constrained by examining the spectral behavior of short GRB afterglows by radio through X-ray observations. Only $\approx 30\%$ of *Swift* short GRBs have detected optical afterglows (Berger 2010a), and prior to this work, only two radio afterglows existed for short GRBs (Berger et al. 2005; Panaitescu 2006; Soderberg et al. 2006b). Since the brightness of the afterglow depends on a combination of the burst distance and explosion properties (Granot & Sari 2002), the paucity of short GRB afterglow detections suggest that they have low kinetic energies and/or circumburst densities. However, this conjecture is only based on a handful of events. *A characterization of the distribution of circumburst densities thus requires a concerted study of broad-band short GRB afterglows.*

Event rates

The event rate of NS-NS mergers extrapolated from the Galactic population is $\approx 30 - 3000$ Gpc^{-3} yr^{-1} (Fryer et al. 1999; Kalogera et al. 2004; Kim et al. 2006;

Dominik et al. 2012), and are broadly consistent with the volumetric rates predicted from population synthesis rates of ≈ 100 Gpc^{-3} yr^{-1} at $z = 0$. Since no NS-BH systems have been detected, rate estimates of these systems rely on population synthesis and is much lower, ≈ 10 Gpc^{-3} yr^{-1} (Fryer et al. 1999; Dominik et al. 2012). These rate estimates have large uncertainties due to the small number of observed systems and the uncertainties in the theoretical inputs.

The true short GRB event rate relies on the degree of collimation in short GRBs. Numerous simulations of post-merger black hole accretion have predicted collimated outflows with opening angles of $\sim 5 - 20^\circ$ (Popham et al. 1999; Aloy et al. 2005; Rosswog 2005; Rezzolla et al. 2011) up to several tens of degrees (Ruffert & Janka 1999b; Popham et al. 1999; Rezzolla et al. 2011). If short GRBs are collimated, the true event rate is significantly larger than the observed rate. The observed rate of short GRBs is ≈ 10 Gpc^{-3} yr^{-1} (Nakar et al. 2006), a factor of 10-100 times lower than estimates for NS-NS binaries (Kalogera et al. 2004). This discrepancy could be explained if short GRBs are beamed. Prior to this work, only two short GRBs have jet angle measurements: GRB 051221A ($\approx 7^\circ$; Soderberg et al. 2006b) and GRB 090426A ($5 - 7^\circ$; Nicuesa Guelbenzu et al. 2011), and thus the degree of collimation in short GRBs is highly uncertain. Thus, it is necessary to *understand the distribution of opening angles for short GRBs*. Such studies will also have implications on the joint detections of on-axis short GRBs with compact object mergers detected with Advanced LIGO/VIRGO. Also, a well-constrained short GRB rate will help us to understand what fraction of compact object mergers produce short GRBs.

Heavy element nucleosynthesis

One of the predicted outcomes following compact object mergers is the ejection of neutron-rich material at subrelativistic velocities for both the NS-NS (Eichler et al. 1989) and NS-BH cases (Lattimer & Schramm 1974, 1976). These early theories also showed that such an environment could produce radioactive heavy elements via the r-process, and was later confirmed by simulations of binary compact object coalescence (Rosswog et al. 1999). The radioactive decay of these elements is expected to produce transient emission, termed a "Li-Paczynski mini-supernova" or more recently, a "kilonova" (Li & Paczyński 1998; Metzger et al. 2010; Goriely et al. 2011; Roberts et al. 2011; Rosswog et al. 2013), which is expected to peak in the NIR on $\approx 1-$week timescales (Barnes & Kasen 2013; Kasen et al. 2013; Tanaka & Hotokezaka 2013; Rosswog et al. 2014). Thus, searches for kilonovae following short GRBs will be imperative in constraining the progenitor. *HST* imaging following the short GRB 130603B revealed a NIR counterpart at ≈ 10 days after the burst, which is interpreted as the first detection of a kilonova (Berger et al. 2013a; Tanvir et al. 2013a). One other event, the short GRB 080503, had a late-time re-brightening in the optical and X-ray bands which loosely matched the expected light curve behavior of a kilonova, although there are other viable explanations for such behavior, such as refreshed shocks or a clumpy medium (Perley et al. 2009a; Hascoët et al. 2012).

1.4 Key Questions and Thesis Summary

At the *Swift* detection rate of ≈ 8 short GRBs per year, the growing population of well-localized events allows for comprehensive studies based on large samples for the first time. In this thesis, I take advantage of the past and incoming flow of events to address four overarching aspects of short GRBs, motivated by the aforementioned predictions for the progenitors. Through a multi-wavelength observational campaign of their host galaxies and afterglows, I address the following key questions:

1. Where do short GRBs occur with respect to their host galaxies?
2. What types of galaxies host short GRBs and what are the demographics?
3. What is the distribution of jet opening angles for short GRBs?
4. What are the energies and circumburst densities of short GRBs?

In Chapters 2 and 3, I address the local environments of short GRBs and the locations of short GRBs with respect to their host galaxies using a combination of ground-based afterglow and *Hubble Space Telescope* (*HST*) host galaxy observations. I characterize the host morphological properties, measure precise physical and host-normalized offsets with respect to the galaxy centers, and study the locations of short GRBs relative to their host light distributions. The high angular resolution of *HST* enables a detailed characterization of their surface brightness profiles, measurements of the host galaxy sizes, and the most precise short GRB-host galaxy offsets to date. These samples enable comparisons to the distributions for long GRBs, and I show that short GRBs originate from distinct local environments than long GRBs. In Chapter 2, I perform these studies

for 10 bursts discovered in 2005-2006, while in Chapter 3, I present 16 additional bursts discovered in 2007-2013. In this latter study, I also take advantage of the Wide-field Camera 3 on-board *HST* with both UV and IR channels to study the locations of short GRBs with respect to their host galaxy rest-frame UV and optical light. These studies provide direct insight to their relationship with the distribution of their host star formation and stellar mass for the first time. I also use the deep IR limits of short GRBs which seem to lack coincident hosts to place meaningful limits on the luminosities and redshifts of underlying host galaxies.

In Chapters 4 and 5, I investigate the galactic-scale environments of short GRBs and the implications for the progenitors. In Chapter 4, I focus on the discovery of the short GRB 100117A and its early-type host galaxy. This event is the second short GRB to be unambiguously associated with an early-type galaxy, implying that a fraction of short GRBs originate from ≈ 1 Gyr old stellar populations. To quantify the early-type fraction and the overall diversity of short GRB galactic-scale environments, in Chapter 5, I use a sample of 36 *Swift* short GRBs with robust associations to an environment and classify bursts originating from four types of environments: late-type, early-type, inconclusive, and "host-less" (lacking a coincident host galaxy to limits of $\gtrsim 26$ mag). I investigate the redshift distribution, implications for the delay time distributions, the short GRB rate as a function of star formation and stellar mass, and correlations with γ-ray properties.

In Chapters 6 and 7, I present evidence for collimation in the afterglow light curves of two events: short GRBs 111020A and 130603B. In Chapter 6, I present the discovery of a steepening in the X-ray afterglow light curve of GRB 111020A, best explained as a jet break with an inferred opening angle of $\approx 3 - 8^{\circ}$. In Chapter 7, I present the radio and optical afterglow light curves of GRB 130603B, which uncover a multi-wavelength

jet break, and the first in a short GRB to date. GRB 130603B is also the third discovery of a radio afterglow in a short GRB. I uncover evidence for significant excess emission in the X-ray afterglow, and investigate scenarios to explain this emission component. I explore the impact that these two events have on the true event rate of short GRBs and compact object mergers, as well as the true, beaming-corrected energy scale.

In Chapter 8, I present the most comprehensive catalog to date of short GRB broad-band afterglow observations for 86 bursts discovered between November 2004 and March 2014. I study a subset of 32 bursts with well-sampled light curves to investigate the energetics and circumburst densities. I then investigate relationships between the inferred explosion properties and host galaxy properties, and also the impact of the energy and density scales on other counterparts to compact object mergers. This study will serve as a crucial input to joint electromagnetic-gravitational wave searches.

In Chapter 9, I present concluding remarks and provide some of the fruitful future directions to take in the context of current and future facilities.

Chapter 2

Hubble Space Telescope Observations of Short GRB Host Galaxies: Morphologies, Offsets, and Local Environments

W. Fong, E. Berger, & D. B. Fox

The Astrophysical Journal, Vol. 708, pp. 9-25, 2010

Abstract

We present the first comprehensive analysis of *Hubble Space Telescope* (*HST*) observations of short-duration gamma-ray burst (GRB) host galaxies. These observations allow us to characterize the galactic and local environments of short GRBs as a powerful constraint on the nature of their progenitors. Using the *HST* data for 10 short GRB hosts we determine the host morphological properties, measure precise physical and host-normalized offsets relative to the galaxy centers, and study the locations of short GRBs relative to their host light distributions. We find that most short GRB hosts have exponential disk profiles, characteristic of late-type galaxies, but with a median size that is twice as large as that of long GRB hosts, commensurate with their higher luminosities. The observed distribution of projected physical offsets, supplemented by ground-based measurements, has a median of ≈ 5 kpc, about 5 times larger than for long GRBs, and in good agreement with predicted offset distributions for NS-NS binary mergers. For the short GRB population as a whole we find the following robust constraints: (i) $\gtrsim 25\%$ have projected offsets of $\lesssim 10$ kpc; and (ii) $\gtrsim 5\%$ have projected offsets of $\gtrsim 20$ kpc. We find no clear systematic trends for the offset distribution of short GRBs with and without extended soft emission. While the physical offsets are larger than for long GRBs, the distribution of host-normalized offsets is nearly identical due to the larger size of short GRB hosts. Finally, unlike long GRBs, which are concentrated in the brightest regions of their host galaxies, short GRBs appear to under-represent the light distribution of their hosts; this is true even in comparison to core-collapse and Type Ia supernovae. Based on these results, we conclude that short GRBs are consistent with a progenitor population of NS-NS binaries, but partial contribution from prompt or delayed magnetar formation

is also consistent with the data. Our study underscores the importance of future *HST* observations of the larger *existing* and growing sample of short GRB hosts, which will allow us to delineate the properties of the progenitor population.

2.1 Introduction

The galactic and local environments of cosmic explosions provide powerful insight into the nature of their progenitors. For example, past studies of supernova (SN) environments have demonstrated that Type Ia and Type Ib/Ic/II events arise from distinct progenitor systems since the former are located in all types of galaxies, while the latter occur only in star forming galaxies, pointing to a direct link with massive stars (e.g., van den Bergh et al. 2005). In a similar vein, long-duration gamma-ray bursts (GRBs; duration, T90 $\gtrsim$ 2 s) have been linked with massive stars through their exclusive association with star forming galaxies (e.g., Bloom et al. 1998; Djorgovski et al. 1998; Fruchter et al. 1999). Short-duration GRBs, on the other hand, are now known to reside in all types of galaxies (Berger et al. 2005; Fox et al. 2005; Gehrels et al. 2005; Bloom et al. 2006; Berger 2009). Moreover, even the star forming host galaxies of short GRBs differ from those of long GRBs; they have higher luminosities and metallicities, and lower specific star formation rates (Berger 2009). The difference between long and short GRB host galaxies, along with the lack of SN associations for short GRBs (Berger et al. 2005; Fox et al. 2005; Gehrels et al. 2005; Hjorth et al. 2005b; Bloom et al. 2006; Soderberg et al. 2006b), demonstrate that they have distinct progenitor populations. In particular, at least some short GRBs are associated with an older progenitor population.

Equally important are the local, sub-galactic environments. In the case of long GRBs, the distribution of their projected physical and host-normalized offsets relative to the host centers matches the overall expected distribution for massive stars in an exponential disk (Bloom et al. 2002). An analysis of the brightness distribution at the locations of long GRBs indicates that they are disproportionately concentrated on the

brightest regions of their hosts, primarily in comparison to core-collapse SNe, which follow the overall light distribution of their hosts (Fruchter et al. 2006). Both of these studies have relied on high angular resolution *Hubble Space Telescope* (*HST*) imaging observations. Preliminary studies of short GRB offsets (Berger et al. 2005; Fox et al. 2005; Bloom & Prochaska 2006; Soderberg et al. 2006b; Troja et al. 2008b; D'Avanzo et al. 2009) reveal somewhat larger projected physical offsets than for long GRBs, and have also led to a claimed trend of smaller offsets for short GRBs with extended X-ray emission (Troja et al. 2008b). No study of the locations of short GRBs relative to their hosts light distribution has been published so far.

Progenitor models of short GRBs lead to distinct predictions about the distribution of host properties and the local environments of short GRBs (measured by their offsets and location relative to the host light distribution). In particular, the popular model of neutron star and/or black hole binary mergers (NS-NS/NS-BH; Eichler et al. 1989; Narayan et al. 1992) predicts larger offsets than for the massive star progenitors of long GRBs due to potential systemic velocity kicks. Various authors have employed population synthesis models to predict the distribution of offsets by convolving distributions of kick velocities, merger timescale, and galaxy masses (Bloom et al. 1999; Fryer et al. 1999; Belczynski et al. 2006). For Milky Way mass galaxies, appropriate for short GRB hosts (Berger 2009), the predicted offset distributions have a median of $\sim 5-10$ kpc, with a broad tail extending to tens of kpc. On the other hand, progenitor models that invoke magnetars, either from a young population or through delayed formation in a WD-WD merger or white dwarf accretion-induced collapse (Levan et al. 2006a; Metzger et al. 2008a), are expected to have a modest offset distribution since these systems do not experience kicks. Similarly, any systematic differences in the progenitors of short GRBs

with and without extended X-ray emission may be revealed in the offset distribution and specific sub-galactic environments.

To confront these models with observations we require high angular resolution imaging, best provided by *HST*. Such observations provide detailed information on the host galaxy morphological properties (e.g., exponential disk versus de Vaucoulers profile, effective radius), as well as the ability to precisely measure offsets and the distribution of short GRBs relative to their host light. *HST* observations have served as the backbone for detailed studies of long GRB environments and host galaxy morphologies (Bloom et al. 2002; Fruchter et al. 2006; Wainwright et al. 2007b). To date, *HST* observations of only 3 short GRBs have been published (050709: Fox et al. 2005; 060121: Levan et al. 2006b; 080503: Perley et al. 2009a), and in only one case (050709) was the host morphology addressed.

Here we present the first comprehensive analysis of all short GRB host galaxies observed with *HST* to date[1]. Using these observations we determine the host morphologies and structural properties (§2.3), we calculate precise physical and host-normalized offsets using accurate astrometry relative to ground-based afterglow images (§2.4), and we construct the first distribution of short GRB locations relative to their host light (§2.5). We draw conclusions in the context of progenitor models in §8.5. Throughout the paper we compare and contrast the results of our analysis with similar studies of long GRBs.

We find that: (i) the short GRB hosts have systematically larger effective radii than

[1]We do not repeat the analysis for GRB 080503 since no convincing host galaxy was identified (Perley et al. 2009a). Future *HST* ACS or WFPC3 observations will provide better constraints on an underlying host than available from the existing WFPC2 observations.

long GRB hosts, in good agreement with their higher luminosities; (ii) the observed short GRB projected physical offset distribution has a median of about 5 kpc, about a factor of 5 times larger than long GRBs, while for the population as a whole $\gtrsim 25\%$ have projected offsets of $\lesssim 10$ kpc, and $\gtrsim 5\%$ have projected offsets of $\gtrsim 20$ kpc; (iii) both the observed physical offset distribution and the robust constraints closely match the predicted offset distribution of NS-NS binaries; and (iv) short GRBs uniformly trace the light distribution of their hosts, similar to core-collapse SNe, but distinct from long GRBs.

2.2 Hubble Space Telescope Data Reduction and Analysis

2.2.1 Sample

We present *HST* optical observations of ten short GRB host galaxies obtained with the Advanced Camera for Surveys (ACS) and the Wide-Field Planetary Camera 2 (WFPC2). The data were obtained as part of programs 10119, 10624, and 10917 (PI: Fox), as well as 10780 and 11176 (PI: Fruchter). These programs targeted all short GRBs with optical and X-ray (XRT) positions from May 2005 to December 2006, which were visible during *HST* 2-gyro operations. In this time frame, the only short burst that was not observed was GRB 060801. Thus, the sample in this paper is nearly complete in relation to the short GRBs with optical/X-ray afterglows[2]. The *HST* observations of GRBs 050709 and

[2]We do not include in this analysis GRBs 051227, 060505, and 060614 all of which had durations well beyond 2 s, even when isolating the initial "short" emission episode. The *HST* data for GRBs 060505

060121 have been published previously by Fox et al. (2005) and Levan et al. (2006b), respectively, but we re-analyze them here in a uniform fashion and perform a more comprehensive analysis of the host morphology and burst environment. Seven of the nine bursts have been localized to sub-arcsecond precision from optical afterglow detections, and five have known redshifts (Table 2.1); we use a constraint of $z \gtrsim 1.4$ for GRB 051210 (Berger et al. 2007b).

Six of the seven short GRBs with sub-arcsecond localization are robustly associated with host galaxies[3] (we present a host identification for GRB 060313 in this paper; see Appendix 2.8.1). The sole exception is GRB 061201, for which we explore two possible host galaxy associations based on the *HST* observations (see Appendix 2.8.2); previously only one galaxy (at $z = 0.111$) was considered a potential host (Berger et al. 2007b; Stratta et al. 2007). Details of the GRB properties and the *HST* observations are provided in Table 2.1.

Throughout the paper we use the standard cosmological parameters, $H_0 = 71$ km s^{-1} Mpc^{-1}, $\Omega_m = 0.27$, and $\Omega_\Lambda = 0.73$. All reported magnitudes are corrected for Galactic extinction using Schlegel et al. (1998) dust maps.

---

and 060614 were published in Ofek et al. (2007) and Gal-Yam et al. (2006), respectively.

[3]For a complete discussion of the galaxy associations we refer the reader to the following papers: GRB 050709: Fox et al. (2005); GRB 050724: Berger et al. (2005); GRB 051221: Soderberg et al. (2006b); GRB 060121: Levan et al. (2006b); GRB 061006: Berger et al. (2007b) and D'Avanzo et al. (2009).

Table 2.1. *HST* Observations of Short GRB Host Galaxies

GRB	RA (J2000)	Dec (J2000)	Uncert. ($''$)	OA?	z	Instrument	Filter	Date (UT)	Exp. Time (s)	AB mag [a]	A_λ [b] (mag)
050509b	$12^h36^m14.06^s$	$+28°59'07.2''$ [c]	3.4	N	0.226	ACS	F814W	2005 May 14	6870	16.32	0.037
	$12^h36^m13.76^s$	$+28°59'03.2''$	3.3								
050709	$23^h01^m26.96^s$	$-38°58'39.5''$	0.2	Y	0.1606	ACS	F814W	2006 Jul 16	6981	21.09	0.02
						WFPC2	F450W	2007 Jul 29	3200	21.43	0.045
050724	$16^h24^m44.38^s$	$-27°32'27.5''$	0.1	Y	0.257	WFPC2	F450W	2008 Apr 07	3200	19.98	2.645
						WFPC2	F814W	2008 May 18	3200	18.74	1.189
051210	$22^h00^m41.26^s$	$-57°36'46.5''$	2.9	N	> 1.4	WFPC2	F675W	2007 Apr 03	2800	21.14	0.052
	$22^h00^m41.33^s$	$-57°36'49.4''$	1.7								
051221a	$21^h54^m48.63^s$	$+16°53'27.4''$	0.2	Y	0.5465	WFPC2	F555W	2007 Aug 13	3200	21.86	0.227
						WFPC2	F814W	2007 Aug 22	1600	21.42	0.133
060121	$09^h09^m51.99^s$	$+45°39'45.6''$	0.1	Y	···	ACS	F606W	2006 Feb 27	4400	26.22	0.047
060313	$04^h26^m28.42^s$	$-10°50'39.9''$	0.2	Y	···	ACS	F475W	2006 Oct 13	2088	26.38	0.300
						ACS	F775W	2006 Oct 14	2120	25.61	0.135
060502b	$18^h35^m45.53^s$	$+52°37'52.9''$	3.7	N	···	ACS	F814W	2006 May 15-Jul 16	25224	17.88 / 24.8-27.5 [d]	0.085
	$18^h35^m45.28^s$	$+52°37'54.7''$	5.8								
061006	$07^h24^m07.78^s$	$-79°11'55.5''$	0.2	Y	0.4377	ACS	F814W	2006 Oct 14	6054	21.67	0.616
						WFPC2	F555W	2008 May 22	3200	23.90	1.052
061201	$22^h08^m32.09^s$	$-74°34'47.1''$	0.2	Y	0.111 / ··· [e]	ACS	F606W	2006 Dec 11	2178	18.17 / 25.34 [f]	0.251

Table 2.1—Continued

GRB	RA (J2000)	Dec (J2000)	Uncert. ($''$)	OA?	z	Instrument	Filter	Date (UT)	Exp. Time (s)	AB mag [a]	A_λ [b] (mag)
						ACS	F814W	2006 Dec 11	2244	17.82 / 25.03 [f]	0.147

Note. — Summary of short GRB positions and redshifts, *HST* observations, and host galaxy magnitudes (calculated using IRAF/`ellipse`).

[a] These values have been corrected for Galactic extinction.

[b] Galactic extinction.

[c] In all cases with *Swift*/XRT positions the top and bottom set of coordinates are from the catalogs of Butler (2007) and Evans et al. (2009), respectively.

[d] These magnitudes correspond to galaxy "A" and galaxies "B"– "G" in Figure 2.8.

[e] We consider two possible host galaxies for this burst (see Appendix 2.8.2).

[f] The first value is for galaxy "A" and the second is for galaxy "B" in Figure 2.10.

2.2.2 Hubble Space Telescope Data Reduction

We retrieved pre-processed images from the *HST* archive[4] for all available short GRBs. We distortion-corrected and combined the individual exposures using the IRAF task `multidrizzle` (Fruchter & Hook 2002; Koekemoer et al. 2003). For the ACS images we used pixfrac = 0.8 and pixscale = 0.05 arcsec pixel^{-1}, while for the WFPC2 images, we used pixfrac = 1.0 and pixscale = 0.0498 arcsec pixel^{-1}, half of the native pixel scale. The final drizzled images, flux-calibrated to the AB magnitude system according to the ACS and WFPC2 zeropoints, are shown in Figures 2.1-2.10.

2.2.3 Surface Brightness Profile Fitting

We use two methods to fit the surface brightness profiles of the short GRB host galaxies. First, we use the `galfit` software package (Peng et al. 2007) to construct the best two-dimensional ellipsoidal model of each galaxy image. Second, we use the IRAF task `ellipse` to produce elliptical intensity isophotes and to construct one-dimensional radial surface brightness profiles. We further use `ellipse` to measure the integrated AB magnitude for each galaxy (listed in Table 2.1).

`galfit`

As an input to `galfit` we generate point-spread-function (PSF) models for each instrument and filter combination using the `tinytim` software package. We assume a constant spectrum in F_ν; the difference in the 90% encircled energy width of the PSF for

[4]see http://archive.stsci.edu/hst/.

a spectral index ranging from -2 to 0 is only 1%. We additionally correct for distortion in the ACS instrument, and use a sub-sampling factor of 2 for WFPC2 to appropriately account for the reduced pixel scale in the drizzled images.

In each observation we fit the host galaxy image with a PSF-convolved Sérsic profile:

$$\Sigma(r) = \Sigma_e \exp\{-\kappa_n[(r/r_e)^{1/n} - 1]\}, \tag{2.1}$$

where n is the concentration parameter ($n = 1$ is equivalent to an exponential disk profile, while $n = 4$ is the de Vaucouleurs profile), $\kappa_n \approx 2n - 1/3 + 4/405n + 46/25515n^2$ is a constant that is coupled to the value of n (Ciotti & Bertin 1999)), r_e is the effective radius, and Σ_e is the effective surface brightness in flux units. In the subsequent discussion, tables, and figures we use surface brightness in units of mag arcsec^{-2}, designated as μ_e.

In all cases we fit the host galaxies with a single[5] Sérsic profile and allow the parameters to vary freely. The resulting best-fit values of n, r_e, and μ_e, as well as the integrated AB magnitudes are provided in Table 3.3. For host galaxies that are detected at a low signal-to-noise ratio we find that a wide range of n values can account for the observed morphology. In these cases we fit the host galaxies with n fixed at values of 1 and 4, and provide the results of both models in Table 3.3.

The `galfit` models and residual images for all instrument/filter combinations are shown in Figures 2.1-2.9. Objects for which both $n = 1$ and $n = 4$ models provide an adequate fit are shown for both cases.

[5]In the case of GRBs 050509b, 050709, 060121, and 061006 we fit additional Sérsic and point-source components to account for foreground/background objects. These components are not considered to be part of the host galaxy.

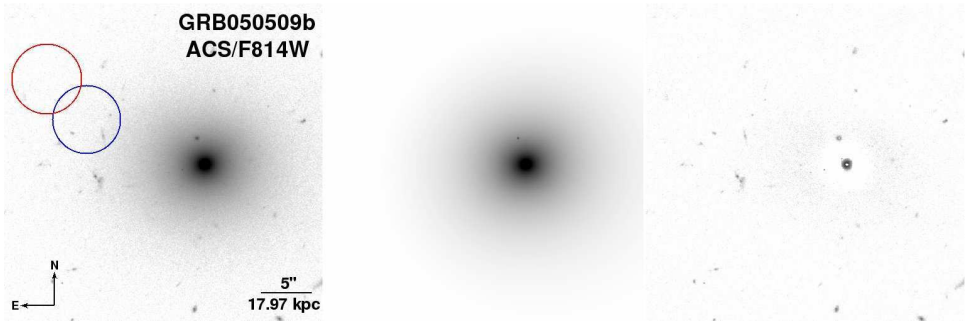

Figure 2.1.—: *Left: HST*/ACS/F814W image of the location of GRB 050509b. The circles mark the X-ray positions of the afterglow from the analysis of Butler (2007) (red) and Evans et al. (2009) (blue). *Center:* Sérsic model fit from `galfit`. *Right:* Residual image.

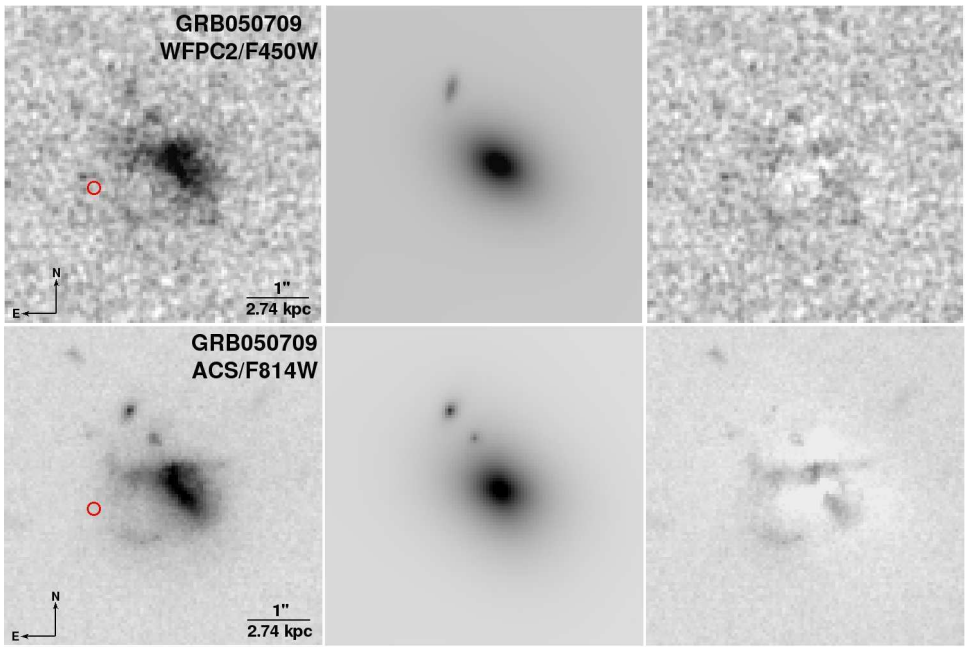

Figure 2.2.—: *Top-left: HST*/ACS/F450W image of the host galaxy of GRB 050709 with a 10σ error circle representing the afterglow position. *Top-center:* Sérsic model fit from `galfit`. *Top-right:* Residual image. *Bottom:* Same, but for the *HST*/WFPC2/F814W observations.

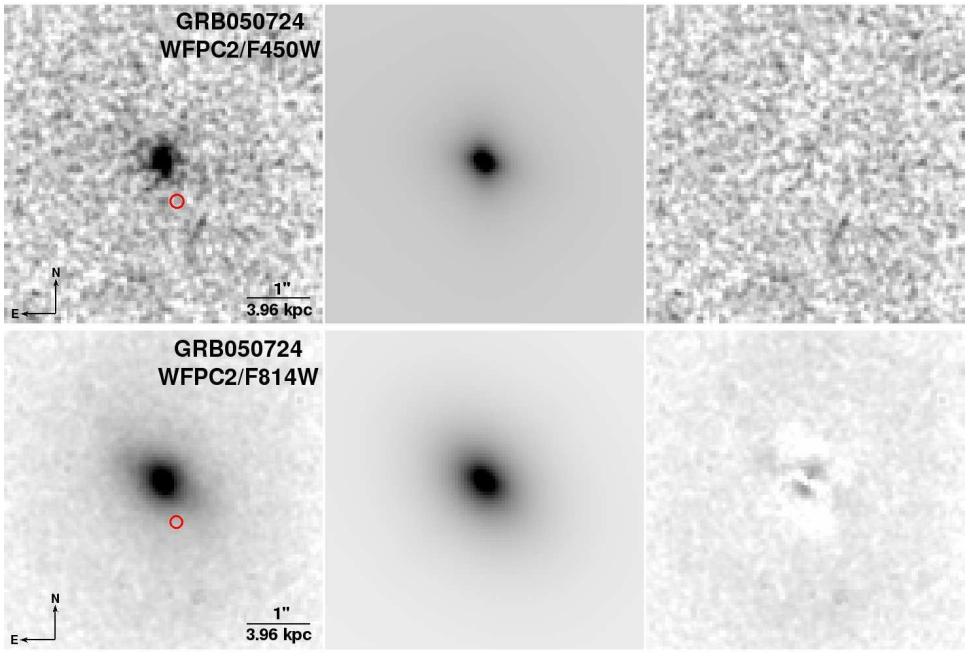

Figure 2.3.—: *Top-left: HST*/WFPC2/F450W image of the host galaxy of GRB 050724 with a 5σ error circle representing the afterglow position. *Top-center:* Sérsic model fit from `galfit`. *Top-right:* Residual image. *Bottom:* Same, but for the *HST*/WFPC2/F814W observations.

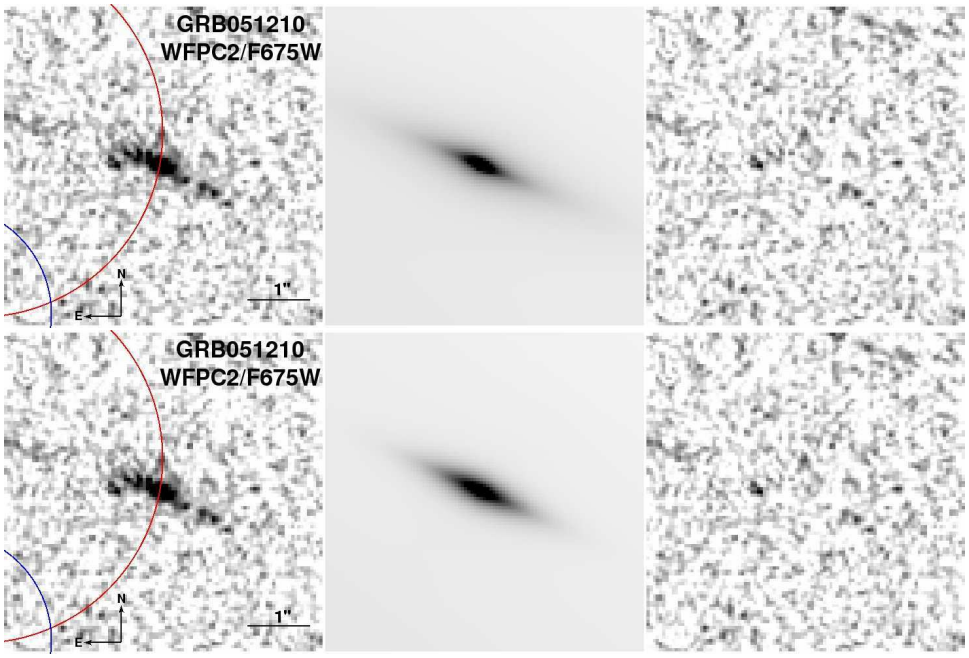

Figure 2.4.—: *Top-left: HST*/WFPC2/F675W image of the location of GRB 051210. The circles mark the X-ray positions of the afterglow from the analysis of Butler (2007) (red) and Evans et al. (2009) (blue). *Top-center:* Sérsic model fit from `galfit` with a fixed value of $n = 1$. *Top-right:* Residual image. *Bottom:* Same, but for Sérsic model fit from `galfit` with a fixed value of $n = 4$.

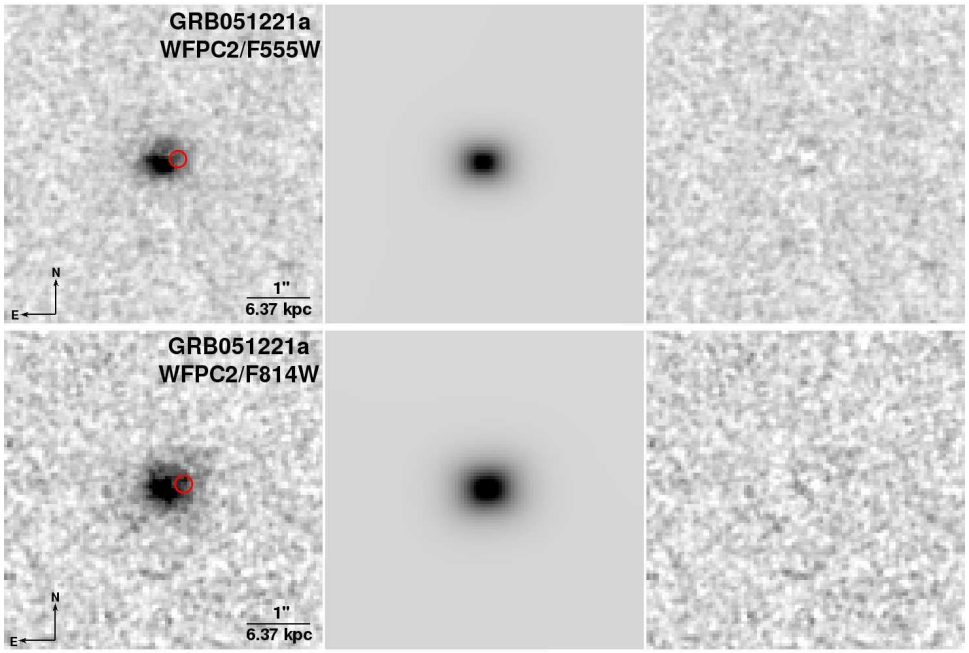

Figure 2.5.—: *Top-left: HST*/WFPC2/F555W image of the host galaxy of GRB 051221 with a 5σ error circle representing the afterglow position. *Top-center:* Sérsic model fit from `galfit`. *Top-right:* Residual image. *Bottom:* Same, but for the *HST*/WFPC2/F814W observations.

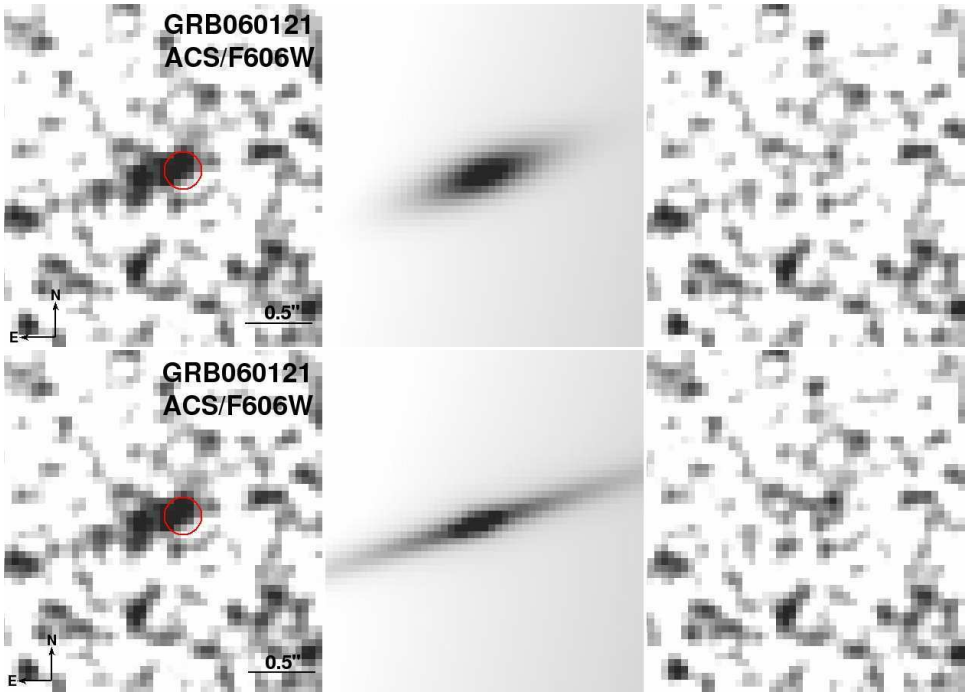

Figure 2.6.—: *Top-left: HST*/ACS/F606W image of the host galaxy of GRB 060121 with a 3σ error circle representing the afterglow position. The image has been smoothed with a 2×2 pixel Gaussian. *Top-center:* Sérsic model fit from `galfit` with a fixed value of $n = 1$. *Top-right:* Residual image. *Bottom:* Same, but for Sérsic model fit from `galfit` with a fixed value of $n = 4$.

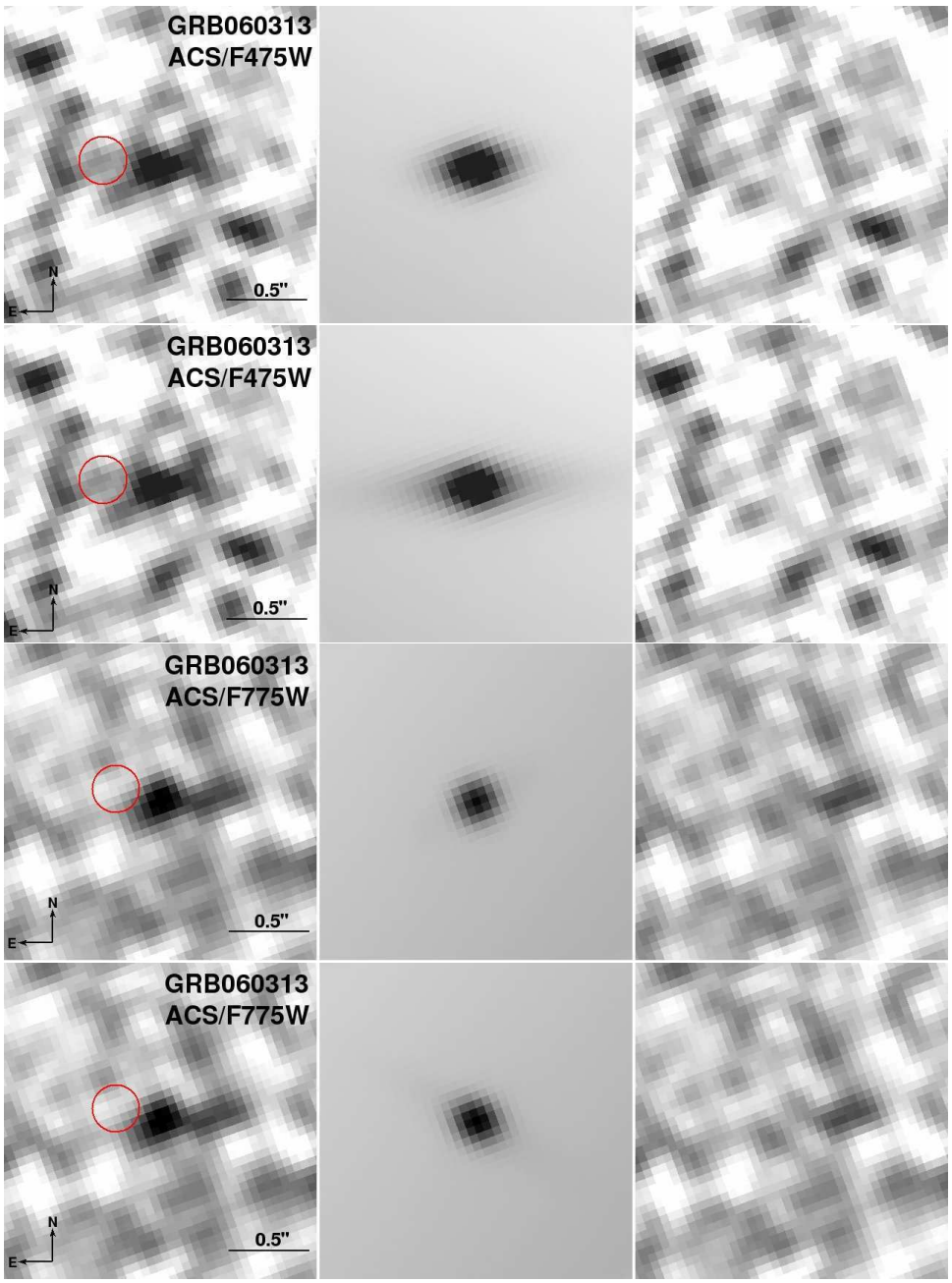

Figure 2.7.—: *Top-left: HST*/ACS/F475W image of the host galaxy of GRB 060313 with a 3σ error circle representing the afterglow position. The image has been smoothed with a 3×3 pixel Gaussian. *Top-center:* Sérsic model fit from `galfit`.with a fixed value of $n = 1$. *Top-right:* Residual image. *Second panel:* Same, but for Sérsic model fit from `galfit` with a fixed value of $n = 4$. *Third panel:* Same, but for the *HST*/WFPC2/F775W observations with a fixed value of $n = 1$. *Bottom panel:* Same, but for the *HST*/WFPC2/F775W observations with a fixed value of $n = 4$.

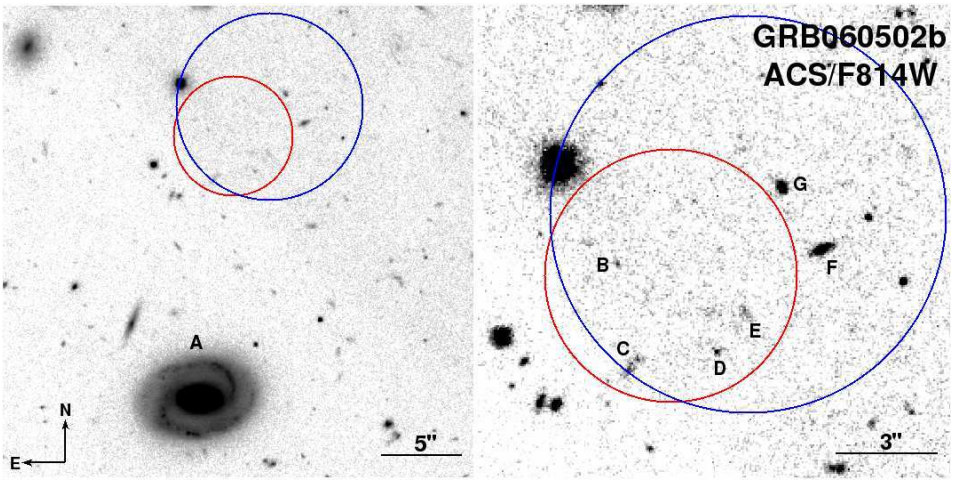

Figure 2.8.—: *HST*/ACS/F814W images of the host galaxy of GRB 060502b. The circles mark the X-ray positions of the afterglow from the analysis of Butler (2007) (red) and Evans et al. (2009) (blue). The bright galaxy marked "A" is located at $z = 0.287$ (Bloom et al. 2007). Several fainter galaxies ("B"–"G") are located within the XRT error circles (see Appendix 2.8.3).

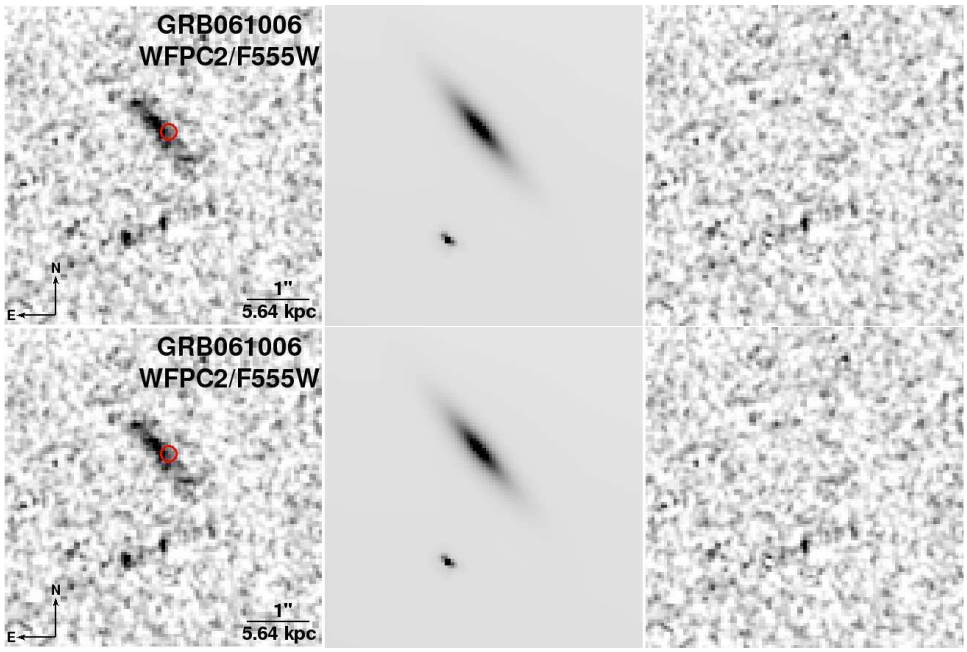

Figure 2.9.—: *Top-left: HST*/ACS/F555W image of the host galaxy of GRB 061006 with a 3σ error circle representing the afterglow position. *Top-center:* Sérsic model fit from `galfit`. *Top-right:* Residual image. *Bottom:* Same, but for the *HST*/ACS/F814W observations.

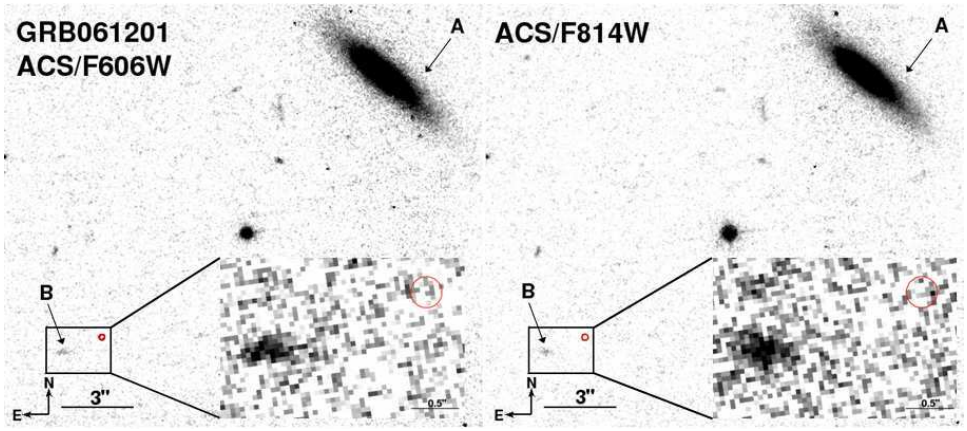

Figure 2.10.—: *Left: HST*/ACS/F606W image of the location of GRB 061201. The bright galaxy at the upper right-hand corner ("A") is located at $z = 0.111$ (Berger 2006a; Stratta et al. 2007) with an offset of about 32.5 kpc. A second, fainter galaxy ("B") is located about $1.8''$ away from the optical afterglow position (see Appendix 2.8.2). *Right:* Same, but for the *HST*/ACS/F814W observations.

Table 2.2. Morphological Properties of Short GRB Host Galaxies

			galfit					IRAF/ellipse			
GRB	Instrument	Filter	n [a]	r_e ($''$)	r_e [c] (kpc)	μ_e [b] (AB mag arcsec^{-2})	AB Mag [b]	n	r_e ($''$)	r_e [c] (kpc)	μ_e [b] (AB mag arcsec^{-2})
050509b	ACS	F814W	5.6	5.84	20.98	23.5	16.2	5.6	5.84	20.98	23.4
050709	ACS	F814W	1.1	0.76	2.08	23.0	21.2	0.6	0.64	1.75	22.4
	WFPC2	F450W	1.1	0.71	1.94	23.5	21.9	0.9	0.71	1.94	23.4
050724	WFPC2	F450W	4	1.35	5.34	23.2	19.4	1.3	0.36	1.42	20.8
	WFPC2	F814W	3.0	0.82	3.24	20.5	18.0	2.9	1.01	4.00	20.8
051210	WFPC2	F675W	1	0.70	5.63	23.8	23.7	1.0	0.63	5.07	24.2
			4	2.38	19.14	26.3	22.8				
051221a	WFPC2	F555W	0.9	0.36	2.29	23.3	23.1	0.8	0.34	2.17	23.1
	WFPC2	F814W	0.9	0.41	2.61	22.7	22.1	0.9	0.39	2.49	22.7
060121	ACS	F606W	1	0.36	2.89	25.9	27.1	1.4	0.67	5.39	27.2
			4	1.22	9.81	27.4	26.6				
060313	ACS	F475W	1	0.14	1.13	23.7	27.3	0.6	0.17	1.37	24.9
			4	0.32	2.57	26.2	26.7				
	ACS	F775W	1	0.07	0.56	21.4	26.1	1.3	0.23	1.85	25.0
			4	0.10	0.80	23.6	26.3				
061006	ACS	F814W	0.7	0.57	3.22	22.3	22.7	0.7	0.65	3.67	22.9
	WFPC2	F555W	1	0.63	3.55	23.3	23.4	0.8	0.55	3.10	23.6

Note. — Results of morphological analysis performed with `galfit` and IRAF/`ellipse` (§2.3).

[a] For the Sérsic index n in `galfit`, exact values of 1 and 4 indicate a fit with n as a fixed parameter.

[b] These values have been corrected for Galactic extinction.

[c] For the hosts with unknown redshift (GRBs 051210, 060121, and 060313) we assume $z = 1$.

Radial Profiles from IRAF/`ellipse`

We use `ellipse` to generate elliptical isophotes for each host galaxy, with the center and ellipticity of each isophote allowed to vary[6]. The resulting radial surface brightness profiles in units of AB mag arcsec^{-2} are shown in Figure 2.11. We fit each profile with a Sérsic model (Equation 3.1) using n, r_e, and μ_e as free parameters. The best-fit values are listed in Table 3.3, and the resulting models are shown in Figure 2.11. We find adequate fits in all cases, although some host galaxies clearly exhibit radial complexity due to irregular structure and/or an edge-on orientation.

2.2.4 Astrometry

To determine the location of each short GRB relative to its host galaxy we perform differential astrometry using optical and near-IR images of the afterglows[7]. With the exception of GRB 050709, whose afterglow is directly detected in *HST*/ACS observations, we use ground-based images from Magellan, Gemini, and the VLT. The astrometric tie between the afterglow and host images is performed using point sources in common between the two images; the source of the afterglow image and the number of astrometric tie objects are listed in Table 3.2. In the case of ground-based to *HST* astrometry we use a range of $15 - 85$ common objects, with the number depending on the density of stellar sources in the field, the depth of the images, and the field-of-view. To determine the astrometric tie we use the IRAF astrometry routine `ccmap`. We find that a second-order

[6]For the hosts of GRBs 060121 and 060313, with low signal-to-noise detections, the center and ellipticity were held fixed throughout the fit.

[7]Optical afterglows have not been detected in the case of GRBs 050509b and 051210.

Table 2.3. Short GRB Angular, Physical, and Host-Normalized Offsets

GRB	Instrument	Filter	z	Reference	No.	$\sigma_{\rm GB\rightarrow HST}$ (mas)	$\sigma_{\theta,\rm GRB}$ (mas)	$\sigma_{\theta,\rm gal}$ (mas)	δRA ($''$)	δDec ($''$)	Offset ($''$)	Offset (kpc)	Offset (r_e [a])
050509b	ACS	F814W	0.226	SDSS	10	30	3400	1.0	+15.61	+8.40	17.73 ± 3.4	63.7 ± 12.2	3.04 ± 0.58
							3300	1.0	+11.68	+4.40	12.48 ± 3.3	44.8 ± 11.9	2.14 ± 0.57
050709	ACS	F814W	0.1606	HST/ACS	35	8	1.0	1.4 [b]	+1.294	−0.310	1.331 ± 0.010	3.64 ± 0.027	2.08 ± 0.02
	WFPC2	F450W		HST/ACS	12	14	1.0	4.7	+1.306	−0.360	1.355 ± 0.020	3.71 ± 0.055	1.91 ± 0.03
	ACS	F814W		self	···	···	1.0	1.4	+1.329	−0.310	1.365 ± 0.002	3.74 ± 0.005	2.13 ± 0.01
050724	WFPC2	F450W	0.257	Magellan/PANIC	60	15	5.0	4.7 [c]	−0.226	−0.640	0.679 ± 0.025	2.69 ± 0.099	1.89 ± 0.07
	WFPC2	F814W		Magellan/PANIC	85	14	5.0	1.4	−0.213	−0.630	0.665 ± 0.020	2.63 ± 0.079	0.66 ± 0.02
	PANIC	K_s		self	···	···	5.0	1.0	−0.253	−0.650	0.697 ± 0.006	2.76 ± 0.024	···
051210	WFPC2	F675W	> 1.4	2MASS	12	29	2900	8	+2.89	+0.50	2.93 ± 2.9	24.9 ± 24.6	4.65 ± 4.60
							1700	8	+3.45	−2.40	4.20 ± 1.7	35.7 ± 14.4	6.67 ± 2.70
051221	WFPC2	F555W	0.5465	Gemini-N/GMOS	45	23	2.5	3.1	−0.287	+0.090	0.301 ± 0.029	1.92 ± 0.18	0.88 ± 0.08
	WFPC2	F814W		Gemini-N/GMOS	45	24	2.5	3.1	−0.330	+0.090	0.342 ± 0.030	2.18 ± 0.19	0.88 ± 0.08
060121	ACS	F606W	···	Gemini-N/GMOS	25	18	16	12	−0.115	+0.030	0.119 ± 0.046	0.96 ± 0.37 [d]	0.18 ± 0.07

Table 2.3—Continued

GRB	Instrument	Filter	z	Reference	No.	$\sigma_{\rm GB\rightarrow HST}$ (mas)	$\sigma_{\theta,\rm GRB}$ (mas)	$\sigma_{\theta,\rm gal}$ (mas)	δRA ($''$)	δDec ($''$)	Offset ($''$)	Offset (kpc)	Offset (r_e [a])
060313	ACS	F475W	···	Gemini-S/GMOS	30	30	19	19.4	+0.354	+0.040	0.356 ± 0.068	2.86 ± 0.55 [d]	2.09 ± 0.40
	ACS	F775W		Gemini-S/GMOS	15	30	19	13.2	+0.280	+0.050	0.284 ± 0.062	2.28 ± 0.50 [d]	1.23 ± 0.23
060502b	ACS	F814W		USNO-B	47	120	3700	··· [e]	···	···	···	···	···
							5800	··· [e]	···	···	···	···	···
061006	ACS	F814W	0.4377	VLT/FORS1	75	17	21	4.9	−0.155	−0.170	0.230 ± 0.043	1.30 ± 0.24	0.35 ± 0.07
	WFPC2	F555W		VLT/FORS1	45	20	21	11	−0.171	−0.190	0.256 ± 0.052	1.44 ± 0.29	0.46 ± 0.10
061201	ACS	F814W	···	VLT/FORS2	24	13	41	··· [e]	···	···	···	···	···
	ACS	F606W	···	VLT/FORS2	24	13	41	··· [e]	···	···	···	···	···

Note. — Projected angular, physical, and host-normalized offsets for the short GRBs with *HST* observations.

[a] Values for r_e are from `ellipse` (Table 3.3).

[b] Systematic uncertainty in host center is 50 mas.

[c] Systematic uncertainty in host center is 20 mas.

[d] Assuming $z = 1$.

[e] We do not claim a unique host galaxy identification for this burst.

polynomial, with six free parameters corresponding to a shift, scale, and rotation in each coordinate, provides a robust astrometric tie in all cases. The resulting rms values are $\sigma_{\rm GB\rightarrow HST} = 13 - 30$ mas (Table 3.2).

We next consider the uncertainty in the afterglow position from each ground-based image. The centroiding accuracy depends on the size of the PSF and the signal-to-noise ratio (S/N) of the afterglow detection, $\sigma_\theta = \theta_{\rm FWHM}/({\rm S/N})$. We determine $\sigma_{\theta,{\rm GRB}}$ for each GRB using the `SExtractor` program[8] (Table 3.2). In the case of GRBs 050724 and 051221 we find that $\sigma_{\theta,{\rm GRB}}$ is significantly smaller than $\sigma_{\rm GB\rightarrow HST}$; for GRBs 060121, 060313, and 061006 the two sources of uncertainty are comparable; and for GRB 061201 $\sigma_{\theta,{\rm GRB}}$ dominates. The afterglows of GRBs 050509b, 051210, and 060502b have only been detected in X-rays, with the *Swift* X-ray Telescope (XRT), and as a result their positional uncertainty is $\sigma_{\theta,{\rm GRB}} \sim 1.7 - 5.8''$ (Table 3.2). We note that the XRT positions from the catalogs of Butler (2007) and Evans et al. (2009) exhibit relative offsets of $5.6''$ (GRB 050509b), $3.0''$ (GRB 051210), and $2.9''$ (GRB 060502b) suggesting that the true positional uncertainties (including systematics) are larger than their quoted statistical uncertainties.

The final source of uncertainty in the relative position of the GRB and host galaxy is the centroiding accuracy of the host in the *HST* images. To determine this uncertainty we again use `SExtractor`. The resulting values of $\sigma_{\theta,{\rm gal}}$ are listed in Table 3.2. We find that for GRBs 050724, 051221, and 061006 the host centroid uncertainty is smaller than both $\sigma_{\rm GB\rightarrow HST}$ and $\sigma_{\theta,{\rm GRB}}$, while for GRBs 060121 and 060313 $\sigma_{\theta,{\rm gal}}$ is comparable to $\sigma_{\theta,{\rm GRB}}$. The combined offset uncertainties are listed in Table 3.2.

[8] `http://sextractor.sourceforge.net/`

A much more accurate relative position is available for GRB 050709 since the afterglow was detected in *HST*/ACS images (Fox et al. 2005). The limiting factor is thus σ_θ for the afterglow and host. We find from the first *HST*/ACS observation (2005 July 15.6 UT) that $\sigma_{\theta,\rm GRB} = 1$ mas, while $\sigma_{\theta,\rm gal} = 1.4$ mas. In addition, we also astrometrically tie the final epoch of ACS imaging and the WFPC2 image to the first epoch. Since the afterglow is no longer detected in these images, this allows us to study the burst environment. For the final ACS image we find $\sigma_{\rm HST\rightarrow HST} = 8$ mas, while for the WFPC2 image we find $\sigma_{\rm HST\rightarrow HST} = 14.5$ mas. These uncertainties clearly dominate over the centroiding errors of the afterglow and host galaxy. We do note, however, that the complex morphology of the host galaxy (§2.3) introduces a systematic uncertainty in the definition of the host "center". By varying the signal-to-noise threshold in `SExtractor`, we find that the centroid of the host shifts by as much as 50 mas, which dominates over the statistical uncertainty in the source position.

Similarly, we find a more accurate offset for GRB 050724 from a detection of the afterglow and host in ground-based near-IR images (Berger et al. 2005). The combined afterglow and host centroid uncertainty in these images is about 6 mas, compared to a total uncertainty of $20 - 25$ mas for the *HST* images.

2.2.5 Host Light Distribution

To determine the brightness of the GRB location relative to the host light distribution, we follow the methodology of Fruchter et al. (2006) and Kelly et al. (2008) and calculate from each galaxy image the fraction of total light in pixels fainter than the afterglow position. Six bursts have differential astrometric positions of better than 1 pixel (050709,

050724, 051221a, 060121, 060313 and 061006; Table 3.2). For each image we create an intensity histogram of a $5'' \times 5''$ region centered on the host galaxy and determine a 1σ cut-off level for the host by fitting a Gaussian profile to the sky brightness distribution (equivalent to a signal-to-noise ratio cut-off of 1). We then plot the pixel flux distribution above the appropriate cut-off level for a region surrounding the host, and determine the fraction of light in pixels fainter than the afterglow pixel; see Table 3.4.

2.3 Morphological Analysis

Using the results of the `galfit` analysis and the radial surface brightness profiles we first classify the short GRB hosts in terms of their Sérsic n values. From the `galfit` analysis we find that three hosts (GRBs 050709, 051221a, and 061006) are best modeled with $n \approx 1$, corresponding to an exponential disk profile, while two hosts (GRBs 050509b and 050724) are best modeled with $n \approx 3$ and ≈ 5.6, respectively, typical of elliptical galaxies. We note that GRB 050724 possibly exhibits weak spiral structure, which may explain the resulting value of $n \approx 3$ (see Figure 2.3 and Malesani et al. 2007b), but this putative spiral structure is clearly sub-dominant relative to the elliptical structure. The final three hosts (GRBs 051210, 060121, and 060313) are equally well modeled in `galfit` with a wide range of n values, and we provide results for both $n = 1$ and $n = 4$ in Table 3.3.

We find identical results using Sérsic model fits to the one-dimensional radial surface brightness profiles generated with `ellipse` (Figure 2.11 and Table 3.3). However, with this approach we find best-fit values of $n \sim 1$ for the three host galaxies with ambiguous `galfit` results, suggesting that they are indeed better modeled as exponential disks.

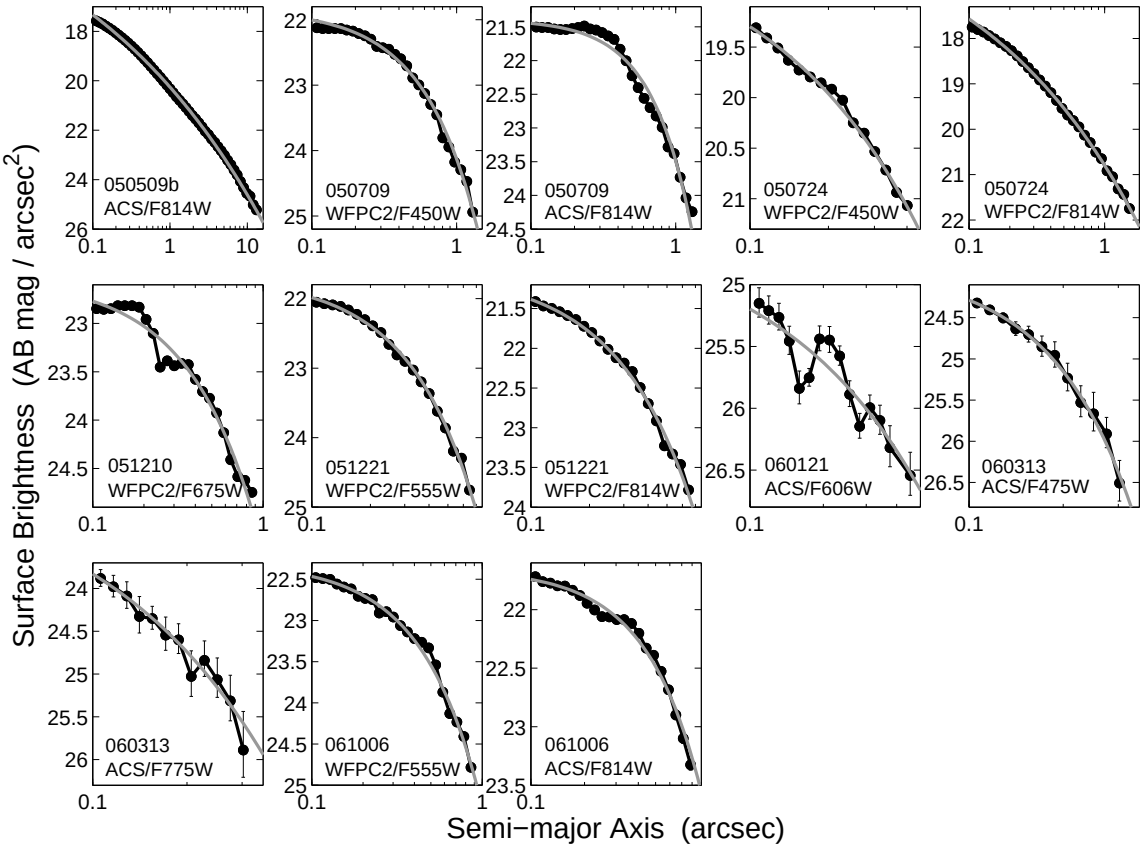

Figure 2.11.—: One-dimensional radial surface brightness profiles for short GRB host galaxies derived from IRAF/`ellipse`. The gray lines are Sérsic model fits (Equation 3.1) to the surface brightness profiles. The results of the fits are listed in Table 3.3.

We therefore conclude that of the eight short GRB host galaxies studied here only two can be robustly classified as elliptical galaxies based on their morphology. A similar fraction was determined independently from spectroscopic observations (Berger 2009). The distribution of n values is shown in Figure 2.12.

As can be seen from the `galfit` results, the Sérsic models of the two elliptical hosts exhibit significant residuals (Figures 2.1 and 2.3). This is a well-known effect for bright elliptical galaxies, which generally require a multi-parameter power-law plus Sérsic fit that accounts for a flatter core than expected in the de Vaucouleurs model (Trujillo et al. 2004). Since we are here mainly interested in the distribution of n values and a comparison to long GRB hosts, we retain the simple Sérsic formulation.

We also find significant residuals for a one-component Sérsic fit of the host galaxy of GRB 050709, which has an irregular morphology dominated by an exponential profile (Figure 2.2). This is the only clearly irregular galaxy in the sample. Finally, we find that the hosts of GRBs 051210, 060121, and 061006 exhibit significant bulges, clearly seen in their radial surface brightness profiles (Figure 2.11). For the host of GRB 061006, which was observed in two filters, the bulge component is more significant in the F814W filter than in the F555W filter, as expected for an older stellar population; the burst appears to coincide with this bulge component (Figure 2.9).

The `galfit` and radial profile fits also yield values of the effective radius, r_e, for each host galaxy. We find a range of $\approx 0.2 - 5.8''$, corresponding to physical scales[9] of about

[9]For the faint hosts without a known redshift (GRBs 051210, 060121, 060313, and possibly 061201) we assume $z = 1$ (Berger et al. 2007b), and take advantage of the relative flatness of the angular diameter distance as a function of redshift beyond $z \sim 0.5$.

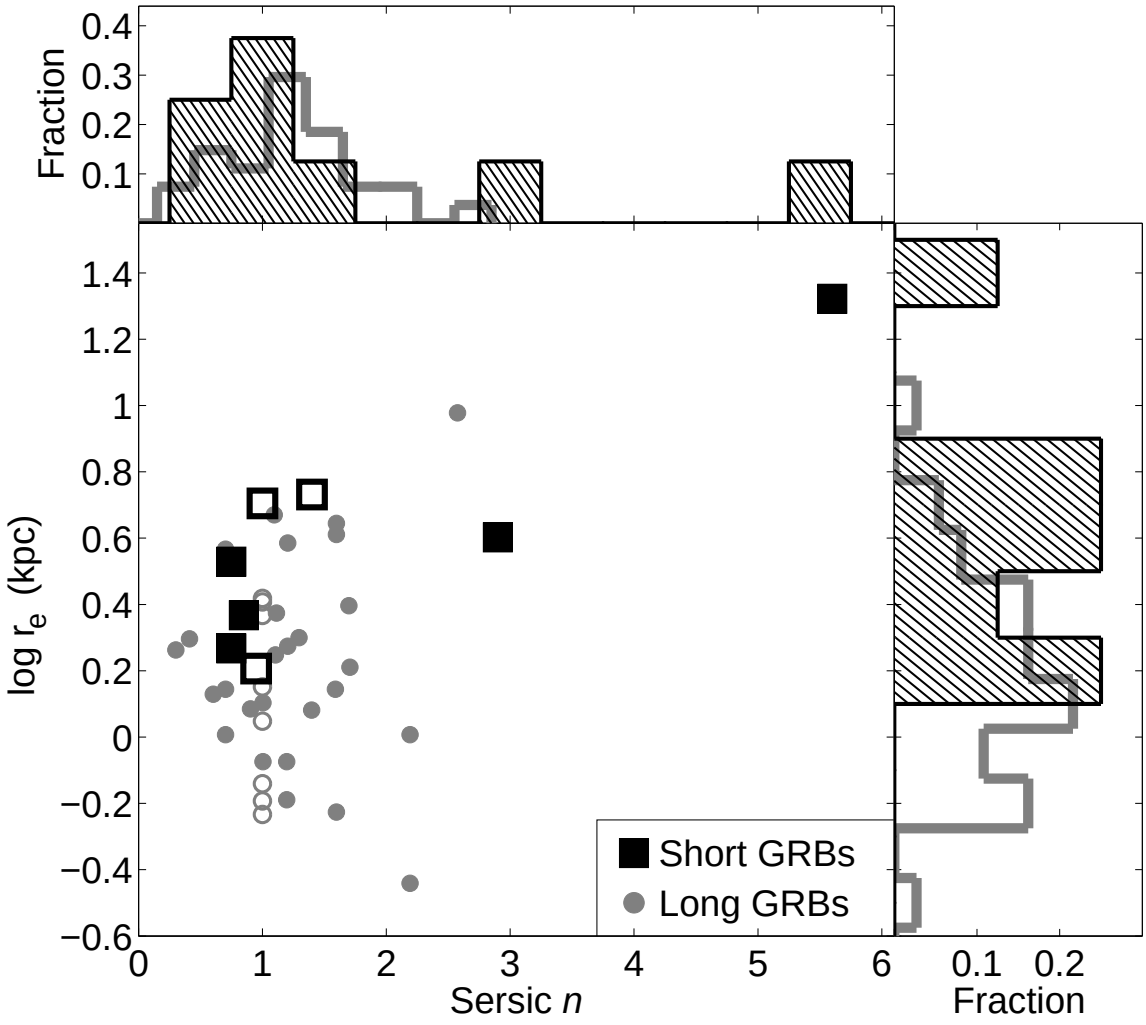

Figure 2.12.—: Effective radii for the short GRB hosts with *HST* observations plotted as a function of their Sérsic n values. We use the results of the IRAF/`ellipse` analysis; see Figure 2.11 (open squares designate hosts for which `galfit` models with $n = 1$ and $n = 4$ provide an equally good fit). Also shown are the data for long GRB hosts based on *HST* observations from the sample of Wainwright et al. (2007b). The hosts of GRBs 050509b and 050724 have n values typical of elliptical galaxies, but the remaining hosts have a similar distribution to that of long GRBs (i.e., a median of $n \sim 1$, or an exponential disk profile). On the other hand, the hosts of short GRBs are larger by about a factor of 2 than the hosts of short GRBs, in agreement with their higher luminosities.

$1.4 - 21$ kpc. The smallest effective radius is measured for the host of GRB 060313, while the host of GRB 050509b has the largest effective radius. The median value is $r_e \approx 3.5$ kpc. We adopt the best-fit values from the radial surface brightness profiles, and plot the resulting distribution, as well as r_e as a function of n, in Figure 2.12.

Finally, the effective surface brightness values range from $\mu_e \approx 21$ to ≈ 27 AB mag arcsec^{-2}. The galaxy with the highest surface brightness is the host of GRB 050724, while the lowest surface brightness is measured for the host of GRB 060121. The integrated magnitudes range from about 16.3 AB mag (GRB 050509b) to 26.4 AB mag (GRB 060313).

2.3.1 Comparison to Long GRB Host Galaxies

A comprehensive morphological analysis of long GRB host galaxies using *HST* observations with the STIS, WFPC2, and ACS instruments has been carried out by Conselice et al. (2005) and Wainwright et al. (2007b). In Figure 2.12 we compare the values of n and r_e measured for long GRB hosts by Wainwright et al. (2007b) to the values measured here for short GRB hosts. Two clear trends emerge from this comparison. First, all long GRB hosts have $n \lesssim 2.5$, and the median value for the population is $\langle n \rangle \approx 1.1$ (Wainwright et al. 2007b). Thus, all long GRB hosts are morphologically classified as exponential disks, while 2 of the 8 short GRB hosts studied here exhibit de Vaucouleurs profiles. However, for the hosts with $n \lesssim 2$, the distributions of n values for both populations appear to be similar.

Second, short GRB hosts have larger effective radii, with $\langle r_e \rangle \approx 3.5$ kpc, compared to $\langle r_e \rangle \approx 1.7$ kpc for long GRB hosts (Wainwright et al. 2007b). A Kolmogorov-Smirnov

(K-S) test indicates that the probability that the short and long GRB hosts are drawn from the same underlying distribution of host galaxy effective radii is only 0.04. If we remove from the sample GRBs 050509b and 051210 (which have only XRT positions) we find that the K-S probability is still only 0.09. Thus, we conclude with high significance that short GRB host galaxies are systematically larger than long GRB hosts, and that this result is not affected by host associations based on XRT positions. The larger sizes of short GRB hosts are expected in the context of the galaxy size-luminosity relation (e.g., Freeman 1970). We recently showed that short GRB hosts are systematically more luminous than long GRB hosts by about $\Delta M_B \approx 1.2$ mag (Berger 2009) and therefore their sizes are expected to be correspondingly larger.

An additional striking difference between the hosts of long and short GRBs is the apparent dearth of interacting or irregular galaxies in the short GRB sample. Of the eight host galaxies studied here, we find only one irregular galaxy (GRB 050709) and none that appear to be undergoing mergers. In contrast, the fraction of long GRB hosts with an irregular or merger/interaction morphology is about $30 - 60\%$ (Wainwright et al. 2007b). The interpretation for this high merger/interaction fraction in the long GRB sample is that such galaxies are likely undergoing intense star formation activity triggered by the merger/interaction process, and are therefore suitable sites for the production of massive stars. The lack of morphological merger signatures in the short GRB sample indicates that if any of the hosts have undergone significant mergers in the past, the delay time between the merger and the production of a short GRB is $\gtrsim 10^9$ yr (e.g., Barnes & Hernquist 1992).

2.4 Offsets

We next turn to an analysis of short GRB offsets relative to the centers of their host galaxies. Based on the astrometric tie of the *HST* host observations to ground-based afterglow observations, we find that the projected offsets are in the range of $\approx 0.12 - 17.7''$ (Table 3.2). The corresponding projected physical offsets are about $1 - 64$ kpc, with a median value of about 3 kpc. The largest offsets are measured for GRBs 050509b and 051210, but these are based on *Swift*/XRT positions with statistical uncertainties of about 12 and 18 kpc, respectively (and possibly larger if we consider systematic uncertainties; §3.2.4). If we consider only the bursts with sub-arcsecond afterglow positions we find that the largest offset is 3.7 kpc (GRB 050709), and that the median offset for the 6 bursts is 2.2 kpc. In the case of GRB 061201 the host association remains ambiguous (see Appendix 2.8.2), but even for the nearest detected galaxy the offset is about 14.2 kpc. The obvious caveat is that an undetected fainter host, with $\gtrsim 25.5$ AB mag, may be located closer to the GRB position.

To investigate the offset distribution in greater detail we supplement the values measured here with offsets for GRBs 070724, 071227, and 090510 from ground-based observations (Berger et al. 2009; Rau et al. 2009). In the case of GRBs 070724 and 071227 the optical afterglows coincide with the disks of apparent edge-on spiral galaxies (Berger et al. 2009; D'Avanzo et al. 2009). The offsets of the three bursts are 4.8, 14.8, and 5.5 kpc, respectively (Berger et al. 2009; Rau et al. 2009). For GRB 071227 we calculate the relative offset from our Magellan/IMACS observations and find a total $(\sigma_{\theta,\rm GRB} + \sigma_{\theta,\rm gal})$ uncertainty of 65 mas, corresponding to 0.34 kpc at the redshift of the

host[10].

There are 7 additional events with optical afterglow identifications. Of these bursts, two (070707 and 070714b) coincide with galaxies (Piranomonte et al. 2008; Graham et al. 2009), but their offsets have not been measured by the respective authors. Based on the claimed coincidence we conservatively estimate an offset of $\lesssim 0.5''$, corresponding[11] to $\lesssim 4$ kpc. Two additional bursts (070809 and 080503) do not have coincident host galaxies to deep limits, but the nearest galaxies are located about 6.5 and 20 kpc from the afterglow positions, respectively[12] (Perley et al. 2008, 2009a). For the final three bursts (080905, 090305, and 090426) no deep host galaxy searches exist in the literature.

In addition to the bursts with sub-arcsecond positions, several hosts have been identified within XRT error circles in follow-up observations (GRBs 060801, 061210, 061217, 070429b, 070729, and 080123; Berger et al. 2007b; Berger 2009), but in all of these cases the offsets are consistent with zero, or may be as large as ~ 30 kpc (e.g., Berger et al. 2007b). For example, the offsets for GRBs 060801, 061210, and 070429b are 19 ± 16 kpc, 11 ± 10 kpc, and 40 ± 48 kpc. We use 30 kpc as a typical upper limit on the offset for these 6 events. We note that no follow-up observations are available

[10]This is significantly more precise than the large uncertainty of $0.4''$ quoted by D'Avanzo et al. (2009) based on *absolute* astrometry; for offset measurements differential astrometry provides a better approach.

[11]GRB 070714b is located at $z = 0.923$, while the redshift of GRB 070707 is not known. Based on the faintness of the host, $R \approx 27.3$ mag, we assume $z = 1$ to calculate the physical offset.

[12]GRB 070809 is located 19.6 kpc from a galaxy at $z = 0.219$, and about $2.3''$ from a much fainter galaxy, which at $z \gtrsim 1$ corresponds to 18.4 kpc. No host is detected at the position of GRB 080503 in deep *HST* observations, but a faint galaxy is located about $0.8''$ away, which at $z \gtrsim 1$ corresponds to 6.5 kpc.

in the literature for most short GRBs with X-ray positions from 2008-2009. Finally, about $1/4 - 1/3$ of all short GRBs discovered to date have only been detected in γ-rays, precluding a unique host galaxy association and an offset measurement.

The cumulative distribution of projected physical offsets for the GRBs with *HST* observations from this work, supplemented by the bursts with offsets or limits based on optical afterglow positions (070707, 070714b, 070724, 070809, 071227, 080503, and 090510) is shown in Figure 2.13. Also shown is the differential probability distribution, $P(\delta r)d(\delta r)$, taking into account the non-Gaussian errors on the radial offsets (see discussion in Appendix B of Bloom et al. 2002). We find that the median for this sample is about 5 kpc.

As evident from the discussion above, this is not a complete offset distribution; roughly an equal number of short GRBs have only limits or undetermined offsets due to their detection in just the X-rays or γ-rays[13]. Taking these events into account, our most robust inferences about the offset distribution of short GRBs are as follows:

- At least 25% of all short GRBs have projected physical offsets of $\lesssim 10$ kpc.
- At least 5% of all short GRBs have projected physical offsets of $\gtrsim 20$ kpc.
- At least 50% of all short GRBs have projected physical offsets of $\lesssim 30$ kpc; this value includes the upper limits for the hosts identified within XRT error circles.

These robust constraints are shown in Figure 2.13.

[13]We do not consider the bursts that lack host searches since there is no a priori reason that these events (mainly from 2008-2009) should have a different offset distribution compared to the existing sample from 2005-2007.

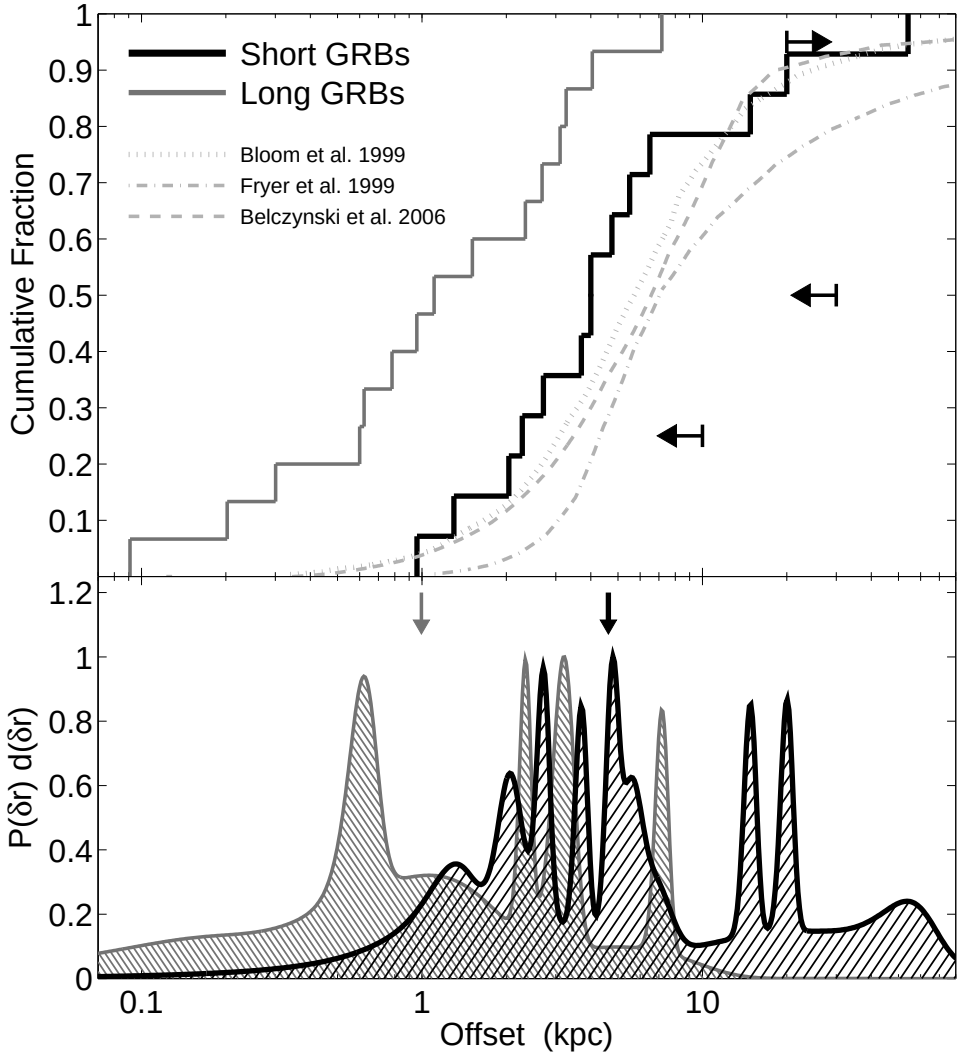

Figure 2.13.—: Projected physical offsets for short GRBs (black) and long GRBs (gray; Bloom et al. 2002). The top panel shows a cumulative distribution, while the bottom panel shows the differential distribution taking into account the non-Gaussian errors on the offsets. The arrows in the bottom panel mark the median value for each distribution. The median value for short GRBs, $\approx$ 5 kpc, is about a factor of 5 times larger than for long GRBs. The arrows in the top panel exhibit the most robust constraints on the offset distribution (§2.4), taking into account the fraction of short GRBs with only γ-ray positions, as well as short GRBs for which hosts have been identified within XRT error circles (thereby providing a typical range of $\sim 0 - 30$ kpc). Also shown in the top panel are predicted offset distributions for NS-NS binary mergers in Milky Way type galaxies based on population synthesis models. We find good agreement between the observed distribution and models, as well as between the robust constraints and models.

Using the observed distribution and the robust constraints outlined above, we now provide a comparison with predicted distributions for NS-NS binaries in Milky Way type galaxies (Bloom et al. 1999; Fryer et al. 1999; Belczynski et al. 2006), appropriate for the observed luminosities of short GRB host galaxies (Berger 2009). We find good agreement between the observed distribution and those predicted by Bloom et al. (1999) and Belczynski et al. (2006). The offset distribution of Fryer et al. (1999), with a median of about 7 kpc, predicts larger offsets and therefore provides a poorer fit to the observed distribution, which has a median of about 5 kpc. However, all three predicted distributions accommodate the offset constraints. In particular, they predict about $60 - 75\%$ of the offsets to be $\lesssim 10$ kpc, about $80 - 90\%$ to be $\lesssim 30$ kpc, and about $10 - 25\%$ of the offsets to be $\gtrsim 20$ kpc. Thus, the projected physical offsets of short GRBs are consistent with population synthesis predictions for NS-NS binaries. However, the observations are also consistent with partial contribution from other progenitor systems with no expected progenitor kicks, such as WD-WD binaries.

2.4.1 Host-Normalized Offsets

To compare the offsets in a more uniform manner, we normalize the measured values by r_e for each host galaxy. We use the r_e values measured from the one-dimensional radial surface brightness profiles from `ellipse` (see Figure 2.14 and Table 3.2) and find values ranging from about 0.2 r_e for GRB 060121 to 6.7 ± 2.7 r_e for the Evans et al. (2009) XRT position of GRB 051210. The Butler (2007) position for GRB 051210, however, leads to an offset of 4.65 ± 4.60 r_e, consistent with a negligible offset. For the subset of 6 bursts with optical afterglow positions and secure host associations, 4 are located within 1 r_e,

while the remaining 2 bursts are located at about 2 r_e (Figure 2.14). GRB 050509b, which has the largest physical offset, has a normalized offset of $2 - 3$ r_e, depending on which XRT position is used. Thus, with the exception of the ambiguous case of GRB 061201, we find that all of the available offsets are consistent with $\lesssim 2$ r_e. The large additional sample of physical offsets that we used above cannot be easily translated to host-normalized offsets at the present since none of the hosts have been observed with *HST*, thereby precluding a robust morphological analysis. This provides an impetus for future *HST* observations.

The differential probability distribution of host-normalized offsets for our *HST* sample, taking into account the non-Gaussian errors, is shown in Figure 2.15. We find that the median value for all 8 bursts is ≈ 1 r_e. Moreover, $\lesssim 20\%$ of the probability distribution is at large offsets of $\gtrsim 2.5$ r_e.

2.4.2 Comparison to Long GRB Host Galaxies

We compare our observed short GRB offsets with those of long GRBs from the sample of Bloom et al. (2002) in Figures 2.13-2.15. The offset distribution of long GRBs has been used to argue for a massive star progenitor population, and against NS-NS binaries (Bloom et al. 2002). The offset distribution for short GRBs is clearly shifted to larger physical scales. In particular, the median offset for the long GRBs is 1.1 kpc, about a factor of 5 times smaller than the median value for short GRBs. Similarly, no long GRB offsets are larger than about 7 kpc, whereas at least some short GRBs appear to have offsets in excess of 15 kpc.

However, the distinction between the two offset distributions is significantly reduced

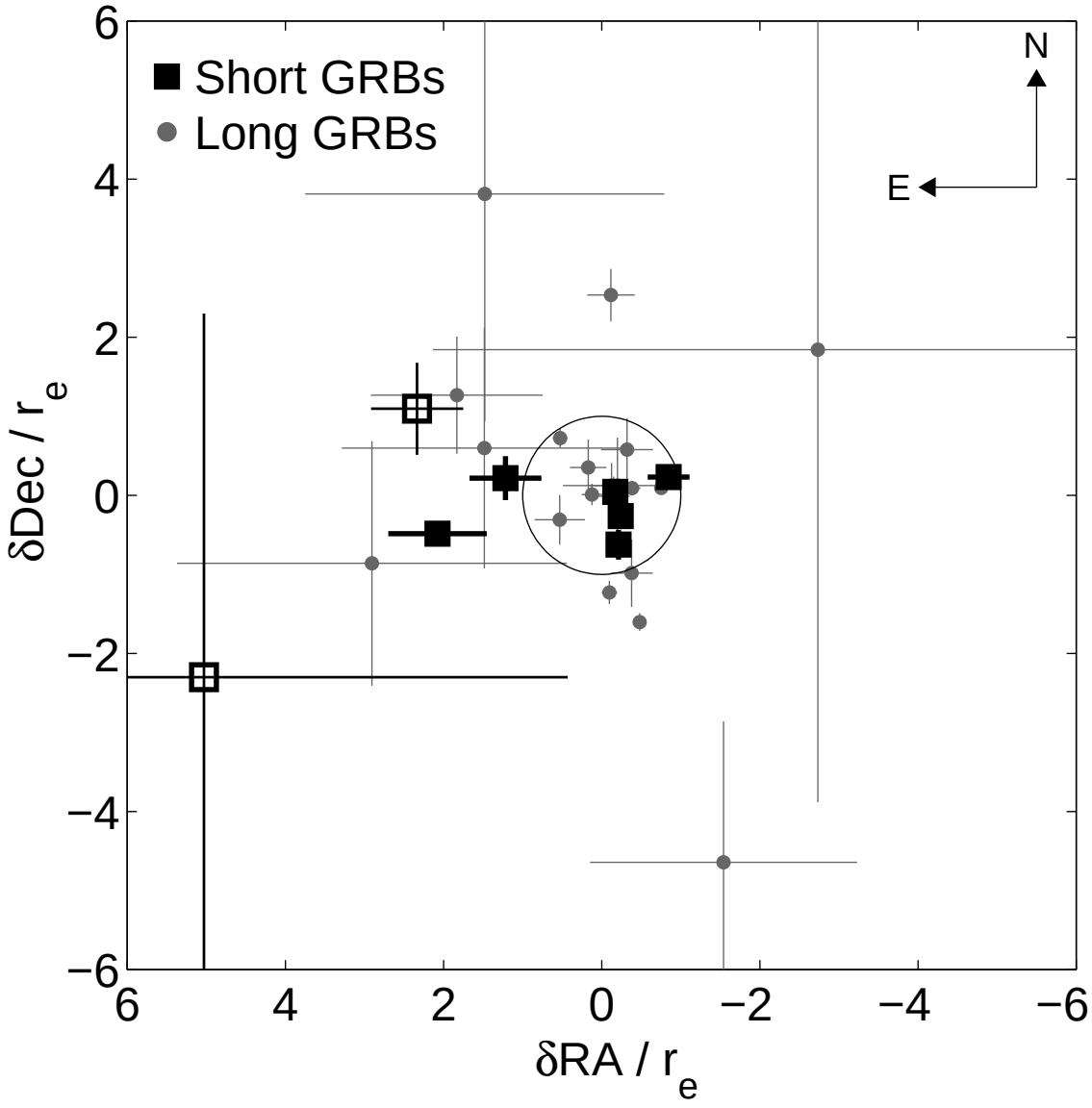

Figure 2.14.—: Host-normalized offsets in right ascension and declination for the short GRBs in our *HST* sample (black; open symbols mark the GRBs with X-ray positions, 050509b and 051210). Also shown are the offsets for long GRBs from the sample of Bloom et al. (2002). The circle marks an offset of 1 r_e. About half of all long GRBs have offsets of $\lesssim 1$ r_e, and we find a similar result for short GRBs.

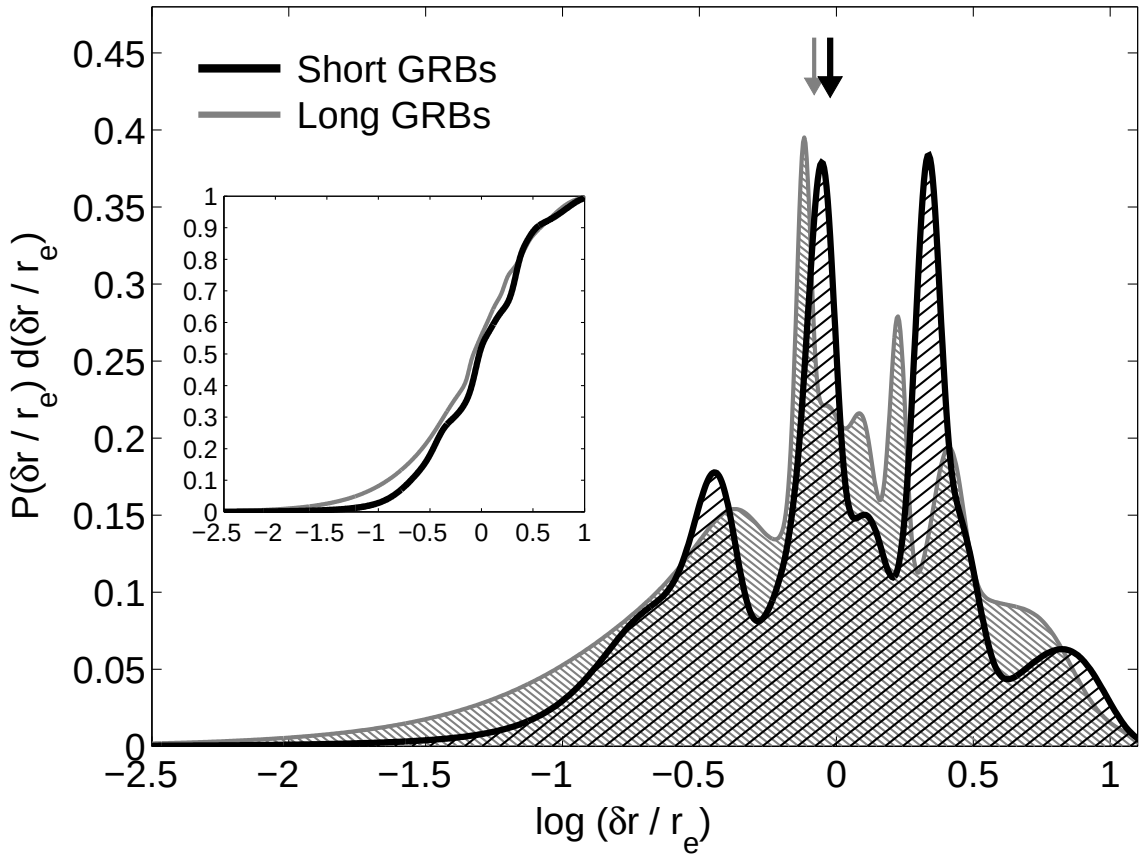

Figure 2.15.—: Probability distributions of the host-normalized offsets of short GRBs (black) and long GRBs (gray; Bloom et al. 2002). For each burst we include the host-normalized offset taking into account the non-Gaussian errors. The arrows mark the median value of each distribution, and the inset shows the cumulative distribution.

when we take into account the systematically larger sizes of short GRB host galaxies (Figure 2.12). The median normalized offset for long GRBs is about 0.8 r_e, compared to about 1 r_e for short GRBs. Similarly, 20% of the long GRB cumulative distribution has offsets of $\gtrsim 2.5$ r_e, identical to the statistics for the short GRB offsets. Indeed, as can be see from Figure 2.15, the cumulative host-normalized offset distributions for long GRBs and short GRBs with *HST* observations are nearly identical.

In the context of NS-NS binary progenitors, the close similarity in the normalized offset distributions can be interpreted to mean that most systems likely remain bound to their hosts (rather than ejected into the intergalactic medium), and/or have a relatively short delay time. These conclusions are tentative due to the small number of events with host-normalized offsets, but they can be further tested with future *HST* observations.

2.5 Light Distribution Analysis

In addition to the offset analysis in the previous section, we study the local environments of short GRBs using a comparison of their local brightness to the host light distribution. This approach is advantageous because it is independent of galaxy morphology, and does not suffer from ambiguity in the definition of the host center (see Fruchter et al. 2006). We note that for the overall regular morphology of short GRB hosts the definition of the host center is generally robust, unlike in the case of long GRBs (Fruchter et al. 2006; Wainwright et al. 2007b). On the other hand, this approach has the downside that it requires precise pixel-scale positional accuracy. In our sample, this is the case for only 6 short bursts.

Table 2.4. Short GRB Fractional Flux

GRB	Instrument	Filter	Fractional Flux
050709	WFPC2	F450W	0
	ACS	F814W	0.09
050724	WFPC2	F450W	0.03
	WFPC2	F814W	0.33
051221	WFPC2	F555W	0.54
	WFPC2	F814W	0.65
060121	ACS	F606W	0.41
060313	ACS	F475W	0.04
	ACS	F775W	0
061006	WFPC2	F555W	0.56
	ACS	F814W	0.63

Note. — Fraction of host galaxy light in pixels fainter than the GRB position.

The fraction of host light in pixels fainter than the afterglow pixel brightness for each host/filter combination is summarized in Table 3.4. The cumulative light distribution histogram is shown in Figure 2.16. The shaded histogram represents the range defined by the dual filters for 5 of the 6 bursts. We find that the upper bound of the distribution is defined by the blue filters, indicating that short GRBs trace the rest-frame optical light of their hosts better than the rest-frame ultraviolet. This indicates that short GRB progenitors are likely to be associated with a relatively old stellar population, rather than a young and UV bright population.

The overall distribution has a median value of $\approx 0.1 - 0.4$ (red); namely, only in about one-quarter of the cases, 50% of the host light is in pixels fainter than at the GRB location. Thus, the overall distribution of short GRB locations under-represents the host galaxies' light distribution. This is also true in comparison to the distribution for core-collapse SNe, which appear to track their host light (Fruchter et al. 2006), and even Type Ia SNe, which have a median of about 0.4 (Kelly et al. 2008). Thus, the progenitors of short GRBs appear to be more diffusely distributed than Type Ia SN progenitors.

2.5.1 Comparison to Long GRB Host Galaxies

An extensive analysis of the brightness distribution at the location of long GRBs has been carried out by Fruchter et al. (2006). These authors find that long GRBs are more concentrated on the brightest regions of their hosts than expected from the light distribution of each host. In particular, they conclude that the probability distribution of GRB positions is roughly proportional to the surface brightness squared. As can be seen from Figure 2.16, short GRBs have a significantly more diffuse distribution relative

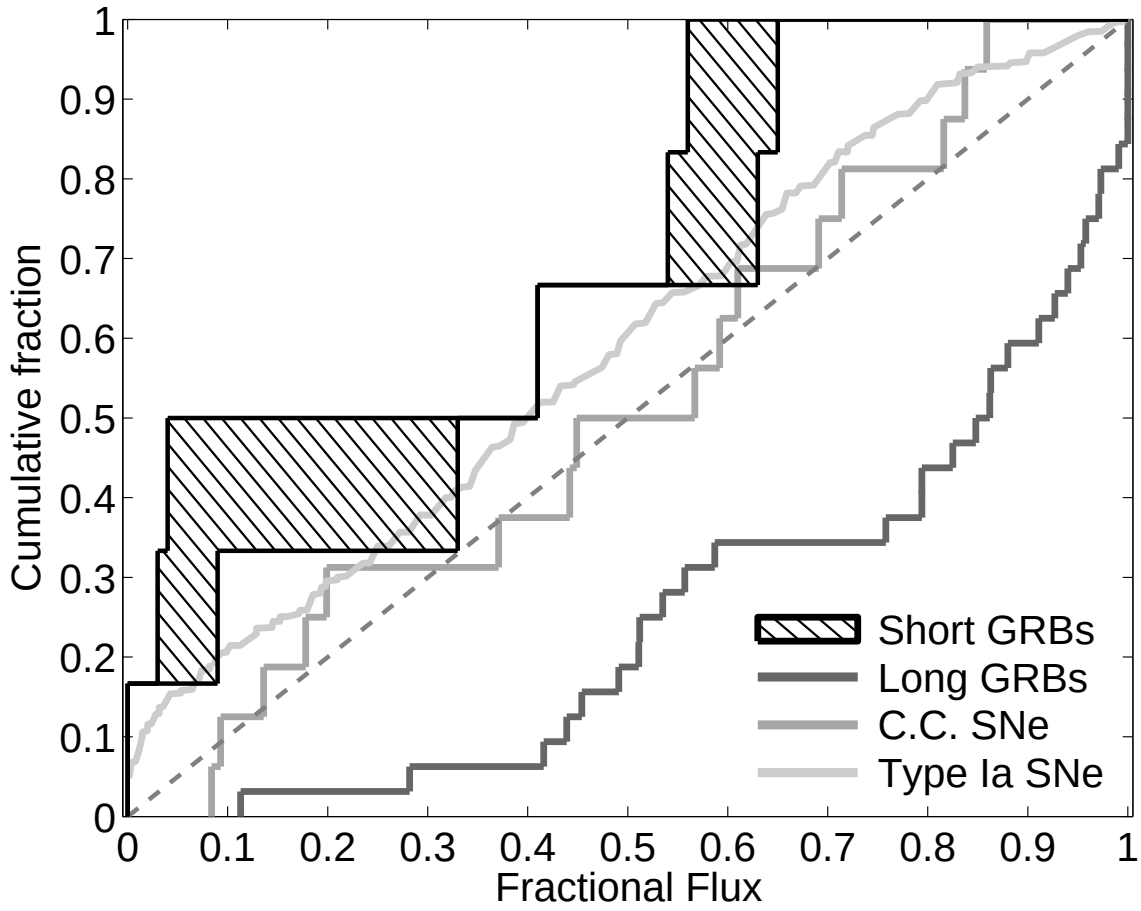

Figure 2.16.—: Cumulative distribution of fractional flux at the location of short GRBs relative to their host light. For each burst we measure the fraction of host light in pixels fainter than the GRB pixel location. The shaded area is defined by the results for the two available filters for each short GRB. Also shown are data for long GRBs (dark gray line) and for core-collapse and Type Ia SNe (light gray lines) from Fruchter et al. (2006) and Kelly et al. (2008). The dashed line marks the expected distribution for objects which track their host light distribution. Short GRBs appear to under-represent their host light, while long GRBs tend to be concentrated in the brightest regions of their hosts (Fruchter et al. 2006).

to the host light than long GRBs. In particular, for the latter, the median light fraction is about 0.85 compared to about 0.25 ± 0.15 for the short GRBs.

2.6 Discussion and Implications

Our extensive analysis of short GRB host galaxy morphologies and the burst local environments has important implications for the progenitor population. We address in particular the popular NS-NS merger model, as well as delayed magnetar formation via WD-WD mergers or WD accretion-induced collapse (Metzger et al. 2008a).

2.6.1 Morphology

From the morphological analysis we find continued evidence that the bulk of short GRB host galaxies ($\sim 3/4$) are late-type galaxies, in agreement with results from spectroscopic observations (Berger 2009). Moreover, as demonstrated by the systematic differences in luminosity, star formation rates, and metallicities between the star forming hosts of long and short GRBs (Berger 2009), we find here that short GRB hosts are systematically larger than long GRB hosts. These results indicate that the progenitors of the two GRB classes select different environments. The higher luminosities, larger sizes, and lower specific star formation rates of short GRB hosts suggest that their rate of occurrence is tied to galactic mass rather than to star formation activity. This result is in broad agreement with old progenitor populations such as NS-NS, NS-BH, or WD-WD binaries, but it indicates that the bulk of short GRB progenitors are not young magnetars. This conclusion is also supported by the dearth of merger signatures, which point to delays of

$\gtrsim 10^9$ yr relative to any merger-triggered star formation episodes.

2.6.2 Offsets

The differential offsets measured here from the *HST* observations provide the most precise values to date for short GRBs, with a total uncertainty of only $\sim 10 - 60$ mas, corresponding to $\sim 30 - 500$ pc. We find that none of the offsets are smaller than ~ 1 kpc, while this is the median offset for long GRBs. On the other hand, a substantial fraction of the *measured* offsets are only a few kpc. The median offset for the *HST* observations supplemented by ground-based data is about 5 kpc (Figure 2.13), about 5 times larger than for long GRBs.

As discussed in detail in §2.4, the observed offset distribution is incomplete. About $1/4 - 1/3$ of all short GRBs have only γ-ray positions ($\sim 1 - 3'$), and a similar fraction have only XRT positions, which generally lead to a range of offsets of $\sim 0 - 30$ kpc. Taking these limitations into account we find that the most robust constraints on the offset distribution are that $\gtrsim 25\%$ of all short GRBs have offsets of $\lesssim 10$ kpc, and that $\gtrsim 5\%$ have offsets of $\gtrsim 20$ kpc. Both the observed offset distribution and these constraints are in good agreement with predictions for the offset distribution of NS-NS binaries in Milky Way type galaxies (Bloom et al. 1999; Fryer et al. 1999; Belczynski et al. 2006). However, at the present they cannot rule out at least a partial contribution from other progenitor systems such as delayed magnetar formation and even young magnetar flare. The apparent existence of large offsets in the sample suggests that these latter models are not likely to account for *all* short GRBs.

In contrast to the larger physical offsets of short GRBs, we find that the distribution

of offsets normalized to the host galaxy effective radii exhibits much better agreement between long and short GRBs (Figure 2.15). The medians of the two distributions are similar (1 versus 0.8 r_e for short and long GRBs, respectively), and both populations have $\approx 20\%$ probability for offsets of $\gtrsim 2.5$ r_e. Naturally, due to the lack of *HST* observations for short GRBs from 2007-2009, the sample for which this analysis is possible is smaller than the sample with physical offsets. Thus, further *HST* observations of existing and future short GRB hosts are essential in order to determine whether the broad similarity in host-normalized offsets is robust. We stress that in the context of comparing short GRBs with various progenitor populations and with long GRBs, host-normalized offsets are the more relevant quantity. For example, the host-normalized distributions for massive stars in small and large galaxies will be similar even though their physical offsets will differ. We stress that population synthesis modelers should include an appropriate distribution of host galaxy sizes, and thereby provide predictions for host-normalized offsets.

In the context of implications for the progenitor population, a recent study of short GRB physical offsets by Troja et al. (2008b) led these authors to claim that short GRBs with extended X-ray emission have systematically smaller offsets, possibly due to a systematic difference in the progenitors. Our *HST* sample includes three short GRBs with strong extended emission (050709, 050724, and 061006), and one GRB (060121) with possible extended emission (4.5σ significance; Donaghy et al. 2006). The physical offsets of these bursts are about 3.7, 2.7, 1.3, and 1 kpc, respectively, leading to a mean offset of about 2.2 kpc. The physical offsets of the bursts without extended emission, but with precise afterglow positions (051221, 060313, and 061201) are 2.0, 2.3, and 14.2 or 32.5 kpc, respectively. The two events with no extended emission and with

XRT positions (050509b and 051210) have offsets of about 54 ± 12 and 28 ± 23 kpc, respectively. If we include the ground-based sample with optical afterglow positions (see §2.4), we find that the bursts with apparent extended emission (070714b, 071227, 080513, and 090510; Barbier et al. 2007; Sakamoto et al. 2007a; Ukwatta et al. 2009; Perley et al. 2009a) have offsets of $\lesssim 4$, 14.8, ~ 20, and ~ 5.5 kpc, while the bursts without extended emission (070724 and 070809) have offsets of 4.8 and ~ 6.5 kpc. Thus, based on the sample of events with sub-arcsecond positions we find that 6/8 bursts with extended emission have offsets of $\lesssim 5$ kpc and 2/8 have likely offsets of $\sim 15 - 20$ kpc. In the sample without extended emission we find that 4/5 have offsets of $\lesssim 6$ kpc and 1/5 has a likely offset of $\sim 14 - 32$ kpc. Thus, we conclude that there is no significant difference in the two offset distributions.

The inclusion of events with only XRT positions does not change this conclusion. In particular, of the subset with no extended emission only GRB 050509b is likely to have a significant offset, while GRBs 051210, 060801, and 070429b have offsets (28 ± 23, 19 ± 16, and 40 ± 48 kpc, respectively) that are consistent with zero. Similarly, GRB 061210 with extended emission has an offset of 11 ± 10 kpc. An examination of the sample of Troja et al. (2008b) reveals that their claim that short GRBs without extended emission have systematically larger offsets rests on four events in particular: GRBs 050509b, 060502b, 061217, and 061201. As noted above, GRBs 050509b and 061201 indeed appear to have substantial offsets[14], but so do GRBs 071227 and 080503 with extended emission and offsets of about $15 - 20$ kpc. Next, the large offset for GRB 060502b relies on its claimed

[14]We note that Troja et al. (2008b) assume that the host of GRB 061201 is the galaxy at $z = 0.111$ at an offset of about 32 kpc. However, as we have shown here based on the *HST* observations (Appendix 2.8.2), there is a fainter potential host at a smaller offset.

association with an elliptical galaxy 70 ± 16 kpc from the XRT position (Bloom et al. 2007). However, the XRT error circle contains additional galaxies with negligible offsets (Berger et al. 2007b). Finally, we note that the offset for GRB 061217 is unreliable due to a substantial discrepancy of about $33''$ in the XRT positions from Butler (2007) and Evans et al. (2009). A continued investigation of the difference between short GRBs with and without extended emission will greatly benefit from the use of host-normalized offsets.

2.6.3 Light Distribution

In addition to projected offsets relative to the host center, we find that the locations of the short GRBs with *HST* imaging and sub-arcsecond positions are more diffusely distributed relative to their host light than long GRBs. In particular, we find that short GRB positions under-represent their host light, even in comparison to core-collapse and Type Ia SNe. This result is likely an upper limit on the brightness of short GRB locations since only the subset of events with optical afterglow positions can be studied with this approach. Thus, short GRBs arise from a population of events with a more diffuse distribution than massive stars and Type Ia SN progenitors. This result also indicates that the bulk of the progenitors of long and short GRBs cannot both be magnetars.

There are currently 10 known short GRBs with optical afterglows for which *HST* observations will enable a similar analysis. This is twice the number of the current sample, and we can therefore make significant progress in understanding the relation of short GRB environments to the overall distribution of light in their host galaxies with future observations.

2.7 Conclusions

We presented the first comprehensive analysis of short GRB *HST* observations, and used these data to extract the morphological properties of the host galaxies, the projected physical and host-normalized GRB offsets, and the brightness at the location of the bursts relative to the overall light distribution of their hosts. The main conclusions of our analysis are as follows:

- The majority of short GRB hosts are consistent with or have exponential surface brightness profiles, typical of late-type galaxies. This conclusion is in good agreement with results from spectroscopic observations that reveal star formation activity in $\sim 3/4$ of short GRB hosts (Berger 2009).

- The host galaxies of short GRBs are on average larger by about a factor of 2 than the hosts of long GRBs.

- The observed short GRB offset distribution extends from ~ 1 to 50 kpc, with a median of about 5 kpc. Including the short GRBs with only γ-ray or X-ray positions, we find that $\gtrsim 25\%$ of all events have offsets of $\lesssim 10$ kpc, and $\gtrsim 5\%$ have offsets of $\gtrsim 20$ kpc. A additional, though softer, limit is that $\gtrsim 50\%$ have offsets of $\lesssim 30$ kpc.

- The observed physical offset distribution and the robust constraints compare favorably with the predicted distribution for NS-NS binaries. However, they do not rule out at least a partial contribution from other progenitors systems such as WD-WD binaries.

- We find no convincing evidence that short GRBs with extended emission have

smaller physical offsets than those without extended emission. In both sub-samples we find examples of both small offsets ($\sim$ few kpc) and possibly large offsets (tens of kpc).

- The distribution of host-normalized offsets for the subset of short GRBs with *HST* observations is nearly identical to that of long GRBs. This is due to the systematically larger size of short GRB hosts, and indicates that a comparison with long GRBs and progenitor models will benefit from the use of host-normalized (rather than physical) offsets.

- The locations of short GRBs with sub-arcsecond positions and *HST* imaging under-represent the overall light distribution of their hosts, but less so in the red. This result differs substantially from long GRBs, core-collapse SNe, and even Type Ia SNe.

The results derived in this paper are based mainly on a small sample of short GRBs (9 events) from 2005-2006. Seven of these objects have precise positions based on optical afterglow detections. Ten additional events with precise afterglow positions, and a similar number with XRT positions (some of which with identified hosts), are now available for a similar study. It is essential to observe this existing sample, as well as new events from *Swift* and *Fermi*, with the refurbished *HST* using the ACS and WFPC3 instruments. In conjunction with constraints on the progenitor population from the redshift distribution (Berger et al. 2007b) and spectroscopic studies of the host galaxies (Berger 2009), the continued use of high angular resolution imaging will provide crucial insight into the nature of the progenitors and the potential for multiple populations.

2.8 Appendix

2.8.1 The Host Galaxy of GRB 060313

We present the first host galaxy association for GRB 060313, using *HST*/ACS observations in the F475W and F775W filters. The offset between the GRB position (determined from Gemini-South observations; Berger et al. 2007b) and the galaxy center is about $0.32''$ (Table 3.2). The galaxy brightness is $m(\mathrm{F475W}) = 26.4$ AB mag and $m(\mathrm{F775W}) = 25.6$ AB mag (Table 2.1). The probability of chance coincidence at this offset and galaxy brightness is only about 3×10^{-3} (Beckwith et al. 2006). We thus conclude that this galaxy is the likely host of GRB 060313.

2.8.2 Possible Host Galaxies of GRB 061201

The *HST* observations of GRB 061201 and its environment are shown in Figure 2.10. We explore two possibilities for the host galaxy. First, the burst is located $16.2''$ (32.5 kpc) from a relatively bright galaxy at $z = 0.111$ (marked "A" in Figure 2.10; Berger 2006a; Stratta et al. 2007), for which we measure $m(\mathrm{F606W}) = 18.17$ and $m(\mathrm{F814W}) = 17.82$ AB mag. Second, we identify from the *HST*/ACS observations a second, fainter galaxy (marked "B" in Figure 2.10) located $1.8''$ from the GRB position, and with $m(\mathrm{F606W}) = 25.34$ and $m(\mathrm{F814W}) = 25.03$ AB mag. The redshift of this galaxy is not known, but assuming $z \gtrsim 1$ the inferred projected offset is 14.2 kpc. The probability of chance coincidence for both galaxies is about 20% (Beckwith et al. 2006). We therefore do not claim a unique host galaxy association for this burst, and stress that both galaxies should be considered as potential hosts. Deeper *HST* observations may

also uncover an underlying host.

2.8.3 Possible Host Galaxies of GRB 060502b

The *HST* observations of GRB 060502b and its environment are shown in Figure 2.8. Previously, Bloom et al. (2007) claimed that the host is likely an early type galaxy at $z = 0.287$ located about 70 kpc away from the burst XRT position. These authors also note the presence of fainter objects within the XRT error circle. A galaxy with $R \approx 25.2$ mag was also found by Berger et al. (2007b). In the combined *HST*/ACS/F814W we find 6 faint galaxies within the XRT error circles of GRB 060502b (Figure 2.8). These galaxies have the following AB magnitudes: 27.5 (B), 25.9 (C), 27.2 (D), 26.1 (E), 24.8 (F), 25.7 (G). The probability of chance coincidence for these galaxies within the XRT error circles is of the order of unity.

Chapter 3

The Locations of Short Gamma-ray Bursts as Evidence for Compact Object Binary Progenitors

W. Fong & E. Berger

The Astrophysical Journal, Vol. 776, No. 18, 2013

Abstract

We present a detailed investigation of *Hubble Space Telescope* rest-frame UV/optical observations of 22 short gamma-ray burst (GRB) host galaxies and sub-galactic environments. Utilizing the high angular resolution and depth of *HST* we characterize the host galaxy morphologies, measure precise projected physical and host-normalized offsets between the bursts and host centers, and calculate the locations of the bursts with respect to their host light distributions (rest-frame UV and optical). We calculate a median short GRB projected physical offset of 4.5 kpc, about 3.5 times larger than that for long GRBs, and find that $\approx 25\%$ of short GRBs have offsets of $\gtrsim 10$ kpc. When compared to their host sizes, the median offset is 1.5 half-light radii (r_e), about 1.5 times larger than the values for long GRBs, core-collapse supernovae, and Type Ia supernovae. In addition, $\approx 20\%$ of short GRBs have offsets of $\gtrsim 5r_e$, and only $\approx 25\%$ are located within $1r_e$. We further find that short GRBs severely under-represent their hosts' rest-frame optical and UV light, with $\approx 30-45\%$ of the bursts located in regions of their host galaxies that have no detectable stellar light, and $\approx 55\%$ in the regions with no UV light. Therefore, short GRBs do not occur in regions of star formation or even stellar mass. This demonstrates that the progenitor systems of short GRBs must migrate from their birth sites to their eventual explosion sites, a signature of kicks in compact object binary systems. Utilizing the full sample of offsets, we estimate natal kick velocities of $\approx 20-140$ km s^{-1}. These independent lines of evidence provide the strongest support to date that short GRBs result from the merger of compact object binaries (NS-NS/NS-BH).

3.1 Introduction

The environments of cosmic explosions and their locations within their hosts provide invaluable insight on the nature of their progenitors. For instance, the spatial locations of long gamma-ray bursts (GRBs; $T_{90} \gtrsim 2$ s; Kouveliotou et al. 1993) within their exclusively star-forming host galaxies are consistent with the expected distribution for massive stars in exponential disks (Bloom et al. 2002). The result is similar for core-collapse supernovae (SNe; Prieto et al. 2008), which are only found in spiral and irregular galaxies (van den Bergh et al. 2005; Hakobyan et al. 2008; Li et al. 2011), indicative of a young, massive star origin. In contrast, Type Ia SNe originate in both star-forming and elliptical galaxies (Oemler & Tinsley 1979; van den Bergh et al. 2005; Mannucci et al. 2005; Li et al. 2011), and their locations do not coincide with star-forming regions (Prieto et al. 2008; Wang et al. 2013), consistent with an evolved progenitor system.

Equally important to the spatial offsets are the locations of these transients with respect to the distribution of the underlying host galaxy light. Using *Hubble Space Telescope (HST)* observations, it has been shown that long GRBs are concentrated on the brightest ultra-violet (UV) regions of their host galaxies (Fruchter et al. 2006; Svensson et al. 2010), pointing to explosion sites within unusually bright star-forming regions. Similarly, core-collapse SNe tend to explode in bright UV regions within their hosts (Kelly et al. 2008; Svensson et al. 2010). In contrast, Type Ia SNe under-represent their hosts' rest-frame UV light, suggesting that they do not tend to occur in regions of star formation (Kelly et al. 2008; Wang et al. 2013), but may correlate with optical light, suggesting a dependence on stellar mass (Kelly et al. 2008; Wang et al. 2013) as

expected for their white dwarf progenitors.

For short GRBs ($T_{90} \lesssim 2$ s), several theoretical progenitor systems have been proposed, including NS-NS/NS-BH mergers (Eichler et al. 1989; Narayan et al. 1992), accretion-induced-collapse of a WD or NS (Qin et al. 1998; Levan et al. 2006a; Metzger et al. 2008a) and magnetar flares (Levan et al. 2006a; Chapman et al. 2008). Studies of the short GRB host galaxy demographics have shown that $\approx 1/4$ of these events explode in elliptical galaxies with no signs of star formation (Fong et al. 2013), but the majority occur in star-forming galaxies (Berger 2009; Fong et al. 2013). The inferred progenitor ages are $\approx 0.1-$few Gyr (Leibler & Berger 2010; Fong et al. 2013), pointing to an origin from older stellar populations.

In Fong et al. 2010, we used *HST* observations of ten short GRB host galaxies to study their sub-galactic environments. For the seven bursts with sub-arcsecond localizations, and thus robust associations to a host galaxy, we constrained their host morphologies, spatial and host-normalized offsets, light distributions, and compared these results to the distributions for long GRBs. We found spatial offsets that are five times greater than those for long GRBs, but with a similar median host-normalized offset of ≈ 1 half-light radius. In addition, we found preliminary evidence that short GRBs under-represent their hosts' rest-frame optical and UV light, in stark contrast to long GRBs and core-collapse SNe. Due to the small number of events, the light distribution results were only suggestive, and not statistically significant. Separately, we also used *HST* data to study an emerging population of bursts with no obvious coincident host galaxy to optical limits of $\gtrsim 26$ mag and found that these bursts likely have large offsets of $30 - 100$ kpc from their hosts (Berger 2010a).

These initial studies demonstrate that *HST* observations are essential for characterizing the local environments of short GRBs, and thus their progenitors. The angular resolution is important in measuring precise offsets and locating the afterglow to sub-pixel precision, critical to analyzing the placement within the host light distributions. In addition, the depth of *HST* allows for the potential detections of faint coincident host galaxies, surpassing the capabilities of ground-based instuments in the optical and and near-infrared.

Expanding on this initial work, we present here *HST* observations of 16 additional short GRB host galaxies, 15 of which have sub-arcsecond positions. We describe the data reduction procedures, including photometry, astrometry, surface brightness profile fits, offsets and fractional flux determination in Section 3.2. We combine the results with those from Fong et al. (2010) and analyze the entire sample of 22 events in Section 3.3. Finally, in Section 8.5, we consider the implications for the progenitor systems

Throughout the paper we use the standard cosmological parameters, $H_0 = 71$ km s^{-1} Mpc^{-1}, $\Omega_m = 0.27$, and $\Omega_\Lambda = 0.73$. All reported magnitudes are corrected for Galactic extinction using dust maps (Schlafly & Finkbeiner 2011) and are calibrated to the AB magnitude system.

Table 3.1. *HST* Observations of Short GRB Host Galaxies

GRB	RA (J2000)	Dec (J2000)	Uncert. ($''$)	z	Instrument	Filter	Date (UT)	Exp. Time (s)	AB mag[a]	A_λ (mag)
061201	$22^h08^m32.13^s$	$-74°34'47.05''$	0.12	0.111?	WFC3/IR	F160W	2012 Jun 11	6397	$> 26.4/18.63 \pm 0.01$ / 24.46 ± 0.03[b]	0.039
070429B	$21^h52^m03.81^s$	$-38°49'42.0''$	1.5[c]	0.9023	WFC3/IR	F160W	2010 Apr 26	2797	20.59 ± 0.03	0.012
					WFC3/UVIS	F475W	2010 Apr 26	2797	24.31 ± 0.20	0.096
070707	$17^h50^m58.59^s$	$-68°55'27.59''$	0.16	< 3.6	WFC3/IR	F160W	2010 Jun 24	6397	26.16 ± 0.24	0.035
					ACS	F606W	2010 Jun 30	5644	26.68 ± 0.12	0.177
070714B	$03^h51^m22.28^s$	$+28°17'51.75''$	0.20	0.923	WFC3/IR	F160W	2009 Aug 16	2798	22.99 ± 0.02	0.069
					WFC3/UVIS	F475W	2009 Aug 16	2698	24.89 ± 0.06	0.467
070724A	$01^h51^m14.10^s$	$-18°35'39.28''$	0.08	0.4571	WFC3/IR	F160W	2011 Oct 3	2396	19.89 ± 0.02	0.006
070809	$13^h35^m04.55^s$	$-22°08'30.8''$	0.40	0.473?	WFC3/IR	F160W	2010 May 5	5597	$> 26.2/18.22 \pm 0.01$[d]	0.041
					ACS	F606W	2009 Aug 9	5150	$> 28.1/20.47 \pm 0.03$[d]	0.210
071227	$03^h52^m31.25^s$	$-55°59'02.63''$	0.22	0.381	WC3/IR	F160W	2010 Jun 11	2797	18.73 ± 0.01	0.006
					WFC3/UVIS	F438W	2010 Jun 12	2900	22.35 ± 0.05	0.042
080503	$19^h06^m28.77^s$	$+68°47'35.32''$	0.14	< 4.2	WFC3/IR	F160W	2011 Dec 26	5597	$> 26.2/25.84 \pm 0.07$[d]	0.028
080905A	$19^h10^m41.74^s$	$-18°52'47.44''$	0.18	0.1218	WFC3/IR	F160W	2011 Oct 16	2397		
					WFC3/IR	F160W	2012 Apr 14	2397	25.97 ± 0.11[e,f]	0.014
					WFC3/UVIS	F814W	2012 Apr 14	2600	> 27.5[f]	0.040
					WFC3/UVIS	F606W	2012 Apr 14	2600	27.29 ± 0.14[f]	0.066
090305A	$16^h07^m07.59^s$	$-31°33'22.12''$	0.20	< 4.1	WFC3/IR	F160W	2012 Feb 22	5597	25.20 ± 0.10	0.092
090426	$12^h36^m18.05^s$	$+32°59'09.42''$	0.12	2.609	WFC3/IR	F160W	2011 Oct 28	2397	25.56 ± 0.07	0.008

Table 3.1—Continued

GRB	RA (J2000)	Dec (J2000)	Uncert. ($''$)	z	Instrument	Filter	Date (UT)	Exp. Time (s)	AB mag[a]	A_λ (mag)
090510	$22^h14^m12.53^s$	$-26°34'59.0''$	0.20	0.903	WFC3/IR	F160W	2011 Oct 11	2397	21.79 ± 0.01	0.009
090515	$10^h56^m36.10^s$	$+14°26'29.37''$	0.16	0.403?	WFC3/IR	F160W	2011 Oct 24	5597	$> 26.1/18.42 \pm 0.02$[d]	0.001
091109B	$07^h30^m56.61^s$	$-54°05'23.11''$	0.16	< 4.4	WFC3/IR	F160W	2012 Feb 26	5596	$> 25.0/19.74 \pm 0.03$[d]	0.075
100117A	$00^h45^m04.65^s$	$-01°35'41.99''$	0.16	0.915	WFC3/IR	F160W	2011 Sep 29	2397	21.37 ± 0.04	0.011
130603B	$11^h28^m48.17^s$	$+17°04'18.03''$	0.09	0.3564	WFC3/IR	F160W	2013 Jun 13	2612	19.83 ± 0.02	0.012
					ACS	F606W	2013 Jun 13	2216	21.08 ± 0.04	0.057

Note. — [a] Corrected for Galactic extinction, A_λ (Schlafly & Finkbeiner 2011).

[b] For GRB 061201, we report the 3σ limit on a coincident host galaxy, photometry for "G1" and for "G2", respectively.

[c] 1σ positional error radius from *Swift*/XRT (Goad et al. 2007; Evans et al. 2009)

[d] For GRBs 070809, 080503, 090515 and 091109B, we report both the 3σ limit on a coincident host galaxy and the magnitude of the galaxy with the lowest probability of chance coincidence.

[e] To attain a higher signal-to-noise ratio, photometry is reported for the 2011 October 16 and 2012 April 14 observations combined.

[f] The position of "G1" is contaminated with saturated stars, so photometry is reported here only for "G2". The F814W limit corresponds to 3σ.

3.2 Data Reduction

3.2.1 Sample

We study *HST* observations of 16 short GRB host galaxies and environments obtained with the Advanced Camera for Surveys (ACS/WFC) and the infrared and ultraviolet-visual channels on the Wide-Field Camera 3 (WFC3/IR and WFC3/UVIS). The data were obtained as part of programs 11669 and 12502 (PI: Fruchter), which targeted all short GRBs with optical positions from April 2007 to January 2010, and the Director's Discretionary Time program 13497 (PI: Tanvir) for GRB 130603B. We combine these public *HST* data with ground-based observations of optical afterglows to astrometrically locate the burst positions within the host galaxies.

Ten of the 16 bursts have apparent host galaxies based on ground-based imaging (GRBs 070429B, 070707, 070714B, 070724A, 071227, 080905A, 090426A, 090510, 100117A, and 130603B), and all of these except GRB 070707 have spectroscopic redshifts (Cenko et al. 2008; Piranomonte et al. 2008; Berger et al. 2009; D'Avanzo et al. 2009; Graham et al. 2009; Kocevski et al. 2010; Levesque et al. 2010; McBreen et al. 2010; Rowlinson et al. 2010a; Fong et al. 2011; Cucchiara et al. 2013). We note that for GRB 080905A, the host association is less secure (probability of chance coincidence, $P_{cc}(< \delta R) \approx 0.01$) than the remaining bursts with $P_{cc}(< \delta R) \approx 10^{-4} - 10^{-3}$ (Fong et al. 2013 and Section 3.3.1), due to the large separation from its claimed host galaxy (Rowlinson et al. 2010a). All of these hosts (except GRB 070429B) have reported near-infrared (NIR) detections or limits (Piranomonte et al. 2008; Berger et al. 2009; Graham et al. 2009; Leibler & Berger 2010; Levesque et al. 2010; Rowlinson et al. 2010a;

Fong et al. 2011; Berger et al. 2013a; Tanvir et al. 2013a).

The remaining six short GRBs have no known coincident host galaxies to optical limits of $\gtrsim 26$ mag from previous ground-based or previous *HST* observations (GRBs 061201, 070809, 080503, 090305A, 090515, and 091109B; Perley et al. 2008, 2009a; Berger 2010a; Fong et al. 2010; Rowlinson et al. 2010b; Levan et al. 2009). These events have been termed "host-less", but appear to have host galaxies at separations of $\approx 30 - 100$ kpc with low probability of chance coincidence (Berger 2010a).

With the exception of GRB 130603B (Berger et al. 2013a; Tanvir et al. 2013a), all of the *HST* observations presented here have not been published in the literature thus far. The results in this work, combined with the *HST* data from Fong et al. (2010), GRB 080503 (Perley et al. 2009a; Berger 2010a), and GRB 130603B (Berger et al. 2013a; Tanvir et al. 2013a), comprise the full available sample of short GRB hosts with *HST* observations. Details of the GRB properties and the observations are provided in Table 3.1.

3.2.2 Image Processing

We retrieved pre-processed images for the 16 short GRBs from the *HST* archive[1]. We apply distortion corrections and combine the individual exposures using the `astrodrizzle` package in PyRAF (Gonzaga et. al. 2012). For the ACS images we use `pixfrac` = 1.0 and `pixscale` = 0.05″ pixel^{-1}. For the WFC3/IR images, we use the recommended values of `pixfrac` = 1.0 and `pixscale` = 0.0642″ pixel^{-1}, half of

[1]http://archive.stsci.edu/hst/.

the native pixel scale, while for the WFC3/UVIS images, we use `pixscale` $= 0.033''$ pixel^{-1}. The final drizzled images are shown for ten events with established host galaxies (Figure 3.1), multi-band observations of GRB 080905A (Figure 3.2) and five events termed as "host-less" (Figure 3.3).

We obtained public optical/NIR afterglow discovery images for each burst. These images are from the UV-Optical Telescope (UVOT) on-board the *Swift* satellite, the twin 6.5-m Magellan telescopes, the Gemini-North and South 8-m telescopes, and the 8-m Very Large Telescope (VLT). The telescope and instrument for each afterglow image is listed in Table 3.2. For the observations from Magellan, Gemini, and VLT, we use standard IRAF tasks to process the data. For GRBs 070429B and 070714B, which have reported UVOT afterglows (Holland et al. 2007; Landsman et al. 2007), we use the `uvotimsum` task as part of the HEASOFT package to create co-added images for each of the seven UVOT filters.

We confirm the afterglow detection of GRB 070714B in multiple filters (Landsman et al. 2007). For GRB 070429B, the afterglow is reported to be weak (3.9σ) and detectable only by combining the data from all filters at $\delta t \approx 600 - 2660$ s. To assess whether this is a real detection, we combine the UVOT observations in the same manner as described in Holland et al. (2007), but we do not detect any source at the reported position, nor within the XRT error circle. We therefore do not consider the reported afterglow to be real, and use the XRT position (Table 3.1) in our analysis presented here.

3.2.3 Photometry

We perform aperture photometry for the galaxy with the lowest probability of chance coincidence in each field (see Section 3.3.1) using standard tasks in IRAF and the tabulated zeropoints for ACS, WFC3/IR and WFC3/UVIS calibrated to the AB magnitude system (Table 3.1). In addition, for the bursts previously termed as "host-less" (GRBs 061201, 070809, 080503, 090515, and 091109B; Figure 3.3), we determine the 3σ limit at the afterglow position.

We note that for GRB 080905A, we can only perform photometry for "G2", because "G1", claimed to be the host galaxy by Rowlinson et al. (2010a), is contaminated by foreground saturated stars which we cannot reliably subtract (Figure 3.2). The position of GRB 090305A, which was previously reported to have no coincident host to $r \gtrsim 25.6$ mag (Berger 2010a), coincides with an extended NIR source with $m_{\rm F160W} = 25.20 \pm 0.10$ mag which we consider to be the host galaxy (Figure 3.1; Section 3.3.1). For GRB 090426A, we consider the host galaxy to be the source directly coincident with the afterglow position (Figure 3.1; Section 3.3.1), previously reported to be a "compact knot" within a multi-component host galaxy complex from ground-based observations (Antonelli et al. 2009a; Levesque et al. 2010). For GRB 091109B, for which a host galaxy has not been previously reported, the afterglow position is contaminated by a diffraction spike from a nearby star (Figure 3.3). We perform photometry at the afterglow position using an aperture radius of $2.5\theta_{\rm FWHM}$, and place a 3σ limit of $m_{\rm F160W} \gtrsim 25$ mag on a coincident host galaxy. We note that this NIR limit is substantially shallower than the 3σ limit of the image, $\gtrsim 26$ mag. Finally, the F160W observation of GRB 130603B has additional flux from a point source at the optical afterglow position that is not part of the host

galaxy (Berger et al. 2013a; Tanvir et al. 2013a). We perform point spread function (PSF) subtraction of the point source as described in Berger et al. (2013a) and calculate the host photometry from the PSF-subtracted image (Figure 3.1).

The photometry for all events, as well as 3σ upper limits for "host-less" events are listed in Table 3.1. All of our values are consistent with those published in the literature from ground-based data except for GRB 070714B, where we calculate $m_{\rm F160W} = 22.99 \pm 0.11$ mag while the previously published value is $H = 23.58 \pm 0.20$ mag (Graham et al. 2009).

3.2.4 Absolute Astrometry

To determine the position of each short GRB afterglow, we perform absolute astrometry using point sources in common between the afterglow discovery images and source catalogs (2MASS, SDSS, or USNO-B depending on availability). If the position of the afterglow is contaminated by host galaxy light in the discovery image, we perform image subtraction using the ISIS package (Alard 2000) relative to late-time observations when the afterglow contribution is negligible. We then use `SExtractor`[2] to determine the afterglow position in the subtracted image. To determine the astrometric tie from the ground-based image to the catalog, we use the IRAF astrometry routine `ccmap` and find that a second-order polynomial with six free parameters corresponding to a shift, scale, and rotation in each coordinate, provides a robust tie in all cases with an average $\sigma_{\rm cat\rightarrow GRB} \approx 160$ mas. Our afterglow positions are consistent with published positions in all relevant cases, albeit with higher precision. In the cases of GRBs 070809 and 090510,

[2] `http://sextractor.sourceforge.net/`

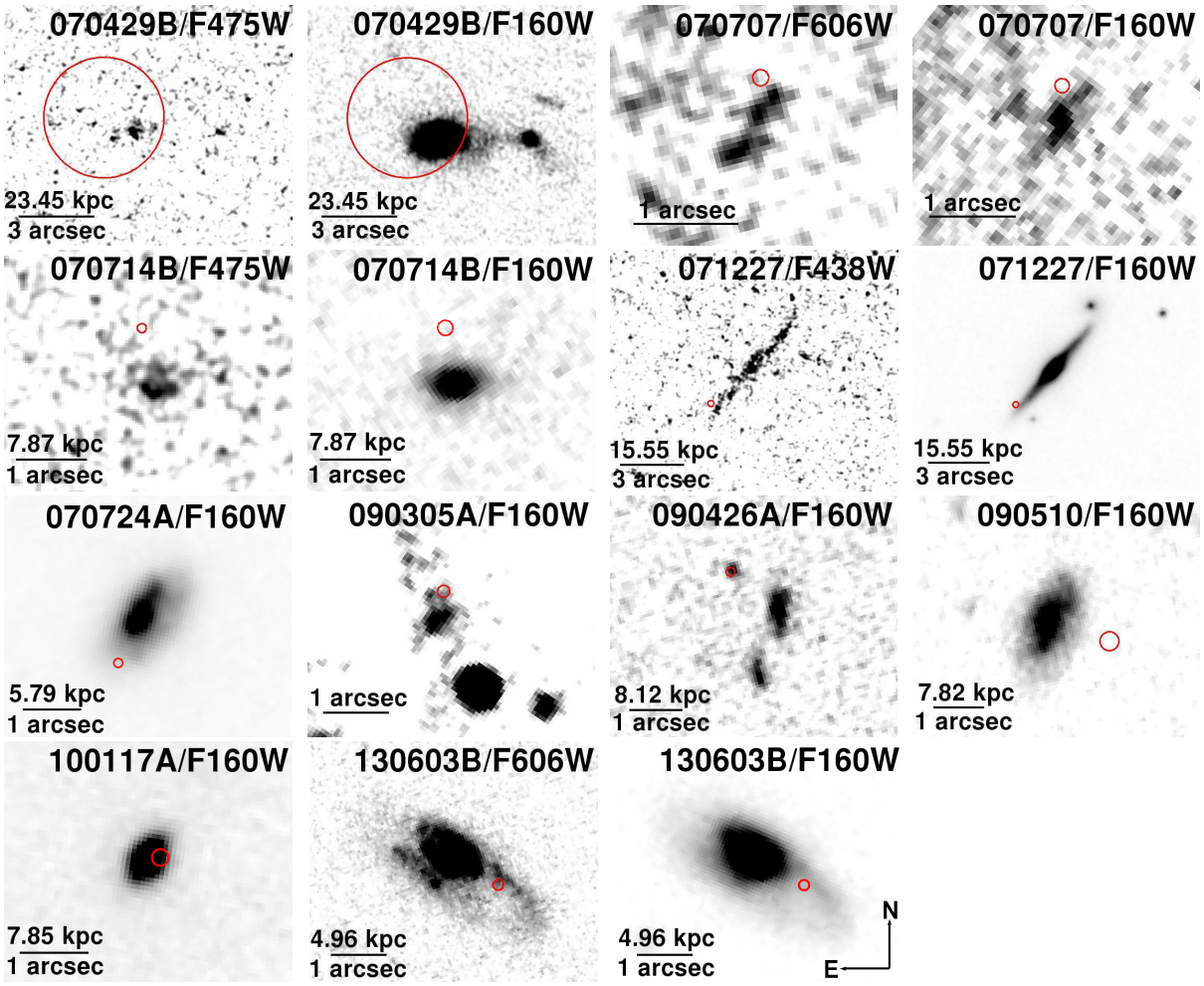

Figure 3.1.—: *HST* observations of ten short GRBs with robust associations to a host galaxy ($P_{cc}(< \delta R) \approx 10^{-4} - 10^{-3}$) based on previous ground-based observations. The afterglow positions are represented by a 3σ error circle in each frame, except for GRBs 070714B and 090510, where the afterglow positional uncertainties are larger, and the circles correspond to 1σ. For GRB 070429B, the position of the X-ray afterglow from *Swift*/XRT is shown (red circle; 90% containment, Goad et al. 2007; Evans et al. 2009). For GRB 130603B/F160W, the image after PSF subtraction of the point source associated with the GRB (see Section 3.2.3 and Berger et al. 2013a) is shown. All images are oriented with North up and East to the left.

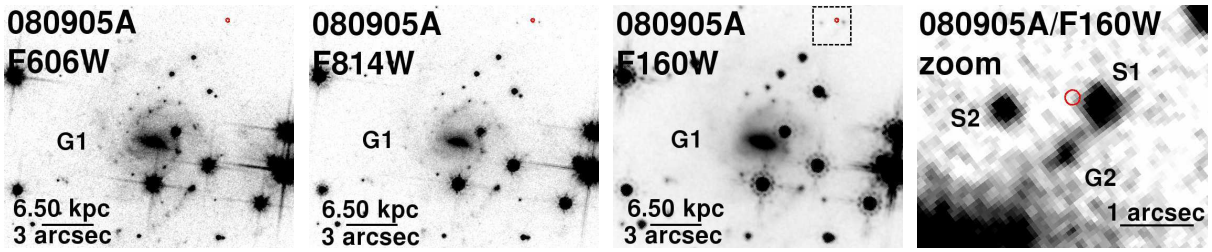

Figure 3.2.—: *HST* observations of GRB 080905A with the optical afterglow position (3σ; red circle) indicated. The face-on spiral galaxy at $z = 0.1218$, claimed as the host by Rowlinson et al. (2010a), is labeled as "G1" ($P_{cc}(< \delta R) \approx 0.01$) in each of the 3 filters, while a zoomed version of the F160W observation shows a new extended source, "G2" ($P_{cc}(< \delta R) \approx 0.08$), as well as two sources with stellar PSFs denoted as "S1" and "S2". All images are oriented with North up and East to the left.

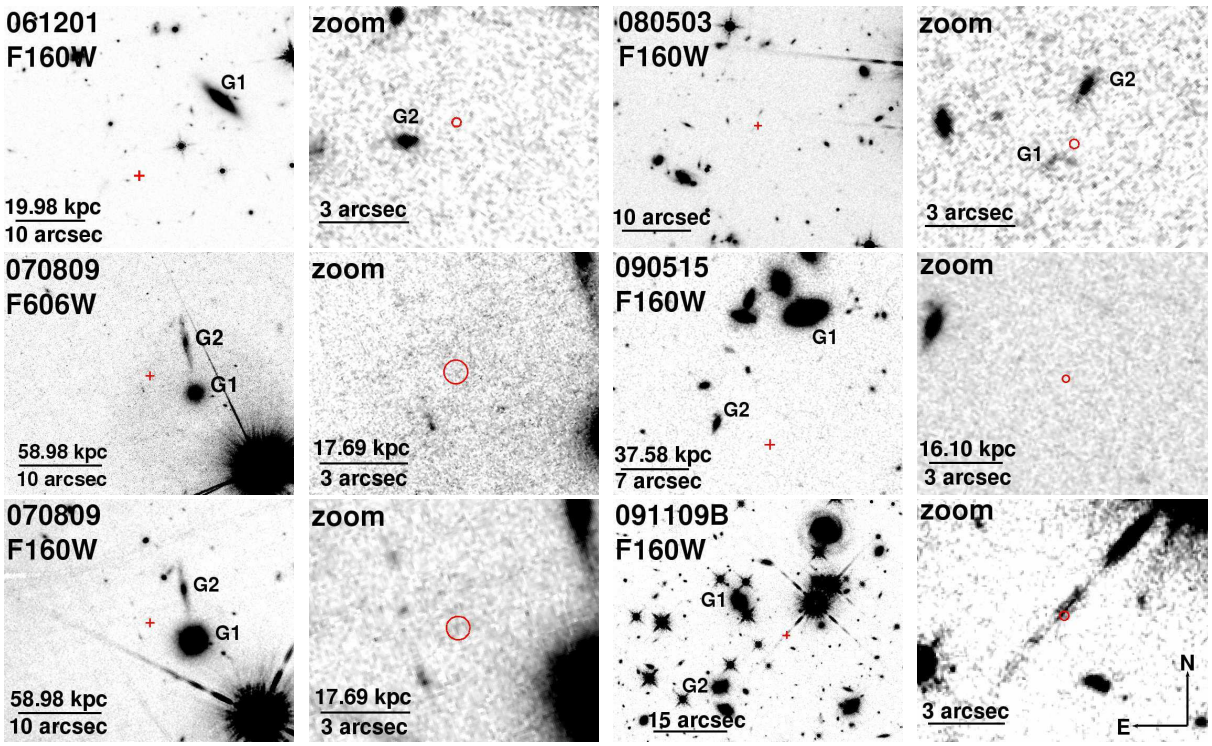

Figure 3.3.—: *HST* observations of 5 short GRBs with no coincident host galaxy to $m_{160\mathrm{W}} \gtrsim 26.2$ mag ("host-less" bursts). We note that the afterglow position of GRB 091109B is contaminated by a diffraction spike so we place a comparatively shallow limit on a coincident host galaxy of $m_{160\mathrm{W}} \gtrsim 25$ mag. The large-scale environments (left) and the 10″ surrounding the afterglow position (right) are shown for each burst. The most probable and second most probable host galaxies from probability of chance coincidence analysis are labeled ("G1" and "G2", respectively). The afterglow positions are shown by the red cross or error circle in each frame. Error circles are 5σ in radius except for GRB 070809, which is 1σ because the uncertainty is based on absolute astrometry. Physical scales in kpc are based on the redshift of "G1" for each burst, if known. All images are oriented with North up and East to the left.

Table 3.2. Short GRB Astrometry and Offsets

GRB	Instrument	Filter	z	Reference	No.	$\sigma_{\rm cat\rightarrow GRB}$ (mas)	$\sigma_{\rm GB\rightarrow HST}$ (mas)	$\sigma_{\rm GRB}$ (mas)	$\sigma_{\rm gal}$ (mas)	δRA ($''$)	δDec ($''$)	Offset ($''$)	Offset (kpc)	Offset (r_e)
061201	VLT/FORS2	I	0.111?	2MASS	17	115	···	17						
G1	WFC3	F160W		VLT	14	···	25	···	1	−11.82	11.14	16.25 ± 0.03	32.47 ± 0.06	14.91 ± 0.03
G2	WFC3	F160W		VLT	14	···	25	···	2	1.69	−0.62	1.80 ± 0.03	14.47 ± 0.24^a	6.43 ± 0.11
070429B	WFC3	F160W	0.902	USNO-B	4	150	···	1460	1.0	···	···	< 1.46	< 11.41	< 2.25
	WFC3	F475W		USNO-B	6	290	···	1460	1.0	···	···	< 1.46	< 11.41	··· ^{b}
070707	VLT/FORS1	R	< 3.6	2MASS	50	156	···	10						
	WFC3	F160W		VLT	76	···	26	···	4.3	−0.16	−0.01	0.40 ± 0.03	3.22 ± 0.24^a	1.11 ± 0.08
	ACS	F606W		VLT	97	···	24	···	12.5	−0.16	0.05	0.40 ± 0.03	3.22 ± 0.24^a	··· ^{b}
070714B	Swift/UVOT	*white*	0.923	2MASS	30	199	···	13						
	WFC3	F160W		Swift	6	···	110	···	1	−0.40	−1.50	1.55 ± 0.11	12.21 ± 0.87	4.56 ± 0.33
	UVIS	F475W		Swift	5	···	66	···	7	−0.40	−1.50	1.55 ± 0.07	12.21 ± 0.53	5.55 ± 0.24
070724A	Gemini-N/GMOS	i	0.4571	2MASS	6	81	···	13						
	WFC3	F160W		Gemini	32	···	22	···	1	−0.48	0.81	0.94 ± 0.03	5.46 ± 0.14	1.50 ± 0.04
070809	WFC3	F160W	0.473?	USNO-B	5	234	···	400	1	−5.18	−2.21	5.63 ± 0.46^c	33.22 ± 2.71	9.25 ± 0.75
	ACS	F606W		2MASS	7	220	···	400	2	−5.47	−2.10	5.86 ± 0.46^c	35.58 ± 2.71	9.29 ± 0.71
071227	VLT/FORS2	R	0.381	2MASS	11	214	···	22						
	WFC3	F160W		VLT	11	···	40	···	6	−2.11	2.11	2.98 ± 0.05	15.50 ± 0.24	3.28 ± 0.05
	UVIS	F438W		VLT	10	···	43	···	4	−2.02	1.83	2.72 ± 0.02	14.18 ± 0.25	··· ^{b}
080503	Gemini-N/GMOS	r	···	2MASS	22	139	···	10						
	WFC3	F160W		Gemini	58	···	29	···	9	0.72	−0.53	0.90 ± 0.03^c	7.24 ± 0.24^a	3.46 ± 0.12
080905A	VLT/FORS2	R	0.1218	2MASS	116	159	···	78						
G1	WFC3	F160W		VLT	46	···	41	···	1	4.34	−7.06	8.29 ± 0.08	17.96 ± 0.19	10.36 ± 0.10
G1	WFC3/UVIS	F814W		VLT	61	···	32	···	1	4.30	−7.07	8.28 ± 0.08	17.92 ± 0.19	10.35 ± 0.10
G1	WFC3/UVIS	F606W		VLT	102	···	34	···	1	4.34	−7.07	8.30 ± 0.09	17.97 ± 0.18	10.38 ± 0.11
G2	WFC3	F160W		VLT	46	···	41	···	13	0.07	−0.69	0.69 ± 0.09	5.55 ± 0.72^a	3.45 ± 0.45
G2	WFC3/UVIS	F606W		VLT	102	···	34	···	7	0.07	−0.79	0.79 ± 0.09	6.35 ± 0.72^a	3.97 ± 0.43

Table 3.2—Continued

GRB	Instrument	Filter	z	Reference	No.	$\sigma_{\rm cat\rightarrow GRB}$ (mas)	$\sigma_{\rm GB\rightarrow HST}$ (mas)	$\sigma_{\rm GRB}$ (mas)	$\sigma_{\rm gal}$ (mas)	δRA ($''$)	δDec ($''$)	Offset ($''$)	Offset (kpc)	Offset (r_e)
090305A	Gemini-S/GMOS	r	< 4.1	2MASS	122	198	···	6						
	WFC3	F160W		Gemini	115	···	31	···	5	0.09	−0.42	0.43 ± 0.03	3.46 ± 0.24^a	1.19 ± 0.08
090426	VLT/FORS2	R	2.609	SDSS	60	120	···	10						
	WFC3	F160W		VLT	9	···	29	···	4	−0.04	0.04	0.06 ± 0.03^d	0.45 ± 0.25	0.29 ± 0.14
090510	WFC3	F160W	0.903	USNO-B	7	370	···	200	2	1.24	0.45	1.33 ± 0.37	10.37 ± 2.89	1.99 ± 0.39^e
090515	Gemini-N/GMOS	r	0.403?	SDSS	109	160	···	15						
	WFC3	F160W		Gemini	61	···	22	···	1	−3.73	13.47	13.98 ± 0.03^c	75.03 ± 0.15	15.53 ± 0.03^e
091109B	VLT/FORS2	R	···	2MASS	20	154	···	28						
	WFC3	F160W		VLT	39		21	···	1	9.53	6.79	11.70 ± 0.03^c	94.07 ± 0.24	···
100117A	Gemini-N/GMOS	r	0.915	SDSS	95	154	···	26						
	WFC3	F160W		Gemini	21	···	33	···	1	0.16	0.03	0.17 ± 0.04	1.32 ± 0.33	0.57 ± 0.13^e
130603B	Magellan/IMACS	r	0.3564	SDSS	17	85	···	10						
	WFC3	F160W		Magellan	12	···	34	···	1	0.93	0.48	1.05 ± 0.04	5.21 ± 0.17	1.05 ± 0.04^e
	ACS	F606W		Magellan	9	···	34	···	1	0.93	0.58	1.09 ± 0.04	5.41 ± 0.17	1.36 ± 0.05^e

Note. — [a] We assume $z = 1$ to calculate these projected physical offsets.
[b] The r_e measurement is highly uncertain due to the low signal-to-noise ratio of the observation.
[c] Offsets are calculated for the galaxy with the lowest probability of chance coincidence.
[d] The offset is calculated relative to the source in direct coincidence with the burst position (Figure 3.1).
[e] Effective radii r_e representative of the combined inner and outer Sérsic components are used to compute offsets: GRB 090510: $0.95''$, GRB 090515: $0.9''$, GRB 100117A: $0.3''$, GRB 130603B/F160W: $1''$ and GRB 130603B/F606W: $0.8''$.

the afterglow discovery images are not available to us so we use the published positions and uncertainties in our analysis (Perley et al. 2007c; Nicuesa Guelbenzu et al. 2012b). The absolute afterglow positions and uncertainties are listed in Table 3.1.

3.2.5 Relative Astrometry and Offsets

To determine the position of each GRB relative to its host galaxy, and thus measure precise offsets, we perform relative astrometry by aligning each of the *HST* observations to the afterglow discovery images. We consider three sources of uncertainty: the afterglow position ($\sigma_{\rm GRB}$), the astrometric tie uncertainty between the ground-based and *HST* images ($\sigma_{\rm GB\rightarrow HST}$), and the host galaxy position ($\sigma_{\rm gal}$).

We measure $\sigma_{\rm GRB}$ from each afterglow image, where the centroiding accuracy depends on the size of the PSF and the signal-to-noise ratio of the afterglow detection using `SExtractor`, and find values of $\sigma_{\rm GRB} \approx 10 - 80$ mas (Table 3.2), except in the case of GRB 070429B which has an uncertainty of $1.5''$ (1σ) from the *Swift*/XRT detection of the afterglow. The second source of uncertainty is the astrometric tie between the afterglow and host galaxy *HST* images ($\sigma_{\rm GB\rightarrow HST}$), which is determined using the same method described in Section 3.2.4. We use a range of $5 - 120$ common point sources, depending on the depth of the image and source density and find values of $\sigma_{\rm GB\rightarrow HST} \approx 20 - 110$ mas. The number of astrometric tie objects and resulting RMS values are listed in Table 3.2. The final source of uncertainty is the centroiding accuracy of the host in the *HST* images. To determine this uncertainty we again use `SExtractor`, and find values of $\sigma_{\rm gal} \approx 1 - 13$ mas. This is generally the smallest source of uncertainty (Table 3.2).

For each galaxy/filter combination, we use the afterglow and host position to measure angular offsets, and for the galaxies with known redshifts we also calculate physical offsets (Table 3.2). We assume $z = 1$ for host galaxies without known redshift, taking advantage of the relatively flat value of the angular diameter distance at $z \gtrsim 0.5$. Finally, we use the effective radii, r_e, determined from surface brightness profile fits (Section 3.2.6 and Table 3.3) to calculate host-normalized offsets. The offsets and accompanying combined uncertainties are listed in Table 3.2. For GRBs 070809 and 090510, where we do not have the afterglow discovery images, we use the published uncertainties of $0.4''$ and $0.2''$, respectively (Perley et al. 2007c; Nicuesa Guelbenzu et al. 2012b), which dominate over all other sources of uncertainty.

3.2.6 Surface Brightness Profile Fitting

We use the IRAF/`ellipse` routine to generate elliptical intensity isophotes and construct one-dimensional radial surface brightness profiles for each galaxy/filter combination. For each observation, we allow the center, ellipticity, and position angle of each isophote to vary. In two cases (GRB 070707/F606W and GRB 071227/F438W), the isophotal fit does not converge, which can be attributed to the low signal-to-noise ratio of these observations. The surface brightness profiles are displayed in Figure 3.4.

Using a χ^2-minimization grid search, we fit each profile with a Sérsic model given by

$$\Sigma(r) = \Sigma_e \exp\{-\kappa_n[(r/r_e)^{1/n} - 1]\}, \tag{3.1}$$

where n is the concentration parameter ($n = 1$ is equivalent to an exponential

disk profile, while $n = 4$ is the de Vaucouleurs profile typical of elliptical galaxies), $\kappa_n \approx 2n - 1/3 + 4/405n + 46/25515n^2$ is a constant that depends on n (Ciotti & Bertin 1999), r_e is the effective radius, and Σ_e is the effective surface brightness in flux units. We convert Σ_e to units of mag arcsec^{-2}, designated as μ_e. In our grid search, n, r_e, and μ_e are the three free parameters. A single Sérsic component provides an adequate fit ($\chi^2_\nu \approx 0.4 - 1.5$) for most of the host galaxies. In four cases (GRBs 090510, 090515, 100117A, and 130603B) a single component fit yields $\chi^2_\nu \gtrsim 2$. To improve the fit for these cases, we use two separate Sérsic components corresponding to the inner and outer regions of each galaxy. The resulting values for n, r_e and μ_e are listed in Table 3.3. We do not perform a surface brightness fit for GRB 080905A/"G1" since it is contaminated by saturated foreground sources (Figure 3.2), but given the prominent spiral structure, the morphology of this host is likely characterized by a disk profile with $n \sim 1$, and we estimate the size of the bulge component to be $\approx 1.8''$ (≈ 3.9 kpc). The surface brightness profiles and resulting models are shown in Figure 3.4.

3.2.7 Host Light Distributions

To determine the brightness of the galaxy at the GRB location relative to the host light distribution, we follow the methodology of Fruchter et al. (2006), Kelly et al. (2008), and Fong et al. (2010), and calculate for each galaxy image the fraction of total light in pixels fainter than the afterglow position ("fractional flux"; Table 3.4). Eleven bursts have differential astrometric positions of better than one pixel (Table 3.2). If the afterglow position spans multiple pixels, we take the average brightness among those pixels to be the representative flux of the afterglow position. For each image, we create an intensity

Table 3.3. Short GRB Host Galaxy Morphological Properties

GRB	Filter	n	r_e ($''$)	r_e (kpc)	μ_e (AB mag arcsec^{-2})
061201/G1	160W	1.03	1.09	2.18	21.86
061201/G2	160W	0.73	0.28	2.25[a]	25.34
070429B	160W	2.15	0.65	5.08	23.61
	475W	1.54	0.08[b]	0.62	24.69
070707	160W	0.97	0.36	2.89[a]	27.01
070714B	160W	0.76	0.34	2.68	24.35
	475W	1.18	0.28	2.20	27.17
070724A	160W	0.92	0.63	3.64	22.16
070809	160W	3.03	0.61	3.59	21.47
	606W	3.38	0.65	3.83	23.64
071227	160W	1.05	0.91	4.72	21.64
080503	160W	0.32	0.26	2.09[a]	26.81
080905A/G1[c]	160W	≈ 1	≈ 1.8	≈ 3.9	$\cdots$
080905A/G2	160W	0.70	0.20	1.60[a]	25.72
090305A	160W	0.57	0.36	2.89[a]	25.96
090426A	160W	0.89	0.21	1.70	25.78
090510 ($a < 0.4''$)	160W	1.27	0.93	7.27	24.92
090510 ($a > 0.4''$)	160W	0.44	0.74	5.79	24.26
090515 ($a < 0.85''$)	160W	2.95	0.79	4.24	22.02
090515 ($a > 0.85''$)	160W	0.73	1.19	6.39	22.47
100117A ($a < 0.6''$)	160W	0.86	0.28	2.20	22.04
100117A ($a > 0.6''$)	160W	4.95	0.07	0.55	18.66
130603B ($a < 1''$)	160W	0.96	0.62	3.07	22.51
130603B ($a > 1''$)	160W	3.81	3.25	2.02	25.71
130603B ($a < 0.2''$)	606W	1.98	0.79	3.92	24.97
130603B ($a > 0.2''$)	606W	1.29	0.68	3.37	24.29

Note. — [a] Calculated assuming $z = 1$.

[b] Due to the low signal-to-noise ratio of this observation, this measurement likely corresponds to a smaller region within the galaxy, and not the entire galaxy itself.

[c] Although we cannot perform a surface brightness profile fit for GRB 080905A/"G1", these parameters are estimated from the apparent morphology and effective radius of the bulge component.

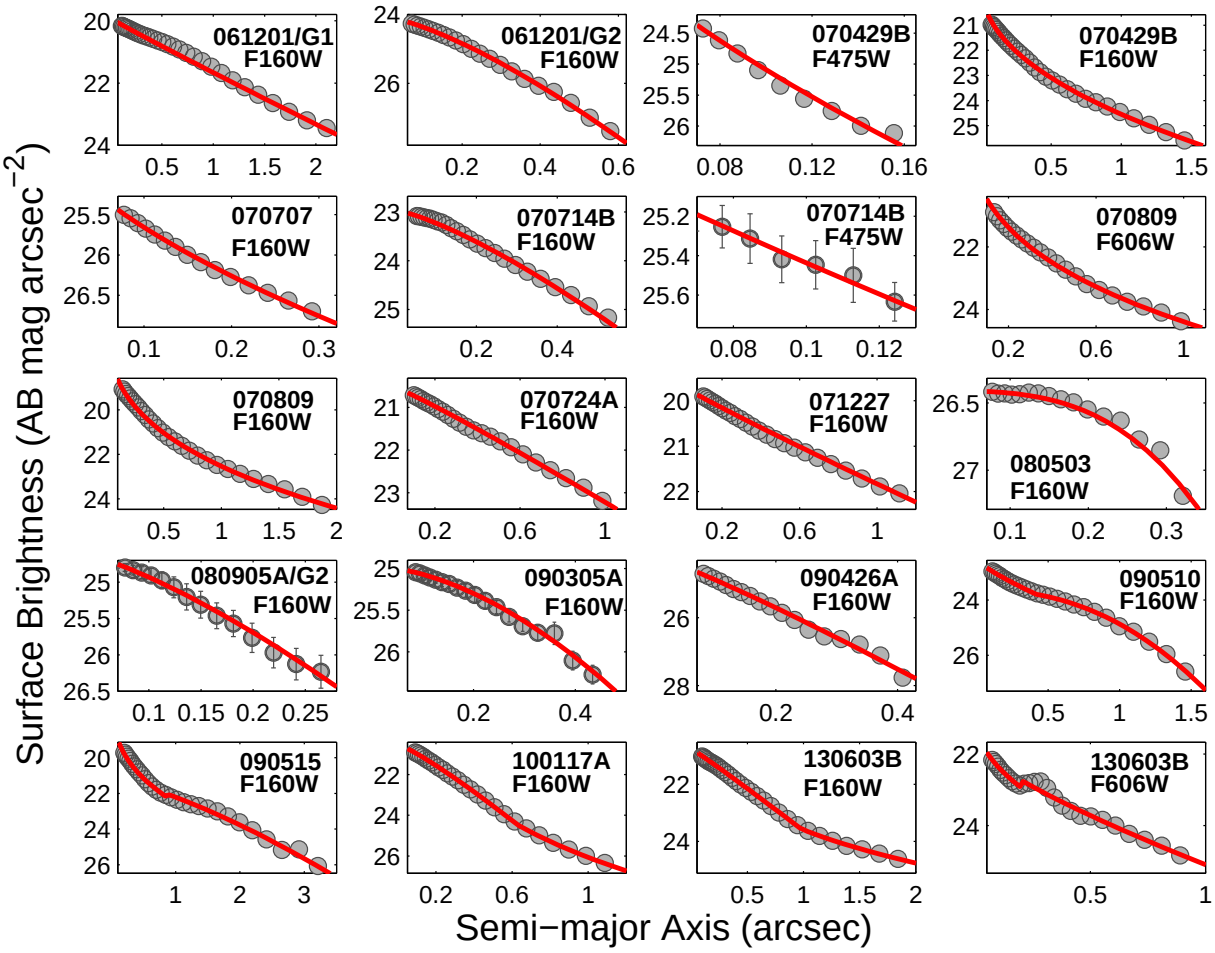

Figure 3.4.—: Radial surface brightness profiles as determined from IRAF/`ellipse` (grey circles) and the corresponding best-fit Sérsic models (red line) for 16 host galaxies. For GRBs 070809, 080503, and 090515, the surface brightness profile for the most probable host galaxy is shown while for GRB 061201, the profiles for both "G1" and "G2" are shown. For GRB 080905A, the profile is shown for the extended source closest to the afterglow position (Source "G2" in Figure 3.1).

histogram of a region centered on the host galaxy and determine a 1σ cut-off level for the host by fitting a Gaussian profile to the sky brightness distribution (equivalent to a signal-to-noise ratio cut-off of 1). We then plot the pixel flux distribution above the appropriate cut-off level for a region surrounding the host, and determine the fraction of light in pixels fainter than the afterglow pixel (see Table 3.4).

Table 3.4. Short GRB Fractional Flux

GRB	Instrument	Filter	1σ Fractional Flux
050709[a]	WFPC2	F450W	0
	ACS	F814W	0.09
050724[a]	WFPC2	F450W	0.03
	WFPC2	F814W	0.33
051221[a]	WFPC2	F555W	0.54
	WFPC2	F814W	0.65
060121[a]	ACS	F606W	0.41
060313[a]	ACS	F475W	0.04
	ACS	F775W	0
061006[a]	WFPC2	F555W	0.56
	ACS	F814W	0.63
061201[ab]	ACS	F606W	0
	ACS	F814W	0
	WFC3/IR	F160W	0
070707	WFC3/IR	F160W	0
	ACS	F606W	0
070714B	WFC3/IR	F160W	0
	WFC3/UVIS	F475W	0
070724A	WFC3/IR	F160W	0.23
070809[b]	WFC3/IR	F160W	0
	ACS	F606W	0
071227	WFC3/IR	F160W	0.19
	WFC3/UVIS	F438W	0
080503[b]	WFC3/IR	F160W	0
080905A	WFC3/IR	F160W	0
	WFC3/UVIS	F814W	0
	WFC3/UVIS	F606W	0
090305A	WFC3/IR	F160W	0.30
090426	WFC3/IR	F160W	0.82
090510	WFC3/IR	F160W	0
090515[b]	WFC3/IR	F160W	0
100117A	WFC3/IR	F160W	0.54
130603B	WFC3/IR	F160W	0.27
	ACS/606W	F606W	0.35

Note. — Fraction of host galaxy light in pixels fainter than the GRB position.

[a] From Fong et al. (2010).

[b] No coincident host to the depth of available *HST* imaging.

For GRBs 071227/F160W and 130603B/F606W, we mask sources contaminating the position of the galaxy and set these pixels to the brightness level of the surrounding pixels. We note that for GRB 080905A, we are unable to explicitly calculate the fractional flux with respect to "G1" due to the presence of saturated stars, while for GRB 061201 we cannot make a unique host association (Section 3.3.1). However, both of these bursts have afterglow locations at the level of the sky background, and thus have fractional flux values of zero regardless of their host associations. Table 3.4 also includes the values for seven bursts from Fong et al. (2010).

3.3 Analysis

3.3.1 Probabilities of Chance Coincidence

To assess the probability that each of the bursts originated from a coincident galaxy or from another galaxy in the field, we perform aperture photmetry for galaxies within the *HST* field of view, discarding noticeably fainter galaxies with increasing distance from the burst since these objects will have a lower probability of being the host galaxy. We then calculate the probability of chance coincidence, $P_{cc}(< \delta R)$ for each galaxy based on the distance from the burst position (δR) and apparent magnitude (m) (c.f., Bloom et al. 2002; Berger 2010a). For bursts at offsets of $< 1r_e$ (GRBs 090426 and 100117A), we use the effective size of the galaxy, $\delta R = r_e$, while for the remaining cases, we take δR to be the projected distance between the burst and candidate host center. For the bursts with previously established hosts (Figure 3.1), we find $P_{cc}(< \delta R) \approx 10^{-4} - 10^{-3}$, consistent with ground-based results (Fong et al. 2013); the next probable hosts have values at least

one order of magnitude greater, with $P_{cc}(< \delta R) \approx 0.02 - 0.30$. The lowest value of 0.02 is for GRB 090426A, which has two galaxies within $1''$ of the optical afterglow position, in addition to the source at the GRB position. From previous ground-based observations, these sources were considered to comprise a single host galaxy complex (Antonelli et al. 2009b; Levesque et al. 2010). However, given the lack of apparent interaction between these sources in the *HST* image (see Figure 3.1) and the comparatively low value of $P_{cc}(< \delta R) \approx 10^{-4}$ for the source at the afterglow position, we consider the latter to be the host galaxy. For GRB 080905A/"G1" (Figure 3.2), we are unable to accurately determine the brightness in any of the filters due to the presence of foreground saturated stars, but using $R \sim 18$ mag determined from Rowlinson et al. (2010a) and our offset of $8.3''$, we find that "G1" has $P_{cc}(< \delta R) \approx 0.01$, while "G2" has $P_{cc}(< \delta R) \approx 0.08$. Therefore, "G1" is the more likely host galaxy, although this case is less clear than the other previously established host associations at small offsets.

For bursts with no obvious host galaxy at small offsets from previous ground-based or *HST* observations (Figure 3.3), termed "host-less" (GRBs 061201, 070809, 080503, 090305A, 090515: Berger 2010a; 091109B: Levan et al. 2009), we calculate a range of probabilities, $P_{cc}(< \delta R) \approx 6 \times 10^{-3} - 0.08$. The associations are most robust for GRBs 070809 and 090305A with the most probable hosts at offsets of $5.7''$ ($P_{cc}(< \delta R) \approx 6 \times 10^{-3}$) and $0.43''$ ($P_{cc}(< \delta R) \approx 7 \times 10^{-3}$), respectively. The host association for GRB 070809 is the same as that made in Berger (2010a), although here we calculate a lower probability of chance coincidence by a factor of three. We note that the extended source we associate with GRB 090305A was not detected in ground-based observations to $r \gtrsim 25.6$ mag (Berger 2010a). Due to the low probability of chance coincidence and the lack of more likely host galaxy candidates in the *HST* observation,

we consider this to be the host galaxy. We calculate moderate probabilities of ≈ 0.05 for GRBs 080503 and 090515, with the most probable hosts at offsets of $0.90''$ and $14''$, respectively. These associations are the same as those previously published (Berger 2010a; Perley et al. 2009a) but the probabilities of chance coincidence are lower by a factor of two in this work.

The associations are more ambiguous for GRBs 061201 and 091109B. For GRB 061201, the two most probable host galaxies ("G1" and "G2"; Figure 3.3) have offsets of $16.3''$ and $1.8''$, respectively, and both have $P_{cc}(< \delta R) \approx 0.07$ so the host association is inconclusive. However, "G1" is at a relatively low redshift of $z = 0.111$ (Stratta et al. 2007) while "G2" is likely at $z \approx 1$; thus the physical offsets are $\gtrsim 15$ kpc in both cases (Table 3.2). For GRB 091109B, the position is contaminated by a diffraction spike, but if there is no coincident host galaxy at $\gtrsim 25$ mag, the most probable host has $m_{\rm F160W} \approx 19.8$ mag at an offset of $11.7''$, yielding $P_{cc}(< \delta R) \approx 0.08$. We note that *HST* imaging at a different rotation angle will be essential in determining whether this burst originates from a host galaxy at $\lesssim 1''$ separation or from a galaxy at a larger offset. Due to the uncertainty of the associations for GRBs 061201 and 091109B, we do not include these bursts in our subsequent offset analysis.

Overall, these probability of chance coincidence results agree with those in the literature (Perley et al. 2009a; Berger 2010a; Rowlinson et al. 2010a), and provide deep NIR limits of $\gtrsim 26.2$ mag for bursts which lack hosts at $\delta R \lesssim$few arcsec. We discuss the possibility that such bursts originated from galaxies fainter than the detection threshold of the *HST* observations (and demonstrate that this is unlikely) in more detail in Section 8.5.

3.3.2 Morphological Properties

Using the results from the radial surface brightness profiles (Figure 3.4), we classify the short GRB hosts in terms of their morphological parameters: Sérsic value, n, and effective size, r_e. We find two elliptical galaxies, the hosts of GRBs 070809 and 090515, with $n \approx 3.0 - 3.4$ while the remaining galaxies have disk-like morphologies with $n \approx 0.3 - 2.1$ (Table 3.3). We note that GRB 100117A exhibits a complex morphology in the NIR, with Sérsic indices of $n \approx 0.9$ and ≈ 5 for its inner and outer regions, respectively, although it is spectroscopically classified as an early-type galaxy with a stellar population age of $\approx 1 - 2$ Gyr and no evidence for star formation activity (Fong et al. 2011). GRB 130603B, which is a star-forming galaxy with SFR$\gtrsim 1.3\,M_{\odot}$ yr^{-1} (Cucchiara et al. 2013), has an inner component in the NIR with $n \approx 1$ and a broad outer component with $n \approx 3.8$. This host galaxy has an irregular, asymmetric morphology in the optical band with excess flux at radial distances of $a \approx 0.2 - 0.4''$ in the surface brightness profile (Figure 3.4) and Sérsic components with $n \approx 2$ and 1.3.

The effective radii range from $\approx 0.2 - 1.2''$ with a median size of $0.36''$. We note that the signal-to-noise ratio of the GRB 070429B/F475W observation is low and the r_e measurement likely corresponds to a smaller region within the galaxy, and not the entire galaxy. For the host galaxies that require two Sérsic components, we use the radius which encloses half of the flux as the effective size when computing the host-normalized offsets. These values are $0.95''$ (GRB 090510), $0.9''$ (GRB 090515), $0.3''$ (GRB 100117A), $1''$ (GRB 130603B/F160W) and $0.8''$ (GRB 130603B/F606W). For the short GRBs with known redshifts, the median physical size is about $r_e \approx 3.6$ kpc. The smallest hosts are GRBs 070714B and 100117A while the largest are GRBs 090510 and 090515. The median

value for this sample is the same as the value of 3.5 kpc reported in Fong et al. (2010) for a preliminary sample of hosts. Compared to the long GRB median host galaxy size of 1.7 kpc (Wainwright et al. 2007b), short GRB host galaxies are twice as large. This is consistent with their larger luminosities (Berger 2009) and stellar masses (Leibler & Berger 2010).

3.3.3 Offsets

To study the locations of short GRBs with respect to their host galaxies, we first consider the distribution of projected angular offsets. The range of angular offsets is $\approx 0.1 - 14''$ with GRB 090426 as the smallest offset[3] and GRB 090515 as the largest. From the angular offsets, we calculate projected physical offsets, assuming $z \approx 1$ for bursts without known redshift. We find a range of $\approx 0.5 - 75$ kpc (Figure 3.5).

We supplement this sample of offsets with six measurements from Fong et al. (2010). In addition, we use offset measurements from ground-based observations of all of the remaining short GRBs with sub-arcsecond positions: GRB 111020A with 6 ± 1 kpc (assuming $z \approx 1$, Fong et al. 2012b), GRB 111117A with 10.5 ± 1.7 kpc (Margutti et al. 2012; Sakamoto et al. 2013), and GRB 120804A with 2.2 ± 1.2 kpc (Berger et al. 2013b). Therefore, the full sample of offsets includes 22 short GRBs (Figure 3.5) with a resulting median offset of 4.5 kpc. We compare the short GRB physical offset distribution to those determined from *HST* observations of long GRBs (Bloom et al. 2002), and ground-based observations of core-collapse and Type Ia SNe (Prieto et al. 2008), where the offsets have

[3]Calculated from the galaxy in direct coincidence with the optical afterglow position, using $z = 2.609$ as determined from afterglow spectroscopy (Antonelli et al. 2009a; Levesque et al. 2010).

been calculated in a similar manner as that described in this work. In comparison to the long GRB median offset of 1.3 kpc (Bloom et al. 2002), the short GRB median offset is ≈ 3.5 times larger. The short GRB median offset is comparable to those for Type Ia and core-collapse SNe of ≈ 3 kpc (Figure 3.5; Prieto et al. 2008), but the short GRB offset distribution extends to much larger offsets: only 10% of both SN types have offsets of $\gtrsim 10$ kpc, compared to 25% for short GRBs. Furthermore, no SNe have offsets of $\gtrsim 20$ kpc, while 10% of short GRBs do.

In Figure 3.5, we also show a comparison of the short GRB offset distribution to the predicted distributions from independent population synthesis models of NS-NS binary mergers in Milky Way type galaxies (Fryer et al. 1999; Bloom et al. 1999; Belczynski et al. 2006). The short GRB distribution is broadly consistent with the NS-NS binary merger predictions, and is in very good agreement with two of the three models (Bloom et al. 1999; Belczynski et al. 2006). The discrepancies between the models themselves can be attributed to uncertainties in their inputs, such as the distribution of kick velocities, orbital separations and details of common envelope evolution. The median offset for the predicted distributions is $5 - 7$ kpc, slightly larger than the observed median of 4.5 kpc. We note that the observed distribution is mainly derived from short GRBs with optical afterglows and may be missing a few bursts with less precise localization from X-ray afterglows (Fong et al. 2013) that may occur outside of their host galaxies. Thus, while the observed distribution of offsets should be fairly representative of the true distribution, accounting for such missing events would only extend the distribution to larger offsets, in even better agreement with the NS-NS merger models.

A study by Troja et al. (2008b) suggested that short GRBs with extended emission in the X-rays have smaller offsets than short GRBs with no such emission. Two

bursts in our sample, GRBs 070714B and 080503 have reported evidence for extended emission at $\gtrsim 5\sigma$ significance (Racusin et al. 2007; Mao et al. 2008; Perley et al. 2009a). GRB 070714B has an offset of ≈ 12.2 kpc while GRB 080503 has an offset of ≈ 7.2 kpc from its most probable host assuming $z \approx 1$. Combining these two bursts with four bursts analyzed in Fong et al. (2010) with sub-arcsecond positions and extended emission (GRBs 050709, 050724, 061006, and 060121), the median offset for the population is 3.2 kpc, with a range of $\approx 1 - 12$ kpc. For the remaining 16 bursts with no extended emission and precise offset measurements, the median offset is 5.3 kpc. A Kolmogorov-Smirnov (K-S) test comparing the two populations gives a p-value of 0.9, supporting the null hypothesis that the two populations are drawn from the same underlying distribution. Therefore, there is no clear evidence from their locations that short GRBs with and without extended emission require different progenitor systems.

To compare the offset distributions in a more uniform manner, we calculate host-normalized offsets, $\delta R/r_e$, using the effective radii as determined from our morphological analysis (Section 3.2.6). We find a range of host-normalized offsets of $\approx 0.3 - 15.5\ r_e$ for the bursts with sub-arcsecond positions (Table 3.2). We supplement this sample with seven measurements from Fong et al. (2010), one of which has only an XRT position and thus a more uncertain offset (GRB 050509B). To account for the varying uncertainty in each offset, we plot a differential distribution of host-normalized offsets following the methodology of Bloom et al. (2002), as well as the resulting cumulative distribution (Figure 3.6). The total sample of short GRBs with host-normalized offsets is comprised of 20 events, with a median of $\approx 1.5\ r_e$ and only about 25% of the events at $\lesssim 1 r_e$. For comparison, the host-normalized offset distributions for long GRBs (Fruchter et al. 2006), core-collapse SNe (Kelly et al. 2008) and Type Ia SNe (Galbany et al. 2012) have

median offsets of $\approx 1\ r_e$. Furthermore, a K-S test comparing the host-normalized offsets for long and short GRBs does not support the null hypothesis that the two populations are drawn from the same underlying distribution ($p = 0.03$). A K-S test between short GRBs and Type Ia SNe yields $p = 10^{-3}$, indicating that the two populations are drawn from different host-normalized offset distributions. Indeed, $\approx 20\%$ of short GRBs have offsets of $\gtrsim 5r_e$, compared to only $\approx 5\%$ for Type Ia SNe.

3.3.4 Light Fraction

To further study the local explosion environments of short GRBs, we utilize the fractional flux method which, unlike the spatial offset method, is independent of host morphology. We divide the fractional flux values into two categories based on the bursts' observed filters and redshifts: rest-frame UV ($\lambda_{\rm rest} \lesssim 0.4\,\mu$m) tracking star formation activity and rest-frame optical ($\lambda_{\rm rest} \gtrsim 0.4\,\mu$m) tracking stellar mass. For bursts with no redshift, we assume fiducial values of $z = 1$ to determine the proper rest-frame band. For the 14 bursts in this analysis, all have rest-frame optical measurements while only three have rest-frame UV measurements (GRB 070707 assuming $z = 1$, GRBs 070714B and 071227; Table 3.4). Despite having coincident host galaxies, these three bursts are located on the lowest level of their hosts' UV light with fractional flux measurements of zero. The rest-frame optical measurements span a range of $0 - 0.8$, with GRB 090426 as the highest measurement (Table 3.4).

We supplement these data with six additional bursts analyzed in Fong et al. (2010), bringing the total sample size to 20 events. We find that the resulting distributions are strongly skewed to low fractional flux measurements: 45% of short GRBs are located on

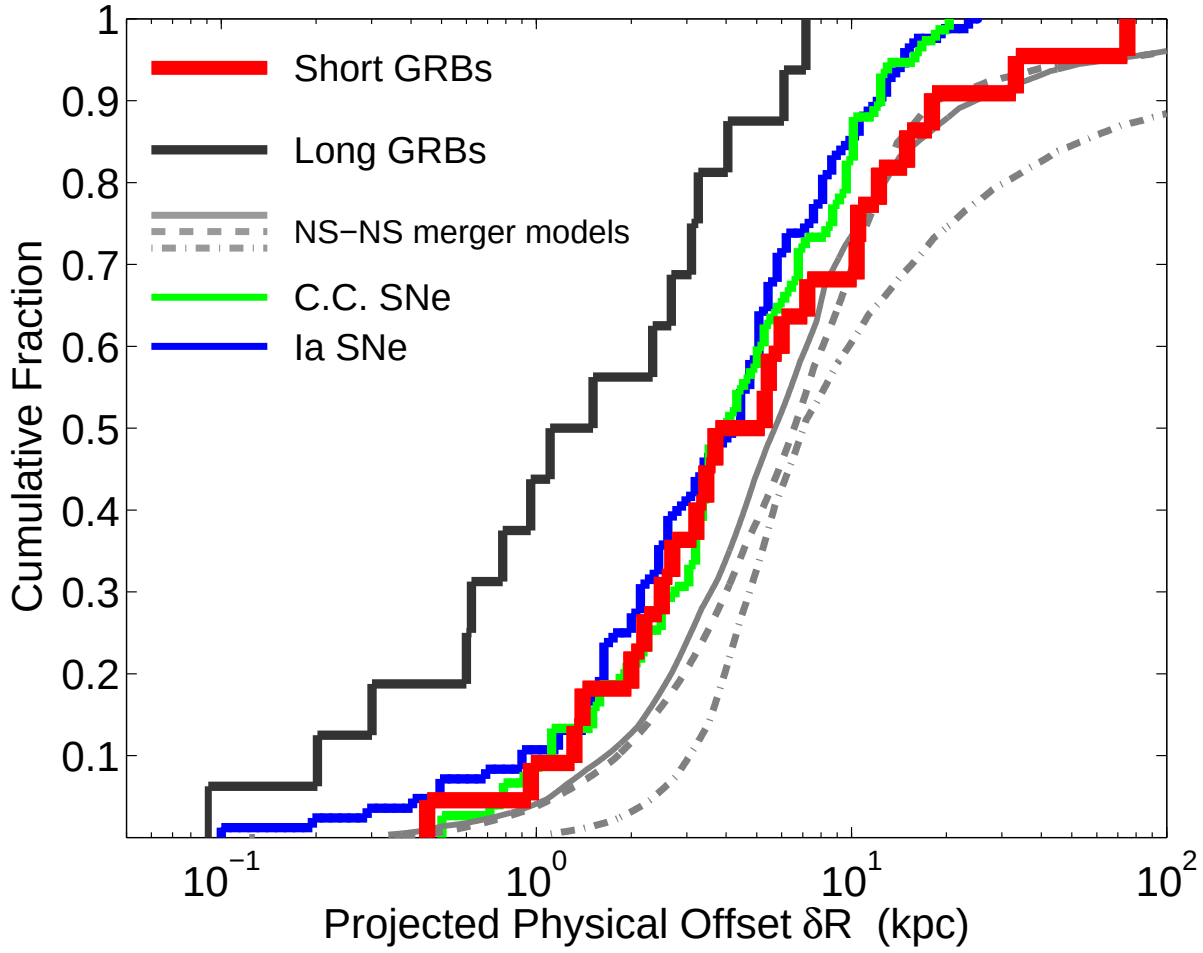

Figure 3.5.—: Cumulative distribution of projected physical offsets for 22 short GRBs with sub-arcsecond positions (red; Fong et al. 2010, this work, and 3 ground-based measurements: Fong et al. 2012b; Margutti et al. 2012; Sakamoto et al. 2013; Berger et al. 2013b). For five bursts with no spectroscopic redshifts (GRBs 060121, 070707, 080503, 090305A, and 111020A), we have assumed $z = 1$. Also shown are the cumulative distributions for long GRBs (black; Bloom et al. 2002), core-collapse SNe (green; Prieto et al. 2008), Type Ia SNe (blue; Prieto et al. 2008), and predicted offsets for NS-NS binaries (grey line Bloom et al. 1999; grey dashed line Belczynski et al. 2006; grey dot-dashed line Fryer et al. 1999).

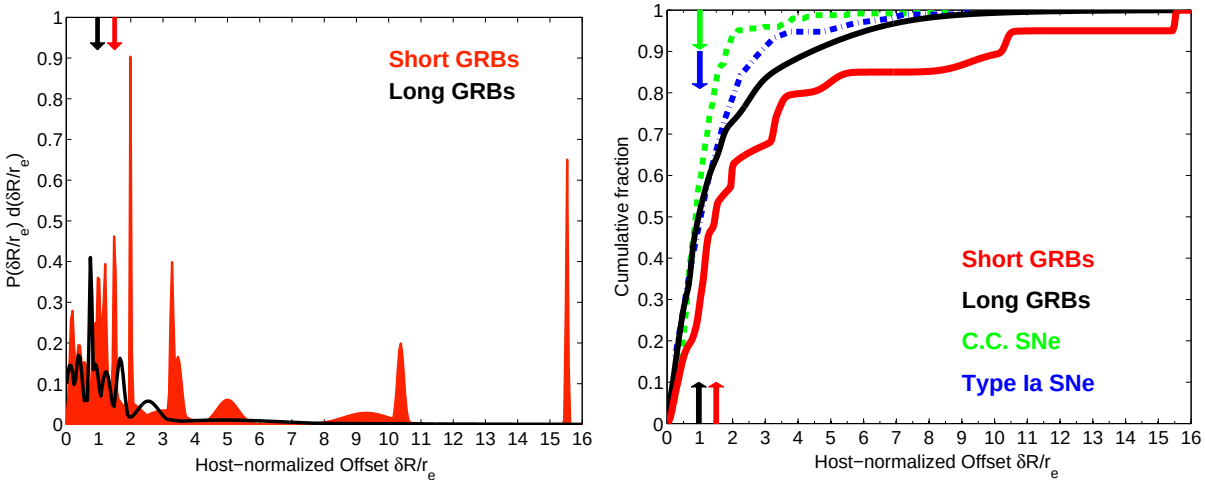

Figure 3.6.—: *Left*: Differential distributions of host-normalized offsets in units of effective radius, r_e, accounting for the uncertainty in each offset measurement, for short GRBs (red shaded region) and long GRBs (black line). The sample is comprised of 20 short GRBs with resolved host galaxies from *HST* data (Fong et al. 2010 and this work), including GRB 050509B which has only an XRT position. Arrows denote the weighted median offset for each population: $1.0r_e$ (long) and $1.5r_e$ (short). *Right*: Cumulative host-normalized offset distributions for short GRBs (red) and long GRBs (black). Also shown are the distributions for core-collapse supernovae (green dashed; Kelly & Kirshner 2012) and Type Ia supernovae (blue dot-dashed; Galbany et al. 2012). Arrows denote the weighted median offset for each population; the median for SNe is also $\approx 1r_e$.

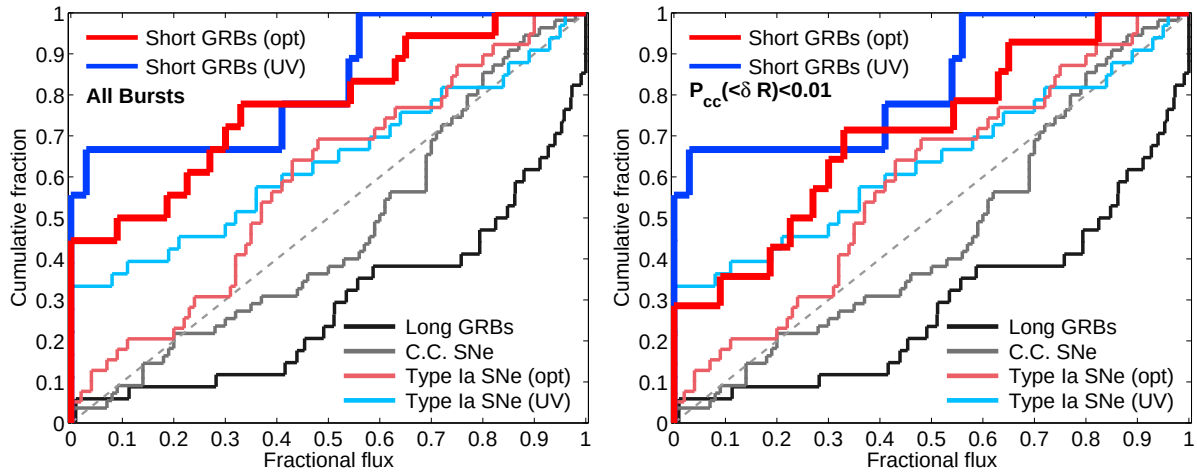

Figure 3.7.—: *Left:* Cumulative distribution of the fractional flux at short GRB locations relative to their host light. The rest-frame optical ($0.4 - 1.2\,\mu$m; red) and rest-frame UV ($< 0.4\,\mu$m; blue) for 20 short GRBs with *HST* observations are shown (Fong et al. 2010 and Table 3.4 in this work). For the purpose of determining the rest-frame band, bursts without known redshifts are assigned $z = 1$. Also shown are the distributions for "normal-velocity" Type Ia supernovae for u'-band (light blue) and r'-band (pink; Wang et al. 2013), core-collapse supernovae (grey; Svensson et al. 2010) and long GRBs (black; Fruchter et al. 2006; Svensson et al. 2010). *Right:* Cumulative distribution of fractional flux including only bursts with host associations with $P_{cc}(< \delta R) \lesssim 0.01$. This case excludes four bursts: GRBs 061201, 080503, 080905A and 090515.

Table 3.5. Fractional Flux Statistics

				K-S test p-values			
Sample	Band	Median	Percentage at zero[a]	Linear[b]	Long GRBs	C. C. SNe	Type Ia SNe
Short GRBs (all)[c]	Optical	0.15	45	0.04	···	···	0.02
Short GRBs ($P_{cc}(< \delta R) \lesssim 0.01$)	Optical	0.25	29	0.07	···	···	0.16
Short GRBs	UV	0	55	0.01	0.002	0.002	0.34
Long GRBs	UV	0.83	6	0.01	···	0.001	3.8×10^{-4}
C. C. SNe	UV	0.60	5	0.42	0.001	···	0.04
Type Ia SNe	Optical	0.34	6	0.35	···	···	···
Type Ia SNe	UV	0.35	34	0.08	3.8×10^{-4}	0.04	···

Note. — [a] Percentage of a given population with fractional flux values of zero.

[b] Corresponds to a distribution that linearly tracks host galaxy light.

[c] All 20 short GRBs with sub-arcsecond positions.

the lowest optical brightness level of their hosts (fractional flux ≈ 0), and 55% are on the lowest UV level (Figure 3.7 and Table 3.5). The short GRB distributions have very low median fractional flux values of ≈ 0.15 for the optical and zero for the UV (Table 3.5). Furthermore, $\approx 75\%$ of the events are located on the faint end (fractional flux $\lesssim 0.5$) of their hosts' optical and UV regions (Figure 3.7). A K-S test comparing the observed short GRB distribution to a distribution that is linearly correlated with host galaxy light (diagonal line in Figure 3.7) yields p-values of 0.04 and 0.01 for the optical and UV, respectively (Table 3.5). These results demonstrate that short GRBs are not correlated with their hosts' rest-frame UV and optical light, i.e., they do not trace regions of star formation or even stellar mass.

The short GRB distribution is particularly striking when compared to long GRBs, which lie on the brightest UV regions of their host galaxies and have a median fractional flux of 0.83 (Figure 3.7 and Table 3.5; Fruchter et al. 2006; Svensson et al. 2010). Core-collapse SNe, which have a median value of 0.60, may slightly over-represent their hosts' UV light (Svensson et al. 2010), commensurate with their origin in star-forming regions. Furthermore, at most a few percent of long GRBs and core-collapse SNe lie on the faintest regions of their host galaxies (Table 3.5).

On the other hand, Type Ia SNe, which result from older stellar progenitor systems, slightly under-represent their hosts' UV and optical light distributions, although K-S test results indicate that this is only marginal (Table 3.5). In particular, 34% of Type Ia SNe have UV fractional flux values of zero, compared to 55% for short GRBs. The difference is more apparent in the optical, with only 6% of the Type Ia SNe population located on the faintest regions of their hosts, compared to 45% for short GRBs (Table 3.5). A K-S test comparing the distributions of short GRBs and Type Ia SNe indicates that

the populations are not drawn from the same underlying distribution in the optical ($p = 0.02$).

We cannot completely rule out the remote possibility that the events with less robust host associations ($P_{cc}(< \delta R) \gtrsim 0.01$) and fractional flux values of zero instead originate from faint host galaxies with $m_{\rm F160W} \gtrsim 26.2$ mag, below the detection threshold of the *HST* images. In this scenario, the fractional flux values for these events may be greater than zero. Therefore, if we only include events with $P_{cc}(< \delta R) < 0.01$ (thereby excluding GRBs 061201, 080503, 080905A and 090515 from the distribution), we find that the short GRBs are still uncorrelated with their hosts' optical light ($p = 0.07$; Table 3.5), with a median value of ≈ 0.25 (Figure 3.7). It is important to note that even in this conservative case, $\approx 30\%$ of the bursts lie on the lowest optical flux levels of their hosts (Figure 3.7). The short GRB UV distribution is unaffected since there are no excluded bursts with rest-frame UV measurements.

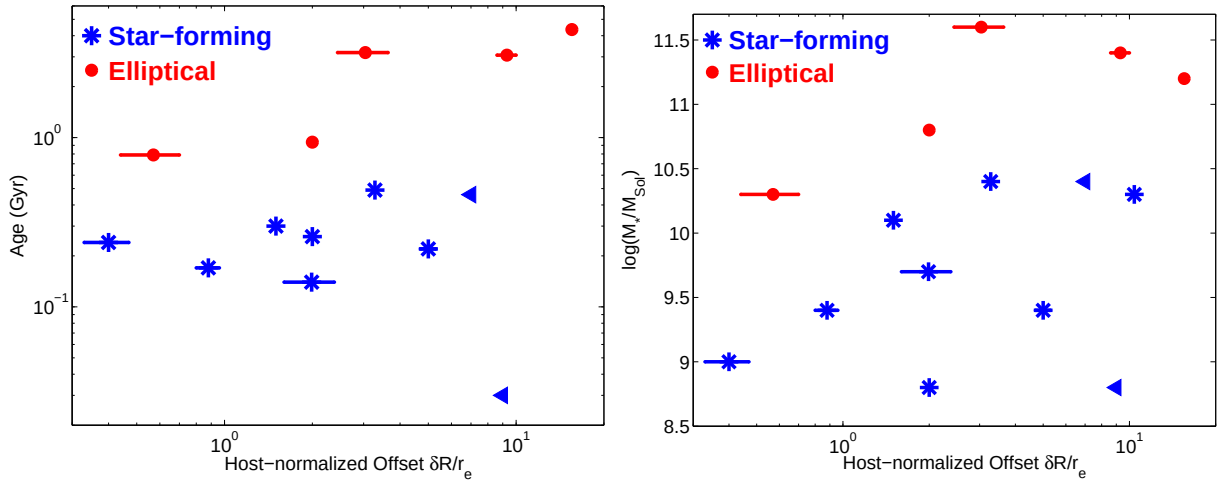

Figure 3.8.—: Stellar population age (left) and stellar mass (right) versus host-normalized offsets for 15 short GRB host galaxies (Leibler & Berger 2010; Rowlinson et al. 2010a), including three bursts with only XRT positions (GRBs 050509B, 051210 and 070429B). Star-forming (blue stars) and elliptical hosts (red circles), as determined from spectroscopy, are indicated. Triangles denote bursts with no detected optical afterglow but that have a single galaxy within the XRT error circle and therefore an upper limit on the offset. We find no obvious trends between stellar mass and host-normalized offsets, or between stellar population age and host-normalized offsets.

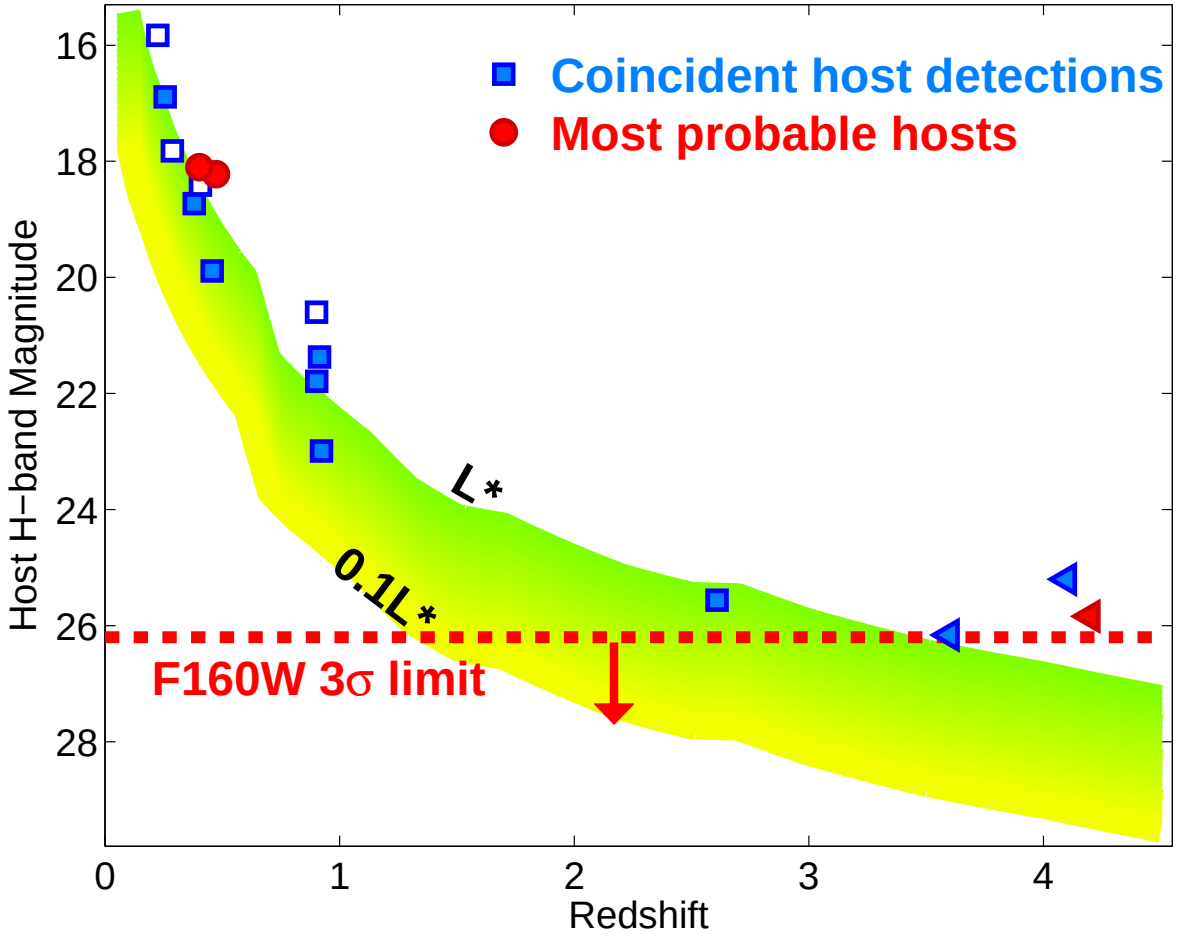

Figure 3.9.—: H-band host galaxy apparent magnitudes from ground-based and *HST* observations versus redshift for short GRBs with coincident host galaxies (blue squares and triangles) and the most probable hosts of GRBs 070809, 080503 and 090515 (red circles and triangle). Triangles denote upper limits on the burst redshift from the detection of the optical afterglow in a particular band. Open symbols correspond to bursts with XRT positions only and a probable host galaxy (GRBs 050509B, 060502B, 070429B and 100206A; Bloom et al. 2007; Perley et al. 2012). The average 3σ upper limit of $m_{\rm F160W} \approx 26.2$ mag for the bursts lacking coincident host galaxies (dotted red line) and the evolving luminosity function for $0.1L^*$ to L^* galaxies (green shaded area; Chen et al. 2003; Poli et al. 2003; Saracco et al. 2006; Marchesini et al. 2007; Hill et al. 2010; Ramos et al. 2011; Marchesini et al. 2012; Stefanon & Marchesini 2013) are shown.

3.4 Implications for the Progenitors

Using the host associations, morphologies, offset distributions, and light distributions presented in the previous sections, we draw implications about the progenitor systems of short GRBs. We first note that the morphological analysis for the 16 host galaxies presented in this paper continues to support the apparent dominance of late-type host galaxies (star-forming with disk morphologies), with only $\approx 1/4$ of short GRBs in hosts with elliptical morphologies (Berger 2009; Fong et al. 2010, 2013). We note that at redshifts of $z \lesssim 1$, we do not expect there to be significant selection effects against detecting short GRBs in elliptical galaxies. Therefore, the tendency for short GRBs to occur in star-forming galaxies indicates that the rate of short GRBs is driven by both recent star formation activity and stellar mass, as also inferred from the distribution of host galaxy masses (Leibler & Berger 2010). In addition, the effective sizes of short GRB hosts are significantly larger than those for long GRB hosts, consistent with their larger luminosities, stellar masses, and metallicities (Berger 2009; Leibler & Berger 2010).

In terms of locations relative to the host centers, we find that short GRBs span a wide range of projected physical offsets of $\sim 0.5 - 75$ kpc, with a median value of about 4.5 kpc and with about 25% of all events occurring at $\gtrsim 10$ kpc. The median offset is 3.5 times larger than for long GRBs (Bloom et al. 2002; Fong et al. 2010). The larger offsets of short GRBs are also evident when normalizing by the effective radii of their hosts, with $\delta R/r_e \approx 0.3 - 16$ and a median value of $\delta R/r_e \approx 1.5$. In addition, only 25% of short GRBs have offsets of $\lesssim r_e$. The median value is 1.5 times larger than for long GRBs, core-collapse SNe, and even Type Ia SNe, which have $\langle \delta R/r_e \rangle \approx 1$. The broader distribution relative to long GRBs and SNe, and the fact that only about 20% of short

GRBs occur within the radius that contains half the light indicate that short GRB progenitors migrate from their birth-sites before producing the bursts. Taken together with the overall match to population synthesis predictions (Figure 3.5), the physical and host-normalized offsets point to compact object binary progenitors with significant kicks.

In this context, the observed offset distribution depends on the combined distributions of kick velocities, merger timescales, and host galaxy masses. Therefore, the observed offset distribution, combined with estimates of the host galaxy stellar masses and merger timescales (Leibler & Berger 2010) can provide insight into the kick velocity distribution. Considering the host stellar population ages as a proxy for the merger timescale, we expect the bursts with the largest offsets to originate from elliptical galaxies, since these systems have had the most time to travel prior to merger. However, the offsets are also sensitive to the escape velocities, and thus stellar masses, of the hosts, and we therefore expect short GRBs in low-mass galaxies to have larger offsets (Perna & Belczynski 2002; Rosswog et al. 2003; Belczynski et al. 2006; Zemp et al. 2009). We investigate these effects using the host-normalized offsets from this work and Fong et al. (2010) in conjuncion with inferred stellar masses and stellar population ages from Leibler & Berger (2010). In Figure 3.8 we plot the values of $\delta R/r_e$ versus stellar mass and population age for both early- and late-type hosts. We calculate the Kendall τ coefficient, (where a value of $\tau = 1$ indicates statistical correlation), to assess whether the stellar population properties are correlated with host-normalized offsets, discarding the offset upper limits. We find that $\tau \approx 0.34$ ($p = 0.09$) for stellar mass and $\tau \approx 0.26$ ($p = 0.20$) for stellar population age. Both results agree with the null hypothesis that there is no strong correlation, and thus we find no clear trend between stellar population properties and offsets. In particular, we find that short GRBs in both elliptical and

star-forming galaxies span the full range of host-normalized offsets. This result suggests that the observed offset distribution is primarily determined by the distribution of kick velocities.

Using the projected physical offsets and the stellar population ages as a proxy for the merger timescale we can calculate the minimum projected kick velocities if the progenitors originate at the host centers ($v_{\rm kick,min}$). We find a range of $v_{\rm kick,min} \approx 2-150$ km s^{-1}, with a median of about 16 km s^{-1}. However, a more reasonable value for the kick velocity of each system needs to take into account the host velocity dispersion ($v_{\rm disp}$), and we therefore use the geometric mean, $\sqrt{v_{\rm kick,min}\, v_{\rm disp}}$ (c.f., Bloom et al. 2007). Using a fiducial value for the late-type hosts of $v_{\rm disp} \approx 120$ km s^{-1}, as measured for the Milky Way (Battaglia et al. 2005; Xue et al. 2008), and ≈ 250 km s^{-1} inferred for $\sim 10^{11}$ M$_\odot$ elliptical galaxies (Forbes & Ponman 1999), we find projected kick velocities of $\approx 20-140$ km s^{-1} with a median of ≈ 60 km s^{-1}. This range is consistent with the inferred natal kick velocities for the eight known Galactic NS-NS binaries, which range from $\approx 5-500$ km s^{-1} (Fryer & Kalogera 1997; Wang et al. 2006; Wong et al. 2010).

Independent of the offset distribution, the locations of short GRBs relative to their hosts' light distribution also point to explosion sites that are distinct from the progenitor birth sites. In particular, our analysis clearly demonstrates that short GRBs are not spatially correlated with either star forming regions or even with the underlying distribution of stellar mass. This is unlike long GRBs and core-collapse SNe, which track UV light (Fruchter et al. 2006; Svensson et al. 2010), or Type Ia SNe, which generally track stellar mass (Kelly et al. 2008). Most strikingly, about $30-45\%$ of all short GRBs occur in regions that effectively contain no rest-frame optical light, and hence negligible stellar mass (Figure 3.7), indicating that the progenitors were not formed at the explosion

sites. Moreover, studies of the host galaxy demographics and stellar mass distribution show that the short GRB rate depends on both stellar mass and star formation activity (Leibler & Berger 2010; Fong et al. 2013), while the light distributions point to explosion sites that are de-coupled from both star-forming regions and the stellar mass distribution. The combination of these results, along with the large host-normalized offsets, provides the strongest support to date for NS-NS/NS-BH progenitors with significant migration from their birth sites to their eventual explosion sites.

Finally, the *HST* observations presented here provide unprecedented NIR limits on coincident hosts for short GRBs previously termed as host-less based on ground-based optical data (GRBs 061201, 070809, 080503 and 090515). Using these limits we investigate the possibility that these events are not at large offsets from their hosts (as appears to be the case based on probability of chance coincidence arguments; Berger 2010a and this paper), but instead originate from coincident hosts that are below the *HST* detection limit.

To determine the combination of luminosity and redshift required for such faint coincident hosts, we compare the average 3σ limit of the *HST* observation, $m_{160\rm W} \gtrsim 26.2$ mag, to the observer-frame H-band galaxy luminosity function taking into account its evolution with redshift (Figure 3.9). We find that if these hosts are $\sim L^*$ galaxies, typical of other short GRB hosts (Figure 3.9; Berger 2009), they would need to originate at $z \gtrsim 3.5$. The highest known short GRB redshift is $z = 2.609$ (GRB 090426), while typical redshifts are $\sim 0.2 - 1$, so in this scenario, these bursts would represent a distinct population of the highest redshift short GRBs. If instead the bursts have redshifts following the observed redshift distribution, this would require the hosts to have luminosities well below $0.1\,L^*$ (Figure 3.9), at least an order of magnitude below the

typical luminosities of short GRB hosts. Furthermore, Berger (2010a) show that these bursts have systematically fainter optical afterglows than bursts with coincident hosts, which is at odds with the scenario of similar redshifts and sub-luminous hosts. Thus, we do not consider the possibility that the host-less events have coincident hosts below the detection limit of the *HST* data as likely. Instead, when combined with a probability of chance coincidence analysis (Berger 2010a and this paper), these bursts appear to be associated with galaxies that are typical of the short GRB host population (Figure 3.9), with resulting offsets of $\sim 10 - 100$ kpc. Thus, the deep NIR limits presented here provide further evidence for large offsets consistent with NS-NS/NS-BH progenitors.

3.5 Conclusions

We presented *HST* observations and a detailed analysis of 22 short GRB host galaxies. Based on this analysis combined with the results from Fong et al. 2010, we draw several key conclusions:

1. Short GRB host galaxies with disk morphologies dominate the sample, with only $\approx 1/4$ of the hosts having elliptical morphologies. The median effective size of short GRB hosts is ≈ 3.6 kpc, about twice as large as long GRB hosts, which are exclusively associated with late-type, star-forming galaxies.

2. Short GRBs have projected physical offsets from their host galaxies of $\approx 0.5-75$ kpc, with a median of ≈ 4.5 kpc, 3.5 times larger than the offsets for long GRBs. Compared to the distributions for core-collapse and Type Ia SNe, short GRBs extend to larger offsets, with $\approx 25\%$ of events at $\gtrsim 10$ kpc, compared to only 10%

for both SN types.

3. Taking into account their host sizes, short GRBs have host-normalized offsets of $0.3 - 15.5r_e$ with a median of $\approx 1.5r_e$, approximately 1.5 times larger than those for long GRBs, core-collapse SNe, and Type Ia SNe. Furthermore, $\approx 20\%$ of short GRBs have offsets of $\gtrsim 5r_e$, compared to only 5% for Type Ia SNe, which also result from old stellar progenitors.

4. In the context of NS-NS/NS-BH progenitors, we use the offset distribution, stellar population age distribution, and typical velocity dispersions for star-forming and elliptical galaxies, to infer kick velocities of $\approx 20 - 140$ km s^{-1} with a median of ≈ 60 km s^{-1}. This is generally consistent with the range of kick velocities inferred for Galactic NS-NS binaries.

5. Short GRBs severely under-represent their hosts' rest-frame UV or optical light. In particular, $30 - 45\%$ of short GRBs are located on the faintest optical regions of their host galaxies, while $\approx 55\%$ occur in the faintest UV regions, showing that short GRBs do not spatially track star formation or stellar mass. Combined with the host galaxy demographics which imply a short GRB rate driven by both star formation and stellar mass, this demonstrates that short GRBs migrate from their birth sites to their eventual explosion sites and provides strong support for progenitor kicks, ie., NS-NS/NS-BH mergers.

6. For bursts with no robust association to a host galaxy within ∼few arcsec, we consider a faint coincident host origin by comparing the NIR limit of $m_{\rm F160W} \gtrsim 26.2$ mag to the H-band galaxy luminosity function and other short GRB hosts. If these hosts are $\sim L^*$ galaxies, typical of other short GRB hosts,

they are constrained to $z \gtrsim 3.5$. Alternatively, if these bursts occur at typical short GRB redshifts of $z \sim 0.5$, this requires sub-luminous hosts compared to the population, with $\lesssim 0.1L^*$. Instead, it is more likely that these bursts originate from $\sim L^*$ galaxies at $\approx 10 - 100$ kpc offsets as indicated by probability of chance coincidence analysis.

Through this analysis, we have provided independent lines of evidence which argue for NS-NS/NS-BH mergers as the progenitors of short GRBs. In particular, both the spatial offsets and their locations on the faintest regions of their hosts demonstrate that the progenitors must migrate between their formation and the eventual explosions. In addition, we have made detailed comparisons between short GRBs and Type Ia SNe which, unlike long GRBs and core-collapse SNe, result from old stellar progenitors. We find that the two populations differ in their distributions of host-normalized offsets and rest-frame optical light locations, with short GRBs having larger offsets and a weaker correlation with stellar mass. Finally, we note that the large fraction of short GRBs with a weak correlation to stellar light agrees with the overall indication from the afterglow emission that the parsec-scale densities around the progenitors are generally low, $\lesssim 0.1$ cm^{-3} (Soderberg et al. 2006b).

The Berger GRB group is supported by the National Science Foundation under Grant AST-1107973, and previously by NASA/Swift AO6 grant NNX10AI24G and A07 grant NNX12AD69G. This paper includes data gathered with the 6.5 meter Magellan Telescopes located at Las Campanas Observatory, Chile. This work is based in part on observations obtained at the Gemini Observatory, which is operated by the Association of Universities for Research in Astronomy, Inc., under a cooperative agreement with

the NSF on behalf of the Gemini partnership: the National Science Foundation (United States), the Science and Technology Facilities Council (United Kingdom), the National Research Council (Canada), CONICYT (Chile), the Australian Research Council (Australia), Ministrio da Cincia, Tecnologia e Inovao (Brazil) and Ministerio de Ciencia, Tecnologa e Innovacin Productiva (Argentina). This work made use of data supplied by the UK Swift Science Data Centre at the University of Leicester. Based on observations made with ESO Telescopes at the La Silla Paranal Observatory under programme IDs 59.A-9002(D), 079.D-0909(C), 080.D-0906(G), 081.D-0588(C), 083.D-0606(C), and 084.D-0621(B). Based on observations made with the NASA/ESA Hubble Space Telescope, obtained from the data archive at the Space Telescope Science Institute. STScI is operated by the Association of Universities for Research in Astronomy, Inc. under NASA contract NAS 5-26555.

Chapter 4

The Optical Afterglow and $z = 0.92$ Early-Type Host Galaxy of the Short GRB 100117A

W. Fong, E. Berger, R. Chornock, N.R. Tanvir, A.J. Levan, A.S. Fruchter, J.F. Graham, A. Cucchiara & D.B. Fox

The Astrophysical Journal, Vol. 730, No. 26, 2011

Abstract

We present the discovery of the optical afterglow and early-type host galaxy of the short-duration GRB 100117A. The faint afterglow is detected 8.3 hr after the burst with $r_{\rm AB} = 25.46 \pm 0.20$ mag. Follow-up optical and near-IR observations uncover a coincident compact red galaxy, identified as an early-type galaxy at a spectroscopic redshift of $z \approx 0.915$ with a mass of $\sim 3 \times 10^{10}$ $M_\odot$, an age of ~ 1 Gyr, and a luminosity of $L_{\rm B} \simeq 0.5\,L_*$. From a possible weak detection of [O II]λ3727 emission at $z = 0.915$ we infer an upper bound on the star formation rate of ~ 0.1 $M_\odot$ yr^{-1}, leading to a specific star formation rate of $\lesssim 0.004$ Gyr^{-1}. Thus, GRB 100117A is only the second short burst to date with a secure early-type host (the other being GRB 050724 at $z = 0.257$) and it has one of the highest short GRB redshifts. The offset between the host center and the burst position, 470 ± 310 pc, is the smallest to date. Combined with the old stellar population age, this indicates that the burst likely originated from a progenitor with no significant kick velocity. However, from the brightness of the optical afterglow we infer a relatively low density of $n \approx 3 \times 10^{-4}\,\epsilon_{e,-1}^{-3}\epsilon_{B,-1}^{-1.75}$ cm^{-3}. The combination of an optically faint afterglow and host suggest that previous such events may have been missed, thereby potentially biasing the known short GRB host population against $z \gtrsim 1$ early-type hosts.

4.1 Introduction

Progress in our understanding of short-duration gamma-ray bursts (GRBs) and their progenitors relies on detailed studies of their afterglows and host galaxy environments. Of particular interest are bursts with precise sub-arcsecond positions, which can provide unambiguous host galaxy associations, redshifts, and burst properties (energy, density). Such localizations require the detection of ultraviolet, optical, near-infrared, and/or radio afterglows; or alternatively an X-ray detection with the *Chandra* X-ray Observatory. As of December 2010, only 20 short bursts have been precisely localized in this manner. Of these, 14 have clearly identified hosts[1] (10 with spectroscopic redshifts), 5 do not have unambiguous host associations[2] (Berger 2010b), and 1 has not been reported in the literature so far[3]. For a recent summary see Berger (2010d).

Only in a single case out of the 10 hosts with spectroscopic identifications is the galaxy known to be early-type with no evidence for on-going star formation activity (GRB 050724: Berger et al. 2005; Gorosabel et al. 2006; Prochaska et al. 2006); the remaining hosts are star forming galaxies, albeit at a level that is on average significantly

[1]These bursts are 050709: (Fox et al. 2005; Hjorth et al. 2005b); 050724: (Berger et al. 2005); 051221A: (Soderberg et al. 2006b); 060121 (Levan et al. 2006b; de Ugarte Postigo et al. 2006a); 060313: (Roming et al. 2006); 061006: (D'Avanzo et al. 2009); 070707: (Piranomonte et al. 2008); 070714B: (Graham et al. 2009); 070724: (Berger et al. 2009); 071227: (D'Avanzo et al. 2009); 080905: (Rowlinson et al. 2010a); 090426: (Antonelli et al. 2009b; Levesque et al. 2010); 090510: (McBreen et al. 2010); and 100117A: this paper.

[2]GRBs 061201: (Stratta et al. 2007), 070809: (Perley et al. 2007d), 080503: (Perley et al. 2009a), 090305: (Berger & Kelson 2009; Cenko et al. 2009), and 090515: (Rowlinson et al. 2010b).

[3]GRB 091109B: (Malesani et al. 2009).

lower than in long GRB hosts (Berger 2009), particularly when accounting for their higher luminosities and stellar masses (Berger 2009; Leibler & Berger 2010). The hosts with measured redshifts span a range of $z \approx 0.1 - 1$ (e.g., Berger 2009), with the exception of the possible short GRB 090426 at $z = 2.609$ (Antonelli et al. 2009b; Levesque et al. 2010); in the three remaining cases the hosts are too faint for a spectroscopic redshift determination, but are likely to be located at $z \gtrsim 1$ (Berger et al. 2007b). At the same time, there is tentative evidence for early-type hosts in the sample of short bursts with optical positions and no coincident hosts based on chance coincidence probabilities (GRBs 070809 and 090515; Berger 2010b).

The host demographics and redshift distribution provide important constraints on the nature of the progenitors. For example, an abundance of low redshifts and early-type hosts would point to a population that is skewed to old ages, $\gtrsim$ few Gyr (Zheng & Ramirez-Ruiz 2007). However, from the existing host galaxy demographics and redshift distributions it appears that the progenitors span a broad range of ages, $\sim 0.1 -$ few Gyr, and may indeed be over-represented in late-type galaxies with intermediate-age populations (~ 0.3 Gyr; Berger et al. 2007b; Leibler & Berger 2010).

Afterglow detections are also important for determining the GRB and circumburst medium properties. To date, however, little detailed information about these properties has been drawn from the existing (though sparse) broad-band afterglow detections (e.g., Berger et al. 2005; Panaitescu 2006; Roming et al. 2006; Soderberg et al. 2006b; Berger 2010b), mainly due to the faintness of short GRB afterglows. Early time optical observations also probe possible emission from radioactive material synthesized and ejected in a binary compact object merger, a so-called Li-Paczynski mini-supernova (Li & Paczyński 1998; Kann et al. 2008; Perley et al. 2009a; Metzger et al. 2010). No such

emission has been conclusively detected to date (e.g., Hjorth et al. 2005a; Bloom et al. 2006; Berger et al. 2009).

Here we report the discovery of the optical afterglow and host galaxy of the short GRB 100117A. From spectroscopy and optical/near-IR imaging we find that the host is an early-type galaxy at $z = 0.915$, making it only the second unambiguous early-type host association for a short GRB with a significantly higher redshift than the previous event, GRB 050724 at $z = 0.257$ (Berger et al. 2005). The precise position also allows us to measure the burst offset, while the optical flux provides constraints on the circumburst density. We present the afterglow and host discovery in §8.2. In §4.3 we study the host redshift and stellar population properties, while in §4.4 we analyze the afterglow properties. Finally, we draw conclusions about the nature of this burst and implications for the short GRB sample in §4.5.

Throughout the paper we use the standard cosmological parameters, $H_0 = 71$ km s^{-1} Mpc^{-1}, $\Omega_m = 0.27$, and $\Omega_\Lambda = 0.73$.

4.2 Observations of GRB 100117A

GRB 100117A was detected by the *Swift* satellite on 2010 January 17.879 UT, and an X-ray counterpart was promptly localized by the on-board X-ray Telescope (XRT) with a final positional accuracy of 2.4″ radius (de Pasquale et al. 2010). No optical/UV source was detected by the co-aligned UV/Optical Telescope (UVOT). The burst duration is $T_{90} = 0.30 \pm 0.05$ s, and its $15 - 150$ keV fluence is $F_\gamma = (9.3 \pm 1.3) \times 10^{-8}$ erg cm^{-2}. The burst was also detected by the *Fermi* Gamma-Ray Burst Monitor (GBM) with a

duration of about 0.4 s, an $8 - 1000$ keV fluence of $F_\gamma = (4.1 \pm 0.5) \times 10^{-7}$ erg cm^{-2}, and a peak energy of $E_p = 287^{+74}_{-50}$ keV (Paciesas 2010; de Pasquale et al. 2010). These properties clearly classify GRB 100117A as a short burst.

The X-ray light curve exhibits a complex behavior at early time, with an initial flare lasting until about 200 s, followed by a steep decline with $F_X \propto t^{-3.5\pm0.2}$. Subsequent data collected at $\sim 5 - 690$ ks lead to an upper limit of $F_X \lesssim 2.5 \times 10^{-14}$ erg cm^{-2} s^{-1} (unabsorbed; Evans et al. 2007a, 2009). A fit to the X-ray spectrum indicates that $F_{\nu,X} \propto \nu^{-0.70\pm0.14}$ and $N_H = (1.2 \pm 0.4) \times 10^{21}$ cm^{-2}, in excess of the expected Galactic column of $N_H = 2.7 \times 10^{20}$ cm^{-2} (de Pasquale et al. 2010). Using the counts to unabsorbed flux conversion (1 cps $= 5.2 \times 10^{-11}$ erg cm^{-2} s^{-1}) and the measured spectral index, we find a flux density limit at $\gtrsim 5$ ks of $F_\nu(1\,\mathrm{keV}) \lesssim 2.3 \times 10^{-3}$ μJy.

Inspection of archival optical images from the Canada-France-Hawaii MegaCam survey led to the detection of four faint sources within the initial XRT error circle with $R, I \approx 23 - 24.5$ mag, while i-band imaging at about 4.7 hr revealed that the brightest of these sources had a comparable brightness to the archival data (Cenko et al. 2010a).

4.2.1 Afterglow Discovery

We initiated R-band observations of GRB 100117A with the Inamori Magellan Areal Camera and Spectrograph (IMACS) on the Magellan/Baade 6.5-m telescope on 2010 January 18.04 UT (3.9 hr after the burst) and detected the four sources noted by Cenko et al. (2010a) within the initial XRT error circle. We subsequently obtained two deeper epochs of imaging in the r-band with the Gemini Multi-Object Spectrograph (GMOS-N) on the Gemini-North 8-m telescope on 2010 January 18.21 and 19.22 UT (7.9 and 33.2

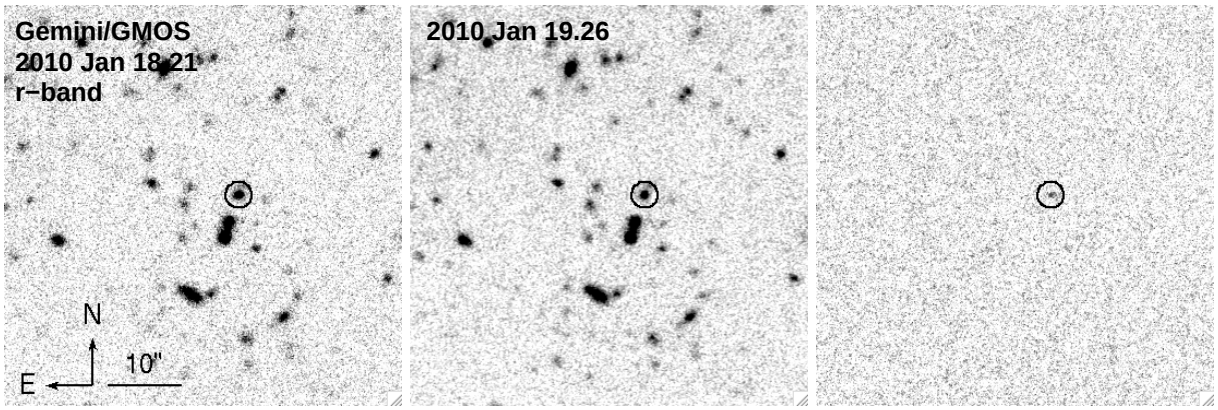

Figure 4.1.—: Gemini/GMOS r-band images obtained starting 7.9 hr (left) and 33.2 hr (center) after the burst. Digital subtraction of the two images reveals a fading source in the residual image (right), which we identify as the afterglow. The afterglow position is denoted by the black circle.

hr after the burst); see Table 7.1. The IMACS observations were reduced using standard procedures in IRAF, while the GMOS-N observations were analyzed using the IRAF `gemini` package. Photometric calibration was performed through observations of the standard star field E3A.

Digital image subtraction of the two GMOS-N observations using the ISIS software package (Alard 2000) reveals the presence of a fading source, which we identify as the optical afterglow of GRB 100117A; see Figure 4.1. Comparing these two epochs, we calculate an afterglow magnitude of $r_{\rm AB} = 25.46 \pm 0.20$ mag (0.24 ± 0.05 μJy) at a median time of 8.3 hr after the burst. We confirm that the afterglow contribution in the second epoch is negligible because the measured host magnitude is consistent with late-time (300 days after the burst) r-band IMACS observations (Table 7.1). A comparison of our early-time IMACS observation with the second epoch of GMOS-N imaging yields an afterglow magnitude of $r_{\rm AB} > 23.93$ mag (3σ) at a median time of 4.1 hr after the burst.

Astrometry relative to the USNO-B catalog provides an absolute position for the

Table 4.1. Log of Optical and Near-IR Observations of GRB 100117A

Date (UT)	Δt (d)	Telescope	Instrument	Filter	Exposures (s)	$\theta_{\rm FWHM}$ ($''$)	Afterglow[a] (AB mag)	F_ν^a (μJy)	Host[a] (AB mag)	A_λ^b (mag)
2010 Jan 18.040	0.162	Magellan	IMACS	R	4×300	1.25	> 23.93	< 0.97	$\cdots$	0.064
2010 Jan 18.207	0.329	Gemini-North	GMOS	r	15×180	0.80	25.46 ± 0.20	0.24 ± 0.05	$\cdots$	0.07
2010 Jan 19.262	1.383	Gemini-North	GMOS	r	15×180	0.76	$\cdots$	0[c]	24.30 ± 0.10	0.07
2010 Feb 2.208	15.3	Gemini-North	NIRI	K	19×60	0.51			21.24 ± 0.20	0.01
2010 Feb 2.229	15.4	Gemini-North	NIRI	H	19×60	0.56			21.26 ± 0.21	0.01
2010 Feb 4.208	17.3	Gemini-North	NIRI	J	14×60	0.80			21.87 ± 0.25	0.02
2010 Feb 4.229	17.4	Gemini-North	GMOS	g	7×240	1.15			26.17 ± 0.30	0.1
2010 Nov 14.042	300.2	Magellan	IMACS	z	5×180	0.70			22.33 ± 0.10	0.035
2010 Nov 14.057	300.2	Magellan	IMACS	i	3×240	0.63			22.85 ± 0.10	0.045
2010 Nov 14.083	300.2	Magellan	IMACS	r	8×360	0.61			24.33 ± 0.10	0.07

Note. — [a] These values are corrected for Galactic extinction.

[b] Galactic extinction.

[c] We assume the afterglow contribution is negligible 1.383 d after the burst.

optical afterglow of $\alpha = 00^{\rm h}45^{\rm m}04.660^{\rm s}$, $\delta = -01^\circ35'41.89''$ (J2000), with an uncertainty of $0.26''$ in each coordinate. This position is $1.5''$ away from the center of the XRT error circle, which has an uncertainty of $2.4''$. We additionally measure the relative position of the afterglow and host galaxy (using the second Gemini epoch) and find an offset of $\delta{\rm RA} = 60$ mas and $\delta{\rm Dec} = 0$ mas. The uncertainty in the offset includes contributions from the astrometric tie of the two ground-based Gemini observations ($\sigma_{\rm GB\rightarrow GB} = 9$ mas), the positional accuracy of the afterglow residual ($\sigma_{\theta,{\rm GRB}} = 10$ mas), and uncertainty in the centroid of the host galaxy ($\sigma_{\theta,{\rm gal}} = 20$ mas), which is itself dominated by systematic uncertainty rather than just the signal-to-noise ratio. Thus, the total angular offset between the afterglow and host center is 60 ± 40 mas.

4.2.2 Host Galaxy Observations

Subsequent to the discovery of the afterglow we obtained follow-up observations of the host galaxy in the g-band with GMOS-N and in the JHK bands with the Near Infra-Red Imager and Spectrometer (NIRI) on the Gemini-North 8-m telescope. We also obtained IMACS observations in the riz bands (Table 7.1). Photometry of the host was extracted in a $1.6''$ radius aperture, and is summarized in Table 7.1. We note that the errors are dominated by uncertainty in the zeropoint in the H and K bands. The host appears to be mildly resolved with a FWHM of $0.6''$ in the K-band (PSF = $0.5''$). Images of the host in the $grizJHK$ filters, and a combined color image are shown in Figure 4.2. A combined color image of the $2' \times 2'$ field covered by NIRI is shown in Figure 4.3.

We obtained spectroscopic observations of the host on 2010 January 19.22 using GMOS-N at a mean airmass of 1.4. A dithered pair of 1500 s exposures were obtained

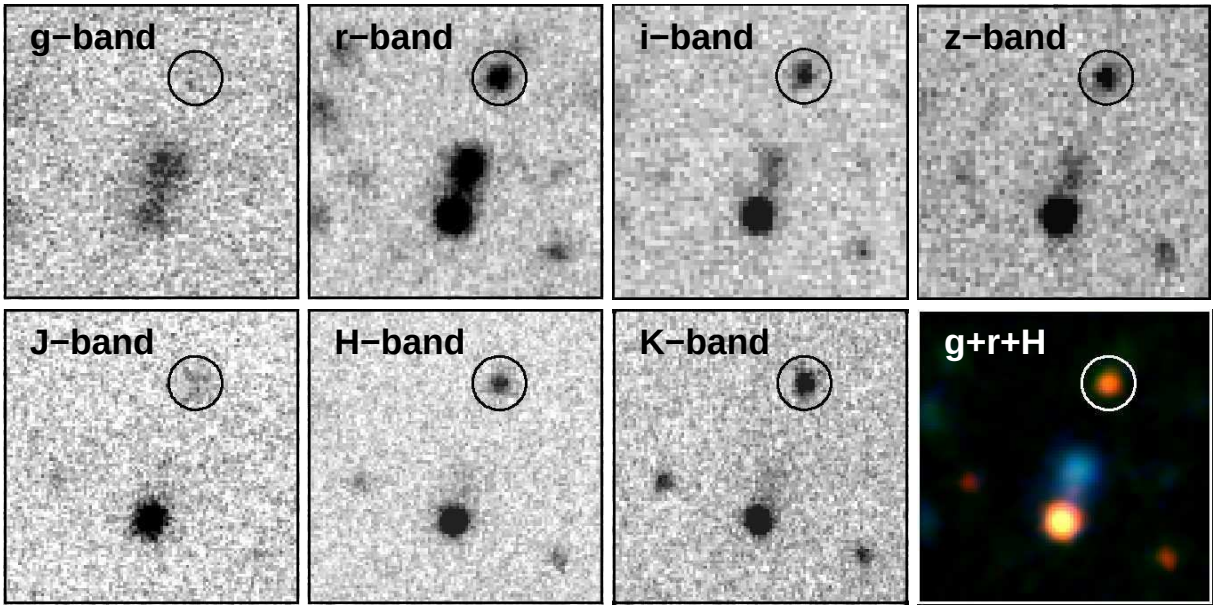

Figure 4.2.—: Gemini and Magellan optical and near-IR images of the host galaxy of GRB 100117A obtained with GMOS, NIRI and IMACS (Table 7.1). Each panel is $0.2'$ on a side with an orientation of north up and east to the left. Also shown is a grH color composite highlighting the red color of the host galaxy.

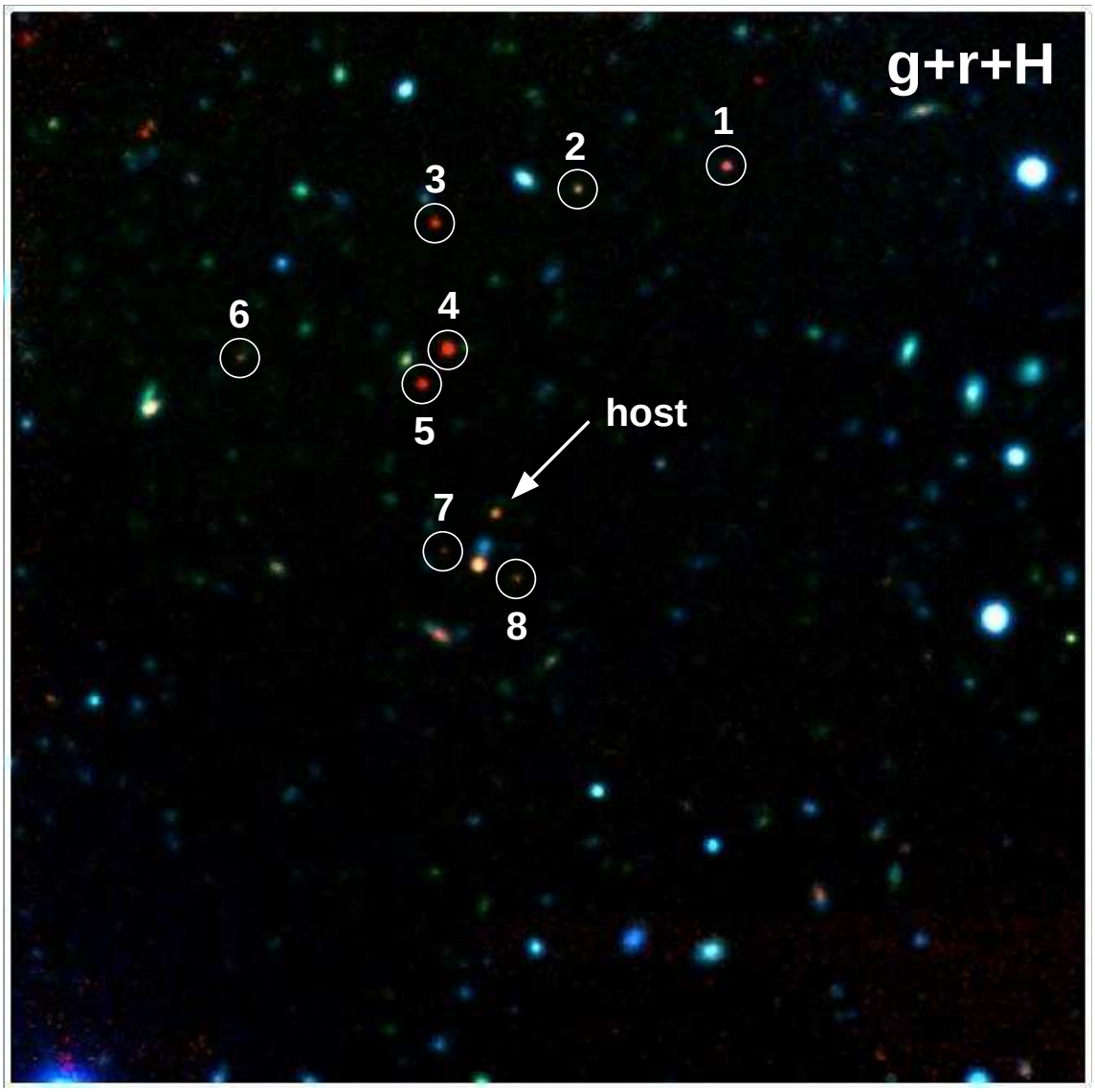

Figure 4.3.—: Gemini optical and near-IR grH color composite image of a $2' \times 2'$ field around GRB 100117A. The environment around the host contains several red galaxies, whose colors are plotted in Figure 4.8 (see §4.3.3).

with the R400 grating covering $3900 - 8130$ Å at a spectral resolution of about 7 Å. We obtained a second, deeper set of observations (4×1460 s) on 2010 November 2.12 with GMOS-S on the Gemini-South 8-m telescope at a mean airmass of 1.15 in the nod-and-shuffle mode. These observations were also obtained with the R400 grating covering $5400 - 9650$ Å with the OG515 order-blocking filter. The data were reduced using standard tasks in IRAF and wavelength calibration was performed using CuAr arc lamps. Archival observations of the smooth-spectrum standard star EG 131 (Bessell 1999) and custom IDL programs were used to apply a flux calibration and remove the telluric absorption bands. An overall flux calibration was applied using the measured r- and i-band fluxes. In order to maximize the signal-to-noise ratio, we use a weighted co-addition of the two epochs in our subsequent analysis. The resulting spectrum is shown in Figure 4.4.

We detect continuum emission from the host beyond ≈ 5000 Å, with a notable increase in the flux redward of 7650 Å. No obvious emission features are detected. Interpreting the break as the Balmer/4000 Å break we find an estimated redshift of $z \approx 0.9$.

4.3 Host Galaxy Redshift and Properties

4.3.1 Spectroscopy

To quantitatively assess the host galaxy's redshift, we fit a weighted co-addition of the GMOS spectra described in §4.2.2 over the wavelength range $6000 - 8500$ Å with spectral evolution models of simple stellar populations (SSPs) at fixed ages provided

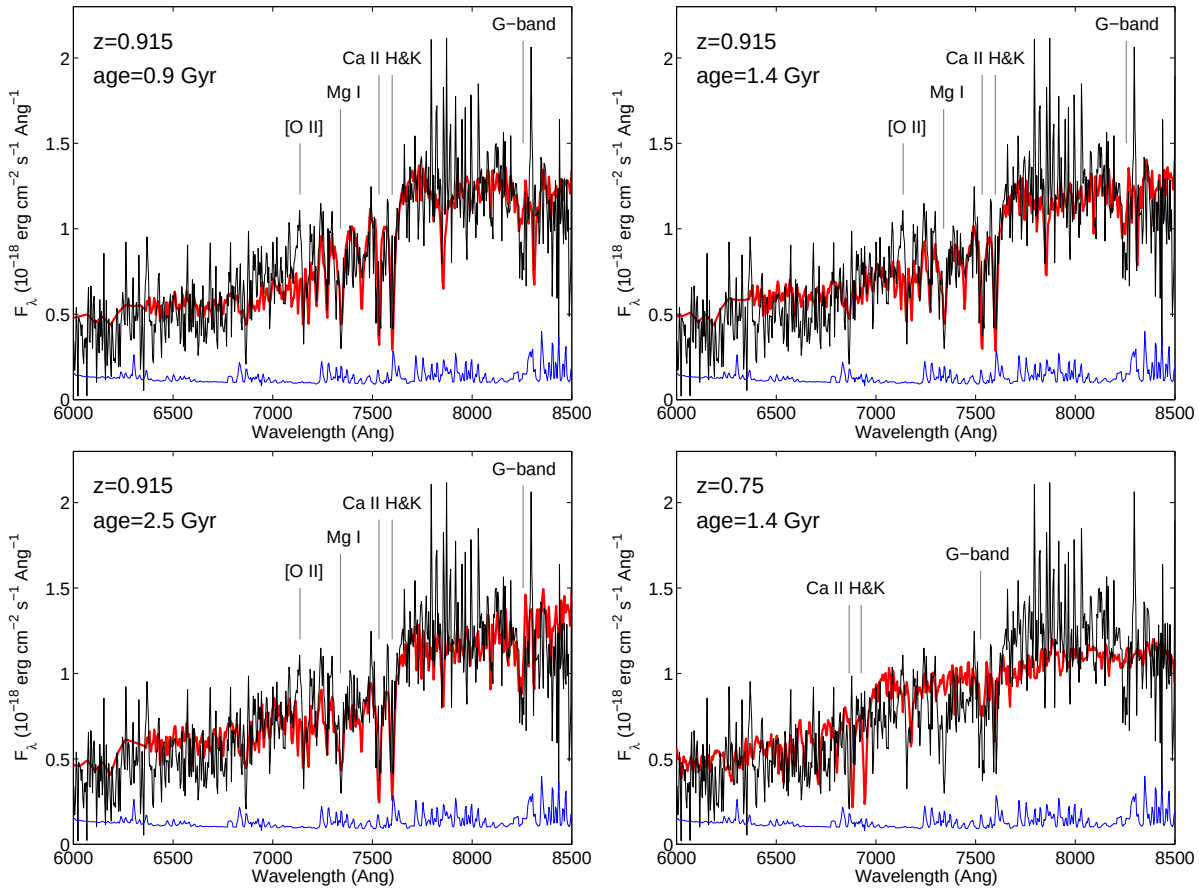

Figure 4.4.—: Gemini spectrum of the host galaxy of GRB 100117A binned with 3-pixel (2 Å) boxcar (black: data; blue: error spectrum). Also shown are SSP templates (red; Bruzual & Charlot 2003) with stellar population ages of 0.9 Gyr (top left), 1.4 Gyr (top right), and 2.5 Gyr (bottom left) at the best-fit spectroscopic redshift of $z = 0.915$. We also show a 1.4 Gyr SSP template at the preferred photometric redshift of $z = 0.75$ (bottom right). Fits are performed on the unbinned data. The latter fit provides a poorer match to both the sharpness of the break and the main spectral features. Absorption line locations corresponding to Ca II H&K, Mg I λ3830, and G-band λ4300 are indicated. Also shown is the expected location of the [O II] λ3727 emission doublet.

as part of the GALAXEV library (Bruzual & Charlot 2003); at wavelengths outside this range, the signal-to-noise ratio is too low to contribute significantly to the fit. We use χ^2 minimization with redshift as the single free parameter and the best-fit flux

normalization determined by the equation,

$$C_{0,\rm bf} = \frac{\sum_{i=1}^{n} \frac{F_{\lambda,model,i} \times F_{\lambda,gal,i}}{\sigma^2_{\lambda,gal,i}}}{\sum_{i=1}^{n} \frac{F^2_{\lambda,model,i}}{\sigma^2_{\lambda,gal,i}}}, \quad (4.1)$$

where $F_{\lambda,model,i}$ are the model fluxes, and $F_{\lambda,gal,i}$ and $\sigma_{\lambda,gal,i}$ are the observed galaxy fluxes and uncertainties, respectively. The fit is performed on the unbinned data. The resulting best-fit redshift is $z = 0.915$ ($\chi^2_\nu = 1.26$ for 1841 degrees of freedom at 1.4 Gyr) for SSPs with an age of $0.9 - 2.5$ Gyr; see Figure 4.4. Significantly poorer fits are found with SSPs outside of this age range, or with late-type templates. At this redshift, there is a clear match between absorption features in the spectrum and the expected dominant lines (i.e., Ca II H&K, Mg I, and G-band). The distribution of χ^2_ν as a function of redshift is shown in Figure 4.5 revealing a secondary broad minimum at $z \approx 0.75$. This solution provides a much poorer fit to the data with $\chi^2_\nu = 1.60$, corresponding to about 10σ away from the best fit. The main reason for the poor fit is that it misses the key spectral absorption features and the clear break at 7650 Å (Figure 4.4).

At the best-fit spectroscopic redshift of $z = 0.915$ we find a marginal feature corresponding to [O II]λ3727 with a flux of $F_{\rm [OII]} \approx 3 \times 10^{-18}$ erg cm^{-2} s^{-1}, or $L_{\rm [OII]} \approx 7 \times 10^{39}$ erg s^{-1}. Given the marginal detection we use this luminosity to derive an upper limit on the star formation rate, with SFR $= (1.4 \pm 0.4)$ M$_\odot$ yr^{-1} L$_{\rm [OII]}$/(10^{41} erg s^{-1}) $\lesssim 0.1$ M$_\odot$ yr^{-1} (Kennicutt 1998). This is smaller than the star formation rates inferred for the star forming hosts of short GRBs (Berger 2009).

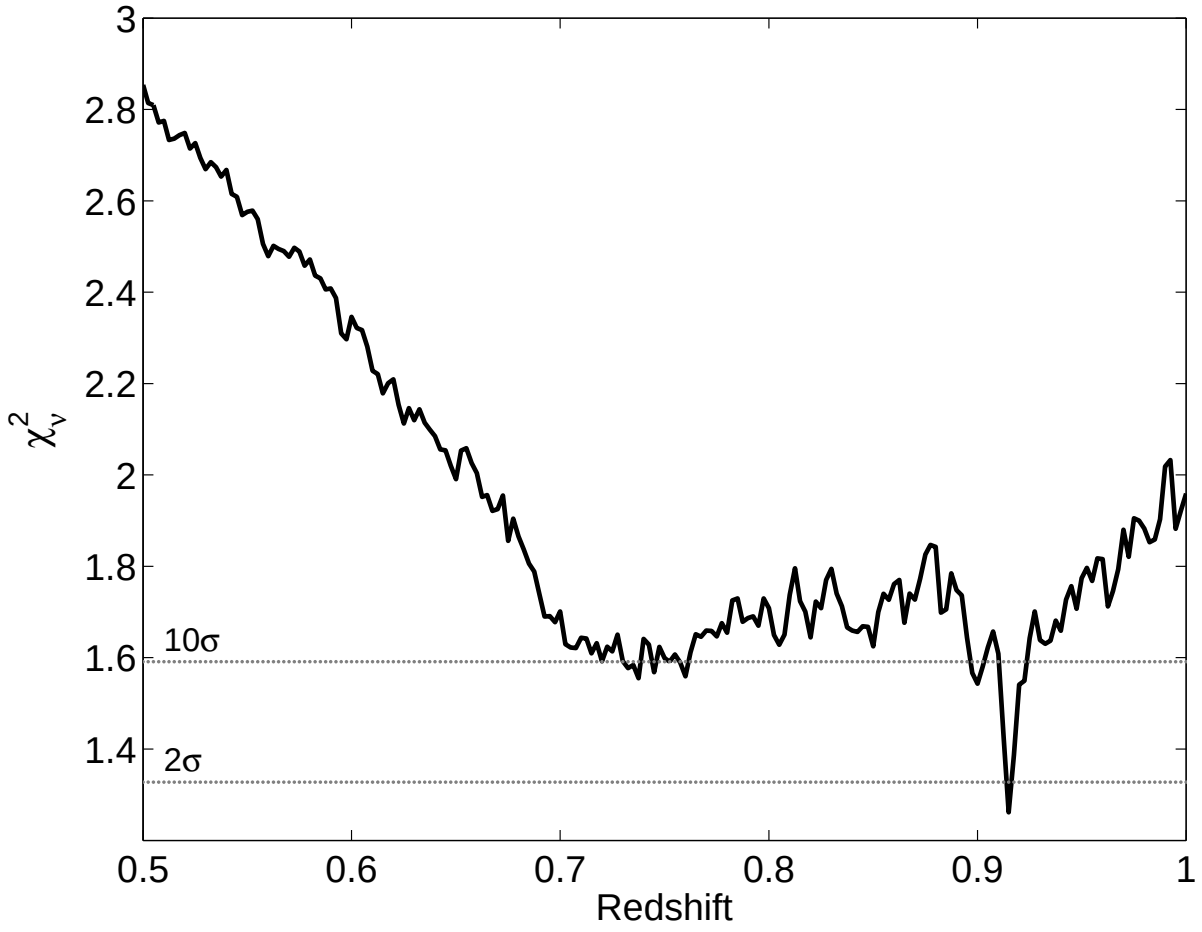

Figure 4.5.—: χ^2_ν as a function of redshift for the spectroscopic fit to a 1.4 Gyr SSP template (performed on the unbinned data, described in §4.3.1). The 2σ and 10σ levels are labeled. We find a sharp minimum at $z = 0.915$ with $\chi^2_\nu = 1.26$ and a broad minimum at $z \sim 0.75$, which is only consistent with the data at the 10σ level.

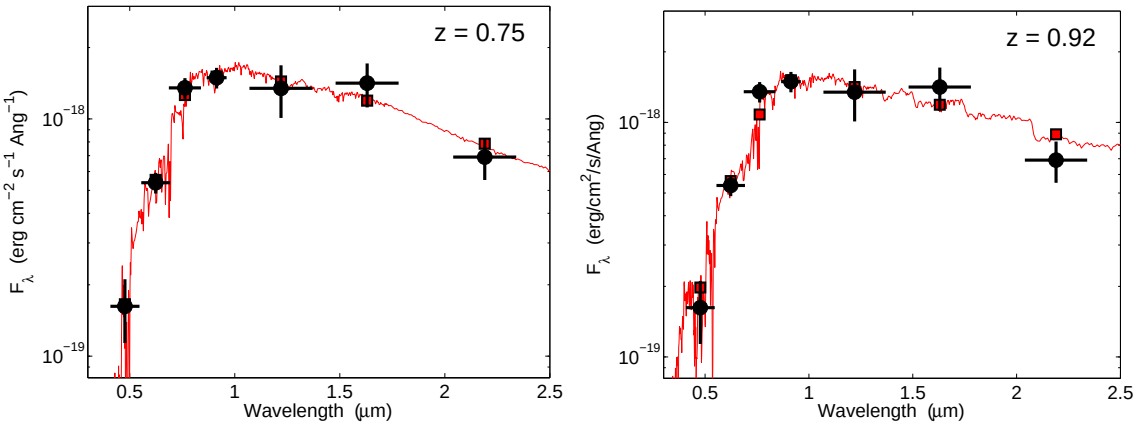

Figure 4.6.—: Optical and near-IR spectral energy distribution of the host galaxy of GRB 100117A (black circles). Each SED is fit with a Maraston (2005) single stellar population model (red line) through a maximum likelihood fit of the synthesized photometry (red squares, §4.3.2). We show the fits at the photometric best-fit $z = 0.75$ (left), and also at the preferred spectroscopic redshift $z = 0.915$ (right).

4.3.2 Broad-band Photometry

To extract additional information about the host galaxy we fit the broad-band photometry with Maraston (2005) evolutionary stellar population synthesis models. We use the subset of models described in Leibler & Berger (2010), with a Salpeter initial mass function, solar metallicity, and a red horizontal branch morphology, leaving redshift as a free parameter; see Figure 7.1. We find the best-fit solution to be $z = 0.75$ ($\chi^2_\nu = 0.3$ for 5 degrees of freedom) with a 2σ range of $z \approx 0.57 - 0.92$ (Figure 4.7), consistent with our spectroscopic redshift determination. Since $z = 0.75$ is ruled out at high confidence from the spectroscopic fit, we adopt $z = 0.915$ as the redshift of the host. At this redshift, the inferred stellar mass is 2.6×10^{10} $M_\odot$ and the stellar population age is about 1.1 Gyr, in good agreement with the spectroscopic results. The absolute B-band magnitude is $M_B \simeq -20.3$ mag, corresponding to $L_B \simeq 0.5\, L_*$ in comparison to the DEEP2 luminosity function at $z = 0.9$ (Willmer et al. 2006). We generally find poorer fits for models with

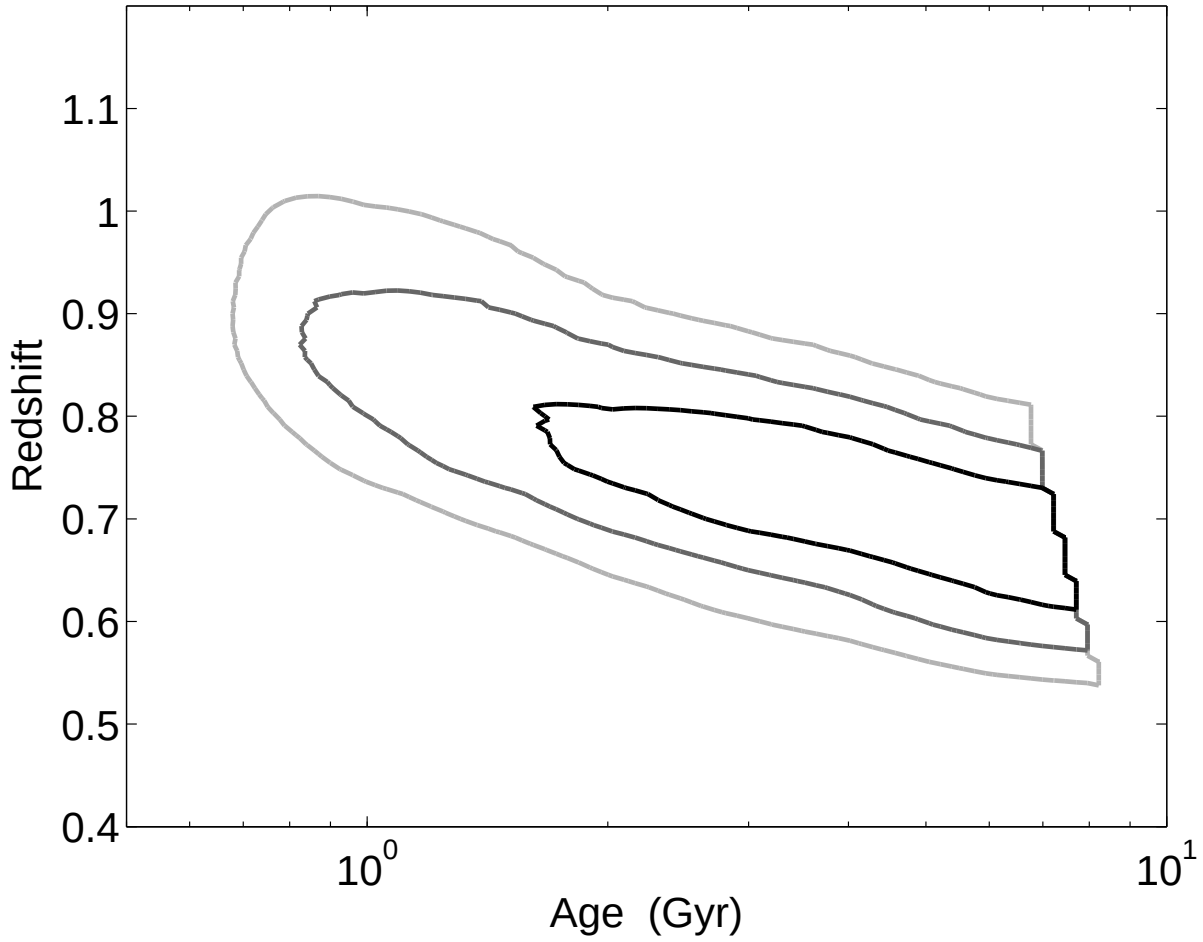

Figure 4.7.—: χ^2_ν contours for redshift and stellar population age using the Maraston (2005) single stellar population model ($1, 2, 3\sigma$ in order of decreasing darkness). The jagged edge at large ages is due to truncation at the appropriate age of the universe as a function of redshift. The 2σ contour leads to a best-fit redshift of $z = 0.57 - 0.92$.

0.5 and 2 $Z_\odot$.

Combining the upper limit on the star formation rate with the inferred stellar mass, the resulting limit on the specific star formation rate is $\mathrm{SSFR} \equiv \mathrm{SFR}/M_* \lesssim 0.004$ Gyr^{-1}. This confirms that the host galaxy is quiescent, since the characteristic growth timescale, $\mathrm{SSFR}^{-1} \approx 260$ Gyr, is significantly larger than the Hubble time.

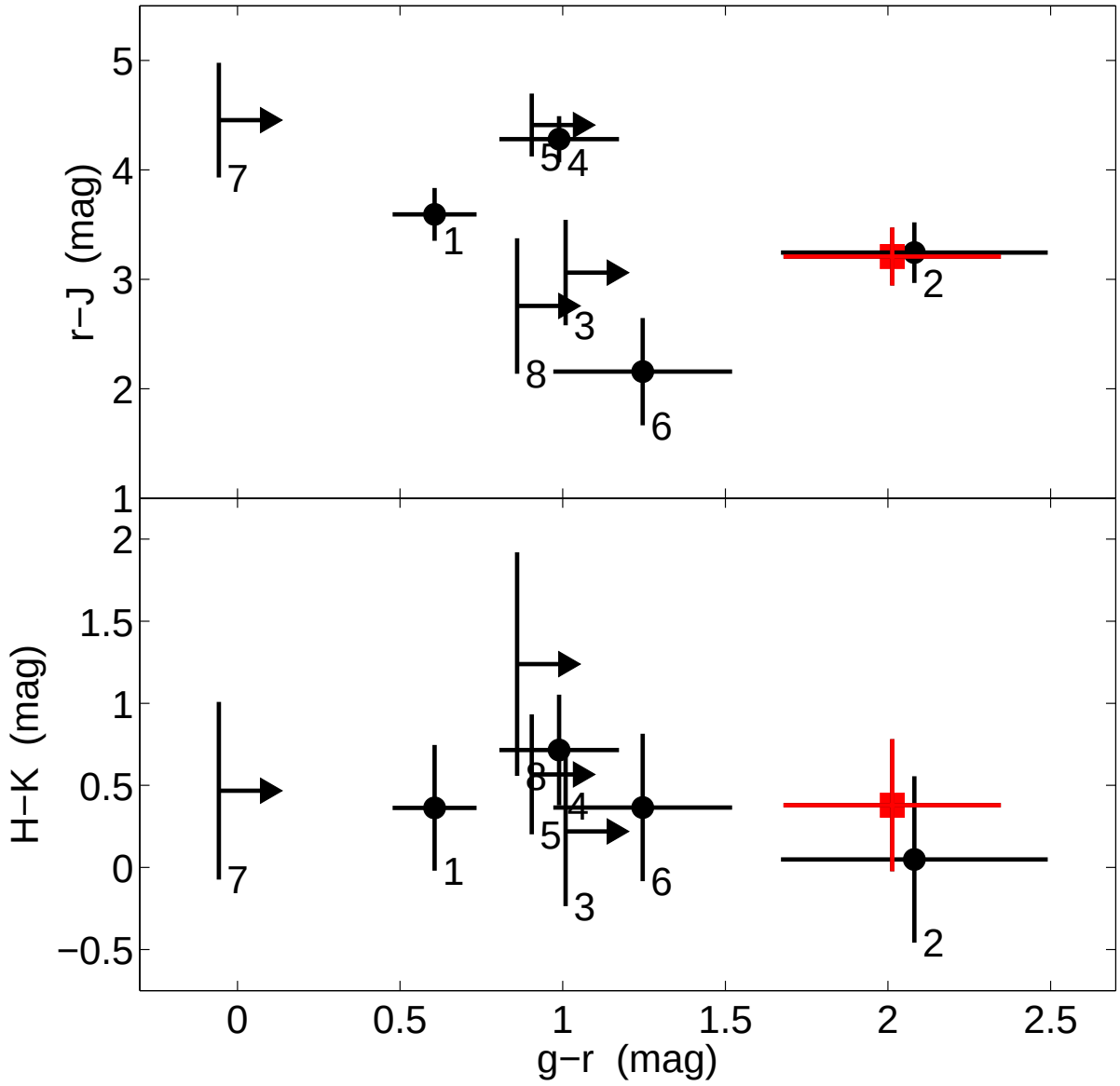

Figure 4.8.—: Color-color plots for red galaxies in a $2' \times 2'$ field around GRB 100117A (Figure 4.3). The host galaxy is marked by a red square. We identify an additional galaxy with similar colors (#2), and two potential galaxies with similar colors (although only lower limits in $g - r$; #3 and #8).

4.3.3 Large-Scale Environment

As shown in Figure 4.3, the field around GRB 100117A contains several red galaxies in addition to the host galaxy itself. We investigate whether the host and these galaxies

are part of a large-scale structure similar to some previous short GRB environments (Bloom et al. 2006; Berger et al. 2007a), using color-color plots (Figure 4.8). We find that only one galaxy has similar colors to the host, and is therefore potentially located at the same redshift. Two additional galaxies have similar $r-J$ and $H-K$ colors to the host, with limits on their $g-r$ colors (due to g-band non-detections) that are consistent with the host of GRB 100117A. These galaxies may be less luminous members of the same large-scale structure. Additional spectroscopic observations are required to assess whether the host is part of a $z \approx 0.9$ galaxy group. However, we note that even if it is part of a real group, it is not a rich group or cluster.

4.4 GRB and Afterglow Properties

At the best-fit redshift of $z = 0.915$ the isotropic-equivalent γ-ray energy of GRB 100117A is $E_{\gamma,\rm iso} = 9.2 \times 10^{50}$ erg ($16 - 2000$ keV in the rest-frame). This is similar to the values inferred for previous short GRBs at a similar redshift (Berger et al. 2007b; Berger 2007, 2010b).

To extract additional information about the burst we use the measured brightness of the optical afterglow in conjunction with the limit on the X-ray flux (§8.2). The inferred optical to X-ray spectral index is $\beta_{\rm OX} \lesssim -0.75$ ($F_\nu \propto \nu^{\beta_{\rm OX}}$), in agreement with the range of $\langle \beta_{\rm OX} \rangle = -0.72 \pm 0.17$ measured for short GRBs with X-ray and optical afterglow detections (Nysewander et al. 2009; Berger 2010b). Assuming the standard synchrotron emission spectrum from a relativistic blast wave (Sari et al. 1998), this value of $\beta_{\rm OX}$ indicates $p \gtrsim 2.5$ if $\nu_c > \nu_{\rm X}$, or $p \gtrsim 1.5$ if $\nu_c < \nu_{\rm O}$; here ν_c is the synchrotron cooling frequency and p is the power law index of the electron energy distribution, $N(\gamma) \propto \gamma^{-p}$.

Since these values are not atypical, we cannot robustly locate ν_c based on the optical to X-ray flux ratio.

However, we can still constrain the circumburst density (n) by making the reasonable assumption that the cooling frequency is located above the optical band, while the synchrotron peak frequency, ν_m, is located below the optical band since the optical afterglow is fading at discovery. Using the observed optical afterglow brightness and assuming a constant density medium at $p = 2.5$, we find (Granot & Sari 2002):

$$n \approx 7.3 \times 10^{-12} \epsilon_e^{-3} \epsilon_B^{-1.75} E_{52}^{-2.75} \ \mathrm{cm}^{-3}, \tag{4.2}$$

where ϵ_e and ϵ_B are the fractions of energy in the radiating electrons and magnetic field, respectively, and E_{52} is the energy in units of 10^{52} erg. Assuming that $E \approx E_{\gamma,\mathrm{iso}}$ and using $\epsilon_e, \epsilon_B \lesssim 1/3$ we infer a lower limit on the density of $n \gtrsim 10^{-6}$ cm^{-3}, which is similar to IGM densities. For more typical values of $\epsilon_e \approx \epsilon_B \approx 0.1$, we find $n \approx 3 \times 10^{-4}$ cm^{-3}. Since generally $\epsilon_e, \epsilon_B \gtrsim 0.01$ (Panaitescu & Kumar 2002; Yost et al. 2003), a likely upper bound on the density is $n \lesssim 20$ cm^{-3}.

4.5 Discussion and Conclusions

In the sample of 14 short GRBs with optical afterglows and coincident hosts, GRB 100117A is only the second event unambiguously associated with an early-type galaxy (the other being GRB 050724; Berger et al. 2005). Additional cases of early-type hosts have been proposed. In particular, GRB 050509B is likely associated with an early-type cluster galaxy but this is based on only an X-ray position (Bloom et al. 2006). Two additional bursts (070809 and 090515) lack coincident hosts despite optical

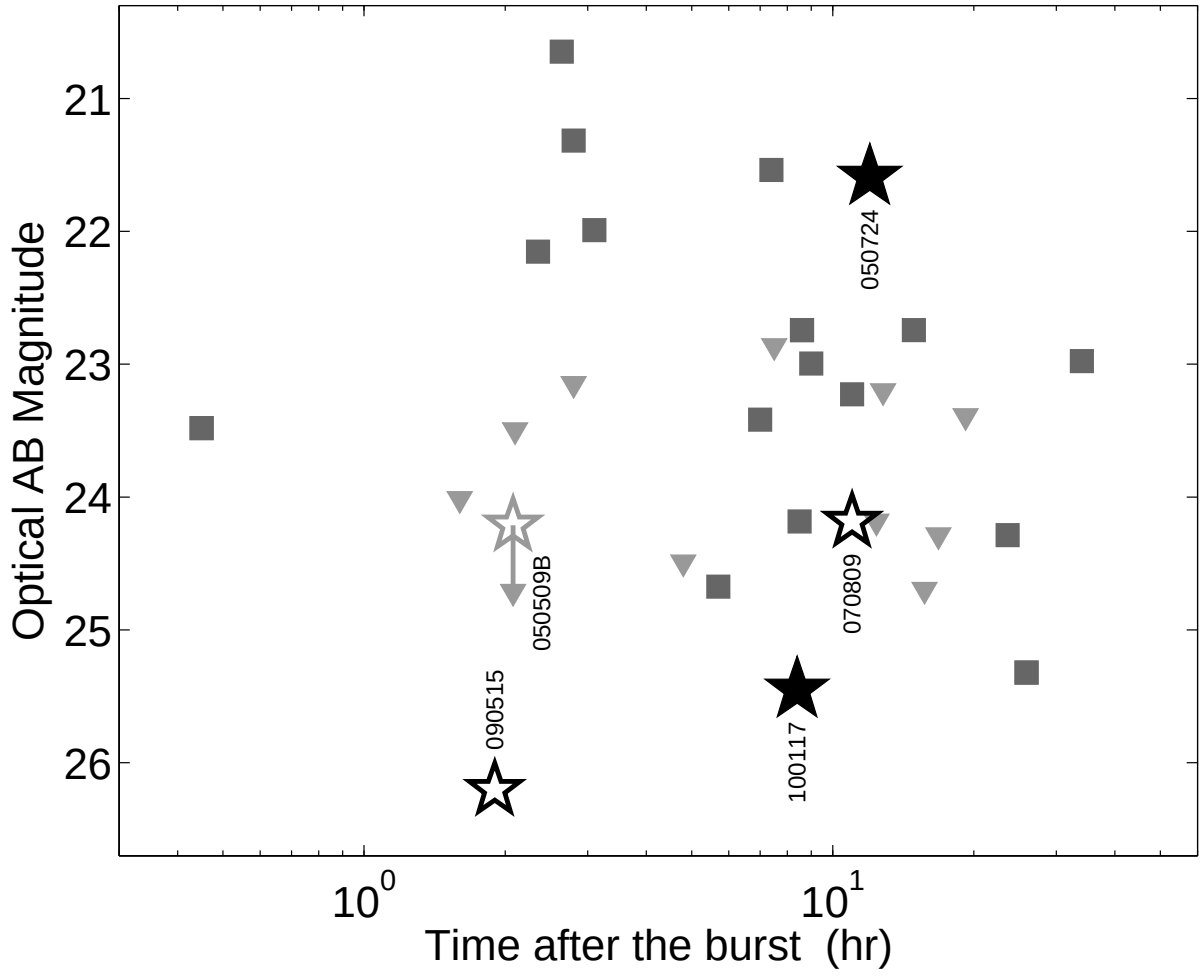

Figure 4.9.—: Short GRB optical afterglow brightness at the time of discovery for bursts with detected optical afterglows (squares) and upper limits (arrows). The two short GRBs with secure early-type hosts are denoted by solid stars, while bursts with putative early-type hosts are marked by open stars (Berger 2010b and references therein).

afterglow detections, but in both cases the galaxies with the lowest probability of chance coincidence are early-type galaxies (Berger 2010b). Even if we accept these additional early-type host associations as genuine, the host of GRB 100117A is located at a significantly higher redshift than the previous events, with $z \approx 0.23 - 0.47$. GRB 100117A also has the highest isotropic-equivalent gamma-ray energy of these events by a factor of a few, with $E_{\gamma,\rm iso} = 2.1 \times 10^{50}$ erg $(15 - 150$ keV). These results suggest that some of the optically-faint host galaxies identified to date (e.g., Berger et al. 2007b) may be bright near-IR sources due to a dominant old population. It also indicates that the presence of short GRBs in early-type galaxies does not necessarily point to progenitor ages of ~ 10 Gyr. Instead, the typical ages of short GRB progenitors in early-type hosts appear to be $\sim 1 - 4$ Gyr (Leibler & Berger 2010), which may lead to early-type hosts even at $z \approx 3$.

At the inferred redshift of $z = 0.915$ the projected physical offset of GRB 100117A is only 470 ± 310 pc. Our previous analysis of short GRB offsets revealed a median projected offset of about 5 kpc (Fong et al. 2010). In this context, GRB 100117A has the smallest offset measured to date. We note that the only other burst with a secure early-type host (GRB 050724) also has a small offset of about 2.7 kpc. Given the age of the stellar population of ~ 1 Gyr in both cases (see also Leibler & Berger 2010), these small offsets indicate that GRB 100117A and GRB 050724 did not originate from progenitors with a substantial kick (unless the kick direction in both cases is nearly aligned with our line of sight). Given the lack of any recent star formation activity, we can also rule out the possibility of a highly kicked progenitor system with a short merger time. On the other hand, the proposed associations of short GRBs 050509B, 070809, and 090515 with early-type hosts at offsets of tens of kpc (Bloom et al. 2006; Berger 2010b) indicates that some progenitors may experience large kicks, unless they have coincident

host galaxies that are very faint and therefore undetected. The cases of GRBs 070809 and 090515 are particularly intriguing since both had optical afterglows of comparable brightness to GRB 100117A (Figure 4.9), suggestive of a similar circumburst density despite a potential large difference in offsets.

Only a few short GRBs have circumburst density measurements, reflecting a general lack of multi-wavelength afterglow detections. GRB 051221A had an estimated density of $n \sim 10^{-3}$ cm^{-3} (Soderberg et al. 2006b), GRB 050724 had $n \approx 0.01 - 0.1$ cm^{-3} (Berger et al. 2005), GRB 050709 had[4] $n \lesssim 0.1$ cm^{-3} (Panaitescu 2006), and GRB 080503 had a very faint optical afterglow ($r_{\rm AB} > 25$) implying a low density of $n \sim 10^{-6}$ cm^{-3} (Perley et al. 2009a). For GRB 100117A we estimate $n \sim 10^{-4} - 10$ cm^{-3}, continuing the trend of relatively low circumburst densities for short GRBs. This is particularly striking in comparison to the circumburst densities inferred for long GRBs, with a median of $\langle n \rangle \approx 1 - 10$ cm^{-3} (e.g., Soderberg et al. 2006b).

Our discovery of the afterglow and $z = 0.915$ early-type host of GRB 100117A continues to support the conclusion that short GRBs exist at $z \sim 1$ and beyond (Berger et al. 2007b). However, unlike all previous short GRB hosts at these redshifts (Berger et al. 2007b; Graham et al. 2009; Antonelli et al. 2009b; Levesque et al. 2010), the host of GRB 100117A exhibits no evidence for star formation activity and is instead dominated by a ~ 1 Gyr old stellar population. With its faint optical afterglow it is possible that previous such events have been missed due to shallow optical afterglows searches, thereby potentially biasing the known host population against $z \gtrsim 1$ early-type hosts.

We thank Rik Williams and Daniel Kelson for obtaining rapid observations of

[4]Only an upper bound is available due to the lack of a radio detection.

GRB 100117A with IMACS. This paper includes data gathered with the 6.5 meter Magellan Telescopes located at Las Campanas Observatory, Chile. Observations were also obtained at the Gemini Observatory, which is operated by the Association of Universities for Research in Astronomy, Inc., under a cooperative agreement with the NSF on behalf of the Gemini partnership: the National Science Foundation (United States), the Particle Physics and Astronomy Research Council (United Kingdom), the National Research Council (Canada), CONICYT (Chile), the Australian Research Council (Australia), CNPq (Brazil) and CONICET (Argentina). This work also made use of data supplied by the UK Swift Science Data Center at the University of Leicester. This work was partially supported by Swift AO5 grant #5080010 and AO6 grant #6090612.

Chapter 5

Demographics of the Galaxies Hosting Short Gamma-Ray Bursts

W. Fong, E. Berger, R. Chornock, R. Margutti, A. J. Levan, N. R. Tanvir, R. L. Tunnicliffe, I. Czekala, D. B. Fox, D. A. Perley, S. B. Cenko, B. A. Zauderer, T. Laskar, S. E. Persson, A. J. Monson, D. D. Kelson, C. Birk, D. Murphy, M. Servillat, & G. Anglada

The Astrophysical Journal, Vol. 769, No. 56, 2013

Abstract

We present observations of the afterglows and host galaxies of three short-duration gamma-ray bursts (GRBs): 100625A, 101219A and 110112A. We find that GRB 100625A occurred in a $z = 0.452$ early-type galaxy with a stellar mass of $\approx 4.6 \times 10^9\,M_\odot$ and a stellar population age of ≈ 0.7 Gyr, and GRB 101219A originated in a star-forming galaxy at $z = 0.718$ with a stellar mass of $\approx 1.4 \times 10^9\,M_\odot$, a star formation rate of ≈ 16 $M_\odot$ yr^{-1}, and a stellar population age of ≈ 50 Myr. We also report the discovery of the optical afterglow of GRB 110112A, which lacks a coincident host galaxy to $i \gtrsim 26$ mag and we cannot conclusively identify any field galaxy as a possible host. From afterglow modeling, the bursts have inferred circumburst densities of $\approx 10^{-4} - 1$ cm^{-3}, and isotropic-equivalent gamma-ray and kinetic energies of $\approx 10^{50} - 10^{51}$ erg. These three events highlight the diversity of galactic environments that host short GRBs. To quantify this diversity, we use the sample of 36 *Swift* short GRBs with robust associations to an environment ($\sim 1/2$ of 68 short bursts detected by *Swift* to May 2012) and classify bursts originating from four types of environments: late-type ($\approx 50\%$), early-type ($\approx 15\%$), inconclusive ($\approx 20\%$), and "host-less" (lacking a coincident host galaxy to limits of $\gtrsim 26$ mag; $\approx 15\%$). To find likely ranges for the true late- and early-type fractions, we assign each of the host-less bursts to either the late- or early-type category using probabilistic arguments, and consider the scenario that all hosts in the inconclusive category are early-type galaxies to set an upper bound on the early-type fraction. We calculate most likely ranges for the late- and early-type fractions of $\approx 60 - 80\%$ and $\approx 20 - 40\%$, respectively. We find no clear trend between gamma-ray duration and host type. We also find no change to the fractions when excluding events recently claimed as possible

contaminants from the long GRB/collapsar population. Our reported demographics are consistent with a short GRB rate driven by both stellar mass and star formation.

5.1 Introduction

Observations of the galactic environments of cosmic explosions provide invaluable insight into their underlying progenitor populations. For example, Type Ia supernovae (SNe) originate in both star-forming and elliptical galaxies (Oemler & Tinsley 1979; van den Bergh et al. 2005; Mannucci et al. 2005; Li et al. 2011) consistent with an evolved progenitor and an event rate that traces both stellar mass and star formation (Sullivan et al. 2006). In contrast, SNe of types II and Ib/c are found to occur only in spiral and irregular galaxies, indicating that these events result from the core-collapse of young, massive stars (van den Bergh et al. 2005; Hakobyan et al. 2008; Li et al. 2011) and a rate tracing recent star formation (Kelly & Kirshner 2012; Anderson et al. 2012).

In the case of long-duration gamma-ray bursts, (GRBs; $T_{90} \gtrsim 2$ s; Kouveliotou et al. 1993) the link to star-forming host galaxies helped to establish that their progenitors are massive stars (Djorgovski et al. 1998; Le Floc'h et al. 2003; Fruchter et al. 2006; Wainwright et al. 2007a). Furthermore, a decade of concerted efforts to characterize the stellar populations of long GRB hosts revealed young stellar population ages of $\lesssim 0.2$ Gyr, a mean stellar mass of $\approx 2 \times 10^9\,M_\odot$, and inferred UV/optical star formation rates (SFR) of $\approx 1 - 50\,M_\odot$ yr^{-1} (Christensen et al. 2004; Savaglio et al. 2009; Leibler & Berger 2010; Laskar et al. 2011). In addition, the spatial locations of long GRBs with respect to their host galaxy centers (with a mean of ~ 1 half-light radius; Bloom et al. 2002) and their concentration in bright UV regions of their hosts (Fruchter et al. 2006) provided a direct association between long GRBs and star formation.

In contrast, the origin of short GRBs ($T_{90} \lesssim 2$ s) is less clear, as the first few afterglow discoveries led to associations with both elliptical (Berger et al. 2005;

Castro-Tirado et al. 2005b; Gehrels et al. 2005; Hjorth et al. 2005a; Bloom et al. 2006) and star-forming (Fox et al. 2005; Hjorth et al. 2005b; Soderberg et al. 2006b; Grupe et al. 2006; Burrows et al. 2006) host galaxies, demonstrating that at least some short GRBs originate from older stellar populations. Studies primarily focused on the sample of bursts with sub-arcsecond localization have shown the population of hosts to be dominated by late-type galaxies, albeit with lower specific SFRs, higher luminosities, and higher metallicities than the star-forming hosts of long GRBs (Berger 2009). Modeling of the spectral energy distributions of short GRB host galaxies has led to a broad range of inferred ages, $\tau \approx 0.03 - 4.4$ Gyr, and an average stellar mass of $\approx 2 \times 10^{10}\,M_{\odot}$ (Leibler & Berger 2010). A detailed analysis of their sub-galactic environments through *Hubble Space Telescope* observations has demonstrated that on average, short GRBs have offsets from their hosts of ≈ 5 kpc (Fong et al. 2010), while a growing subset which lack coincident hosts may have offsets of $\gtrsim 30$ kpc (Berger 2010a). Finally, an examination of short GRB locations with respect to their host light distributions revealed that they under-represent their host UV/optical light (Fong et al. 2010). These results are consistent with theoretical expectations for NS-NS/NS-BH mergers (Eichler et al. 1989; Narayan et al. 1992), with potential minor contribution from other proposed progenitors, such as the accretion-induced-collapse of a WD or NS (Qin et al. 1998; Levan et al. 2006a; Metzger et al. 2008a) or magnetar flares (Levan et al. 2006a; Chapman et al. 2008).

However, the majority of short GRB host galaxy studies published thus far primarily concentrate on bursts with sub-arcsecond localization from optical afterglows. While these events have the most unambiguous associations with host galaxies, the fraction is only $\sim 1/3$ (23/68 to May 2012) of all short GRBs detected by the *Swift* satellite

(Gehrels et al. 2004). The faintness of their optical afterglows ($\approx$ 23 mag at $\sim$ 10 hr after the burst; Berger 2010a) is likely attributed to a combination of a low energy scale (Panaitescu et al. 2001) and circumburst densities. Therefore, if there exist correlations between these basic properties and host galaxy type, the selection by optical afterglows may affect the relative rates of short GRBs detected in early- and late-type host galaxies. An alternative route to sub-arcsecond localization is through the X-ray detection of an afterglow, which does not necessarily depend on circumburst density (Granot & Sari 2002) with *Chandra*; however, only two such cases have been reported thus far (Fong et al. 2012b; Margutti et al. 2012; Sakamoto et al. 2013).

Demographics which accurately represent the bulk of the short GRB population are imperative in understanding the link to the progenitors. In particular, the late-to-early-type host galaxy ratio will inform whether stellar mass or SFR drives the short GRB rate (Leibler & Berger 2010), and will help to constrain the delay time distribution (Zheng & Ramirez-Ruiz 2007). Furthermore, a recent study based on γ-ray properties (spectral hardness and duration) claims that there is a non-negligible fraction of contaminants from collapsars in the *Swift* short GRB population (Bromberg et al. 2013). Thus, an examination of how this fraction affects the environment demographics will aid in assessing the true contamination.

Fortunately, the detection of X-ray afterglows with *Swift*/XRT (Gehrels et al. 2004; Burrows et al. 2005) enables positions with $\sim$few arcsecond precision in $\approx$ 60% (40/68) of all *Swift* short GRBs. In the majority of such cases, these XRT positions coupled with dedicated optical/NIR searches for host galaxies have provided meaningful associations

to a galactic environment[10]. While such bursts with XRT positions have been studied as single events (e.g. Gehrels et al. 2005; Bloom et al. 2006, 2007; Perley et al. 2012), the entire sample has not been studied in detail alongside bursts with sub-arcsecond localization.

To this end, we present here X-ray and optical/NIR observations of the afterglows and environments of three short GRBs[11] localized by *Swift*/XRT, which highlight the diversity of their galactic environments: GRBs 100625A, 101219A, and 110112A. We also present the discovery of the optical afterglow of GRB 110112A. While GRBs 100625A and 101219A have robust associations with host galaxies, GRB 110112A lacks a coincident host to deep optical limits. We describe the X-ray, optical and NIR observations for these three events (§2), present their energy scales and circumburst densities inferred from afterglow modeling (§3), and host galaxy stellar population ages, masses and SFRs extracted from spectroscopy and broad-band SEDs (§4). We discuss the stellar population characteristics of these three host galaxies compared to previous short GRB hosts (§5). Putting these bursts into the context, we undertake the first comprehensive study of host galaxy demographics of both sub-arcsecond localized and XRT-localized bursts, by investigating the late- and early-type host galaxy fractions for the bulk of the short GRB population, and compare host galaxy type to γ-ray properties (§6).

[10]The large majority of the remaining $\approx$ 40% of *Swift* short GRBs lack afterglow follow-up due to observing constraints unrelated to the burst properties; see §5.

[11]We present observations of two additional short GRBs, 100628A and 100702A, both with published *Swift*/XRT localizations (see Appendix). We show that the XRT afterglow of GRB 100628A is of low significance, while the XRT position of GRB 100702A is contaminated, preventing an unambiguous association with a host galaxy.

Unless otherwise noted, all magnitudes are in the AB system and are corrected for Galactic extinction in the direction of the burst (Schlegel et al. 1998; Schlafly & Finkbeiner 2011), and uncertainties correspond to 1σ confidence. We employ a standard ΛCDM cosmology with $\Omega_M = 0.27$, $\Omega_\Lambda = 0.73$, and $H_0 = 71$ km s^{-1} Mpc^{-1}.

5.2 Observations

5.2.1 GRB 100625A

GRB 100625A was detected by three γ-ray satellites on 2010 June 25.773 UT: the Burst Alert Telescope (BAT) on-board the *Swift* satellite (Gehrels et al. 2004; Holland et al. 2010b), *Konus-Wind* (Golenetskii et al. 2010a) and the Gamma-Ray Burst Monitor (GBM) on-board *Fermi* (Bhat 2010). BAT localized the burst to a ground-calculated position of RA=$01^{\rm h}03^{\rm m}11.1^{\rm s}$, Dec=$-39°05'29''$ (J2000) with an uncertainty of $1.0'$ radius (90% containment; Holland et al. 2010a), and the burst consisted of two pulses with a total duration of $T_{90} = 0.33 \pm 0.03$s ($15 - 350$ keV) and a fluence of $f_\gamma = (2.3 \pm 0.2) \times 10^{-7}$ erg cm^{-2} ($15 - 150$ keV; Holland et al. 2010a). *Fermi*/GBM observations determined $E_{\rm peak} = 509^{+77}_{-61}$ keV and $f_\gamma = (1.32 \pm 0.05) \times 10^{-6}$ erg cm^{-2} ($8 - 1000$ keV; Bhat 2010), while *Konus-Wind* observations determined $E_{\rm peak} = 418^{+128}_{-78}$ keV and $f_\gamma = (8.3 \pm 1.5) \times 10^{-7}$ erg cm^{-2} ($20 - 2000$ keV; Golenetskii et al. 2010a). Based on the short duration and high $E_{\rm peak}$, GRB 100625A can be classified as a short, hard burst. The γ-ray properties are listed in Table 8.1.

X-ray Observations

The X-ray Telescope (XRT) on-board *Swift* began observing the field at $\delta t = 43$ s (δt is the time after the BAT trigger) and detected a fading, uncatalogued X-ray source at RA=$01^{\rm h}03^{\rm m}10.91^{\rm s}$ and Dec=$-39°05'18.4''$ with a final positional accuracy of $1.8''$ radius (90%; Goad et al. 2007; Evans et al. 2009; Holland et al. 2010a; Table 8.1).

We analyze the XRT data using HEASOFT (v.6.11) and relevant calibration files. We apply standard filtering and screening criteria, and generate a count rate light curve following the prescriptions from Margutti et al. (2010) and Margutti et al. (2013). Our re-binning scheme ensures a minimum signal-to-noise ratio of $S/N = 4$ for each temporal bin. To extract a spectrum, we use Cash statistics and fit the XRT data with an absorbed power law model (*tbabs* × *ztbabs* × *pow* within the XSPEC routine) characterized by photon index, Γ, and intrinsic neutral hydrogen absorption column density, $N_{\rm H,int}$, in excess of the Galactic column density in the direction of the burst, $N_{\rm H,MW} = 2.1 \times 10^{20}\,{\rm cm}^{-2}$ (typical uncertainty of $\sim 10\%$; Kalberla et al. 2005; Wakker et al. 2011). We utilize the entire PC data set ($\delta t = 60 - 10^5$ s), where there is no evidence for spectral evolution. Our best-fit spectrum (C-stat$_\nu = 0.92$ for 95 d.o.f.) is characterized by $\Gamma = 2.5 \pm 0.2$ and $N_{\rm H,int} \lesssim 1.7 \times 10^{21}$ cm^{-2} (3σ) at $z = 0.452$ (see §5.4.1 for the redshift determination). Our best-fit parameters are consistent with the automatic spectrum fit produced by Page & Holland (2010). Applying these parameters to the data, we calculate the count rate-to-flux conversion factors, and hence the unabsorbed fluxes (Figure 5.1).

To quantify the decay rate, we utilize χ^2-minimization to fit a power law to the data in the form $F_X(t) \propto t^{\alpha_X}$, with α_X as the free parameter. The entire XRT light

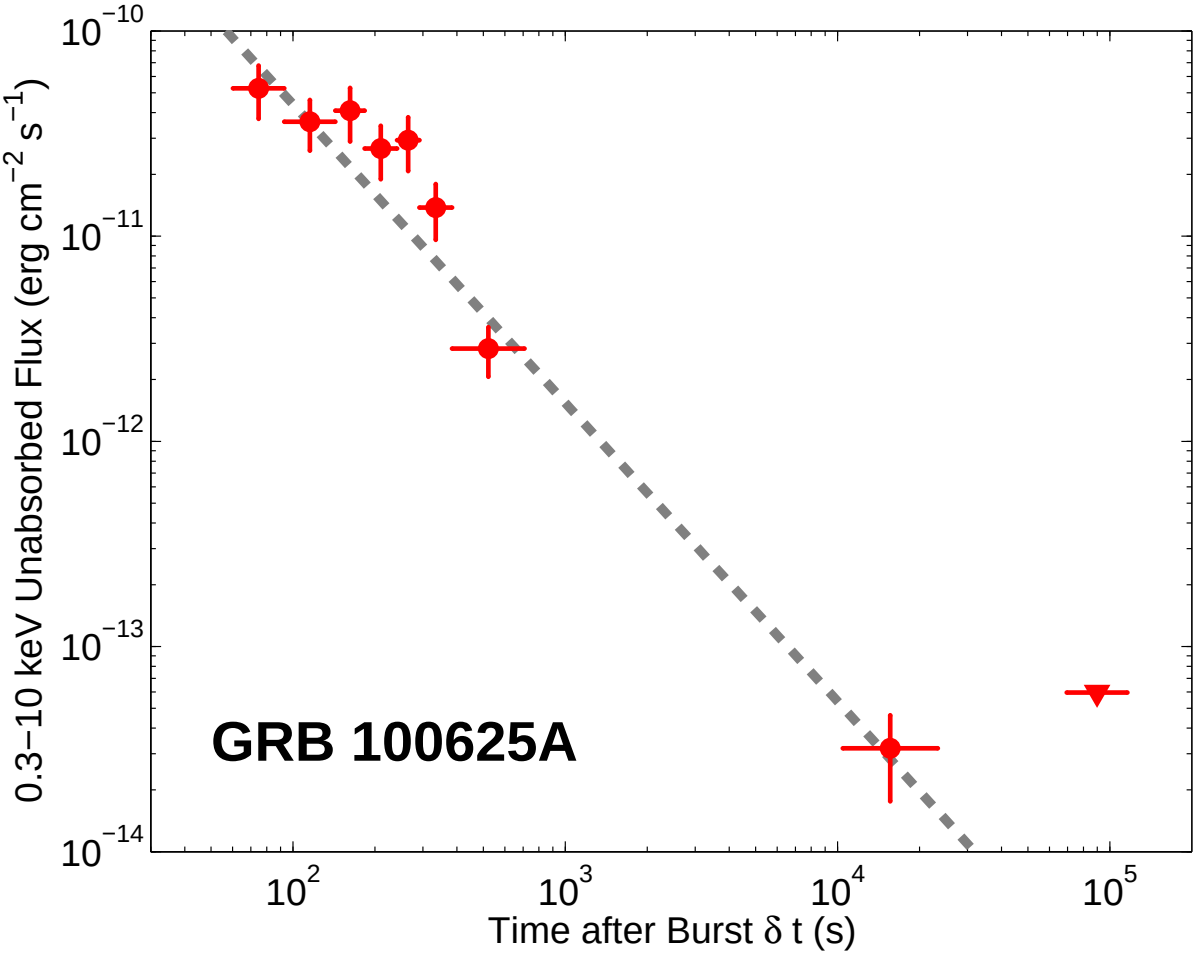

Figure 5.1.—: *Swift*/XRT light curve of GRB 100625A. The triangle is a 3σ upper limit. The entire light curve is best fit with a power law characterized by $\alpha_X = -1.45 \pm 0.08$ (grey dashed line).

curve ($\delta t \approx 80 - 10^5$ s, PC mode) is best fit with a single power law with index $\alpha_X = -1.45 \pm 0.08$ ($\chi^2_\nu = 2.1$ for 7 d.o.f.; Figure 5.1).

Optical/NIR Observations and Afterglow Limits

The UV-Optical Telescope (UVOT) on-board *Swift* commenced observations at $\delta t = 56$ s but no corresponding source was found within the XRT position. The 3σ limit over $\delta t \approx 87 - 1.2 \times 10^4$ s in the *white* filter, which transmits over $\lambda = 1600$-7000 Å (Poole et al. 2008), is $\gtrsim 22.6$ mag (not corrected for Galactic extinction; Holland et al. 2010a). Rapid ground-based follow-up in the optical and NIR provided early limits on the afterglow of $I \gtrsim 22.8$ mag at $\delta t \approx 17$ min (Suzuki et al. 2010) and $J \gtrsim 19.4$ mag at $\delta t \approx 8.6$ hr (Naito et al. 2010). GROND observations at $\delta t \approx 12.2$ hr place limits of $g \gtrsim 23.6$ mag, and $riz \gtrsim 23$ mag (Nicuesa Guelbenzu et al. 2012a).

We obtained optical observations of GRB 100625A with the Gemini Multi-Object Spectrograph (GMOS) mounted on the Gemini-South 8-m telescope, starting at $\delta t = 12.4$ hr in the riz filters in poor seeing conditions (Table 7.1). We analyze the data using the IRAF `gemini` package, and detect a single source within the enhanced XRT error circle in all three filters. To assess any potential fading of the source, we obtained a second set of observations at $\delta t \approx 2.6$ d, where the source is clearly extended. Digital image subtraction using the ISIS software package (Alard 2000) shows no residuals in all three filters (Figure 5.2). We therefore place 3σ limits of $r \gtrsim 22.6$ mag, $i \gtrsim 22.7$ mag and $z \gtrsim 22.8$ mag on the optical afterglow at $\delta t \approx 12.7$ hr (Table 7.1). The GMOS zeropoints are determined by sources in common with late-time IMACS observations (see below), which are calibrated to a standard star field at a similar airmass. Our limits match the

Table 5.1. Short GRB Properties

GRB	R.A. (J2000)	Decl (J2000)	Uncert. ($''$)	z	T_{90} ($15-350$ keV) (s)	f_γ ($15-150$ keV) (erg cm^{-2})	References
GRB 100625A	$01^h03^m10.91^s$	$-39°05'18.4''$	1.8	0.452	0.33 ± 0.03	$(2.3 \pm 0.2) \times 10^{-7}$	1
GRB 101219A	$04^h58^m20.49^s$	$-02°32'23.0''$	1.7	0.718	0.6 ± 0.2	$(4.6 \pm 0.3) \times 10^{-7}$	2
GRB 110112A	$21^h59^m43.85^s$	$+26°27'23.9''$	0.14	···	0.5 ± 0.1	$(3.0 \pm 0.9) \times 10^{-8}$	3, This work

Note. — **References**: (1) Holland et al. 2010a; (2) Krimm et al. 2010b; (3) Barthelmy et al. 2011

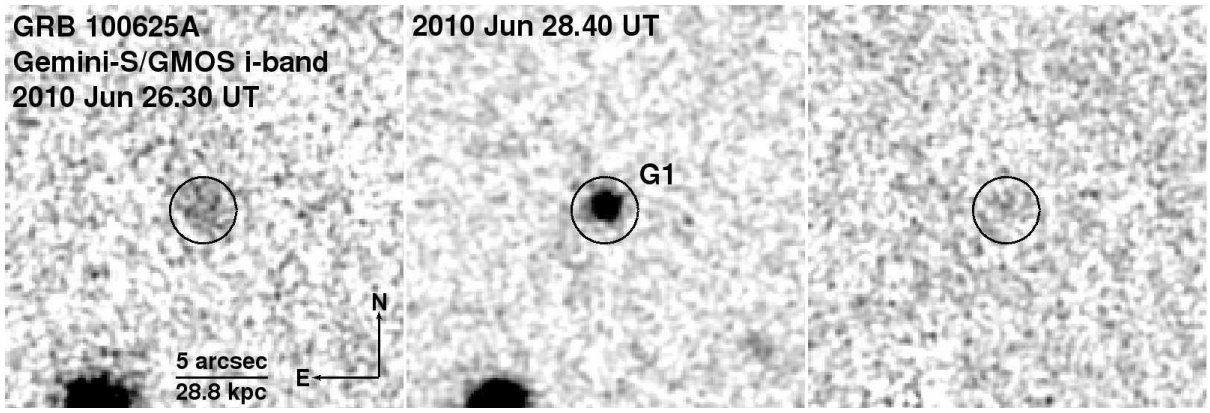

Figure 5.2.—: Gemini-South/GMOS i-band observations of GRB 100625A. The XRT error circle has a radius of $1.8''$ (90% containment; black). Images are smoothed with a 2-pixel Gaussian. *Left:* $\delta t = 0.53$ d in poor seeing conditions ($\theta_{\rm FWHM} = 1.9''$) with a faint host detection. *Center:* $\delta t = 2.63$ d with $0.9''$ seeing. *Right:* Digital image subtraction of the two epochs reveals no afterglow to a 3σ limit of $i \gtrsim 22.7$ mag. The host galaxy is marked as G1.

GROND limits reported at $\delta t \approx 12.2$ hr (Nicuesa Guelbenzu et al. 2012a).

In addition, we obtained two epochs of J-band observations with the Persson's Auxilliary Nasmyth Infrared Camera (PANIC) mounted on the 6.5-m Magellan/Baade telescope at $\delta t \approx 1.6$ and 6.6 d. We analyze the data using standard procedures in IRAF. Digital image subtraction shows no evidence for fading, with a 3σ limit of $J \gtrsim 23.9$ mag (photometrically tied to the 2MASS catalog and converted to the AB system) at $\delta t \approx 1.6$ d (Table 7.1).

We obtained late-time *griz* observations of the the field of GRB 100625A with the Inamori Magellan Areal Camera and Spectrograph (IMACS) mounted on Magellan/Baade starting on 2010 November 14.11 UT. We also obtained K_s-band observations with the FourStar Infrared Camera mounted on Magellan/Baade on 2011 December 07.16 UT (Table 7.1). The *griz* zeropoints are calculated using a standard star field at a similar airmass, while the K_s-band zeropoint is determined from point sources in common with 2MASS. Our afterglow limit and host galaxy photometry are summarized in Table 7.1.

We obtained a spectrum of the putative host galaxy with the Low Dispersion Survey Spectrograph 3 (LDSS3) mounted on the 6.5-m Magellan/Clay telescope on 2011 October 21.27 UT. A dithered pair of 2700 s exposures was obtained with the VPH-ALL grating, which has a wavelength coverage of $4000 - 10000$ Å and a spectral resolution of ≈ 8 Å. We used standard tasks in IRAF for data reduction, HeNeAr arc lamps for wavelength calibration, and observations of the smooth-spectrum standard star EG131 for flux calibration. We discuss the spectral features and redshift determination in §5.4.1.

Table 5.2. Log of Optical/NIR Afterglow and Host Galaxy Photometry

GRB	Date (UT)	δt (d)	Telescope	Instrument	Filter	Exposures (s)	θ_{FWHM} ($''$)	Afterglow[a] (AB mag)	F_ν^a (μJy)	Host[a] (AB mag)	$A_{\lambda,\rm MW}$ (mag)
GRB 100625A	2010 Jun 26.288	0.52	Gemini-S	GMOS	r	5×120	2.31	> 22.6	< 3.3	22.76 ± 0.23	0.027
	2010 Jun 26.301	0.53	Gemini-S	GMOS	i	3×120	1.91	> 22.7	< 2.9	22.10 ± 0.15	0.020
	2010 Jun 26.314	0.54	Gemini-S	GMOS	z	5×120	1.95	> 22.8	< 2.8	22.23 ± 0.15	0.015
	2010 Jun 27.392	1.62	Magellan	PANIC	J	35×60	0.76	> 23.9	< 1.0	21.48 ± 0.05	0.008
	2010 Jun 28.394	2.62	Gemini-S	GMOS	r	5×120	1.10			22.63 ± 0.09	0.027
	2010 Jun 28.404	2.63	Gemini-S	GMOS	i	5×120	0.87			22.14 ± 0.04	0.020
	2010 Jun 28.414	2.64	Gemini-S	GMOS	z	5×120	0.95			22.07 ± 0.10	0.015
	2010 Jul 02.398	6.63	Magellan	PANIC	J	18×180	0.53			21.40 ± 0.06	0.008
	2010 Nov 14.114	141.3	Magellan	IMACS	g	2×420	0.65			23.87 ± 0.19	0.039
	2010 Nov 14.123	141.4	Magellan	IMACS	i	1×240	0.47			22.04 ± 0.07	0.020
	2010 Nov 14.196	141.4	Magellan	IMACS	r	1×360	0.65			22.59 ± 0.13	0.027
	2010 Nov 14.200	141.4	Magellan	IMACS	z	1×180	0.52			21.88 ± 0.22	0.015
	2011 Dec 07.16	529.4	Magellan	FourStar	K_s	90×10	0.55			20.76 ± 0.10	0.008
GRB 100702A	2010 Jul 02.10	0.05	Magellan	PANIC	J	9×180	0.53	$> 23.3^b$	$< 1.70^b$	20.54 ± 0.05 / 21.30 ± 0.07^c	0.284
	2010 Jul 02.30	0.25	Magellan	PANIC	J	9×180	0.75			$\cdots$ [d] / 21.49 ± 0.11	0.284
	2011 Mar 06.37	247.3	Magellan	IMACS	i	2×240	0.83			> 22.7	0.679
GRB 101219A	2010 Dec 19.15	0.04	Gemini-S	GMOS	i	9×180	0.66	> 24.9	< 0.40	23.20 ± 0.11	0.097
	2010 Dec 19.16	0.05	Magellan	FourStar	J	25×60	0.46	> 23.6	< 1.36	22.43 ± 0.13	0.041
	2010 Dec 19.17	0.07	Gemini-S	GMOS	r	9×180	0.80	> 24.9	< 0.40	23.83 ± 0.26	0.131

Table 5.2—Continued

GRB	Date (UT)	δt (d)	Telescope	Instrument	Filter	Exposures (s)	θ_{FWHM} ($''$)	Afterglow[a] (AB mag)	F_ν^a (μJy)	Host[a] (AB mag)	$A_{\lambda,\mathrm{MW}}$ (mag)
	2010 Dec 19.20	0.09	Gemini-S	GMOS	i	9×180	0.69	> 24.9	< 0.40	23.40 ± 0.09	0.097
	2010 Dec 19.27	0.16	Gemini-S	GMOS	r	12×180	0.67	> 25.1	< 0.34	23.73 ± 0.10	0.131
	2010 Dec 19.30	0.20	Gemini-S	GMOS	i	12×180	0.67			23.19 ± 0.08	0.097
	2010 Dec 28.16	9.05	Gemini-S	GMOS	r	12×240	0.65			23.95 ± 0.05	0.131
	2011 Jan 12.15	24.05	Magellan	LDSS3	z	6×180	0.68			23.22 ± 0.16	0.072
	2011 Jan 12.17	24.06	Magellan	LDSS3	g	5×180	1.05			24.57 ± 0.08	0.189
	2011 Dec 07.24	353.1	Magellan	FourStar	J	15×60	0.56			22.11 ± 0.19	0.041
	2011 Dec 07.25	353.1	Magellan	FourStar	K_s	90×10	0.44			21.55 ± 0.21	0.017
GRB 110112A	2011 Jan 12.18	0.64	WHT	ACAM	i	2×300	1.10	22.77 ± 0.29	2.84 ± 0.75	$\cdots$	0.104
	2011 Jun 27.83	166.2	Magellan	LDSS3	i	5×240	0.94			> 24.7	0.104
	2011 Jun 27.83	166.3	Magellan	LDSS3	r	3×360	1.11			> 25.5	0.140
	2011 Jul 28.46	197.3	Gemini-N	GMOS	i	15×180	0.61			> 26.2	0.104

Note. — Limits correspond to a 3σ confidence level.

[a] These values are corrected for Galactic extinction (Schlafly & Finkbeiner 2011).

[b] Only applies to approximately half of the error circle.

[c] Magnitudes for S1 and S4, respectively.

[d] S1 is blended with a neighboring bright star (Figure 5.16) so we cannot perform photometry.

5.2.2 GRB 101219A

GRB 101219A was detected by *Swift*/BAT (Gelbord et al. 2010) and *Konus-Wind* (Golenetskii et al. 2010b) on 2010 December 19.105 UT. BAT localized the burst at a ground-calculated position of RA=$04^{\rm h}58^{\rm m}20.7^{\rm s}$ and Dec=$-02^\circ31'37.1''$ with a $1.0'$ radius uncertainty (90% containment; Krimm et al. 2010b). The γ-ray light curve exhibits a double-peaked structure with $T_{90} = 0.6 \pm 0.2$ s ($15 - 350$ keV) and $f_\gamma = (4.6 \pm 0.3) \times 10^{-7}$ erg cm^{-2} ($15 - 150$ keV; Krimm et al. 2010b). *Konus-Wind* observations determined $E_{\rm peak} = 490^{+103}_{-79}$ keV and $f_\gamma = (3.6 \pm 0.5) \times 10^{-6}$ erg cm^{-2} ($20 - 10^4$ keV; Golenetskii et al. 2010b). Based on the short duration and high $E_{\rm peak}$, GRB 101219A can be classified as a short, hard burst. The γ-ray properties are listed in Table 8.1.

X-ray Observations

Swift/XRT began observing the field at $\delta t = 40$ s and detected a fading, uncatalogued X-ray source at RA=$04^{\rm h}58^{\rm m}20.49^{\rm s}$ and Dec=$-02^\circ32'23.0''$ with final accuracy of $1.7''$ (Goad et al. 2007; Evans et al. 2009; Table 8.1). We re-bin the XRT data and extract the best-fit spectrum for GRB 101219A as described in §5.2.1. We utilize the PC data set, $\delta t = 70 - 10^4$ s, where there is no evidence for spectral evolution. We find an average best-fitting spectrum characterized by $\Gamma = 1.8 \pm 0.1$ and $N_{\rm H,int} = 6.6^{+2.3}_{-1.8} \times 10^{21}$ cm^{-2} at $z = 0.718$ (C-stat$_\nu = 0.97$ for 211 d.o.f.; see §5.4.2 for redshift determination) in excess of the Galactic absorption, $N_{\rm H,MW} = 4.9 \times 10^{20}$ cm^{-2} (Kalberla et al. 2005). Our best-fit parameters are consistent with the automatic spectrum fit produced by Gelbord & Grupe (2010). Applying these parameters to the XRT data, we calculate the count rate-to-flux conversion factors, and hence the unabsorbed fluxes (Figure 5.3).

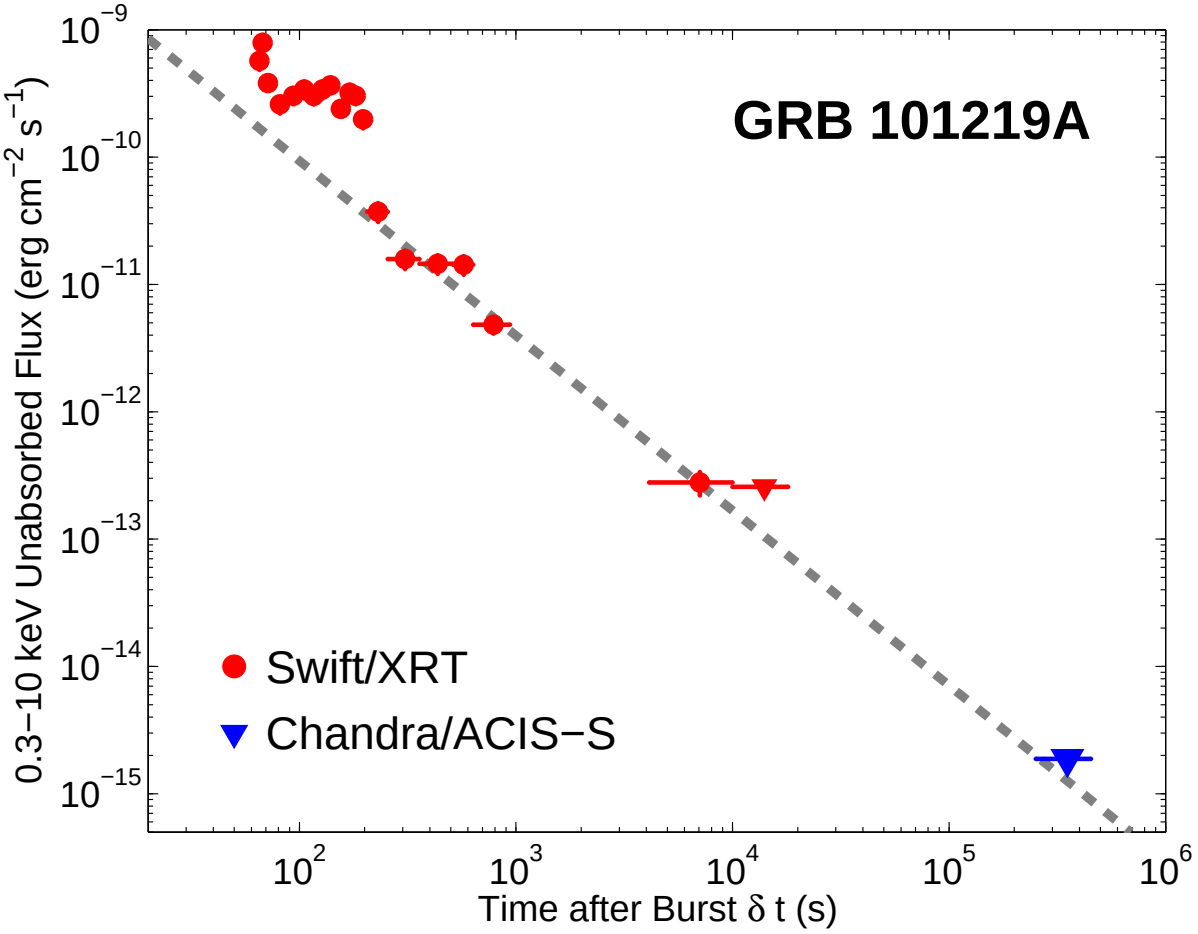

Figure 5.3.—: X-ray afterglow light curve of GRB 101219A, including *Swift*/XRT observations (red points) and a *Chandra*/ACIS-S observation (blue point). Triangles denote 3σ upper limits. The data over $\delta t \approx 200 - 10^4$ s are best fit with a power law characterized by $\alpha_X = -1.37 \pm 0.13$ (grey dashed line).

In addition, we obtained a 20 ks observation with the Advanced CCD Imaging Spectrometer (ACIS-S) on-board the *Chandra* X-ray Observatory starting at $\delta t = 4.1$ days. We analyze the *Chandra* data with the `CIAO` data reduction package. In an energy range of $0.5-8$ keV, we extract 4 counts in a $2.5''$ aperture centered on the XRT position, consistent with the average 3σ background level calculated from source-free regions on the same chip. We take this count rate of $\lesssim 2 \times 10^{-4}$ counts s^{-1} to be the 3σ upper limit on the X-ray afterglow flux at $\delta t \approx 4.1$ days. Applying the spectrum extracted from the XRT data, this count rate corresponds to $F_X \lesssim 1.9 \times 10^{-15}$ erg cm^{-2} s^{-1}.

The X-ray light curve is characterized by a steep decay and a short plateau for $\delta t < 200$ s, followed by a steady decline to the end of XRT observations at $\delta t \approx 10^4$ s. To quantify this decay rate, we utilize the single-parameter χ^2-minimization method described in §5.2.1. Excluding the XRT data at $\delta t \lesssim 200$ s and the late-time upper limits, the best-fit power law index is $\alpha_X = -1.37 \pm 0.13$ ($\chi^2_\nu = 1.1$ for 5 d.o.f.). The full X-ray afterglow light curve, along with the best-fit model is shown in Figure 5.3.

Optical/NIR Observations and Afterglow Limits

UVOT commenced observations at $\delta t = 67$ s. Over $\delta t = 67 - 5500$ s, no corresponding source was found within the XRT position to a 3σ limit of $\gtrsim 21.4$ in the *white* filter (Kuin & Gelbord 2010).

We observed the field of GRB 101219A in both r- and i-bands with GMOS on Gemini-South, and in J-band with FourStar, starting at $\delta t \approx 0.96$ hr (Table 7.1). We detect a single extended source within the XRT error circle in all filters. To assess any fading, we obtained additional observations in the ri-bands at $\delta t \approx 0.2$ d (Table 7.1).

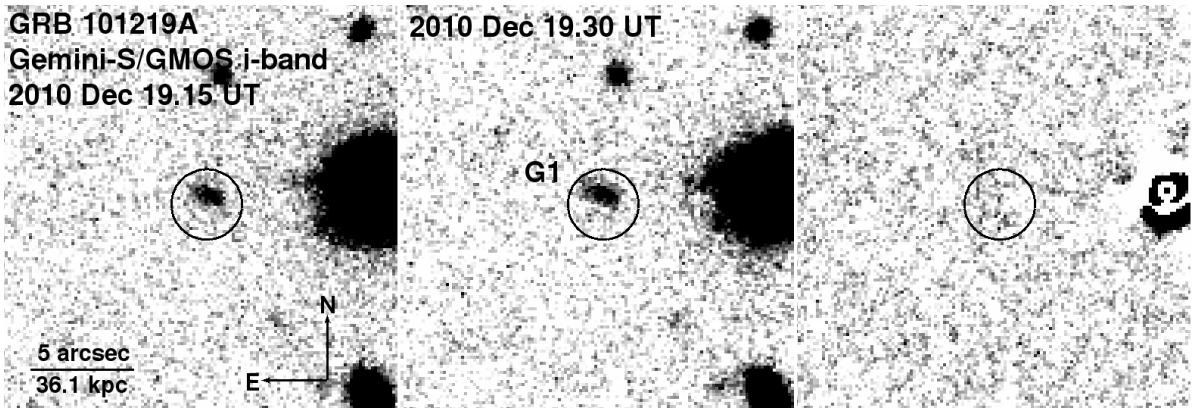

Figure 5.4.—: Gemini-South/GMOS i-band observations of the host galaxy of GRB 101219A. The XRT error circle has a radius of 1.7″ (90% containment; black). An additional i-band observation at $\delta t = 2.2$ hr, adds no additional constraints so is not shown here. *Left:* $\delta t = 0.96$ hr. *Center:* $\delta t = 4.8$ hr. *Right:* Digital image subtraction of the two epochs reveals no afterglow to a 3σ limit of $i \gtrsim 24.9$ mag.

Digital image subtraction between these epochs does not reveal any residuals (Figure 5.4), allowing us to place limits on the optical afterglow of $i \gtrsim 24.9$ mag and $r \gtrsim 24.9$ mag at the time of the first epoch for each filter: $\delta t \approx 0.96$ and 2.2 hr, respectively (Table 7.1). To assess the fading on timescales $\gtrsim 1$ day, we obtained a third set of observations in the r-band at $\delta t \approx 9$ d. Image subtraction with each of the first and second r-band observations also show no evidence for fading (Table 7.1). A second set of J-band observations at $\delta t \approx 350$ d and a clean image subtraction with the first epoch allows us to place a limit on the NIR afterglow of $J \gtrsim 23.6$ mag at $\delta t = 1.7$ hr. Finally, to complement our early optical/NIR observations, we obtained imaging of the putative host galaxy in the gz-bands with LDSS3 starting on 2011 January 12.15 UT, and in the K_s-band with FourStar on 2011 December 07.24 UT. Our limits for the afterglow and photometry of the putative host galaxy are summarized in Table 7.1.

We obtained spectroscopic observations of the host on 2011 January 2.25 UT

using GMOS on Gemini-North at a mean airmass of 1.2. We obtained a set of 4×1800 s exposures with the R400 grating and an order-blocking filter, OG515 in the nod-and-shuffle mode, covering $5860 - 10200$ Å at a spectral resolution of ≈ 7 Å. We used standard tasks in IRAF for data reduction, CuAr arc lamps for wavelength calibration, and archival observations of the smooth-spectrum standard star BD+28 4211 for flux calibration. We discuss the characteristics of the spectrum and redshift determination in §5.4.2.

5.2.3 GRB 110112A

Swift/BAT detected GRB 110112A on 2011 January 12.175 UT (Stamatikos et al. 2011), with a single spike with $T_{90} = 0.5 \pm 0.1$ s $(15 - 350$ keV) and $f_\gamma = (3.0 \pm 0.9) \times 10^{-8}$ erg cm^{-2} $(15 - 150$ keV; Barthelmy et al. 2011). The BAT ground-calculated position is RA=$21^{\rm h}59^{\rm m}33.6^{\rm s}$ and Dec=$+26°28'10.6''$ with $2.6'$ radius uncertainty (90% containment; Barthelmy et al. 2011). The γ-ray properties are listed in Table 8.1.

X-ray Observations

XRT commenced observations of the field of GRB 110112A at $\delta t = 76$ s and located a fading X-ray counterpart with a UVOT-enhanced positional accuracy of $1.6''$ radius (Evans et al. 2011; Goad et al. 2007; Evans et al. 2009; Table 8.1). We extract the XRT light curve and spectrum in the manner described in Section 5.2.1, requiring a minimum $S/N = 3$ for each bin, and use the Galactic absorption in the direction of the burst of $N_{\rm H,MW} = 5.5 \times 10^{20}$ cm^{-2} (Kalberla et al. 2005). The light curve is characterized by a short plateau for $\delta t \lesssim 200$ s, followed by a steady decline (Figure 5.5). Performing

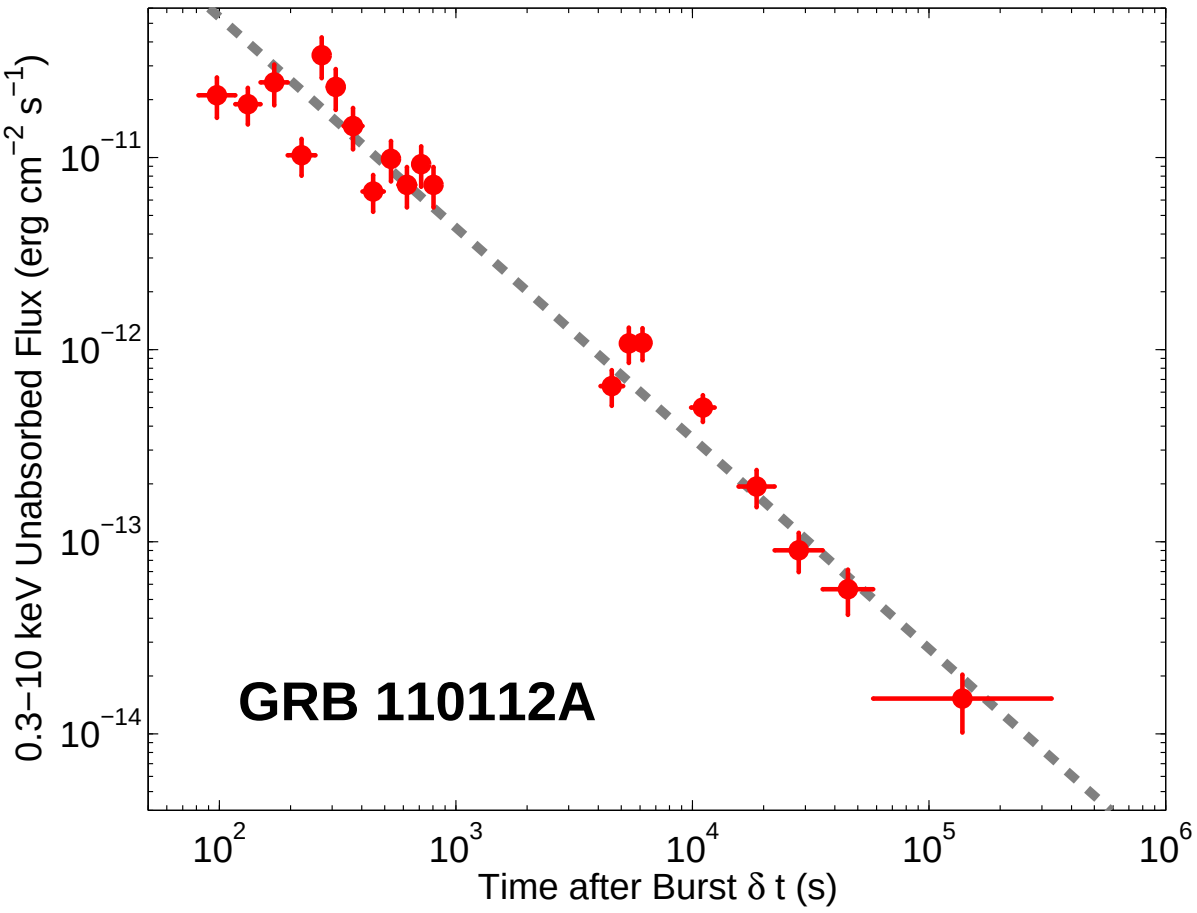

Figure 5.5.—: *Swift*/XRT light curve of GRB 110112A. The data (red points) for $\delta t \gtrsim 200$ s is best fit with a single power law characterized by $\alpha_X = -1.10 \pm 0.05$ (grey dashed line).

χ^2-minimization, we find the XRT light curve for $\delta t \gtrsim 200$ s is best fit with a single power law characterized by index $\alpha_X = -1.10 \pm 0.05$ ($\chi^2_\nu = 1.0$ for 17 d.o.f.). Our best-fitting spectral parameters over the entire data set, where there is no evidence for spectral evolution, are $\Gamma = 2.2 \pm 0.2$ and an upper limit of $N_{\rm H,int} \lesssim 1.6 \times 10^{21}$ cm^{-2} (3σ at $z = 0$; C-stat = 0.82 for 156 d.o.f.).

Optical Afterglow Discovery

UVOT commenced observations at $\delta t = 80$ s, and no corresponding source was found within the XRT position to a 3σ limit in the *white* filter of $\gtrsim 21.3$ mag using data over $\delta t = 4400 - 6100$ s (uncorrected for Galactic extinction; Breeveld & Stamatikos 2011).

We obtained i-band observations with ACAM mounted on the 4.2-m William Herschel Telescope (WHT) at $\delta t = 15.4$ hr. In a total exposure time of 600 s (Table 7.1), we detect a single source within the enhanced XRT error circle with $i = 22.77 \pm 0.29$ mag, where the zeropoint has been determined using sources in common with the SDSS catalog (Figure 5.6). To assess any fading associated with this source or within the XRT position, we obtained i-band imaging with LDSS3 starting on 2011 June 27.83 UT and no longer detect any source within the error circle to $i \gtrsim 24.7$ mag, confirming that the source has faded by $\gtrsim 2$ mag. Therefore, we consider this source to be the optical afterglow of GRB 110112A.

To determine the position of the afterglow, we perform absolute astrometry using 108 point sources in common with SDSS and calculate an astrometric tie RMS of $0.11''$. The resulting afterglow position is RA=$21^{\rm h}59^{\rm m}43.85^{\rm s}$ and Dec=$+26^\circ27'23.89''$ (J2000) with a centroid uncertainty of $0.09''$ determined with Source Extractor, which, together

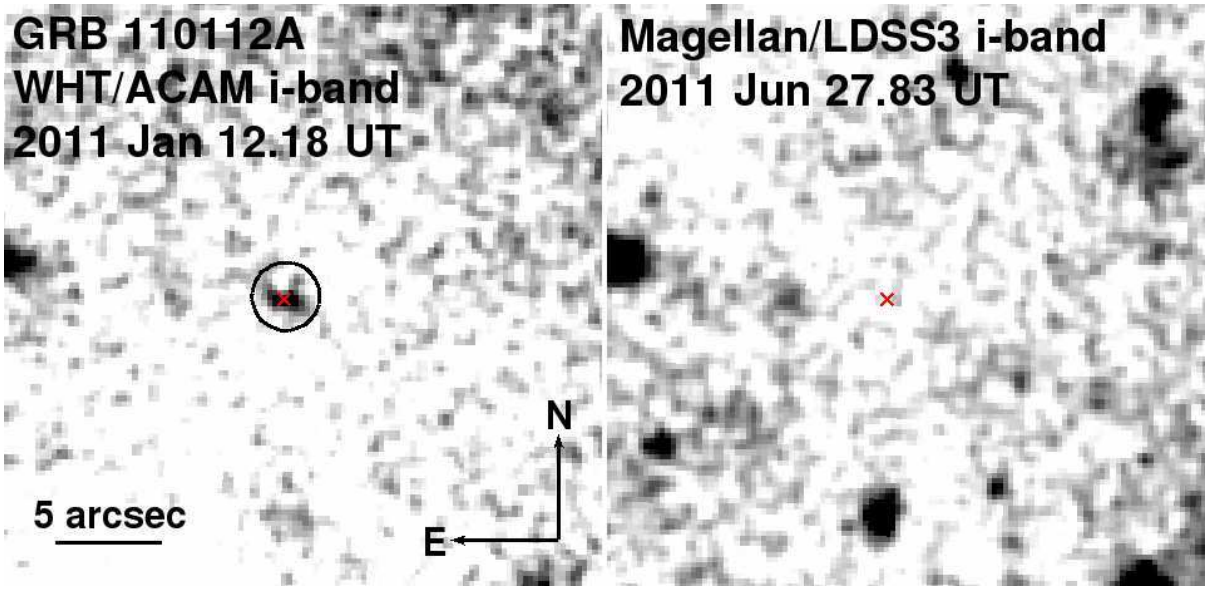

Figure 5.6.—: The optical afterglow of GRB 110112A. The XRT error circle has a radius of 1.6″ (90% containment; black) and the red cross marks the centroid of the optical afterglow, with a 1σ uncertainty of 0.14″ (afterglow centroid + absolute tie to SDSS) and $i = 22.77 \pm 0.29$. *Left:* WHT/ACAM i-band observations at $\delta t = 0.64$ days. *Right:* Magellan/LDSS3 i-band observations at $\delta t = 166$ days.

with the astrometric tie uncertainty, gives a total positional uncertainty of $0.14''$. We note that this source's position is not consistent with the $R = 19.6 \pm 0.3$ source claimed by Xin et al. (2011a). Furthermore, we do not detect any source at this position in any of our observations.

To perform a more thorough search for a coincident host galaxy, we obtained r-band observations with LDSS3 on 2011 June 27.83 UT and i-band observations with Gemini-North/GMOS on 2011 July 28.46 UT. In these deeper observations, we do not detect any sources within the XRT error circle to limits of $r \gtrsim 25.5$ mag and $i \gtrsim 26.2$ mag (Table 7.1). We further assess the probability of potential host galaxies outside the XRT position in §5.4.3.

5.3 Afterglow Properties

We utilize the X-ray and optical/NIR observations to constrain the explosion properties and circumburst environments of GRBs 100625A, 101219A and 110112A. We adopt the standard synchrotron model for a relativistic blastwave in a constant density medium (ISM), as expected for a non-massive star progenitor (Sari et al. 1999; Granot & Sari 2002). This model provides a mapping from the broad-band afterglow flux densities to physical parameters: isotropic-equivalent kinetic energy ($E_{\rm K,iso}$), circumburst density (n_0), fractions of post-shock energy in radiating electrons (ϵ_e) and magnetic fields (ϵ_B), and the electron power-law distribution index, p, with $N(\gamma) \propto \gamma^{-p}$ for $\gamma \gtrsim \gamma_{\rm min}$. Since we have optical and X-ray observations for these three bursts, we focus on constraining the location of the cooling frequency (ν_c) with respect to the X-ray band because it affects the afterglow flux dependence on $E_{\rm K,iso}$ and n_0. For each burst, we determine this by

comparing the temporal (α_X) and spectral ($\beta_X \equiv 1 - \Gamma$) indices to the closure relation $\alpha - 3\beta/2$: for $p > 2$, if $\nu_c > \nu_X$, $\alpha - 3\beta/2 = 0$, while for $\nu_c < \nu_X$, $\alpha - 3\beta/2 = 1/2$. We also infer the extinction, $A_V^{\rm host}$ by a comparison of the optical and X-ray data.

5.3.1 GRB 100625A

From the X-ray light curve and spectrum of GRB 100625A, we measure a temporal decay index of $\alpha_X = -1.45 \pm 0.08$ and a spectral index of $\beta_X = -1.5 \pm 0.2$, which gives $\alpha_X - 3\beta_X/2 = 0.79 \pm 0.34$. This indicates that $\nu_c < \nu_X$ and therefore $p = 2.7 \pm 0.2$.

From our derived value of $N_{\rm H,int} \lesssim 1.7 \times 10^{21}$ cm^{-2}, we infer $A_V^{\rm host} \lesssim 0.8$ mag (3σ) in the rest-frame of the burst using the Galactic N_H-to-A_V conversion, $N_{\rm H,int}/A_V \approx 2.0 \times 10^{21}$ (Predehl & Schmitt 1995; Watson 2011). We can also investigate the presence of extinction by comparing the X-ray flux and the optical upper limit at $\delta t \approx 0.5$ d. If we assume a maximum value of $\nu_{c,\rm max} \approx 2.4 \times 10^{17}$ Hz (1 keV) and extrapolate the X-ray flux density of $\approx 9 \times 10^{-3}\,\mu$Jy to the optical band using $\beta = -(p-1)/2 = -0.85$ to obtain the lowest bound on the expected afterglow flux in the absence of extinction, we estimate $F_{\nu,\rm opt} \approx 0.24\,\mu$Jy ($i = 25.4$ mag). Given the observed limit of $F_{\nu,\rm opt} \lesssim 2.9\,\mu$Jy ($i \gtrsim 22.7$ mag), this does not conflict with this lower bound, the afterglow observations are consistent with no extinction.

We can therefore use the X-ray data and optical afterglow limits to constrain $E_{\rm K,iso}$ and n_0. Assuming that the X-ray flux is from the forward shock, we can directly obtain $E_{\rm K,iso}$ by (Granot & Sari 2002)

$$E_{\rm K,iso,52}^{4.7/4} \epsilon_{e,-1}^{1.7} \epsilon_{B,-1}^{0.7/4} \approx 5.7 \times 10^{-3}, \tag{5.1}$$

where $E_{\rm K,iso,52}$ is in units of 10^{52} erg, and ϵ_e and ϵ_B are in units of 10^{-1}, and we have used $z = 0.452$. The X-ray flux density at $\delta t \approx 10^4$ s is $F_{\nu,X} \approx 9.1 \times 10^{-3}\,\mu$Jy (1 keV), and therefore $E_{\rm K,iso} \approx 1.2 \times 10^{50}$ erg ($\epsilon_e = \epsilon_B = 0.1$). At $z = 0.452$, $E_{\gamma,\rm iso} \approx 4.3 \times 10^{50}$ erg ($20 - 2000$ keV from the *Konus-Wind* fluence), which gives a γ-ray efficiency of $\eta_\gamma \approx 0.8$. If we instead assume $\epsilon_e = 0.1$ and $\epsilon_B = 0.01$, then $E_{\rm K,iso} \approx 1.7 \times 10^{50}$ erg, and $\eta_\gamma \approx 0.7$.

For $\nu_m < \nu_{\rm opt} < \nu_c$ (where ν_m is the synchrotron peak frequency), the optical afterglow brightness depends on a combination of $E_{\rm K,iso}$ and n_0. Therefore, the riz-band observed limits on the afterglow translate to an upper limit on the physical parameters, given by

$$E_{\rm K,iso,52}^{5.7/4} n_0^{0.5} \epsilon_{e,-1}^{1.7} \epsilon_{B,-1}^{3.7/4} \lesssim 2.5 \times 10^{-3}, \tag{5.2}$$

where n_0 is in units of cm^{-3}. Assuming $\epsilon_e = \epsilon_B = 0.1$ and using $E_{\rm K,iso} = 1.2 \times 10^{50}$ erg, we obtain $n \lesssim 1.5$ cm^{-3}. If we instead assume $\epsilon_e = 0.1$ and $\epsilon_B = 0.01$, then $n_0 \lesssim 40$ cm^{-3}. For both scenarios, we obtain $\nu_c \gtrsim 4 \times 10^{15}$ Hz ($\gtrsim 0.02$ keV), consistent with our assumption that $\nu_c < \nu_X$.

5.3.2 GRB 101219A

From the X-ray light curve and spectrum, we measure $\alpha_X = -1.37 \pm 0.13$ and $\beta_X = -0.8 \pm 0.1$, which gives $\alpha_X - 3\beta_X/2 = 0.17 \pm 0.23$, suggesting that $\nu_c > \nu_X$. The resulting value of p is 2.7 ± 0.1. We note that the closure relation is consistent with the alternative scenario for $> 2\sigma$.

Since the optical afterglow flux may be subject to an appreciable amount of

extinction, as suggested by the intrinsic absorption in the X-ray spectrum (§5.2.2), the most reliable proxy for $E_{\rm K,iso}$ and n_0 is the X-ray afterglow flux. Using the last XRT data point at $\delta t \approx 7 \times 10^3$ s, which has $F_{\nu,X} \approx 0.03\,\mu$Jy (1 keV), we infer the following relationship between $E_{\rm K,iso}$ and n_0,

$$E_{\rm K,iso,52}^{5.7/4} n_0^{0.5} \epsilon_{e,-1}^{1.7} \epsilon_{B,-1}^{3.7/4} \approx 1.3 \times 10^{-3}, \tag{5.3}$$

where we have used $z = 0.718$. At this redshift, we find $E_{\gamma,\rm iso} \approx 4.8 \times 10^{51}$ erg ($20 - 10^4$ keV using the *Konus-Wind* fluence). Assuming $E_{\gamma,\rm iso} \approx E_{\rm K,iso}$, we infer $n_0 \approx 1.3 \times 10^{-5}$ cm^{-3} for $\epsilon_e = \epsilon_B = 0.1$. With these values, $\nu_c \approx 6 \times 10^{19}$ Hz (250 keV), consistent with our assumption that $\nu_c > \nu_X$. We note that this assumption is violated for $n_0 \gtrsim 4 \times 10^{-3}$ cm^{-3}. If instead we use $\epsilon_e = 0.1$ and $\epsilon_B = 0.01$, then we obtain $n_0 \approx 9 \times 10^{-4}$ cm^{-3} and $\nu_c \approx 2 \times 10^{19}$ Hz (80 keV), which is again self-consistent, and find this assumption is violated for $n_0 \gtrsim 0.1$ cm^{-3}. Therefore, the X-ray data suggest an explosion environment with $n_0 \approx 10^{-5} - 10^{-3}$ cm^{-3} for GRB 101219A.

We investigate the presence of extinction intrinsic to the host galaxy by comparing the X-ray and NIR observations, since the NIR data provide a stronger constraint than the optical band. Since the X-ray and NIR bands lie on the same segment of the synchrotron spectrum, the spectral slope is given by $\beta_{\rm NIR-X} = \beta_X \approx -0.8$. At the time of our first J-band observations at $\delta t \approx 1$ hr, the X-ray flux density is $0.06\,\mu$Jy, leading to an expected J-band flux density of $F_{\nu,J} \approx 14.7\,\mu$Jy (21 mag). This is above the limit of our observations, $\lesssim 1.4\,\mu$Jy ($\gtrsim 23.6$ mag), indicating that $A_J \gtrsim 2.5$ mag. Using a Milky Way extinction curve (Cardelli et al. 1989), this indicates that $A_V^{\rm host} \gtrsim 4.2$ mag

in the rest-frame of the burst. In addition, using the Galactic relation between N_H and A_V, this implies $N_{\rm H,int} \gtrsim 7.5 \times 10^{21}$ cm^{-2}, which does not necessarily violate our inferred value from the X-ray spectrum of $N_{\rm H,int} = (6.6 \pm 2.0) \times 10^{21}$ cm^{-2}. Therefore, the broad-band afterglow spectrum requires an appreciable amount of extinction.

5.3.3 GRB 110112A

From the X-ray light curve and spectrum, we measure $\alpha_X = -1.10 \pm 0.05$ and $\beta_X = -1.2 \pm 0.2$, giving $\alpha_X - 3/2\beta_X = 0.70 \pm 0.30$ indicating $\nu_c < \nu_X$. The resulting value of p is 2.1 ± 0.1.

From our derived value of $N_{\rm H,int} \lesssim 1.6 \times 10^{21}$ cm^{-2}, we infer $A_V^{\rm host} \lesssim 0.9$ mag in the rest-frame of the burst using the Galactic relation. We can measure the cooling frequency by comparing the X-ray and optical fluxes at $\delta t \approx 0.64$ d. At this time, $F_{\nu,X} \approx 6.6 \times 10^{-3}\,\mu$Jy and $F_{\nu,\rm opt} \approx 2.8\,\mu$Jy. Using $p = 2.1$ and the location of the optical and X-ray bands, we then estimate that $\nu_c \approx 1.6 \times 10^{15}$ Hz ($\approx 7 \times 10^{-3}$ keV) which agrees with our assumption that $\nu_c < \nu_X$. The cooling frequency is dependent on a combination of physical parameters and gives the constraint:

$$E_{\rm K,iso,52}^{-0.5} n_0^{-1} \epsilon_{B,-1}^{-1.5} \approx 5.4, \tag{5.4}$$

where we have assumed a fiducial redshift of $z = 0.5$, the median of the observed short GRB population. We then use the X-ray afterglow flux at $\delta t \approx 0.64$ d to determine $E_{\rm K,iso}$ by

$$E_{\rm K,iso,52}^{4.1/4}\epsilon_{e,-1}^{1.1}\epsilon_{B,-1}^{0.1/4} \approx 0.023. \quad (5.5)$$

Our final constraint comes from the optical afterglow brightness, given by

$$E_{\rm K,iso,52}^{5.1/4}n_0^{0.5}\epsilon_{e,-1}^{1.1}\epsilon_{B,-1}^{3.1/4} \approx 0.01. \quad (5.6)$$

Assuming $\epsilon_e = 0.1$ and $z = 0.5$, we obtain the solution $E_{\rm K,iso} \approx 2.5 \times 10^{50}$ erg, $n_0 \approx 1.5$ cm^{-3} and $\epsilon_B \approx 0.08$. At this redshift, $E_{\gamma,\rm iso} \approx 9.5 \times 10^{49}$ erg (determined from the *Swift* fluence and applying a correction factor of 5 to represent $\approx 1 - 10^4$ keV). If we consider a high-redshift origin for GRB 110112A of $z = 2$, then we infer larger energies of $E_{\rm K,iso} \approx 3.6 \times 10^{51}$ erg and $E_{\gamma,\rm iso} \approx 1.5 \times 10^{51}$ erg, a lower value of $\epsilon_B \approx 0.01$, and a lower density, $n_0 \approx 0.18$ cm^{-3}. In both cases, $\eta_\gamma \approx 0.3$.

5.4 Host Galaxy Properties

5.4.1 GRB 100625A

The XRT position of GRB 100625A fully encompasses a single galaxy, which we call G1 (Figure 5.2). To assess the probability that the burst originated from G1, we calculate the probability of chance coincidence, $P_{cc}(< \delta R)$, at a given angular separation, (δR) and apparent magnitude (m) for galaxies within $15'$ (the field of view of our images) of the burst position (Bloom et al. 2002; Berger 2010a). For G1, we conservatively assume $\delta R = 3\sigma_{\rm XRT} \approx 3.4''$, and calculate $P_{cc}(< \delta R) \approx 0.04$. The remaining bright galaxies in

the field have substantially higher values of $P_{cc}(< \delta R) \gtrsim 0.17$, and a search for galaxies within 5° of the GRB position using the NASA/IPAC Extragalactic Database (NED) yields only objects with $P_{cc} \gtrsim 0.98$. From these probabilistic arguments, we consider G1 to be the host galaxy of GRB 100625A.

To determine the host galaxy's redshift, we fit the LDSS3 spectrum over the wavelength range of $5200 - 8000$ Å with simple stellar population (SSP) spectral evolution models at fixed ages ($\tau = 0.29, 0.64, 0.90, 1.4$ and 2.5 Gyr) provided as part of the GALAXEV library (Bruzual & Charlot 2003); at wavelengths outside this range, the signal-to-noise is too low to contribute significantly to the fit. We use χ^2-minimization with redshift as the single free parameter, and perform the fit on the unbinned data. The resulting best-fit redshift is $z = 0.452 \pm 0.002$ ($\chi^2_\nu = 1.3$ for 1861 degrees of freedom), determined primarily by the location of the 4000 Å break and the main absorption features of Ca II H&K, Hβ, Hγ, and Hδ. The shape of the break is best fit by the template with $\tau = 0.64$ Gyr (Figure 5.7), and poorer fits ($\chi^2_\nu \gtrsim 2$) are found for SSPs with younger or older ages. Due to the strength of the 4000 Å break, deep absorption features, lack of emission lines, and old age, we classify this host as an early-type galaxy. We note that the shape of the spectrum does not require any intrinsic extinction, which is consistent with the results from the afterglow observations.

We do not find an emission feature corresponding to [O II]λ3727. Using the error spectrum, we calculate the expected integrated flux for a 3σ emission doublet centered at $\lambda = 3727$ Å with a width of ≈ 10 Å. We find an expected upper limit of $F_{[\rm OII]} \lesssim 4.3 \times 10^{-17}$ erg cm^{-2} s^{-1}, which translates to $L_{[\rm OII]} \lesssim 2.2 \times 10^{40}$ erg s^{-1} at the redshift of the burst. Using the standard relation, SFR $= (1.4 \pm 0.4)$ M$_\odot$ yr^{-1} L$_{[\rm OII],41}$ (Kennicutt 1998), we derive a 3σ upper limit of SFR$\lesssim 0.3\, M_\odot$ yr^{-1} for the host galaxy.

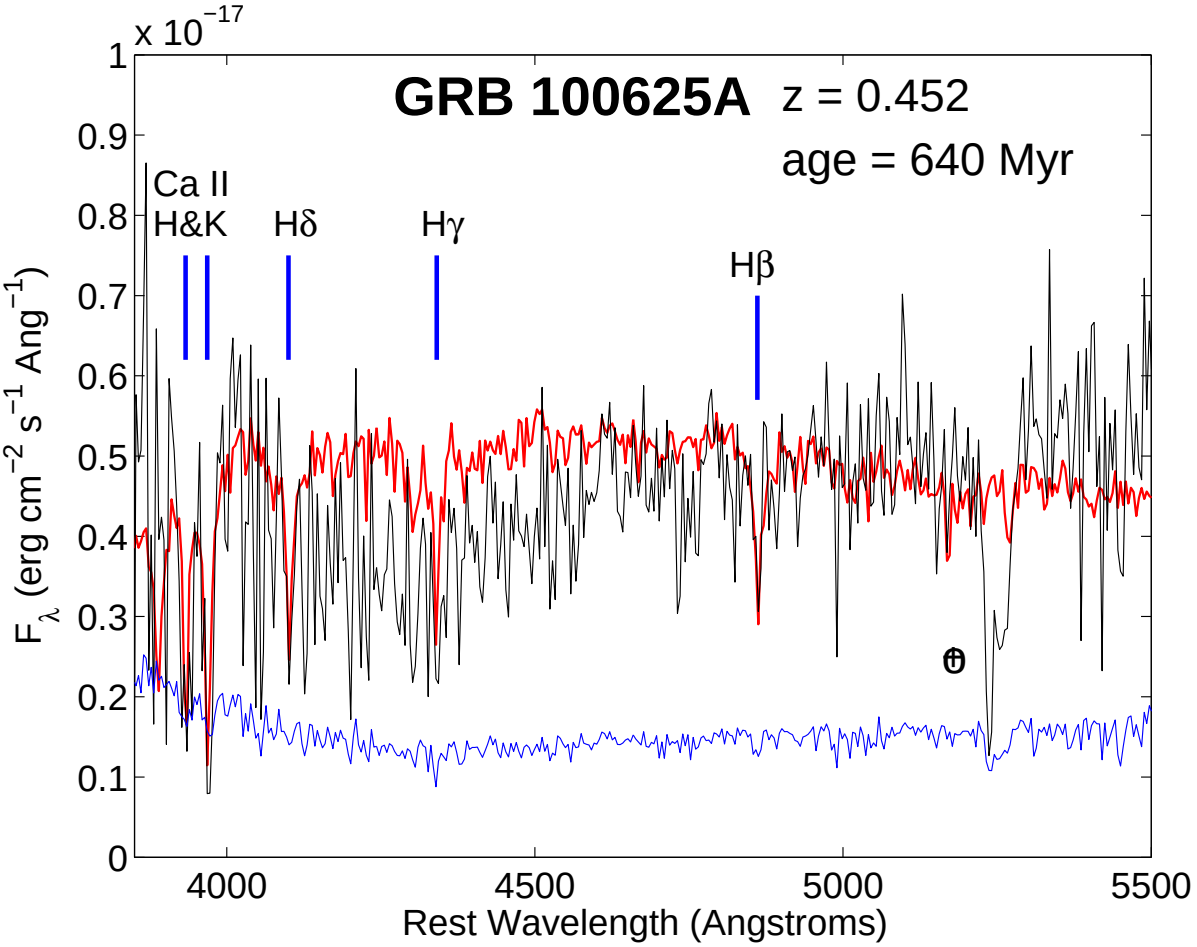

Figure 5.7.—: LDSS3 spectrum of the early-type host galaxy of GRB 100625A, binned with a 3-pixel boxcar (black: data; blue: error spectrum). Also shown is the best-fit SSP template (red; Bruzual & Charlot 2003) with a stellar population age of 640 Myr at a redshift of $z = 0.452 \pm 0.002$. Fits are performed on the unbinned data. The locations of the Balmer absorption lines and Ca II H&K are labelled.

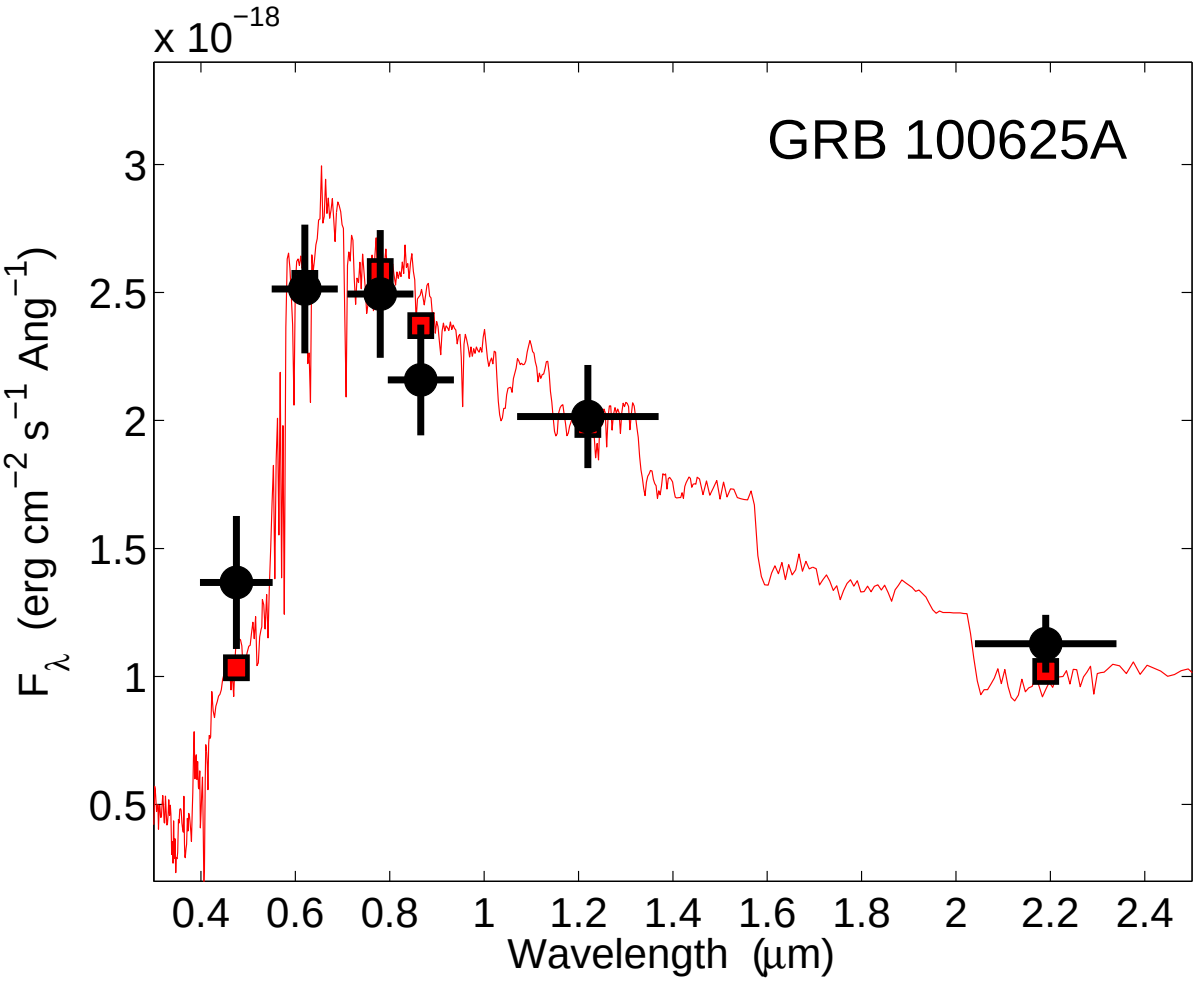

Figure 5.8.—: $grizJK_s$ photometry for the host galaxy of GRB 100625A (black circles). The best-fit model (red squares and line; Maraston 2005) is characterized by $\tau \approx 0.8$ Gyr and $M_* \approx 4.6 \times 10^9\, M_\odot$.

We use the $grizJK_s$-band photometry to infer the stellar population age and mass of the host galaxy with the Maraston (2005) evolutionary stellar population synthesis models, employing a Salpeter initial mass function and a red giant branch morphology. We fix $A_V^{\rm host} = 0$ mag as inferred from the absence of $N_{\rm H,int}$ (§5.2.1), $z = 0.452$ as inferred from the spectrum, and metallicity $Z = Z_\odot$, and allow the stellar population age (τ) and stellar mass (M_*) to vary. The resulting best-fit model is characterized by $\tau \approx 0.8$ Gyr, in good agreement with the fit to the spectrum, and $M_* \approx 4.6 \times 10^9\,M_\odot$. The model and broad-band photometry are shown in Figure 5.8.

5.4.2 GRB 101219A

The XRT position of GRB 101219A fully encompasses a single galaxy (G1; Figure 5.4). We perform the same probability of chance coincidence analysis described in §5.4.1 using $\delta R = 3\sigma_{\rm XRT}$ and find $P_{cc}(< \delta R) \approx 0.06$ for G1, while the remaining bright galaxies within $5'$ of the burst have $P_{cc}(< \delta R) \gtrsim 0.23$. Furthermore, a search within 5° of the position with NED yields only galaxies with $P_{cc}(< \delta R) \approx 1$. We therefore consider G1 to be the most probable host galaxy of GRB 101219A.

We examine the host spectrum of GRB 101219A to determine the redshift and physical characteristics of the stellar population. We identify two emission features in the co-added spectrum at $\lambda_{\rm obs} = 6401.65$ Å and $\lambda_{\rm obs} = 8599.50$ Å that are also present in the individual 2D spectra prior to co-addition. If these features correspond to [O II]λ3727 and [O III]λ5007, their locations give a common redshift of $z = 0.718$. Furthermore, we do not find a common redshift solution for an alternative set of features, so we consider the host galaxy to be at $z = 0.718$. In addition, we note the presence of marginal

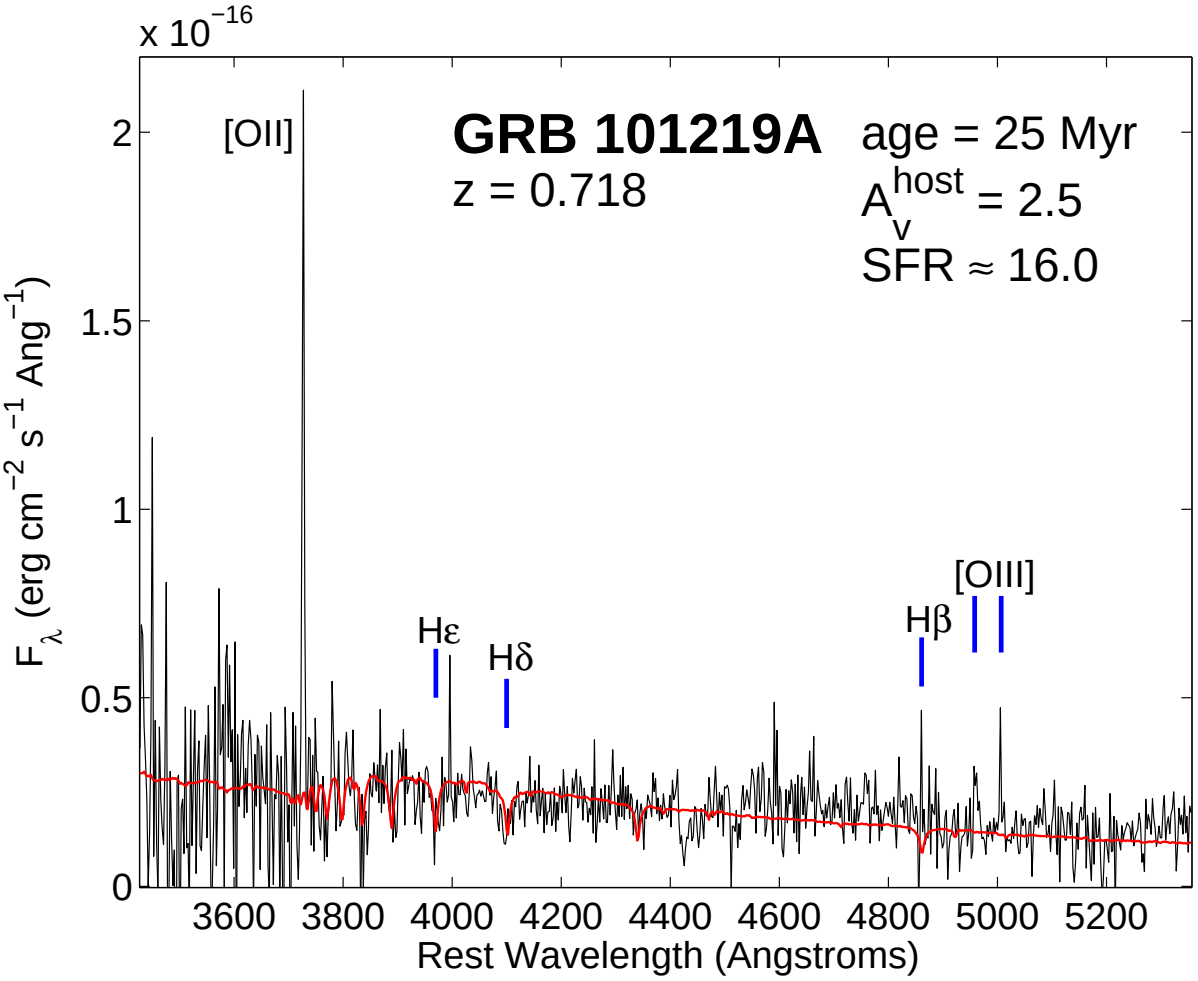

Figure 5.9.—: GMOS-N spectrum of the host galaxy of GRB 101219A, binned with a 3-pixel boxcar (black). The spectrum is corrected for Galactic extinction and $A_V^{\rm host} = 2.5$ mag. The stellar population model has $\tau = 25$ Myr (red; Bruzual & Charlot 2003). The [O II] λ3727 and [O III] λ5007 emission features are at a common redshift of $z = 0.718$. Also labeled are the locations of the Balmer lines Hϵ and Hδ, and marginal emission features at Hβ and the [O III] doublet. From [O II] λ3727 we deduce SFR $= 16.0 \pm 4.6$ $M_\odot$ yr^{-1}. (Kennicutt 1998).

emission features at the expected locations of Hβ and [O III]λ4959; however, these locations are contaminated by sky line residuals. Finally, we detect absorption at the locations of $H\varepsilon$ and $H\delta$ (Figure 5.9).

To determine the age and host extinction, we use stellar population spectral templates with fixed ages of $\tau = 5, 25, 100$ and 290 Myr (Bruzual & Charlot 2003) to fit the continuum; ages outside this range do not fit the overall shape of the spectrum. We apply corrections for both Galactic extinction ($A_V = 0.16$ mag at $z = 0$; Schlafly & Finkbeiner 2011) and $A_V^{\rm host}$ at $z = 0.718$ using a Milky Way extinction curve (Cardelli et al. 1989). The spectrum is best matched with the $\tau = 25$ Myr template and $A_V^{\rm host} = 2.5$ mag. Since there is some degeneracy between age and $A_V^{\rm host}$, imposing an older stellar population of $\tau = 100$ Myr also provides a reasonable match, but requires a smaller amount of extinction of $A_V^{\rm host} \approx 2$ mag. Older spectral templates predict a large break at 4000 Å not seen in the spectrum, while younger templates lack the observed absorption lines. Therefore, a likely range of ages for the host galaxy is $\tau \approx 25 - 100$ Myr. Given the emission features and relatively young age, we classfiy this galaxy as late-type. The de-reddened spectrum for GRB 101219A, along with the 25 Myr model, is shown in Figure 5.9.

From the extinction-corrected flux of [O II]λ3727, $F_{\rm [OII]} \approx 8.5 \times 10^{-16}$ erg cm^{-2} s^{-1}, we find $L_{\rm [OII]} \approx 1.1 \times 10^{42}$ erg s^{-1} at the redshift of the burst. Using the standard relation (Kennicutt 1998), we derive a SFR of 16.0 ± 4.6 M$_\odot$ yr^{-1}.

We use the same procedure described in §5.4.1 to model the SED of the host galaxy to infer τ and M_*. We fix $z = 0.718$ as inferred from the spectrum, $Z = Z_\odot$, and allow τ, M_*, and $A_V^{\rm host}$ to vary. The resulting best-fit model is characterized by $A_V^{\rm host} \approx 1.5$

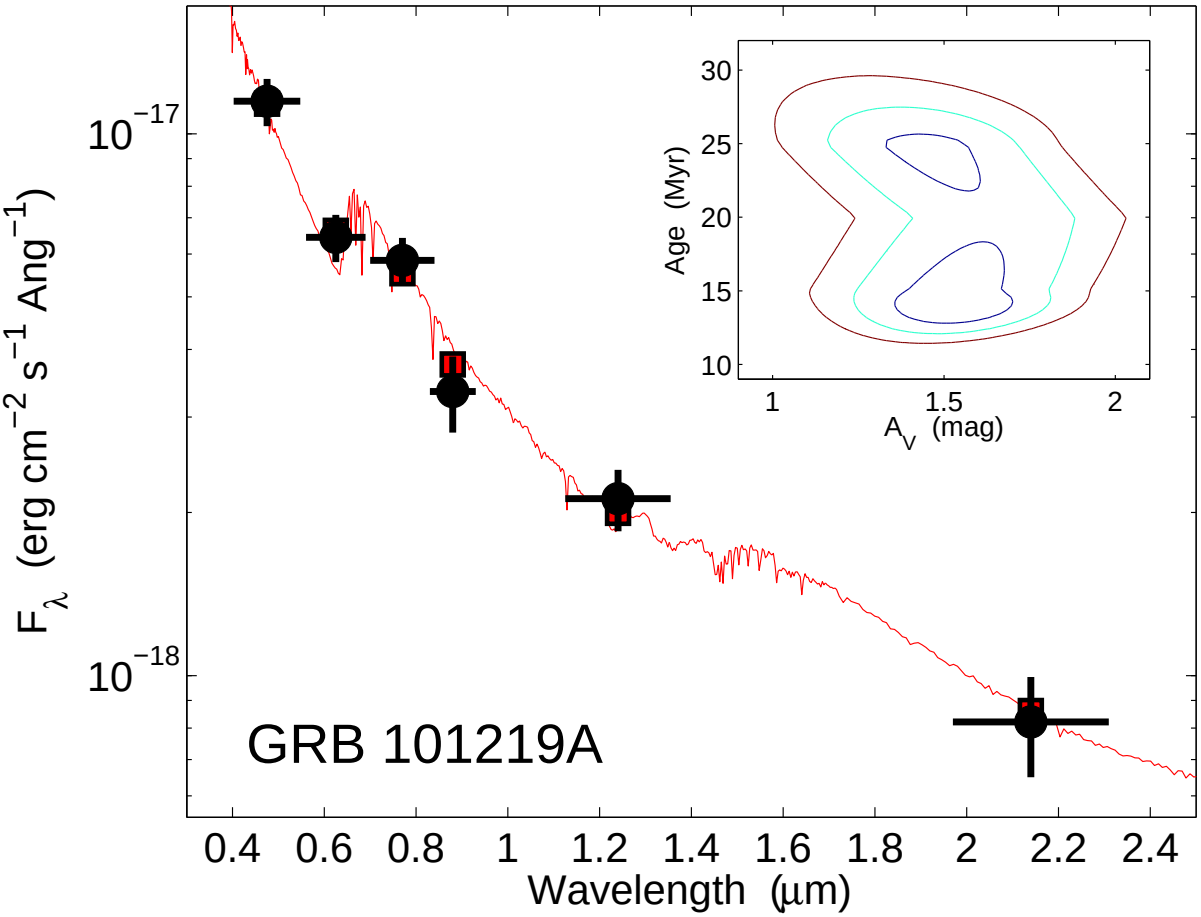

Figure 5.10.—: $grizJK_s$-band photometry of the host galaxy of GRB 101219A (black circles). The best-fit model (red squares and line; Maraston 2005) is characterized by $A_V^{\rm host} \approx 1.5$ mag, $\tau \approx 15 - 25$ Myr and $M_* \approx 1.4 \times 10^9\,M_\odot$. The age-$A_V^{\rm host}$ contours of 1σ (blue), 2σ (cyan), and 3σ (red) solutions are shown in the inset.

mag, $\tau \approx 15 - 25$ Myr, and $M_* \approx 1.4 \times 10^9\, M_\odot$, which is consistent with the parameters derived from the spectrum and afterglow. The broad-band photometry and best-fit stellar population model are shown in Figure 5.10.

5.4.3 GRB 110112A

For GRB 110112A, we do not detect a source in coincidence with the optical afterglow position or within the XRT error circle to a 3σ limit of $i \gtrsim 26.2$ mag in our GMOS-N image (Figure 5.11). To determine which sources in the field are probable hosts, we calculate $P_{cc}(< \delta R)$ for 15 galaxies within $\sim 3'$ of the GRB position, the field of view of our GMOS-N i-band image. These galaxies were selected by discarding noticeably fainter galaxies with increasing δR since these objects will have $P_{cc}(< \delta R) \sim 1$. We find that 9 of these galaxies have $P_{cc}(< \delta R) \lesssim 0.85$ (Figure 5.12). The two most probable host galaxies, G1 and G4 (Figures 5.11 and 5.12), have $P_{cc}(< \delta R) = 0.43$ and 0.54, respectively, and offsets of $\delta R = 4.8''$ and $11.1''$. In addition, we search for bright galaxies within 5° of the GRB position using NED, but all additional catalogued galaxies have $P_{cc}(< \delta R) \gtrsim 0.98$. Given the relatively high values for $P_{cc}(< \delta R)$, we do not find a convincing putative host for GRB 110112A.

It is also plausible that GRB 110112A originated from a galaxy fainter than the detection threshold of our observations. For instance, a ≈ 27 mag host would require $\delta R \lesssim 2.0''$ while a ≈ 28 mag host would require $\delta R \lesssim 1.3''$, to be a more probable host than G1. However, to be a $27 - 28$ mag galaxy convincing enough to make a host association ($P_{cc}(< \delta R) \lesssim 0.05$) would require a smaller offset of $\delta R \lesssim 0.5''$. We note that the lack of potential host is in contrast to previous "host-less" short GRBs (Berger

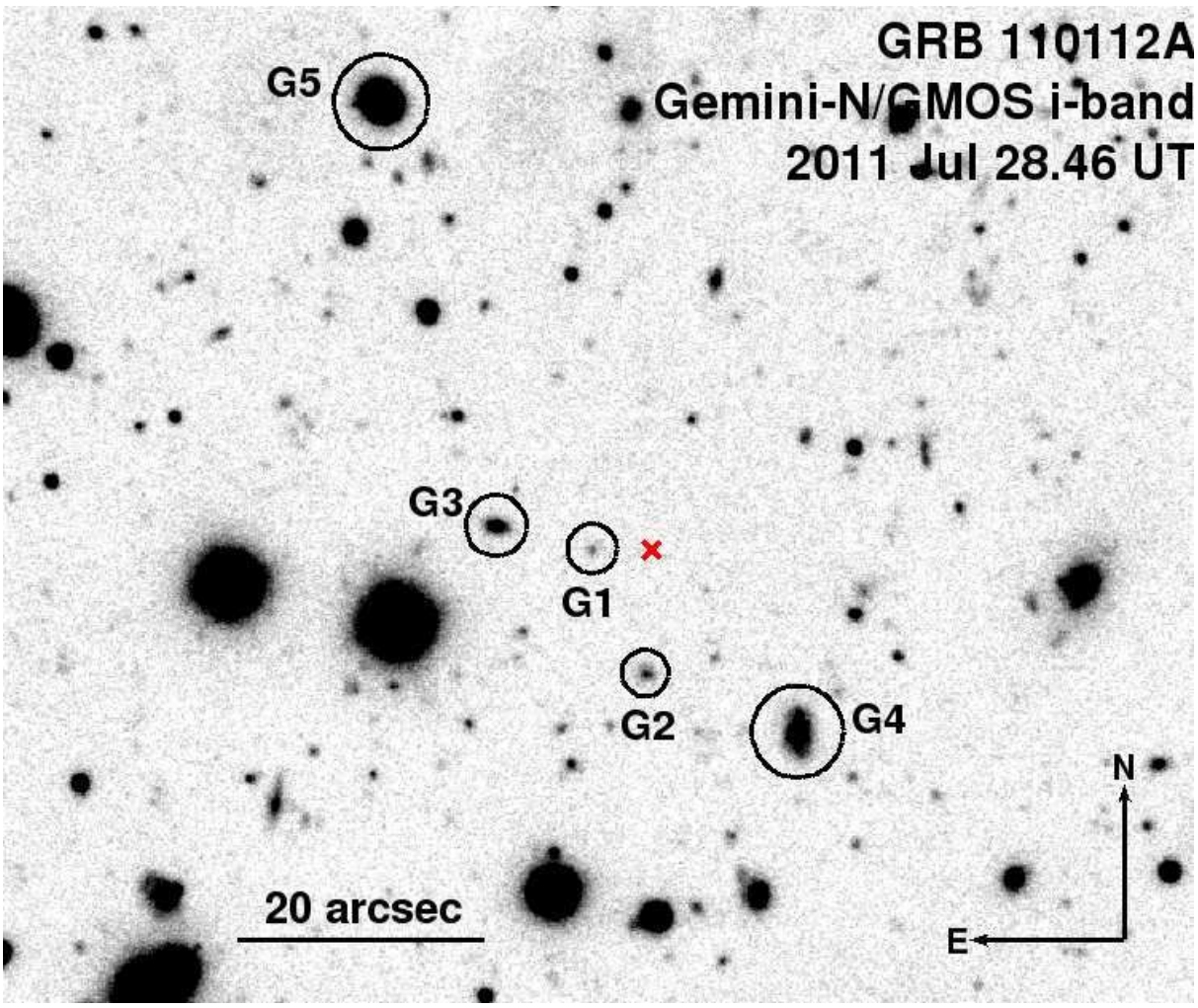

Figure 5.11.—: *Left:* Gemini-N/GMOS i-band observations of the field of GRB 110112A on 2011 Jul 28.46 UT. The position of the optical afterglow is marked by the red cross. The five galaxies with the lowest probabilities of chance coincidence are circled and labeled G1-G5. The galaxy with the lowest value of $P(< \delta R)$ is G1, located $4.8''$ from the optical afterglow position.

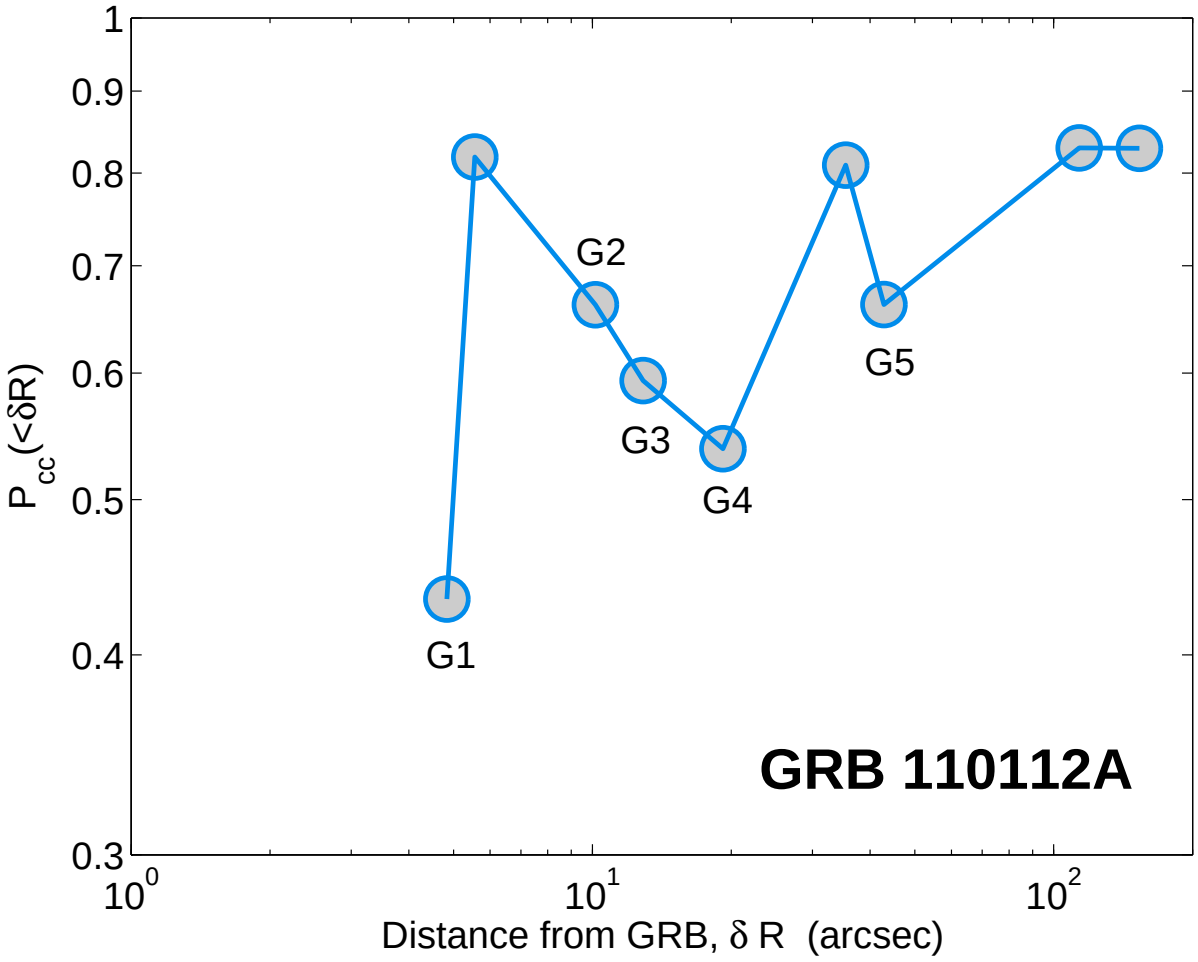

Figure 5.12.—: Probability of chance coincidence, $P_{cc}(< \delta R)$, as a function of angular distance from the optical afterglow position of GRB 110112A. There are nine galaxies in the $2'$ field with $P_{cc}(< \delta R) < 0.85$. The five galaxies with the lowest $P(< \delta R)$ are labeled G1-G5. The galaxy G1 has the lowest probability of chance coincidence $P(< \delta R) = 0.43$.

2010a). The high inferred density due to the bright optical afterglow (§3) is suggestive of a high-redshift origin as opposed to a progenitor system that was kicked outside of its host galaxy.

5.5 Stellar Population Characteristics

Of the 30 short GRBs with host associations ($P_{cc} \lesssim 0.05$; Table 5.3), GRB 100625A is the fifth short GRB associated with a spectroscopically-confirmed early-type host galaxy (Gehrels et al. 2005; Berger et al. 2005; Bloom et al. 2006, 2007; Fong et al. 2011), near the median redshift of the short GRB population (Figure 5.13). In contrast, GRB 101219A is associated with a $z = 0.718$ late-type galaxy that is actively star-forming with characteristics similar to the majority of the short GRB late-type host population (Berger 2009). Finally, GRB 110112A joins a growing number of short GRBs with sub-arcsecond positions but no obvious coincident host galaxy to deep limits of $\gtrsim 26$ mag (Berger 2010a), although unlike previous events, the case for a large offset is less clear.

Short GRBs with sub-arcsecond positions and coincident hosts have a median projected physical offset of ~ 5 kpc (Fong et al. 2010) which, in the context of a NS-NS/NS-BH progenitor, can be interpreted as the result of natal kicks and moderate delay times (Fryer et al. 1999; Belczynski et al. 2006). At the inferred redshifts of GRBs 100625A and 101219A, the upper limits on the projected physical offsets set by the radii of the X-ray positions are $\lesssim 10.3$ and $\lesssim 12.3$ kpc respectively, which agree with the observed offset distribution. Assuming a fiducial redshift of $z = 0.5$, GRB 110112A would be located 29 ± 3 kpc away from the closest and most probable host galaxy, but this association is much less definitive ($P_{cc}(< \delta R) \approx 0.43$) than previous host-less bursts

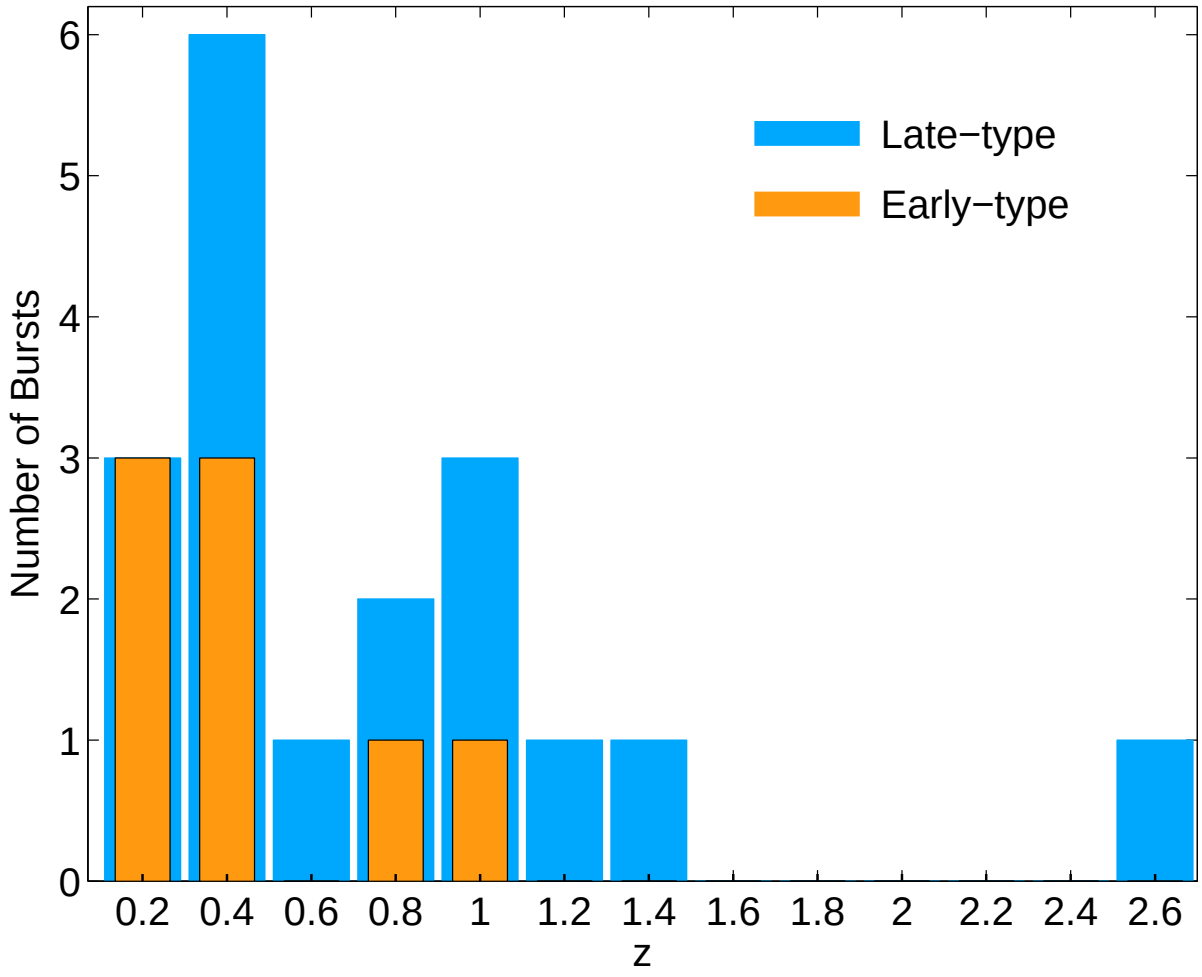

Figure 5.13.—: Redshift distribution of 26 short GRBs with host associations and redshifts, classified by type of the host galaxy, either late-type (blue) or early-type (orange). Redshifts and classifications are based on spectroscopy, with the exception of two hosts, GRBs 070729 and 111117A, which are based on well-sampled broad-band photometry (Table 5.3; Leibler & Berger 2010; Margutti et al. 2012).

(Berger 2010a). Imaging with the *Hubble Space Telescope* may enable the detection of a faint coincident host. These offsets are in contrast to long GRBs which have relatively small offsets of ≈ 1 kpc (Bloom et al. 2002; Fruchter et al. 2006). From afterglow observations, the inferred densities for these three events may span a wide range, $n_0 \sim 10^{-4} - 1$ cm^{-3}, while long GRBs have values of $n_0 \gtrsim 0.1$ cm^{-3} (Soderberg et al. 2006b).

The host galaxies of GRBs 100625A and 101219A have stellar populations that span the observed distribution of short GRB hosts. With $\tau \approx 25 - 100$ Myr and $\log(M_*/M_\odot) \approx 9.1$, GRB 101219A is at the low end of both the short GRB age and mass distributions (Leibler & Berger 2010). This host also has one of the most vigorous star formation rates reported for a short GRB host to date (Berger 2009; Perley et al. 2012; Berger et al. 2013b), and an appreciable extinction of $A_V^{\rm host} \gtrsim 2$ mag. These characteristics match more closely with the median parameters observed for long GRB host galaxies (Christensen et al. 2004; Wainwright et al. 2007b; Leibler & Berger 2010). However, an independent study based on the γ-ray properties report a probability that GRB 101219A is not a collapsar of 94% (Bromberg et al. 2013). Compared to other early-type hosts, GRB 100625A has a similar age ($0.6 - 0.8$ Gyr) and SFR limit (Bloom et al. 2006; Berger 2009; Leibler & Berger 2010; Fong et al. 2011), but its stellar mass, $\log(M_*/M_\odot) \approx 9.7$, is the lowest by an order of magnitude (Leibler & Berger 2010).

5.6 Host Galaxy Demographics

To broadly determine and utilize the short GRB host population, we expand upon the observations presented here and investigate the demographics of the bulk of the

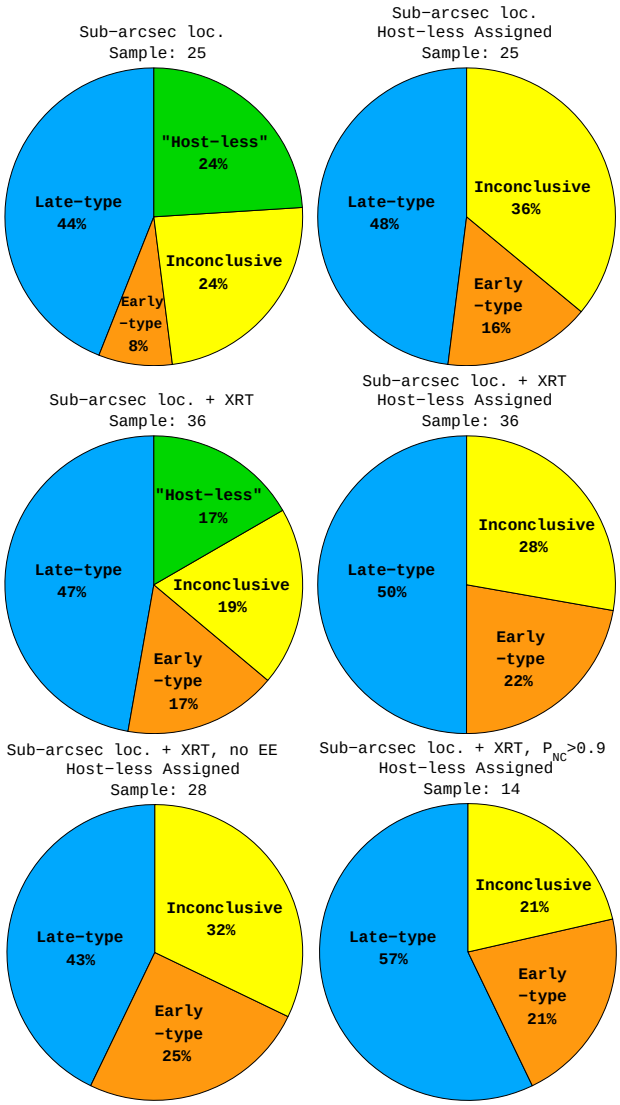

Figure 5.14.—: Distribution of short GRB environments, according to Table 5.3. The fractions of late-type (blue), early-type (orange), host-less (green) and inconclusive (yellow) environments are shown. *Top:* The distribution of 25 short GRBs with sub-arcscond localization are divided into all four categories (left), and the 6 host-less bursts are each assigned to their most probable host galaxy (right; Berger 2010a and this work). *Middle:* Our full sample, including 11 short GRBs with XRT localizations and probable hosts, is divided into all four categories (left), and with the 6 host-less bursts assigned (right). *Bottom:* Distribution of our sample for which there is no evidence for extended emission (left) and for which $P_{\rm NC} > 0.9$ (right; Bromberg et al. 2013).

Table 5.3. Short GRB Host Galaxy Morphologies

GRB	T_{90}^a (s)	z^b	Type^c	90% XRT uncert.^{d} (arcsec)	$P_{cc}(< \delta R)$	References
			Sub-arcsecond localized			
050709	0.07 / 130	0.161	L		3×10^{-3}	1 – 3
050724A	3	0.257	E		2×10^{-5}	4 – 5
051221A	1.4	0.546	L		5×10^{-5}	6 – 7
060121	2.0	< 4.1	?		2×10^{-3}	8 – 9
060313	0.7	< 1.7	?		3×10^{-3}	10 – 11
061006	0.4 / 130	0.4377	L		4×10^{-4}	12 – 15
061201	0.8	0.111	H/L		$\cdots$ /0.08	9, 16 – 17
070429B	0.5	0.9023	L		3×10^{-3}	18 – 19
070707	1.1	< 3.6	?		7×10^{-3}	20 – 21
070714B	2.0 / 64	0.9224	L		5×10^{-3}	19, 22 – 23
070724A	0.4	0.457	L		8×10^{-4}	24 – 25
070809	1.3	0.473	H/E		$\cdots$ /0.03	9, 26
071227	1.8^e	0.381	L		0.01	27 – 29
080503	0.3 / 170	< 4.2	H/?		$\cdots$ /0.1	9, 30 – 31
080905A	1.0	0.1218	L		0.01	32 – 33
081226A	0.4	< 4.1	?		0.01	34 – 35
090305	0.4	< 4.1	H/?		$\cdots$ /0.06	9, 36
090426A	1.3	2.609	L		1.5×10^{-4}	37 – 38
090510	0.3	0.903	L		8×10^{-3}	39 – 40
090515	0.04	0.403	H/E		$\cdots$ /0.15	9, 41
091109B	0.3	< 4.4	?		$\cdots$	42 – 43
100117A	0.3	0.915	E		7×10^{-5}	44 – 45
110112A	0.5	< 5.3	H/?		0.43	46, This work
111020A^f	0.4	$\cdots$	?		0.01	47 – 48
111117A^{fg}	0.5	1.3	L		0.02	49 – 50
			XRT only			
050509B	0.04	0.225	E	3.8	5×10^{-3}	51 – 52
050813^h	0.6	0.72/1.8	E/?	2.9	$\cdots$	53 – 57
051210	1.3	> 1.4	?	1.6	0.04	14, 58
060502B	0.09	0.287	E	5.2	0.03	59 – 60
060801	0.5	1.130	L	1.5	0.02	61 – 62
061210	0.2 / 85	0.4095	L	3.9	0.02	14, 63
061217	0.2	0.827	L	5.5	0.24^i	14, 64
070729^g	0.9	0.8	E	2.5	0.05	65 – 66

Table 5.3—Continued

GRB	T_{90}^{a} (s)	z^{b}	Type^{c}	90% XRT uncert.^{d} (arcsec)	$P_{cc}(<\delta R)$	References
080123	0.4 / 115	0.495	L	1.7	0.004	67 – 68
100206A	0.1	0.4075	L	3.3	0.02	69 – 70
100625A	0.3	0.452	E	1.8	0.04	71, This work
101219A	0.6	0.718	L	1.7	0.06	72, This work

Note. — [a] *Swift* $15-150$ keV. For bursts with extended emission, both the duration of the prompt spike and the duration including extended emission are reported.

[b] Upper limits on redshift are based on the detection of the UV/optical afterglow and therefore the lack of suppression blueward of the Lyman limit ($\lambda_0 = 912$ Å) or Lyman-α line ($\lambda_0 = 1216$ Å).

[c] L=late-type, E=early-type, ?=inconclusive type, H="host-less". For each host-less burst, we also list the type of the galaxy with the lowest P_{cc} (Berger 2010a and this work).

[d] Only listed for XRT bursts. (Goad et al. 2007; Evans et al. 2009)

[e] Evidence at the 4σ level for extended emission is reported to $\delta t \approx 100$ s.

[f] Bursts with no optical afterglow, localized by *Chandra*.

[g] Bursts with galaxy type classifications based on extensive broad-band photometry (Leibler & Berger 2010; Margutti et al. 2012). In particular, the host of GRB 070729 has an inferred age (≈ 0.98 Gyr) and stellar mass ($\approx 4 \times 10^{10}\,M_{\odot}$; Leibler & Berger 2010) more consistent with an early-type designation.

[h] There exists disagreement in the literature regarding the association of GRB 050813 with an early-type cluster galaxy at $z = 0.72$ (Berger 2005; Foley et al. 2005; Prochaska et al. 2006) or a high redshift cluster at $z = 1.8$ (Berger 2006b); thus, we only display this burst for completeness but do not include it in our demographics.

[i] Despite the relatively high P_{cc}, all surrounding galaxies have P_{cc} of order unity (Berger et al. 2007b).

References: (1) Villasenor et al. 2005; (2) Fox et al. 2005; (3) Hjorth et al. 2005b; (4) Krimm et al. 2005; (5) Berger et al. 2005; (6) Cummings et al. 2005; (7) Soderberg et al. 2006b; (8) de Ugarte Postigo et al. 2006b; (9) Berger 2010a; (10) Markwardt et al. 2006; (11) Roming et al. 2006; (12) Urata et al. 2006 (13) Schady et al. 2006; (14) Berger et al. 2007b; (15) D'Avanzo et al. 2009; (16) Marshall et al. 2006; (17) Stratta et al. 2007; (18) Markwardt et al. 2007; (19) Cenko et al. 2008; (20) Gotz et al. 2007; (21) Piranomonte et al. 2008; (22) Kodaka et al. 2007; (23) Racusin et al. 2007; (24) Ziaeepour et al. 2007; (25) Berger et al. 2009; (26) Marshall et al. 2007; (27) Sato et al. 2007b; (28) D'Avanzo et al. 2007; (29) Sakamoto et al. 2007b; (30) Mao et al. 2008; (31) Perley et al. 2009a; (32) Pagani et al. 2008; (31) Rowlinson et al. 2010a; (34) Krimm et al. 2008; (35) Nicuesa Guelbenzu et al. 2012a; (36) Krimm et al. 2009; (37) Antonelli et al. 2009a; (38) Levesque et al. 2010; (39) Hoversten et al. 2009; (40) McBreen et al. 2010; (41) Barthelmy et al. 2009; (40) Oates et al. 2009; (43) Levan et al. 2009; (44) de Pasquale et al. 2010; (45) Fong et al. 2011; (46) Barthelmy et al. 2011; (47) Sakamoto et al. 2011b; (48) Fong et al. 2012b; (49) Sakamoto et al. 2013; (50) Margutti et al. 2012; (51) Gehrels et al. 2005; (52) Bloom et al. 2006; (53) Sato et al. 2005; (54) Berger 2005; (55) Foley et al. 2005; (56) Berger 2006b; (57) Prochaska et al. 2006; (58) La Parola et al. 2006; (59) Sato et al. 2006a; (60) Bloom et al. 2007; (61) Sato et al. 2006b; (62) Berger 2009; (63) Cannizzo et al. 2006; (64) Ziaeepour et al. 2006; (65) Sato et al. 2007a; (66) Leibler & Berger 2010; (67) Uehara et al. 2008; (68) Ukwatta et al. 2008; (69) Krimm et al. 2010a; (70) Perley et al. 2012; (71) Holland et al. 2010a; (72) Krimm et al. 2010b

Swift short GRB sample, quantifying the fractions of events that explode in different types of environments. We divide the population into four host galaxy categories: late-type, early-type, inconclusive (coincident hosts that are too faint to classify as late- or early-type), and "host-less" (lack of coincident hosts to $\gtrsim 26$ mag). All late- and early-type designations are based on spectroscopic classification, with the exception of two hosts, GRBs 070729 and 111117A, which are based on well-sampled broad-band photometry (Table 5.3; Leibler & Berger 2010; Margutti et al. 2012).

We then use our classifications to examine the relative rates of short GRBs detected in early- and late-type galaxies. In the absence of observational selection effects, if the overall short GRB rate tracks stellar mass alone, the relative detection rates in early- and late-type galaxies should match the distribution of stellar mass, which is roughly equal at $z \sim 0$ (Kochanek et al. 2001; Bell et al. 2003; Driver et al. 2007) and shows little evolution to $z \sim 1$ (Ilbert et al. 2010). On the other hand, if the short GRB rate depends on a combination of stellar mass and star formation, as in the case of Type Ia supernovae (Sullivan et al. 2006), we expect a distribution skewed toward star-forming galaxies, with a late-to-early-type ratio of >1:1.

5.6.1 Environment Fractions

We first analyze the subset of bursts with sub-arcsecond localization because they have the most unambiguous associations. Of the 68 short GRBs detected with *Swift*[12] as of May 2012, there are 25 such events (Table 5.3), 2 of which have been localized

[12]We note that two of the bursts in our sample, GRBs 050709 and 060121, were first discovered by the High Energy Transient Explorer 2 (HETE-2) satellite.

with *Chandra* (GRB 111020A: Fong et al. 2012b; GRB 111117A; Margutti et al. 2012; Sakamoto et al. 2013), an alternative route to sub-arcsecond positions in the absence of an optical afterglow. This population is divided as follows: 11 (44%) originate in late-type galaxies, 2 (8%) are in early-type galaxies, 6 (24%) have hosts of inconclusive type, and 6 (24%) are host-less (Berger 2010a and this work; Figure 5.14 and Table 5.4). From probability of chance coincidence arguments, we can assign the 6 host-less GRBs to a most probable host galaxy. Berger (2010a) investigated 5 events, finding 2 which likely originated in early-type hosts (GRBs 070809 and 090515), 1 with a late-type host (GRB 061201), and 2 with hosts of inconclusive type (GRBs 080503 and 090305). We have shown that the remaining host-less burst, GRB 110112A lacks an obvious host galaxy (§5.4.3), and we classify it as inconclusive.

Accounting for these host-less assignments in the distribution of galaxy types, we do not find a substantial change in the relative fractions (Figure 5.14). Considering the 16 bursts with definitive host types, the late-to-early-type ratio is 3:1 which deviates from the expected 1:1 distribution if the short GRB rate depends only on stellar mass. Using binomical statistics, we test the null hypothesis of a distribution that is intrinsically 1:1 and find that the observed ratio has a p-value of only 0.04, indicating that the null hypothesis is disfavored (Table 5.4).

Because the optical afterglow brightness depends on the circumburst density, n_0 (Granot & Sari 2002), the requirement of an optical afterglow for precise positions (with the exception of the two bursts localized by *Chandra*) may affect the relative rates of short GRB detection in early- and late-type hosts if there is a correlation between average density and galaxy type. To assess this potential effect, we broaden our analysis to include bursts with a single probable host galaxy ($P_{cc}(< \delta R) \lesssim 0.05$) within or on

Table 5.4. Short GRB Environment Distributions

Sample	Late-type	Early-type	Inconclusive	Host-less	Total	L:E ratio[a]	$P_{\rm binom}(\geq$L:E$)$[b]	Reject 1:1 distribution?[c]
Sub-arcsec.	11 (44%)	2 (8%)	6 (24%)	6 (24%)	25	5.5:1	0.01	Yes
Sub-arcsec., Host-less assigned	12 (48%)	4 (16%)	9 (36%)		25	3:1	0.04	Yes, marginal
Sub-arcsec. + XRT	17 (47%)	6 (17%)	7 (19%)	6 (17%)	36	2.8:1	0.02	Yes
Sub-arcsec. + XRT, Host-less assigned	18 (50%)	8 (22%)	10 (28%)		36	2.3:1	0.04	Yes, marginal
Sub-arcsec. + XRT, All Inc. are Early-type	18 (50%)	18 (50%)			36	1:1	0.5	No
Sub-arcsec. + XRT, EE excluded	12 (43%)	7 (25%)	9 (32%)		28	1.7:1	0.19	No
Sub-arcsec. + XRT, $P_{\rm NC} > 0.9$	8 (58%)	3 (21%)	3 (21%)		14	2.7:1	0.11	No

Note. — [a] Late-to-early-type ratio

[b] p value for finding greater than or equal to the observed L:E ratio from a 1:1 binomial distribution.

[c] Assumes a significance level of 0.05.

the outskirts of XRT error circles. This sample comprises 11 additional events[13] with localizations of $1.5 - 5.5''$ in radius (90% containment; Table 5.3), bringing the total sample size to 36 bursts. Since we require sub-arcsecond localization for a burst to be classified as host-less, the relative fraction of these events is artificially diluted by the addition of bursts with XRT positions (Figure 5.14).

Assigning the host-less bursts to their most probable host galaxies, we recover a similar distribution to the sub-arcsecond localized sample: $\approx 50\%$ late-type, $\approx 20\%$ early-type, and $\approx 30\%$ inconclusive, (Figure 5.14 and Table 5.4). Based on the 26 bursts with early- and late-type designations, this gives a late-to-early-type ratio of 2.3:1 and a low p-value of 0.04 for the null hypothesis that this distribution is drawn from an intrinsically 1:1 distribution. To directly compare this 2.3:1 ratio to the 3:1 observed ratio for sub-arcsecond localized bursts, we compute the probability of obtaining a ratio $\leq$2.3:1 from a population with a true ratio of 3:1 using Monte Carlo simulations for the binomial distribution. In 10^5 trials, we calculate a high probability of 0.82, suggesting that there is no bias to the environment fractions when analyzing only sub-arcsecond localized bursts.

Next, we address the remaining population of 32 *Swift* short GRBs excluded from the discussion thus far. The majority, 80%, are affected by observing constraints that are dependent on factors completely decoupled from any intrinsic properties of the bursts: 15 had *Swift* re-pointing constraints (Sun or Moon) and thus have only γ-ray positions, 7 have XRT positions that are highly contaminated (in the direction of the Galactic plane or near a saturated star, e.g. GRB 100702A, see Appendix), and 4 have XRT

[13]We exclude GRB 050813 from our sample; see Table 5.4.

afterglows but so far lack adequate optical/NIR follow-up to determine the presence of a host galaxy; thus, we cannot currently distinguish between a faint coincident host and a host-less origin for these 4 bursts. The remaining 20% (6 events) have no XRT localization despite rapid *Swift* re-pointing ($\delta t \lesssim 2$ min), but have a low median fluence of $f_\gamma \approx 2 \times 10^{-8}$ erg cm^{-2} compared to the rest of the population with $\langle f_{\gamma,\mathrm{SGRB}} \rangle \approx 2 \times 10^{-7}$ erg cm^{-2} ($15 - 150$ keV; Figure 5.15). Therefore, the lack of detectable emission with XRT may be related to an intrinsically lower energy scale. In summary, we do not expect the exclusion of these 32 bursts to have a substantial effect on the relative morphological fractions.

The low observed early-type fraction is likely attributed to one of two possibilities: (1) it is more challenging to identify early-type galaxies at higher redshifts, and thus a disproportionate fraction of the bursts designated as inconclusive are in fact early-type; or (2) short GRBs preferentially occur in late-type galaxies due to the intrinsic properties of their progenitors.

We explore the former option by investigating the inconclusive population in more detail. Spectral energy distributions of early-type galaxies generally lack strong emission lines, and the most prominent features, the 4000 Å break and the Ca II H&K absorption lines, are redshifted out of the range of most optical spectrographs for $z \gtrsim 1.5$, making spectroscopic identifications particularly difficult at these redshifts. However, more effective studies selecting for distant early-type field galaxies by their photometric optical/NIR colors detect a nearly constant number of early-types between $z \approx 1 - 1.5$ (Stanford et al. 2004), with a typical AB color of $1 - 4$ mag, depending on the choice of optical/NIR filters (Stanford et al. 2004; Tamura & Ohta 2004). Of the 10 inconclusive host galaxies, 4 have optical/NIR color information but yield only poor

constraints of $\lesssim 3-5$ mag due to NIR non-detections and faint optical magnitudes, and 5 lack reported NIR observations. The only inconclusive host galaxy with multi-band detections, GRB 060121, has $R-H \approx 2.4$ mag; however, the optical afterglow and objects in the vicinity are comparably red, suggesting a $z > 2$ origin as an explanation for the red host color (Levan et al. 2006b). K-band imaging to depths of $\gtrsim 23$ AB mag might enable progress in deducing what fraction of the inconclusive population is more likely early-type. To set an extreme upper bound on the true early-type fraction, if we assume that all inconclusive hosts are early-types, the projected early-type fraction is $\sim 50\%$ (Table 5.4).

We now turn to the second option, that short GRBs preferentially originate from late-type galaxies. The predicted demographics of NS-NS/NS-BH merger populations show a preference toward late-type galaxies of $\gtrsim 70\%$ (O'Shaughnessy et al. 2008), so we can use the observed short GRB population to assess the implications for the progenitors. We expect to find roughly equal early- and late-type fractions if stellar mass is the sole parameter determining the short GRB rate. However, we only observe this for $z < 0.4$ (6 events; Figure 5.13). For $z > 0.4$, the late-type fraction is consistently higher, with a late-to-early-type ratio of $\gtrsim$2:1. These results, along with the previous finding that the short GRB rate per unit stellar mass is $2-5$ times higher in late-type hosts (Leibler & Berger 2010), suggest that the short GRB rate is dependent upon a combination of stellar mass and star formation. In the context of NS-NS/NS-BH mergers, if the delay times of the systems which give rise to short GRBs are very long ($\gtrsim$ few Gyr), we would expect a dominant population of early-type hosts at $z \sim 0$. Instead, the current demographics show a preference for late-type galaxies.

Along with the inferred stellar population ages from SED modeling (Leibler &

Berger 2010), this suggests moderate delay times of $\lesssim$ few Gyr. For a delay time distribution of the form $P(\tau) \propto \tau^n$, this translates to $n \lesssim -1$, in contrast to previous short GRB results which claimed substantially longer average delay times of $\sim 4-8$ Gyr for lognormal lifetime distributions based on smaller numbers of events (Nakar et al. 2006; Zheng & Ramirez-Ruiz 2007; Gal-Yam et al. 2008). These results are in good agreement with predictions for populations of NS-NS/NS-BH mergers from population synthesis (Dominik et al. 2012). We also note the similarity to the delay time distribution of Type Ia supernovae, which have $n \approx -1.1$ (Maoz et al. 2010, 2012).

In summary, we find that unless all inconclusive hosts are early-type, the short GRB host distribution is skewed toward late-type galaxies, with the most likely ranges for the early- and late-type fractions of $\approx 20-40\%$ and $\approx 60-80\%$, respectively, for the entire short GRB population. Furthermore, for most cuts on the sample we find that the null hypothesis of a 1:1 distribution can be mildly or strongly rejected.

5.6.2 Comparison with γ-ray Properties

We next investigate whether there is contamination in our sample from collapsars by analyzing trends between morphological type and γ-ray properties. We find that bursts in early- and late-type galaxies span the entire distribution of observed T_{90} for short GRBs, with a median value of 0.4 s (Figure 5.15). Using a Kolmogorov-Smirnov (K-S) test, we find that the two populations are consistent with being drawn from the same underlying distribution ($p = 0.43$). The claim becomes stronger when we compare the combined early-type and inconclusive distribution with the late-type distribution ($p = 0.94$). On the other hand, the corresponding K-S tests for the fluence distributions

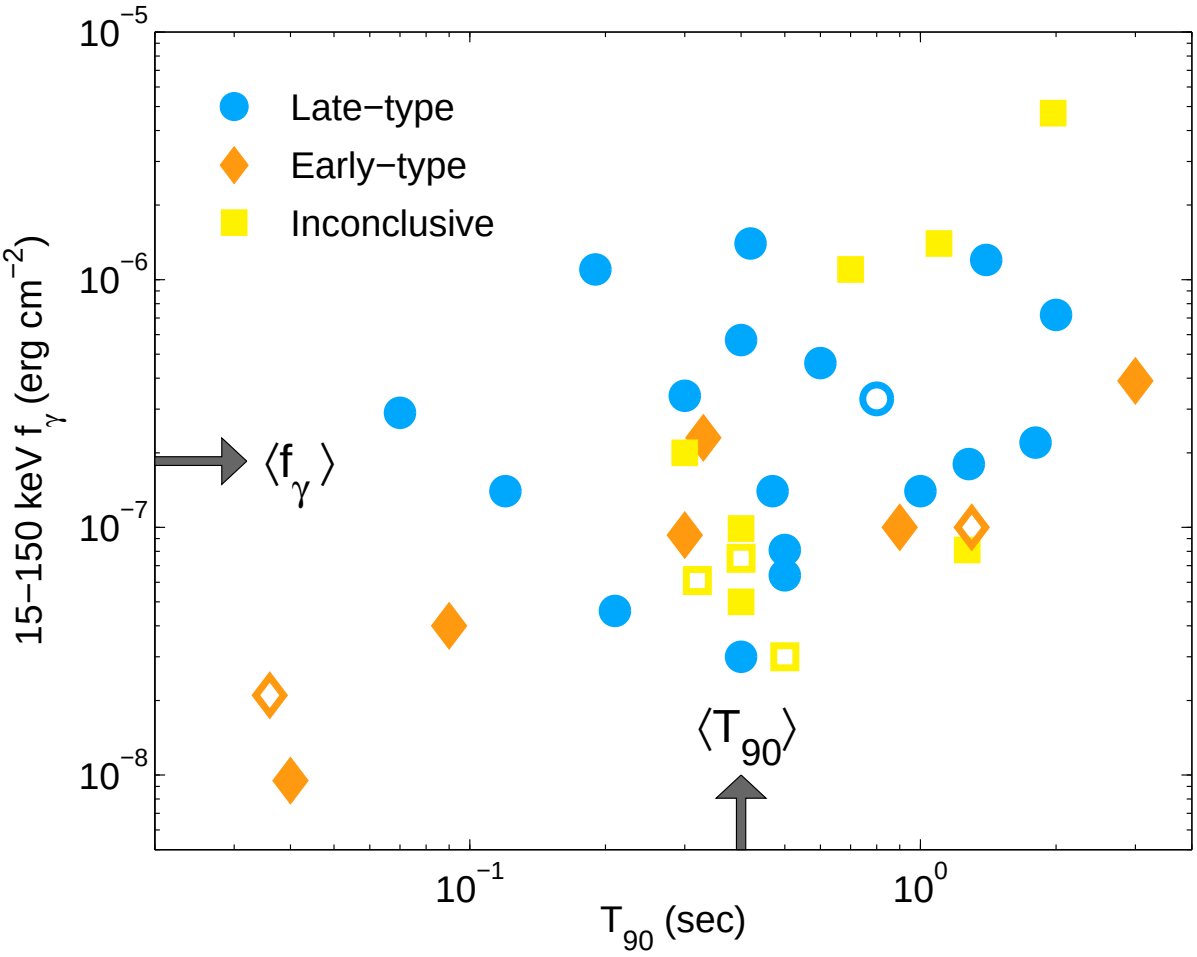

Figure 5.15.—: Fluence, f_γ, $(15-150$ keV) versus duration, T_{90} for the sub-arcsecond localized + XRT sample of 36 *Swift* short GRBs. Bursts are classified by morphological type (Table 5.3) as late-type (blue), early-type (orange) and inconclusive (yellow). Open symbols denote host-less assignments. The median $f_\gamma \approx 2\times10^{-7}$ erg cm^{-2} and $T_{90} \approx 0.4$ s are labeled. The majority of events have $f_\gamma \approx 10^{-8}-10^{-6}$ erg cm^{-2}.

(Figure 5.15) yield marginal p-values of 0.05, suggesting that bursts associated with early- and late-types may not be drawn from the same underlying distribution in f_γ.

A recent study by Bromberg et al. (2013) used the γ-ray properties (T_{90} and spectral hardness) to derive a probability that each event is *not* a collapsar ($P_{\rm NC}$), excluding 8 bursts which have reported evidence for extended emission. Of the 29 bursts that overlap in our samples, 14 have a high probability of not arising from a collapsar ($P_{\rm NC} > 0.9$). If these probabilities are robust, and there is contamination from collapsars in our full sample, we would expect the galaxy type fractions for the population with $P_{\rm NC} > 0.9$ to differ from the overall sample. In particular, by including only high-probability non-collapsar events, we would presumably be excluding mostly late-type galaxies since all long GRBs/collapsars are found in star-forming galaxies. Therefore, one would naively expect the late-to-early-type ratio to *decrease* with respect to the full sample. However, we find that the late-to-early-type ratio for this sample is 2.7:1 (Table 5.4; Figure 5.14) which is higher than the 2.3:1 ratio inferred for the sample of 36 short GRBs.

However, $P_{\rm NC}$ values are not reported for bursts with extended emission. Thus, for a more direct comparison, we evaluate the subset of 28 short GRBs without extended emission (Figure 5.14), and calculate a late-to-early-type ratio of 1.7:1 (Table 5.4). Interestingly, all bursts with extended emission originate in late-type (or inconclusive) galaxies, with the exception of GRB 050724A. Since the ratio for the $P_{\rm NC} > 0.9$ population is more skewed toward late-type galaxies with 2.7:1, the probability of obtaining a $\geq$2.7:1 ratio in 14 events from an intrinsically 1:7:1 distribution is moderate, 0.37. This not only demonstrates no noticeable contamination to the short GRB host type distribution when including bursts with reportedly high probabilities of being

collapsars, but also calls into question the reliability or importance of these probabilities in assessing the true population of short GRBs.

5.7 Conclusions

We present broad-band observations of three short GRBs: GRB 100625A associated with an early-type galaxy at $z = 0.452$, GRB 101219A associated with an active star-forming galaxy at $z = 0.718$, and GRB 110112A which has a sub-arcsecond localization from an optical afterglow but no coincident host galaxy to deep optical limits, and no convincing putative host within 5° of the burst location. These observations showcase the diversity of short GRB environments and give direct clues to the nature of the short GRB progenitor: the moderate physical offsets and low inferred densities can be interpreted as evidence for a compact binary progenitor.

We also undertake the first comprehensive study of host demographics for the full *Swift* short GRB population, classifying bursts by their host galaxy type. We emphasize several key conclusions:

1. The sample of sub-arcsecond localized bursts have a host galaxy distribution of $\approx 50\%$ late-type, $\approx 20\%$ early-type and $\approx 30\%$ of inconclusive type after assigning host-less bursts. The inclusion of bursts with *Swift*/XRT positions and convincing host associations ($P_{cc}(< \delta R) \lesssim 0.05$) does not affect the relative fractions.

2. The observed late-to-early-type ratio is $\gtrsim$2:1, and most cuts to the sample demonstrate that an intrinsically 1:1 distribution is improbable. The only way to obtain equal fractions with the observed events is by assuming that all inconclusive

hosts are early-type galaxies at $z \gtrsim 1$.

3. The most likely ranges for the early- and late-type fractions are $\approx 20 - 40\%$ and $\approx 60 - 80\%$. The preference toward late-type galaxies suggests that both stellar mass and star formation play roles in determining the short GRB rate. Furthermore, in the context of the NS-NS/NS-BH mergers, the observed short GRB population is not dominated by systems with very long delay times, but instead with typical delay times of $\lesssim$ few Gyr.

4. There is no clear trend between T_{90} and host galaxy type, while there may be a relationship between f_γ and host type. When excluding the population of bursts reported to be likely collapsars ($> 90\%$ probability), the late-type fraction increases relative to the overall short GRB sample, suggesting that these probabilities are not reliable in assessing the true population.

Looking forward, our study has demonstrated that detailed observations of short GRB afterglows and environments hold the key to understanding the underlying population of progenitors. In particular, we emphasize the importance of deep NIR observations to determine the early-type fraction within the inconclusive population of hosts, and *Hubble Space Telescope* observations of short GRBs which lack coincident host galaxies to ground-based optical limits (≈ 26 mag). A concerted analysis of broad-band short GRB afterglows would complement this study by providing constraints on the basic properties of the bursts (i.e., energy scale, circumburst density), and help to determine whether there are any correlations between these basic properties and galactic environment. Finally, these updated short GRB demographics now enable a more detailed comparison to published theoretical predictions for the relative fractions of

early- and late-type galaxies which host NS-NS/NS-BH mergers (O'Shaughnessy et al. 2008) and their delay time distributions (Dominik et al. 2012).

5.8 Appendix A

5.8.1 GRB 100628A

GRB 100628A was detected by *Swift*/BAT and the Anti-Coincidence System on INTEGRAL on 2010 June 28.345 UT with $T_{90} = 0.036 \pm 0.009$ s $(15 - 350$ keV), $f_\gamma = 2.5 \pm 0.5 \times 10^{-8}$ erg cm^{-2} $(15 - 150$ keV), and peak energy $E_{\rm peak} = 74.1 \pm 11.4$ keV. The ground-calculated position is RA=$15^{\rm h}03^{\rm m}46.2^{\rm s}$, Dec=$-31°39'10.2''$ with an uncertainty of $2.1'$ (Immler et al. 2010).

X-ray Observations

XRT began observing the field at $\delta t = 86$ s and detected an X-ray source in coincidence with the core of a bright galaxy. The lack of fading of this source confirmed by *Chandra*/ACIS-S observations at $\delta t = 4.4$ days suggests an AGN origin (Immler et al. 2010; Berger 2010c). Furthermore, we use binomial statistics and a 10-pixel region centered on the source to calculate the probability of a chance fluctuation, finding a high probability of 15%. Thus, this source is ruled out as the afterglow of GRB 100628A. A second candidate afterglow was reported based on 7 counts over 3.8 ks in the time interval $\delta t = 92 - 7200$ s, which translates to a count rate of $0.0017^{+0.0008}_{-0.0006}$ counts s^{-1} $(0.3 - 10$ keV; Immler et al. 2010). UVOT, which commenced observations at $\delta t = 90$ s, did not detect a coincident source to $\gtrsim 20.2$ mag (*white* filter; Immler et al. 2010).

We re-analyze the same time interval of XRT data and use the `ximage` routine in the HEASOFT package to measure the significance of the source. In a blind search, we find the source has a significance of 2.3σ. Late-time XRT and *Chandra* observations confirm that the source has faded by a factor of ~ 15 from the claimed initial X-ray flux (Berger 2010c). However, we do not include this burst in our sample of short GRBs with XRT positions due to the low significance of the initial source. We caution against classifying this burst as XRT-localized in future short GRB samples.

5.9 Appendix B

5.9.1 GRB 100702A

Swift/BAT detected GRB 100702A on 2010 July 02.044 UT with $T_{90} = 0.16 \pm 0.03$ s $(15-350$ keV) and $f_\gamma = (1.2 \pm 0.1) \times 10^{-7}$ erg cm^{-2} $(15-150$ keV) at a ground-calculated position of RA=$16^{\rm h}22^{\rm m}46.4^{\rm s}$ and Dec=$-56^\circ 32' 57.4''$ with an uncertainty of $1.4'$ in radius (Siegel et al. 2010).

X-ray Observations

XRT started observing the field at $\delta t = 94$ s and identified a fading X-ray counterpart with a final UVOT-enhanced positional accuracy of $2.4''$ (Table 8.1; Goad et al. 2007; Evans et al. 2009). UVOT commenced observations at $\delta t = 101$ s and no source was identified in the *white* filter to a limit of $\gtrsim 18$ mag (Siegel et al. 2010). The XRT light curve is best fit with a broken power law with decay indices of $\alpha_{X,1} = -0.86^{+0.17}_{-0.24}$ and $\alpha_{X,2} = -5.04^{+0.34}_{-0.37}$, and a break time at $\delta t = 202$ s (Evans et al. 2009).

We extract a spectrum from the XRT data (method described in §5.2.1) and utilize the full PC data set, where there is no evidence for spectral evolution. Our best-fit model is characterized by $\Gamma = 2.7 \pm 0.3$ and $(4.4 \pm 2.0) \times 10^{21}$ cm^{-2} in excess of the substantial Galactic value, $N_{\rm H,MW} = 2.8 \times 10^{21}$ cm^{-2} (Kalberla et al. 2005). We note that the burst is in the direction of the Galactic Center ($b = -4.8^{\circ}$) and therefore the uncertainties on $N_{\rm H,MW}$ are likely larger than the typical 10%. Our results are consistent with the automatic fits by Evans et al. (2009).

Optical/NIR Observations and Afterglow Limits

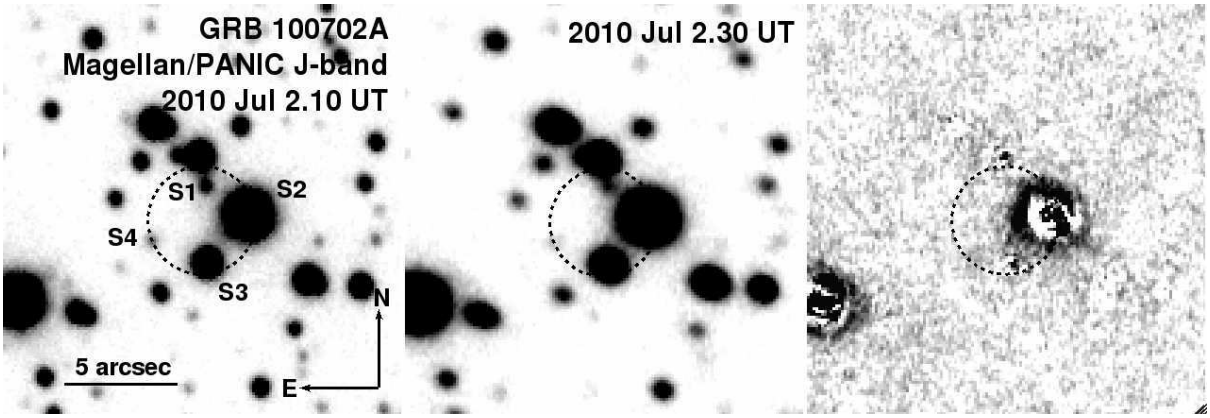

Figure 5.16.—: Magellan/PANIC J-band observations of the host galaxy of GRB 100702A. The XRT error circle has a radius of 2.4″ (90% containment; black). *Left:* $\delta t = 1.3$ hr. *Center:* $\delta t = 6.1$ hr. *Right:* Digital image subtraction of the two epochs reveals no afterglow to a 3σ limit of $J \gtrsim 23.3$ mag.

We obtained J-band observations of the field of GRB 100702A with PANIC at $\delta t = 1.3$ hr (Figure 5.16). We detect 4 sources within or near the outskirts of the XRT error circle (S1-S4 in Figure 5.16). S2 and S3 have stellar PSFs, while S1 and S4 have non-stellar PSFs. Previously reported J-band observations also confirm that S2 and S3 are stars (Nicuesa Guelbenzu et al. 2012a), while S1 and S4 have not been reported in

the literature[14] To assess any fading within the XRT position, we obtained a second set of J-band observations at $\delta t = 6.1$ hr. Digital image subtraction reveal no residuals to a 3σ limit of $J \gtrsim 23.3$ mag (Table 7.1). We caution that this limit only applies to 2/3 of the error circle due to contamination from the saturated star, S2 (Figure 5.16). In addition, we obtained i-band observations with IMACS at $\delta t = 247.3$ days and we do not detect any additional sources in or around the XRT error circle (Table 7.1).

5.9.2 Probabilities of Chance Coincidence

We calculate $P_{cc}(< \delta R)$ for S1 and S4 to assess either source as a putative host galaxy for GRB 100702A. Source S1 is fully inside the XRT error circle while S4 lies on the outskirts of the XRT error circle. We perform PSF photometry for both sources (Table 7.1), and calculate their probabilities of chance coincidence: $P_{cc}(< \delta R) \approx 0.02$ for S1 and $P(< \delta R) \approx 0.04$ for S2 using the 3σ XRT position radius of $4.5''$. This analysis suggests that either source is a likely host for GRB 100702A, and we cannot currently distinguish which is more likely. We also note that the significant contamination makes it difficult to exclude the possibility that there is a brighter galaxy within the XRT error circle. Therefore, we do not include GRB 100702A in our sample of bursts with XRT localization, and consider this field to have observing constraints which prevent more in-depth analysis.

We thank F. di Mille for observing on behalf of the Berger GRB group at Harvard. The Berger GRB group is supported by the National Science Foundation under

[14]Our PANIC observations show that source "C" in Nicuesa Guelbenzu et al. (2012a) is actually three blended sources, including S1. The remaining two sources are outside of the XRT error circle.

Grant AST-1107973, and by NASA/Swift AO6 grant NNX10AI24G and A07 grant NNX12AD69G. Partial support was also provided by the National Aeronautics and Space Administration through Chandra Award Number GO1-12072X issued by the Chandra X-ray Observatory Center, which is operated by the Smithsonian Astrophysical Observatory for and on behalf of the National Aeronautics Space Administration under contract NAS8-03060. This paper includes data gathered with the 6.5 meter Magellan Telescopes located at Las Campanas Observatory, Chile. This work is based in part on observations obtained at the Gemini Observatory, which is operated by the Association of Universities for Research in Astronomy, Inc., under a cooperative agreement with the NSF on behalf of the Gemini partnership: the National Science Foundation (United States), the Science and Technology Facilities Council (United Kingdom), the National Research Council (Canada), CONICYT (Chile), the Australian Research Council (Australia), Ministrio da Cincia, Tecnologia e Inovao (Brazil) and Ministerio de Ciencia, Tecnologa e Innovacin Productiva (Argentina). This work made use of data supplied by the UK Swift Science Data Centre at the University of Leicester. SBC acknowledges generous support from Gary & Cynthia Bengier, the Richard & Rhoda Goldman Fund, the Christopher R. Redlich Fund, the TABASGO Foundation, and NSF grants AST-0908886 and AST-1211916

Chapter 6

A Jet Break in the X-ray Light Curve of Short GRB 111020A Implications for Energetics and Rates

W. Fong, E. Berger, R. Margutti, B. A. Zauderer, E. Troja, I. Czekala, R. Chornock, N. Gehrels, T. Sakamoto, D. B. Fox & P. Podsiadlowski

The Astrophysical Journal, Vol. 756, No. 189, 2012

Abstract

We present broad-band observations of the afterglow and environment of the short GRB 111020A. An extensive X-ray light curve from *Swift*/XRT, XMM-Newton and *Chandra*, spanning ~ 100 seconds to 10 days after the burst, reveals a significant break at $\delta t \approx 2$ days with pre- and post-break decline rates of $\alpha_{X,1} \approx -0.78$ and $\alpha_{X,2} \lesssim -1.7$, respectively. Interpreted as a jet break, we infer a collimated outflow with an opening angle of $\theta_j \approx 3 - 8^{\circ}$. The resulting beaming-corrected γ-ray ($10 - 1000$ keV band) and blastwave kinetic energies are $(2 - 3) \times 10^{48}$ erg and $(0.3 - 2) \times 10^{49}$ erg, respectively, with the range depending on the unknown redshift of the burst. We report a radio afterglow limit of < 39 μJy (3σ) from EVLA observations which, along with our finding that $\nu_c < \nu_X$, constrains the circumburst density to $n_0 \sim 0.01 - 0.1$ cm^{-3}. Optical observations provide an afterglow limit of $i \gtrsim 24.4$ mag at 18 hours after the burst, and reveal a potential host galaxy with $i \approx 24.3$ mag. The sub-arcsecond localization from *Chandra* provides a precise offset of $0.80'' \pm 0.11''$ (1σ) from this galaxy corresponding to an offset of $5 - 7$ kpc for $z = 0.5 - 1.5$. We find a high excess neutral Hydrogen column density of $(7.5 \pm 2.0) \times 10^{21}$ cm^{-2} ($z = 0$). Our observations demonstrate that a growing fraction of short GRBs are collimated which may lead to a true event rate of $\gtrsim 100 - 1000$ Gpc^{-3} yr^{-1}, in good agreement with the NS-NS merger rate of $\approx 200 - 3000$ Gpc^{-3} yr^{-1}. This consistency is promising for coincident short GRB-gravitational wave searches in the forthcoming era of Advanced LIGO/VIRGO.

6.1 Introduction

Observations of the temporal and spectral evolution of short-duration gamma-ray burst (GRB; $T_{90} < 2$ sec; Kouveliotou et al. 1993) afterglows are crucial to our understanding of the basic properties of these events: their energetics, parsec-scale environments, and geometries. From observations over the past 7 years, we now know that short GRBs have isotropic-equivalent energies of $\sim 10^{50} - 10^{52}$ erg (Berger 2007) and circumburst densities of $\sim 10^{-6} - 1$ cm^{-3} (Soderberg et al. 2006b; Panaitescu 2006; Stratta et al. 2007; Perley et al. 2009a; Berger 2010a; Fong et al. 2011); however these ranges are based on only a handful of events. The geometry, or degree of collimation, is the least constrained property, but is of particular interest because it directly affects the true energy scale and event rates. These parameters aid our understanding of the explosion physics, the nature of the progenitors, and the potential detectability of short GRBs as gravitational wave sources. In particular, knowledge of the true energy scale may constrain the mechanism of energy extraction from the central engine and the ejecta composition: $\nu\bar{\nu}$ annihilation powering a baryonic jet (Jaroszynski 1993; Mochkovitch et al. 1993) or magnetohydrodynamic (MHD) processes in a magnetically-dominated outflow (Blandford & Znajek 1977; Rosswog et al. 2003). Significant improvement on the short GRB observed rate of $\gtrsim 10$ Gpc^{-3} yr^{-1} (Nakar & Granot 2007) will have a critical impact on estimates for coincident short GRB-gravitational wave detections in the era of Advanced LIGO/VIRGO (Abadie et al. 2010).

The opening angles (θ_j) of GRBs can be inferred from temporal breaks in the afterglow light curves ("jet breaks"), which occur at the time, t_j, when the Lorentz factor of the outflow is $\Gamma(t_j) \approx 1/\theta_j$; a later break corresponds to a wider opening angle

(Sari et al. 1999; Rhoads 1999). Jet breaks in the light curves of long-duration GRBs have led to an opening angle distribution with a range of $\sim 2 - 20^\circ$ and a median of 7°, leading to beaming-corrected energies of $E_\gamma = [1 - \cos(\theta_j)]E_{\gamma,\rm iso} \sim 10^{50} - 10^{51}$ erg (Bloom et al. 2003; Frail et al. 2001; Friedman & Bloom 2005; Kocevski & Butler 2008; Racusin et al. 2009). For short GRBs, there is mounting theoretical (Eichler et al. 1989; Narayan et al. 1992) and observational (Fong et al. 2010; Berger 2010a; Church et al. 2011) evidence that the progenitors are NS-NS/NS-BH mergers and numerous simulations of post-merger black hole accretion have predicted collimated outflows with $\theta_j \sim 5 - 20^\circ$ (Popham et al. 1999; Aloy et al. 2005; Rosswog 2005; Rezzolla et al. 2011) up to several tens of degrees (Ruffert & Janka 1999b; Popham et al. 1999; Rezzolla et al. 2011).

However, the detection of jet breaks in the afterglow light curves of short GRBs has proved to be challenging. They can in principle be measured from optical or radio observations, but there are several caveats that make this particularly difficult for short GRBs. First, the brightness of optical and radio afterglows are sensitive to the circumburst densities, which are typically low, $\sim 10^{-2}$ cm^{-3} (Soderberg et al. 2006b). Indeed, of nearly 70 short bursts detected by *Swift*, only 2 radio afterglows have been detected over the past 7 years (Berger et al. 2005; Soderberg et al. 2006b; Chandra & Frail 2011). Similarly, only $\sim 30\%$ of *Swift* bursts have detected optical afterglows, with a typical brightness at $\lesssim 1$ day of ≈ 23 mag (Berger 2010a; Fong et al. 2011), making long-term temporal monitoring nearly impossible with ground-based facilities. Second, in the optical band there can be significant contamination from the host galaxies, which are generally brighter than the afterglows at $\gtrsim 1$ day (Berger 2010a).

On the other hand, the X-ray afterglow brightness is independent of the circumburst density (as long as the density is $\gtrsim 10^{-5}$ cm^{-3} and hence $\nu_c > \nu_X$; Granot & Sari 2002),

and host contamination is not an issue. In addition, the well-sampled *Swift*/XRT light curves from ~ 1 min to ~ 1 day provide an unambiguous baseline against which we can measure a subsequent break. Therefore, it is no surprise that the X-rays enabled the discovery of the first jet break in a short GRB. The X-ray afterglow light curve of GRB 051221A exhibited a break at ≈ 5 days, leading to $\theta_j \approx 7^\circ$ (Soderberg et al. 2006b; Burrows et al. 2006). Similarly, *Chandra* observations of GRB 050724A out to 22 days placed a meaningful lower limit of $\theta_j \gtrsim 25^\circ$ (Grupe et al. 2006), consistent with a spherical explosion. Temporal breaks on timescales of $\lesssim$ few hours were observed in the XRT light curves of GRBs 061201 (Stratta et al. 2007) and 090510[1] (De Pasquale et al. 2010). If these are interpreted as jet breaks, they would lead to $\theta_j \sim 1^\circ$; however, they also match the timescale and behavior of early breaks in long GRBs, which are not due to collimation (Nousek et al. 2006; Zhang et al. 2006; Liang et al. 2007). Finally, there is tentative evidence for beaming in the light curves of GRBs 050709 (Fox et al. 2005) and 061210[2] (Berger 2007); however, these are based on sparsely-sampled light curves without a definitive break (e.g., Watson et al. 2006). No other jet breaks in the light curves of unambiguous short GRBs have been reported to date[3] and the lack of jet breaks in *Swift*/XRT observations out to $\sim 1-2$ days can provide only weak lower bounds of $\theta_j \gtrsim 2-6^\circ$ (revised from Coward et al. 2012 with more realistic density values;

[1]GRB 090510 also exhibits a post-jet break-like decay in its optical light curve (Nicuesa Guelbenzu et al. 2012b).

[2]Please note that Berger (2007) erroneously refers to GRB 061006.

[3]A jet break was reported in the light curve of GRB 090426A (Nicuesa Guelbenzu et al. 2011); however the characteristics of its environment and prompt emission are more similar to those of long GRBs (Levesque et al. 2010; Xin et al. 2011b).

see Section 6.4.2).

Against this backdrop, we present here the discovery of a break in the X-ray light curve of GRB 111020Aat $\delta t \approx 2$ days, best explained as a jet break. We also present contemporaneous radio and optical limits on the afterglow, allowing a characterization of the broad-band synchrotron spectrum and constraints on the energy and density. In addition, we report the discovery of a putative host galaxy. A comparison of our X-ray and optical data may require an appreciable amount of extinction and the highest intrinsic neutral Hydrogen column density for a short GRB to date. Our results have implications for the opening angle distribution, and therefore the observed short GRB rate and true energy release.

Unless otherwise noted, all magnitudes in this paper are in the AB system and are corrected for Galactic extinction in the direction of the burst using $E(B-V) = 0.432$ mag (Schlegel et al. 1998; Schlafly & Finkbeiner 2011). We employ a standard ΛCDM cosmology with $\Omega_M = 0.27$, $\Omega_\Lambda = 0.73$, and $H_0 = 71$ km s^{-1} Mpc^{-1}.

6.2 Observations of GRB 111020A

6.2.1 *Swift* Observations

GRB 111020A was detected on 2011 October 20 at 06:33:49.0 UT by the Burst Alert Telescope (BAT) on-board the *Swift* satellite (Gehrels et al. 2004; Sakamoto et al. 2011c). BAT located the burst at a ground-calculated position of RA=$19^{\rm h}08^{\rm m}06.9^{\rm s}$ and Dec=$-38^\circ01'50.3''$ (J2000) with $2.1'$ accuracy (90% containment; Sakamoto et al.

2011b). The X-ray Telescope (XRT) commenced observations of the location of the burst at $\delta t = 72.8$ s (where δt is the time after the BAT trigger) and detected a fading X-ray source (Section 6.2.2). The UV-Optical Telescope (UVOT) began observations of the field at $\delta t = 79$ s but no corresponding UV or optical source was found within the XRT position. The 3σ limit in the *white* filter, which transmits over $\lambda = 1600$-8000 Å (Poole et al. 2008), is 20.3 mag (not corrected for Galactic extinction; Oates & Sakamoto 2011).

The gamma-ray emission consists of a single pulse with a duration of $T_{90} = 0.40 \pm 0.09$ s in the $15 - 350$ keV band, classifying GRB 111020A as a short burst (Sakamoto et al. 2011b). The spectrum is best fit with a single power law with index 1.37 ± 0.26 and a fluence of $f_\gamma = (6.5 \pm 1.0) \times 10^{-8}$ erg cm^{-2} ($15 - 150$ keV). Spectral lag analysis is not conclusive, and there is no clear evidence for extended emission (Sakamoto et al. 2011a).

6.2.2 X-ray Observations

The XRT promptly located a fading, uncatalogued X-ray source (Evans et al. 2007a, 2009; Sakamoto et al. 2011c) with a UVOT-enhanced position of RA=$19^{\rm h}08^{\rm m}12.53^{\rm s}$ and Dec=$-38°00'43.8''$ (J2000) and an uncertainty of $1.6''$ (Osborne et al. 2011). XRT observations of the field continued until the source faded below the detection threshold at $\delta t \approx 3.5$ days.

We also observed the field of GRB 111020A with the European Photon Imaging Camera (EPIC-PN) on-board the X-ray Multi-Mirror Mission (XMM-Newton) starting at $\delta t = 0.65$ days. With 13.5 ks of on-source observations, we clearly detect a source in the energy range $0.5 - 10$ keV, consistent with the *Swift*-XRT position. In addition, we obtained two sets of 20-ks observations with the Advanced CCD Imaging Spectrometer

(ACIS-S; $0.3 - 10\,\mathrm{keV}$) on-board the *Chandra* X-ray Observatory at $\delta t = 2.9$ and 10.1 days to refine the astrometry and monitor the light curve evolution. We detect the X-ray afterglow in the first *Chandra* observation but do not detect any source at the same location in the second epoch.

Data Analysis and Spectral Fitting

We analyze the XRT data using the latest version of the HEASOFT package (v.6.11) and relevant calibration files. We apply standard filtering and screening criteria, and generate a count rate light curve following the prescriptions from Margutti et al. (2010) and Margutti et al. (2013). Our re-binning scheme ensures a minimum signal-to-noise ratio of $S/N = 4$ for each temporal bin. We analyze the XMM data using standard routines in the Scientific Analysis System (SAS) v.11. We remove the first 5 ks of data due to high background contamination, giving a total exposure time of 13.5 ks. We extract count rates from a $20''$ radius aperture and the background is calculated using $20''$ radius source-free regions on the same chip. We use the `CIAO` data reduction package for the *Chandra* data. For the first epoch, we use a $2.5''$ radius source aperture centered on the *Chandra* position and a background annulus with inner and outer radii of $10''$ and $35''$, respectively, giving a source detection significance of $\sim 30\sigma$. For the second epoch, we extract 1 count in a $2.5''$ aperture at the location of the source, consistent with the average background level calculated from source-free regions on the same chip. We therefore take the 3σ background count rate as an upper limit on the X-ray afterglow.

To extract a spectrum from the X-ray data, we fit each of the data sets with an absorbed power law model ($tbabs \times ztbabs \times pow$ within the XSPEC routine) characterized

by a photon index, Γ, and intrinsic neutral hydrogen absorption column, $N_{\rm H,int}$, in excess of the Galactic column density in the direction of the burst, $N_{\rm H,MW} = 6.9 \times 10^{20}\,{\rm cm}^{-2}$ (typical uncertainty of $\sim 10\%$; Kalberla et al. 2005; Wakker et al. 2011), using Cash statistics. For XRT, we utilize data in the time interval $0.08 - 60$ ks where there is no evidence for spectral evolution. We find an average best-fitting (C-stat$_\nu = 0.86$ for 188 d.o.f.) spectrum characterized by $\Gamma = 2.2 \pm 0.5$ and $N_{\rm H,int} = (1.0 \pm 0.3) \times 10^{22}\,{\rm cm}^{-2}$ at $z = 0$ (Table 8.5). Uncertainties correspond to the 90% confidence level. Our best-fit parameters are fully consistent with the automatic spectrum fit produced by Mangano & Sakamoto (2011). The XMM data are best modeled with a power law characterized by $\Gamma = 2.0 \pm 0.4$ and $N_{\rm H,int} = (0.65 \pm 0.22) \times 10^{22}$ cm^{-2} (C-stat$_\nu = 1.0$ for 256 d.o.f.), consistent with the XRT model parameters. We also fit the first epoch of *Chandra* data and the resulting parameters are consistent with those from XRT and XMM, albeit with large error bars due to low count statistics (Table 8.5). Since we find no evidence for spectral evolution in the XRT data, we perform a joint XRT+XMM spectral analysis to obtain the best constraints on Γ and $N_{\rm H,int}$. The resulting best-fit model has $\Gamma = 2.0 \pm 0.3$ and $N_{\rm H,int} = (0.8 \pm 0.2) \times 10^{22}$ cm^{-2} (90% c.l.; C-stat$_\nu = 0.94$ for 446 d.o.f.). Although the redshift of the burst is unknown, we note that Γ remains unchanged within its 1σ value for $z \lesssim 3$ and we find evidence for intrinsic $N_{\rm H,int}$ in excess of the Galactic value at 6.5σ confidence. The best-fitting spectral parameters for each of the three data sets and the joint fit are summarized in Table 8.5.

Applying these parameters to the individual XRT, XMM, and *Chandra* data sets, we calculate the count rate-to-flux conversion factors, and hence their absorbed and unabsorbed fluxes (Table 6.2). Applying these conversion factors results in the X-ray light curve shown in Figure 6.1.

Table 6.1. GRB 111020A X-ray Spectral Fit Parameters

Telescope	Detector	δt (ks)	$N_{H,int}^{ab}$ (10^{22} cm^{-2})	Γ^{ab}	C-stat$_\nu$/d.o.f.
Swift	XRT	$0.08 - 60$	1.0 ± 0.3	2.2 ± 0.5	0.86/188
XMM	EPIC-PN	$61.4 - 76.8$	$0.65^{+0.21}_{-0.23}$	2.0 ± 0.4	1.0/256
Chandra	ACIS-S	$250.5 - 268.5$	$0.4^{+2.3}_{-0.4}$	$1.1^{+2.7}_{-0.8}$	0.32/661
Swift+XMM	XRT+EPIC-PN	see above	$0.75^{0.20}_{-0.18}$	2.0 ± 0.3	0.94/446

Note. — [a] These values assume a Galactic column density of $N_{H,gal} = 6.9 \times 10^{20}$ cm^{-2} (Kalberla et al. 2005), using an `XSPEC` model of $tbabs \times ztbabs \times pow$ at $z = 0$. [b] Uncertainties correspond to a 90% confidence level.

Table 6.2. GRB 111020A X-ray Observations

δt (s)	Time Bin Duration (s)	Unabs. Flux ($0.3-10$ keV) (erg cm^{-2} s^{-1})
	Swift/XRT	
6.18×10^{1}[a]	7.44×10^{0}	$(2.38 \pm 0.79) \times 10^{-10}$
1.35×10^{2}	4.64×10^{1}	$(3.80 \pm 1.03) \times 10^{-11}$
2.66×10^{2}	1.71×10^{2}	$(1.64 \pm 0.42) \times 10^{-11}$
4.15×10^{2}	1.26×10^{2}	$(2.43 \pm 0.64) \times 10^{-11}$
5.96×10^{2}	2.36×10^{2}	$(1.03 \pm 0.26) \times 10^{-11}$
7.97×10^{2}	1.66×10^{2}	$(1.83 \pm 0.49) \times 10^{-11}$
1.14×10^{3}	5.20×10^{2}	$(8.85 \pm 1.72) \times 10^{-12}$
5.94×10^{3}	2.46×10^{3}	$(1.65 \pm 0.33) \times 10^{-12}$
1.17×10^{4}	2.46×10^{3}	$(1.07 \pm 0.27) \times 10^{-12}$
1.94×10^{4}	6.38×10^{3}	$(9.19 \pm 2.28) \times 10^{-13}$
2.58×10^{4}	6.28×10^{3}	$(1.19 \pm 0.32) \times 10^{-12}$
3.19×10^{4}	5.90×10^{3}	$(1.05 \pm 0.27) \times 10^{-12}$
4.29×10^{4}	1.61×10^{4}	$(8.36 \pm 2.41) \times 10^{-13}$
1.26×10^{5}	1.51×10^{5}	$(1.63 \pm 0.55) \times 10^{-13}$
3.09×10^{5}	2.14×10^{5}	$(1.11 \pm 0.42) \times 10^{-13}$
	XMM/EPIC-PN	
6.91×10^{4}	1.35×10^{4}	$(2.66 \pm 0.19) \times 10^{-13}$
	Chandra/ACIS-S	
2.61×10^{5}	1.98×10^{4}	$(5.96 \pm 0.89) \times 10^{-14}$
8.84×10^{5}	1.98×10^{4}	$< 8.95 \times 10^{-15}$

Note. — Upper limits are 3σ.

[a] These points were excluded from the broken power law fit.

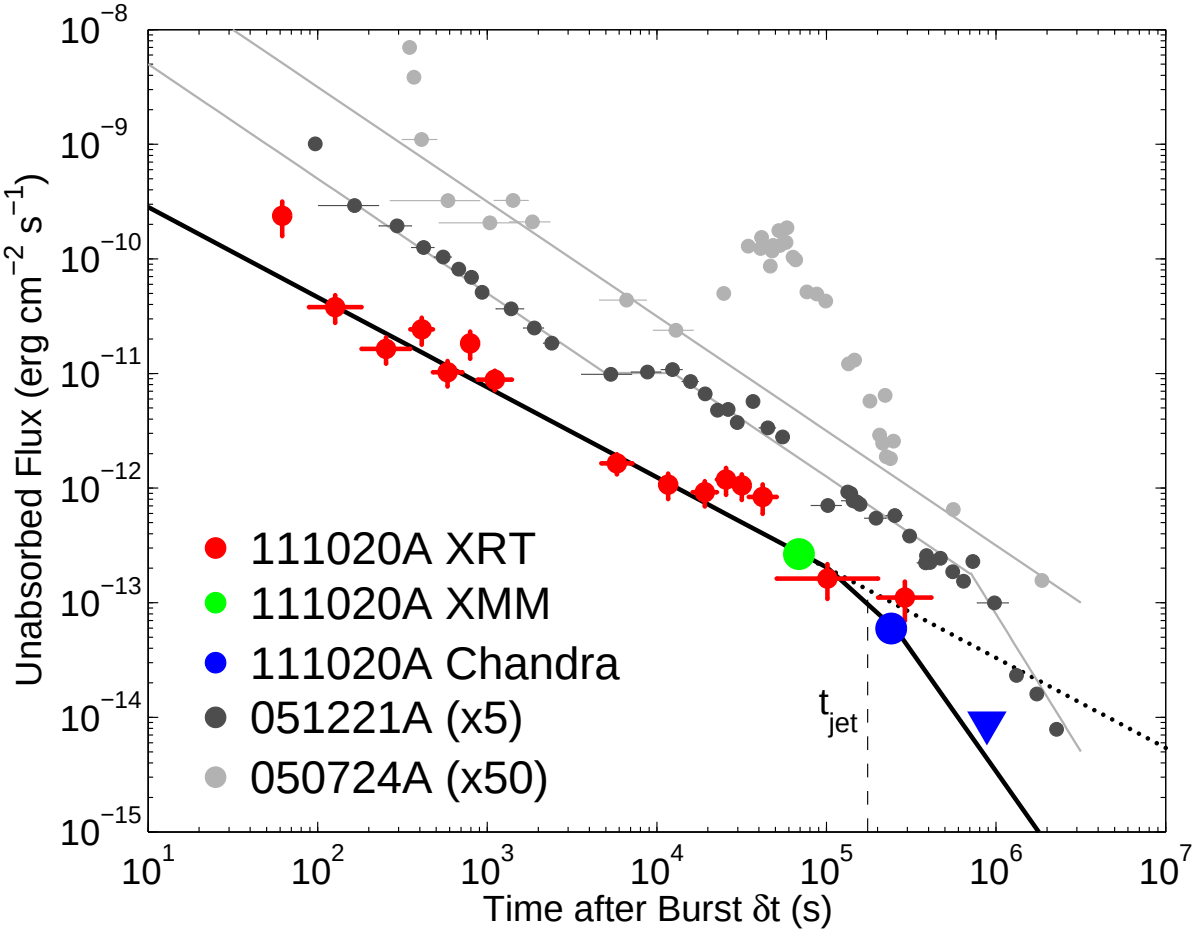

Figure 6.1.—: Unabsorbed X-ray flux light curve for GRB 111020A from *Swift*-XRT (red), XMM (green), and *Chandra* (blue). Flux errors are 1σ. The *Chandra* 3σ upper limit is denoted by the blue triangle. The best-fit broken power law model (black solid line) for GRB 111020A is characterized by $\alpha_1 = -0.78$, $\alpha_2 = -2.1$, and $t_j = 2.0$ days. A single power law model with $\alpha = -0.78$ (black dotted) violates the *Chandra* upper limit. Also plotted are X-ray light curves for short GRBs 051221A (dark grey circles; Soderberg et al. 2006b; Burrows et al. 2006) and 050724 (light grey circles; Grupe et al. 2006). The data for GRBs 051221A and 050724 have been scaled for clarity. Grey lines trace the afterglow evolution with a break for GRB 051221A at ≈ 5 days and no break for GRB 050724A to ≈ 22 days.

Differential Astrometry

In the absence of the detection of an optical afterglow (Section 6.2.3), we use our *Chandra* observations to refine the *Swift*/XRT position (1.6″ uncertainty) to sub-arcsecond accuracy. We perform differential astrometry between our *Chandra* and GMOS observations (Section 6.2.3). To achieve the maximum signal-to-noise ratio, we combine both epochs of GMOS *i*-band observations and use `SExtractor`[4] to determine the positions and centroid uncertainty of sources in the field. Performing an absolute astrometric tie to 2MASS using ∼70 common point sources, we find a resulting rms value of $\sigma_{\rm GMOS-2MASS} = 0.17''$ ($0.12''$ in each coordinate).

To refine the native *Chandra* astrometry and determine the location of the X-ray afterglow relative to the GMOS image, we perform differential astrometry. We use `CIAO` routines `mergeall` to combine the two *Chandra* epochs and `wavdetect` to obtain positions and 1σ centroid uncertainties of X-ray sources in the field. We also use `wavdetect` to determine the *Chandra* position of the afterglow from the first epoch and find a 1σ centroid statistical uncertainty $\sigma_{\rm X,ag} = 0.08''$. We calculate an astrometric tie based on two X-ray and optically bright common sources and find weighted mean offsets of δRA$= -0.27'' \pm 0.06''$ and δDec$= +0.05'' \pm 0.05''$ giving a tie uncertainty of $\sigma_{\rm CXO-GMOS} = 0.08''$. There are three additional common, but fainter sources. An astrometric tie using all five sources gives weighted mean offsets and errors of δRA$= -0.29'' \pm 0.15''$ and δDec$= +0.06'' \pm 0.16''$, fully consistent with our results from using the two bright sources alone. We therefore use the astrometric solution from the two bright sources only. Applying this solution, we obtain a *Chandra* X-ray afterglow

[4]http://sextractor.sourceforge.net/.

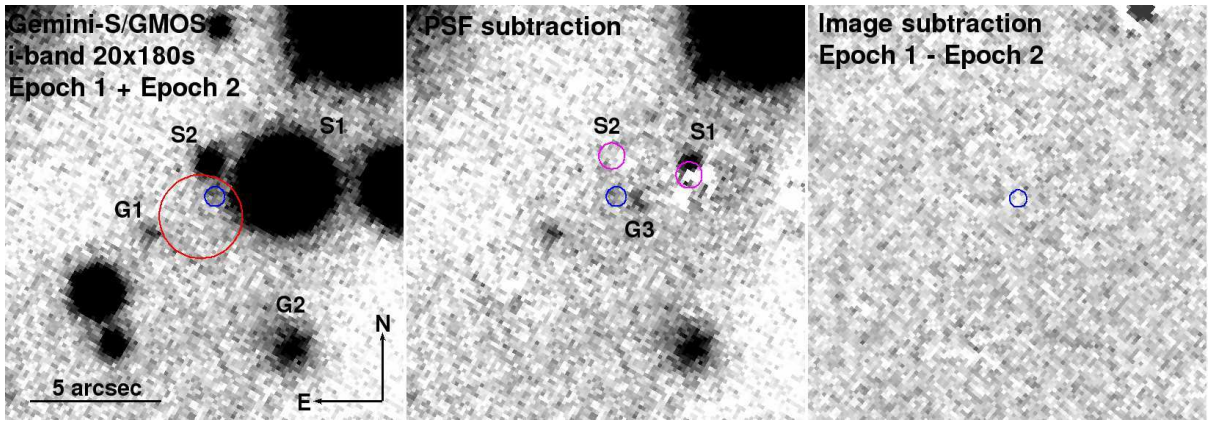

Figure 6.2.—: Optical i-band observations obtained with GMOS on Gemini-South. *Left*: Combined stack of two nights of GMOS i-band data. Stars S1 and S2 are labeled, as well as galaxies G1 and G2. X-ray positions of GRB 111020A are denoted by the circles (red: *Swift*-XRT, 1.6″ radius, 90% containment; blue: *Chandra*, 0.33″ radius, 90% confidence). *Center*: PSF-subtracted image with the centroids of S1 and S2 (magenta circles). The subtraction reveals a third source, G3, with $i \approx 24.3$ mag. *Right*: Digital image subtraction of the two epochs obtained at 17.7 hours and 1.7 days, respectively, reveals no residuals in or around the *Chandra* position.

position of RA=$19^{\rm h}08^{\rm m}12.49^{\rm s}$ and Dec=$-38°00'42.9''$ (denoted by the blue circle in Figure 6.2) with a total 1σ uncertainty of $0.20''$, accounting for the 2MASS-GMOS astrometric tie, GMOS-*Chandra* tie, and afterglow positional uncertainty. This position is consistent with the XRT position and is offset by $0.94''$ from the XRT centroid.

6.2.3 Optical Observations and Putative Host Galaxies

We initiated i-band observations of GRB 111020A with the Gemini Multi-Object Spectrograph (GMOS) mounted on the Gemini-South 8-m telescope on 2011 October 21.01 UT ($\delta t = 17.7$ hours). The data were reduced using the `gemini/gmos` package in IRAF. In a stack of 9×180 s exposures in $0.74''$ seeing and photometric conditions (Figure 6.2), we do not detect any sources within the enhanced XRT error circle or

coincident with the *Chandra* position. However, the outskirts of the XRT position are partially contaminated by emission from a nearby $i = 17.7$ mag star (S1) and a fainter star (S2) with $i = 22.7$ mag (corrected for $A_i = 0.73$ mag; Figure 6.2). We detect two additional nearby sources: a faint galaxy (G1) located $2.8''$ away from the center of the *Chandra* position and a brighter galaxy (G2) with a $6.5''$ offset (Figure 6.2).

To search for a fading optical afterglow, we obtained a second, deeper set of i-band observations (11×180 s) with GMOS at $\delta t = 1.74$ days in $0.67''$ seeing. Digital image subtraction using the ISIS software package (Alard 2000) reveals no variation between the two epochs inside or near the X-ray afterglow error circles (Figure 6.2). To calculate the upper limit on the afterglow, we add several point sources of varying magnitudes between $i = 24 - 26$ mag around the position in the first epoch using IRAF routine `addstar`. We perform photometry in the residual image in $2''$ apertures using the standard published i-band zeropoint for GMOS-S and place a 3σ limit on the afterglow of $i \gtrsim 24.4$ mag ($F_\nu \lesssim 0.63$ μJy). We also perform photometry in a $1.8''$ aperture for G1 and a $2.3''$ aperture for G2, giving magnitudes of $i = 23.9 \pm 0.2$ mag and $i = 21.9 \pm 0.1$, respectively (Table 6.3).

In addition, we obtained r-band observations (3×360 s in $0.62''$ seeing) with the Low Resolution Survey Spectrograph 3 (LDSS3) mounted on the Magellan/Clay 6.5-m telescope concurrent to the first epoch of GMOS observations ($\delta t = 17.7$ hours). We obtained a second, deeper set of observations (16×150 s in $0.66''$ seeing) at $\delta t \approx 180$ days, and digital image subtraction reveals no evidence for a fading source within the X-ray positions to a 3σ limit of $r \gtrsim 24.1$ mag, where the zeropoint is determined from several standard stars at similar airmass. We easily detect G2, with $r = 21.9 \pm 0.1$ mag, but do not detect G1 to a 3σ limit of $r \gtrsim 24.8$ (corrected for $A_r = 0.99$ mag;

Table 6.3. GRB 111020A Optical Photometry

Date (UT)	δt (d)	Telescope	Instrument	Filter	Exposures (s)	$\theta_{\rm FWHM}$ (arcsec)	Afterglow[ab] (AB mag)	F_ν[ab] (μJy)	G1[a] (AB mag)	G2[a] (AB mag)	G3[a] (AB mag)	A_λ (AB mag)
2011 October 21.01	0.74	Magellan/Clay	LDSS3	r	3×360	0.62	> 24.1	< 0.83	> 24.1	22.00 ± 0.08	> 24.1	0.987
2011 October 21.01	0.74	Gemini-S	GMOS	i	9×180	0.74	> 24.4	< 0.63				0.734
2011 October 22.01	1.74	Gemini-S	GMOS	i	11×180	0.67						0.734
2011 October 21+22		Gemini-S	GMOS	i	20×180	0.72			23.89 ± 0.17	21.91 ± 0.05	24.27 ± 0.16	0.734
2012 May 17.25	179.0	Magellan/Clay	LDSS3	z	15×180	0.60			24.05 ± 0.41	21.67 ± 0.08	> 23.6	0.546
2012 May 17.30	179.1	Magellan/Clay	LDSS3	r	16×180	0.66			> 24.8	21.84 ± 0.05	> 24.8	0.987

Note. — [a] These values have been corrected for Galactic extinction A_λ (Schlafly & Finkbeiner 2011).

[b] Limits are 3σ.

Table 6.3). Finally, we obtained z-band observations with LDSS3 (15×180 s in $0.60''$ seeing) at $\delta t \approx 180$ days. We detect G1 at 2.5σ significance, $z = 24.1 \pm 0.4$, and G2 with $z = 21.7 \pm 0.1$ (corrected for $A_z = 0.55$ mag).

Since S1 and S2 contaminate the *Chandra* position, we subtract their contribution using point-spread-function (PSF) subtraction on the individual observations and a combined stack of the two GMOS epochs. We use standard PSF-fitting routines in the IRAF `daophot` package. Modelling the PSF using 4 bright, unsaturated stars in the field out to a radius of $3''$ ($\sim 4\theta_{\rm FWHM}$) from the center of each star, we subtract several stars in the field including S1 and S2. The clean subtraction of these stars indicates a model PSF representative of the PSF of the field. We uncover a faint, mildly extended source (G3) on the outskirts of S1 at coordinates RA=$19^{\rm h}08^{\rm m}12.43^{\rm s}$ and Dec=$-38^\circ00'43.07''$ (J2000). This source, which lies $0.80''$ from the center of the *Chandra* error circle, has a magnitude of $i = 24.3 \pm 0.2$ and is a potential host of GRB 111020A (Section 6.3.1). G3 is not detected in the r or z filters to 3σ limits of $r > 24.8$ and $z > 23.6$ (Table 6.3). Based on the limited color information, $r - i \gtrsim 0.5$ and $i - z \gtrsim -0.67$, we cannot rule out the possibility that this source is a faint star.

6.2.4 Radio Observations and Possible Afterglow

We observed the position of GRB 111020A with the Expanded Very Large Array[5] (EVLA) beginning on 1 October 20.95 UT ($\delta t = 16.1$ hours; Program $10C - 145$) at a mean frequency of 5.8 GHz with a total on-source integration time of 65 min. We observed 3C295 and J1937−1958 for bandpass/flux and gain calibration, respectively,

[5]Newly renamed the Karl G. Jansky Very Large Array.

and used standard procedures in the Astronomical Image Processing System (AIPS; Greisen 2003) for data calibration and analysis. With the new wideband capabilities of the EVLA (Perley et al. 2011), our data have an effective bandwidth of $\sim$1.5 GHz after excising edge channels and data affected by radio frequency interference. The low declination of GRB 111020A and the compact D configuration of the array at the time of observation caused significant shadowing and required the removal of 7 out of 27 antennas (the north arm of the EVLA).

Taking into account the highly-elongated beam ($33'' \times 7''$ with a position angle of 170°), we detect a 3.7σ source with an integrated flux density of $48 \pm 13\,\mu$Jy located at RA=$19^{\rm h}08^{\rm m}12.40^{\rm s}$, Dec=$-38°00'41.2''$ (δRA= $1.1''$, δDec= $3.6''$, 1σ uncertainty), consistent with the *Chandra* position. The position, peak flux and integrated flux of the source are consistent regardless of our choice of weighting, or if we analyze the upper and lower sidebands separately. However, despite the statistical significance of the detection, we cannot completely rule out sidelobe contribution from nearby bright sources in the field due to the low declination of the burst. Therefore, we conservatively adopt a 3σ upper limit of $39\,\mu$Jy on the radio afterglow of GRB 111020A for our analysis. We note that if the source is indeed real then upper limits inferred from the radio data can be treated as actual values.

6.3 Results

6.3.1 Galaxy Probabilities of Chance Coincidence

To assess which galaxy is the most probable host of GRB 111020A we adopt the methodology of Bloom et al. (2002) and Berger (2010a) to calculate the probability of chance coincidence $P(< \delta R)$ at a given angular separation δR. We determine the expected number density of galaxies brighter than a measured apparent magnitude, m, using the results of deep optical galaxy surveys (Hogg et al. 1997; Beckwith et al. 2006):

$$\sigma(\leq m) = \frac{1}{0.33 \times \ln(10)} \times 10^{0.33(m-24)-2.44} \ \text{arcsec}^{-2}. \tag{6.1}$$

Then the probability of chance coincidence is given by (Bloom et al. 2002)

$$P(< \delta R) = 1 - \mathrm{e}^{-\pi(\delta R)^2 \sigma(\leq m)}. \tag{6.2}$$

We calculate $P(< \delta R)$ for each of the three host galaxy candidates (Figure 6.3), and find that G3 is the most probable host of GRB 111020A with $P(< \delta R) = 0.01$, while for G1 and G2, the values are $P(< \delta R) = 0.10$ and 0.12, respectively.

6.3.2 X-ray Light Curve Fitting and a Jet Break

The temporal behavior of the X-ray afterglow flux is characterized by a steady power-law decline until $\delta t \approx 2$ days when there is a significant steepening in the light curve (Figure 6.1). A single power law model with a decline rate determined by the X-ray

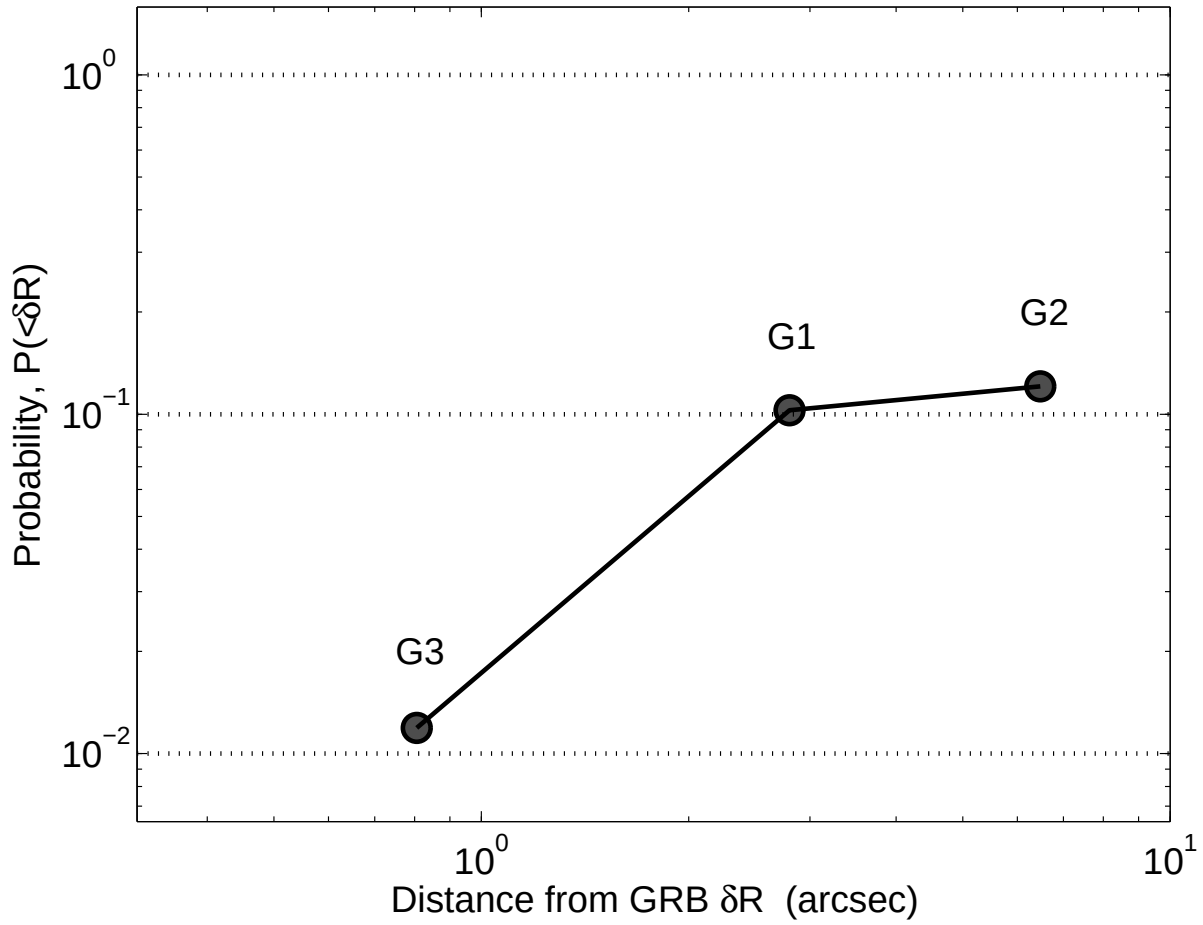

Figure 6.3.—: Probability of chance coincidence, $P(< \delta R)$, as a function of angular distance from the center of the *Chandra* afterglow position for the three host galaxy candidates of GRB 111020A. The galaxy G3 has the lowest probability of chance coincidence $P(< \delta R) = 0.01$, and is therefore the most probable host of GRB 111020A.

data at early times ($t \lesssim 2$ days) provides a poor fit to the late-time data (dotted line in Figure 6.1); in particular, it overestimates the *Chandra* detection and upper limit. To quantitatively assess the shape of the X-ray light curve, we therefore invoke a broken power law model, given by

$$F_X = F_{X,0}\left[\left(\frac{t}{t_j}\right)^{\alpha_{X,1}s} + \left(\frac{t}{t_j}\right)^{\alpha_{X,2}s}\right]^{1/s}, \tag{6.3}$$

where $F_{X,0} = 2^{1/s}F_X(t = t_j)$, $\alpha_{X,1}$ and $\alpha_{X,2}$ are the power law indices pre- and post-break, respectively, t_j is the break time in seconds, and s is a dimensionless smoothness parameter that characterizes the sharpness of the break. We perform a three-parameter χ^2-grid search over $F_{X,0}$, $\alpha_{X,1}$ and t_j. If we use a relatively sharp break (e.g. $s \approx -10$), the *Chandra* 3σ upper limit constrains $\alpha_{X,2} \lesssim -1.7$. If we allow for a smoother break (e.g. $s \approx -1$), $\alpha_{X,1}$ remains unchanged but the break occurs at later times ($t_j \approx 4$ days) and $\alpha_{X,2}$ is required to have a steeper value of $\lesssim -2.2$ to accommodate the *Chandra* upper limit. This scenario generally provides a poorer fit to the last *Chandra* and *Swift*/XRT points. We therefore adopt the sharp-break scenario. Fixing $s = -10$ and $\alpha_{X,2} = -2.1$, we find a best-fit broken power law model characterized by $F_X(t_j) = (1.36 \pm 0.45) \times 10^{-13}$ erg cm^{-2} s^{-1}, $\alpha_{X,1} = -0.78 \pm 0.05$, and $t_j = 2.0 \pm 0.5$ days (1σ, $\chi^2_\nu = 1.1$ with 15 d.o.f.; Figure 6.1). This best-fit model is shown in Figure 6.1. The best fit parameters are independent of our choice of $\alpha_{X,2}$ between -1.7 and -3. We also note the presence of a slight flux enhancement relative to the power law decay at $\delta t \approx 3 \times 10^4$ s (0.35 days). If we remove these points from our fits, the resulting best-fit parameters remain unaffected.

The required change in the temporal index is $\Delta\alpha_{12} \gtrsim 0.9$. There are several

possibilities that can explain breaks in GRB afterglow light curves. The first scenario is the transition of the cooling frequency across the band, but this only predicts $\Delta\alpha = 0.25$ (Sari et al. 1998). An alternative possibility is the cessation of energy injection, either from refreshed shocks or a long-lasting central engine (e.g., Rees & Meszaros 1998; Sari & Mészáros 2000; Zhang & Mészáros 2002), which has been used to explain the termination of a shallow decay or plateau phase in the X-ray and optical light curves of several long GRBs. However, these cases all exhibit earlier temporal breaks at $\sim 10^3 - 10^4$ sec with $\Delta\alpha_{12} \sim 0.7$ ($\alpha_{X,1} \approx -0.5$, $\alpha_{X,2} \approx -1.2$; Nousek et al. 2006; Zhang et al. 2006; Liang et al. 2007). Attributing the break in GRB 111020A to the cessation of central engine activity would require sustained energy injection from the start of XRT monitoring to the break time, ~ 100 seconds to 2 days, whereas the timescales of energy injection for long GRBs are $\lesssim$ few hours (Nousek et al. 2006; Zhang et al. 2006; Liang et al. 2007; Racusin et al. 2009). Single episodes of energy injection have also been observed in two short GRBs: 051221A and 050724A (Berger et al. 2005; Soderberg et al. 2006b; Burrows et al. 2006; Grupe et al. 2006)). The light curve of GRB 051221A, which exhibits a power law decay with index $\alpha_{X,1} = -1.1$, a plateau, and a return to the same power law ($\Delta\alpha_{12} = 0$), is interpreted as a single period of energy injection (Soderberg et al. 2006b; Burrows et al. 2006). A super-imposed flare on the light curve of GRB 050724A with a single underlying decay index of $\alpha_{X,1} = -0.98$ is also possibly related to late-time reactivation of the central engine (Berger et al. 2005; Grupe et al. 2006; Figure 6.1). Neither of these light curves resemble the behavior of GRB 111020A, where the change in slope is substantially greater.

Yet another possibility to explain the break is a sharp change in the external density. However, models for density jumps in a uniform medium (Nakar & Granot 2007) predict

that the density would need to decrease by greater than a factor of $\sim 10^3$ to account for the observed $\Delta\alpha_{12} > 0.9$ steepening. More realistic density contrasts of ~ 10 predict $\Delta\alpha_{\rm max} \approx 0.4$ in optical and X-ray afterglow light curves (Nakar & Granot 2007).

Finally, we consider that the observed steepening is a jet break, when the edge of a relativistically-beamed outflow becomes visible to the observer and the jet spreads laterally (Sari et al. 1999; Rhoads 1999). This model is often adopted to explain $\Delta\alpha_{12} \sim 1$ in the light curves of long GRBs (e.g., Frail et al. 2001; Bloom et al. 2003; Racusin et al. 2009) and has been observed in one other short burst, GRB 051221A ($\Delta\alpha_{12} \sim 0.9$, Figure 6.1; Soderberg et al. 2006b; Burrows et al. 2006). Given the similarity in $\Delta\alpha_{12}$ and the timescales of jet breaks in both short and long GRBs, we conclude that the observed steepening in the light curve of GRB 111020A is best explained by a jet break at $t_j = 2.0 \pm 0.5$ days.

6.3.3 Afterglow Properties

We utilize our radio, optical and X-ray observations to constrain the explosion properties and circumburst environment of GRB 111020A. In particular, we adopt the standard synchrotron model for GRB afterglows (Sari et al. 1998; Granot & Sari 2002) which provides a mapping from observable properties to the isotropic-equivalent kinetic energy ($E_{\rm K,iso}$), circumburst density (n_0), and the fractions of post-shock energy in radiating electrons (ϵ_e) and magnetic fields (ϵ_B). We use data at the time of the radio and first optical observations ($\delta t = 17.7$ hours), as well as the decay indices from the full X-ray light curve.

First, we constrain the electron power-law index p, using a combination of temporal

and spectral information. From the X-ray light curve, we measure $\alpha_{X,2} \lesssim -1.7$ (Section 7.4). For $p = -\alpha_{X,2}$, appropriate for a spreading jet (Sari et al. 1999), we can then constrain $p \gtrsim 1.7$. To further constrain p and investigate the location of the cooling frequency, ν_c, we compare the values $\alpha_{X,1} = -0.78 \pm 0.05$ and $\beta_X = -1.04 \pm 0.16$ ($\beta_X = 1 - \Gamma$; 1σ) to the closure relations for a relativistic blastwave in a constant density ISM-like medium for $p > 2$, a typical environment expected for a short GRB from a non-massive star progenitor (Sari et al. 1999; Granot & Sari 2002). If $\nu_c > \nu_X$ then the independently-derived values for p from the temporal and spectral indices are inconsistent: $p = 2.0 \pm 0.07$ from $\alpha_{X,1}$, and $p = 3.1 \pm 0.32$ from β_X (errors are 1σ).

However, if $\nu_c < \nu_X$ we obtain $p = 1.7 \pm 0.07$ from $\alpha_{X,1}$, (Granot & Sari 2002) which is consistent with the p value inferred from $\alpha_{X,2}$, but yields a divergent total integrated energy in electrons unless a break at high energies in the distribution is invoked. Although a flat electron distribution ($p < 2$) is possible and not uncommon (e.g. Dai & Cheng 2001; Panaitescu & Kumar 2001; Racusin et al. 2009), the standard relations for $1 < p < 2$ yield $p = 0.84 \pm 0.25$ from $\alpha_{X,1}$. This solution is not self-consistent, and would also require an unusually sharp break of $\Delta p \gtrsim 1.2$ in the electron distribution. Continuing with the assumptions that $\nu_c < \nu_X$ and $p > 2$, we obtain $p = 2.1 \pm 0.32$ from β_X, which is marginally consistent with the value inferred from the temporal index. Put another way, $\alpha - 3\beta/2 = 0.77 \pm 0.30$, which satisfies the closure relation for $\nu_c < \nu_X$ (Sari et al. 1998). We therefore conclude that $\nu_c < \nu_X$. We note that the spectral index is generally more reliable in the determination of p because it remains constant over time and is not subject to alternative processes such as energy injection or flaring. In this case, the same β_X was also independently determined from both the XMM and XRT data sets (Table 8.5). Therefore for the rest of our calculations, we take a reasonable

value of $p = 2.1$ as determined from β_X.

We next determine a set of constraints on n_0 and $E_{\rm K,iso}$ based on the X-ray flux density, radio limit, and the condition that $\nu_c < \nu_X$. First, we use the X-ray afterglow emission as a proxy for $E_{\rm K,iso}$ assuming the X-ray emission is from the forward shock. For $\nu_c < \nu_X$ at the time of our broad-band observations ($\delta t = 17.7$ hours), we use $F_X = 0.032\,\mu$Jy at $\nu_X = 2.4 \times 10^{17}$ Hz (1 keV), and $p = 2.1$ to obtain (Granot & Sari 2002)

$$E_{\rm K,iso} \approx 2.2 \times 10^{50} (1+z)^{-1} \epsilon_e^{-1.07} \epsilon_B^{-0.024} d_{\rm L,28}^{1.95} \ {\rm erg} \tag{6.4}$$

where $d_{\rm L,28}$ is the luminosity distance in units of 10^{28} cm. Next, we use $E_{\rm K,iso}$ to constrain n_0. Using our 3σ EVLA limit of $F_{\nu,\rm rad} \lesssim 39$ μJy, we can determine an upper limit on n_0 under the reasonable assumption that our observed radio band ($\nu = 5.8$ GHz) is above the self-absorption frequency ($\nu_a < \nu_{\rm rad} < \nu_m$; $F_{\nu,\rm rad} \propto n_0^{1/2}$) at the time of observations. For this scenario (Granot & Sari 2002),

$$n_0 \lesssim 1.7 \times 10^{-3} E_{\rm K,iso,52}^{-5/3} (1+z)^{-5/3} d_{L,28}^4 \epsilon_e^{4/3} \epsilon_B^{-2/3} \ {\rm cm}^{-3}, \tag{6.5}$$

where $E_{\rm K,iso,52}$ is in units of 10^{52} erg and n_0 is in cm^{-3}. As noted in Section 6.2.4, if the marginal radio detection is indeed real, then this upper bound can be replaced with an equality. Finally, we can place a lower limit on the density using the condition that $\nu_c < \nu_X$ (i.e., $\nu_c \lesssim 2.4 \times 10^{16}$ Hz; 0.1 keV)

$$n_0 \gtrsim 4.5 \times 10^{-4} (1+z)^{-1/2} \epsilon_B^{-3/2} E_{\rm K,iso,52}^{-1/2} \ {\rm cm}^{-3}. \tag{6.6}$$

It is clear that $E_{\rm K,iso}$ and n_0 depend sensitively on our choice of z, ϵ_e and ϵ_B. The fractions ϵ_e, ϵ_B are not expected to exceed $\sim 1/3$. We therefore calculate $E_{\rm K,iso}$ for two representative cases: I: $\epsilon_e = \epsilon_B = 1/3$, and II: more typical values of $\epsilon_e = \epsilon_B = 0.1$. We then calculate the range of allowed n_0 set by Equations 6.5 and 6.6, which becomes wider as the redshift increases[6]. For Case I, this requires that $z \gtrsim 0.2$, below which the constraints on n_0 conflict (Figure 6.4). At the median observed redshift of the short GRB population, $z \sim 0.5$, we obtain $E_{\rm K,iso} \approx 3.7 \times 10^{50}$ erg and $n_0 = 0.01 - 0.06$ cm^{-3}. For Case II, the constraints on n_0 require a higher redshift of $z \gtrsim 1.5$ (Figure 6.4). For a fiducial redshift of $z = 1.5$, we obtain $E_{\rm K,iso} \approx 1.2 \times 10^{52}$ erg and $n_0 = 0.008$ cm^{-3}. The parameters for the two cases are listed in Table 6.4. Although we cannot distinguish between these two scenarios, both cases require low circumburst densities of $n \sim 0.01 - 0.1$ cm^{-3}.

6.3.4 Jet Opening Angle

In the context of a jet break, we use the time of the break from the X-ray light curve (2.0 ± 0.5 days) and the circumburst density and energy estimates from the previous section to constrain θ_j. The time of the break is a direct reflection of the jet opening angle (Sari et al. 1999; Frail et al. 2001),

[6]Assuming non-equipartition in two alternative cases: $\epsilon_B = 0.01$, $\epsilon_e = 0.1$ and $\epsilon_B = 0.1$, $\epsilon_e = 0.01$, our constraints on n_0 conflict unless $z \gtrsim 3$, and result in $n_0 \sim 0.01 - 1$ cm^{-3}. Based on our observations of the putative host galaxies and the typical luminosity of short GRB hosts, we find a high-z origin unlikely (See Section 6.4.2)

Table 6.4. Physical Parameters of GRB 111020A

Parameter	Case I $[z = 0.5, \epsilon_e = \epsilon_B = 1/3]$	Case II $[z = 1.5, \epsilon_e = \epsilon_B = 0.1]$
t_j	2.0 ± 0.5 days[a]	2.0 ± 0.5 days[a]
$E_{\gamma,\rm iso}$	2.1×10^{50} erg	1.9×10^{51} erg
$E_{\rm K,iso}$	3.7×10^{50} erg	1.2×10^{52} erg
n_0	$0.01 - 0.06$ cm^{-3}	0.008 cm^{-3}
θ_j	$7 - 8^\circ$	3°
f_b	$0.007 - 0.01$	0.001
E_γ	2×10^{48} erg	3×10^{48} erg
E_K	$(3 - 4) \times 10^{48}$ erg	2×10^{49} erg
$E_{\rm tot}$	$(5 - 6) \times 10^{48}$ erg	2×10^{49} erg
η_γ	$0.3 - 0.4$	0.15

Note. — [a] Uncertainties correspond to a 1σ confidence level.

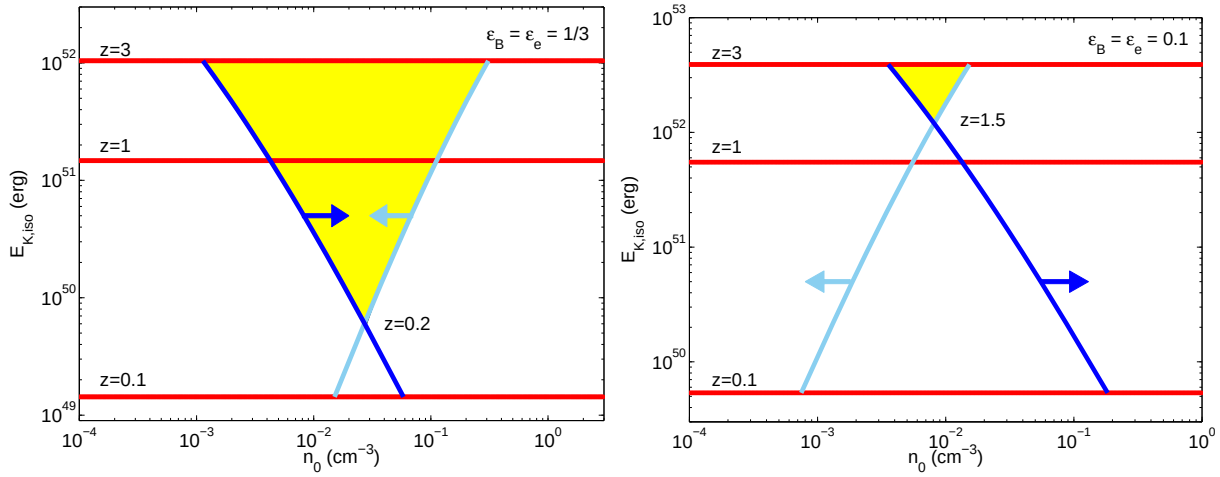

Figure 6.4.—: Isotropic-equivalent kinetic energy and circumburst density parameter space for GRB 111020A assuming $\epsilon_e = \epsilon_B = 1/3$ (left) and $\epsilon_e = \epsilon_B = 0.1$ (right). The lower limit on the density (dark blue) is set by the condition that $\nu_c < \nu_X$ (Equation 6.6) while the upper limit (light blue) is set by radio observations (Equation 6.5). Also plotted are the values for $E_{\rm K,iso}$ at $z = 0.1, 1$ and 3 (red). The allowable parameter space set by these constraints is filled in yellow.

$$\theta_j = 0.1 t_{j,\rm d}^{3/8} (1+z)^{-3/8} E_{\rm K,iso,52}^{-1/8} n_0^{1/8} \tag{6.7}$$

where $t_{j,\rm d}$ is expressed in days. For our fiducial Case I ($z = 0.5, \epsilon_e = \epsilon_B = 1/3$), $E_{\rm K,iso} \approx 3.7 \times 10^{50}$ erg and $n \approx 0.01 - 0.06$ cm^{-3} give $\theta_j = 7 - 8°$. This leads to a beaming correction on the energy of $f_b \equiv [1 - \cos(\theta_j)] = 0.007 - 0.01$, and therefore a true kinetic energy $E_K = f_b E_{\rm K,iso} \approx (3 - 4) \times 10^{48}$ erg (Table 6.4). To estimate the beaming-corrected γ-ray energy, we infer $E_{\gamma,\rm iso}$ from the *Swift*/BAT fluence and apply a bolometric correction factor of 5 to roughly convert to a representative observed γ-ray energy range of $\sim 10 - 1000$ keV. This factor is derived from short GRBs observed by satellites with wider energy coverage (Berger 2010a; Margutti et al. 2013). We obtain $E_{\gamma,\rm iso} = 2.1 \times 10^{50}$ erg and therefore a true γ-ray energy of $E_\gamma \approx 2 \times 10^{48}$ erg.

For Case II ($z = 1.5, \epsilon_e = \epsilon_B = 0.1$), where $n_0 \approx 0.008$ cm^{-3} and $E_{\rm K,iso} \approx 1.2 \times 10^{52}$ erg, we obtain a smaller opening angle of $\theta_j \approx 3^\circ$. This leads to $f_b \approx 1.4 \times 10^{-3}$ and hence, $E_\gamma \approx 3 \times 10^{48}$ erg and $E_K \approx 2 \times 10^{49}$ erg.

In both cases, the true γ-ray energy is few $\times 10^{48}$ erg while the kinetic energy is an order of magnitude higher at $z = 1.5$ than at $z = 0.5$. This results in a *lower* γ-ray conversion efficiency ($\eta_\gamma \equiv E_\gamma/E_{\rm tot}$) for Case II of 0.15 compared to $0.3 - 0.4$ for Case I (Table 6.4). The total energy even for Case II is $\sim 10 - 100$ times lower that for long GRBs.

6.3.5 Extinction

We investigate the presence of extinction by comparing the unabsorbed X-ray flux and the optical non-detection at $\delta t = 17.7$ hour. Since we do not know the exact location of the cooling frequency, we assume a maximum value $\nu_{c,\rm max}$ of 2.4×10^{17} Hz (1 keV) and extrapolate the X-ray flux to the optical band using the shallowest possible slope of $\beta = -(p-1)/2 = -0.55$ to obtain the lowest bound on the expected optical afterglow flux in the absence of extinction; any other assumption for the location of $\nu_c < \nu_X$ would result in a higher predicted optical flux density. For $p = 2.1$ we estimate $F_{\nu,\rm opt} \approx 1.1$ μJy ($i = 23.8$ mag). Given that our observed 3σ upper limit is $i \gtrsim 24.4$ mag, this implies a lower limit on the optical extinction in excess of the Galactic value of $A_i \gtrsim 0.6$ mag[7]. In the rest frame of the burst for a Milky Way extinction curve, this translates to $A_V^{\rm host} \gtrsim 0.6$ mag for $z = 0.5$ and $A_V^{\rm host} \gtrsim 0.2$ at $z = 1.5$ (Cardelli et al. 1989). Using Galactic relations between N_H and A_V, $N_{\rm H,int}/A_V \approx (1.7 - 2.2) \times 10^{21}$ (Predehl & Schmitt 1995; Watson

[7]We note that for $p \lesssim 1.9$, no host galaxy extinction is required

2011), we infer lower limits of $N_{\rm H,int} \gtrsim 10^{21}$ cm^{-2} at $z = 0.5$ and $N_{\rm H,int} \gtrsim 4.4 \times 10^{20}$ cm^{-2} at $z = 1.5$, consistent with our value of 7.5×10^{21} cm^{-2} ($z = 0$) derived from the X-ray spectrum (Table 8.5). However, an appreciable extinction is unexpected given the burst's location on the outskirts of its potential host galaxy. We note that the burst is located at Galactic coordinates $(l, b) = (359.3^\circ, -19.4^\circ)$ which is toward the Galactic Bulge on a steep gradient in the dust map (Schlegel et al. 1998) and thus may be subject to substantial ($\sim 30\%$) uncertainties in the Galactic extinction[8]. Taking this uncertainty into account reduces the required $A_V^{\rm host}$ to $\gtrsim 0.2 - 0.3$ mag depending on the redshift of the burst.

6.4 Discussion

6.4.1 Environment

From our broad-band observations, we constrain the circumburst density of GRB 111020A to $n_0 \sim 0.01 - 0.1$ cm^{-3} which is consistent with the low values inferred for a few previous short GRBs (Soderberg et al. 2006b; Panaitescu 2006; Stratta et al. 2007; Perley et al. 2009a; Berger 2010a; Fong et al. 2011). The inferred density fits well with the framework of NS-NS/NS-BH binary progenitor systems, which may be subject to substantial kicks from their host galaxies and are predicted to typically occur at densities of $\sim 10^{-6} - 1$ cm^{-3} (Perna & Belczynski 2002; Belczynski et al. 2006).

[8]Using a high-resolution ($\theta_{\rm FWHM} = 15''$) WISE 12 μm map, we do not see strong evidence for any thin dust filaments at the location of the burst which would result in $> 30\%$ uncertainties in the Galactic A_V (D. Finkbeiner, private comm.)

Table 6.5. Intrinsic X-ray Column Density of Hydrogen, $N_{\rm H,int}$ for *Swift* Short GRBs

GRB	z	$N_{\rm H,int}$ (10^{21} cm^{-2})	σ above zero
050724	0.258	$3.20^{+0.97}_{-0.86}$	5.7
051210	···	< 0.54	
051221A	0.547	$1.92^{+0.73}_{-0.68}$	4.5
060313	···	$0.45^{+0.36}_{-0.33}$	2.1
060801	1.131	$3.02^{+2.22}_{-1.88}$	2.4
061006	0.438	< 2.04	
061201	···	$0.94^{+0.60}_{-0.53}$	2.7
070714B	0.923	$3.89^{+1.87}_{-1.61}$	4.2
070724A	0.457	< 1.89	
071227	0.383	$2.84^{+0.72}_{-0.65}$	6.8
080123	···	$1.12^{+0.28}_{-0.26}$	6.8
080905A	0.122	$2.04^{+1.58}_{-1.33}$	2.3
090510	0.903	< 0.80	
090515	···	$0.56^{+0.30}_{-0.27}$	3.2
090607	···	< 0.79	
091109B	···	< 1.58	
100117A	0.915	$4.10^{+3.41}_{-2.71}$	2.2
100702A	···	$4.37^{+3.67}_{-3.05}$	2.1
101219A	0.718	$6.61^{+3.73}_{-2.82}$	3.3
110112A	···	< 0.92	
111020A	···	$7.50^{+2.0}_{-1.8}$	6.5
111117A	···	$1.84^{+1.28}_{-1.05}$	2.6
111121A	···	$2.41^{+0.82}_{-0.74}$	5.1

Note. — Errors and upper limits quoted correspond to a 90% confidence level; $z = 0$ is assumed when the redshift is not known.

GRB 111020A has an offset of $\approx 0.80''$ from its most probable host galaxy (G3; Figure 6.2). For redshifts between $z = 0.5 - 1.5$, this translates to a projected physical offset of $\approx 5 - 7$ kpc, which is comparable to the median value of ~ 5 kpc for well-localized short GRBs with host associations (Fong et al. 2010; Church et al. 2011). Although G3 has the lowest probability of chance coincidence by an order of magnitude (Figure 6.3), we cannot rule out the possibility that G3 is a faint star. The next most probable galaxies, G1 and G2, are situated $2.8''$ ($17 - 24$ kpc) and $6.5''$ ($40 - 56$ kpc), respectively, from GRB 111020A (Figure 6.2). If the burst originated from one of these galaxies, this would put GRB 111020A at the high end of the observed offset distribution, similar to the growing sub-class of apparently "hostless" short GRBs which likely occur $\gtrsim 30$ kpc from their host galaxies (Berger 2010a). All of these inferred offsets are consistent with predicted offset distributions of NS-NS/NS-BH binaries originating in Milky Way-type galaxies (Bloom et al. 1999; Fryer et al. 1999; Belczynski et al. 2006; Salvaterra et al. 2010).

Most short GRB host galaxies with confirmed spectroscopic redshifts have measured luminosities of $L_B \approx 0.1 - 1L_*$ (Berger et al. 2007b). The apparent magnitude of G3 is $i \approx 24.3$, which corresponds to $L_B \approx 0.1 - 1L_*$ over $z \approx 0.5 - 2.3$ when compared to the luminosity function of galaxies at corresponding redshifts in the DEEP2 and LBG surveys (Willmer et al. 2006; Reddy & Steidel 2009). This is consistent with the redshift range inferred from the afterglow.

We next investigate the nature of the dust and gas in the environment of GRB 111020A through an analysis of $A_V^{\rm host}$ and $N_{\rm H,int}$. We have shown that the burst requires dust extinction of $A_V^{\rm host} \gtrsim 0.2 - 0.6$ mag, depending on the redshift of the burst and the uncertainty in Galactic extinction. We have also measured a neutral Hydrogen

column density intrinsic to the burst environment of $N_{\rm H,int} = (7.5 \pm 2.0) \times 10^{21}$ cm^{-2} at $z = 0$, which becomes higher for any other choice of z. High values of both dust extinction and X-ray absorption have been linked to "dark" GRBs (e.g. Perley et al. 2009b; Campana et al. 2011) which have optically sub-luminous afterglows compared to their X-ray or NIR counterparts and can quantitatively be classified by $|\beta_{OX}| \lesssim |\beta_X| - 0.5$ (van der Horst et al. 2009; see also Jakobsson et al. 2004). With $|\beta_X| = 1.0$ and $|\beta_{OX}| \lesssim 0.46$, GRB 111020A is consistent with this definition of dark GRBs. While optical extinction intrinsic to long GRB environments is not uncommon and commensurate with their origin in dusty, star-forming regions, evidence for substantial extinction has been reported for only one other short burst, GRB 070724A, which required $A_V^{\rm host} \gtrsim 2$ mag to explain the suppression of optical emission relative to the NIR (Berger et al. 2009; Kocevski et al. 2010). The location of GRB 070724A on the outskirts of its host galaxy, ~ 5 kpc from the center, suggested either an origin in a star-forming region or a progenitor system which produced the dust itself (Berger et al. 2009). The potentially appreciable extinction and the location with respect to its putative host suggests that the same conclusions may be drawn for GRB 111020A.

On the other hand, the relation between $N_{\rm H,int}$ and the darkness of a burst is less clear. A recent study of long dark GRBs shows them to have higher intrinsic column densities than non-dark GRBs, which suggests that the darkness of a burst is largely due to absorption by circumburst material (Campana et al. 2011). To investigate this relationship for GRB 111020A, we extract spectra and best-fitting $N_{\rm H,int}$ for all short GRBs with XRT-detected afterglows in the same manner as GRB 111020A (see Section 6.2.2), over time ranges with no evidence for spectral evolution. There are 22 short bursts with sufficient X-ray counts to perform spectral analysis, 11 of

which have known redshifts (Table 6.5). We find a short GRB weighted average of $N_{\rm H,int}(z = 0) = (1.1 \pm 0.14) \times 10^{21}$ cm^{-2} (90% c.l.; Figure 6.5). In comparison, GRB 111020A has a high value of $N_{\rm H,int} = (7.5 \pm 2.0) \times 10^{21}$ cm^{-2} at $z = 0$ (Figure 6.5). Taken at face value, it is surprising to find a large $N_{\rm H,int}$ for a substantial offset, and may suggest that the burst occurred in a relatively metal-rich environment.

6.4.2 Beaming, Energetics, and Rates

We uncover a break in the X-ray light curve of GRB 111020A at ≈ 2 days, which we interpret as a jet break (Section 7.4). Depending on our values for z, ϵ_e and ϵ_B, we infer an opening angle of $\approx 3 - 8^\circ$. This is reminiscent of the first jet break discovery in GRB 051221A, with $\theta_j \approx 7^\circ$ (Soderberg et al. 2006b; Burrows et al. 2006), and suggests that at least a fraction of these events are highly collimated. In addition, temporal breaks at $t_j \lesssim$ few hours in GRBs 061201 (Stratta et al. 2007) and 090510 (De Pasquale et al. 2010; Nicuesa Guelbenzu et al. 2012b), if interpreted as jet breaks, lead to $\theta_j \approx 1^\circ$ (Figure 7.3). However, these two cases resemble early breaks in long GRBs that are generally attributed to the cessation of energy injection, and not collimation.

Although the remaining short GRB afterglow data is sparse, the lack of observed jet breaks in their X-ray light curves can be used to place lower limits on the opening angles. Indeed, *Chandra* observations of GRB 050724A out to 22 days indicated $\theta_j \gtrsim 25^\circ$, consistent with a spherical explosion (Grupe et al. 2006). A recent study by Coward et al. (2012) analyzed the sample of short GRB *Swift*/XRT light curves up to August 2011 with monitoring $\gtrsim 1$ day which included 6 additional events, and inferred $\theta_j \gtrsim 6 - 16^\circ$, assuming $n_0 = 1$ cm^{-3} for all bursts. We revise this analysis for 3 of the

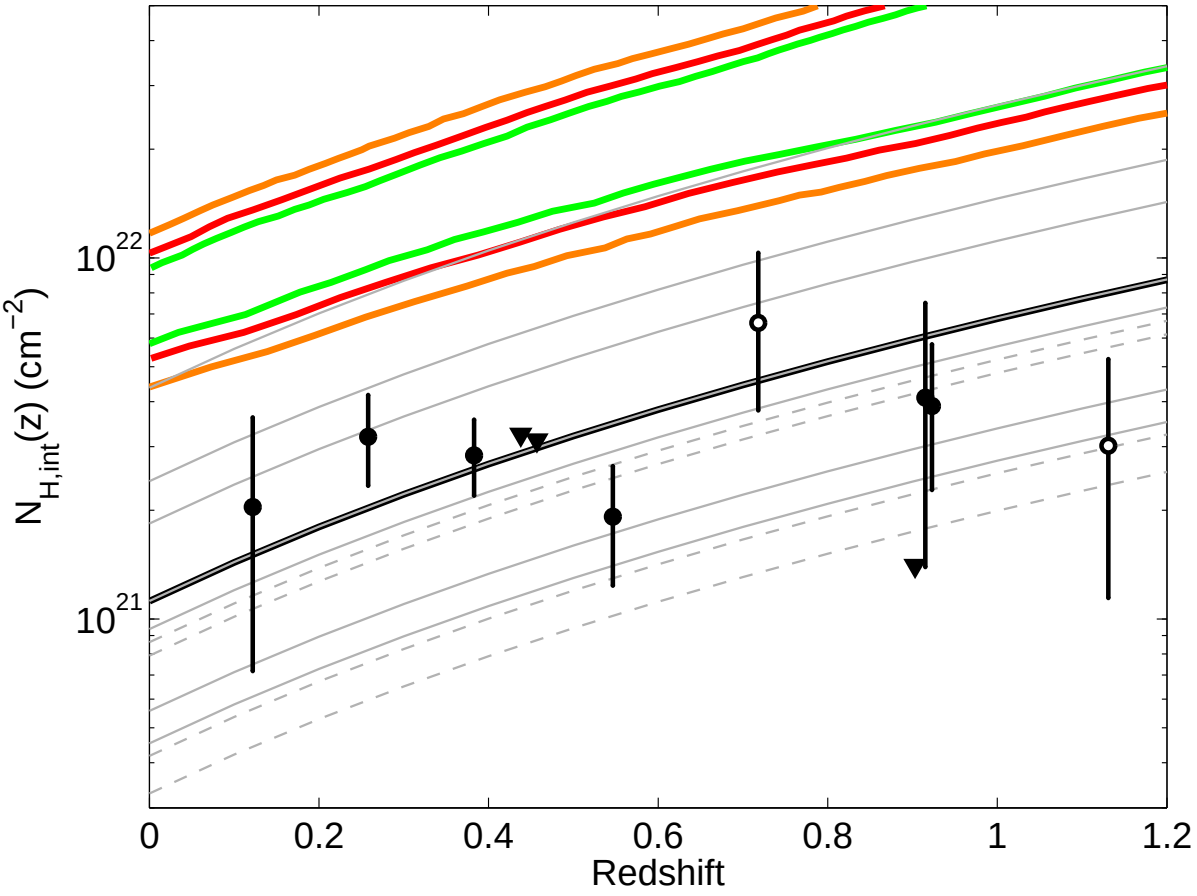

Figure 6.5.—: Excess neutral hydrogen column density, $N_{\rm H,int}$, versus redshift for GRB 111020A (1, 2 and 3σ intervals denoted by green, red and orange lines) along with 6 *Swift* short GRBs with measured redshifts and optical afterglows (black filled circles) and 2 (GRBs 060801 and 101219A) with only X-ray afterglows (open circles). Also plotted are 11 short GRBs without secure redshifts (grey lines), 4 of which have only upper limits on $N_{\rm H,int}$ (grey dashed). For GRBs without redshifts, the $N_{\rm H,int}$ value at $z = 0$ is scaled by $(1 + z)^{2.6}$ (Galama & Wijers 2001). Errors and upper limits are at the 90% confidence level. The weighted mean for all short GRBs (black line) over the redshift interval $z = 0 - 1.2$ is also shown. GRB 111020A has the highest $N_{\rm H,int}$ of a short GRB to date and is well above the mean for short GRBs.

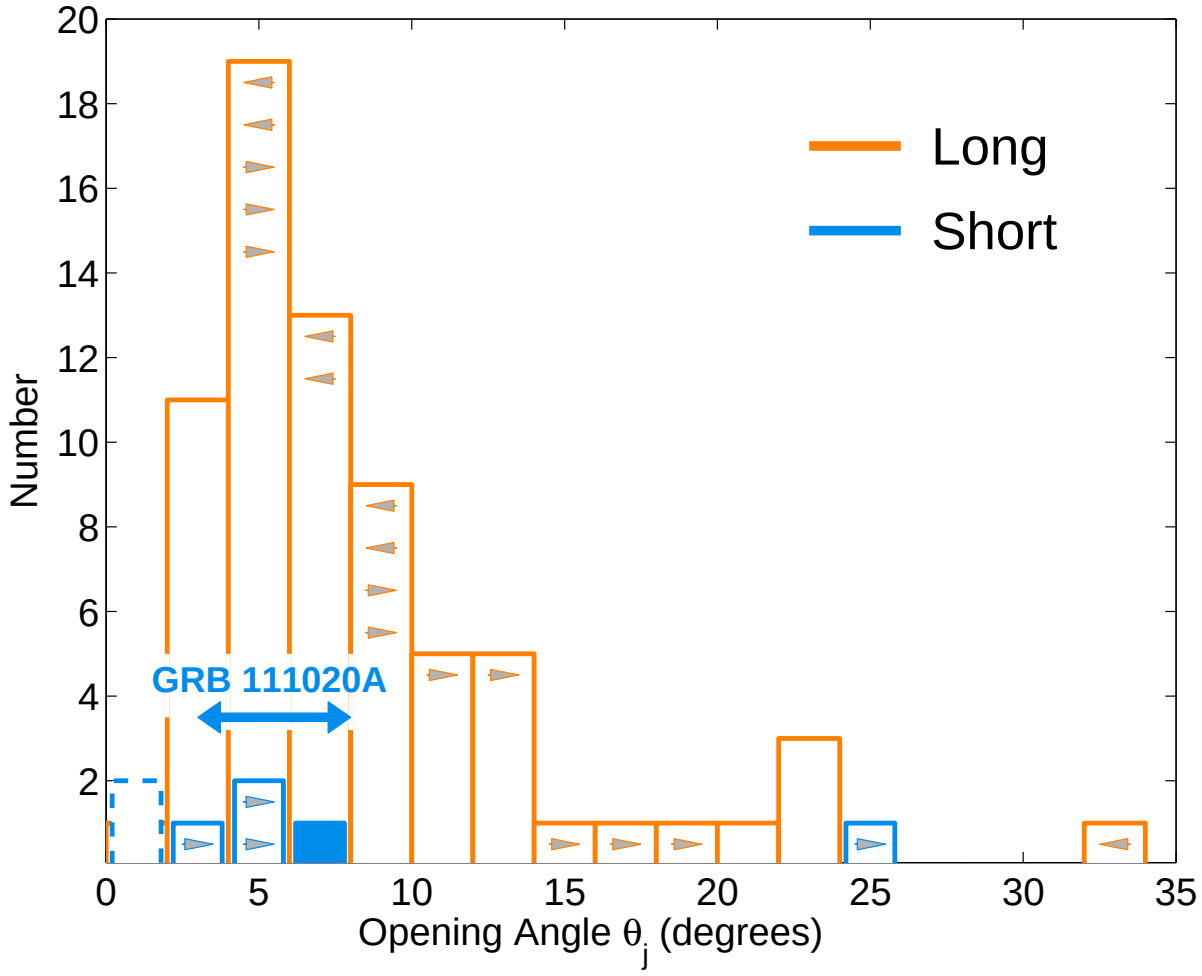

Figure 6.6.—: Distribution of opening angles for long (orange) and short (blue) GRBs. Arrows represent upper and lower limits. The long GRB population includes pre-*Swift* (Frail et al. 2001; Berger et al. 2003a; Bloom et al. 2003; Ghirlanda et al. 2004; Friedman & Bloom 2005), *Swift* (Racusin et al. 2009; Filgas et al. 2011), and *Fermi* (Cenko et al. 2010b; Goldstein et al. 2011; Cenko et al. 2011) bursts. The opening angle for GRB 111020A ranges from $\sim 3 - 8^\circ$ (depending on the redshift), while GRB 051221A has $\theta_j \approx 7^\circ$ (Soderberg et al. 2006b; Burrows et al. 2006). Tentative jet breaks (blue dashed) for GRBs 061201 (Stratta et al. 2007) and 090510 (De Pasquale et al. 2010; Nicuesa Guelbenzu et al. 2012b) are at $\sim 1^\circ$. Short GRB lower limits are from the non-detection of jet breaks in *Swift*/XRT data (this work, revised from Coward et al. 2012) and *Chandra* data for GRB 050724A (Berger et al. 2005; Grupe et al. 2006).

events with robust X-ray light curves (GRBs 070714B, 070724A, 071227; data analysis prescriptions from Margutti et al. 2013) employing a more representative $n_0 \approx 10^{-2}$ cm^{-3} (e.g. Soderberg et al. 2006b and this work). We derive $E_{\gamma,\rm iso}$ from the reported fluences, applying a bolometric correction when necessary to represent an energy range of $\sim 10 - 1000$ keV, and infer more realistic lower limits of $\gtrsim 2 - 6^\circ$ (Figure 7.3). These limits are indeed lower than the detected values for GRBs 051221A and 111020A, and therefore do not add strong constraints on the distribution. We caution that the sample presented here represents only the $\sim 30\%$ of the *Swift* short GRB population that have bright X-ray afterglows and relatively slow flux decline rates; the remaining fraction do not have detectable X-ray afterglows or fade too quickly so constraints cannot be placed on their collimation.

There are now two short GRBs with opening angle measurements, two with measurements based on more tentative early breaks, and an additional four with lower limits (Figure 7.3). These early constraints create a distribution that may mimic the distribution for long GRBs, which ranges from $\sim 2 - 20^\circ$ with a median of 7° (Figure 7.3; Frail et al. 2001; Berger et al. 2003a; Bloom et al. 2003; Ghirlanda et al. 2004; Friedman & Bloom 2005; Racusin et al. 2009; Cenko et al. 2010b; Filgas et al. 2011; Goldstein et al. 2011; Cenko et al. 2011). More events are needed to assess the real differences between the distributions. However, simulations of post-merger black hole accretion predict jets with $\theta_j \sim 5 - 20^\circ$ (Aloy et al. 2005; Rosswog 2005; Rezzolla et al. 2011) to several tens of degrees (Ruffert & Janka 1999b; Rezzolla et al. 2011) depending on the mechanism of energy extraction and Lorentz factor, so there are expectations on theoretical grounds that the short GRB distribution is wider.

The first major ramification of collimation is the correction to the total energy

release: the true energy is lower than the isotropic-equivalent value by the beaming factor, f_b. For GRB 111020A with an opening angle of $\approx 3-8^\circ$, this correction factor is substantial, $0.001-0.01$. Depending on the redshift, the beaming-corrected energy of GRB 111020A is $E_\gamma \approx (2-3)\times 10^{48}$ erg (Table 6.4) which is an order of magnitude lower than for GRB 051221A with $E_\gamma \approx (1-2)\times 10^{49}$ erg (Soderberg et al. 2006b; Burrows et al. 2006) and GRB 050724A with $E_\gamma \approx (0.4-4)\times 10^{50}$ erg (Grupe et al. 2006). The three remaining events with opening angle lower limits, GRBs 070714B, 070724A and 071227, have ranges of $E_\gamma \approx 10^{48}-10^{51}$ erg, where the upper bound is set by the isotropic-equivalent γ-ray energy in the $\approx 10-1000$ keV band. The small population of short GRBs with measured E_γ therefore has a median value of $E_\gamma \sim 10^{49}$ erg, which is an order of magnitude below *Swift* long GRBs (Kocevski & Butler 2008; Racusin et al. 2009) and 2 orders of magnitude below the pre-*Swift* population (Frail et al. 2001; Bloom et al. 2003). Again, this sample is incomplete because we can only measure E_γ for bursts with well-constrained opening angles.

In a similar vein, we compare the beaming-corrected kinetic energy and total energy (E_K, $E_{\rm tot}$) of GRB 111020A to the values for other short bursts. Because $E_{\rm K,iso}$ is more sensitive to our choices for z, ϵ_e and ϵ_B, we infer different values for Case I and II. For Case I, we infer $E_K \approx (3-4)\times 10^{48}$ erg, $E_{\rm tot} = E_\gamma + E_K \approx (5-6)\times 10^{48}$ erg, and $\eta_\gamma \approx 0.3-0.4$. For Case II, we calculate $E_K \approx 2\times 10^{49}$ erg, $E_{\rm tot} \approx 2\times 10^{49}$ erg and $\eta_\gamma \approx 0.15$. GRB 051221A had $E_K \approx 8\times 10^{48}$ erg and a total energy release of $\approx 2.5\times 10^{49}$ erg (Soderberg et al. 2006b; Burrows et al. 2006) while GRB 050724 had a total energy of $10^{50}-10^{51}$ erg. With $E_{\rm tot} \approx (0.5-2)\times 10^{49}$ erg, GRB 111020A may be on the low end of the total energy distribution, but more events with beaming-corrected energies are needed to better characterize the distribution for short GRBs.

The true total energy release of short GRBs has strong implications on the energy extraction mechanism. Two primary mechanisms, the thermal energy release from $\nu\bar{\nu}$ annihilation in a baryonic outflow (Jaroszynski 1993; Mochkovitch et al. 1993) and magnetohydrodynamic (MHD) processes in the black hole's accretion remnant (e.g. Blandford & Znajek 1977; Rosswog et al. 2003), give different estimates for the expected energy release. Predictions for $\nu\bar{\nu}$ annihilation are largely dependent on the mass of the disc and efficiency to produce pairs. Simulations of an outflow due to $\nu\bar{\nu}$ annihilation suggest beaming-corrected total energy releases could reach $10^{48} - 10^{49}$ erg (Ruffert & Janka 1999b,a; Popham et al. 1999; Rosswog 2005; Birkl et al. 2007; Lee & Ramirez-Ruiz 2007). Higher energy releases can be obtained from MHD processes, which can produce luminosities of $\gtrsim 10^{52}$ erg s^{-1} ($\gtrsim 10^{50}$ erg s^{-1} when corrected for beaming; Popham et al. 1999; Rosswog et al. 2003; Lee & Ramirez-Ruiz 2007) depending on the nature of the magnetic field amplification. While the true energy releases of GRBs 051221A and 050724A suggest that MHD processes may be powering these events (Berger et al. 2005; Grupe et al. 2006; Soderberg et al. 2006b; Burrows et al. 2006), the total energy of GRB 111020A is consistent with predictions for both scenarios.

The second major consequence of beaming is that the true event rate is *higher* than the observed rate by the inverse of the beaming factor (i.e., $R_{\rm true} = f_b^{-1} R_{\rm obs}$). Thus, beaming provides essential information for understanding the relation to various progenitor systems and is of particular interest since the NS-NS/NS-BH merger rates, which are a critical input for estimates of Advanced LIGO gravitational wave detections, are highly uncertain (e.g., Abadie et al. 2010; Metzger & Berger 2012). The current estimated *observed* short GRB volumetric rate is $\sim$10 Gpc^{-3} yr^{-1} (Nakar et al. 2006). The estimated NS-NS merger rate is much higher: $\sim$200-3000 Gpc^{-3} yr^{-1} (Kalogera

et al. 2004; Nakar et al. 2006).

The discrepancy in these rates can be explained if short GRBs have typical $\theta_j \sim 8^\circ$ ($f_b^{-1} \sim 100$; see also Metzger & Berger 2012). The determination of GRB 111020A's opening angle of $3 - 8^\circ$ ($f_b^{-1} = 100 - 730$), along with the small but increasing sample of opening angle constraints for short GRBs, implies that at least a fraction of these events are significantly beamed and that the true rate of short GRBs is at least $\sim 100 - 1000$ Gpc^{-3} yr^{-1}. With a few additional opening angle measurements, this value can be significantly improved. Other proposed progenitor models, e.g., WD-WD mergers or accretion-induced collapse of a WD/NS (Qin et al. 1998; Levan et al. 2006a; Metzger et al. 2008a) have estimated rates of $\lesssim 1000$ Gpc^{-3} yr^{-1} and $\sim 0.1 - 100$ Gpc^{-3} yr^{-1}, respectively (Lee & Ramirez-Ruiz 2007; Darbha et al. 2010), so if a large fraction of short GRBs have opening angles of $\lesssim 25^\circ$, these systems may not contribute significantly to the progenitor population.

6.5 Conclusions and Future Work

We have presented observations of GRB 111020A, utilizing extensive coverage in the X-rays with *Swift*/XRT, XMM and *Chandra* to uncover a temporal break, most naturally explained as a jet break. Our limit on the radio afterglow from EVLA combined with the inference that $\nu_c < \nu_X$ leads to a robust range on the circumburst density of $\sim 0.01 - 0.1$ cm^{-3}. The jet break time of ≈ 2 days leads to an opening angle of $3 - 8^\circ$, depending on the redshift and equipartition fractions, which leads to beaming-corrected energies of $E_\gamma \approx (2 - 3) \times 10^{48}$ erg, $E_K \approx (0.3 - 2) \times 10^{49}$ erg and $E_{\rm tot} \approx (0.5 - 2) \times 10^{49}$ erg. This result, along with the previous jet break constraints for GRBs 051221A and 050724A

suggests that there may be a spread in true energy release, $\sim 10^{48} - 10^{50}$ erg for short GRBs (Berger et al. 2005; Grupe et al. 2006; Soderberg et al. 2006b; Burrows et al. 2006).

Furthermore, our optical observations provide a limit on the afterglow and enabled the discovery of a putative host galaxy with $i \approx 24.3$ mag. A comparison of the X-ray and optical data at $\delta t = 17.7$ hours provides a lower limit on the host galaxy extinction of $A_V^{\rm host} \gtrsim 0.2 - 0.6$ mag. This is consistent with the high intrinsic column density from X-ray absorption when compared to the mean for the short GRB population.

GRB 111020A demonstrates that rapid multi-wavelength follow-up is vital to our understanding of the basic properties of short GRBs: the geometry, energetics, and circumburst densities. In particular, the search for jet breaks on timescales of $\gtrsim$ few days is imperative for placing meaningful constraints on the opening angle distribution. Ideally, the detection of breaks in both optical and X-ray data leads to an unambiguous and tight constraint on the opening angle; however, optical afterglows are only detected in $\sim 30\%$ of *Swift* short GRBs, while X-ray afterglows have been detected in $\sim 70\%$. Furthermore, optical afterglows are intrinsically faint and subject to host galaxy contamination, making long-term monitoring highly challenging. Therefore, the jet break search is optimized in the X-ray band where the burst is not subject to such contamination and the afterglow brightness is virtually independent of the typically low circumburst densities. The X-rays also allow for a measurement of the kinetic energy of the outflow. Deep radio limits provide additional constraints on the circumburst density and energy. The EVLA upgrade is now enabling us to probe events with relatively low energy scales of $\sim 10^{48}$ erg and densities of $\lesssim 10^{-2}$ cm^{-2}.

The collimation of short GRBs will undoubtedly further our knowledge of their true energetics and rates. While the former provides information on the explosion and energy extraction mechanisms, the latter is crucial for understanding the relation to various progenitor systems (e.g., NS-NS mergers). Significant improvement on the estimated short GRB observed rate of ~ 10 Gpc^{-3} yr^{-1} (Nakar et al. 2006) will have a critical impact on estimates for coincident short GRB-gravitational wave detections in the era of Advanced LIGO/VIRGO (Abadie et al. 2010). Furthermore, a more complete knowledge of the short GRB redshift distribution will inform our understanding of the fraction of short GRBs which may originate in globular clusters, highly relevant to gravitational wave event rate estimates (Hopman et al. 2006; Salvaterra et al. 2008; Guetta & Stella 2009). The uncertainty in the observed short GRB rate is dominated by the uncertainty in the beaming fraction and with only a handful of short GRB opening angles measured to date, the discovery of even a few additional jet breaks in the coming years will enable significant progress.

We thank D. Finkbeiner for helpful discussions. The Berger GRB group at Harvard is supported by the National Science Foundation under Grant AST-1107973. Partial support was also provided by the National Aeronautics and Space Administration through Chandra Award Number GO1-12072X issued by the Chandra X-ray Observatory Center, which is operated by the Smithsonian Astrophysical Observatory for and on behalf of the National Aeronautics Space Administration under contract NAS8-03060. Additional support was provided by NASA/Swift AO6 grant NNX10AI24G. Observations were obtained with the EVLA (program 10C-145) operated by the National Radio Astronomy Observatory, a facility of the National Science Foundation operated under cooperative agreement by Associated Universities, Inc. This paper includes data gathered with the

6.5 meter Magellan Telescopes located at Las Campanas Observatory, Chile. This work is based in part on observations obtained at the Gemini Observatory, which is operated by the Association of Universities for Research in Astronomy, Inc., under a cooperative agreement with the NSF on behalf of the Gemini partnership: the National Science Foundation (United States), the Science and Technology Facilities Council (United Kingdom), the National Research Council (Canada), CONICYT (Chile), the Australian Research Council (Australia), Ministrio da Cincia, Tecnologia e Inovao (Brazil) and Ministerio de Ciencia, Tecnologa e Innovacin Productiva (Argentina).

Chapter 7

Short GRB 130603B: Discovery of a jet break in the optical and radio afterglows, and a mysterious late-time X-ray excess

W. Fong, E. Berger, B. D. Metzger, R. Margutti, R. Chornock, G. Migliori, R. J. Foley, B. A. Zauderer, R. Lunnan, T. Laskar, S. J. Desch, K. J. Meech, S. Sonnett, C. Dickey, A. Hedlund & P. Harding

The Astrophysical Journal, Vol. 780, No. 118, 2014

Abstract

We present radio, optical/NIR, and X-ray observations of the afterglow of the short-duration *Swift* and *Konus-Wind* GRB 100117A, and uncover a break in the radio and optical bands at ≈ 0.5 d after the burst, best explained as a jet break with an inferred jet opening angle of $\approx 4 - 8^{\circ}$. GRB 130603B is only the third short GRB with a radio afterglow detection to date, and the first time that a jet break is evident in the radio band. We model the temporal evolution of the spectral energy distribution to determine the burst explosion properties and find an isotropic-equivalent kinetic energy of $\approx (0.6 - 1.7) \times 10^{51}$ erg and a circumburst density of $\approx 5 \times 10^{-3} - 30$ cm^{-3}. From the inferred opening angle of GRB 100117A, we calculate beaming-corrected energies of $E_{\gamma} \approx (0.5 - 2) \times 10^{49}$ erg and $E_K \approx (0.1 - 1.6) \times 10^{49}$ erg. Along with previous measurements and lower limits we find a median opening angle of $\approx 10^{\circ}$. Using the all-sky observed rate of 10 Gpc^{-3} yr^{-1}, this implies a true short GRB rate of ≈ 20 yr^{-1} within 200 Mpc, the Advanced LIGO/VIRGO sensitivity range for neutron star binary mergers. Finally, we uncover evidence for significant excess emission in the X-ray afterglow of GRB 100117A at $\gtrsim 1$ d and conclude that the additional energy component could be due to fall-back accretion or spin-down energy from a magnetar formed following the merger.

7.1 Introduction

The broad-band afterglows of short-duration gamma-ray bursts (GRBs; $T_{90} < 2$ sec; Kouveliotou et al. 1993) provide a unique opportunity to study the basic properties of these events: their energetics, circumburst densities, and jet opening angles. While the energy scales and densities provide fundamental insight to the explosion physics and progenitors, the geometry provides direct information on the population's true energy scale and event rate. The most likely progenitors, neutron star-neutron star (NS-NS) and/or neutron star-black hole (NS-BH) mergers (Eichler et al. 1989; Narayan et al. 1992; Fong et al. 2010; Berger 2010a; Fong & Berger 2013), are the premier candidates of gravitational waves for Advanced LIGO/VIRGO. Thus, an inference on the opening angle distribution will aid our expectations for coincident electromagnetic-gravitational wave detections.

Over the past ~ 9 years, the *Swift* satellite (Gehrels et al. 2004) has discovered 77 short GRBs, with a median γ-ray fluence of $\approx 2 \times 10^{-7}$ erg cm^{-2} ($15 - 150$ keV; Gehrels et al. 2008; Nysewander et al. 2009). Coupled with redshift measurements from their host galaxies, this has demonstrated a range of isotropic-equivalent γ-ray energies of $E_{\gamma,\rm iso} \approx 10^{48} - 10^{52}$ erg (Berger 2007; Nysewander et al. 2009). Temporal monitoring of their broad-band afterglows has led to a similarly broad range of inferred isotropic-equivalent kinetic energies, $E_{\rm K,iso} \approx 10^{48} - 10^{52}$ erg, circumburst densities of $\lesssim 1$ cm^{-3} (Soderberg et al. 2006b; Panaitescu 2006; Stratta et al. 2007; Perley et al. 2009a; Berger 2010a; Fong et al. 2011), and opening angles of $\gtrsim 3 - 25^{\circ}$ (Fox et al. 2005; Grupe et al. 2006; Soderberg et al. 2006b; Fong et al. 2012b; Margutti et al. 2012; Nicuesa Guelbenzu et al. 2012a; Berger et al. 2013b; Sakamoto et al. 2013).

Collimation in GRBs is determined from temporal steepenings in afterglow light curves, termed "jet breaks", which are expected to be achromatic (Sari et al. 1999; Rhoads 1999; Panaitescu 2005). Jet breaks in the light curves of long GRBs translate to an opening angle distribution with a range of $\theta_j \approx 2 - 25^\circ$ and a median of $\approx 7^\circ$, leading to beaming-corrected energies of $E_\gamma = [1 - \cos(\theta_j)]E_{\gamma,\rm iso} \approx 10^{51}$ erg (Bloom et al. 2003; Frail et al. 2001; Friedman & Bloom 2005; Kocevski & Butler 2008; Racusin et al. 2009). For short GRBs, the search for jet breaks has been more challenging, primarily due to the intrinsic faintness of their afterglows, a direct reflection of their low energy scales and circumburst densities. There are only three robust cases of jet breaks for short GRBs based on well-sampled light curves thus far (GRB 051221A: Soderberg et al. 2006b, GRB 090426: Nicuesa Guelbenzu et al. 2011; GRB 111020A: Fong et al. 2012b), with $\theta_j \approx 3 - 8^\circ$. The non-detection of jet breaks to $\gtrsim 1$ day after the burst has also provided lower limits on the jet opening angles of $\gtrsim 3 - 25^\circ$ (Fox et al. 2005; Grupe et al. 2006; Fong et al. 2012b; Coward et al. 2012; Margutti et al. 2012; Berger et al. 2013b), suggesting that short GRBs may have wider jets than their long-duration counterparts.

In addition to an inference on the opening angles, afterglows can also provide unique constraints on the energy scales and circumburst densities through multi-wavelength detections and modeling of the spectral energy distributions. However, of the 77 *Swift* short GRBs detected to present, only two have been detected in the radio band (GRB 050724A: Berger et al. 2005; GRB 051221A: Soderberg et al. 2006b). Both of these events have inferred densities of $\approx 10^{-2}$ cm^{-3} and isotropic-equivalent energies of $\approx 10^{51}$ erg. The upgrade of the VLA with a ten-fold increase in sensitivity (Perley et al. 2011) provides a promising route to increase radio afterglow detections, and thus substantially tighter constraints on these properties.

Temporal afterglow information, particularly in the X-ray band, has also revealed cases of anomalous behavior that do not fit with the standard synchrotron picture of afterglows. For short GRBs, there have been observed cases of flares at $\lesssim 1000$ s after the burst (Grupe et al. 2006; Margutti et al. 2011), shallow decays attributed to energy injection (e.g., Soderberg et al. 2006b), putative early plateaus attributed to the spin-down power of a hyper-massive and highly-magnetized neutron star remnant (Fan & Xu 2006; Rowlinson et al. 2010b, 2013) and two cases of late-time X-ray re-brightenings on $\sim$ day timescales (GRB 050724A: Grupe et al. 2006; GRB 080503: Perley et al. 2009a).

Recently, the short-duration GRB 130603B sparked much interest, because its bright optical afterglow enabled the first afterglow spectrum of a short GRB and thus an unambiguous redshift determination of $z = 0.3565 \pm 0.0002$ (Cucchiara et al. 2013; de Ugarte Postigo et al. 2013). It also led to the first claimed detection of a "kilonova" associated with a short GRB (Berger et al. 2013a; Tanvir et al. 2013a), providing direct evidence for a compact object binary progenitor. Here, we present and model the broad-band afterglow of GRB 130603B. In Section 2, we present the X-ray, optical/NIR and radio data sets. In Section 3, we model the evolution of the spectral energy distribution (SED) and constrain the burst explosion properties. In Section 4, we discuss the steepening in the radio and optical light curves, best explained as a jet break. In Section 5, we investigate several possibilities to explain excess X-ray emission at $\gtrsim 1$ day. Finally in Section 6, we discuss GRB 130603B in the context of the short GRB population, and investigate implications for the energy scale and event rate.

Unless otherwise noted, all magnitudes in this paper are in the AB system and are corrected for Galactic extinction in the direction of the burst using $E(B-V) = 0.02$ mag

(Schlegel et al. 1998; Schlafly & Finkbeiner 2011). Reported uncertainties correspond to 68% confidence. We employ a standard ΛCDM cosmology with $\Omega_M = 0.27$, $\Omega_\Lambda = 0.73$, and $H_0 = 71$ km s^{-1} Mpc^{-1}.

7.2 Observations

GRB 130603B was detected on 2013 June 3 at 15:49:14 UT by the Burst Alert Telescope (BAT; Barthelmy et al. 2005) on-board the *Swift* satellite (Melandri et al. 2013), and by *Konus-Wind* (Golenetskii et al. 2013). *Swift*/BAT localized the burst to RA=$11^{\rm h}28^{\rm m}53.2^{\rm s}$ and Dec=$+17°03'48.2''$ (J2000) with $1.0'$ accuracy (90% containment; Barthelmy et al. 2013). The γ-ray emission consists of a single pulse with a duration of $T_{90} = 0.18 \pm 0.02$ s ($15 - 150$ keV; Barthelmy et al. 2013), a fluence of $f_\gamma = (6.6 \pm 0.7) \times 10^{-6}$ erg cm^{-2} ($20 - 10^4$ keV; Golenetskii et al. 2013), and a peak energy of $E_{\rm pk} = 660 \pm 100$ keV (Golenetskii et al. 2013). The spectral lags are 0.6 ± 0.7 ms ($15 - 25$ keV to $50 - 100$ keV) and -2.5 ± 0.7 ms ($25 - 50$ keV to $100 - 350$ keV; Norris et al. 2013). The combination of the duration, high peak energy, and small (or negative) lag unambiguously classifies GRB 130603B as a short-hard burst. At $z = 0.3565$ (Cucchiara et al. 2013; de Ugarte Postigo et al. 2013), the isotropic-equivalent gamma-ray energy is $E_{\gamma,\rm iso} \approx 2.1 \times 10^{51}$ erg ($20 - 10^4$ keV, rest-frame).

7.2.1 X-rays

Observations with the X-ray Telescope (XRT; Burrows et al. 2005) on-board *Swift* commenced at $\delta t = 59$ s (where δt is the time after the BAT trigger) and revealed a

Table 7.1. GRB 130603B Afterglow Photometry

δt (d)	Exposure Time (hr)	Telescope	Instrument	Band	F_ν (μJy)	σ_ν (μJy)	References
			X-rays				
2.69	5.14	*XMM-Newton*	EPIC-pn	1 keV	2.44×10^{-3}	4.59×10^{-4}	This work
6.50	8.38	*XMM-Newton*	EPIC-pn	1 keV	8.25×10^{-4}	5.03×10^{-4}	This work
			Optical				
0.008	0.05	Swift	UVOT	V	< 199.5		1
0.089	1.42	Swift	UVOT	V	< 53.95		1
0.24	0.50	NOT	MOSCA	r	12.59	0.23	1
0.25	0.25	WHT	ACAM	z	25.35	1.36	1
0.27	0.25	WHT	ACAM	i	16.44	0.88	1, 2
0.28	0.50	CAHA	DLR-MKIII	V	8.32	0.73	1
0.29	0.008	GTC	OSIRIS	r	10.96	0.20	1, 2
0.29	0.25	WHT	ACAM	g	6.31	0.34	1, 2
0.33	0.40	Gemini-South	GMOS	g	5.30	0.19	3
0.34	0.17	Magellan/Baade	IMACS	r	8.64	0.14	4
0.37	0.40	Gemini-South	GMOS	i	12.25	1.18	3
0.60	0.14	Gemini-North	GMOS	z	6.54	0.18	1, 2
0.60	0.19	UKIRT	WFCAM	K	13.68	1.32	1, 2
0.61	0.14	Gemini-North	GMOS	i	4.53	0.12	1, 2
0.61	0.19	UKIRT	WFCAM	J	9.29	1.12	1, 2
0.62	0.14	Gemini-North	GMOS	r	2.88	0.08	1, 2
0.62	0.14	Gemini-North	GMOS	g	1.60	0.06	1, 2
1.30	0.15	Gemini-South	GMOS	r	< 0.30		3
1.30	0.15	Gemini-South	GMOS	i	< 0.58		3
1.34	0.33	Magellan/Baade	IMACS	r	< 0.46		4
1.59	0.17	Gemini-North	GMOS	g	< 0.19		1, 2
1.60	0.17	Gemini-North	GMOS	r	0.21	0.05	1, 2
1.61	0.17	Gemini-North	GMOS	i	< 0.48		1, 2
1.61	0.39	UKIRT	WFCAM	J	< 1.25		1, 2
1.62	0.17	Gemini-North	GMOS	z	< 1.00		1, 2
2.32	0.37	VLT	HAWK-I	J	< 1.25		1, 2
3.26	0.17	GTC	OSIRIS	r	< 0.33		1, 2
4.26	0.17	GTC	OSIRIS	r	< 0.23		1, 2
7.30	0.37	VLT	HAWK-I	J	< 1.45		1, 2
8.23	0.33	TNG	DOLoRes	r	< 1.15		1
8.25	0.33	TNG	DOLoRes	i	< 0.52		1

Table 7.1—Continued

δt (d)	Exposure Time (hr)	Telescope	Instrument	Band	F_ν (μJy)	σ_ν (μJy)	References
8.41	0.33	Magellan/Baade	IMACS	r	< 0.40		This work
9.37	0.62	HST	ACS	F606W	< 0.03		2, 4
[a]9.41	0.73	HST	WFC3	F160W	0.17	0.03	2, 4
21.26	0.67	TNG	DOLoRes	r	< 1.49		1
21.29	0.67	TNG	DOLoRes	i	< 0.93		1
21.52	0.28	MMT	MMTCam	r	< 1.91		This work
29.57	0.73	HST	WFC3	F160W	< 0.10		2, 4
37.34	0.75	Magellan/Clay	LDSS3	r	< 0.40		This work
			Radio				
0.37	2.00	VLA		4.9 GHz	125.1	14.4	This work
0.37	2.00	VLA		6.7 GHz	118.6	9.1	This work
1.43	1.00	VLA		4.9 GHz	< 56.7		This work
1.43	1.00	VLA		6.7 GHz	64.9	15.2	This work
1.44	1.00	VLA		21.8 GHz	< 50.0		This work
4.32	2.00	VLA		4.9 GHz	< 51.0		This work
4.32	2.00	VLA		6.7 GHz	< 25.8		This work
84.31	1.00	VLA		4.9 GHz	< 68.6		This work
84.31	1.00	VLA		6.7 GHz	< 33.7		This work

Note. — All upper limits correspond to 3σ confidence. Optical flux densities are corrected for Galactic extinction in the direction of the burst, but are not corrected for extinction in the rest-frame of the burst.
[a] The reported flux and uncertainty are of the claimed kilonova detection (Berger et al. 2013a; Tanvir et al. 2013a).
References: (1) de Ugarte Postigo et al. 2013; (2) Tanvir et al. 2013a; (3) Cucchiara et al. 2013; (4) Berger et al. 2013a

fading, uncatalogued X-ray source with a UVOT-enhanced position of RA=$11^{\rm h}28^{\rm m}48.15^{\rm s}$ and Dec=$+17^\circ04'16.9''$ (J2000) and an uncertainty of $1.4''$ radius (90% containment; Goad et al. 2007; Evans et al. 2007a, 2009). The source faded below the XRT detection threshold by $\delta t \approx 2$ d. We analyze the XRT data using the HEASOFT package (v.6.13) and relevant calibration files. To generate a count-rate light curve, we apply standard filtering and screening criteria (see Margutti et al. 2013), ensuring a minimum signal-to-noise ratio of 4 for each temporal bin.

We initiated a target-of-opportunity program on *XMM-Newton* (ID: 072257, PI: Fong) with the European Photon Imaging Camera (EPIC-PN) and obtained observations at $\delta t \approx 2.7$ d and ≈ 6.5 d with net exposure times of 18.5 ks and 30.2 ks, respectively. We analyze these data using standard routines in the Scientific Analysis System (SAS) and detect a fading source coincident with the XRT position. We find ≈ 60 counts ($\sim 4\sigma$) in the first observation in a $30''$-radius aperture, and ≈ 10 counts (3σ) in the second observation in a $15''$-radius aperture, where the aperture size is adjusted to maximize the signal-to-noise ratio.

To determine the flux calibration, we model the XRT data with an absorbed single power-law spectrum, using the Galactic neutral Hydrogen absorption column ($N_{\rm H,MW} = 1.93 \times 10^{20}\,{\rm cm}^{-2}$; Kalberla et al. 2005). We fit for the photon index, Γ and the intrinsic Hydrogen absorption column ($N_{\rm H,int}$ at $z = 0.3565$). Using all of the available XRT data, we find $N_{\rm H,int} = (2.4 \pm 0.4) \times 10^{21}\,{\rm cm}^{-2}$ and $\Gamma = 2.2 \pm 0.1$. We apply these spectral parameters to the XRT and XMM data. The resulting fluxes from XMM are listed in Table 7.1.

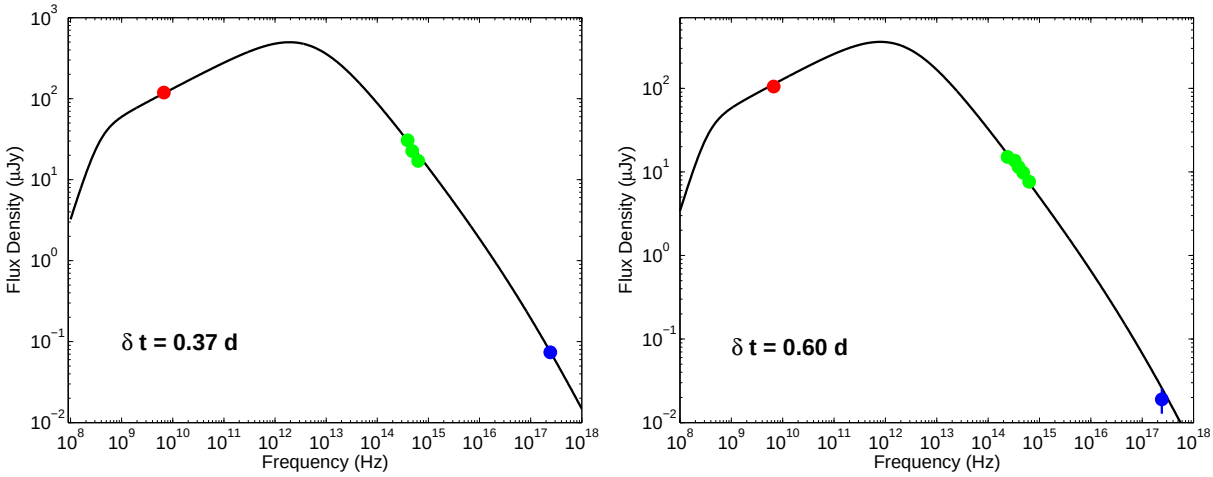

Figure 7.1.—: Radio (red; 6.7 GHz), optical/NIR (green; $griJ$-band; Berger et al. 2013a; Cucchiara et al. 2013; Tanvir et al. 2013a) and X-ray (blue; 1 keV) afterglow spectral energy distributions of GRB 130603B at $\delta t = 0.37$ d (left) and 0.60 d (right). The $grizJ$ afterglow observations are corrected for $A_V^{\rm host} = 1$ mag. Error bars correspond to 1σ confidence. A representative best-fit model (black line) is shown in each panel.

7.2.2 Optical

Subsequent to the discovery of the X-ray afterglow (Melandri et al. 2013), ground-based optical/NIR observations began at $\delta t \approx 2.7$ hr to search for an optical counterpart (Berger et al. 2013a; Cucchiara et al. 2013; de Ugarte Postigo et al. 2013; Tanvir et al. 2013a). We initiated four sets of r-band observations of GRB 130603B using instruments on the twin Magellan 6.5-m telescopes, spanning $\delta t \approx 8.1$ hr to ≈ 37 d (Table 7.1). The description of these observations and the optical afterglow discovery are provided in Berger et al. (2013a). In addition, we obtained a set of r-band observations with MMTCam on the 6.5-m Multi-Mirror Telescope (MMT) and processed these data using standard procedures in IRAF. All of the published optical/NIR afterglow photometry (Berger et al. 2013a; Cucchiara et al. 2013; de Ugarte Postigo et al. 2013; Tanvir et al. 2013a), are listed in Table 7.1.

7.2.3 Radio

We observed the position of GRB 130603B with the Karl G. Jansky Very Large Array (VLA; Program 13A-046, PI: Berger) starting at $\delta t \approx 8.8$ hr at a mean frequency of 5.8 GHz (upper and lower side-bands centered at 6.7 GHz and 4.9 GHz) using 3C286 and J1120-1420 for bandpass/flux and gain calibration, respectively. We follow standard procedures in the Astronomical Image Processing System (AIPS; Greisen 2003) for data calibration and analysis. We detect a source located at RA=$11^{\rm h}28^{\rm m}48.15^{\rm s}$, Dec=$+17^\circ04'18.0''$ (J2000; δRA= $0.21''$, δDec= $0.14''$), consistent with the optical and X-ray afterglow positions. We obtained three subsequent 5.8 GHz observations at $\delta t \approx 1.4$ d, ≈ 4.3 d, and ≈ 84.3 d in which the source faded, indicating that it is the radio afterglow. We also obtained observations at a mean frequency of 21.8 Hz at $\delta t \approx 1.4$ d (using J1118+1234 as the phase calibrator), where the afterglow is not detected.

We measure flux densities for the upper and lower side-bands from each epoch using AIPS/`JMFIT`, and calculate 3σ upper limits from source-free regions using AIPS/`IMSTAT`. The radio afterglow detections and upper limits are listed in Table 7.1.

7.3 Broad-band Afterglow Properties

We utilize the broad-band afterglow observations to constrain the explosion properties and circumburst environment of GRB 130603B. We emphasize that this is only the third radio afterglow detection of a short GRB, thereby enabling substantially tighter constraints on the physical properties than for the majority of short GRBs. We adopt the standard synchrotron model for a relativistic blastwave in a constant density

medium (ISM; Sari et al. 1999; Granot & Sari 2002). This model provides a mapping from the broad-band afterglow flux densities to physical parameters of the explosion and circumburst environment: isotropic-equivalent kinetic energy ($E_{\rm K,iso}$), circumburst density (n_0), fractions of post-shock energy in radiating electrons (ϵ_e) and magnetic fields (ϵ_B), and the electron power-law distribution index (p), with $N(\gamma) \propto \gamma^{-p}$ for $\gamma \gtrsim \gamma_{\rm min}$.

To determine the locations of the break frequencies with respect to the X-ray, optical and radio bands, we first compare the spectral indices from the afterglow observations. From the X-ray spectral fit, we find $\beta_X \equiv 1 - \Gamma = -1.2 \pm 0.1$ (Section 7.2.1), while from the optical *griz*-band afterglow photometry at $\delta t \approx 0.6$ d (Table 7.1; Cucchiara et al. 2013; Tanvir et al. 2013a), we measure an observed spectral index of $\beta_{\rm opt,obs} = -2.0 \pm 0.1$. The NIR spectral index measured from the JK-bands at the same epoch is substantially shallower, $\beta_{\rm NIR} = -0.6 \pm 0.2$, indicating that the optical flux is suppressed by extinction in the host galaxy. To determine the amount of extinction, we apply a Milky Way extinction curve (Cardelli et al. 1989) to the *grizJK* photometry, fitting for the spectral index and rest-frame extinction ($A_V^{\rm host}$), and find best-fit values of $\beta_{\rm opt} = -0.84 \pm 0.10$ and $A_V^{\rm host} = 1.0 \pm 0.1$ mag, similar to the values found from other analyses (de Ugarte Postigo et al. 2013; Jin et al. 2013). Using standard Galactic relations between the intrinsic hydrogen column density and rest-frame extinction (Predehl & Schmitt 1995; Watson 2011), we find an inferred extinction of $A_V^{\rm host} = 0.9 - 1.6$ mag from the $N_{\rm H,int}$ value determined in Section 7.2.1, consistent with $A_V^{\rm host} \approx 1$ mag. A comparison of $\beta_{\rm opt}$ and β_X indicates that the cooling frequency, ν_c, lies between the optical and X-ray bands, and that $p = 2.55 \pm 0.15$.

To determine the location of the self-absorption and peak frequencies (ν_a and ν_m, respectively) with respect to the optical and radio bands, we compare the radio spectral

slope determined from VLA observations at $\delta t \approx 0.37$ d and 1.43 d (Table 7.1) to $\beta_{\rm opt}$. We find that $\beta_{\rm rad}$ does not match the optical slope and furthermore is consistent with $F_\nu \propto \nu^{1/3}$, as expected for $\nu_a < \nu_{\rm rad} < \nu_m$.

Knowing the relative locations of the break frequencies with respect to our observing bands, we use the standard synchrotron model to determine allowable ranges for the physical parameters. We use the afterglow SED at two common epochs, $\delta t = 0.37$ d and 0.60 d, where the optical/NIR fluxes are corrected for $A_V^{\rm host} = 1$ mag (Figure 7.1). We also use the constraints $\epsilon_e, \epsilon_B < 1/3$ and determine:

$$3.3 \times 10^8 < \nu_a < 2.6 \times 10^9 \text{ Hz} \tag{7.1a}$$

$$5.8 \times 10^{-2} < \epsilon_e < 1/3 \tag{7.1b}$$

$$2.0 \times 10^{-3} < \epsilon_B < 1/3 \tag{7.1c}$$

$$0.6 \times 10^{51} \text{ erg} < E_{\rm K,iso} < 1.7 \times 10^{51} \text{ erg} \tag{7.1d}$$

$$4.9 \times 10^{-3} \text{ cm}^{-3} < n_0 < 30 \text{ cm}^{-3} \tag{7.1e}$$

where the ranges are set by the uncertainty in ν_a. We note that the inferred isotropic-equivalent kinetic energy is comparable to $E_{\gamma,\rm iso} \approx 2.1 \times 10^{51}$ erg. These parameters give rise to a family of models, and we show representative model SEDs along with the broad-band afterglow observations in Figure 7.1.

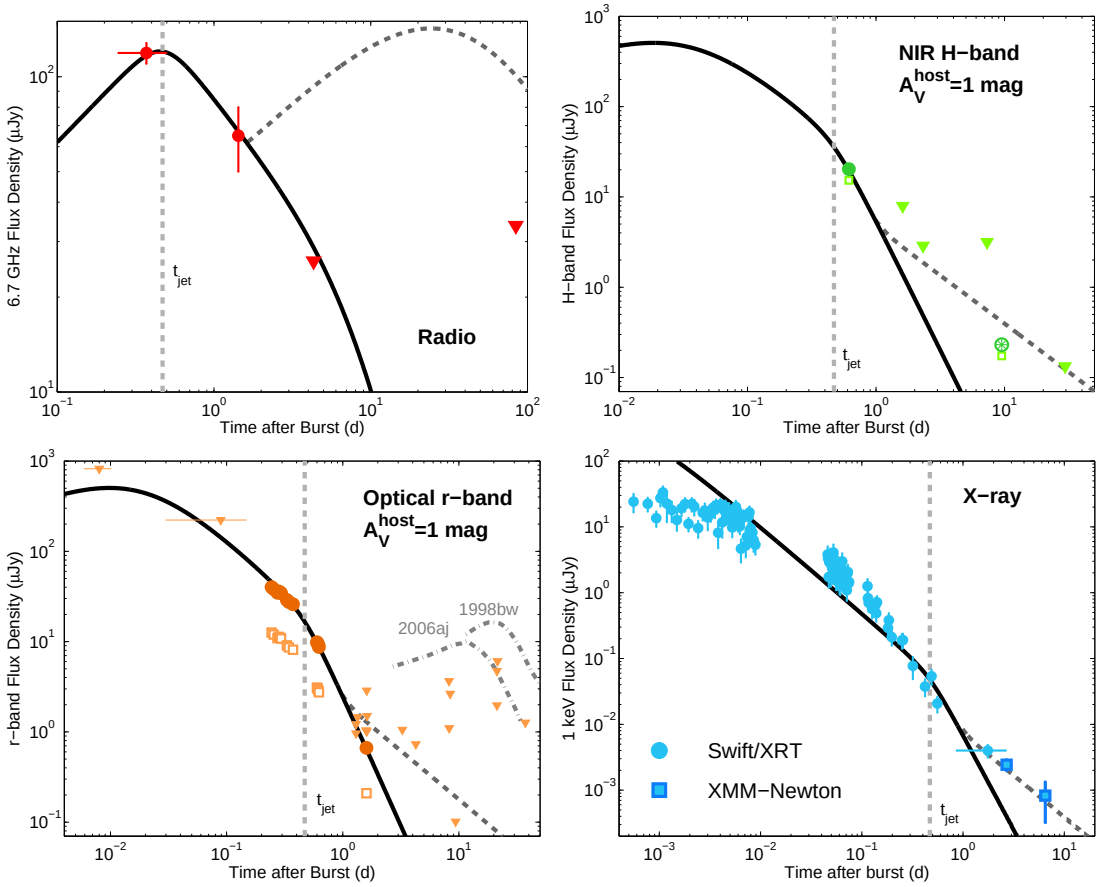

Figure 7.2.—: Radio through X-ray afterglow light curves of GRB 130603B. Error bars correspond to 1σ confidence, and triangles denote 3σ upper limits. The afterglow model is shown as a black line, while the jet break time of $t_j \approx 0.47$ d is marked by a vertical grey dashed line. Also shown is a model with energy injection (dark grey dashed line) that adequately fits the X-ray excess and is consistent with most of the optical and NIR limits. However, this model is not consistent with the 3σ upper limits in the radio band. *Top left:* 6.7 GHz observations with the VLA (red). *Top right:* H-band observations (green; Berger et al. 2013a; de Ugarte Postigo et al. 2013; Tanvir et al. 2013a), where JK-band observations are extrapolated to H-band using $\beta_{\rm opt} = -2$. The observed values (open green squares) are corrected for $A_V^{\rm host} = 1$ mag (filled green symbols). The circled asterisk at $\delta t \approx 9$ d is the "kilonova" associated with GRB 130603B (Berger et al. 2013a; Tanvir et al. 2013a). *Bottom left:* Optical r-band observations (orange; this work, Cucchiara et al. 2013; de Ugarte Postigo et al. 2013; Tanvir et al. 2013a), where giz-band observations are extrapolated to r-band using $\beta_{\rm opt} = -2$. The observed values (open orange squares) are corrected for $A_V^{\rm host} = 1$ mag (filled orange symbols). The displayed upper limits (orange triangles) are also corrected for extinction. Also shown are the optical light curves of GRB-SN 1998bw (Galama et al. 1998; Clocchiatti et al. 2011) and GRB-SN 2006aj (dot-dashed lines; Mirabal et al. 2006) corrected for extinction and redshifted to $z = 0.3565$. *Bottom right:* Observations from *Swift*/XRT (blue circles) and *XMM-Newton* (blue squares) at 1 keV.

7.4 Afterglow Evolution: Jet Break

To investigate the temporal behavior of the optical/NIR afterglow, we extrapolate all of the available afterglow data (Table 7.1) to the optical r-band using the observed spectral slope (Section 7.3) and then correct these fluxes for $A_V^{\rm host} = 1$ mag. The resulting temporal behavior of the optical afterglow flux is characterized by a broken power law (Figure 8.1). Invoking a broken power law model with two segments, we find pre- and post-break decay indices of $\alpha_1 \approx -1.26 \pm 0.05$ and $\alpha_2 = -2.73 \pm 0.08$, with a break time of $t_b = 0.47^{+0.02}_{-0.06}$ d. The required change in the temporal index is therefore $\Delta\alpha \approx 1.5$. Although there are several possibilities that can explain breaks in GRB afterglow light curves, most of these cannot explain the large change in slope and the steep post-break decline seen here. For instance, the transition of the cooling frequency across the band predicts $\Delta\alpha = 0.25$ (Sari et al. 1998), while the cessation of energy injection observed in long GRBs typically leads to $\Delta\alpha \approx 0.7$ with moderate decline rates of $\alpha_1 \approx -0.5$ and $\alpha_2 \approx -1.2$ (Nousek et al. 2006; Zhang et al. 2006; Liang et al. 2007). A steep drop in the density is predicted to cause maximum changes of $\Delta\alpha \approx 0.4$ for density contrasts of ~ 10 (Nakar & Granot 2007), and would require a density contrast of $\gtrsim 1000$ to account for $\Delta\alpha = 1.5$.

We therefore conclude that the temporal steepening is instead a jet break, when the edge of a relativistically-beamed outflow becomes visible to the observer (Sari et al. 1999; Rhoads 1999). In this scenario, the post-break flux declines as t^{-p} (Sari et al. 1999). Indeed, we find good agreement between $\alpha_2 = -2.7 \pm 0.1$ determined from the optical light curve and $p = 2.55 \pm 0.15$ independently determined from the broad-band SED (Section 7.3).

In addition, since the radio band lies between ν_a and ν_m (Section 7.3), the radio flux density should increase as $F_\nu \propto t^{1/2}$ in the spherical regime (Granot & Sari 2002), while the flux will decrease as $F_\nu \propto t^{-1/3}$ in a post-jet break scenario (Sari et al. 1999). We find that the observed radio flux of GRB 130603B declines with $\alpha \approx -0.45$ between $\delta t \approx 0.4$ d and 1.3 d, demonstrating that the evolution is not isotropic (Figure 8.1). Thus, the temporal behavior of both the optical and radio afterglows support a jet break at $t_j \approx 0.47$ d, making this the first detection of a jet break in the radio afterglow of a short GRB.

In conjunction with the energy, density, and redshift, the time of the break can be converted to a jet opening angle (Sari et al. 1999; Frail et al. 2001),

$$\theta_j = 9.51 t_{j,\rm d}^{3/8} (1+z)^{-3/8} E_{\rm K,iso,52}^{-1/8} n_0^{1/8} \ \deg \tag{7.2}$$

where $t_{j,\rm d}$ is in days, $E_{\rm K,iso,52}$ is in units of 10^{52} erg and n_0 is in units of cm^{-3}. For the ranges of $E_{\rm K,iso}$ and n_0 in Equations 7.1d-7.1e, we calculate $\theta_j \approx 4 - 14^\circ$. However, given a NS-NS/NS-BH progenitor as indicated by the likely detection of a kilonova (Berger et al. 2013a; Tanvir et al. 2013a), the circumburst density is likely more typical of ISM densities ($n \lesssim 1$ cm^{-3}), leading to $\theta_j \approx 4 - 8^\circ$.

7.5 Late-time X-ray Excess

The synchrotron afterglow model with a jet break at $t_j \approx 0.47$ d provides a good match to the radio and optical light curves (Figure 8.1). However, unlike the optical afterglow behavior, we do not observe significant steepening in the X-ray light curve,

and instead the afterglow flux at $\delta t \gtrsim 0.03$ d can be characterized by a single power law with $\alpha_X = -1.88 \pm 0.15$. Thus, our afterglow model underpredicts the X-ray flux by a factor of ≈ 5 at $\delta t \gtrsim 2$ d (see Figure 8.1). We note that Tanvir et al. (2013a) and de Ugarte Postigo et al. (2013) previously claimed that the same broken power-law fits both the optical and X-ray data, but this was based on the XRT data alone. The *XMM-Newton* observations do not support these claims. We are thus motivated to consider an additional energy source for this X-ray emission excess, which follows $L_{\rm X} \simeq 4 \times 10^{43} t_d^{-1.88}$ erg s^{-1} (where t_d is in units of days).

One possible source of late-time excess X-ray emission is continued energy injection into the blastwave from ongoing central engine activity (Zhang & Mészáros 2002; Zhang et al. 2006). We first consider continuous power law energy injection with $L \propto t^q$. We find that energy injection beginning at $\delta t \approx 1$ d characterized by $q = 0.3$ (e.g., $E \propto t^{1.3}$) provides an adequate fit to the late-time X-ray light curve (Figure 8.1). Assuming that the injection extends to $\delta t \approx 10$ d, the energy injection factor is ≈ 9.5. However, this energy injection model is not consistent with the 3σ radio upper limits, which are a factor of ≈ 3 below the predicted flux with energy injection (Figure 8.1). Therefore, continuous energy injection is not a viable explanation for the excess X-ray emission.

We are therefore motivated to consider a source of emission that predominantly contributes in the X-rays with negligible effects on the other bands. We focus on scenarios in which this emission originates from the central engine, but which we now assume can be viewed directly through the merger ejecta (we justify this assumption below). We first consider ongoing accretion ("fall-back") onto the newly-formed black hole following a compact object merger. By extrapolating the matter trajectories from numerical simulations of the merger process to late times, Rosswog (2007) predicts

accretion luminosities of $L_{\rm acc} \sim 10^{43} - 10^{45}$ erg s^{-1} on a timescale of ~ 1 d, with a temporal decay of $L_{\rm acc} \sim t^{-\alpha}$ similar to the canonical prediction of $\alpha = -5/3$ for a tidally disrupted star (Rees 1988). Assuming a radiative efficiency of $\gtrsim 10\%$, this scenario is well matched to the X-ray light curve of GRB 130603B. However, such efficiencies are optimistic and more detailed models of the fall-back process from compact object mergers (Rossi & Begelman 2009) predict much lower X-ray luminosities of $L_{\rm X} \lesssim 10^{-3} L_{\rm acc}$, which would not be large enough to explain the observed excess.

Another possibility is that the X-ray emission is powered by the spin-down of a massive magnetar remnant (Metzger et al. 2008b; Bucciantini et al. 2012; Zhang 2013), a process that has been used to explain putative plateaus in the X-ray afterglows of short GRBs (Rowlinson et al. 2013). Such remnants may be at least temporarily stable to gravitational collapse, if they rotate with spin periods of $\lesssim$few ms (e.g. Özel et al. 2010; Giacomazzo & Perna 2013). The remnant may also acquire strong magnetic fields of $\gtrsim 10^{14} - 10^{15}$ G, similar to those of Galactic magnetars (Duncan & Thompson 1992; Zrake & MacFadyen 2013). The magnetar model predicts that the late-time spin-down luminosity should decay as $L_{\rm sd} \propto t^{-2}$, consistent with the observed temporal decay of $\alpha_X = -1.88 \pm 0.15$. The predicted spectrum is $F_\nu \propto \nu^{-1}$ (Metzger et al. 2013), also consistent with the observed spectral index $\beta_X \approx -1.2 \pm 0.1$. Fitting the entire X-ray light curve with a magnetar model characterized by the duration and luminosity of the plateau (Zhang & Mészáros 2001), and assuming $M_{\rm NS} = 1.4 - 2.5\ M_\odot$ and $R_{\rm NS} = 10^6$ cm, we find best-fit parameters of $B \approx 2 \times 10^{16}$ G and $P \approx 15 - 25$ ms (where higher mass corresponds to slower spin periods)[1]. However, such slow spin periods are likely

[1]From an independent fit of the XRT data alone, de Ugarte Postigo et al. (2013) find $P \approx 8.4$ ms and $B \approx 8.6 \times 10^{15}$ G

unphysical in the merger context due to the substantial angular momentum of the initial binary. Instead, assuming a more reasonable initial spin period of 1 ms, the required magnetic field strength to produce the observed X-ray luminosity at $\gtrsim 1$ d assuming 10% radiative efficiency, is $B \approx 10^{15}$ G, but such a model would under-predict the light curve at $\delta t \lesssim 3000$ s by a factor of a few. We thus conclude that the magnetar scenario could potentially explain the late-time X-ray excess for $\delta t \gtrsim 3000$ s.

To justify that we can observe the central engine directly, as is required in either the fall-back or magnetar models, the merger ejecta must be transparent to soft X-rays. Due to the high bound-free X-ray opacity of neutral matter, this in turn requires that the engine be sufficiently luminous to re-ionize the merger ejecta (Metzger et al. 2013). The ejecta becomes transparent to X-rays once two conditions are satisfied: (1) the opacity becomes dominated by electron scattering ($\kappa_{\rm bf}/\kappa_{\rm es} \lesssim 1$, where $\kappa_{\rm bf}$ and $\kappa_{\rm es}$ are the bound-free and electron scattering opacities, respectively) and (2) the electron scattering optical depth, $\tau_{\rm es}$, through the ejecta decreases to $\lesssim 1$. Assuming ejecta mainly composed of hydrogen-like iron[2] and an ejecta temperature of $T_{\rm ej} = 10^4$ K, we derive the following expressions (see Appendix for details):

$$\frac{\kappa_{\rm bf}}{\kappa_{\rm es}} \approx 0.13 \left(\frac{L_X}{4 \times 10^{43} {\rm erg\,s^{-1}}}\right)^{-1} \left(\frac{M_{\rm ej}}{10^{-3} M_\odot}\right) \left(\frac{t}{1\ {\rm d}}\right)^{-1} \left(\frac{v_{\rm ej}}{c}\right)^{-1}, \tag{7.3}$$

$$\tau_{\rm es} = \rho_{\rm ej} \kappa_{\rm es} R_{\rm ej} \simeq 0.02 \left(\frac{M_{\rm ej}}{10^{-3} M_\odot}\right) \left(\frac{v_{\rm ej}}{c}\right)^{-2} \left(\frac{t}{1\,{\rm d}}\right)^{-2} \tag{7.4}$$

[2]Outflows along the polar direction arise chiefly from the accretion disk and are expected to be composed of Fe-like nuclei (e.g. Metzger et al. 2008b).

where $M_{\rm ej}, R_{\rm ej} = v_{\rm ej}t$, and $v_{\rm ej}$ are the (effective) mass, radius, and velocity of the ejecta along the observer line of sight, respectively. Using fiducial values for $M_{\rm ej}$ and $v_{\rm ej}$ of the merger (Hotokezaka et al. 2013; Fernández & Metzger 2013), we find that both conditions are satisfied on timescales $\delta t \gtrsim$ few hr given the observed X-ray luminosity. We thus conclude that the ejecta are indeed transparent to the soft X-rays at late times, supporting the idea that direct radiation from the central engine could produce the observed X-ray excess emission in GRB 130603B.

We note that of the ≈ 10 short GRBs with X-ray observations to $\delta t \gtrsim 1$ d, two events, GRBs 050724 and 080503, also exhibited late-time X-ray excess emission on timescales of $\delta t \sim 1 - 2$ d (Grupe et al. 2006; Perley et al. 2009a). However, unlike GRB 130603B, these bursts both had corresponding behavior in the optical bands (Malesani et al. 2007b; Perley et al. 2009a), suggesting that the optical and X-ray emission were from the same emitting region.

7.6 Comparison to Previous Short GRBs

The broad-band afterglow observations of GRB 130603B provide the second detection of a multi-wavelength jet break in a short GRB, and the first detection of a jet break in the radio band. Radio afterglow emission has thus far been detected in two short GRBs: GRB 050724A (Berger et al. 2005), GRB 051221A (Soderberg et al. 2006b). The ability to monitor the radio afterglow of GRB 130603B at a flux density level of $\lesssim 0.1$ mJy highlights the improved sensitivity of the VLA.

Indeed, the radio evolution can provide an important constraint on the progenitor.

In the context of the compact object binary progenitor, the radioactive decay of r-process elements in the sub-relativistic merger ejecta is predicted to produce transient emission, termed a "kilonova" (Li & Paczyński 1998; Metzger et al. 2010; Goriely et al. 2011; Roberts et al. 2011; Rosswog et al. 2013), which is expected to peak in the NIR (Barnes & Kasen 2013; Kasen et al. 2013; Tanaka & Hotokezaka 2013). Late-time NIR emission in GRB 130603B detected with the *Hubble Space Telescope* (Figure 8.1; Berger et al. 2013a; Tanvir et al. 2013a) has been interpreted as the first detection of a r-process kilonova. An alternative scenario to explain the excess NIR emission of GRB 130603B may be a wide, mildly relativistic component of a structured jet (Jin et al. 2013) which has been used to explain the light curve behavior of a handful of long GRBs (e.g., Berger et al. 2003b; Sheth et al. 2003; Peng et al. 2005; Racusin et al. 2008). In this scenario, the predicted radio emission is similarly boosted, and will be $\approx 80\,\mu$Jy at $\delta t \approx 84$ d, the time of our final radio observations (Jin et al. 2013). Instead, the non-detection of any radio emission to $\lesssim 34\,\mu$Jy provides a strong constraint on the existence of a two component jet, and supports the kilonova interpretation of the NIR emission.

The detection of a jet break in GRB 130603B leads to an opening angle measurement of $4 - 14^\circ$, with a more likely range of $4 - 8^\circ$. This opening angle is the fourth[3] such measurement for a short GRB after GRB 051221A (7°; Soderberg et al. 2006b), GRB 090426 ($5 - 7^\circ$; Nicuesa Guelbenzu et al. 2011), and GRB 111020A ($3 - 8^\circ$; Fong et al. 2012b). From these four short GRB opening angle measurements, the median is $\langle \theta_j \rangle \approx 6^\circ$ (Figure 7.3).

[3]We note that Nicuesa Guelbenzu et al. (2012a) claimed a jet break in the GRB 090305A afterglow but this is based on a single optical data point.

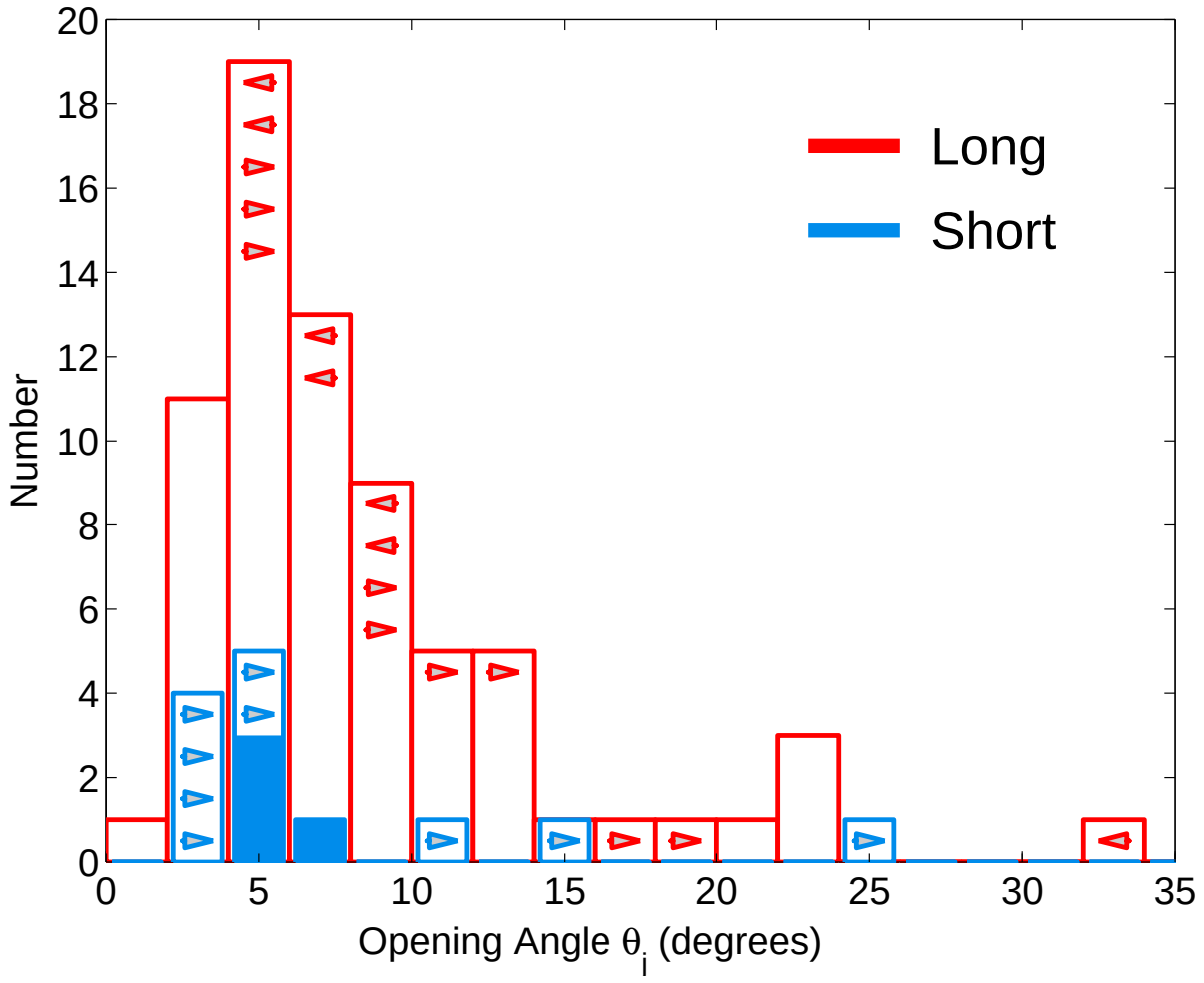

Figure 7.3.—: Distribution of opening angles for long (red) and short (blue) GRBs, updated from Fong et al. (2012b). Arrows represent upper and lower limits. The long GRB population includes pre-*Swift* (Frail et al. 2001; Berger et al. 2003a; Bloom et al. 2003; Ghirlanda et al. 2004; Friedman & Bloom 2005), *Swift* (Racusin et al. 2009; Filgas et al. 2011), and *Fermi* (Cenko et al. 2010b; Goldstein et al. 2011; Cenko et al. 2011) bursts. For short GRBs, the existing measurements are GRB 051221A (7°; Soderberg et al. 2006b), GRB 090426 ($5-7°$, assigned 6° here; Nicuesa Guelbenzu et al. 2011), GRB 111020A ($3-8°$, assigned 5.5° here; Fong et al. 2012b) and GRB 130603B ($4-8°$, assigned 6° here; this work). Short GRB lower limits are from the non-detection of jet breaks in *Swift*/XRT data (Fong et al. 2012b), *Chandra* data for GRBs 050724A (Grupe et al. 2006), 101219A (Fong et al. 2013), 111117A (Margutti et al. 2012; Sakamoto et al. 2013), and 120804A (Berger et al. 2013b) and optical data for GRBs 050709 (Fox et al. 2005) and 081226A (Nicuesa Guelbenzu et al. 2012a).

The non-detections of jet breaks can provide lower limits on the opening angles, assuming on-axis orientation, as off-axis observing angles could disguise jet breaks (van Eerten & MacFadyen 2012, 2013). Indeed, such non-detections to timescales of ~ 1 day with *Swift*/XRT have led to lower limits of $\theta_j \gtrsim 2 - 6^\circ$ (Fong et al. 2012b), while monitoring with more sensitive instruments such as *Chandra* and *XMM-Newton* to timescales of ~ 1 week has led to more meaningful limits of $\theta_j \gtrsim 10 - 25^\circ$ (Figure 7.3; Fox et al. 2005; Grupe et al. 2006; Berger et al. 2013b). The search for jet breaks has been less fruitful in the optical bands, primarily due to the intrinsic faintness of the optical afterglows and contamination from host galaxies. Indeed, the sole lower limit from a well-sampled optical light curve is from GRB 081226A, with $\theta_j \gtrsim 3^\circ$ (Nicuesa Guelbenzu et al. 2012a), while we conservatively adopt a lower limit of $\theta_j \gtrsim 15^\circ$ for GRB 050709 based on a sparsely-sampled optical light curve (Fox et al. 2005). Using the measured opening angles and lower limits of $\gtrsim 10 - 25^\circ$, a likely median for short GRBs is $\langle \theta_j \rangle \approx 10^\circ$.

The opening angle distribution of short GRBs impacts the true energy scale and event rate. The true energy is lower than the isotropic-equivalent value by the beaming factor, f_b ($f_b \equiv 1 - \cos(\theta_j)$, $E = f_b E_{\rm iso}$), while the actual event rate is increased by f_b^{-1}. For GRB 130603B, with an opening angle of $\approx 4 - 8^\circ$, the resulting beaming factor is $f_b \approx (0.2 - 1) \times 10^{-2}$. Therefore, the true energies are $E_\gamma \approx (0.5 - 2) \times 10^{49}$ erg and $E_K \approx (0.1 - 1.6) \times 10^{49}$ erg. The small population of short GRBs with well-constrained opening angles have beaming-corrected energies of $E_\gamma \approx E_K \approx 10^{49}$ erg (Soderberg et al. 2006b; Burrows et al. 2006; Grupe et al. 2006; Fong et al. 2012b; Nicuesa Guelbenzu et al. 2012a), roughly two orders of magnitude below the inferred true energies for long GRBs (Frail et al. 2001; Bloom et al. 2003; Kocevski & Butler 2008; Racusin et al. 2009).

The true event rate is elevated compared to the observed rate by f_b^{-1}. The current estimated observed short GRB volumetric rate is ≈ 10 Gpc^{-3} yr^{-1} (Nakar et al. 2006). For a median opening angle of $\approx 10^\circ$, the median inverse beaming factor is $f_b^{-1} \approx 70$, resulting in a true rate of ≈ 700 Gpc^{-3} yr^{-1}. The observed all-sky event rate of ≈ 0.3 yr^{-1} within 200 Mpc (Guetta & Piran 2005) then becomes ≈ 20 yr^{-1}. This rate is comparable to estimates for NS-NS merger detections with Advanced LIGO/VIRGO (LIGO Scientific Collaboration et al. 2013).

7.7 Conclusions

We presented broad-band observations of the afterglow of GRB 130603B, uncovering a jet break in the optical and radio light curves at $\delta t \approx 0.47$ d. This comprehensive data set marks the first detection of a jet break in the radio band and the third radio afterglow detection in nearly a decade of follow-up. The inferred opening angle is $\theta_j \approx 4 - 8^\circ$, leading to true energy releases of $E_\gamma \approx E_K \approx 10^{49}$ erg.

We observe excess X-ray emission at $\gtrsim$1 day with no corresponding emission in the other bands. We rule out energy injection from ongoing activity from the central engine due to the non-detection of any radio or optical emission on a similar timescale. We find that fall-back accretion can explain the late-time excess only if the radiative efficiency is $\gtrsim 10\%$. Finally, we consider that the emission is due to the spin-down of a massive magnetar and find that a model characterized by a spin period of ≈ 1 ms and magnetic field of $\approx 10^{15}$ G provides a good fit to the emission at $\delta t \gtrsim 1$ d, but underpredicts the X-ray emission at $\lesssim 3000$ s. Furthermore, we show that the merger ejecta are transparent to soft X-rays (also see Appendix), ensuring that the engine can be viewed in X-rays.

GRB 130603B highlights the importance of multi-wavelength afterglow observations, which provide the only route to constraints on the basic explosion properties of GRBs. In particular, the radio band is advantageous because unlike the optical, it does not typically suffer from host galaxy contamination, and can provide an additional constraint on the circumburst density. Thus, continued target-of-opportunity efforts at the VLA will provide invaluable information on the sub-parsec explosion environments. In addition, the non-detection of late-time radio emission, coupled with the detection of NIR excess emission, can provide unambiguous support for the kilonova interpretation for future events, as it has for GRB 130603B.

The opening angle determination for GRB 130603B is the fourth robust jet break measurement for a short GRB. Using realistic assumptions for the opening angle distribution, this implies a conservative volumetric event rate of ≈ 700 Gpc^{-3} yr^{-1}, and an all-sky event rate of ≈ 20 yr^{-1} within 200 Mpc, consistent with the predictions of NS-NS merger detections with Advanced LIGO/VIRGO. However, the opening angle distribution for wider jets of $\gtrsim 5^\circ$ is poorly constrained, and it is necessary to continue monitoring short GRB afterglows to late times to characterize this part of the distribution.

7.8 Appendix

7.8.1 Re-ionization Model

The average density of the freely-expanding ejecta decreases with time as $\rho_{\rm ej} \simeq M_{\rm ej}/(4\pi/3R_{\rm ej}^3)$, where $M_{\rm ej}, R_{\rm ej} = v_{\rm ej}t$ is the ejecta radius, and $v_{\rm ej}$ is the ejecta velocity.

The ionization state of the ejecta is determined by comparing the absorption rate of ionizing photons $\mathcal{R}_{\rm ion} = \mathcal{C} n_{\gamma,\nu\gtrsim\nu_1}\sigma_{\nu_1}c$ (per ion) to the rate of recombination $\mathcal{R}_{\rm rec} = n_e\alpha_{\rm rec}$, where $n_{\gamma,\nu>\nu_1} = L_{\rm X}/4\pi h\nu_1 R_{\rm ej}^2 c$ is the number density of ionizing photons; $\mathcal{C}$ is a constant of order unity that depends on the spectrum of the ionizing radiation; L_{ν_1} is the specific X-ray luminosity near the ionization threshold energy $h\nu_1 \sim 10$ keV; $\sigma_{\nu_1} \simeq 8\times10^{-21}$ cm^2 is the photoionization cross section at $\nu = \nu_1$ and $n_e \simeq \rho_{\rm ej}/2m_p$ is the number density of electrons in the ejecta; $\alpha_{\rm rec} \approx 2.0\times10^{-10}T_4^{-0.8}$ cm^3 s^{-1} is the [type 2] recombination coefficient (e.g. Osterbrock & Ferland 2006); and $T_4 \sim 1$ is the ejecta temperature in units of 10^4 K. The above results can be combined to determine the ratio of the bound-free $\kappa_{\rm bf} = f_{\rm n}\sigma_{\nu_1}/26m_p$ and electron scattering $\kappa_{\rm es} = 0.2$ cm^2 g^{-1} opacities of the ejecta, where $f_{\rm n} \approx \mathcal{R}_{\rm rec}/\mathcal{R}_{\rm ion} \ll 1$ is the neutral fraction (set by the balance between ionization and recombination rates). The resulting coefficient is in Equation 7.3, from which it is shown that the ejecta is sufficiently ionized for the observed X-rays to originate directly from the central engine interior to the ejecta.

One might be concerned that an X-ray source of sufficient luminosity to ionize the ejecta along the observer line of site (perpendicular to the merger plane) would also be sufficient to ionize matter ejected in the equator, the radioactive heating of which powers the optical/NIR kilonova emission. Indeed, the red colors of the kilonova result from the high line opacity of the lanthanides, which would vanish were the ejecta ionized by the central engine. However, equation (7.3) shows that $\kappa_{\rm bf}/\kappa_{\rm es} \propto L_X^{-1}t^{-1}$ is larger for the equatorial ejecta (due to its larger mass $M_{\rm ej}$ and lower velocity $v_{\rm ej}$), and that this ratio increases with time $\propto t$ (since $L_X \propto t^{-2}$, approximately). The fact that $\kappa_{\rm bf}/\kappa_{\rm es}$ may be sigificantly $\gg 1$ for the equatorial kilonova ejecta implies that the latter may remain neutral, preserving the kilonova emission. However, more detailed calculations, including

the different (and uncertain) recombination rates of the lanthanides, is necessary to verify this conclusion.

We thank Barry Madore for obtaining Magellan observations. We thank the VLA staff for rapid response capabilities, and especially Joan Wrobel for scheduling of VLA observations. The Berger GRB group is supported by the National Science Foundation under AST- 1107973. BAZ is supported by an NSF Astronomy and Astrophysics Postdoctoral Fellowship under award AST-1302954. VLA observations were obtained under Program 13A-046. The National Radio Astronomy Observatory is a facility of the National Science Foundation operated under cooperative agreement by Associated Universities, Inc. This paper includes data gathered with the 6.5 meter Magellan Telescopes located at Las Campanas Observatory, Chile. This work made use of data supplied by the UK Swift Science Data Centre at the University of Leicester. This work is based on observations obtained with XMM-Newton, an ESA science mission with instruments and contributions directly funded by ESA Member States and the USA (NASA).

Chapter 8

A Decade of Short-duration Gamma-ray Burst Broad-band Afterglows: Energetics and Circumburst Densities

W. Fong, E. Berger, R. Margutti & B. A. Zauderer

Abstract

We present the first comprehensive catalog and analysis of broad-band afterglow observations for 86 short-duration gamma-ray bursts (GRBs). This sample comprises all short GRBs from November 2004 to March 2014 with prompt follow-up observations in the X-ray, optical, near-infrared and/or radio bands. These observations have uncovered 60 X-ray afterglows, 26 optical/NIR afterglows, and 3 radio afterglows. Employing the standard synchrotron model for the afterglow emission, we perform joint probability analysis for a subset of 32 short GRBs with well-sampled light curves to infer the burst isotropic-equivalent energies and circumburst densities. We find median isotropic-equivalent γ-ray and kinetic energies of $\approx (1-2) \times 10^{51}$ erg. Our results also indicate that short GRBs occur in low-density environments, with a median density scale of $\approx (0.4-2) \times 10^{-3}$ cm^{-3}, depending on the microphysical parameters. Furthermore, $\gtrsim 75\%$ have densities of $\lesssim 1$ cm^{-3}. We investigate trends between the circumburst densities and host galaxy properties, and find that events located at large projected offsets from their hosts of $\gtrsim 10$ effective radii have very low densities of $\lesssim 10^{-4}$ cm^{-3}, consistent with an IGM-like environment. We otherwise find no other obvious trends between circumburst density, the locations within their hosts, and host galaxy type. Finally, we investigate the effects of the inferred energy and circumburst density scales on the detectability of other electromagnetic counterparts to compact object binary mergers, which are the leading progenitors of short GRBs.

8.1 Introduction

The afterglows of gamma-ray bursts (GRBs) provide a unique way to probe their basic properties: the energetics, circumburst densities, and jet opening angles. Over fifteen years of long GRB ($T_{90} > 2$ s; Kouveliotou et al. 1993) afterglow observations have led to beaming-corrected kinetic energy releases of $\approx 10^{51}$ erg (Frail et al. 2001; Berger et al. 2003a; Friedman & Bloom 2005; Gehrels et al. 2008; Nysewander et al. 2009; Laskar et al. 2014), circumburst densities of $\approx 0.1 - 100$ cm^{-3} (Panaitescu & Kumar 2002; Yost et al. 2003), and opening angles of $\approx 2 - 20^{\circ}$ (Bloom et al. 2003; Frail et al. 2001; Friedman & Bloom 2005; Kocevski & Butler 2008; Racusin et al. 2009). In some cases, the radial density profiles of their circumburst environments reflect the wind environments expected for massive stars (Chevalier & Li 2000; Yost et al. 2003).

In contrast, the afterglows of short GRBs ($T_{90} \lesssim 2$ s) are uniformly fainter (Gehrels et al. 2008; Nysewander et al. 2009; Berger 2010a). Therefore, they have primarily been utilized for providing precise burst localization, and thus robust associations to host galaxies. These host studies have revealed that at least some short GRBs originate from older stellar populations, and are distinct in their global properties from the hosts of long GRBs (Berger 2009; Leibler & Berger 2010; Fong et al. 2013). The local and galactic environments of short GRBs have provided observational support for a compact object binary merger progenitor involving two neutron stars (NS-NS) or a neutron star and a stellar mass black hole (NS-BH), consistent with theoretical predictions (Eichler et al. 1989; Narayan et al. 1992).

As studies of short GRB host galaxies and their demographics have progressed at a rapid pace, knowledge of their basic explosion properties has been limited by both the

paucity of afterglow detections and the relatively low detection rate of well-localized (∼few arcmin uncertainty) short GRBs from the *Swift* satellite. Furthermore, broad-band information serves to provide tighter constraints on these parameters than single band observations. In the X-ray band, long and short GRBs have comparable afterglow detection rates. While long GRB afterglows are routinely detected in the optical and radio bands (e.g., Kann et al. 2010; Chandra & Frail 2012; Zaninoni et al. 2013), only $\approx 30\%$ of *Swift* short GRBs have detected optical afterglows (Berger 2010a; Fong et al. 2013), and only three radio afterglows have been detected for short GRBs. For these three events, GRBs 050724A, 051221A and 130603B, the inferred densities span a wide range, $\approx 10^{-4} - 10$ cm^{-3}, although they extend to much lower densities than those inferred for long GRBs (Berger et al. 2005; Panaitescu 2006; Soderberg et al. 2006b; Fong et al. 2014). They also have isotropic-equivalent γ-ray and kinetic energies of $\approx 10^{50} - 10^{51}$ erg, two orders of magnitude lower than long GRB values (Soderberg et al. 2006b; Fong et al. 2012b).

The relative difficulty of detecting short GRB afterglows is a direct reflection of a combination of low energies and circumburst densities. Predictions for NS-NS/NS-BH mergers span several orders of magnitude in density, depending on the precise distribution of natal kick velocities, merger timescales, and host galaxy type (Perna & Belczynski 2002; Belczynski et al. 2006). Similarly, different mechanisms of energy extraction to power a relavistic blast-wave can produce energy scales which differ by three orders of magnitude (e.g., Ruffert & Janka 1999b; Rosswog 2005). Constraints on the energies and densities from short GRB afterglows thus offer a way to study these fundamental questions. These basic properties also serve as critical inputs for the detectability of other electromagnetic counterparts to compact object mergers, and will directly affect

follow-up strategies to gravitational wave signals detected with Advanced LIGO/VIRGO.

Taking advantage of the dedicated searches for short GRB afterglows at all wavelengths, we are now in a position to explore these basic properties for a large population of events for the first time. We present the first comprehensive broad-band catalog of short GRB afterglows, representing a decade of observations since the launch of *Swift* in 2004, and use this sample to constrain short GRB energies and circumburst densities. In Section 8.2, we introduce the sample and data reduction methods for X-ray through radio observations. In Section 8.3, we model the temporal and spectral behavior of the afterglows, and use the observations to infer constraints on the energetics and circumburst densities for each burst. In Section 8.4, we present the energetics and circumburst densities for 32 events with well-sampled afterglow data sets. Finally, in Section 8.5, we discuss statistics of afterglow follow-up, implications for the progenitors, and the effect of the basic inferred properties on the detectability of alternative electromagnetic counterparts to gravitational wave sources.

All magnitudes are in the AB system and are corrected for Galactic extinction in the direction of the burst (Schlegel et al. 1998; Schlafly & Finkbeiner 2011), and unless otherwise noted, uncertainties correspond to 1σ confidence. We employ a standard ΛCDM cosmology with $\Omega_M = 0.27$, $\Omega_\Lambda = 0.73$, and $H_0 = 71$ km s^{-1} Mpc^{-1}.

8.2 Observations

8.2.1 Sample

We present radio through X-ray afterglow observations for 86 short GRBs discovered by the *Swift* satellite (Gehrels et al. 2004), *Fermi* satellite (Atwood et al. 2009; Meegan et al. 2009), *Konus-Wind* (Aptekar et al. 1995), High Energy Transient Explorer 2 (HETE-2; Ricker et al. 2003), or the Interplanetary Network (IPN; Hurley et al. 2010) between November 2004 and March 2014. We restrict our sample to all bursts with $T_{90} \lesssim 2$ s and follow-up observations in any of the X-ray, optical, near-infrared (NIR) or radio bands on timescales of $\delta t \lesssim$ few days (where δt corresponds to the time after the γ-ray trigger). We also include three events, GRBs 050724A, 090607 and 100213A, which have $T_{90} \approx 2.5 - 3$ s but which exhibit the spectral hardness and negligible spectral lags typical of short GRBs. Furthermore, for bursts with optical/NIR follow-up, we only include bursts with afterglow detections or meaningful limits of $\gtrsim 20$ mag at $\delta t \lesssim 1$ day. Basic information for the sample of 86 events, including durations, redshifts, and the available follow-up in each observing band is presented in Table 8.1.

Of the 86 bursts in our sample, 78 (91%) have X-ray follow-up observations, 72 (84%) have optical/NIR observations, and 50 (58%) have radio observations. These observations have uncovered 60 X-ray afterglows, 26 optical/NIR afterglows, and 3 radio afterglows. If we only consider the bursts with follow-up observations, the detection fractions increase to 77%, 36%, and 6% in the X-ray, optical/NIR, radio bands, respectively.

We note that 13 of the bursts with X-ray observations had a delayed *Swift* response

due to an observing constraint or burst discovery from another satellite. Likewise, eight bursts with optical/NIR observations have an observing constraint (e.g., crowded field, high Galactic extinction sightline, position contaminated by a bright star), making the detection of an optical afterglow particularly challenging. Taking these observing constraints in to account, we find that 92% (40%) of bursts that have X-ray (optical/NIR) follow-up and no observing constraints result in an afterglow detection.

Twenty-seven bursts in this sample have redshifts from robust associations to a host galaxy, while two events have spectroscopic redshifts from afterglows themselves, GRB 090426A: (Antonelli et al. 2009b; Levesque et al. 2010) and GRB 130603B (Cucchiara et al. 2013; de Ugarte Postigo et al. 2014). In addition to the broad-band afterglow observations that have been published thus far, we present new optical/NIR observations for four bursts, and new radio observations for 15 events.

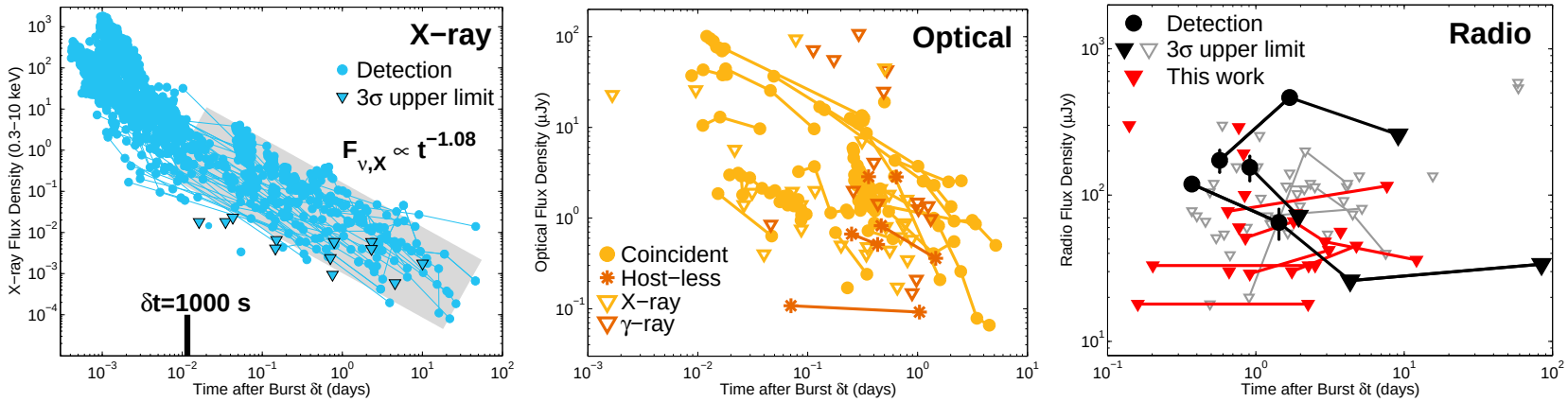

Figure 8.1.—: Broad-band afterglow light curves of all short GRBs with follow-up observations between November 2004 and March 2014. Circles denote detections while triangles indicate 3σ upper limits. Lines connect observations for the same burst. *Left:* 0.3-10 keV X-ray afterglow light curves for 72 short GRBs with X-ray observations. The triangles correspond to 12 bursts with a γ-ray trigger but no detected X-ray afterglow. The data for $\delta t \gtrsim 1000$ sec are used in our subsequent analysis and are listed in Table 8.2. The grey band indicates the median decline rate at $\delta t \gtrsim 1000$ sec of $F_{\nu,X} \propto t^{-1.08}$. *Center:* Optical afterglow light curves for 72 short GRBs corresponding to the events in Table 8.3. The light curves are divided in to four categories: bursts with optical afterglows and coincident host galaxies (orange circles), bursts with optical afterglows and no coincident host (brown asterisks; Berger 2010a; Fong et al. 2013; Tunnicliffe et al. 2013), bursts with an X-ray detection but no optical afterglow (orange triangles) and bursts neither optical nor X-ray afterglow detections (brown triangles). *Right:* Radio afterglow data for 50 short GRBs corresponding to the events in Table 8.4. The light curves for three short GRBs with radio afterglow detections are shown (black; GRBs 050724A, 051221A and 130603B). Fifteen bursts have observations published for the first time in this work (red triangles), while the rest of the limits are collected from the literature (grey triangles; see Table 8.4 for references).

Table 8.1. Short GRB Basic Information

GRB	T_{90} (s)	z	X-ray?	Opt/NIR?	Radio?
050202[a]	0.27	···	···	N	N
050509B	0.04	0.225	Y	N	N
050709	0.07	0.161	Y	Y	N
050724A	3.0	0.257	Y	Y	Y
050813	0.6	0.72/1.8	Y	N	N
050906	0.26	···	N	N	N
050925	0.07	···	N	···	N
051105A	0.09	···	···	N	N
051210	1.3	> 1.4	Y	N	···
051221A	1.4	0.546	Y	Y	Y
060121	2.0	< 4.1	Y	Y	···
060313	0.7	< 1.7	Y	Y	N
060502B	0.09	0.287	Y	N	···
060801	0.5	1.130	Y	N	N
061006	0.4	0.438	Y	Y	···
061201	0.8	0.111?	Y	Y	···
061210	0.2	0.41	Y	N	N
061217	0.2	0.827	Y	N	···
070209	0.09	···	···	N	···

Table 8.1—Continued

GRB	T_{90} (s)	z	X-ray?	Opt/NIR?	Radio?
070406[a]	1.20	···	···	N	···
070429B	0.5	0.902	Y	N	N
070707[a]	1.1	< 3.6	Y	Y	···
070714B	2.0	0.923	Y	Y	N
070724A	0.4	0.457	Y	Y	N
070729	0.9	0.8	Y	N	N
070809	1.3	0.473?	Y	Y	···
070810B	0.08	···	N	N	···
070923[a]	0.05	···	N	···	N
071017[a]	0.5	···	N	···	N
071112B[a]	0.30	···	N	N	N
071227	1.8	0.381	Y	Y	···
080121[a]	0.7	···	N	N	···
080123	0.4	···	Y	N	···
080426	1.7	···	Y	N	···
080503	0.3	< 4.2	Y	Y	N
080702A	0.5	···	Y	N	N
080905A	1.0	0.122	Y	Y	···
080919	0.6	···	Y	N	···
081024A	1.8	···	Y	N	N
081024B[a]	0.4	···	···	N	N

Table 8.1—Continued

GRB	T_{90} (s)	z	X-ray?	Opt/NIR?	Radio?
081226A	0.4	< 4.1	Y	Y	N
081226B[a]	0.7	···	N	N	N
090305A	0.4	< 4.1	Y	Y	···
090417A[a]	0.07	···	···	···	N
090426	1.3	2.609	Y	Y	···
090510	0.3	0.903	Y	Y	N
090515	0.04	0.403?	Y	Y	N
090607	2.3[b]	···	Y	N	···
090621B	0.14	···	Y	N	N
090715A[a]	0.5	···	···	N	N
090916[a]	0.3	···	N	N	···
091109B	0.3	< 4.4	Y	Y	···
091117[a]	0.43	···	···	N	N
100117A	0.30	0.915	Y	Y	···
100206A	0.1	0.407	Y	N	···
100213A	2.4[c]	···	Y	···	···
100625A	0.3	0.452	Y	N	N
100628A	0.04	···	N	N	N
100702A	0.16	···	Y	N	···

Table 8.1—Continued

GRB	T_{90} (s)	z	X-ray?	Opt/NIR?	Radio?
101219A	0.6	0.718	Y	N	···
101224A	0.2	···	Y	···	N
110112A	0.5	< 5.3	Y	Y	N
110112B[a]	0.5	···	N	N	N
110420B[a]	0.08	···	···	N	N
111020A	0.4	···	Y	N	N
111117A	0.5	1.3	Y	N	N
111121A	0.45	···	Y	···	N
111222A[a]	0.3	···	Y	···	···
120229A[a]	0.22	···	···	N	···
120305A	0.1	···	Y	N	N
120521A	0.45	···	Y	N	N
120630A[d]	0.6	···	Y	N	···
120804A	0.81	1.3	Y	Y	N
120817B[a]	0.19	···	N	N	···
121226A	1.0	···	Y	N	N
130313A	0.26	···	Y	N	N

Table 8.1—Continued

GRB	T_{90} (s)	z	X-ray?	Opt/NIR?	Radio?
130515A	0.29	···	Y	N	···
130603B	0.18	0.356	Y	Y	Y
130626A	0.16	···	N	···	···
130716A	0.8	···	Y	N	N
130822A	0.04	···	Y	N	N
130912A	0.28	···	Y	Y	N
131004A	1.54	0.717	Y	Y	N
131125A[e]	0.5	···	···	N	···
131126A[e]	0.3	···	···	N	···
131224A[a]	0.8	···	N	N	N

Note. — Short GRBs with X-ray, optical/NIR or radio follow-up observations. "Y" = detection, "N" = non-detection, and ··· means there is no useful follow-up in that band.

[a] Observing constraint or delayed *Swift*/XRT observations.

[b] This burst has $T_{90} = 2.3 \pm 0.1$ s but is spectrally hard (Marshall et al. 2009).

[c] This burst has $T_{90} = 2.4 \pm 0.4$ s, but the spectral lag of 5 ± 15 ms indicates this is a short-hard burst (Grupe et al. 2010).

[d] Delayed reporting of burst due to power outage, preventing useful optical follow-up.

[e] IPN-localized burst with no *Swift*/ follow-up.

8.2.2 X-rays

We gather all available X-ray afterglow observations from the *Swift* light curve repository[1] (Evans et al. 2007a, 2009), the GRB Coordinates Network (GCN) Circulars, and the literature (Table 8.2). The data were taken with the X-ray Telescope (XRT) on-board *Swift*, the *Chandra* X-ray Observatory, and the X-ray Multi-Mirror Mission (*XMM-Newton*). We use unabsorbed fluxes and uncertainties in the 0.3-10 keV energy band when they are available; otherwise, we use the count-rate light curves in the same energy range. Since early-time X-ray afterglow light curves are often subject to steep decays, plateaus, or flares which may contaminate the afterglow emission (Nousek et al. 2006; Zhang et al. 2006; Margutti et al. 2011, 2013), we only collect X-ray data for $\delta t \gtrsim 1000$ s, when bursts have typically settled in to the power-law afterglow phase. For bursts with multiple upper limits, we only include those which help to constrain the temporal behavior of the X-ray light curve. Of the 78 short GRBs with X-ray observations, six events[2] have no reported measurements or upper limits beyond 1000 s. Therefore, the resulting late-time X-ray afterglow catalog is comprised of 72 events (Table 8.2).

When applicable, we convert the count rate light curves to unabsorbed fluxes using the count-rate-to-unabsorbed-flux conversion factors provided by the *Swift* light curve repository. These factors are derived from the automatic spectral fitting routine (Evans et al. 2009). This routine fits the X-ray spectrum for each burst to an absorbed power law model characterized by photon index, Γ, and the intrinsic neutral hydrogen absorption

[1] `http://www.swift.ac.uk/xrt_curves`

[2] These events are GRBs 051105A, 070209, 070406, 081024B, 091117, and 110420B.

column, $N_{\rm H,int}$, in excess of the Galactic column density in the direction of the burst (Kalberla et al. 2005; Wakker et al. 2011). We use spectral parameters extracted in the Photon Counting (PC) mode when possible; otherwise, we use parameters from the Windowed Timing (WT) mode. In seven cases, the value of $N_{\rm H,int}$ is highly uncertain, but consistent with zero. Therefore, utilizing the median value of $N_{\rm H,int}$ may result in an over-estimate of the true unabsorbed flux. Instead of using the given conversion factors for these bursts, we calculate the unabsorbed fluxes using WebPIMMS[3], setting $N_{\rm H,int} = 0$. In seven events, no count-rate-to-unabsorbed-flux conversion factor is available, so we employ a fiducial value of 1×10^{-11} erg cm^{-2} s^{-1} ct^{-1} set by the median value for the events in our sample (Table 8.2). Applying these conversion factors to each of the count-rate light curves from *Swift*/XRT, *Chandra* and *XMM-Newton*, we obtain the unabsorbed fluxes and 3σ upper limits for each burst.

To enable comparison of the X-ray light curves to the optical and radio data, we convert the X-ray fluxes to flux densities, $F_{\nu,X}$, at a fiducial energy of 1 keV ($F_{\nu,X} \propto \nu^{\beta_X}$ where $\beta_X \equiv 1 - \Gamma$). When no spectral information is available, we use a fiducial spectral index of $\beta_X = -1$, set by the median value of the events in our sample. The flux densities, uncertainties, and 3σ upper limits are listed in Table 8.2, and the resulting light curves are shown in Figure 8.1.

We perform our own light curve extraction for eighteen bursts which were studied in Fong et al. (2012b). For these bursts, we generate count-rate light curves using the HEASOFT package following the prescriptions from Margutti et al. (2013). Our re-binning scheme ensures a minimum signal-to-noise ratio of $S/N = 4$ for each temporal

[3]https://heasarc.gsfc.nasa.gov/Tools/w3pimms.html

bin. To extract a spectrum, we fit each of the data sets with an absorbed power law model (*tbabs* × *ztbabs* × *pow* within the XSPEC routine) using Cash statistics to obtain Γ, $N_{\rm H,int}$, and thus the count-rate-to-unabsorbed-flux conversion factors. We present these light curves in Table 8.2 and Figure 8.1.

Finally, we present the *Chandra* observation of GRB 120804A at $\delta t \approx 46$ days (PI: D. Burrows), since the afterglow brightness has not been published in the literature thus far. We retrieve the pre-processed Level 2 data from the *Chandra* archive. We use the `CIAO` data reduction package to extract a count-rate within a $2.5''$-radius source aperture centered on the X-ray afterglow position, and utilize source-free regions on the same chip to estimate the background. Using WebPIMMS and the spectral parameters derived from earlier epochs of *Chandra* data for the same burst (Berger et al. 2013b), we convert the count-rate to flux density (Table 8.2).

8.2.3 Optical/NIR

For each burst, we gather all available optical and NIR afterglow observations from the literature and GCN Circulars (see Table 8.3 for references). When there are multiple upper limits for a given burst, we include only the most meaningful limits, set by a combination of the timescale and depth of the observation. We convert all magnitudes to the AB system using instrument-specific conversion factors when available, or the standard conversions following Blanton & Roweis (2007). We correct all observations for Galactic extinction in the direction of each burst (Schlegel et al. 1998; Schlafly & Finkbeiner 2011), and convert AB magnitudes to flux densities, $F_{\nu,\rm opt}$. A log of observations for 72 events with optical/NIR follow-up is provided in Table 8.3, and the light curves and upper limits are shown in Figure 8.1.

We also present optical/NIR observations of four short GRBs that have not been published in the literature thus far: GRBs 100628A, 110420B, 120229A, 130716A. These observations were enabled by Target-of-Opportunity programs on the twin 6.5-m Magellan telescopes (PI: E. Berger) and the 8-m Gemini telescopes (PI: E. Berger, D. Fox, N. Tanvir, A. Cucchiara). We use standard tasks in the IRAF `ccdred` package to process the Magellan data and the IRAF `gemini` package to process the Gemini data. For each of these bursts, we obtained the first epoch of observations at $\delta t \lesssim 1 - 20$ hr and a second set of observations at $\delta t \gtrsim 24$ hr (Table 8.3). To assess any fading between the two epochs, we perform digital image subtraction for each burst and filter using the ISIS software (Alard 2000). Using the second epoch as a template, we find no residuals in any of the subtracted images. We therefore use aperture photometry to place 3σ upper limits on the optical/NIR afterglow brightness. The observational details and 3σ

Table 8.2. Short GRB Late-time X-ray afterglow catalog

GRB	δt (s)	Exposure Time (s)	F_X (μJy)	σ_X (μJy)	References
050509B	831	381	0.07	0.02	Gehrels et al. (2005)
	6.2×10^3	2.0×10^3	< 0.02		
	$^{+}2.1 \times 10^5$	5.0×10^4	$< 8.0 \times 10^{-3}$		
050709	1.4×10^5	1.5×10^4	1.9×10^{-3}	1.4×10^{-4}	Fox et al. (2005)
	2.1×10^5	5.0×10^3	$< 1.5 \times 10^{-3}$		
	$^{+}2.2 \times 10^5$	3.8×10^4	1.1×10^{-3}	2.0×10^{-5}	
	2.8×10^5	6.4×10^3	$< 7.3 \times 10^{-4}$		
	3.7×10^5	2.1×10^3	$< 5.9 \times 10^{-3}$		
	$^{+}1.4 \times 10^6$	6.1×10^3	1.3×10^{-3}	6.0×10^{-5}	
	$^{+}1.4 \times 10^6$	1.2×10^4	1.1×10^{-4}	2.0×10^{-5}	
050724A	1.0×10^3	514	0.43	0.086	Grupe et al. (2006)
	1.4×10^3	323	0.68	0.14	
	1.9×10^3	493	0.44	0.090	
	6.6×10^3	2.0×10^3	0.091	0.022	
	1.3×10^4	3.4×10^3	0.050	0.013	
	2.5×10^4	1.9×10^3	0.10	0.023	
	3.5×10^4	805	0.27	0.056	
	3.7×10^4	1.2×10^3	0.19	0.039	
	4.1×10^4	830	0.26	0.053	
	4.2×10^4	652	0.32	0.068	
	4.2×10^4	772	0.27	0.057	
	4.7×10^4	1.2×10^3	0.18	0.038	
	4.8×10^4	880	0.24	0.050	
	4.8×10^4	790	0.27	0.056	
	5.2×10^4	587	0.37	0.075	
	5.3×10^4	800	0.27	0.055	
	5.8×10^4	759	0.29	0.058	
	5.9×10^4	554	0.39	0.080	
	6.3×10^4	972	0.22	0.046	
	6.6×10^4	1.0×10^3	0.20	0.044	
	7.7×10^4	1.6×10^3	0.11	0.027	
	8.8×10^4	2.0×10^3	0.10	0.023	
	9.9×10^4	1.2×10^3	0.090	0.028	
	1.4×10^5	4.4×10^3	0.025	8.4×10^{-3}	
	1.5×10^5	4.0×10^3	0.027	9.5×10^{-3}	
	1.8×10^5	7.0×10^3	0.012	5.5×10^{-3}	
	2.2×10^5	2.1×10^3	0.014	8.4×10^{-3}	
	5.6×10^5	4.7×10^4	1.4×10^{-3}	7.8×10^{-4}	

Table 8.2—Continued

GRB	δt (s)	Exposure Time (s)	F_X (μJy)	σ_X (μJy)	References
	$^{+}2.1 \times 10^5$	8.3×10^3	6.0×10^{-3}	1.1×10^{-3}	
	$^{+}2.1 \times 10^5$	9.6×10^3	5.1×10^{-3}	9.7×10^{-4}	
	$^{+}2.3 \times 10^5$	1.2×10^4	3.9×10^{-3}	7.5×10^{-4}	
	$^{+}2.4 \times 10^5$	1.3×10^4	3.8×10^{-3}	7.2×10^{-4}	
	$^{+}2.5 \times 10^5$	6.5×10^3	5.4×10^{-3}	1.2×10^{-3}	
	$^{+}1.9 \times 10^6$	4.3×10^4	3.3×10^{-4}	1.2×10^{-4}	
050813	4.7×10^3	2.7×10^5	3.4×10^{-3}	1.0×10^{-3}	Evans et al. (2007a, 2009)
	6.5×10^5	3.4×10^5	$<2.7 \times 10^{-3}$		
050906	3.0×10^3	5.2×10^3	< 0.018		Pagani et al. (2005)
050925	1.4×10^3	1.4×10^3	$<6.6 \times 10^{-3}$		Beardmore et al. (2005)
051210	894	840	0.40	0.15	This work
051221A	1.4×10^3	512	0.86	0.10	Burrows et al. (2006)
	1.9×10^3	512	0.59	0.085	Soderberg et al. (2006b)
	2.4×10^3	512	0.43	0.082	
	5.3×10^3	3.5×10^3	0.23	0.033	
	8.8×10^3	3.5×10^3	0.24	0.035	
	1.2×10^4	3.5×10^3	0.25	0.026	
	1.6×10^4	3.5×10^3	0.20	0.076	
	1.9×10^4	3.5×10^3	0.16	0.021	
	2.3×10^4	3.5×10^3	0.11	0.023	
	2.6×10^4	3.5×10^3	0.11	0.026	
	3.0×10^4	3.5×10^3	0.088	0.015	
	3.7×10^4	3.5×10^3	0.13	0.020	
	4.5×10^4	1.0×10^4	0.079	0.011	
	5.5×10^4	1.0×10^4	0.066	0.010	
	1.0×10^5	4.1×10^4	0.017	2.7×10^{-3}	
	1.4×10^5	4.1×10^4	0.018	2.9×10^{-3}	
	2.0×10^5	5.7×10^4	0.013	1.9×10^{-3}	
	2.5×10^5	5.7×10^4	0.014	2.0×10^{-3}	
	3.1×10^5	5.7×10^4	9.0×10^{-3}	1.7×10^{-3}	
	3.8×10^5	8.6×10^4	5.2×10^{-3}	1.0×10^{-3}	
	4.7×10^5	8.6×10^4	5.8×10^{-3}	1.1×10^{-3}	
	5.5×10^5	8.6×10^4	4.4×10^{-3}	9.4×10^{-4}	
	6.4×10^5	8.3×10^4	3.6×10^{-3}	9.4×10^{-4}	
	7.3×10^5	8.2×10^4	5.4×10^{-3}	1.0×10^{-3}	
	9.8×10^5	4.1×10^5	2.3×10^{-3}	4.1×10^{-4}	
	$^{+}1.3 \times 10^5$	5.4×10^3	0.022	2.2×10^{-3}	
	$^{+}1.4 \times 10^5$	5.5×10^3	0.021	2.1×10^{-3}	

Table 8.2—Continued

GRB	δt (s)	Exposure Time (s)	F_X (μJy)	σ_X (μJy)	References
	$^{+}1.4 \times 10^5$	6.4×10^3	0.018	1.9×10^{-3}	
	$^{+}1.5 \times 10^5$	6.6×10^3	0.018	1.8×10^{-3}	
	$^{+}1.6 \times 10^5$	6.3×10^3	0.017	1.8×10^{-3}	
	$^{+}3.9 \times 10^5$	9.5×10^3	6.1×10^{-3}	8.8×10^{-4}	
	$^{+}4.0 \times 10^5$	1.0×10^4	5.5×10^{-3}	8.0×10^{-4}	
	$^{+}4.1 \times 10^5$	1.0×10^4	5.3×10^{-3}	7.9×10^{-4}	
	$^{+}1.3 \times 10^6$	1.8×10^4	5.5×10^{-4}	1.9×10^{-4}	
	$^{+}1.7 \times 10^6$	2.5×10^4	3.8×10^{-4}	1.4×10^{-4}	
	$^{+}2.3 \times 10^6$	4.8×10^4	1.9×10^{-4}	7.2×10^{-5}	
060121	1.1×10^4	153	0.61	0.14	Evans et al. (2007a, 2009)
	1.1×10^4	221	0.42	0.095	
	1.1×10^4	206	0.45	0.10	
	1.1×10^4	198	0.47	0.11	
	1.1×10^4	208	0.34	0.087	
	1.2×10^4	178	0.52	0.12	
	1.2×10^4	183	0.51	0.12	
	1.2×10^4	155	0.60	0.14	
	1.2×10^4	193	0.36	0.094	
	1.2×10^4	338	0.37	0.072	
	1.6×10^4	281	0.27	0.069	
	1.6×10^4	308	0.24	0.063	
	1.6×10^4	196	0.39	0.10	
	1.7×10^4	258	0.29	0.076	
	1.7×10^4	246	0.31	0.080	
	1.7×10^4	236	0.32	0.083	
	1.8×10^4	221	0.34	0.089	
	1.8×10^4	201	0.38	0.10	
	1.8×10^4	617	0.19	0.039	
	2.2×10^4	361	0.23	0.056	
	7.0×10^4	1.3×10^3	0.060	0.015	
	7.5×10^4	2.5×10^3	0.030	7.9×10^{-3}	
	8.1×10^4	2.3×10^3	0.053	0.011	
	8.9×10^4	7.6×10^3	0.043	8.0×10^{-3}	
	1.6×10^5	1.2×10^4	0.021	4.9×10^{-3}	
	1.7×10^5	1.9×10^3	0.038	0.010	
	1.8×10^5	7.3×10^3	0.033	7.2×10^{-3}	

Table 8.2—Continued

GRB	δt (s)	Exposure Time (s)	F_X (μJy)	σ_X (μJy)	References
	2.0×10^5	3.6×10^4	0.012	3.2×10^{-3}	
	2.5×10^5	4.9×10^4	0.013	3.4×10^{-3}	
	3.1×10^5	6.5×10^4	7.7×10^{-3}	2.1×10^{-3}	
	4.2×10^5	1.5×10^5	4.1×10^{-3}	1.2×10^{-3}	
	6.3×10^5	2.8×10^5	3.5×10^{-3}	9.7×10^{-4}	
	1.0×10^6	8.3×10^4	1.8×10^{-3}	8.5×10^{-4}	
060313	4.2×10^3	161	1.3	0.52	This work
	4.3×10^3	92	1.4	0.52	
	4.4×10^3	97	1.7	0.62	
	4.5×10^3	128	1.2	0.43	
	4.7×10^3	113	1.2	0.45	
	4.8×10^3	113	1.1	0.39	
	4.9×10^3	128	1.1	0.43	
	5.0×10^3	65	2.4	0.91	
	5.1×10^3	133	0.91	0.33	
	5.2×10^3	146	0.83	0.30	
	5.4×10^3	176	0.64	0.23	
	5.5×10^3	163	0.75	0.27	
	5.7×10^3	95	1.4	0.54	
	5.8×10^3	211	0.61	0.23	
	6.0×10^3	125	1.2	0.46	
	6.1×10^3	153	0.85	0.31	
	6.3×10^3	125	1.0	0.38	
	6.5×10^3	286	0.96	0.30	
	1.0×10^4	301	0.38	0.14	
	1.0×10^4	309	0.43	0.16	
	1.1×10^4	228	0.66	0.25	
	1.1×10^4	243	0.47	0.17	
	1.1×10^4	266	0.44	0.16	
	1.1×10^4	384	0.346	0.13	
	1.2×10^4	344	0.36	0.13	
	1.2×10^4	459	0.37	0.12	
	1.6×10^4	602	0.19	0.069	
	1.6×10^4	412	0.29	0.11	
	1.7×10^4	414	0.27	0.10	
	1.8×10^4	1.1×10^3	0.25	0.078	
	2.2×10^4	934	0.11	0.043	
	2.3×10^4	545	0.20	0.075	

Table 8.2—Continued

GRB	δt (s)	Exposure Time (s)	F_X (μJy)	σ_X (μJy)	References
	2.3×10^4	1.1×10^3	0.13	0.047	
	2.8×10^4	781	0.15	0.057	
	2.9×10^4	1.8×10^3	0.089	0.031	
	3.4×10^4	2.5×10^3	0.061	0.022	
	4.2×10^4	6.3×10^3	0.058	0.024	
	5.2×10^4	1.2×10^4	0.036	0.014	
	8.7×10^4	5.9×10^4	0.013	5.4×10^{-3}	
	2.7×10^5	3.1×10^5	3.6×10^{-3}	1.2×10^{-3}	
060502B	3.8×10^4	6.6×10^4	$<1.0 \times 10^{-3}$		Evans et al. (2007a, 2009)
060801	918	954	0.20	0.077	This work
061006	3.6×10^3	670	0.12	0.067	This work
	4.4×10^3	997	0.11	0.060	
	9.4×10^3	4.9×10^3	0.046	0.026	
	1.4×10^4	4.7×10^3	0.054	0.030	
	6.6×10^4	2.4×10^5	6.0×10^{-3}	3.3×10^{-3}	
061201	5.7×10^3	238	0.55	0.31	This work
	5.9×10^3	188	0.56	0.31	
	6.1×10^3	238	0.45	0.26	
	6.4×10^3	264	0.66	0.34	
	1.2×10^4	5.9×10^3	0.11	0.072	
	2.1×10^4	1.2×10^4	0.055	0.036	
	6.7×10^4	1.3×10^5	4.8×10^{-3}	2.9×10^{-3}	
061210	2.3×10^5	5.3×10^4	0.048	0.013	Evans et al. (2007a, 2009)
	3.1×10^5	9.4×10^4	0.026	8.0×10^{-3}	
	4.2×10^5	1.3×10^5	0.018	6.0×10^{-3}	
	7.0×10^5	4.9×10^5	< 0.014		
061217	6.0×10^4	3.2×10^5	$<2.5 \times 10^{-3}$		Evans et al. (2007a, 2009)
070429B	1.6×10^3	2.0×10^3	0.32	0.080	Evans et al. (2007a, 2009)
	1.6×10^4	3.6×10^4	< 0.024		
070707[a]	4.1×10^4	2.2×10^4	0.15	0.032	Evans et al. (2007a, 2009)
	4.1×10^5	1.9×10^5	< 0.032		
070714B	8.5×10^2	116	2.0	0.64	This work
	2.8×10^3	183	0.40	0.18	
	3.1×10^3	311	0.24	0.11	
	3.6×10^3	675	0.19	0.09	
	5.9×10^3	417	0.15	0.075	

Table 8.2—Continued

GRB	δt (s)	Exposure Time (s)	F_X (μJy)	σ_X (μJy)	References
	6.5×10^3	795	0.12	0.058	
	9.2×10^3	1.4×10^3	0.054	0.027	
	2.9×10^4	5.8×10^4	3.0×10^{-3}	1.7×10^{-3}	
070724A	4.6×10^3	4.8×10^3	0.055	0.032	This work
	1.1×10^4	7.6×10^3	0.026	0.014	
	1.8×10^4	5.2×10^3	0.024	0.013	
	2.6×10^4	1.2×10^4	0.014	7.5×10^{-3}	
	5.3×10^4	5.5×10^4	0.010	5.4×10^{-3}	
	1.8×10^5	3.0×10^5	1.8×10^{-3}	5.9×10^{-4}	
070729	2.0×10^4	6.6×10^4	$<3.8 \times 10^{-3}$		Evans et al. (2007a, 2009)
070809	1.1×10^3	271	0.27	0.13	This work
	1.6×10^3	660	0.20	0.080	
	5.5×10^3	321	0.23	0.11	
	5.9×10^3	507	0.14	0.068	
	6.3×10^3	366	0.23	0.11	
	6.8×10^3	555	0.13	0.062	
	7.4×10^3	673	0.12	0.058	
	1.1×10^4	673	0.10	0.047	
	1.2×10^4	803	0.093	0.044	
	1.3×10^4	989	0.085	0.039	
	1.8×10^4	2.6×10^3	0.038	0.017	
	2.4×10^4	2.0×10^3	0.050	0.021	
071017[c]	2.0×10^5	2.1×10^3	$<5.9 \times 10^{-3}$		Evans et al. (2007b)
071112B[a]	3.7×10^3	2.2×10^3	< 0.023		Perri et al. (2007)
071227	6.2×10^3	9.5×10^3	0.022	9.8×10^{-3}	This work
	5.7×10^4	2.5×10^5	2.6×10^{-3}	8.6×10^{-4}	
080121	2.0×10^5	2.2×10^4	$<4.0 \times 10^{-3}$		Troja et al. (2008a)
081023	1.4×10^3	1.7×10^3	0.072	0.024	This work
	1.8×10^4	5.3×10^4	9.5×10^{-3}	3.2×10^{-3}	
080426	1.1×10^3	100	2.13	0.48	Evans et al. (2007a, 2009)
	1.2×10^3	148	1.4	0.32	
	1.3×10^3	95	2.2	0.50	
	1.4×10^3	108	2.1	0.45	
	1.5×10^3	125	1.7	0.38	
	1.7×10^3	211	1.01	0.23	
	1.9×10^3	191	1.44	0.29	

Table 8.2—Continued

GRB	δt (s)	Exposure Time (s)	F_X (μJy)	σ_X (μJy)	References
	6.2×10^3	258	0.65	0.17	
	6.6×10^3	687	0.24	0.063	
	7.5×10^3	978	0.19	0.047	
	1.3×10^4	2.1×10^3	0.11	0.025	
	2.1×10^4	8.1×10^3	0.056	0.012	
	3.8×10^4	2.0×10^4	0.021	5.7×10^{-3}	
	7.0×10^4	4.2×10^4	4.9×10^{-3}	2.8×10^{-3}	
080503	920	1.1×10^3	0.45	0.18	This work
	$^{+c}3.9 \times 10^5$	3.2×10^4	2.1×10^{-3}	9.6×10^{-4}	Perley et al. (2009a)
	$^{+}1.9 \times 10^6$	3.3×10^4	$< 8.0 \times 10^{-5}$		Perley et al. (2009a)
080702A	3.9×10^3	2.2×10^4	0.041	8.9×10^{-3}	Evans et al. (2007a, 2009)
	7.5×10^4	7.6×10^4	< 0.013		
080905A	758	593	0.74	0.31	This work
080919	1.0×10^3	1.5×10^3	0.39	0.20	This work
	3.0×10^4	1.7×10^5	5.9×10^{-3}	5.7×10^{-3}	
081024A	597	1.6×10^3	0.39	0.070	Evans et al. (2007a, 2009)
	1.5×10^4	3.7×10^4	$<3.2 \times 10^{-3}$		
081226A	1.6×10^4	4.3×10^4	0.026	0.014	Evans et al. (2007a, 2009)
081226B[a]	1.3×10^4	8.0×10^3	$<6.6 \times 10^{-3}$		Evans & Hoversten (2008)
090305A[b]	4.8×10^3	1.3×10^4	$<2.0 \times 10^{-3}$		Beardmore et al. (2009)
090426	1.0×10^3	95	1.2	0.26	Evans et al. (2007a, 2009)
	1.1×10^3	108	1.0	0.23	
	1.2×10^3	95	1.2	0.26	
	1.4×10^3	145	0.77	0.17	
	1.5×10^3	92	1.2	0.27	
	1.6×10^3	100	1.1	0.25	
	1.7×10^3	178	0.62	0.14	
	1.9×10^3	243	0.45	0.10	
	2.2×10^3	221	0.68	0.13	
	5.6×10^3	346	0.27	0.072	
	6.0×10^3	351	0.27	0.071	
	6.4×10^3	481	0.20	0.051	
	6.9×10^3	479	0.20	0.051	
	7.6×10^3	938	0.18	0.035	
	1.8×10^4	1.2×10^4	0.060	0.013	
	2.3×10^5	7.5×10^5	1.5×10^{-3}	6.5×10^{-4}	
090510	1.0×10^3	31	2.7	1.0	This work
	2.8×10^3	89	0.61	0.26	

Table 8.2—Continued

GRB	δt (s)	Exposure Time (s)	F_X (μJy)	σ_X (μJy)	References
	2.9×10^3	141	0.47	0.21	
	3.1×10^3	174	0.37	0.17	
	3.3×10^3	338	0.18	0.081	
	3.6×10^3	251	0.22	0.10	
	3.9×10^3	321	0.18	0.084	
	6.2×10^3	770	0.051	0.027	
	6.8×10^3	547	0.073	0.039	
	1.3×10^4	9.2×10^3	0.020	0.010	
	4.1×10^4	7.6×10^4	4.0×10^{-3}	1.3×10^{-3}	
090515	8.1×10^2	2.2×10^3	0.24	0.093	This work
090607	9.3×10^2	2.0×10^3	0.060	0.017	Evans et al. (2007a, 2009)
	2.0×10^4	2.4×10^4	$< 6.6 \times 10^{-3}$		
090621B	7.2×10^3	8.3×10^3	0.04	0.01	Evans et al. (2007a, 2009)
	2.5×10^4	2.5×10^4	6.0×10^{-3}	3.4×10^{-3}	
090916[b]	6.5×10^4	1.2×10^4	$< 9.4 \times 10^{-4}$		Troja et al. (2009)
091109B	5.7×10^3	2.4×10^3	0.097	0.019	Evans et al. (2007a, 2009)
	1.6×10^4	1.3×10^4	0.030	0.023	
	5.8×10^4	5.8×10^4	0.011	7.9×10^{-3}	
	2.0×10^5	1.2×10^5	0.011	9.6×10^{-3}	
100117A	3.1×10^4	3.6×10^5	2.2×10^{-3}	7.2×10^{-4}	This work
100206A	2.4×10^4	9.5×10^4	$<3.3 \times 10^{-3}$		Evans et al. (2007a, 2009)
100213	2.0×10^4	3.1×10^4	< 0.033		Evans et al. (2007a, 2009)
100625A	1.6×10^4	1.3×10^4	4.4×10^{-3}	1.8×10^{-3}	Fong et al. (2013)
	9.0×10^4	4.6×10^4	$< 8.2 \times 10^{-3}$		Fong et al. (2013)
100628A[a]	$^{+}3.9 \times 10^5$	2.0×10^4	$<5.9 \times 10^4$		This work
100702A	1.4×10^4	4.3×10^4	< 0.011		Evans et al. (2007a, 2009)
101219A	7.7×10^2	317	0.58	0.20	Fong et al. (2013)
	8.6×10^3	1.4×10^4	0.038	0.014	
	3.4×10^5	2.0×10^5	$< 1.9 \times 10^{-4}$		
101224A	1.9×10^3	4.0×10^4	0.015	5.0×10^{-3}	Evans et al. (2007a, 2009)
110112A	4.6×10^3	1.0×10^3	0.083	0.028	Fong et al. (2013)
	5.4×10^3	605	0.14	0.047	
	6.2×10^3	941	0.14	0.043	
	1.1×10^4	2.5×10^3	0.064	0.016	

Table 8.2—Continued

GRB	δt (s)	Exposure Time (s)	F_X (μJy)	σ_X (μJy)	References
	1.9×10^4	6.6×10^3	0.025	8.8×10^{-3}	
	2.8×10^4	1.3×10^4	0.012	4.3×10^{-3}	
	4.5×10^4	2.3×10^4	7.3×10^{-3}	3.1×10^{-3}	
	1.4×10^5	2.7×10^5	2.0×10^{-3}	1.0×10^{-3}	
110112B[b]	6.1×10^4	1.2×10^4	$<2.4 \times 10^{-3}$		Littlejohns et al. (2011)
111020A	1.1×10^3	520	1.0	0.20	Fong et al. (2012b)
	5.8×10^3	2.5×10^3	0.19	0.039	
	1.2×10^4	2.5×10^3	0.13	0.032	
	1.9×10^4	6.4×10^3	0.11	0.027	
	2.6×10^4	6.3×10^3	0.14	0.037	
	3.2×10^4	5.9×10^3	0.12	0.031	
	4.2×10^4	1.6×10^4	0.10	0.028	
	1.0×10^5	1.5×10^5	0.019	6.4×10^{-3}	
	2.9×10^5	2.1×10^5	0.013	4.9×10^{-3}	
	$^{++}6.9 \times 10^4$	1.4×10^4	0.031	2.4×10^{-3}	
	$^{+}2.6 \times 10^5$	2.0×10^4	7.0×10^{-3}	1.0×10^{-3}	
	5.1×10^5	2.1×10^5	< 0.019		
	$^{+}8.8 \times 10^5$	2.0×10^4	$< 1.1 \times 10^{-3}$		
111117A	1.0×10^3	178	0.55	0.20	Margutti et al. (2012)
	1.2×10^3	211	0.45	0.15	
	5.0×10^3	881	0.11	0.035	
	5.5×10^4	1.9×10^5	4.0×10^{-3}	1.4×10^{-3}	
	$^{+}2.6 \times 10^5$	4.0×10^4	4.2×10^{-4}	1.6×10^{-4}	
111121A	4.2×10^3	85	2.17	0.47	Evans et al. (2007a, 2009)
	4.3×10^3	133	1.3	0.30	
	4.5×10^3	143	1.4	0.31	
	4.7×10^3	228	1.4	0.26	
	4.9×10^3	113	1.6	0.37	
	5.1×10^3	196	1.1	0.22	
	5.3×10^3	246	0.93	0.21	
	5.6×10^3	326	1.0	0.20	
	6.0×10^3	133	1.3	0.30	
	6.2×10^3	143	1.2	0.28	
	6.3×10^3	160	1.1	0.25	
	6.5×10^3	158	1.1	0.25	
	6.7×10^3	206	1.1	0.21	
	1.0×10^4	155	1.2	0.26	
	1.0×10^4	183	1.0	0.23	

Table 8.2—Continued

GRB	δt (s)	Exposure Time (s)	F_X (μJy)	σ_X (μJy)	References
	1.1×10^4	384	0.34	0.090	
	1.1×10^4	188	0.94	0.21	
	1.1×10^4	181	0.74	0.19	
	1.1×10^4	243	0.54	0.14	
	1.1×10^4	223	0.60	0.16	
	1.2×10^4	268	0.50	0.13	
	1.2×10^4	657	0.37	0.072	
	1.6×10^4	985	0.24	0.063	
	1.8×10^4	1.6×10^3	0.17	0.043	
	2.2×10^4	667	0.22	0.057	
	2.3×10^4	1.8×10^3	0.12	0.026	
	4.2×10^4	3.7×10^4	0.045	8.3×10^{-3}	
	1.4×10^5	6.5×10^4	< 0.020		
111222A	9.7×10^4	7.3×10^3	0.047	9.5×10^{-3}	Evans et al. (2007a, 2009)
	7.8×10^5	5.2×10^4	< 0.027		
	4.0×10^6	1.7×10^5	< 0.014		
120305A	2.3×10^4	9.4×10^4	0.016	8.0×10^{-3}	Evans et al. (2007a, 2009)
120521A	6.8×10^3	7.3×10^3	< 0.020		
120630A	6.6×10^2	1.2×10^3	0.11	0.024	Evans et al. (2007a, 2009)
120804A	4.3×10^3	203	1.1	0.23	Berger et al. (2013b)
	4.5×10^3	211	0.82	0.20	
	4.7×10^3	178	0.85	0.22	
	4.9×10^3	181	1.1	0.26	
	5.2×10^3	281	0.54	0.14	
	5.4×10^3	263	0.58	0.15	
	5.7×10^3	301	0.50	0.13	
	6.0×10^3	349	0.43	0.12	
	6.4×10^3	494	0.34	0.090	
	1.1×10^4	2.6×10^3	0.29	0.056	
	1.7×10^4	2.5×10^3	0.20	0.051	
	2.3×10^4	2.6×10^3	0.11	0.021	
	3.0×10^4	5.7×10^3	0.096	0.026	
	3.4×10^4	2.6×10^3	0.10	0.021	
	4.3×10^4	8.2×10^3	0.049	0.013	
	6.2×10^4	2.3×10^4	0.076	0.016	
	1.4×10^5	9.3×10^4	0.048	0.014	

Table 8.2—Continued

GRB	δt (s)	Exposure Time (s)	F_X (μJy)	σ_X (μJy)	References
	3.1×10^5	2.8×10^5	6.8×10^{-3}	2.2×10^{-3}	
	5.0×10^5	2.3×10^4	< 0.0456		
	$^{+}8.1 \times 10^5$	2.0×10^4	3.5×10^{-3}	6.2×10^{-4}	
	$^{++}1.6 \times 10^6$	2.5×10^4	3.0×10^{-3}	6.2×10^{-4}	
	$^{+}4.0 \times 10^6$	5.9×10^4	6.6×10^{-4}	1.3×10^{-3}	This work
120817B[b]	6.8×10^4	2.8×10^3	$<5.9 \times 10^{-3}$		Pagani (2012)
121226A	4.3×10^3	589	0.58	0.15	Evans et al. (2007a, 2009)
	4.9×10^3	542	0.62	0.16	
	5.5×10^3	679	0.49	0.13	
	7.9×10^3	4.7×10^3	0.36	0.079	
	6.2×10^4	8.3×10^4	0.030	8.6×10^{-3}	
	1.2×10^5	6.2×10^3	0.034	0.027	
130313A[a]	2.1×10^3	5.3×10^4	< 0.013		Evans et al. (2007a, 2009)
130515A	1.2×10^4	3.0×10^4	< 0.014		Evans et al. (2007a, 2009)
130603B	4.0×10^3	33	3.8	1.2	Fong et al. (2014)
	4.0×10^3	41	3.3	1.0	
	4.1×10^3	75	1.7	0.54	
	4.1×10^3	44	2.9	0.95	
	4.2×10^3	44	3.0	0.91	
	4.2×10^3	36	3.5	1.2	
	4.3×10^3	75	1.8	0.53	
	4.3×10^3	44	3.0	1.0	
	4.4×10^3	54	2.5	0.71	
	4.4×10^3	41	3.2	1.1	
	4.5×10^3	65	2.0	0.63	
	4.5×10^3	31	4.1	1.3	
	4.6×10^3	44	3.0	0.99	
	4.6×10^3	52	2.4	0.80	
	4.7×10^3	65	2.0	0.68	
	4.7×10^3	52	2.6	0.74	
	4.8×10^3	98	1.6	0.46	
	4.9×10^3	57	2.2	0.72	
	4.9×10^3	44	3.0	0.98	
	5.0×10^3	59	2.3	0.77	
	5.1×10^3	83	1.5	0.43	

Table 8.2—Continued

GRB	δt (s)	Exposure Time (s)	F_X (μJy)	σ_X (μJy)	References
	5.1×10^3	59	2.5	0.71	
	5.2×10^3	93	1.4	0.43	
	5.3×10^3	96	1.4	0.45	
	5.4×10^3	88	1.6	0.49	
	5.5×10^3	72	1.8	0.59	
	5.5×10^3	41	3.0	0.98	
	5.6×10^3	67	1.9	0.59	
	5.7×10^3	85	1.5	0.44	
	5.8×10^3	78	1.7	0.50	
	5.8×10^3	65	2.0	0.59	
	5.9×10^3	75	1.6	0.54	
	6.0×10^3	67	1.9	0.56	
	6.0×10^3	91	1.4	0.42	
	6.2×10^3	114	1.1	0.34	
	6.2×10^3	65	2.0	0.59	
	6.3×10^3	59	2.1	0.59	
	6.4×10^3	91	1.4	0.42	
	6.5×10^3	122	1.5	0.40	
	9.8×10^3	91	1.3	0.36	
	9.9×10^3	143	0.83	0.23	
	1.0×10^4	166	0.71	0.19	
	1.1×10^4	1.5×10^3	0.57	0.16	
	1.2×10^4	166	0.65	0.19	
	1.2×10^4	226	0.49	0.13	
	1.2×10^4	205	0.72	0.17	
	1.6×10^4	338	0.29	0.076	
	1.6×10^4	252	0.38	0.11	
	1.7×10^4	2.0×10^3	0.21	0.056	
	2.1×10^4	450	0.19	0.048	
	2.2×10^4	463	0.19	0.047	
	2.8×10^4	1.1×10^3	0.077	0.029	
	3.6×10^4	5.9×10^3	0.038	0.011	
	4.2×10^4	5.5×10^3	0.054	0.014	
	4.8×10^4	6.7×10^3	0.021	5.6×10^{-3}	
	1.5×10^5	2.1×10^5	4.0×10^{-3}	8.8×10^{-4}	
	$^{++}2.3 \times 10^5$	1.9×10^4	2.4×10^{-3}	3.2×10^{-4}	
	$^{++}5.6 \times 10^5$	3.0×10^4	8.2×10^{-4}	5.0×10^{-4}	
130626A[b]	8.7×10^5	7.2×10^5	$<1.8 \times 10^{-3}$		Page & de Pasquale (2013)

upper limits for these four bursts are also listed in Table 8.3.

Figure 8.1 shows the photometric data for 26 bursts with optical afterglow detections, and upper limits for the remaining 46 events. The bursts with no detected optical afterglow are further classified by the detection of an X-ray afterglow. The median afterglow brightness is $\approx 2.5\,\mu$Jy (≈ 23 mag) at $\delta t \approx 0.3 - 0.5$ days, while the median limit placed on bursts with no detected optical afterglow is $\lesssim 1.5\,\mu$Jy ($\gtrsim 23.5$ mag) on the same timescale.

Table 8.2—Continued

GRB	δt (s)	Exposure Time (s)	F_X (μJy)	σ_X (μJy)	References
130716A	1.2×10^4	2.5×10^4	0.014	4.0×10^{-3}	Evans et al. (2007a, 2009)
	4.0×10^4	1.3×10^4	$< 7.2 \times 10^{-3}$		
130822A	3.0×10^4	1.9×10^4	$< 4.6 \times 10^{-3}$		Evans et al. (2007a, 2009)
130912A	9.7×10^2	95	5.6	1.3	Evans et al. (2007a, 2009)
	1.1×10^3	103	2.7	0.60	
	1.2×10^3	100	1.3	0.30	
	1.3×10^3	105	1.3	0.29	
	1.4×10^3	95	1.4	0.31	
	1.5×10^3	180	1.6	0.26	
	5.2×10^3	780	0.26	0.068	
	6.4×10^3	1.8×10^3	0.21	0.04	
	1.2×10^4	2.5×10^3	0.066	0.016	
	1.8×10^4	2.5×10^3	0.057	0.015	
	2.8×10^4	1.4×10^4	0.025	4.9×10^{-3}	
	1.1×10^5	5.8×10^4	$< 3.9 \times 10^{-3}$		
131004A	1.8×10^2	306	13.2	3.1	Evans et al. (2007a, 2009)
	4.4×10^2	115	34.8	8.1	
	5.5×10^2	115	33.9	8.1	
	6.9×10^2	158	24.8	5.9	
	8.8×10^2	228	31.9	5.5	
	1.1×10^4	1.5×10^3	0.23	0.049	
	2.4×10^4	1.8×10^4	0.055	0.015	
	5.9×10^4	4.7×10^4	0.050	0.014	
	1.1×10^5	4.1×10^4	< 0.017		
131224A[c]	1.3×10^4	4.0×10^3	$< 4.1 \times 10^{-3}$		Gompertz et al. (2013)

Note. — Upper limits correspond to 3σ. Unless otherwise stated, all data are taken with *Swift*/XRT and X-ray flux densities are at 1 keV.

[a] We employed a fiducial spectral index of $\beta_X = -1$.

[b] We employed a fiducial count rate-to-unabsorbed flux conversion factor of 10^{-11} erg cm^{-2} s^{-1} and spectral index $\beta_X = -1$.

[c] Late-time re-brightening in GRB 080503 light curve is observed in both optical and X-ray bands and is unlikely the afterglow (Perley et al. 2009a).

[+] Chandra observation.

[++] XMM-Newton observation.

Table 8.3. Short GRB Optical/near-IR afterglow catalog

GRB	δt (hr)	Telescope	Instrument	Filter	Exposure Time (s)	F_ν (μJy)	σ (μJy)	References
050202	12.6	Mount John	MOA	R	900	< 42.89		Castro-Tirado et al. (2005a)
050509B	2.1	WIYN	OPTIC	r	600	< 0.75		Bloom et al. (2006)
050709	34.0	Danish tel.	DFOSC	R	7200	2.34	0.12	Hjorth et al. (2005b)
	59.1	VLT	FORS2	V	3600	0.64	0.07	Covino et al. (2006)
	59.3	VLT	FORS2	R	3000	0.90	0.05	Covino et al. (2006)
	60.0	Danish tel.	DFOSC	R	10200	1.17	0.26	Hjorth et al. (2005b)
	104.7	VLT	FORS1	V	3600	< 0.36		Covino et al. (2006)
	134.4	HST	ACS	F814W	6360	0.34	0.006	Fox et al. (2005)
	235.2	HST	ACS	F814W	6360	0.17	0.008	
	832.8	HST	ACS	F814W	6360	< 0.02		
050724A	11.4	VLT	FORS1	V	480	16.0	0.45	Malesani et al. (2007b)
	11.6	Magellan/Baade	PANIC	K	1320	45.6	1.4	Berger et al. (2005)
	11.8	VLT	FORS1	R	540	17.8	0.7	Malesani et al. (2007b)
	11.8	VLT	FORS1	I	540	18.37	0.51	Malesani et al. (2007b)
	12.0	Swope 40-in		I	1800	19.1	0.2	Berger et al. (2005)
	14.2	Swope 40-in		I	1800	25.2	0.9	Berger et al. (2005)
	34.8	VLT	FORS1	I	540	2.81	0.33	Malesani et al. (2007b)
	34.9	Magellan/Baade	PANIC	K	1320	< 5.4		Berger et al. (2005)
	35.0	VLT	FORS1	R	540	3.35	0.29	Malesani et al. (2007b)
	36.7	Swope 40-in		I	2700	< 9.1		Berger et al. (2005)
	83.1	VLT	FORS1	I	540	0.33	0.12	Malesani et al. (2007b)
050813	13.2	CAHA 2.2-m	CAFOS	I	6000	< 1.82		Ferrero et al. (2007)
	14.1	CAHA 2.2-m	CAFOS	R	4140	< 1.43		

Table 8.3—Continued

GRB	δt (hr)	Telescope	Instrument	Filter	Exposure Time (s)	F_ν (μJy)	σ (μJy)	References
050906	21.4	VLT	FORS2	R	1800	< 0.15		Levan et al. (2008)
051210	19.4	Magellan/Clay	LDSS3	r	1200	< 1.6		Berger et al. (2007b)
051221A	3.1	Gemini-N	GMOS	r		16.8	1.3	Soderberg et al. (2006b)
	3.4	Gemini-N	GMOS	r		15.6	1.2	
	26.9	Gemini-N	GMOS	r		2.5	0.19	
	27.2	Gemini-N	GMOS	i		2.3	0.54	
	51.0	Gemini-N	GMOS	i		0.83	0.32	
	51.3	Gemini-N	GMOS	z		1.1	0.47	
	51.6	Gemini-N	GMOS	r		0.93	0.11	
	75.7	Gemini-N	GMOS	r		0.94	0.28	
	123.6	Gemini-N	GMOS	r		0.50	0.11	
	147.8	Gemini-N	GMOS	r		0.32		
060121	0.37	OSN		I	120	19.3	4.4	de Ugarte Postigo et al. (2006b)
	0.70	OSN		I	120	10.0	2.8	de Ugarte Postigo et al. (2006b)
	2.0	NOT	ALFOSC	R		3.3	0.70	Levan et al. (2006b)
	2.6	NOT	ALFOSC	R		6.1	1.9	Levan et al. (2006b)
	2.7	OSN		I	300	10.8	2.5	de Ugarte Postigo et al. (2006b)
	2.8	OSN		R	600	3.7	0.97	de Ugarte Postigo et al. (2006b)
	3.9	CAHA 2.2-m		R	1200	1.1	0.33	de Ugarte Postigo et al. (2006b)
	4.4	CAHA 2.2-m		R	1800	4.6	0.83	de Ugarte Postigo et al. (2006b)
	5.4	CAHA 2.2-m		R	1200	1.2	0.49	de Ugarte Postigo et al. (2006b)

Table 8.3—Continued

GRB	δt (hr)	Telescope	Instrument	Filter	Exposure Time (s)	F_ν (μJy)	σ (μJy)	References
	5.6	Bok	90Prime	R		1.1	0.22	Levan et al. (2006b)
	6.5	Bok	90Prime	B		< 0.96		Levan et al. (2006b)
	7.3	Bok	90Prime	R		1.2	0.18	Levan et al. (2006b)
	7.3	CAHA 2.2-m		R	1800	1.4	0.37	Levan et al. (2006b)
	7.4	WHT		K	750	17.1	1.4	de Ugarte Postigo et al. (2006b)
	7.7	OSN		I	1500	< 2.5		de Ugarte Postigo et al. (2006b)
	11.3	Bok	90Prime	R		1.6	0.41	Levan et al. (2006b)
	13.1	WIYN		R		1.2	0.24	Levan et al. (2006b)
	30.0	OSN		R	10800	< 0.8		de Ugarte Postigo et al. (2006b)
	31.3	WHT		K	1000	6.3	1.6	de Ugarte Postigo et al. (2006b)
	33.5	APO/ARC	NIC-FPS	K	3600	7.5	0.65	de Ugarte Postigo et al. (2006b)
	33.6	WIYN		R		0.41	0.06	Levan et al. (2006b)
	51.5	CAHA 2.2-m		R	5400	0.55	0.14	de Ugarte Postigo et al. (2006b)
	127.8	APO/ARC	NIC-FPS	K	3600	< 2.13		de Ugarte Postigo et al. (2006b)
060313	0.045	*Swift*	UVOT	V	200	55.0	18.8	Roming et al. (2006)
	0.12	*Swift*	UVOT	U	50	22.7	13.0	Roming et al. (2006)
	0.22	*Swift*	UVOT	*white*	50	30.5	11.6	Roming et al. (2006)
	1.2	Gemini-S	GMOS	r	1800	36.6	6.6	Berger et al. (2007b)
	1.3	*Swift*	UVOT	B	886	18.7	5.3	Roming et al. (2006)
	1.5	*Swift*	UVOT	$UVW2$	900	6.4	1.9	Roming et al. (2006)
	1.7	*Swift*	UVOT	V	684	33.7	9.5	Roming et al. (2006)
	2.9	*Swift*	UVOT	$UVM2$	900	4.7	2.3	Roming et al. (2006)
	3.1	*Swift*	UVOT	$UVW1$	900	12.4	2.4	Roming et al. (2006)

Table 8.3—Continued

GRB	δt (hr)	Telescope	Instrument	Filter	Exposure Time (s)	F_ν (μJy)	σ (μJy)	References
	3.3	*Swift*	UVOT	U	708	7.4	1.8	Roming et al. (2006)
	4.5	*Swift*	UVOT	B	886	12.2	5.8	Roming et al. (2006)
	6.1	*Swift*	UVOT	$UVM2$	900	3.4	1.2	Roming et al. (2006)
	6.3	*Swift*	UVOT	$UVW1$	900	3.3	1.5	Roming et al. (2006)
	6.6	*Swift*	UVOT	U	716	8.8	2.1	Roming et al. (2006)
	9.6	*Swift*	UVOT	$UVW1$	900	3.0	1.4	Roming et al. (2006)
	9.8	*Swift*	UVOT	U	658	3.4	1.9	Roming et al. (2006)
	24.2	Gemini-S	GMOS	r	900	3.7	0.75	Berger et al. (2007b)
	48.5	Gemini-S	GMOS	r	1500	1.3	0.18	Berger et al. (2007b)
	240	Gemini-S	GMOS	r	1800	< 0.48		Berger et al. (2007b)
060502B	16.8	Gemini-N	GMOS	R	1500	< 0.62		Price et al. (2006)
060801	16.0	Hale	LFC	r	1500	< 0.83		Berger et al. (2007b)
061006	14.9	VLT	FORS1	I	1800	4.3	0.20	D'Avanzo et al. (2009)
	45.9	VLT	FORS1	I	1800	2.5	0.17	
	60.0	VLT	FORS1	I	1260	2.6	0.22	
	49.7	VLT	FORS1	R	645	1.5	0.17	
061201	8.6	VLT	FORS2	I	3640	2.9	0.22	Stratta et al. (2007)
	9.0	VLT	FORS2	R	780	1.9	0.23	
	33.1	VLT	FORS2	I	5200	< 0.91		
	81.4	VLT	FORS2	I	2400	< 0.63		
061210	2.1	Gemini-N	GMOS	r	5400	< 1.44		Berger et al. (2007b)
061217	2.8	Magellan/Clay	LDSS3	r	300	< 2.0		Berger et al. (2007b)

Table 8.3—Continued

GRB	δt (hr)	Telescope	Instrument	Filter	Exposure Time (s)	F_ν (μJy)	σ (μJy)	References
070209	0.29	PROMPT		V	120	< 81.66		Johnson et al. (2007)
070406	24.5	NOT	ALFOSC	R	1800	< 1.26		Malesani et al. (2007a)
070429B	4.8	Gemini-S	GMOS	R	900	< 0.50		Perley et al. (2007a)
	27.1	Blanco	ISPI	J	1080	< 4.0		Nysewander et al. (2007)
070707	11.0	VLT	FORS1	R	1200	2.1	0.039	Piranomonte et al. (2008)
	33.8	VLT	FORS1	R	1200	1.0	0.047	
	37.4	VLT	FORS1	R	180	0.82	0.10	
	59.3	VLT	FORS1	R	1200	0.26	0.020	
	61.0	VLT	ISAAC	J	1800	< 0.60		
	83.2	VLT	FORS1	R	3600	0.078	0.014	
	108.0	VLT	FORS1	R	5100	0.066	0.015	
070714B	0.21	Liverpool		r	60	37.2	6.7	Graham et al. (2009)
	0.27	Liverpool		r	120	43.1	4.6	
	0.30	Liverpool		i	120	50.7	8.6	
	0.40	Liverpool		r	120	37.9	9.8	
	0.44	Liverpool		r	120	38.3	9.0	
	23.6	WHT		R	2400	1.0	0.22	
	24.0	TNG	NICS	J		< 9.1		Covino et al. (2007)
070724A	2.3	Gemini-N	GMOS	g	360	< 1.5		Berger et al. (2009)
	2.3	Gemini-N	GMOS	i	360	1.1	0.1	Berger et al. (2009)
	2.8	Gemini-N	NIRI	Ks	900	9.3	1.5	Berger et al. (2009)
	3.1	Gemini-N	NIRI	J	900	3.4	0.3	Berger et al. (2009); this work

Table 8.3—Continued

GRB	δt (hr)	Telescope	Instrument	Filter	Exposure Time (s)	F_ν (μJy)	σ (μJy)	References
	3.4	Gemini-N	NIRI	H	450	7.8	0.44	Berger et al. (2009); this work
	3.7	Gemini-N	NIRI	Ks	900	8.9	1.5	Berger et al. (2009)
070729	8.4	ESO/MPG	GROND	r		< 0.48		Nicuesa Guelbenzu et al. (2012a)
	8.4	ESO/MPG	GROND	J		< 3.02		
070809	11.2	Keck I	LRIS	R	640	0.82	0.17	Perley et al. (2007b)
	35.1	Keck I	LRIS	R		0.36	0.11	
	11.21	Keck I	LRIS	g	880	0.25	0.051	
	35.14	Keck I	LRIS	g		< 0.19		
070810B	23.4	Keck I	LRIS	R	630	< 0.21		Kocevski et al. (2007)
071112B	6.3	Magellan/Clay	LDSS3	r	1200	< 2.0		Berger & Challis (2007)
	9.6	ESO/MPG	GROND	J		< 8.32		Nicuesa Guelbenzu et al. (2012a)
071227	4.2	ESO/MPG	GROND	J		< 36.3		Nicuesa Guelbenzu et al. (2012a)
	7.0	VLT	FORS2	R	240	1.6	0.12	D'Avanzo et al. (2009)
	80.9	VLT	FORS2	R	540	0.86	0.15	D'Avanzo et al. (2009)
080121	55.2	*Swift*	UVOT	*white*	2015	< 4.57		Troja et al. (2008a)
080123	0.04	*Swift*	UVOT	*white*	100	< 22.91		Ukwatta et al. (2008)
080426[a]	7.5	CAHA 2.2-m		I	3300	< 7.06		de Ugarte Postigo et al. (2008)
080503	0.037	*Swift*	UVOT	*white*	98	< 14.2		Perley et al. (2009a)
	1.0	Gemini-N	GMOS	r	180	< 0.20		
	1.2	Gemini-N	GMOS	g	900	0.089	0.018	
	1.2	Keck I	LRIS	B	300	< 0.21		

Table 8.3—Continued

GRB	δt (hr)	Telescope	Instrument	Filter	Exposure Time (s)	F_ν (μJy)	σ (μJy)	References
	1.3	Keck I	LRIS	R	630	< 0.21		
	1.5	Gemini-N	GMOS	r	800	< 0.081		
	1.8	Gemini-N	GMOS	i	800	< 0.078		
	2.2	Gemini-N	GMOS	z	800	< 0.16		
	2.4	Gemini-N	GMOS	g	360	< 0.65		
	[b]26.0	Gemini-N	GMOS	r	1800	0.27	0.037	
	[b]47.4	Gemini-N	GMOS	r	1620	0.23	0.038	
	[b]50.2	Gemini-N	GMOS	g	720	0.12	0.024	
	[b]74.0	Gemini-N	GMOS	r	2700	0.19	0.046	
	[b]97.1	Gemini-N	GMOS	r	2880	0.13	0.025	
	125	Gemini-N	NIRI	K_s	2760	< 0.70		
	[b]128.6	*HST*	WFPC2	F606W	0.067	0.011		
080702A	12.06	Loiano		R	1800	< 44.92		Greco et al. (2008)
080905A	8.5	NOT	ALFOSC	R	1800	0.72	0.39	Rowlinson et al. (2010a)
	14.3	VLT	FORS2	R	2400	0.59	0.20	Rowlinson et al. (2010a)
	17.5	ESO/MPG	GROND	r	660	< 3.7		Nicuesa Guelbenzu et al. (2012a)
	17.5	ESO/MPG	GROND	J	660	< 27.5		Nicuesa Guelbenzu et al. (2012a)
	36.0	VLT	FORS2	R	2400	< 0.30		Rowlinson et al. (2010a)
080919[a]	0.19	ESO/MPG	GROND	J		< 73.3		Nicuesa Guelbenzu et al. (2012a)
081024A	1.9	Faulkes North		R	600	< 93.93		Melandri et al. (2008)
081024B	30	P200	LFC		R	< 1.36		Cenko & Kasliwal (2008)
081226A	0.37	ESO/MPG	GROND	r		1.9	0.42	Nicuesa Guelbenzu et al. (2012a)
	1.1	ESO/MPG	GROND	g		0.38	0.12	

Table 8.3—Continued

GRB	δt (hr)	Telescope	Instrument	Filter	Exposure Time (s)	F_ν (μJy)	σ (μJy)	References
	1.1	ESO/MPG	GROND	r		0.63	0.16	
	1.1	ESO/MPG	GROND	i		0.81	0.31	
	1.1	ESO/MPG	GROND	z		1.4	0.35	
	1.1	ESO/MPG	GROND	J		< 7.7		
081226B	2.7	*Swift*	UVOT	B	1414	< 14.45		Evans & Hoversten (2008)
090305	0.47	ESO/MPG	GROND	r		3.0	0.084	Nicuesa Guelbenzu et al. (2012a)
	0.56	ESO/MPG	GROND	r		3.1	0.27	Nicuesa Guelbenzu et al. (2012a)
	0.56	ESO/MPG	GROND	i		3.3	0.59	Nicuesa Guelbenzu et al. (2012a)
	0.60	ESO/MPG	GROND	r		2.9	0.082	Nicuesa Guelbenzu et al. (2012a)
	0.61	Gemini-S	GMOS	r	900	1.8	0.034	Tunnicliffe et al. (2013)
	0.71	ESO/MPG	GROND	g		2.1	0.40	Nicuesa Guelbenzu et al. (2012a)
	0.71	ESO/MPG	GROND	r		2.8	0.35	
	0.79	ESO/MPG	GROND	g		1.9	0.09	
	0.92	ESO/MPG	GROND	g		2.1	0.31	
	0.92	ESO/MPG	GROND	r		2.1	0.32	
	0.92	ESO/MPG	GROND	i		2.5	0.49	
	0.93	ESO/MPG	GROND	g		1.8	0.085	
	1.1	ESO/MPG	GROND	g		1.7	0.11	
	1.1	ESO/MPG	GROND	r		1.9	0.24	
	1.2	ESO/MPG	GROND	r		2.0	0.13	
	1.3	Gemini-S	GMOS	i	900	1.5	0.041	Tunnicliffe et al. (2013)

Table 8.3—Continued

GRB	δt (hr)	Telescope	Instrument	Filter	Exposure Time (s)	F_ν (μJy)	σ (μJy)	References
	1.3	ESO/MPG	GROND	g		1.6	0.14	
	1.3	ESO/MPG	GROND	i		1.9	0.24	
	1.3	ESO/MPG	GROND	r		1.5	0.16	
	1.4	ESO/MPG	GROND	r		1.7	0.082	
	1.5	ESO/MPG	GROND	r		1.7	0.34	
	1.5	ESO/MPG	GROND	i		1.9	0.22	
	1.6	ESO/MPG	GROND	r		1.7	0.078	
	1.6	Gemini-S	GMOS	r	900	1.4	0.026	Tunnicliffe et al. (2013)
	1.6	ESO/MPG	GROND	r		1.8	0.19	
	1.7	ESO/MPG	GROND	r		1.6	0.073	
	1.7	ESO/MPG	GROND	r		1.5	0.12	
	1.8	ESO/MPG	GROND	r		1.4	0.051	
	1.8	ESO/MPG	GROND	g		1.0	0.13	
	1.8	ESO/MPG	GROND	r		1.5	0.12	
	2.0	ESO/MPG	GROND	r		1.6	0.12	
	2.1	ESO/MPG	GROND	r		1.2	0.35	
	2.1	Gemini-S	GMOS	r	900	0.95	0.027	Tunnicliffe et al. (2013)
	2.1	ESO/MPG	GROND	r		1.1	0.040	
	21.7	Gemini-S	GMOS	r	1500	< 0.19		Tunnicliffe et al. (2013)
090426	0.29	TNT		R	60	101	7.8	Xin et al. (2011b)
	0.31	TNT		R	60	95.1	10.1	Xin et al. (2011b)
	0.33	TNT		R	60	89.2	9.5	Xin et al. (2011b)
	0.36	TNT		R	60	77.0	8.2	Xin et al. (2011b)

Table 8.3—Continued

GRB	δt (hr)	Telescope	Instrument	Filter	Exposure Time (s)	F_ν (μJy)	σ (μJy)	References
	0.38	TNT		R	60	74.9	8.8	Xin et al. (2011b)
	0.40	TNT		R	60	69.6	8.1	Xin et al. (2011b)
	0.42	TNT		R	60	73.5	8.6	Xin et al. (2011b)
	0.53	TNT		V	600	49.0	5.7	Xin et al. (2011b)
	0.71	TNT		V	600	36.5	4.3	Xin et al. (2011b)
	0.88	TNT		V	600	34.5	4.0	Xin et al. (2011b)
	1.1	TNT		V	600	36.2	4.2	Xin et al. (2011b)
	1.2	TNT		V	600	32.4	3.8	Xin et al. (2011b)
	1.4	TNT		V	600	31.8	4.4	Xin et al. (2011b)
	1.6	TNT		V	600	28.7	4.0	Xin et al. (2011b)
	2.0	TNT		V	600	24.6	3.9	Xin et al. (2011b)
	2.3	TNT		V	600	20.1	3.4	Xin et al. (2011b)
	2.6	TNT		V	600	20.8	3.5	Xin et al. (2011b)
	3.0	TNT		V	600	19.7	3.6	Xin et al. (2011b)
	7.3	TLS		I		15.8	2.8	Nicuesa Guelbenzu et al. (2011)
	7.5	TLS		R		13.5	1.7	Nicuesa Guelbenzu et al. (2011)
	7.5	TLS		R		13.4	1.8	Nicuesa Guelbenzu et al. (2011)
	7.7	TLS		R		11.8	2.3	Nicuesa Guelbenzu et al. (2011)
	7.8	TLS		R		12.7	1.7	Nicuesa Guelbenzu et al. (2011)
	12.9	ESO/MPG	GROND	g	3.1×10^3	5.8	0.16	Nicuesa Guelbenzu et al. (2011)
	12.9	ESO/MPG	GROND	r	3.1×10^3	7.6	0.21	Nicuesa Guelbenzu et al. (2011)
	12.9	ESO/MPG	GROND	i	3.1×10^3	8.2	0.38	Nicuesa Guelbenzu et al. (2011)
	12.9	ESO/MPG	GROND	z	3.1×10^3	9.8	0.65	Nicuesa Guelbenzu et al. (2011)

Table 8.3—Continued

GRB	δt (hr)	Telescope	Instrument	Filter	Exposure Time (s)	F_ν (μJy)	σ (μJy)	References
	12.9	ESO/MPG	GROND	J	3.1×10^3	15.2	0.28	Nicuesa Guelbenzu et al. (2011)
	12.9	ESO/MPG	GROND	H	3.1×10^3	15.7	3.2	Nicuesa Guelbenzu et al. (2011)
	12.9	ESO/MPG	GROND	K	3.1×10^3	< 33.3		Nicuesa Guelbenzu et al. (2011)
	14.6	ESO/MPG	GROND	g	7.3×10^3	4.7	0.087	Nicuesa Guelbenzu et al. (2011)
	14.6	ESO/MPG	GROND	r	7.3×10^3	6.0	0.11	Nicuesa Guelbenzu et al. (2011)
	14.6	ESO/MPG	GROND	i	7.3×10^3	7.3	0.20	Nicuesa Guelbenzu et al. (2011)
	14.6	ESO/MPG	GROND	z	7.3×10^3	8.3	0.31	Nicuesa Guelbenzu et al. (2011)
	14.6	ESO/MPG	GROND	J	7.3×10^3	10.2	0.89	Nicuesa Guelbenzu et al. (2011)
	14.6	ESO/MPG	GROND	H	7.3×10^3	11.8	1.4	Nicuesa Guelbenzu et al. (2011)
	14.6	ESO/MPG	GROND	K	7.3×10^3	< 21.0		Nicuesa Guelbenzu et al. (2011)
	16.3	LOAO		R	1.8×10^3	< 6.6		Xin et al. (2011b)
090510[c]	6.2	ESO/MPG	GROND	r		5.9	2.5	Nicuesa Guelbenzu et al. (2012b)
	6.3			r		5.5	2.3	
	6.3			r		4.6	1.6	
	6.4			r		2.6	1.8	
	6.4			r		3.0	1.8	
	6.5			r		2.6	1.6	
	6.7			r		2.3	0.71	
	6.8			r		3.8	0.77	
	6.9			r		2.7	0.89	
	7.1			r		3.4	0.79	
	7.2			r		2.9	0.72	
	7.3			r		2.2	0.75	

Table 8.3—Continued

GRB	δt (hr)	Telescope	Instrument	Filter	Exposure Time (s)	F_ν (μJy)	σ (μJy)	References
	7.4			r		3.1	0.77	
	7.6			r		2.3	0.59	
	7.7			r		1.9	0.40	
	7.8			r		1.9	0.50	
	7.9			r		2.2	0.55	
	8.1			r		1.8	0.59	
	8.2			r		2.0	0.52	
	8.3			r		2.0	0.47	
	8.4			r		2.1	0.46	
	8.6			r		2.3	0.48	
	8.6			J		< 4.8		
	8.7			r		2.0	0.47	
	8.8			r		1.9	0.44	
	8.9			r		1.5	0.47	
	9.1			r		1.7	0.43	
	9.2			r		1.3	0.41	
	9.3			r		1.5	0.41	
	9.5			r		1.5	0.40	
	9.7			r		0.88	0.47	
	9.8			r		1.2	0.41	
090515	1.4	WIYN	WHIRC	J	2.4×10^3	< 39.4		Updike et al. (2009)
	1.7	Gemini-N	GMOS	r	1.8×10^3	0.11	0.013	Rowlinson et al. (2010b)
	2.0	MMT	MMIRS	K	810	< 12.0		McLeod & Williams (2009)

Table 8.3—Continued

GRB	δt (hr)	Telescope	Instrument	Filter	Exposure Time (s)	F_ν (μJy)	σ (μJy)	References
	25.0	Gemini-N	GMOS	r	1.8×10^3	0.092	0.033	Rowlinson et al. (2010b)
	4.4×10^3	Gemini-N	GMOS	r	2.8×10^3	< 0.042		Rowlinson et al. (2010b)
090607[a]	0.52	Faulkes North		R	720	< 5.70		Guidorzi et al. (2009)
090621B	0.75	RTT150	TFOSC	R_c	900	< 1.91		Galeev et al. (2009)
090916	2.7	PROMPT		R	480	< 71.4		Haislip et al. (2009)
091109B	6.0	VLT	FORS2	R	2400	0.67	0.092	Tunnicliffe et al. (2013)
	7.2	VLT	HAWK-I	K	1320	< 0.85		Tunnicliffe et al. (2013)
	8.3	VLT	HAWK-I	J	1320	< 2.5		
	10.4	VLT	FORS2	R	1200	0.51	0.11	
	31.7	VLT	FORS2	R	2400	< 0.17		
091117	31.5	ESO/MPG	GROND	J		< 7.59		Nicuesa Guelbenzu et al. (2012a)
	31.7	Magellan	IMACS	r		< 0.98		Berger & Mulchaey (2009)
100117A	3.9	Magellan	IMACS	R	1200	< 0.97		Fong et al. (2011)
	4.3	ESO/MPG	GROND	r		< 0.69		Nicuesa Guelbenzu et al. (2012a)
	8.3	Gemini-N	GMOS	r	2700	0.24	0.05	Fong et al. (2011)
100206A	11.7	ESO/MPG	GROND	i		< 1.8		Nicuesa Guelbenzu et al. (2012a)
	11.7	ESO/MPG	GROND	J		< 9.7		Nicuesa Guelbenzu et al. (2012a)
	15.7	Gemini-N	GMOS	i	1200	< 0.18		Perley et al. (2012)
100625A	12.2	ESO/MPG	GROND	g	≈ 3600	< 1.32		Nicuesa Guelbenzu et al. (2012a)
	33.9	Magellan	PANIC	J	2100	< 1.0		Fong et al. (2013)
100628A	1.1	Gemini-N	GMOS	i	1200	< 0.85		This work

Table 8.3—Continued

GRB	δt (hr)	Telescope	Instrument	Filter	Exposure Time (s)	F_ν (μJy)	σ (μJy)	References
	17.8	Magellan	PANIC	J	1620	< 5.43		This work
100702A[a]	0.16	ESO/MPG	GROND	J		< 27.29		Nicuesa Guelbenzu et al. (2012a)
	1.7	ESO/MPG	GROND	J		r	< 1.96	Nicuesa Guelbenzu et al. (2012a)
101219A	0.96	Gemini-S	GMOS	i	1620	< 0.40		Fong et al. (2013)
	1.20	Magellan	FourStar	J	1500	< 1.36		Fong et al. (2013)
110112A	15.4	WHT	ACAM	i	600	2.8	0.75	Fong et al. (2013)
	4.0×10^3	Magellan	LDSS3	i	1200	< 0.49		
110420B	10.5	Magellan	IMACS	r	1530	< 1.4		This work
111020A[a]	17.8	Magellan/Clay	LDSS3	r	1080	< 0.83		Fong et al. (2012b)
	17.8	Gemini-S	GMOS	i	1620	< 0.63		Fong et al. (2012b)
	18.5	VLT	HAWK-I	J	2640	< 0.57		Tunnicliffe et al. (2013)
111117A	8.2	GTC	OSIRIS	r	1200	< 0.40		Sakamoto et al. (2013)
	13.7	Gemini-S	GMOS	r	1200	< 0.23		Margutti et al. (2012)
120229A	9.6	Magellan/Clay	LDSS3	r	540	< 4.1		This work
120305A	0.23	Liverpool		r		< 25.85		Virgili et al. (2012)
120521A[a]	18.6	ESO/MPG	GROND	r	3000	< 0.88		Rossi et al. (2012)
	18.6	ESO/MPG	GROND	J	2400	< 20.9		Rossi et al. (2012)
120804A	5.5	Gemini-N	GMOS	i	1980	0.17	0.04	Berger et al. (2013b)
120817B	24.0	LCO/duPont	WFCCD	R	900	< 1.5		Fong et al. (2012a)

Table 8.3—Continued

GRB	δt (hr)	Telescope	Instrument	Filter	Exposure Time (s)	F_ν (μJy)	σ (μJy)	References
121226A	11.1	NOT	ALFOSC	R	1800	< 2.1		Xu et al. (2012)
130313A	13.4	TNG		r	1800	< 0.44		D'Avanzo et al. (2013)
130515A	0.63	Gemini-S	GMOS	r	240	< 1.4		Cenko & Cucchiara (2013)
130603B	0.19	*Swift*	UVOT	V	180	< 199.5		de Ugarte Postigo et al. (2013)
	2.1	*Swift*	UVOT	V	5110	< 54.0		de Ugarte Postigo et al. (2013)
	2.4	*Swift*	UVOT	B	7700	17.2	4.5	de Ugarte Postigo et al. (2013)
	5.9	NOT	MOSCA	r	1800	12.6	0.23	de Ugarte Postigo et al. (2013)
	6.1	WHT	ACAM	z	900	25.4	1.4	de Ugarte Postigo et al. (2013)
	6.6	WHT	ACAM	i	900	16.4	0.88	de Ugarte Postigo et al. (2013)
	6.7	CAHA	DLR-MKIII	V	1800	8.3	0.73	de Ugarte Postigo et al. (2013)
	7.0	GTC	OSIRIS	r	30	11.0	0.20	de Ugarte Postigo et al. (2013)
	7.1	WHT	ACAM	g	900	6.3	0.34	de Ugarte Postigo et al. (2013)
	7.9	Gemini-S	GMOS	g	1440	5.3	0.19	Cucchiara et al. (2013)
	8.2	Magellan/Baade	IMACS	r	600	8.6	0.14	Berger et al. (2013a)
	9.0	Gemini-S	GMOS	i	1440	12.3	1.2	Cucchiara et al. (2013)
	14.4	Gemini-N	GMOS	z	500	6.5	0.18	de Ugarte Postigo et al. (2013)
	14.5	UKIRT	WFCAM	K	684	13.7	1.3	de Ugarte Postigo et al. (2013)
	14.6	Gemini-N	GMOS	i	500	4.5	0.12	de Ugarte Postigo et al. (2013)
	14.7	UKIRT	WFCAM	J	500	9.3	1.3	de Ugarte Postigo et al. (2013)
	14.8	Gemini-N	GMOS	r	500	2.9	0.081	de Ugarte Postigo et al. (2013)
	15.0	Gemini-N	GMOS	g	500	1.6	0.06	de Ugarte Postigo et al. (2013)

Table 8.3—Continued

GRB	δt (hr)	Telescope	Instrument	Filter	Exposure Time (s)	F_ν (μJy)	σ (μJy)	References
	31.2	Gemini-S	GMOS	r	540	< 0.30		Cucchiara et al. (2013)
	31.2	Gemini-S	GMOS	i	540	< 0.58		Cucchiara et al. (2013)
	32.2	Magellan/Baade	IMACS	r	1200	< 0.46		Berger et al. (2013a)
	38.2	Gemini-N	GMOS	g	600	< 0.19		de Ugarte Postigo et al. (2013)
	38.4	Gemini-N	GMOS	r	600	0.21	0.05	de Ugarte Postigo et al. (2013)
	38.6	Gemini-N	GMOS	i	600	< 0.48		de Ugarte Postigo et al. (2013)
	38.6	UKIRT	WFCAM	J	1400	< 3.6		de Ugarte Postigo et al. (2013)
130716A	19.5	Gemini-N	GMOS	r	900	< 0.35		This work
130822A	21.1	Gemini-N	GMOS	i	600	< 0.58		Cenko et al. (2013a)
130912A	0.27	ESO/MPG	GROND	r		10.5	2.1	Tanga et al. (2013)
	0.38	P60		r		13.0	2.6	Cenko et al. (2013b)
	0.88	P60		r		9.7	2.5	Cenko et al. (2013b)
	20.0	WHT	ACAM	g		< 0.87		Tanvir et al. (2013b)
	24.8	Johnson	RATIR	r	19200	< 1.8		Butler et al. (2013)
	24.8	Johnson	RATIR	i	19200	< 1.7		Butler et al. (2013)
	24.8	Johnson	RATIR	Z	8060	< 3.7		Butler et al. (2013)
	24.8	Johnson	RATIR	Y	8060	< 5.4		Butler et al. (2013)
	24.8	Johnson	RATIR	J	8060	< 5.3		Butler et al. (2013)
	24.8	Johnson	RATIR	H	8060	< 7.9		Butler et al. (2013)
131004A	0.43	NOT	ALFOSC	R		44.3	4.3	Xu et al. (2013)
	1.1	TNG	DOLoRes	R	60	25.5	2.5	Malesani et al. (2013)
	1.4	Liverpool		i	300	47.4	4.6	Kopac et al. (2013)
	1.9	Liverpool		i	300	32.8	3.2	Kopac et al. (2013)

Table 8.3—Continued

GRB	δt (hr)	Telescope	Instrument	Filter	Exposure Time (s)	F_ν (μJy)	σ (μJy)	References
	2.8	ESO/MPG	GROND	g	460	6.0	0.58	Kopac et al. (2013)
	2.8	ESO/MPG	GROND	r	460	9.6	0.93	Kopac et al. (2013)
	2.8	ESO/MPG	GROND	i	460	13.1	1.3	Kopac et al. (2013)
	2.8	ESO/MPG	GROND	z	460	14.0	1.4	Kopac et al. (2013)
	2.8	ESO/MPG	GROND	J	480	36.5	7.4	Kopac et al. (2013)
	2.8	ESO/MPG	GROND	H	480	34.0	6.9	Kopac et al. (2013)
	2.8	ESO/MPG	GROND	K	480	< 47.3		Kopac et al. (2013)
	7.3	Johnson	RATIR	r	7812	< 1.6		Littlejohns et al. (2013)
	7.3	Johnson	RATIR	i	7812	< 1.9		Littlejohns et al. (2013)
	7.3	Johnson	RATIR	Z	3384	< 2.9		Littlejohns et al. (2013)
	7.3	Johnson	RATIR	Y	3384	< 4.8		Littlejohns et al. (2013)
	7.3	Johnson	RATIR	J	3384	< 3.6		Littlejohns et al. (2013)
	7.3	Johnson	RATIR	H	3384	< 3.6		Littlejohns et al. (2013)
131125A	11.8	iPTF		R		< 24.9		Singer et al. (2013a)
131126A	19.5	iPTF		R		< 107.8		Singer et al. (2013b)

Note. — Upper limits correspond to 3σ. All optical and near-IR fluxes are corrected for Galactic extinction in the directions of each bursts (Schlegel et al. 1998; Schlafly & Finkbeiner 2011). Instruments, exposure times, and flux density uncertainties are provided whenever available.

[a] Optical oserving constraint, due to delayed reporting of XRT position, sightline with high Galactic extinction, crowded field, or proximity to a bright star which contaminates the X-ray position.

[b] Optical re-brightening observed in GRB 080503 is unlikely the afterglow (Perley et al. 2009a).

[c] Simultaneous giz-band light curves are available in Nicuesa Guelbenzu et al. (2012b).

8.2.4 Radio

We gather all available radio afterglow data taken with the Karl G. Jansky Very Large Array (VLA), Westerbork Synthesis Radio Telescope (WSRT), Australia Telescope Compact Array (ATCA), and Combined Array for Research in Millimeter-wave Astronomy (CARMA). The resulting radio afterglow catalog is comprised of 50 short GRBs (Table 8.4). The large majority of events, 86%, were observed with the VLA, and eighteen bursts utilized the upgraded VLA, which has a ten-fold improvement in sensitivity (Perley et al. 2011).

We present new observations enabled by Target-of-Opportunity programming on the upgraded VLA (PI: E. Berger) and CARMA (PI: B. A. Zauderer) for 15 bursts (Table 8.4). In six cases, we obtained multiple sets of observations in order to place constraining limits on the radio afterglow on timescales spanning $\delta t \approx 1 - 10$ days. For data calibration and analysis, we follow standard procedures in the Astronomical Image Processing System (AIPS; Greisen 2003). In all cases, we do not find any uncatalogued radio sources in or around the X-ray or γ-ray positions. To measure 3σ upper limits on the radio afterglow brightness, we use AIPS/`IMSTAT` on source-free regions in the field. The radio afterglow detections and upper limits for 50 short GRBs with radio observations are listed in Table 8.4 and displayed in Figure 8.1. For the observations that are new to this work, flux densities reported here supercede those reported in GCN Circulars.

Three bursts have detected radio afterglows, and all discoveries were made with the VLA (GRB 050724A, Berger et al. 2005; Panaitescu 2006; GRB 051221A, Soderberg et al. 2006b; GRB 130603B, Fong et al. 2014). The median 3σ upper limit for all observations

is $F_{\nu,\rm rad} \approx 77\,\mu$Jy, and the median response time to the first observation is $\delta t \approx 25$ hr.

Table 8.4. Short GRB Radio afterglow catalog

GRB	δt (dy)	Facility	Mean Frequency (GHz)	F_ν (μJy)	σ (μJy)	References
050202	0.52	VLA	4.86	< 120		Frail & Soderberg (2005)
050509B	0.49	WSRT	4.86	< 66		van der Horst et al. (2005)
050709	1.6	VLA	8.46	< 115		Fox et al. (2005)
	2.5	VLA	8.46	< 114		
	4.5	VLA	8.46	< 74		
	7.5	VLA	8.46	< 40		
050724A	0.57	VLA	8.46	173	30	Berger et al. (2005)
	1.68	VLA	8.46	465	29	Berger et al. (2005)
	9.10	VLA	8.46	< 259		Panaitescu (2006)
050813	1.64	VLA	8.46	< 55		Cameron & Frail (2005a)
050906	3.91	VLA	8.46	< 92		Cameron & Frail (2005b)
050925	0.40	WSRT	4.9	< 72		van der Horst (2005)
051105A	0.54	VLA	8.5	< 51		Frail & Cameron (2005)
051221A	0.91	VLA	8.46	155	30	Soderberg et al. (2006b)
	1.94	VLA	8.46	< 72		
060313	2.12	VLA	8.46	< 110		Soderberg & Frail (2006)
060801	0.49	VLA	8.46	< 105		Soderberg et al. (2006a)
	1.2	WSRT	4.9	< 72		van der Horst (2006)
	5.2	WSRT	4.9	< 81		van der Horst (2006)
061210	1.9	VLA	8.46	< 102		Chandra & Frail (2006)
070429B	0.59	VLA	8.46	< 300		Chandra & Frail (2007b)
070714B	15.6	VLA	8.46	< 135		Chandra & Frail (2007d)
070724A	1.06	VLA	8.46	< 255		Chandra & Frail (2007a)
070729	9.49	VLA	8.46	< 255		Chandra & Frail (2007e)
070923	4.98	VLA	8.46	< 135		Chandra & Frail (2007c)
071112B	1.69	ATCA	8.7	< 141		Wieringa et al. (2007)
080503	3.05	VLA	8.46	< 54		Frail & Chandra (2008)

Table 8.4—Continued

GRB	δt (dy)	Facility	Mean Frequency (GHz)	F_ν (μJy)	σ (μJy)	References
080702A	0.74	VLA	8.46	< 156		Chandra & Frail (2008b)
081024A	1.03	VLA	8.46	< 156		Chandra & Frail (2008a)
081024B	4.1	VLA	8.46	< 114		Chandra et al. (2008)
081226A	58.9	ATCA	4.9	< 540		Moin et al. (2009a)
081226B	58.4	ATCA	4.9	< 588		Moin et al. (2009b)
090417A	0.37	VLA	8.46	< 72		Chandra & Frail (2009)
090510	1.98	VLA	8.46	< 84		Frail & Chandra (2009)
090515	0.87	VLA	8.46	< 60		Berger & Fong (2009a)
090621B	0.61	VLA	8.46	< 54		Berger & Fong (2009c)
090715A	1.25	VLA	8.46	< 64		Berger & Fong (2009d)
091117	2.33	VLA	8.46	< 120		Berger & Fong (2009b)
100625A	0.83	VLA	4.90	< 192		This work
100628A	0.77	VLA	5.8	< 291		This work
101224A	3.72	VLA	5.8	< 56		This work
110112A	1.87	VLA	5.0	< 75		This work
110112B	0.85	VLA	5.8	< 51		This work
	1.80	VLA	5.8	< 66		
	2.92	VLA	5.8	< 48		
	12.10	VLA	5.8	< 36		
110420B	0.65	VLA	4.90	< 77		This work
	7.65	VLA	5.8	< 116		
111020A	0.67	VLA	5.8	< 39		Fong et al. (2012b)
111117A	0.49	VLA	5.8	< 18		Margutti et al. (2012)
111121A	0.84	VLA	5.8	< 100		This work
120305A	0.16	VLA	5.8	< 18		This work

8.3 Broad-band Afterglow Analysis

We utilize the broad-band afterglow observations to constrain the explosion properties and circumburst environment of each burst. We adopt the standard synchrotron model for a relativistic blastwave in a constant density medium (ISM; Sari et al. 1999; Granot & Sari 2002), as expected for a non-massive star progenitor. This model provides a mapping from the broad-band afterglow flux densities to the isotropic-equivalent kinetic energy ($E_{\rm K,iso}$), circumburst density (n), fractions of post-shock energy in radiating electrons (ϵ_e) and magnetic fields (ϵ_B), and the electron power-law distribution index (p), with $N(\gamma) \propto \gamma^{-p}$ for $\gamma \gtrsim \gamma_{\rm min}$.

The synchrotron spectrum is characterized by a flux normalization and three break frequencies: the self-absorption frequency (ν_a), the peak frequency (ν_m), and the cooling frequency (ν_c). Constraints on the physical parameters requires knowledge of where the synchrotron break frequencies are located with respect to the observing bands. While in most cases there is not enough information to constrain the locations of ν_a and ν_m, we can use the available data to determine the location of ν_c with respect to the X-ray and optical bands. This then determines how the fluxes map to the inferred basic properties.

To determine the location of ν_c, we first determine the temporal and spectral power-law indices (α and β, respectively, where $F_\nu \propto t^\alpha \nu^\beta$) from the X-ray and optical light curves. We compare these indices to the standard relations given by the synchrotron model to determine whether the cooling frequency is above or below the X-ray band (i.e., whether or not the optical and X-ray bands are on the same part of the spectrum). This allows us to calculate the value of p and use all of the available data to constrain the burst energy and circumburst density.

Table 8.4—Continued

GRB	δt (dy)	Facility	Mean Frequency (GHz)	F_ν (μJy)	σ (μJy)	References
	2.25	VLA	5.8	< 18		
120521A	1.08	ATCA	34	< 95		Hancock et al. (2012a)
120804A	0.9	VLA	5.8	< 20		Berger et al. (2013b)
	2.2	ATCA	34	< 200		Hancock et al. (2012b)
	4.2	ATCA	34	< 120		Hancock et al. (2012b)
121226A	1.75	VLA	5.8	< 30		This work
	4.76	VLA	5.8	< 45		
130313A	0.77	VLA	5.8	< 60		This work
130603B	0.37	VLA	4.9	125	14.4	Fong et al. (2014)
	0.37	VLA	6.7	119	9.1	
	1.43	VLA	4.9	< 57		
	1.43	VLA	6.7	64.9	15.2	
	1.44	VLA	21.8	< 50		
	4.32	VLA	4.9	< 51		
	4.32	VLA	6.7	< 26		
	84.31	VLA	4.9	< 69		
	84.31	VLA	6.7	< 34		
130716A	2.51	VLA	5.8	< 33		This work
130822A	15.9	VLA	5.8	< 30		This work
130912A	0.91	VLA	5.8	< 29		This work
	3.10	VLA	5.8	< 42		
131004A	0.14	CARMA	93	< 100		This work
131224A	0.20	VLA	5.8	< 33		This work
	2.27	VLA	5.8	< 33		

Note. — For bursts with multiple upper limits, we only display the most constraining limits. Upper limits are 3σ.

8.3.1 X-rays

To investigate the temporal behavior of the X-ray afterglows, we utilize χ^2-minimization to fit a single power law model to each light curve in the form $F_{\nu,X} \propto t^{\alpha_X}$, with temporal index α_X as the single free parameter. For the X-ray light curves, we initially include all of the available data at $\delta t \gtrsim 1000$ s in the fit. In a few cases, there are light curve features which significantly affect the fit: super-imposed flares (GRBs 050724A and 111121A), plateaus possibly due to energy injection (GRB 051221A), or steepenings at $\delta t \gtrsim 1000$ s likely due to a jet break (GRBs 051221A and 111020A). For these bursts, we exclude the time intervals that contain such features, and re-fit the light curves. In eight cases, there only exists a single detection and an upper limit beyond 1000 s, so we can only extract an upper limit for α_X. The resulting best-fit values for α_X, along with 1σ uncertainties, are listed in Table 8.5. Also listed are the X-ray spectral indices, β_X, from the relation $\beta_X \equiv 1 - \Gamma$. The X-ray afterglows have weighted average index values of $\langle \alpha_X \rangle = -1.08 \pm 0.03$ (Figure 8.1) and $\langle \beta_X \rangle = -1.05 \pm 0.03$.

Table 8.5. Spectral and Temporal Power-law Indices

GRB	α_X	β_X	$\alpha_{\rm opt}$	$\beta_{\rm opt}$
050509B	-1.10 ± 0.25	-0.88 ± 0.34	$\cdots$	$\cdots$
050709	-1.23 ± 0.10	-1.24 ± 0.35	-1.42 ± 0.08	$\cdots$
050724A	-0.93 ± 0.08	-0.81 ± 0.15	-1.74 ± 0.11^a	-0.82 ± 0.03^a
050813	< -0.004	$-1.3^{+2.1}_{-1.3}$	$\cdots$	$\cdots$
051210	$\cdots$	-2.1 ± 0.5	$\cdots$	$\cdots$
051221A	-1.08 ± 0.12	-1.0 ± 0.2	-0.97 ± 0.06	$\cdots$
060121	-1.23 ± 0.20	-1.07 ± 0.16	-0.60 ± 0.24	$\cdots$
060313	-1.47 ± 0.39	-0.96 ± 0.09	-0.70 ± 0.19	-1.35 ± 0.19
060502B	$\cdots$	$-2.07^{+1.50}_{-0.54}$	$\cdots$	$\cdots$
060801	$\cdots$	-0.68 ± 0.12	$\cdots$	$\cdots$
061006	-0.85 ± 0.30	-0.90 ± 0.25	-0.43 ± 0.08	$\cdots$
061201	-1.96 ± 1.18	-0.66 ± 0.12	$\cdots$	$\cdots$
061210	-1.71 ± 1.15	$-1.86^{+1.26}_{-0.61}$		
070429B	< -1.12	-2.0 ± 0.63	$\cdots$	$\cdots$
070707	< -0.65	$\cdots$	-2.55 ± 0.22	$\cdots$
070714B	-1.96 ± 0.69	-1.07 ± 0.19	-0.81 ± 0.11	$\cdots$
070724A	-0.95 ± 0.33	-0.60 ± 0.25	< -0.15	-0.58 ± 0.02
070729	$\cdots$	$-0.5^{+0.44}_{-0.25}$	$\cdots$	$\cdots$
070809	-1.09 ± 1.10	$-0.37^{+0.13}_{-0.07}$	-0.73 ± 0.33	$\cdots$
071227	-0.97 ± 0.27	-0.90 ± 0.31	$\cdots$	$\cdots$
080123	-0.77 ± 0.19	-1.6 ± 0.4	$\cdots$	$\cdots$
080426	-1.54 ± 0.33	-1.03 ± 0.16	$\cdots$	$\cdots$
080503	$\cdots$	$-1.53^{+0.26}_{-0.12}$	$\cdots$	$\cdots$

Table 8.5—Continued

GRB	α_X	β_X	$\alpha_{\rm opt}$	$\beta_{\rm opt}$
080702A	< -0.38	-1.00 ± 0.43	$\cdots$	$\cdots$
080905A	$\cdots$	-0.53 ± 0.18	-0.39 ± 1.36	$\cdots$
080919	-1.23 ± 0.69	$-1.9^{+0.63}_{-0.38}$	$\cdots$	$\cdots$
081024A	$\cdots$	-0.70 ± 0.38	$\cdots$	$\cdots$
081226A	$\cdots$	$-2.27^{+1.24}_{-0.32}$	-0.95 ± 0.30	-1.67 ± 0.67^a
090305A	$\cdots$	$\cdots$	-0.74 ± 0.09	-0.71 ± 0.27
090426A	-1.15 ± 0.16	-1.04 ± 0.09	-0.58 ± 0.16	-0.94 ± 0.06^b
090510	-1.79 ± 0.63	-0.75 ± 0.08	-2.37 ± 0.29	-0.85 ± 0.05
090515	$\cdots$	$-1.53^{+0.78}_{-0.28}$	< -0.12	$\cdots$
090607	< -0.72	-1.2 ± 0.4	$\cdots$	$\cdots$
090621B	-1.48 ± 0.54	$-2.7^{+0.68}_{-1.0}$	$\cdots$	$\cdots$
091109B	-0.83 ± 0.28	-1.1 ± 0.3	-0.49 ± 0.45	$\cdots$
100117A	$\cdots$	-1.6 ± 0.3	-1.60 ± 0.33	$\cdots$
100206A	$\cdots$	$-2.05^{+1.07}_{-0.53}$	$\cdots$	$\cdots$
100213	$\cdots$	$-2.0^{+1.2}_{-1.0}$	$\cdots$	$\cdots$
100625A	< 0.37	-1.5 ± 0.2	$\cdots$	$\cdots$
100702A	$\cdots$	-1.7 ± 0.3	$\cdots$	$\cdots$
101219A	-1.37 ± 0.13	-0.8 ± 0.1	$\cdots$	$\cdots$
101224A	$\cdots$	$-2.4^{+1.8}_{-0.6}$	$\cdots$	$\cdots$
110112A	-1.10 ± 0.05	-1.2 ± 0.2	< -0.32	$\cdots$
111020A	-0.78 ± 0.05	-1.04 ± 0.16	$\cdots$	$\cdots$
111117A	-1.21 ± 0.05	-1.0 ± 0.2	$\cdots$	$\cdots$
111121A	-1.55 ± 0.30	-0.90 ± 0.12	$\cdots$	$\cdots$

Table 8.5—Continued

GRB	α_X	β_X	$\alpha_{\rm opt}$	$\beta_{\rm opt}$
111222A	< -0.30	$-0.7^{+1.4}_{-0.4}$	$\cdots$	$\cdots$
120305A	$\cdots$	$-2.2^{+0.6}_{-0.4}$	$\cdots$	$\cdots$
120521A	$\cdots$	-0.8 ± 0.25	$\cdots$	$\cdots$
120630A	$\cdots$	-0.8 ± 0.3	$\cdots$	$\cdots$
120804A	-1.02 ± 0.10	-1.1 ± 0.1	$\cdots$	$\cdots$
121226A	-1.12 ± 0.28	-1.5 ± 0.25	$\cdots$	$\cdots$
130313A	$\cdots$	$-1.6^{+2.1}_{-2.5}$	$\cdots$	$\cdots$
130515A	$\cdots$	-0.7 ± 0.31	$\cdots$	$\cdots$
130603B	-1.88 ± 0.15	-1.2 ± 0.1	-1.26 ± 0.05	-2.0 ± 0.1^a
130716A	< -0.52	$-1.1^{+0.56}_{-0.38}$	$\cdots$	$\cdots$
130822A	$\cdots$	$-0.89^{+1.1}_{-0.34}$	$\cdots$	$\cdots$
130912A	-1.33 ± 0.18	-0.57 ± 0.13	< -0.42	$\cdots$
131004A	-1.1 ± 0.61	-0.8 ± 0.3	-1.94 ± 0.25	-1.52 ± 0.13^a

Note. — Error bars correspond to 1σ confidence. Values of $\beta_{\rm opt}$ are observed values and are uncorrected for intrinsic rest-frame extinction, A_V.

[a] These values are computed over the same time interval as the X-ray flare that is super-imposed on the underlying afterglow power-law decay. No optical detections exist for the underlying afterglow. [b] This value corresponds to the spectral behavior after the jet break.

Next, we constrain the location of the cooling frequency, ν_c, with respect to the X-ray band. We use the relations given by Granot & Sari (2002) which relate α_X and β_X to the value of p for the scenarios $\nu_m < \nu_X < \nu_c$ and $\nu_c < \nu_X$ by

$$p = \left\{ \begin{array}{c} 1 - 2\beta_X \\ 1 - \frac{4}{3}\alpha_X \end{array} \right\} \qquad \nu_m < \nu_X < \nu_c \tag{8.1}$$

$$p = \left\{ \begin{array}{c} -2\beta_X \\ \frac{2 - 4\alpha_X}{3} \end{array} \right\} \qquad \nu_c < \nu_X . \tag{8.2}$$

For a given burst, we calculate the values of p and 1σ uncertainties using Equations 8.1 and 8.2 and standard propagation of errors. We select the valid regime under the condition that the values of p independently determined from α_X and β_X for a given scenario agree within the 1σ uncertainties. Following this condition, we can constrain the location of ν_c with respect to the X-ray band for 32 bursts (Table 8.6); for 18 events, the cooling frequency is below the X-ray band. We calculate the weighted mean for the value of p in the valid scenario; the resulting values and uncertainties are listed in Table 8.6. We note that in the case of GRB 071227, the condition is satisfied for $\nu_c < \nu_X$, but has a median of $p < 2$ ($p = 1.92 \pm 0.31$), which yields a divergent total integrated energy. Thus for this burst, we employ $p = 2.05$ in our subsequent analysis (Table 8.6). The weighted mean for the sample of 32 bursts is $\langle p \rangle = 2.36 \pm 0.03$.

Table 8.6. Inferred Basic Properties

GRB	A_V (mag)	$\nu_c < \nu_X$?	p	ϵ_e	ϵ_B	$E_{\gamma,\rm iso,52}$ (10^{52} erg)	$< E_{\rm K,iso,52} >^+$ (10^{52} erg)	η_γ	$< n >^+$ (cm^{-3})
050709	0	Y	2.31 ± 0.13	0.1	0.1	0.09	2.6[-0.6,+0.8] $\times 10^{-3}$	0.97	1.0[-0.5,+0.8]
	0	Y	2.31 ± 0.13	0.1	0.01	0.09	6.2[-0.6,+0.4] $\times 10^{-3}$	0.93	1.6[-0.2,+0.2]
050724A	0	N	2.29 ± 0.10	0.1	10^{-4}	0.24	1.8[-0.05,+0.08]	0.58	0.89[-0.49,+0.58]
051221A	0	Y	2.24 ± 0.07	0.1	0.1	1.3	0.16[-0.01,+0.01]	0.89	3.0[-0.5,+0.6] $\times 10^{-2}$
	0	Y	2.24 ± 0.07	0.1	0.01	1.3	0.27[-0.03,+0.03]	0.83	0.14[-0.04,+0.05]
060121	1.6	Y	2.24 ± 0.20	0.1	0.1	4.5	0.20[-0.04,+0.05]	0.96	5.4[-2.2,+5.6] $\times 10^{-3}$
	1.6	Y	2.24 ± 0.20	0.1	0.01	4.5	0.23[-0.04,+0.05]	0.95	0.16[-0.06,+0.17]
060313[a]	0	Y	2.03 ± 0.20	0.1	0.1	2.9	0.45[-0.05,+0.05]	0.87	3.3[-0.5,+1.0] $\times 10^{-3}$
061006	F	N	2.39 ± 0.31	0.1	0.1	1.1	0.64[-0.37,+0.85]	0.63	2.2[-1.9,+16] $\times 10^{-5}$
	F	N	2.39 ± 0.31	0.1	0.01	1.1	1.1[-0.7,+2.1]	0.50	1.2[-1.1,+29] $\times 10^{-4}$
061201	F	N	2.35 ± 0.24	0.1	0.1	0.05	0.05[-0.03,+0.10]	0.47	5.0[-4.6,+66] $\times 10^{-5}$
	F	N	2.35 ± 0.24	0.1	0.01	0.05	0.1[-0.09,+0.4]	0.29	2.7[-2.6,+120] $\times 10^{-4}$
070714B[b]	0.5	Y	2.30 ± 0.35	0.1	0.1	1.7	0.1[-0.02,+0.02]	0.94	5.6[-1.1,+2.4] $\times 10^{-2}$
070724A	1.5	N	2.24 ± 0.33	0.1	0.1	0.03	0.35[-0.20,+0.49]	0.07	1.9[-1.6,+12] $\times 10^{-5}$
	2.0	N	2.24 ± 0.33	0.1	0.01	0.03	1.1[-0.8,+3.0]	0.02	9.3[-9.2,+210] $\times 10^{-5}$
070809	0	N	2.12 ± 1.47[c]	0.1	0.1	0.09	0.5[-0.3,+0.7]	0.14	2.2[-1.9,+15] $\times 10^{-5}$
	0	N	2.12 ± 1.47[c]	0.1	0.01	0.09	1.1[-0.8,+2.7]	0.07	1.2[-1.1,+30] $\times 10^{-4}$
071227	0	Y	1.92 ± 0.31	0.1	0.1	0.14	8.4[-1.9,+2.5] $\times 10^{-3}$	0.94	1.9[-1.1,+2.4]
	0	Y	1.92 ± 0.31	0.1	0.01	0.14	8.9[-1.8,+2.6] $\times 10^{-3}$	0.94	60[-33,+75]
080426	F	Y	2.29 ± 0.26	0.1	0.1	0.35	0.05[-0.01,+0.01]	0.87	0.04[-0.02,+0.04]
	F	Y	2.29 ± 0.26	0.1	0.01	0.35	0.06[-0.01,+0.01]	0.85	1.2[-0.48,+1.2]
080905A	F	N	2.06 ± 0.36	0.1	0.1	0.02	0.04[-0.03,+0.12]	0.34	1.3[-1.2,+33] $\times 10^{-4}$
	F	N	2.06 ± 0.36	0.1	0.01	0.02	0.08[-0.07,+0.44]	0.21	7.1[-7.1,+610] $\times 10^{-4}$

Table 8.6—Continued

GRB	A_V (mag)	$\nu_c < \nu_X$?	p	ϵ_e	ϵ_B	$E_{\gamma,\mathrm{iso},52}$ (10^{52} erg)	$< E_{\mathrm{K,iso},52} >^+$ (10^{52} erg)	η_γ	$< n >^+$ (cm^{-3})
080919	$\gtrsim 6$	Y	2.97 ± 0.68	0.1	0.1	0.07	1.9[-0.4,+0.5] $\times 10^{-2}$	0.78	0.20[-0.07,+0.19]
	$\gtrsim 6$	Y	2.97 ± 0.68	0.1	0.01	0.07	2.9[-0.6,+0.7] $\times 10^{-2}$	0.70	5.1[-1.7,+4.5]
081024A	F	N	2.40 ± 0.76	0.1	0.1	0.11	0.11[-0.07,+0.22]	0.51	8.1[-7.7,+150] $\times 10^{-5}$
	F	N	2.40 ± 0.76	0.1	0.01	0.11	0.25[-0.20,+0.92]	0.31	4.3[-4.2,260] $\times 10^{-4}$
081226A	1.0	N	2.27 ± 0.39	0.1	0.1	0.09	0.20[-0.13,+0.36]	0.32	3.2[-2.9,+29] $\times 10^{-5}$
	1.0	N	2.27 ± 0.39	0.1	0.01	0.09	0.43[-0.33,+1.5]	0.18	1.7[-1.6,+54] $\times 10^{-4}$
090426A	0	Y	2.13 ± 0.14	0.1	0.1	2.0	1.4[-0.3,+0.4]	0.59	0.04[-0.02,+0.04]
	0	Y	2.13 ± 0.14	0.1	0.01	2.0	1.5[-0.3,+0.4]	0.15	1.2[-0.6,+1.4]
090510	0	N	2.65 ± 0.08	0.1	0.1	0.77	0.77[-0.33,+0.57]	0.50	1.2[-1.0,+5.5] $\times 10^{-5}$
	0	N	2.65 ± 0.08	0.1	0.01	0.77	1.9[-1.2,+3.0]	0.29	6.4[-6.0,+100] $\times 10^{-5}$
090607	F	Y	2.40 ± 0.76	0.1	0.1	0.10	2.1[-0.3,+0.4] $\times 10^{-3}$	0.98	0.84[-0.22,+0.52]
	F	Y	2.40 ± 0.76	0.1	0.01	0.10	2.6[-0.4,+0.5] $\times 10^{-3}$	0.98	24[-6.3,+15]
090621B[b]	2.5	Y	2.64 ± 0.72	0.1	0.1	0.07	2.3[-0.6,+0.7] $\times 10^{-2}$	0.75	0.05[-0.02,+0.06]
	2.5	Y	2.64 ± 0.72	0.1	0.01	0.07	3.1[-0.7,+0.9] $\times 10^{-2}$	0.68	1.0[-0.27,+0.52]
091109B	F	N	2.40 ± 0.32	0.1	0.1	0.18	0.25[-0.16,+0.18]	0.42	2.8[-2.5,+24] $\times 10^{-5}$
	F	N	2.40 ± 0.32	0.1	0.01	0.18	0.8[-0.6,+2.2]	0.18	9.4[-9.0,200] $\times 10^{-5}$
100117A	F	Y	2.36 ± 0.3	0.1	0.1	0.22	1.9[-0.3,+0.3] $\times 10^{-2}$	0.92	0.04[-0.01,+0.03]
	F	Y	2.36 ± 0.3	0.1	0.01	0.22	2.3[-0.4,+0.4] $\times 10^{-2}$	0.90	1.2[-0.3,+0.9]
101219A	$\gtrsim 2.5$	N	2.73 ± 0.13	0.1	0.1	0.74	0.3[-0.2,+0.5]	0.68	4.6[-4.3,+59] $\times 10^{-5}$
	$\gtrsim 2.5$	N	2.73 ± 0.13	0.1	0.01	0.74	0.87[-0.64,+2.3]	0.46	2.4[-2.3,+97] $\times 10^{-4}$
110112A	F	Y	2.49 ± 0.07	0.1	0.1	0.03	6.4[-0.5,+0.8] $\times 10^{-2}$	0.31	2.4[-0.4,+0.4] $\times 10^{-2}$
111020A[ab]	0.5	Y	2.08 ± 0.32	0.1	0.1	0.17	0.48[-0.08,+0.09]	0.26	4.5[-3.8,+6.0] $\times 10^{-3}$
111117A	F	Y	2.27 ± 0.07	0.1	0.1	0.55	0.06[-0.01,+0.01]	0.90	8.3[-2.3,+5.9] $\times 10^{-3}$

Table 8.6—Continued

GRB	A_V (mag)	$\nu_c < \nu_X$?	p	ϵ_e	ϵ_B	$E_{\gamma,\rm iso,52}$ (10^{52} erg)	$< E_{\rm K,iso,52} >^{+}$ (10^{52} erg)	η_γ	$< n >^{+}$ (cm^{-3})
	F	Y	2.27 ± 0.07	0.1	0.01	0.55	0.07[-0.01,+0.02]	0.89	0.25[-0.07,+0.16]
111121A	N/A	N	2.87 ± 0.21	0.1	0.1	2.1	3.1[-1.2,+1.9]	0.40	8.2[-6.3,+27] $\times 10^{-6}$
	N/A	N	2.87 ± 0.21	0.1	0.01	2.1	8.3[-4.8,+11.1]	0.20	4.2[-3.8,+48] $\times 10^{-5}$
120804A[b]	2.5	Y	2.08 ± 0.11	0.1	0.1	3.4	1.1[-0.2,+0.3]	0.76	3.2[-1.5,+3.1] $\times 10^{-3}$
	2.5	Y	2.08 ± 0.11	0.1	0.01	3.4	2.3[-0.2,+0.2]	0.60	1.4[-0.1,+0.2] $\times 10^{-2}$
121226A[a]	1	Y	2.50 ± 0.37	0.1	0.1	0.37	0.6[-0.09,+0.08]	0.37	4.0[-0.6,+1.0] $\times 10^{-3}$
130603B	1.2	Y	2.70 ± 0.06	0.1	0.1	0.37	0.11[-0.01,+0.02]	0.77	0.09[-0.03,+0.04]
	0.3	Y	2.70 ± 0.06	0.1	0.01	0.37	0.15[-0.02,+0.02]	0.72	0.31[-0.04,+0.08]
130912A[b]	1.3	N	2.49 ± 0.17	0.1	0.1	0.16	0.50[-0.20,+0.37]	0.25	1.7[-1.5,+9.9] $\times 10^{-5}$
	1.3	N	2.49 ± 0.17	0.1	0.01	0.16	1.4-0.8,+0.2	0.11	5.2[-4.9,+7.6] $\times 10^{-5}$
131004A	0	N	2.57 ± 0.48	0.1	0.1	0.45	1.2[-0.36,+0.56]	0.28	1.2[-1.0,+5.7] $\times 10^{-5}$
	0	N	2.57 ± 0.48	0.1	0.01	0.45	2.8[-1.5,+3.4]	0.45	6.5[-4.7,+17] $\times 10^{-4}$

Note. — [+] Numbers in square brackets are the 1σ uncertainties about the median.
"F" indicates that the rest-frame extinction is fixed at the fiducial value of $A_V = 0$ mag. All solutions presented here assume a lower density bound of $n_{\rm min} = 10^{-6}$ cm^{-3}.
[a] We assume a redshift of $z = 1$ for this burst.
[b] Value of A_V is determined from a comparison of the optical and X-ray bands, and not directly from the optical/NIR SED.
[c] Determined from α_X alone.

For the remaining bursts, we cannot determine the location of ν_c, and therefore the value of p from the afterglow data. We therefore concentrate on the subset of 32 bursts with determine values of p for our broad-band afterglow analysis.

8.3.2 Optical/NIR

We determine the temporal index of the optical/NIR observations (where $F_{\nu,\rm opt} \propto t^{\alpha_{\rm opt}}$) in the same manner as described in Section 8.3.1, using the filter with the most well-sampled light curve for each burst. If there are multiple filters for which we can determine $\alpha_{\rm opt}$, we independently fit $\alpha_{\rm opt}$ for each filter and report the weighted mean (Table 8.5). We can measure the optical temporal decay for 18 short GRBs and place upper limits in four cases for bursts with only a single detection and upper limit. The best-fit optical temporal indices and uncertainties are listed in Table 8.5.

If there are contemporaneous observations in multiple filters, we use these to determine the spectral slope and to constrain the rest-frame extinction intrinsic to the afterglow environment (A_V). We use χ^2-minimization to fit the optical/NIR photometry to a power law model with rest-frame extinction according to a Milky Way extinction curve (Cardelli et al. 1989). We determine the observed spectral slope, $\beta_{\rm opt}$ ($F_{\nu,\rm opt} \propto \nu^{\beta_{\rm opt}}$) and A_V. We note that a Milky Way extinction curve should be a reasonable approximation as short GRB host galaxies are similar to the Milky Way in terms of their global properties (Berger 2009; Leibler & Berger 2010). The resulting values for the optical spectral indices, uncertainties, and A_V are listed in Table 8.6. We find non-zero extinction values for GRBs 060121, 070724A, 081226A, and 130603B, while in nine cases, we find no evidence for rest-frame extinction (Table 8.6). For bursts where

we do not have enough information to constrain the spectral behavior of the afterglow, we initially assume that there is no rest-frame extinction, $A_V = 0$, as expected for progenitors that do not originate in star-forming regions. However, in seven cases, a comparison to the X-ray data necessitates extinction (see Section 8.3.3); these A_V values are also listed in Table 8.6.

A few short GRBs have well-measured optical spectral indices from contemporaneous multi-band data, but do not have a well-sampled light curve in a single filter, preventing a measurement of $\alpha_{\rm opt}$. For these events, we use the measured value of $\beta_{\rm opt}$ to extrapolate all of the available afterglow data to a single filter, and then determine the temporal decay index from these observations.

Under the reasonable assumption that the optical band lies between the peak frequency, ν_m, and the cooling frequency, ν_c (such that $\nu_m < \nu_{\rm opt} < \nu_c$), we use the available values for $\alpha_{\rm opt}$ and $\beta_{\rm opt}$ and Equation 8.1 to determine the value of p. If this value agrees with that determined from the X-ray band, we include this in our weighted average of p; otherwise, we do not include it.

8.3.3 Constraints on $E_{\rm K,iso}$ and n for Individual Bursts

In the standard synchrotron model from Granot & Sari (2002), the dependencies on the isotropic-equivalent kinetic energy, circumburst density, and the microphysical parameters are as follows for a given flux density, $F_{\nu,i}$ and observing band, ν_i:

$$F_{\nu,i} \propto \begin{cases} n_0^{1/2} E_{\rm K,iso,52}^{5/6} \epsilon_{e,-1}^{-2/3} \epsilon_{B,-1}^{1/3} & \nu_a < \nu_i < \nu_m \\ n_0^{1/2} E_{\rm K,iso,52}^{\frac{3+p}{4}} \epsilon_{e,-1}^{p-1} \epsilon_{B,-1}^{\frac{1+p}{4}} & \nu_m < \nu_i < \nu_c \\ E_{\rm K,iso,52}^{\frac{2+p}{4}} \epsilon_{e,-1}^{p-1} \epsilon_{B,-1}^{\frac{p-2}{4}} & \nu_i > \nu_c \end{cases} \tag{8.3}$$

where n_0 is in units of cm^{-3}, $E_{\rm K,iso,52}$ is in units of 10^{52} erg, and $\epsilon_{e,-1}$ and $\epsilon_{B,-1}$ are in units of 0.1. In addition to these four parameters, $F_{\nu,i}$ is also dependent on the redshift, luminosity distance, ν_i, time after the burst, δt, and the value of p; the exact dependencies are provided in Granot & Sari 2002. For bursts with no spectroscopic redshift, we assume $z = 0.5$ set by the median of the short GRB population (Berger 2013). In all cases, we cannot independently constrain ϵ_e and ϵ_B since this requires well-sampled light curves in several bands. Thus, in order to determine ranges for $E_{\rm K,iso}$ and n, we fix the values of the microphysical parameters. We consider two fiducial cases: $\epsilon_e = 0.1, \epsilon_B = 0.1$, and $\epsilon_e = 0.1, \epsilon_B = 0.01$.

For each burst, we determine the constraints on $E_{\rm K,iso}$ and n by computing individual probability distributions for each observation. We then assign the probabilities to a grid of values, and use joint probability analysis to calculate the distributions in each parameter. For the grid, the ranges of the density and isotropic-equivalent kinetic energy are $n_i = 10^{-6} - 10^{3}$ cm^{-3} and $E_i = 10^{46} - 10^{54}$ erg, with 1000 logarithmically-spaced steps in each parameter. We choose the lower bound of the density range, $n_{\rm min} = 10^{-6}$ cm^{-3} to match the typical density of the intergalactic medium (IGM).

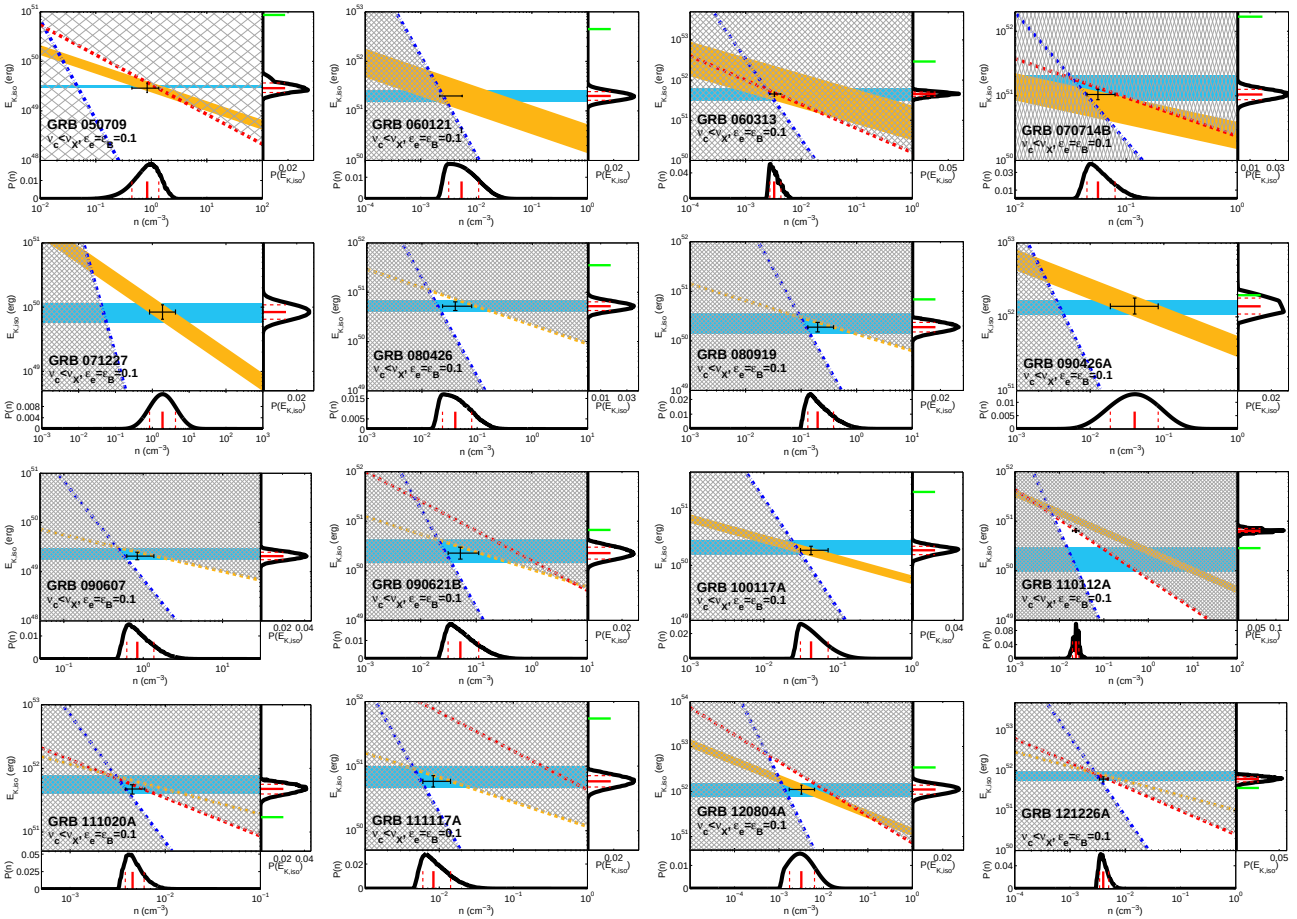

Figure 8.2.—: Isotropic-equivalent kinetic energy versus circumburst density for 16 short GRBs with solutions for $\nu_c < \nu_X$ assuming fiducial values for the microphysical parameters of $\epsilon_e = \epsilon_B = 0.1$. In each panel, the X-rays (light blue), optical (orange) and radio (red) provide independent constraints on the parameter space. In particular, the X-ray band provides an estimate of $E_{\rm K,iso}$. Measurements are shown as solid regions, where the width of the region corresponds to the 1σ uncertainty, while upper limits are denoted as dashed lines. Setting the cooling frequency to a maximum value of $\nu_{c,\rm max} = 7.2 \times 10^{16}$ Hz (0.3 keV) provides an additional constraint (dark blue dot-dashed line). The regions of parameter space ruled out by the observations are denoted (grey hashed regions). The median solution and 1σ uncertainty is indicated by the black cross in each panel, corresponding to the values listed in Table 8.6. For each burst, the joint probability distributions in n (bottom panel) and $E_{\rm K,iso}$ (right panel) are shown. Red lines correspond to the median, and dotted lines are the 1σ uncertainty about the median. The green line corresponds to $E_{\gamma,\rm iso}$.

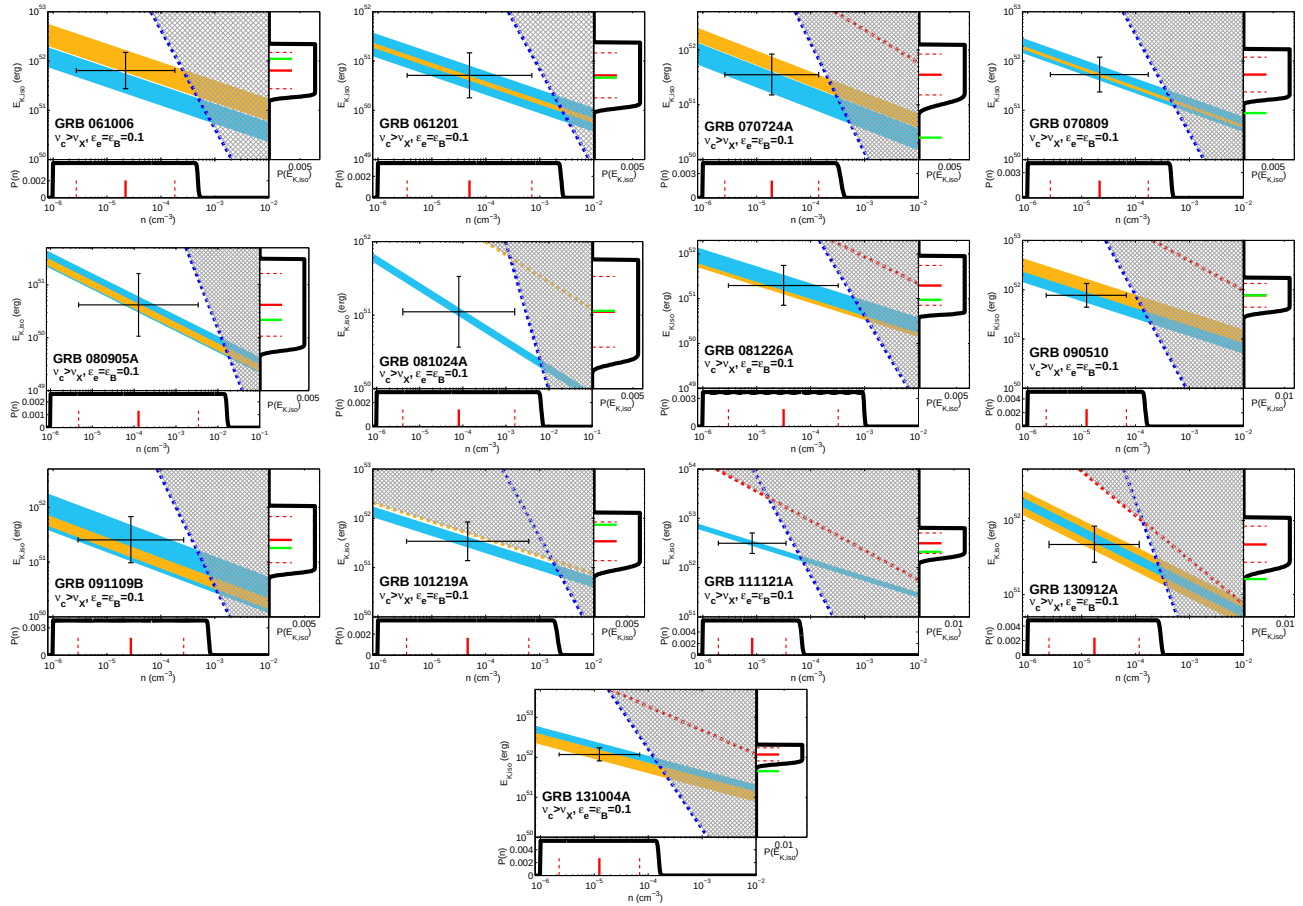

Figure 8.3.—: Isotropic-equivalent kinetic energy versus circumburst density for 13 short GRBs with solutions for $\nu_c > \nu_X$ assuming fiducial values for the microphysical parameters of $\epsilon_e = \epsilon_B = 0.1$. In each panel, the X-rays (light blue), optical (orange) and radio (red) provide independent constraints on the parameter space. Measurements are shown as solid regions, where the width of the region corresponds to the 1σ uncertainty, while upper limits are denoted as dashed lines. Setting the cooling frequency to a *minimum* value of $\nu_{c,\rm min} = 2.4 \times 10^{18}$ Hz (10 keV) provides an additional constraint (dark blue dashed line). The regions of parameter space ruled out by the observations are denoted (grey hashed regions). The median solution and 1σ uncertainty is indicated by the black cross in each panel, corresponding to the values listed in Table 8.6. For each burst, the joint probability distributions in n, with an imposed lower bound of $n_{\rm min} = 10^{-6}$ cm^{-3} (bottom panel), and $E_{\rm K,iso}$ (right panel) are shown. Red lines correspond to the median, and dotted lines are the 1σ uncertainty about the median. The green line corresponds to $E_{\gamma,\rm iso}$.

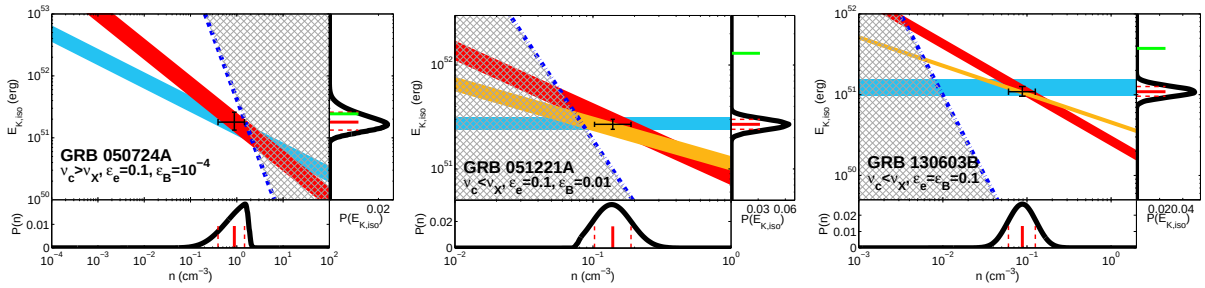

Figure 8.4.—: Isotropic-equivalent kinetic energy versus circumburst density for the three short GRBs with radio afterglow detections. The colors correspond to those in Figures 8.2 and 8.3. The addition of the radio band helps to constrain the best-fit solution, especially in the case of GRB 050724A. For GRB 050724A, at a fixed value of $\epsilon_e = 0.1$, ϵ_B is constrained to $\lesssim 10^{-4}$. The only optical observations available for GRB 050724A are during the steep decline phase of a super-imposed flare; thus we do not include the optical data in our analysis.

To calculate the individual probability distributions, we apply Equation 8.3 to every observation using the relevant regime and observing band, ν_i, and assume that the uncertainties in the flux densities are Gaussian. Each observation thus contributes a unique and log-normal distribution. Since the value of p is determined from the X-ray band, the $E_{\rm K,iso} - n$ relation remains unchanged when using different X-ray observations on the same temporal decline. However, in some cases, individual optical/NIR observations give slightly different relations, where the differences are larger than the 1σ uncertainty in any single relation. In these cases, we use the weighted mean and standard deviation of these relations (i.e., systematic uncertainty) as the optical/NIR solution. For the radio band, we assume that $\nu_a < \nu_{\rm rad} < \nu_m$, which is the case for the three bursts with radio afterglow detections. After calculating the unique probability distribution from each of the radio, optical/NIR and X-ray bands, we normalize the area under each of the distributions to unity. These relations are shown for each of 32 bursts in Figures 8.2-8.4.

For upper limits, we use Equation 8.3 to determine the $E_{\rm K,iso} - n$ relation at the 3σ upper limit. We then assign zero probability to the $E_{\rm K,iso} - n$ parameter space above the relationship, and assign a constant probability to the allowed parameter space below the relationship, normalized to unity. The upper limits are evident in Figures 8.2-8.4, where regions of ruled out parameter space are marked as hashed regions.

We can utilize the relative location of the cooling frequency as a final constraint, since it depends on a combination of energy and density,

$$\nu_c \propto n_0^{-1} E_{\rm K,iso,52}^{-1/2}, \tag{8.4}$$

with other dependencies on ϵ_B, δt, and redshift according to Granot & Sari (2002). For the cases in which the X-ray band is located above the cooling frequency ($\nu_c < \nu_X$), we employ a maximum value at the lower edge of the X-ray band, $\nu_{c,\rm max} = 7.3 \times 10^{16}$ Hz (0.3 keV), to obtain a lower limit on the combination of energy and density. The corresponding probability distribution has zero value in the $E_{\rm K,iso} - n$ parameter space below the relation, and a constant value above the relation, where the area in the allowed parameter space is normalized to unity. In cases where the X-ray band is below the cooling frequency ($\nu_m < \nu_X < \nu_c$), we set the cooling break to a minimum value, $\nu_{c,\rm min} = 2.4 \times 10^{18}$ Hz (10 keV) at the upper edge of the X-ray band, and determine the $E_{\rm K,iso} - n$ relation for each burst using Equation 8.4. This constraint sets an upper limit on the combination of energy and density. We form the probability distribution in the same manner as for afterglow upper limits. The relations for each burst set by the cooling frequency are shown in Figures 8.2-8.4. We also calculate the $E_{\rm K,iso} - n$ relations assuming that the cooling frequency is in the middle of the X-ray band,

$\nu_{c,\rm mid} = 1.2 \times 10^{18}$ Hz (5 keV), to understand the impact of our assumptions on the final energy and density distributions.

In the 18 cases where $\nu_c < \nu_X$, the afterglow brightness is independent of circumburst density, and thus the X-ray afterglow brightness serves as a proxy for the isotropic-equivalent kinetic energy (Equation 8.3). In the 14 cases where $\nu_m < \nu_X < \nu_c$ (Figure 8.3), the X-ray and optical/NIR bands occupy the same spectral regime and the resulting $E_{\rm K,iso} - n$ relations are parallel. The lower bound on the density is set by our minimum grid value of $n_{\rm min} = 10^{-6}$ cm^{-3}; the density is otherwise unconstrained at the low end (Figure 8.3). We note that in seven cases, the solution from the optical band is $\gtrsim 3\sigma$ below that for the X-ray band, suggesting that either there is intrinsic extinction, or that the X-rays do not originate from the forward shock. Assuming the former explanation, we incrementally add extinction until the X-ray and optical solutions agree to within the 1σ uncertainties. The resulting values for A_V are listed in Table 8.6.

To understand the impact of our choice of $n_{\rm min}$ on our results, we repeat the individual probability analysis, employing a more stringent lower bound of $n_{\rm min} = 10^{-4}$ cm^{-3}, at the low end of gas densities for the ISM (Korpi et al. 1999; Murali 2000; Gent et al. 2013). Since kinetic energy and density are inversely related, the upper bound on $E_{\rm K,iso}$ is naturally set by our choice of $n_{\rm min}$.

8.3.4 Joint Probability Distributions

Since each of the observing bands, as well as the location of the cooling frequency, contribute an independent probability distribution, we can calculate the joint probability from a product of these distributions. We integrate over each of the parameters to

obtain 1-dimensional probability distributions. Finally, we normalize the area under each 1-dimensional distribution to unity. The resulting distributions, $P(n)$ and $P(E_{\rm K,iso})$, for 29 bursts are shown in Figures 8.2 and 8.3 for the fiducial microphysical parameters, $\epsilon_e = \epsilon_B = 0.1$. The median values and 1σ uncertainties in isotropic-equivalent kinetic energy and circumburst density are also shown in these figures and listed in Table 8.6.

In some cases, we do not find a valid joint solution on our allowed grid for the fiducial microphysical parameters and redshift. For instance, for three of the bursts without spectroscopic redshifts, GRBs 060313, 111020A, and 121226A, we do not find any valid solutions at $z = 0.5$ on our allowed grid, so we assume $z = 1$ for these bursts. In addition, for five bursts, we find valid solutions for $\epsilon_e = 0.1, \epsilon_B = 0.1$, but not for $\epsilon_e = 0.1, \epsilon_B = 0.01$ (Table 8.6).

Figure 8.4 shows the individual and joint probability distributions for three additional bursts with radio afterglow detections. In two of three cases, we can use the available data to place additional constraints on the microphysical parameters. For GRB 050724A, the radio and X-ray data require that $\epsilon_B \lesssim 10^{-4}$ for $\epsilon_e = 0.1$, while for GRB 051221A, the solution provides a significantly better fit at $\epsilon_B = 0.01$ (for $\epsilon_e = 0.1$), shown in Figure 8.4. In all cases, the addition of the radio band enables tighter distributions in both energy and density.

8.3.5 Comparison to $E_{\gamma,\rm iso}$

To compare the inferred isotropic-equivalent kinetic energy to the γ-ray energy, we compute the isotropic-equivalent γ-ray energy, $E_{\gamma,\rm iso}$, to represent a range of $\approx 10 - 1000$ keV (to match the widest energy ranges for current GRB detection

satellites). We can obtain this value from the fluence, f_γ, redshift, and luminosity distance, by

$$E_{\gamma,\rm iso} = \frac{4\pi d_L^2}{1+z} f_\gamma \times k_{\rm bol} \ {\rm erg} \tag{8.5}$$

where $k_{\rm bol}$ is the bolometric correction factor to convert the fluence to an energy range of $\sim 10 - 1000$ keV, d_L is the luminosity distance in cm, and f_γ is in units of erg cm^{-2}. For cases in which the fluence is calculated over the $15 - 150$ keV *Swift* energy range, we use $k_{\rm bol} = 5$. If a burst is detected by other γ-ray satellites which cover a wider energy range of $\approx 10 - 1000$ keV (e.g., *Fermi*, *Konus-Wind*, *Suzaku*), we utilize the measured fluences from these satellites and $k_{\rm bol} = 1$ to calculate the γ-ray energy. We also calculate the γ-ray efficiency, $\eta_\gamma = E_{\gamma,\rm iso}/(E_{\gamma,\rm iso} + E_{K,\rm iso})$. The resulting values of $E_{\gamma,\rm iso}$ and η are listed in Table 8.6, and the values of $E_{\gamma,\rm iso}$ are shown in Figures 8.2-8.4.

8.4 Density and Energy Scale for Short GRBs

In order to quantify the distributions of circumburst densities and isotropic-equivalent kinetic energies for the entire sample, we calculate the combined probability distributions from the sum of the 1-dimensional probability distributions, $P(n)$ and $P(E_{\rm K,iso})$, for all bursts. We sum the distributions at fixed values of ϵ_B and $n_{\rm min}$, and normalize the area under each of the combined distributions to unity. The combined and cumulative probability distributions for both density and kinetic energy are shown in Figures 8.5 and 8.6, corresponding to the two fiducial cases, $\epsilon_B = 0.1$ and $\epsilon_B = 0.01$. To keep the distributions at a fixed value of ϵ_B, we exclude GRB 050724A in the combined

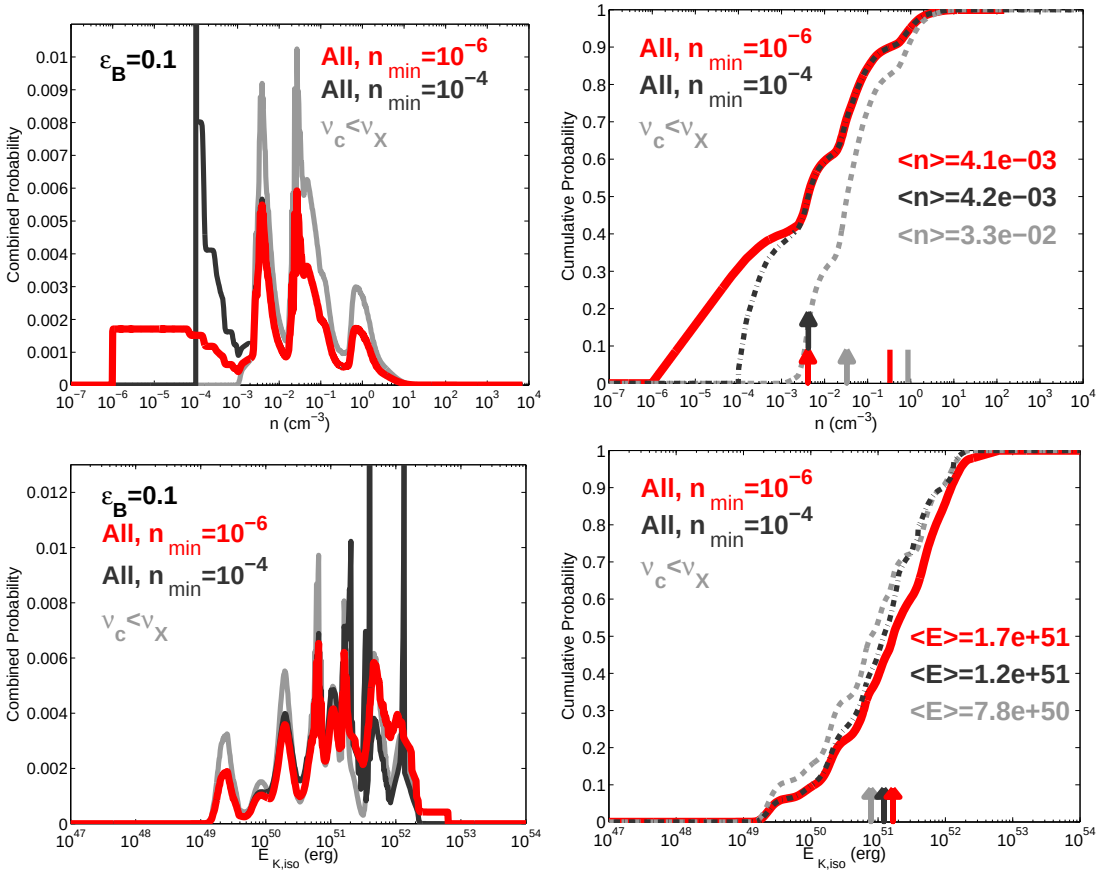

Figure 8.5.—: Combined and cumulative probability distributions in n and $E_{\rm K,iso}$ assuming $\epsilon_e = \epsilon_B = 0.1$. Each panel shows three populations: all 31 bursts with an imposed lower bound of $n_{\rm min} = 10^{-6}$ cm^{-3} (red), all 31 bursts with an imposed lower bound of $n_{\rm min} = 10^{-4}$ cm^{-3} (black or black dot-dashed), and the sub-sample of 18 events with $\nu_c < \nu_X$ (light grey). Color-coded arrows from the bottom denote the median for each distribution, and lines denote 90% upper limits. The cumulative distributions indicate that for $n \gtrsim 3 \times 10^{-3}$ cm^{-3} ($E_{\rm K,iso} \lesssim 3 \times 10^{50}$ erg), the distributions are virtually independent of the choice of $n_{\rm min}$ provided that $n_{\rm min} \gtrsim 10^{-4}$ cm^{-3}. This allows us to place robust 90% upper limits of $n \lesssim 0.33$ cm^{-3} for the entire sample and $n \lesssim 0.86$ cm^{-3} for the well-measured events. In addition, $\approx 95\%$ of the total probability for all events lies below densities of 1 cm^{-3}.

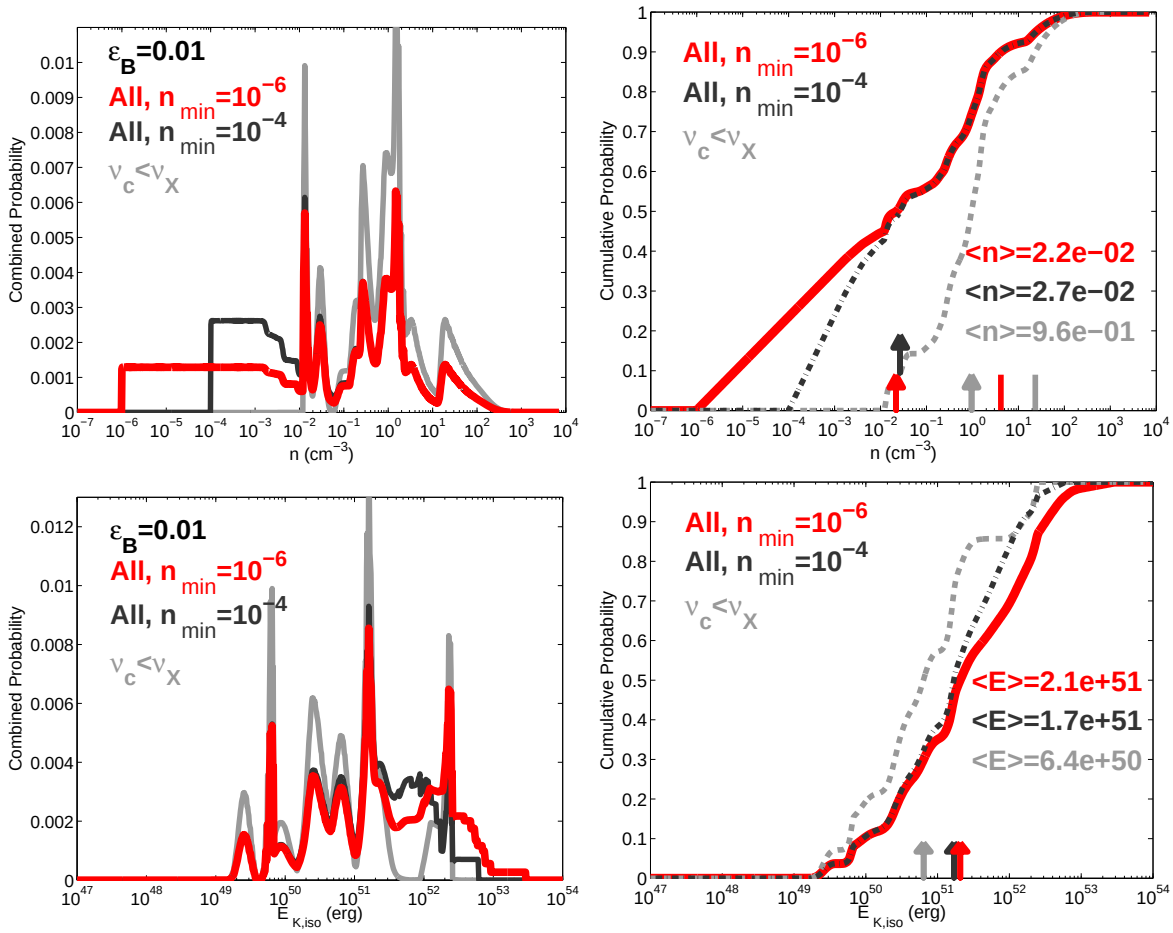

Figure 8.6.—: Combined and cumulative probability distributions in n and $E_{\rm K,iso}$ assuming $\epsilon_e = 0.1$, $\epsilon_B = 0.01$. Each panel shows three populations: all 27 bursts with an imposed lower bound of $n_{\rm min} = 10^{-6}$ cm^{-3} (red), all 27 bursts with an imposed lower bound of $n_{\rm min} = 10^{-4}$ cm^{-3} (black or black dot-dashed), and the sub-sample of 14 events with $\nu_c < \nu_X$ (light grey). Color-coded arrows from the bottom denote the median for each distribution, and lines denote 90% upper limits. The cumulative distributions indicate that for $n \gtrsim 10^{-2}$ cm^{-3} ($E_{\rm K,iso} \lesssim 10^{51}$ erg), the distributions are virtually independent of the choice of $n_{\rm min}$ provided that $n_{\rm min} \gtrsim 10^{-4}$ cm^{-3}. This allows us to place robust 90% upper limits of $n \lesssim 4.2$ cm^{-3} for the entire sample and $n \lesssim 23.3$ cm^{-3} for the well-measured events. In addition, $\approx 75\%$ of the total probability for all events lies below densities of 1 cm^{-3}.

Table 8.7. Circumburst Density and Kinetic Energy Population Statistics

Scenario	No. of Events	ϵ_B	$\langle n \rangle$ (cm^{-3})	n 90% U.L. (cm^{-3})	Fraction < 1 cm^{-3}	$\langle E_{\mathrm{K,iso}} \rangle$ (erg)
All bursts, $n_{\min} = 10^{-6}$ cm^{-3}	31	0.1	4.1×10^{-3}	0.33	0.95	1.7×10^{51}
All bursts, $n_{\min} = 10^{-4}$ cm^{-3}	31	0.1	4.2×10^{-3}	0.33	0.95	1.2×10^{51}
Bursts with $\nu_c < \nu_X$	18	0.1	3.3×10^{-2}	0.86	0.92	7.8×10^{50}
All bursts, $n_{\min} = 10^{-6}$ cm^{-3}, ν_c @ 5 keV	31	0.1	1.8×10^{-3}	0.12	0.96	
All bursts, $n_{\min} = 10^{-4}$ cm^{-3}, ν_c @ 5 keV	31	0.1	2.2×10^{-3}	0.12	0.96	
All bursts, $n_{\min} = 10^{-6}$ cm^{-3}	27	0.01	2.2×10^{-2}	4.2	0.75	2.1×10^{51}
All bursts, $n_{\min} = 10^{-4}$ cm^{-3}	27	0.01	2.7×10^{-2}	4.2	0.75	1.7×10^{51}
Bursts with $\nu_c < \nu_X$	14	0.01	0.96	23.3	0.51	6.4×10^{50}
All bursts, $n_{\min} = 10^{-6}$ cm^{-3}, ν_c @ 5 keV	27	0.01	2.4×10^{-2}	2.2	0.81	
All bursts, $n_{\min} = 10^{-4}$ cm^{-3}, ν_c @ 5 keV	27	0.01	3.5×10^{-2}	2.2	0.81	

distributions since the only valid solutions are for $\epsilon_B \lesssim 10^{-4}$ ($\epsilon_e = 0.1$). Four additional bursts lack valid solutions for $\epsilon_B = 0.01$ (Table 8.6). We therefore have 31 events in our distributions for $\epsilon_B = 0.1$ and 27 events for $\epsilon_B = 0.01$.

We first consider the distributions with a lower bound on the density of $n_{\rm min} = 10^{-6}$ cm^{-3}. For $\epsilon_B = 0.1$, the median values are $\langle n \rangle \approx 4.1 \times 10^{-3}$ cm^{-3} and $\langle E_{\rm K,iso} \rangle \approx 1.7 \times 10^{51}$ erg (Table 8.7 and Figure 8.5). Imposing a more stringent lower bound of $n_{\rm min} = 10^{-4}$ cm^{-3}, set by the typical density scale of the diffuse ISM, we find that for densities of $n \gtrsim 3 \times 10^{-3}$ cm^{-3} ($E_{\rm K,iso} \lesssim 3 \times 10^{50}$ erg), the distributions are virtually independent of our choice of $n_{\rm min}$, provided that $n_{\rm min} \lesssim 10^{-4}$ cm^{-3}. Importantly, this also allows us to place robust upper limits on the density and energy for the entire sample that are independent of $n_{\rm min}$ (Table 8.7). We find that the 90% upper limit only decreases by a factor of three when assuming a cooling frequency value in the middle of the X-ray band (5 keV; Table 8.7). Strikingly, $\approx 95\%$ of the probability for all events lies at densities of $\lesssim 1$ cm^{-3} (Figure 8.5), regardless of $n_{\rm min}$ or the location of the cooling frequency within the X-ray band.

We repeat the same exercise for $\epsilon_B = 0.01$ to create cumulative probability distributions (Figure 8.6). When compared to the $\epsilon_B = 0.1$ case, the median density increases by a factor of five, while $E_{\rm K,iso}$ only increases by a factor of 1.2 (Table 8.7 and Figure 8.6). The cumulative distributions are independent of $n_{\rm min}$ for $n \gtrsim 10^{-2}$ cm^{-3} ($E_{\rm K,iso} \lesssim 10^{51}$ erg). We find that the median and fraction of total probability for all events which lies below $n \lesssim 1$ cm^{-3} are unaffected when assuming a cooling frequency corresponding to 5 keV (Table 8.7).

We also calculate the statistics for the sub-sample of bursts with $\nu_c < \nu_X$ and

therefore relatively well-constrained energies and densities, corresponding to the events in Figure 8.2. We find that for $\epsilon_B = 0.1$ ($\epsilon_B = 0.01$), the distribution has a median of 3.3×10^{-2} cm^{-3} (0.96 cm^{-3}) and furthermore that $\approx 92\%$ (51%) of the total probability lies at circumburst densities of $n \lesssim 1$ cm^{-3} (Figures 8.5-8.6 and Table 8.7).

8.5 Discussion and Implications

8.5.1 Population Statistics

We present the radio through X-ray afterglow afterglows of 86 short GRBs and investigate a sub-sample of 32 bursts in more detail to place constraints on the circumburst densities and energies. In 18 cases, there are X-ray observations following the GRB trigger with no detected afterglow, although most of these are attributed to observing constraints or delayed *Swift*/XRT observations. Thus, we find that the vast majority, $\approx 92\%$ of bursts with prompt X-ray follow-up observations and no observing constraints have detected X-ray afterglows, while $\approx 40\%$ have detected optical afterglows after taking in to account observing constraints. For the 46 bursts with no detected optical afterglow, the median limit placed on the afterglow brightness is $\gtrsim 23.5$ mag at $\delta t \approx 0.3 - 0.5$ days after the burst. In the NIR, the median afterglow limits are $\gtrsim 21.5 - 22.5$ mag ($\lesssim 4 - 8\,\mu$Jy). We find that these limits and timescales are independent of the detection of an X-ray afterglow (Figure 8.1). However, since we only include bursts with optical limits of $\gtrsim 20$ mag ($\lesssim 35\,\mu$Jy), we are excluding a fraction of bursts with very shallow follow-up; thus the limits here for bursts with only γ-ray localizations are an optimistic representation of the entire population.

By fitting the X-ray light curves, we find a median decline rate of $\alpha_X = -1.08$ at $\delta t \gtrsim 1000$ s for 30 bursts with measured temporal indices, similar to the pre-jet break declines measured from long GRB light curves (Nysewander et al. 2009; Racusin et al. 2009; Kann et al. 2010; Zaninoni et al. 2013), and slightly shallower than the value of $\alpha_X \approx -1.2$ found for 11 short GRBs in an earlier study (Nysewander et al. 2009). We measure the optical decline rates and find a shallower median decline rate of $\alpha_{\rm opt} = -0.87$ from 17 well-sampled bursts. From spectral fitting of the optical/NIR data and afterglow modeling, we find 12 cases which require rest-frame extinction (Table 8.6). We note that GRB 080919 has the highest value of rest-frame extinction, with $A_V = 6$ mag. However, this burst has a sightline close to the Galactic plane and therefore has a highly uncertain Galactic extinction, which likely affects the inferred value for A_V. For the radio band, we introduce new observations for 15 bursts, with an average response time of $\delta t \approx 25$ hr and a median 3σ upper limit of $77\,\mu$Jy. In more recent cases, we set unprecedented 3σ limits of $15 - 20\,\mu$Jy using the upgraded VLA on timescales of $\delta t \approx 1 - 10$ days.

8.5.2 Implications for the Progenitors

There is mounting observational evidence from their host galaxies and environments that short GRBs originate from NS-NS/NS-BH merger progenitors (e.g., Fong et al. 2010; Berger 2010a; Fong & Berger 2013; Tunnicliffe et al. 2013). In the context of the compact object merger progenitor, we compare the distribution of energies and densities to those predicted for NS-NS mergers. We find median isotropic-equivalent γ-ray and kinetic energy scales of $\approx 2 \times 10^{51}$ erg and $(1 - 2) \times 10^{51}$ erg, respectively. These values are two orders of magnitude lower than those inferred for long GRBs (Nysewander et al.

2009; Kann et al. 2010). The values for $E_{\rm K,iso}$ span a wide range, $(0.01 - 30) \times 10^{51}$ erg, while the γ-ray energies are more tightly distributed, with $(0.2 - 45) \times 10^{51}$ erg. If short GRBs are collimated in jets of $\approx 5 - 10^{\circ}$ (Soderberg et al. 2006b; Nicuesa Guelbenzu et al. 2011; Fong et al. 2012b, 2014), the beaming-corrected total energy release would be $\approx (0.02 - 8) \times 10^{50}$ erg.

The inferred energy scales can be used to constrain the mechanism of energy extraction to power the relativistic jet: the thermal energy release from $\nu\bar{\nu}$ annihilation in a baryonic outflow (Jaroszynski 1993; Mochkovitch et al. 1993) and magnetohydrodynamic (MHD) processes in the black hole's accretion remnant (e.g. Blandford & Znajek 1977; Rosswog et al. 2003). The general consensus is that $\nu\bar{\nu}$ annihilation can only produce beaming-corrected total energy releases of $10^{48} - 10^{49}$ erg, while MHD processes can more easily produce energy releases in excess of 10^{49} erg (Ruffert & Janka 1999b,a; Popham et al. 1999; Rosswog 2005; Birkl et al. 2007; Lee & Ramirez-Ruiz 2007). Thus, if short GRBs have wider opening angles of $\gtrsim 10^{\circ}$, and thus a smaller correction to the isotropic-equivalent energy scale, it will be necessary to invoke MHD processes to explain the high energy end of the distribution.

We find a wide range of inferred circumburst densities, $10^{-5} - 10$ cm^{-3} for the 32 bursts that we have studied in detail. In particular, there is a population of 18 bursts with well-measured densities which span $10^{-3} - 10$ cm^{-3}. Separating the bursts by host galaxy type according to Fong et al. (2013), we find that bursts in star-forming host galaxies span the full range of densities, while bursts in elliptical hosts hint at a bimodal distribution in density (Figure 8.7). We compare the inferred densities to predictions for NS-NS mergers from population synthesis for varying Galactic potentials, which have input distributions for merger timescales and kick velocities

(Belczynski et al. 2006). Considering only the three bursts with elliptical hosts, we find particularly good agreement with the distributions for the large elliptical galaxy model ($M_* = 10^{11} M_\odot$, $M_{\rm halo} = 10^{12} M_\odot$) which has probability peaks at 10^{-5} cm^{-3} and 1 cm^{-3}, but find the distribution cannot be easily explained by the small elliptical galaxy model ($M_* = 10^8 M_\odot$), which is dominated by very low densities of $\lesssim 10^{-6}$ cm^{-3} (Belczynski et al. 2006). The inferred distribution of densities is also inconsistent with the large starburst model, in which mergers remain bound to the galaxy and also have short merger timescales of $\lesssim 1$ Gyr; consequently these mergers exclusively occur in denser regions of $\gtrsim 10^{-4}$ cm^{-3}.

We next investigate the relationship between the inferred circumburst densities and burst offsets from their host galaxies. If short GRBs trace the large-scale distribution of the ISM, we expect the inferred circumburst densities to decrease as a function of offset. In this simplified picture, we would also expect short GRBs which originate in elliptical galaxies to have lower inferred densities due to the lower average ISM densities in elliptical galaxies (e.g., Fukazawa et al. 2006). In this vein, we gather all available projected physical offsets, δR, between the afterglow location and host galaxy center, derived from ground-based (Margutti et al. 2012; Berger et al. 2013b; Sakamoto et al. 2013) and *Hubble Space Telescope* (*HST*) observations (Fong et al. 2010; Fong & Berger 2013). Since most of these studies have assumed a fiducial redshift of $z = 1$ for bursts with no spectroscopic redshift, we re-calculate the physical offsets at $z = 0.5$ to be consistent with this work. However, for GRBs 060313 and 111020A, afterglow modeling implies that $z > 0.5$ (c.f. Section 8.3.3; Fong et al. 2012b; Roming et al. 2006) so we keep the original fiducial value of $z = 1$. The distribution of circumburst densities with respect to projected physical offset for 20 bursts is shown in Figure 8.7. We find that

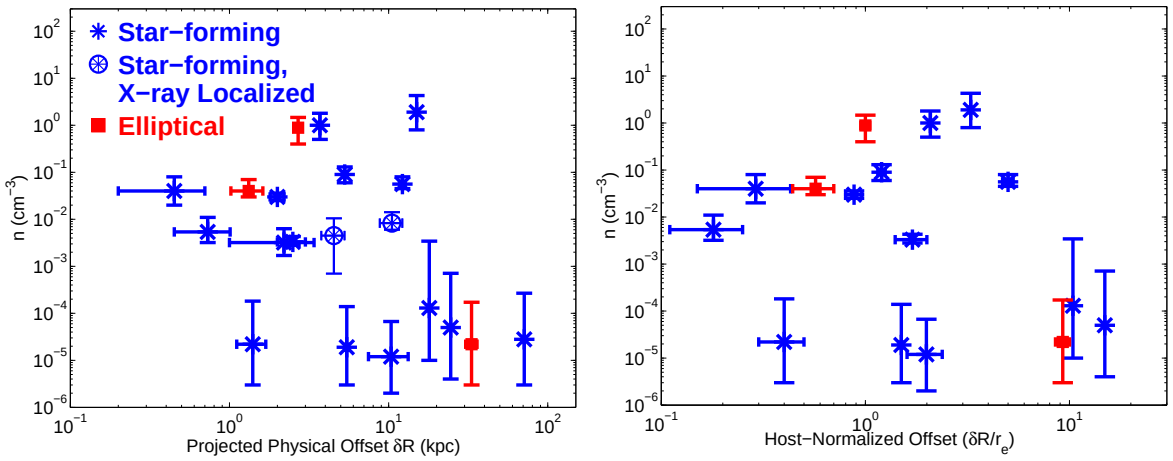

Figure 8.7.—: *Left:* Circumburst density versus projected physical offset, δR, for 20 short GRBs with inferred circumburst densities and sub-arcsecond localization allowing for precise offset measurements. The sample is separated by host galaxy type: star-forming hosts (blue asterisks) and elliptical hosts with no signs of star formation (red squares) according to Fong et al. (2013). In two cases, GRBs 111020A and 111117A, the bursts have no detected optical afterglow and are localized by an X-ray afterglow alone allowing for robust associations to star-forming hosts (blue wheels). For bursts with no spectroscopic redshift, we have assumed $z = 0.5$ to calculate the physical offset, except for two cases, GRBs 060313 and 111020A, where we have assumed $z = 1$ as suggested by the afterglow modeling. *Right:* Circumburst density versus host-normalized offset, $\delta R/r_e$ for 16 bursts with measured host galaxy sizes. Physical and host-normalized offsets are from Fong et al. (2010), Margutti et al. (2012), Berger et al. (2013b), Fong & Berger (2013), and Sakamoto et al. (2013). Error bars correspond to 1σ confidence.

three bursts with $\delta R \gtrsim 15$ kpc have very low densities of $\approx 10^{-4}$ cm^{-3}, while bursts with $\delta R \lesssim 1$ kpc have comparatively higher densities of $\approx (0.5-5) \times 10^{-2}$ cm^{-3}. Furthermore, the two bursts which have sub-arcsecond localizations from X-ray afterglows alone (GRBs 111117A and 111020A), do not appear to be distinct in their offsets or densities than the sample selected by optical afterglows. Overall, we find that for $\delta R \approx 1-15$ kpc, there is no obvious trend between circumburst density and projected physical offset.

To analyze the relationship with offsets in a more uniform manner, we utilize offsets that have been normalized by the sizes of their host galaxies ($\delta R/r_e$ where r_e is the

galaxy half-light radius). The sample of bursts with host-normalized offsets is smaller since precise galaxy size measurements require the resolution of *HST*; thus the sample comprises 16 events (Fong et al. 2010; Fong & Berger 2013). The circumburst densities as a function of projected host-normalized offset is provided in Figure 8.7. Our analysis suggests that for $\lesssim 5\ r_e$, the inferred densities are largely independent of host-normalized offset. We discuss a couple of possible contributing factors. First, since we can only measure projected offsets, we are not sensitive to the distance component along our line of sight, which could contribute a significant amount to the absolute distance. This may explain the case of GRB 061006, which has a small projected offset $\approx 0.4 r_e$ but has a very low density of $\approx 2 \times 10^{-5}$ cm^{-3} (Table 8.6 and Figure 8.7). Second, the afterglow only probes the sub-parsec circumburst environment and to a certain extent will be more sensitive to small-scale fluctuations in the ISM rather than the average ISM density on kiloparsec scales.

However, bursts that appear to have no coincident host galaxy to deep optical/NIR limits of $\gtrsim 26$ mag and are located $\approx 30 - 75$ kpc from the nearest most probable host galaxy ("host-less" bursts; Berger 2010a; Fong & Berger 2013; Tunnicliffe et al. 2013) are expected to have low inferred densities. Indeed, the three bursts located at offsets of $\gtrsim 10 r_e$ have low densities of $\lesssim 10^{-4}$ cm^{-3}, as expected if these bursts occur in the IGM or outer halos of their hosts.

Finally, we note that we have presented results for a fiducial value of $\epsilon_B = 0.1$. If we decrease this value to $\epsilon_B = 0.01$ keeping all other fiducial parameters the same, this will systematically increase all of the densities by a factor of ≈ 4, while the distribution of isotropic-equivalent kinetic energy barely changes. Thus, our conclusions regarding the large-scale trends versus host galaxy offsets are not dependent on our assumed value of

ϵ_B.

8.5.3 Alternative Electromagnetic Counterparts

In addition to informing the behavior of on-axis afterglows, the circumburst density and energy are key parameters which feed in to predictions for alternative isotropic electromagnetic counterparts to compact object mergers, such as off-axis afterglows (Granot et al. 2002; van Eerten et al. 2010) and long-lived radio flares from mildly relativistic ejecta (Nakar & Piran 2011). Advanced LIGO/VIRGO will detect NS-NS mergers within a horizon distance of ≈ 200 Mpc (LIGO Scientific Collaboration et al. 2013), making these alternative electromagnetic signatures promising for joint detection with gravitational waves. We use the median values found for on-axis short GRBs of $E_{\rm K,iso} \approx 10^{51}$ erg and $n \approx 10^{-3} - 10^{-2}$ cm^{-3} and inputs for theoretical models to assess the detectability of off-axis counterparts in the gravitational wave era.

We first investigate the effect of the basic properties on off-axis afterglows. There is observational evidence that short GRBs are collimated in jets with angles of $\theta_j \approx 5 - 10^\circ$ (Fong et al. 2012b, 2014) indicating that for every on-axis event, there are ≈ 100 additional events directed away from Earth which escape detection. These off-axis events are accompanied by off-axis afterglows. The brightness of off-axis afterglows depends on the inferred basic properties of the GRB (e.g., $E_{\rm K,iso}, n, \epsilon_e, \epsilon_B$), the distance to the burst, and the observer angle with respect to the axis of the GRB ($\theta_{\rm obs}$). These parameters also affect the peak timescale; for example, lower densities will result in later peak timescales for the afterglow (Granot et al. 2002; van Eerten et al. 2010). Metzger & Berger (2012) explore a suite of models with varying energy, density, and observer angle for a burst at

200 Mpc (derived from van Eerten & MacFadyen 2011) and compare these light curves to the depth of current and future transient surveys: PanSTARRS, Palomar Transient Factory (PTF), and the Large Synoptic Sky-Survey Telescope (LSST). Given the median inferred values for energy and density of $\approx 10^{51}$ erg and $\approx 10^{-3} - 10^{-2}$ cm^{-3}, they find that off-axis afterglows will likely only be detectable with LSST for $\theta_{\rm obs} \approx 2\theta_j$, and will not detectable with any of these facilities for $\theta_{\rm obs} \approx 4\theta_j$. For the most optimistic case, $n \approx 1$ cm^{-3}, off-axis afterglows will also be detectable with all of these facilities for $\theta_{\rm obs} \approx 2\theta_j$, while these afterglows will only be detectable with LSST if $\theta_{\rm obs} \approx 4\theta_j$. However, we note that $\approx 75 - 95\%$ of bursts fall below densities of 1 cm^{-3} and thus it is very unlikely that current transient surveys will be useful in the detection of off-axis optical afterglows at the horizon distance of 200 Mpc.

Another predicted signature from NS-NS mergers is outflows following the merger at mildly relativistic velocities (Nakar & Piran 2011; Metzger & Bower 2014). These outflows have several predicted origins, including the accretion disk, neutrino-driven winds (Nakar & Piran 2011) or a rapidly spinning hypermassive neutron star (HMNS) remnant (Metzger & Bower 2014). Consequently, up to 10^{52} erg of energy can be coupled to the circumburst medium, creating synchrotron emission which peaks at GHz frequencies. This radio emission has a peak flux and timescale which depend sensitively on the density: $F_{\rm peak} \propto n^{(p+1)/4}$ and $t_{\rm peak} \propto n^{-1/3}$. In Nakar & Piran (2011), the authors assume a density of $n = 1$ cm^{-3} ($\epsilon_e = \epsilon_B = 0.1$) and find that this counterpart will be easily detectable at 1.4 GHz for a source at 200 Mpc with current and upcoming radio facilities. However, given that the observed median density scale is at least two orders of magnitude lower, $10^{-3} - 10^{-2}$ cm^{-3}, the peak flux decreases by a factor of $50 - 350$ and peak timescale is prolonged by a factor of $5 - 10$, with respect to the

1 cm^{-3} case. For instance, assuming a fiducial case ($E = 10^{50}$ erg, $d = 200$ Mpc, $p = 2.4$ and $n = 10^{-2}$ cm^{-3}), the predicted peak flux and timescale at 1.4 GHz is $\approx 160\,\mu$Jy and 0.8 yr, which is feasible with the VLA. However, for bursts with lower densities of 10^{-3} cm^{-3}, the peak flux becomes $\approx 23\,\mu$Jy while the peak timescale increases to 1.8 yr; such a counterpart would be much more challenging to detect and temporally monitor with current or upcoming facilities. The situation quickly becomes more promising at closer distances: the same fiducial case with $n = 10^{-3}$ cm^{-3} at 100 Mpc has a predicted flux of $88\,\mu$Jy. We note that detectability could also become more promising with an increase in the energy of the outflows (e.g., from a HMNS; Metzger & Bower 2014). Thus, late-time radio observations following gravitational wave signals may help to constrain the burst explosion properties in the absence of a multi-wavelength afterglow.

8.6 Conclusions

We present the most comprehensive catalog of short GRB afterglows to date, representing a decade of observations. This catalog is comprised of 86 short GRBs with prompt X-ray, optical/NIR and radio follow-up, enabled by broad-band Target-of-Opportunity programs. Applying the synchrotron afterglow model to the observations, we also place constraints on the isotropic-equivalent kinetic energies and circumburst densities for a subset of 32 events with well-sampled data sets. While a handful of short GRB afterglows have been studied in detail on an individual basis, our work sets the energy and density scales for a large population of events for the first time. We come to the following key conclusions:

- For the sample of 86 bursts, there are 60 X-ray afterglows, 26 optical/NIR afterglows, and 3 radio afterglows, yielding detection fractions of 70%, 30% and 3%, respectively. For bursts with prompt observations and no observing constraints, we find that 92% have X-ray detections and 40% have detected optical detections.

- For bursts with no detected optical afterglow, the median limit placed on the afterglow brightness is $\gtrsim 23.5$ mag at $\delta t \approx 0.3 - 0.5$ days after the burst. In the radio band, the median time to the first radio observation is $\delta t \approx 25$ hr, and the median 3σ upper limit for all observations is $F_{\nu,\rm rad} \approx 77\,\mu$Jy.

- For the subset of 32 bursts studied in more detail, we find a broad range of energies: $E_{\gamma,\rm iso} \approx (0.2 - 45) \times 10^{51}$ erg and $E_{\rm K,iso} \approx (0.01 - 30) \times 10^{51}$ erg. The medians are $\approx (1 - 2) \times 10^{51}$ erg, two orders of magnitude below the values inferred for long GRBs. The beaming-corrected total energy release is $\approx$few $\times 10^{49}$ erg assuming opening angles of $\approx 5 - 15^\circ$. This is broadly consistent with the two primary proposed mechanisms of energy extraction, $\nu\bar{\nu}$ annihilation and MHD processes.

- We find a wide range of inferred circumburst densities, $10^{-5} - 10$ cm^{-3}, with a median density of $\approx (0.4 - 2) \times 10^{-2}$ cm^{-3}. Strikingly, we find that $\approx 75 - 95\%$ of the probability for all events falls *below* densities of 1 cm^{-3}. This indicates that short GRBs explode in low-density environments.

- Our results indicate broad consistency between the inferred densities to those predicted for NS-NS mergers from population synthesis. In particular, we find that inferred densities for the three bursts with elliptical hosts match the predicted bimodal distribution for a large, $\approx 10^{11} M_\odot$ galaxy, while the bursts in star-forming hosts predictably span a wide range of densities.

- We find no obvious trends between circumburst density and host galaxy offset for offsets of $\lesssim 5\ r_e$, and no trend between density and host galaxy type, indicating that the circumburst density is independent of the average ISM density. However, three bursts in our sample with offsets of $\gtrsim 10 r_e$ have low densities of $\lesssim 10^{-4}$ cm^{-3}, as expected if these bursts explode in the IGM.

- The low inferred density scale has strong implications on the detection of alternative electromagnetic counterparts to compact object mergers. In particular, for mergers at the egde of the Advanced LIGO/VIRGO horizon of 200 Mpc, it is unlikely that current transient surveys (e.g., PTF and Pan-STARRS) will be useful in the detection of off-axis optical afterglows, while LSST will be useful in the more optimistic cases ($n \gtrsim 10^{-2}$ cm^{-3}). The detectability of predicted radio flares from mildly relativistic ejecta is only promising for more optimistic cases of $n \gtrsim 10^{-2}$ cm^{-3} and $E \gtrsim 10^{50}$ erg.

Our study highlights the importance of broad-band observations in constraining the basic properties of short GRBs. The detection of an afterglow in the X-ray and optical bands can in some cases break the degeneracies between energy and density, thereby providing tight constraints for these properties. Color information from contemporaneous observations of the optical/NIR afterglow can help to determine the rest-frame extinction intrinsic to the explosion site. The addition of the radio band, which has different dependencies on the energies and densities, can provide an invaluable constraint. Furthermore, for bursts with detected radio afterglows, we can start to constrain the microphysical parameters, which has thus far only been possible for long GRBs.

While our study provides the isotropic-equivalent γ-ray and kinetic energy scales, the true energy release depends on the degree of collimation for short GRBs. Current knowledge of the collimation of short GRBs relies on only a handful of events with measured opening angles from their light curves, primarily due to the faintness of short GRB afterglows which prevent temporal monitoring on timescales longer than $1-2$ days. Therefore, it is imperative to use the most sensitive ground- and space-based resources to uncover additional collimated events or place meaningful lower limits on the opening angles. It is especially important to undertake these studies while *Swift* is in operation, since this satellite has the unique capability of providing multi-wavelength light curves within minutes after the bursts.

We have briefly explored the relationship between the circumburst densities, host galaxy type, and host-burst offsets. A comprehensive study exploring trends between the circumburst densities and specific host properties such as star formation rate, stellar mass, and stellar population age will provide a more complete picture of the burst environments from sub-parsec to kiloparsec scales.

The past decade of short GRB observations has enabled significant progress in understanding the basic properties of short GRBs, namely their energetics, circumburst densities, and opening angles. Furthermore, these properties will serve as essential inputs for the characterization of other electromagnetic counterparts to compact object binary mergers, and will help to inform search strategies in the upcoming revolutionary era of gravitational wave discovery.

We acknowledge Kathy Cooksey, Tolga Guver, Dan Kelson, Nathan Sanders, Anil Seth, Rik Williams, and Amanda Zangari for their assistance in Magellan Target-of-

Opportunity observations. This work made use of data supplied by the UK Swift Science Data Centre at the University of Leicester. This paper includes data gathered with the 6.5 meter Magellan Telescopes located at Las Campanas Observatory, Chile. The National Radio Astronomy Observatory is a facility of the National Science Foundation operated under cooperative agreement by Associated Universities, Inc.

Chapter 9

Conclusions and Future Directions

9.1 Conclusions

Through a multi-wavelength picture of their host galaxies and afterglows, this thesis comprises several lines of independent evidence to demonstrate that short GRBs originate from compact object mergers, and sets the scales for the burst basic explosion properties. Here, we summarize the key conclusions.

- Short GRBs occur at significantly larger offsets from their host galaxies than any known class of cosmic explosions, including long GRBs, core-collapse SNe, and Type Ia SNe. The offset distribution shows remarkable consistency with predictions for NS-NS mergers. The locations with respect to their host rest-frame UV and optical light show that short GRBs do not spatially track star formation or stellar mass. Taken together, their locations demonstrate that the progenitors of short GRBs must migrate between their formation sites and eventual explosions sites.

- For the growing subset of short GRBs with no robust associations to host galaxies within $\approx 5''$, we place stringent limits on a combination of luminosity and redshift for the underlying host galaxies, and find that these bursts likely originate from galaxies at $\approx 30 - 100$ kpc offsets. This subset represents $\approx 15 - 20\%$ of the population which occur at $\gtrsim 5$ half-light radii from their host galaxies, and provides strong support for progenitor kicks, ie., NS-NS/NS-BH mergers.

- Short GRBs show a preference toward star-forming (late-type) host galaxies in an observed late-to-early-type ratio of $\gtrsim$2:1. The most likely ranges for the early- and late-type host fractions for the entire short GRB population are $\approx 20 - 40\%$ and $\approx 60 - 80\%$. The preference toward late-type galaxies indicates that both stellar

mass and star formation play roles in determining the short GRB rate, and that short GRB progenitors have typical delay times of $\lesssim$ few Gyr.

- To date, there are four short GRBs which show evidence for collimation, two of which were uncovered in this work. Along with previous measurements and lower limits, this suggests a median opening angle of $\approx 10^{\circ}$. Using the all-sky observed rate of 10 Gpc^{-3} yr^{-1}, this implies a true short GRB rate of ≈ 20 yr^{-1} within 200 Mpc, the Advanced LIGO/VIRGO sensitivity range for neutron star binary mergers.

- Short GRBs have isotropic-equivalent γ-ray and kinetic energy scales of $\approx (1-2) \times 10^{51}$ erg. If all short GRBs are collimated in jets of $\approx 5-10^{\circ}$, the beaming-corrected total energy release would be $\approx (0.02-8) \times 10^{50}$ erg. These values are roughly two orders of magnitude below the inferred true energy scale for long GRBs.

- The environments of short GRBs on sub-parsec scales have low densities, with a median of $\approx (0.04-2) \times 10^{-2}$ cm^{-3}. Furthermore, $\gtrsim 75\%$ of events have densities below 1 cm^{-3}.

I re-visit the expectations for three progenitors models initially presented in the Introduction of this thesis in Table 9.1: NS-NS/NS-BH mergers, massive stars, and accretion-induced collapse or mergers of two white dwarfs. A comparison of progenitor expectations to the results presented in this thesis show that there is resounding observational support for NS-NS/NS-BH mergers as the progenitors of short GRBs, consistent with the theoretical predictions formulated over the past two decades. This

Table 9.1. Testable Predictions and Expectations for Short GRB Progenitor Models

Testable Prediction	NS-NS/NS-BH	Massive Stars	WD-WD/WD-AIC
Associated SN?	✓**No**	✗ Yes	✓**No**
Spatial offsets	✓**Substantial**	✗ Small	✗ Small
Correlation with SF regions	✓**Weak**	✗ Strong	✓**Weak**
Correlation with stellar mass	✓**Weak**	✗ Strong	✗ Strong
Host Demographics	✓**Mix of elliptical and SF**	✗ SF only	✓**Mix of elliptical and SF**
Immediate environments	✓**Low densities (ISM/IGM)**	✗ High densities	✗ Average densities (ISM)

Note. — ✓= In good agreement with short GRB observations. ✗= Does not agree with short GRB observations.

thesis thus represents a comprehensive body of indirect evidence linking short GRBs to compact object merger progenitors.

9.2 Future Directions

The link between short GRBs and compact object mergers has a broad impact on related areas of astrophysics. In the context of current and upcoming facilities, I focus on three primary directions to take: continued monitoring of short GRBs and their afterglows, searches for a "smoking gun" linking short GRBs to their progenitors, and development of search strategies to identify electromagnetic signatures in gravitational wave localization regions.

9.2.1 Key Areas for Short GRBs

The GRB field has been rich with discovery in the past two decades, thanks to the ongoing suite of GRB-detection satellites in space. It is imperative to take advantage of the current era of GRB detection satellites (e.g., *Swift*, *Fermi*, IPN, INTEGRAL) and utilize the incoming flow of short GRBs to continue to characterize these events. I identify key areas in which it will be especially important to concentrate our observational resources.

Event Rates. The current sample of short GRBs with opening angle measurements is comprised of four events, primarily due to the faint and rapidly-fading afterglows. Thus, even a few additional jet breaks would enable significantly tighter constraints on the rate. The observed short GRB rate is $\sim$1-2 orders of magnitude lower than the predicted

compact object merger rate, but this discrepancy can be explained if short GRBs are collimated in narrow jets. An alternative solution is that short GRBs are isotropic but only $\lesssim 10\%$ of compact object mergers produce such events (Metzger & Berger 2012). Thus it is important to provide an independent estimate of the short GRB rate as a baseline for comparison. While the work in this thesis has taken steps to constrain short GRBs with opening angles of $5-7^\circ$, the opening angle distribution for wider jets of $\gtrsim 5^\circ$ is poorly constrained. Thus, it is necessary to continue monitoring short GRB afterglows to late times to characterize this part of the distribution.

The X-ray band is advantageous in the search for jet breaks because *Swift*/XRT provides afterglow observations within minutes after the bursts, which serve as an unambiguous baseline against which we can measure a subsequent break. The faint afterglows also require the sensitivity of *Chandra* and *XMM-Newton* to track their temporal behavior beyond $\gtrsim 1$ day (Fig. 9.1). Thus, the pursuit of jet breaks for short GRBs requires a combination of these facilities. Contemporaneous searches in the optical and radio bands will also be imperative to unambiguously confirm a jet break.

Central engines. There is broad consensus that GRBs are powered by accretion on to a black hole or by a highly-spinning magnetar which later collapses to a black hole. Well-sampled afterglow light curves have uncovered distinct features that cannot be easily explained by a black-hole accretion central engine. For instance, $\approx 15\%$ of short GRBs have prolonged X-ray emission immediately following the prompt γ-ray emission which lasts for $\sim 10-100$ s (e.g., Norris & Bonnell 2006; Perley et al. 2009a), longer than the expected accretion timescale of $\lesssim 1$ s on to a black hole. This "extended emission" has been proposed to be powered by the spin-down of a magnetar (Bucciantini et al.

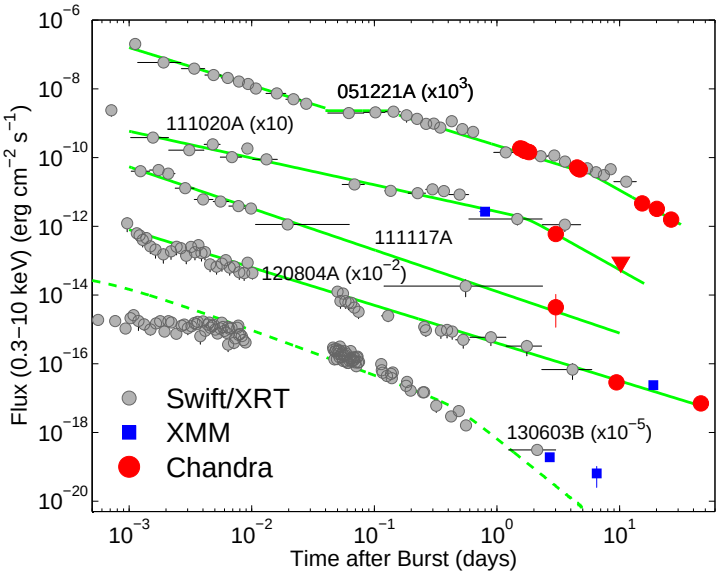

Figure 9.1.—: X-ray afterglow light curves of five short GRBs (051221A, 111020A, 111117A, 120804A and 130603B) with X-ray follow-up at $\gtrsim 1$ day. Data from *Swift*/XRT (grey circles), *Chandra* (red circles), and *XMM-Newton* (blue squares) are shown, along with the best-fit single or broken power-law models (green lines). The best-fit jet break model determined by the optical and radio afterglows is shown for GRB 130603B, revealing excess X-ray emission at $\gtrsim 1$ day (green dashed line). Fluxes are scaled for clarity as marked, and triangles denote 3σ upper limits. The combination of these X-ray facilities will be vital in understanding the late-time X-ray behavior of short GRBs.

2012). Similarly, shallow plateau phases in the X-ray afterglow light curves of some short GRBs may be explained by a magnetar central engine (Rowlinson et al. 2013). Finally, the excess X-ray emission in GRB 130603B at $\approx 2 - 10$ days after the burst could be explained either by a long-lived magnetar remnant or fallback accretion (Figure 9.1; Fong et al. 2014). It will be enlightening to investigate the population of bursts with these anomalous features in more detail; in particular, to study if there are any other properties which set these bursts apart from the rest of the population.

"Host-less bursts." The fraction of bursts which explode in IGM-like environments at large separations from their host galaxies will have low circumburst densities of

$\lesssim 10^{-4}$ cm^{-3}, and thus fainter optical afterglows. Therefore, it is crucial to continue to perform Target-of-Opportunity searches on the most sensitive telescopes to understand the true fraction of bursts which have large offsets from their host galaxies. Furthermore, deep limits on underlying host galaxies enabled by *HST* will strengthen the claim that these bursts are kicked from their hosts.

Complete host galaxy demographics. Demographics which accurately represent the bulk of the short GRB population are imperative in understanding the link to the progenitors, and for galaxy-targeted search strategies following gravitational wave detections. Most short GRB host galaxy studies to date are primarily based on the $\approx 30\%$ of *Swift*-discovered events with sub-arcsecond localization from optical afterglows. Furthermore, the paucity of detected optical afterglows is a direct reflection of the low circumburst densities of their immediate environments. If there exist correlations between average ISM density and host galaxy type, the sample of hosts selected by optical afterglows will not accurately represent the entire population. A unique route to exploring this potential bias is to characterize the host galaxies of short GRBs which lack detected optical afterglows, but which have detected X-ray afterglows. Unlike the optical afterglow, the X-ray afterglow brightness does not necessarily depend on circumburst density, and would thus be more immune to trends with host galaxy type. The high resolution and sensitivity of *Chandra* may lead to sub-arcsecond localization, and has been successful in identifying host galaxies in two cases (GRBs 111020A and 111117A). It will also be essential to explore the environments of bursts with only X-ray positions, which are routinely and promptly provided by *Swift*/XRT.

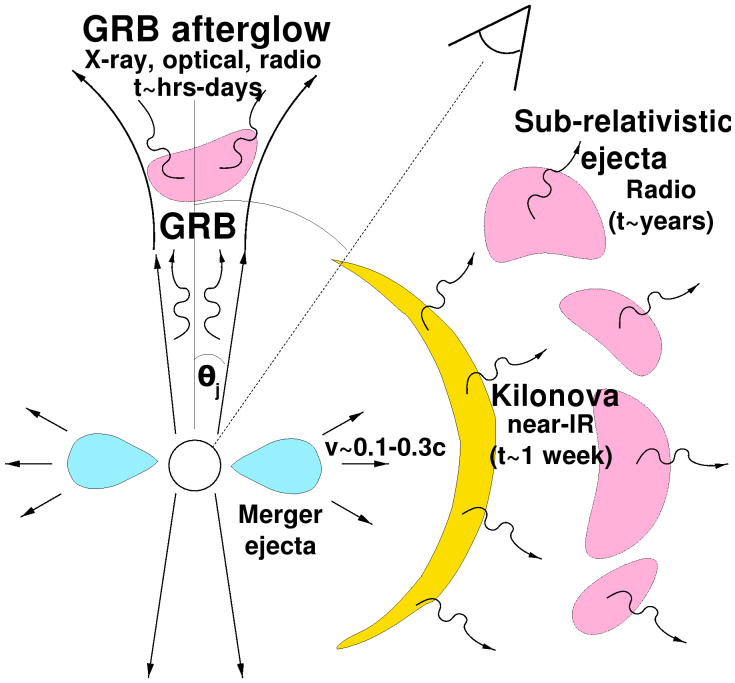

Figure 9.2.—: The expected EM counterparts for a compact object binary merger. Future efforts will focus on characterizing each of these counterparts. Adapted from Metzger & Berger (2012).

9.2.2 Search for a Smoking Gun

One of the predicted outcomes following compact object mergers is transient emission powered by the radioactive decay of heavy elements produced following the merger (c.f. Section 1.5.5), termed a "kilonova". The kilonova emission is expected to be isotropic and peak in the NIR on $\sim 1-$week timescales (Figure 9.2). While there an overwhelming amount of indirect evidence that points to a compact object progenitor, as outlined in this thesis, the detection of a kilonova accompanying a short GRB would provide "smoking gun" evidence. As isotropic counterparts, kilonovae are also important to understand in the context of joint detectability with gravitational waves. Thus, it is important to characterize the brightness distribution of kilonovae. We propose two avenues: perform optical/NIR observations that are matched to the rise timescale of the

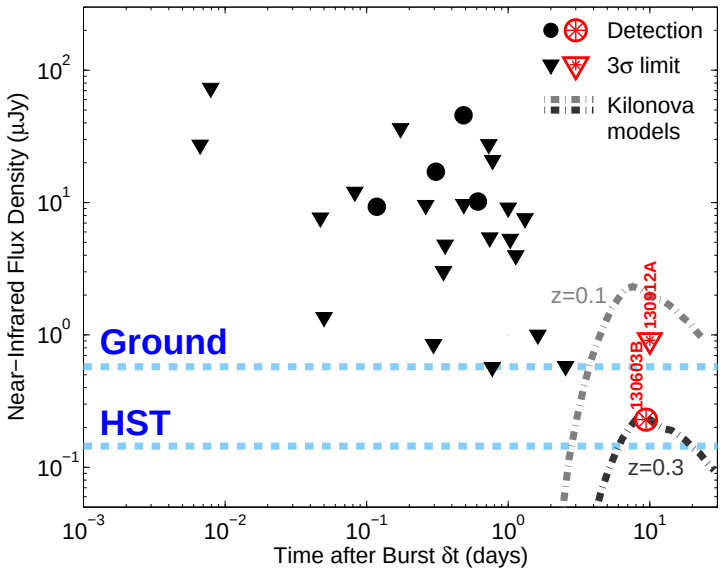

Figure 9.3.—: Near-IR afterglow detections (black circles) and 3σ upper limits (grey triangles) for 25 short GRBs. Red symbols denote two recent kilonova searches, following the short GRBs 130603B (*HST*) and 130912A (Magellan/FourStar). Conservative kilonova models at $z = 0.1$ and $z = 0.3$ are shown (Tanaka & Hotokezaka 2013; grey dot-dashed). A comparison to the depth of ground-based telescopes and *HST* (blue dashed lines) shows that these facilities will be instrumental in kilonova searches for short GRBs at $z \lesssim 0.4$.

kilonova emission following short GRBs, and characterization of their detectability with wide-field untargeted transient surveys.

The community has started to perform deep NIR searches following short GRBs. The excess NIR emission following the short GRB 130603B provided the first tentative "smoking gun" linking a short GRB to a compact object merger progenitor (Fig. 9.3; Berger et al. 2013a; Tanvir et al. 2013a). From the kilonova brightness, the mass and velocity of the ejected radioactive material could be constrained ($M \approx 0.05 M_{\odot}$, $v \approx 0.1$-$0.3c$). Kilonovae have otherwise escaped detection in the past since most searches were optimized in the optical bands, or in the NIR on timescales of $\lesssim 1$ day after the bursts (Fig. 9.3). I recently conducted a kilonova search following the short

GRB 130912A, placing a near-IR limit of $\lesssim 1\mu$Jy ($m_{\rm J,AB} \gtrsim 24$) at 10 days after the burst. Although the redshift is unknown, a comparison to conservative kilonova models of an equal-mass NS-NS binary ($M = 0.01 M_\odot$, $v = 0.1c$) ruled out such a transient for $z \lesssim 0.2$ (Fig. 9.3). These models are conservative because unequal mass binaries (i.e., NS-BH systems) have higher predicted ejecta masses and velocities, and thus higher expected fluxes (Barnes & Kasen 2013; Tanaka & Hotokezaka 2013). Other than these two events, we have no information on the late-time near-IR emission of short GRBs (Fig. 9.3). In this vein, it will be useful to perform kilonova searches on $\sim$ 1-week timescales following short GRBs with $z \lesssim 0.4$ using red-sensitive ground-based instruments and *HST* (ACS/WFC3). This will help to establish the brightness distribution of kilonovae and to distinguish them from background contaminating transients in the era of Advanced LIGO/VIRGO and LSST. Furthermore, the inferred kilonova properties will determine whether compact object mergers are the dominant site of heavy element production. Finally, the non-detection of late-time emission at other wavelengths, coupled with the detection of NIR excess emission, can provide unambiguous support for the kilonova interpretation for future events.

A complementary way of exploring the brightness distribution of kilonovae is through untargeted surveys, taking advantage of the isotropy of kilonova emission. While current wide-field surveys primarily operate in the optical bands, it is a useful exercise to determine whether the optical emission of kilonovae will be detectable with current and future facilities (e.g., PTF, Pan-STARRs, LSST). In Figure 9.4, we compare a Monte Carlo simulation for a standard kilonova model characterized by an ejecta mass and velocity of $0.01\,M_\odot$ and $0.2c$ to the depths for PTF, Pan-STARRs, CTIO/DECam and LSST. The contours demonstrate the detection of a rise, defined as an observed

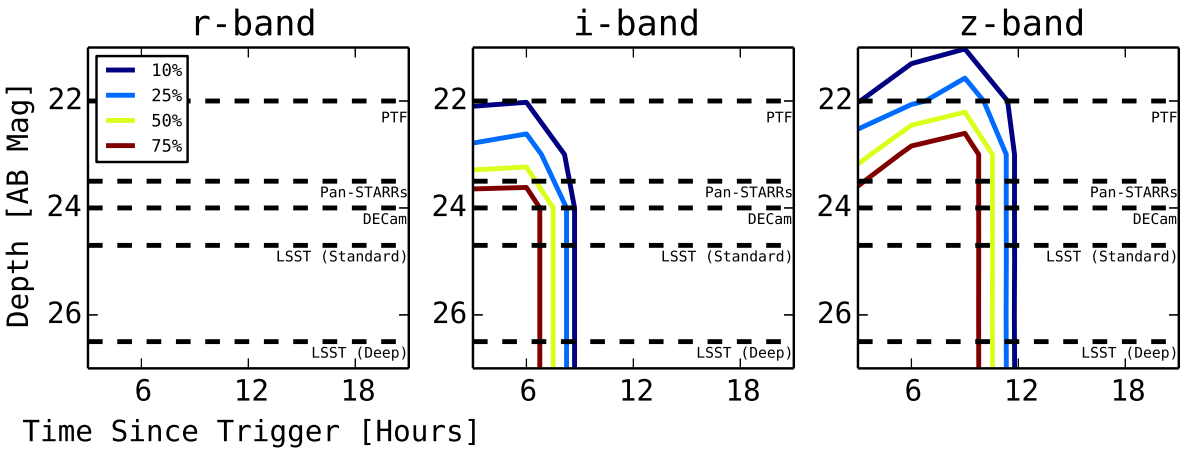

Figure 9.4.—: Detectability of a kilonova rise with current and upcoming facilities as a function of time after the gravitational wave trigger, for optical *riz*-bands. To produce the detectability contours, a Monte Carlo simulation for a standard kilonova model characterized by an ejecta mass and velocity of $0.01\,M_{\odot}$ and $0.2c$ is employed, and the detection of a rise is defined as an observed brightening. These simulations demonstrate that in order to detect kilonovae, the response time will need to be at $\lesssim$ 12 hr, and efforts will need to be concentrated on the redder optical filters. The addition of LSST at the end of the decade will provide improved detectability, but does not negate the need for a quick response time. *From Cowperthwaite et al., in prep.*

brightenings. As expected, the optical r-band will likely not be useful for the median expected ejecta mass and velocity. However, detectability becomes more promising in the $i-$ and z-bands. In the majority of cases, the kilonova rise is detectable with Pan-STARRs, DECam and LSST (Figure 9.4). The primary challenge will be response time of $\lesssim$ 12 hr, and identifying kilonovae amidst the otherwise dynamic sky.

9.2.3 Preparing for the Gravitational Wave Era

Compact object mergers (NS-NS/NS-BH) are the premier candidates of gravitational waves detected by Advanced LIGO. The detection of gravitational waves alone from

such systems will provide uncertain distance measurements and poor localizations of ~ 100 deg^2 (LIGO Scientific Collaboration et al. 2013). Therefore, a coincident detection at electromagnetic wavelengths will significantly leverage the gravitational wave signal by providing sub-arcsecond localization, a precise redshift, and placement within a host galaxy. The key challenge for joint gravitational wave-EM detections will be to distinguish the afterglow from unrelated variable sources that may provide a contaminating background within the ~ 100 deg^2 LIGO localization regions. While short GRBs are unambiguous signals from compact object mergers, only a small fraction may have their jets pointed toward Earth. I explore two additional studies that will inform search strategies in the upcoming decade.

To search for kilonovae, most follow-up observations will be in the red optical bands. High-cadence pilot studies which characterize the red optical transient sky will be imperative in establishing the rates and temporal behavior of red contaminating transients. Currently, we are using CTIO/DECam to reach a depth of $m_{\rm AB} \approx 24$ mag within 75 deg^2 on a nightly cadence. This can be viewed as a "dry run" for searches within LIGO localization regions (Cowperthwaite et al., in prep.). The outcome of this study will also provide invaluable inputs to LSST, where selection of interesting candidates for spectroscopic follow-up will be based on photometry alone.

The incoming flow of poorly-localized short GRBs with localization uncertainties of a $\lesssim 1$ square degree can also be used as tests for gravitational wave follow-up strategies in multiple wavelengths. We have a pilot program on the VLA to search for radio afterglows of short GRBs detected by the Interplanetary Network (IPN). IPN is optimized to detect bright and thus potentially nearby events ($z \lesssim 0.1$). However, the typical localizations are $1-4$ deg^2 reported a few days after the burst, precluding optical

afterglow detections which fade more rapidly. This program takes advantage of the relatively quiet radio transient sky to perform targeted searches around bright galaxies within the localization regions of short GRBs detected by IPN. Such strategies must be tested prior to using radio facilities for gravitational wave follow-up. While the expected rate of such afterglow detections is low, $\lesssim 1$ yr^{-1}, the science return will be very high if such a search strategy is proved successful.

In the context of current and upcoming facilities, it is an extremely exciting time to study short GRBs. The field has been ripe with discovery, and will no doubt continue to satisfy and surprise us for decades to come.

References

Abadie, J., et al. 2010, Classical and Quantum Gravity, 27, 173001

Alard, C. 2000, A&AS, 144, 363

Aloy, M. A., Janka, H.-T., & Müller, E. 2005, A&A, 436, 273

Anderson, J. P., Habergham, S. M., James, P. A., & Hamuy, M. 2012, MNRAS, 424, 1372

Antonelli, L. A., et al. 2009a, A&A, 507, L45

—. 2009b, A&A, 507, L45

Aptekar, R. L., et al. 1995, Space Sci. Rev., 71, 265

Arzoumanian, Z., Chernoff, D. F., & Cordes, J. M. 2002, ApJ, 568, 289

Atwood, W. B., et al. 2009, ApJ, 697, 1071

Barbier, L., et al. 2007, GRB Coordinates Network, 6623, 1

Barnes, J., & Kasen, D. 2013, ArXiv e-prints

Barnes, J. E., & Hernquist, L. 1992, ARA&A, 30, 705

Barthelmy, S. D., Sakamoto, T., & Stamatikos, M. 2011, GRB Coordinates Network, 11557, 1

Barthelmy, S. D., et al. 2005, Space Sci. Rev., 120, 143

—. 2009, GRB Coordinates Network, 9364, 1

—. 2013, GRB Coordinates Network, 14741, 1

Battaglia, G., et al. 2005, MNRAS, 364, 433

Beardmore, A. P., Page, K. L., Evans, P. A., Pagani, C., Kennea, J., & Burrows, D. N. 2009, GRB Coordinates Network, 8937, 1

Beardmore, A. P., Page, K. L., Gehrels, N., Greiner, J., Kennea, J., Nousek, J., Osborne, J. P., & Tagliaferri, G. 2005, GRB Coordinates Network, 4043, 1

Becker, W., Prinz, T., Winkler, P. F., & Petre, R. 2012, ApJ, 755, 141

Beckwith, S. V. W., et al. 2006, AJ, 132, 1729

Belczynski, K., Perna, R., Bulik, T., Kalogera, V., Ivanova, N., & Lamb, D. Q. 2006, ApJ, 648, 1110

Bell, E. F., McIntosh, D. H., Katz, N., & Weinberg, M. D. 2003, ApJS, 149, 289

Berger, E. 2005, GRB Coordinates Network, 3801, 1

—. 2006a, GRB Coordinates Network, 5952, 1

Berger, E. 2006b, in American Institute of Physics Conference Series, Vol. 836, Gamma-Ray Bursts in the Swift Era, ed. S. S. Holt, N. Gehrels, & J. A. Nousek, 33–42

—. 2007, ApJ, 670, 1254

—. 2009, ApJ, 690, 231

—. 2010a, ApJ, 722, 1946

—. 2010b, ApJ, 722, 1946

—. 2010c, GRB Coordinates Network, 10942, 1

—. 2010d, ArXiv e-prints

—. 2013, ArXiv e-prints

Berger, E., Cenko, S. B., Fox, D. B., & Cucchiara, A. 2009, ApJ, 704, 877

Berger, E., & Challis, P. 2007, GRB Coordinates Network, 7085, 1

Berger, E., & Fong, W. 2009a, GRB Coordinates Network, 9373, 1

—. 2009b, GRB Coordinates Network, 10182, 1

Berger, E., Fong, W., & Chornock, R. 2013a, ApJ, 774, L23

Berger, E., & Fong, W.-F. 2009c, GRB Coordinates Network, 9555, 1

—. 2009d, GRB Coordinates Network, 9683, 1

Berger, E., & Kelson, D. 2009, GRB Coordinates Network, 8934, 1

Berger, E., Kulkarni, S. R., & Frail, D. A. 2003a, ApJ, 590, 379

Berger, E., & Mulchaey, J. 2009, GRB Coordinates Network, 10174, 1

Berger, E., Shin, M.-S., Mulchaey, J. S., & Jeltema, T. E. 2007a, ApJ, 660, 496

Berger, E., et al. 2003b, Nature, 426, 154

—. 2005, Nature, 438, 988

—. 2007b, ApJ, 664, 1000

—. 2013b, ApJ, 765, 121

Bessell, M. S. 1999, PASP, 111, 1426

Bhat, P. N. 2010, GRB Coordinates Network, 10912, 1

Birkl, R., Aloy, M. A., Janka, H.-T., & Müller, E. 2007, A&A, 463, 51

Blandford, R. D., & Znajek, R. L. 1977, MNRAS, 179, 433

Blanton, M. R., & Roweis, S. 2007, AJ, 133, 734

Bloom, J. S., Djorgovski, S. G., & Kulkarni, S. R. 2001, ApJ, 554, 678

Bloom, J. S., Djorgovski, S. G., Kulkarni, S. R., & Frail, D. A. 1998, ApJ, 507, L25

Bloom, J. S., Frail, D. A., & Kulkarni, S. R. 2003, ApJ, 594, 674

Bloom, J. S., Kulkarni, S. R., & Djorgovski, S. G. 2002, AJ, 123, 1111

Bloom, J. S., & Prochaska, J. X. 2006, in American Institute of Physics Conference Series, Vol. 836, Gamma-Ray Bursts in the Swift Era, ed. S. S. Holt, N. Gehrels, & J. A. Nousek, 473–482

Bloom, J. S., Sigurdsson, S., & Pols, O. R. 1999, MNRAS, 305, 763

Bloom, J. S., et al. 2006, ApJ, 638, 354

—. 2007, ApJ, 654, 878

Boella, G., Butler, R. C., Perola, G. C., Piro, L., Scarsi, L., & Bleeker, J. A. M. 1997, A&AS, 122, 299

Breeveld, A. A., & Stamatikos, M. 2011, GRB Coordinates Network, 11560, 1

Bromberg, O., Nakar, E., Piran, T., & Sari, R. 2013, ApJ, 764, 179

Bruzual, G., & Charlot, S. 2003, MNRAS, 344, 1000

Bucciantini, N., Metzger, B. D., Thompson, T. A., & Quataert, E. 2012, MNRAS, 419, 1537

Burrows, D. N., et al. 2005, Space Sci. Rev., 120, 165

—. 2006, ApJ, 653, 468

Butler, N., et al. 2013, GRB Coordinates Network, 15226, 1

Butler, N. R. 2007, AJ, 133, 1027

Cameron, P. B., & Frail, D. A. 2005a, GRB Coordinates Network, 3815, 1

—. 2005b, GRB Coordinates Network, 3933, 1

Campana, S., et al. 2006, Nature, 442, 1008

—. 2011, ArXiv e-prints

Cannizzo, J. K., et al. 2006, GCN Report, 20, 1

Cardelli, J. A., Clayton, G. C., & Mathis, J. S. 1989, ApJ, 345, 245

Castro-Tirado, A. J., Bond, I., Kilmartin, P., de Ugarte Postigo, A., Gorosabel, J., Jelinek, M., & Yock, P. 2005a, GRB Coordinates Network, 3018, 1

Castro-Tirado, A. J., et al. 2005b, A&A, 439, L15

Cenko, S. B., Cobb, B. E., Perley, D. A., & Bloom, J. S. 2009, GRB Coordinates Network, 8933, 1

Cenko, S. B., & Cucchiara, A. 2013, GRB Coordinates Network, 14670, 1

Cenko, S. B., & Kasliwal, M. M. 2008, GRB Coordinates Network, 8417, 1

Cenko, S. B., Perley, D. A., Bloom, J. S., Cobb, B. E., & Morgan, A. N. 2010a, GRB Coordinates Network, Circular Service, 10339, 1 (2010), 339, 1

Cenko, S. B., Perley, D. A., Cucchiara, A., Fong, W., & Levan, A. J. 2013a, GRB Coordinates Network, 15121, 1

Cenko, S. B., Sudilovsky, V., Tanga, M., & Greiner, J. 2013b, GRB Coordinates Network, 15222, 1

Cenko, S. B., et al. 2008, ArXiv e-prints

—. 2010b, ApJ, 711, 641

—. 2011, ApJ, 732, 29

Chandra, P., Cenko, S. B., Frail, D. A., & Harrison, F. 2008, GRB Coordinates Network, 8451, 1

Chandra, P., & Frail, D. A. 2006, GRB Coordinates Network, 5910, 1

—. 2007a, GRB Coordinates Network, 6667, 1

—. 2007b, GRB Coordinates Network, 6367, 1

—. 2007c, GRB Coordinates Network, 6831, 1

—. 2007d, GRB Coordinates Network, 6685, 1

—. 2007e, GRB Coordinates Network, 6742, 1

—. 2008a, GRB Coordinates Network, 8419, 1

—. 2008b, GRB Coordinates Network, 7934, 1

—. 2009, GRB Coordinates Network, 9160, 1

—. 2011, Bulletin of the Astronomical Society of India, 39, 451

—. 2012, ApJ, 746, 156

Chapman, R., Levan, A. J., Wynn, G. A., Davies, M. B., King, A. R., Priddey, R. S., & Tanvir, N. R. 2008, in American Institute of Physics Conference Series, Vol. 983, 40 Years of Pulsars: Millisecond Pulsars, Magnetars and More, ed. C. Bassa, Z. Wang, A. Cumming, & V. M. Kaspi, 301–303

Chen, H.-W., et al. 2003, ApJ, 586, 745

Chevalier, R. A., & Li, Z.-Y. 2000, ApJ, 536, 195

Chornock, R., et al. 2010, ArXiv e-prints

Christensen, L., Hjorth, J., & Gorosabel, J. 2004, A&A, 425, 913

Church, R. P., Levan, A. J., Davies, M. B., & Tanvir, N. 2011, MNRAS, 413, 2004

Ciotti, L., & Bertin, G. 1999, A&A, 352, 447

Clocchiatti, A., Suntzeff, N. B., Covarrubias, R., & Candia, P. 2011, AJ, 141, 163

Cobb, B. E., Bloom, J. S., Perley, D. A., Morgan, A. N., Cenko, S. B., & Filippenko, A. V. 2010, ApJ, 718, L150

Conselice, C. J., et al. 2005, ApJ, 633, 29

Costa, E., et al. 1997, Nature, 387, 783

Covino, S., Piranomonte, S., D'Avanzo, P., A., A. L., de Luise, F., Pedani, M., & Pinilla Alfonso, N. 2007, GRB Coordinates Network, 6635, 1

Covino, S., et al. 2006, A&A, 447, L5

Coward, D. M., et al. 2012, MNRAS, 425, 2668

Cucchiara, A., et al. 2013, ApJ, 777, 94

Cummings, J., et al. 2005, GRB Coordinates Network, 4365, 1

Dai, Z. G., & Cheng, K. S. 2001, ApJ, 558, L109

Darbha, S., Metzger, B. D., Quataert, E., Kasen, D., Nugent, P., & Thomas, R. 2010, MNRAS, 409, 846

D'Avanzo, P., Covino, S., Melandri, A., Padilla Torres, C. P., & Andreuzzi, G. 2013, GRB Coordinates Network, 14307, 1

D'Avanzo, P., Fiore, F., Piranomonte, S., Covino, S., Tagliaferri, G., Chincarini, G., & Stella, L. 2007, GRB Coordinates Network, 7152, 1

D'Avanzo, P., et al. 2009, A&A, 498, 711

de Pasquale, M., Markwardt, C., & Sbarufatti, B. 2010, GCN Report, 269, 1

De Pasquale, M., et al. 2010, ApJ, 709, L146

de Ugarte Postigo, A., Kann, D. A., Castro-Tirado, A. J., Aguirre, A., & Jordi, C. 2008, GRB Coordinates Network, 7644, 1

de Ugarte Postigo, A., et al. 2006a, ApJ, 648, L83

—. 2006b, ApJ, 648, L83

—. 2013, ArXiv e-prints

—. 2014, A&A, 563, A62

Dezalay, J.-P., Barat, C., Talon, R., Syunyaev, R., Terekhov, O., & Kuznetsov, A. 1992, in American Institute of Physics Conference Series, Vol. 265, American Institute of Physics Conference Series, ed. W. S. Paciesas & G. J. Fishman, 304–309

Dezalay, J. P., Lestrade, J. P., Barat, C., Talon, R., Sunyaev, R., Terekhov, O., & Kuznetsov, A. 1996, ApJ, 471, L27

Djorgovski, S. G., Kulkarni, S. R., Bloom, J. S., Goodrich, R., Frail, D. A., Piro, L., & Palazzi, E. 1998, ApJ, 508, L17

Dominik, M., Belczynski, K., Fryer, C., Holz, D. E., Berti, E., Bulik, T., Mandel, I., & O'Shaughnessy, R. 2012, ApJ, 759, 52

Donaghy, T. Q., et al. 2006, ArXiv Astrophysics e-prints

Driver, S. P., Allen, P. D., Liske, J., & Graham, A. W. 2007, ApJ, 657, L85

Duncan, R. C., & Thompson, C. 1992, ApJ, 392, L9

Eichler, D., Livio, M., Piran, T., & Schramm, D. N. 1989, Nature, 340, 126

Eldridge, J. J., Langer, N., & Tout, C. A. 2011, MNRAS, 414, 3501

Evans, P. A., Goad, M. R., Osborne, J. P., & Beardmore, A. P. 2011, GRB Coordinates Network, 11556, 1

Evans, P. A., & Hoversten, E. A. 2008, GRB Coordinates Network, 8740, 1

Evans, P. A., et al. 2007a, A&A, 469, 379

—. 2007b, GRB Coordinates Network, 6942, 1

—. 2009, MNRAS, 397, 1177

Fan, Y.-Z., & Xu, D. 2006, MNRAS, 372, L19

Fernández, R., & Metzger, B. D. 2013, ArXiv e-prints

Ferrero, P., et al. 2007, AJ, 134, 2118

Fesen, R. A., et al. 2006, ApJ, 645, 283

Filgas, R., et al. 2011, A&A, 526, A113

Foley, R. J., Bloom, J. S., & Chen, H.-W. 2005, GRB Coordinates Network, 3808, 1

Fong, W., & Berger, E. 2013, ApJ, 776, 18

Fong, W., Berger, E., & Fox, D. B. 2010, ApJ, 708, 9

Fong, W., Berger, E., Kelson, D., & Williams, R. 2012a, GRB Coordinates Network, 13700, 1

Fong, W., et al. 2011, ApJ, 730, 26

—. 2012b, ApJ, 756, 189

—. 2013, ApJ, 769, 56

—. 2014, ApJ, 780, 118

Forbes, D. A., & Ponman, T. J. 1999, MNRAS, 309, 623

Fox, D. B., et al. 2005, Nature, 437, 845

Frail, D. A., & Cameron, P. B. 2005, GRB Coordinates Network, 4199, 1

Frail, D. A., & Chandra, P. 2008, GRB Coordinates Network, 7684, 1

—. 2009, GRB Coordinates Network, 9354, 1

Frail, D. A., & Soderberg, A. M. 2005, GRB Coordinates Network, 3007, 1

Frail, D. A., et al. 2001, ApJ, 562, L55

Freeman, K. C. 1970, ApJ, 160, 811

Friedman, A. S., & Bloom, J. S. 2005, ApJ, 627, 1

Fruchter, A. S., & Hook, R. N. 2002, PASP, 114, 144

Fruchter, A. S., et al. 1999, ApJ, 519, L13

—. 2006, Nature, 441, 463

Fryer, C., Burrows, A., & Benz, W. 1998, ApJ, 496, 333

Fryer, C., & Kalogera, V. 1997, ApJ, 489, 244

Fryer, C. L., Woosley, S. E., & Hartmann, D. H. 1999, ApJ, 526, 152

Fukazawa, Y., Botoya-Nonesa, J. G., Pu, J., Ohto, A., & Kawano, N. 2006, ApJ, 636, 698

Fynbo, J. U., et al. 2000, ApJ, 542, L89

Gal-Yam, A., et al. 2006, Nature, 444, 1053

—. 2008, ApJ, 686, 408

Galama, T., et al. 1997, Nature, 387, 479

Galama, T. J., & Wijers, R. A. M. J. 2001, ApJ, 549, L209

Galama, T. J., et al. 1998, Nature, 395, 670

Galbany, L., et al. 2012, ApJ, 755, 125

Galeev, A., et al. 2009, GRB Coordinates Network, 9549, 1

Gehrels, N., et al. 2004, ApJ, 611, 1005

—. 2005, Nature, 437, 851

—. 2008, ApJ, 689, 1161

Gelbord, J. M., & Grupe, D. 2010, GRB Coordinates Network, 11474, 1

Gelbord, J. M., et al. 2010, GRB Coordinates Network, 11461, 1

Gent, F. A., Shukurov, A., Fletcher, A., Sarson, G. R., & Mantere, M. J. 2013, MNRAS, 432, 1396

Ghirlanda, G., Ghisellini, G., & Lazzati, D. 2004, ApJ, 616, 331

Giacomazzo, B., & Perna, R. 2013, ApJ, 771, L26

Goad, M. R., et al. 2007, A&A, 476, 1401

Goldstein, A., et al. 2011, ArXiv e-prints

Golenetskii, S., et al. 2010a, GRB Coordinates Network, 10890, 1

—. 2010b, GRB Coordinates Network, 11470, 1

—. 2013, GRB Coordinates Network, 14771, 1

Gompertz, B. P., Page, K. L., & de Pasquale, M. 2013, GRB Coordinates Network, 15610, 1

Goriely, S., Bauswein, A., & Janka, H.-T. 2011, ApJ, 738, L32

Gorosabel, J., et al. 2006, A&A, 450, 87

Gotz, D., Beckmann, V., Mereghetti, S., & Paizis, A. 2007, GRB Coordinates Network, 6607, 1

Graham, J. F., et al. 2009, ApJ, 698, 1620

Granot, J., Panaitescu, A., Kumar, P., & Woosley, S. E. 2002, ApJ, 570, L61

Granot, J., & Sari, R. 2002, ApJ, 568, 820

Greco, G., et al. 2008, GRB Coordinates Network, 7977, 1

Greisen, E. W. 2003, Information Handling in Astronomy - Historical Vistas, 285, 109

Grindlay, J., Portegies Zwart, S., & McMillan, S. 2006, Nature Physics, 2, 116

Grupe, D., Burrows, D. N., Patel, S. K., Kouveliotou, C., Zhang, B., Mészáros, P., Wijers, R. A. M., & Gehrels, N. 2006, ApJ, 653, 462

Grupe, D., et al. 2010, GCN Report, 268, 1

Guetta, D., & Piran, T. 2005, A&A, 435, 421

Guetta, D., & Stella, L. 2009, A&A, 498, 329

Guidorzi, C., Melandri, A., O'Brien, P., & Tanvir, N. 2009, GRB Coordinates Network, 9492, 1

Haislip, J., et al. 2009, GRB Coordinates Network, 9921, 1

Hakobyan, A. A., Petrosian, A. R., McLean, B., Kunth, D., Allen, R. J., Turatto, M., & Barbon, R. 2008, A&A, 488, 523

Hancock, P., Murphy, T., Gaensler, B., Bell, M., Burlon, D., & de Ugarte Postigo, A. 2012a, GRB Coordinates Network, 13338, 1

—. 2012b, GRB Coordinates Network, 13611, 1

Hansen, B. M. S., & Phinney, E. S. 1997, MNRAS, 291, 569

Hascoët, R., Daigne, F., & Mochkovitch, R. 2012, A&A, 541, A88

Hill, D. T., Driver, S. P., Cameron, E., Cross, N., Liske, J., & Robotham, A. 2010, MNRAS, 404, 1215

Hjorth, J., et al. 2003, Nature, 423, 847

—. 2005a, ApJ, 630, L117

—. 2005b, Nature, 437, 859

Hogg, D. W., Pahre, M. A., McCarthy, J. K., Cohen, J. G., Blandford, R., Smail, I., & Soifer, B. T. 1997, MNRAS, 288, 404

Holland, S. T., de Pasquale, M., & Markwardt, C. B. 2007, GRB Coordinates Network, 7145, 1

Holland, S. T., Landsman, W. B., Page, K. L., & Stamatikos, M. 2010a, GCN Report, 289, 1

Holland, S. T., et al. 2010b, GRB Coordinates Network, 10884, 1

Hopman, C., Guetta, D., Waxman, E., & Portegies Zwart, S. 2006, ApJ, 643, L91

Hotokezaka, K., Kiuchi, K., Kyutoku, K., Okawa, H., Sekiguchi, Y.-i., Shibata, M., & Taniguchi, K. 2013, Phys. Rev. D, 87, 024001

Hoversten, E. A., Krimm, H. A., Grupe, D., Kuin, N. P. M., Barthelmy, S. D., Burrows, D. N., Roming, P., & Gehrels, N. 2009, GCN Report, 218, 1

Hurley, K., et al. 2002, ApJ, 567, 447

Hurley, K., et al. 2010, in American Institute of Physics Conference Series, Vol. 1279, American Institute of Physics Conference Series, ed. N. Kawai & S. Nagataki, 330–333

Ilbert, O., et al. 2010, ApJ, 709, 644

Immler, S., Starling, R. L. C., Evans, P. A., Barthelmy, S. D., & Sakamoto, T. 2010, GCN Report, 290, 1

Jakobsson, P., Hjorth, J., Fynbo, J. P. U., Watson, D., Pedersen, K., Björnsson, G., & Gorosabel, J. 2004, ApJ, 617, L21

Jaroszynski, M. 1993, AcA, 43, 183

Jin, Z.-P., Xu, D., Fan, Y.-Z., Wu, X.-F., & Wei, D.-M. 2013, ApJ, 775, L19

Johnson, S., et al. 2007, GRB Coordinates Network, 6218, 1

Kalberla, P. M. W., Burton, W. B., Hartmann, D., Arnal, E. M., Bajaja, E., Morras, R., & Pöppel, W. G. L. 2005, A&A, 440, 775

Kalogera, V., et al. 2004, ApJ, 601, L179

Kann, D. A., et al. 2008, ArXiv e-prints

—. 2010, ApJ, 720, 1513

Kasen, D., Badnell, N. R., & Barnes, J. 2013, ApJ, 774, 25

Katz, J. I. 1994, ApJ, 432, L107

Kehoe, R., et al. 2001, ApJ, 554, L159

Kelley, L. Z., Ramirez-Ruiz, E., Zemp, M., Diemand, J., & Mandel, I. 2010, ApJ, 725, L91

Kelly, P. L., & Kirshner, R. P. 2012, ApJ, 759, 107

Kelly, P. L., Kirshner, R. P., & Pahre, M. 2008, ApJ, 687, 1201

Kennicutt, Jr., R. C. 1998, ARA&A, 36, 189

Kim, C., Kalogera, V., & Lorimer, D. R. 2006, ArXiv Astrophysics e-prints

Klebesadel, R. W. 1992, The durations of gamma-ray bursts, ed. C. Ho, R. I. Epstein, & E. E. Fenimore, 161–168

Klebesadel, R. W., Strong, I. B., & Olson, R. A. 1973, ApJ, 182, L85

Kocevski, D., Bloom, J. S., Thoene, C. C., & Prochaska, J. 2007, GRB Coordinates Network, 6771, 1

Kocevski, D., & Butler, N. 2008, ApJ, 680, 531

Kocevski, D., et al. 2010, MNRAS, 404, 963

Kochanek, C. S., et al. 2001, ApJ, 560, 566

Kodaka, N., et al. 2007, GRB Coordinates Network, 6637, 1

Koekemoer, A. M., Fruchter, A. S., Hook, R. N., & Hack, W. 2003, in HST Calibration Workshop : Hubble after the Installation of the ACS and the NICMOS Cooling System, ed. S. Arribas, A. Koekemoer, & B. Whitmore, 337

Kopac, D., Smith, R. J., Mundell, C. G., Tanvir, N. R., & Gomboc, A. 2013, GRB Coordinates Network, 15306, 1

Korpi, M. J., Brandenburg, A., Shukurov, A., Tuominen, I., & Nordlund, Å. 1999, ApJ, 514, L99

Kouveliotou, C., Meegan, C. A., Fishman, G. J., Bhat, N. P., Briggs, M. S., Koshut, T. M., Paciesas, W. S., & Pendleton, G. N. 1993, ApJ, 413, L101

Krimm, H., et al. 2005, GRB Coordinates Network, 3667, 1

Krimm, H. A., Cummings, J. R., Evans, P. A., & Marshall, F. E. 2010a, GCN Report, 271, 1

Krimm, H. A., et al. 2008, GRB Coordinates Network, 8735, 1

—. 2009, GRB Coordinates Network, 8936, 1

—. 2010b, GRB Coordinates Network, 11467, 1

Kuin, N. P. M., & Gelbord, J. M. 2010, GRB Coordinates Network, 11472, 1

La Parola, V., et al. 2006, A&A, 454, 753

Lamb, D. Q., Castander, F. J., & Reichart, D. E. 1999, A&AS, 138, 479

Landsman, W., Marshall, F. E., & Racusin, J. 2007, GRB Coordinates Network, 6689, 1

Laskar, T., Berger, E., & Chary, R.-R. 2011, ApJ, 739, 1

Laskar, T., et al. 2014, ApJ, 781, 1

Lattimer, J. M., & Schramm, D. N. 1974, ApJ, 192, L145

—. 1976, ApJ, 210, 549

Le Floc'h, E., et al. 2003, A&A, 400, 499

Lee, W. H., & Ramirez-Ruiz, E. 2007, New Journal of Physics, 9, 17

Lee, W. H., Ramirez-Ruiz, E., & van de Ven, G. 2010, ApJ, 720, 953

Leibler, C. N., & Berger, E. 2010, ApJ, 725, 1202

Levan, A. J., Tanvir, N. R., Hjorth, J., Malesani, D., de Ugarte Postigo, A., & D'Avanzo, P. 2009, GRB Coordinates Network, 10154, 1

Levan, A. J., Wynn, G. A., Chapman, R., Davies, M. B., King, A. R., Priddey, R. S., & Tanvir, N. R. 2006a, MNRAS, 368, L1

Levan, A. J., et al. 2006b, ApJ, 648, L9

—. 2008, MNRAS, 384, 541

Levesque, E. M., et al. 2010, MNRAS, 401, 963

Li, L.-X., & Paczyński, B. 1998, ApJ, 507, L59

Li, W., Chornock, R., Leaman, J., Filippenko, A. V., Poznanski, D., Wang, X., Ganeshalingam, M., & Mannucci, F. 2011, MNRAS, 412, 1473

Liang, E.-W., Zhang, B.-B., & Zhang, B. 2007, ApJ, 670, 565

LIGO Scientific Collaboration et al. 2013, ArXiv e-prints

Littlejohns, O., et al. 2013, GRB Coordinates Network, 15312, 1

Littlejohns, O. M., de Pasquale, M., & Morris, D. C. 2011, GRB Coordinates Network, 11567, 1

MacFadyen, A. I., & Woosley, S. E. 1999, ApJ, 524, 262

Malesani, D., D'Avanzo, P., di Fabrizio, L., & Tessicini, G. 2013, GRB Coordinates Network, 15305, 1

Malesani, D., de Ugarte Postigo, A., Levan, A. J., Tanvir, N. R., Hjorth, J., & D'Avanzo, P. 2009, GRB Coordinates Network, Circular Service, 156, 1 (2009), 156, 1

Malesani, D., Uthas, H., Thoene, C. C., Fynbo, J. P. U., Hjorth, J., & Andersen, M. I. 2007a, GRB Coordinates Network, 6254, 1

Malesani, D., et al. 2004, ApJ, 609, L5

—. 2007b, A&A, 473, 77

Mangano, V., & Sakamoto, T. 2011, GRB Coordinates Network, 12468, 1

Mannucci, F., Della Valle, M., Panagia, N., Cappellaro, E., Cresci, G., Maiolino, R., Petrosian, A., & Turatto, M. 2005, A&A, 433, 807

Mao, J., Guidorzi, C., Ukwatta, T., Brown, P. J., Barthelmy, S. D., Burrows, D. N., Roming, P., & Gehrels, N. 2008, GCN Report, 138, 1

Maoz, D., Mannucci, F., & Brandt, T. D. 2012, MNRAS, 426, 3282

Maoz, D., Sharon, K., & Gal-Yam, A. 2010, ApJ, 722, 1879

Maraston, C. 2005, MNRAS, 362, 799

Marchesini, D., Stefanon, M., Brammer, G. B., & Whitaker, K. E. 2012, ApJ, 748, 126

Marchesini, D., et al. 2007, ApJ, 656, 42

Margutti, R., et al. 2010, MNRAS, 402, 46

—. 2011, MNRAS, 417, 2144

—. 2012, ApJ, 756, 63

—. 2013, MNRAS, 428, 729

Markwardt, C., Beardmore, A., Marshall, F. E., Schady, P., Barthelmy, S. D., Burrows, D. N., Roming, P., & Gehrels, N. 2007, GCN Report, 51, 1

Markwardt, C., et al. 2006, GRB Coordinates Network, 4873, 1

Marshall, F., Perri, M., Stratta, G., Barthelmy, S. D., Krimm, H., Burrows, D. N., Roming, P., & Gehrels, N. 2006, GCN Report, 18, 1

Marshall, F. E., Barthelmy, S. D., Burrows, D. N., Chester, M. M., Cummings, J., Evans, P. A., Roming, P., & Gehrels, N. 2007, GCN Report, 80, 1

Marshall, F. E., Curran, P. A., Page, K. L., Barthelmy, S. D., Burrows, D. N., Roming, P., & Gehrels, N. 2009, GCN Report, 220, 1

McBreen, S., et al. 2010, A&A, 516, A71+

McLeod, B., & Williams, G. 2009, GRB Coordinates Network, 9370, 1

Meegan, C., et al. 2009, ApJ, 702, 791

Meegan, C. A., Fishman, G. J., Wilson, R. B., Horack, J. M., Brock, M. N., Paciesas, W. S., Pendleton, G. N., & Kouveliotou, C. 1992, Nature, 355, 143

Melandri, A., Burgdorf, M., Smith, R. J., Steele, I. A., Bersier, D. F., Mundell, C. G., Gomboc, A., & Guidorzi, C. 2008, GRB Coordinates Network, 8402, 1

Melandri, A., et al. 2013, GRB Coordinates Network, 14735, 1

Meszaros, P., & Rees, M. J. 1997, ApJ, 476, 232

Metzger, B. D., & Berger, E. 2012, ApJ, 746, 48

Metzger, B. D., & Bower, G. C. 2014, MNRAS, 437, 1821

Metzger, B. D., Quataert, E., & Thompson, T. A. 2008a, MNRAS, 385, 1455

—. 2008b, MNRAS, 385, 1455

Metzger, B. D., Vurm, I., Hascoet, R., & Beloborodov, A. M. 2013, ArXiv e-prints

Metzger, B. D., et al. 2010, MNRAS, 406, 2650

Milisavljevic, D., & Fesen, R. A. 2013, ApJ, 772, 134

Mirabal, N., Halpern, J. P., An, D., Thorstensen, J. R., & Terndrup, D. M. 2006, ApJ, 643, L99

Mochkovitch, R., Hernanz, M., Isern, J., & Martin, X. 1993, Nature, 361, 236

Moin, A., Tingay, S., Phillips, C., Taylor, G., Wieringa, M., & Martin, R. 2009a, GRB Coordinates Network, 8952, 1

—. 2009b, GRB Coordinates Network, 8953, 1

Murali, C. 2000, ApJ, 529, L81

Naito, H., Sako, T., Suzuki, D., Kobara, S., Omori, K., Nagayama, T., Kurita, M., & Oi, N. 2010, GRB Coordinates Network, 10889, 1

Nakar, E., Gal-Yam, A., & Fox, D. B. 2006, ApJ, 650, 281

Nakar, E., & Granot, J. 2007, MNRAS, 380, 1744

Nakar, E., & Piran, T. 2011, Nature, 478, 82

Narayan, R., Paczynski, B., & Piran, T. 1992, ApJ, 395, L83

Nicuesa Guelbenzu, A., et al. 2011, A&A, 531, L6

—. 2012a, A&A, 548, A101

—. 2012b, A&A, 538, L7

Norris, J., Gehrels, N., Barthelmy, S. D., & Sakamoto, T. 2013, GRB Coordinates Network, 14746, 1

Norris, J. P., & Bonnell, J. T. 2006, ApJ, 643, 266

Norris, J. P., Cline, T. L., Desai, U. D., & Teegarden, B. J. 1984, Nature, 308, 434

Nousek, J. A., et al. 2006, ApJ, 642, 389

Nysewander, M., Fruchter, A., & Graham, J. 2007, GRB Coordinates Network, 6604, 1

Nysewander, M., Fruchter, A. S., & Pe'er, A. 2009, ApJ, 701, 824

Oates, S. R., Page, K. L., Evans, P. A., & Markwardt, C. B. 2009, GCN Report, 259, 1

Oates, S. R., & Sakamoto, T. 2011, GRB Coordinates Network, 12466, 1

Oemler, Jr., A., & Tinsley, B. M. 1979, AJ, 84, 985

Ofek, E. O., et al. 2007, ApJ, 662, 1129

Osborne, J. P., Beardmore, A. P., Evans, P. A., & Goad, M. R. 2011, GRB Coordinates Network, 12463, 1

O'Shaughnessy, R., Belczynski, K., & Kalogera, V. 2008, ApJ, 675, 566

O'Shaughnessy, R., Kim, C., Fragos, T., Kalogera, V., & Belczynski, K. 2005, ApJ, 633, 1076

Osterbrock, D. E., & Ferland, G. J. 2006, Astrophysics of gaseous nebulae and active galactic nuclei

Özel, F., Psaltis, D., Ransom, S., Demorest, P., & Alford, M. 2010, ApJ, 724, L199

Paciesas, W. 2010, GRB Coordinates Network, Circular Service, 10345, 1 (2010), 345, 1

Paczynski, B. 1995, PASP, 107, 1167

Paczynski, B., & Rhoads, J. E. 1993, ApJ, 418, L5

Pagani, C. 2012, GRB Coordinates Network, 13680, 1

Pagani, C., La Parola, V., & Burrows, D. N. 2005, GRB Coordinates Network, 3934, 1

Pagani, C., Racusin, J. L., Brown, P., & Cummings, J. 2008, GCN Report, 162, 1

Page, K. L., & de Pasquale, M. 2013, GRB Coordinates Network, 15004, 1

Page, K. L., & Holland, S. T. 2010, GRB Coordinates Network, 10888, 1

Panaitescu, A. 2005, MNRAS, 362, 921

—. 2006, MNRAS, 367, L42

Panaitescu, A., & Kumar, P. 2001, ApJ, 560, L49

—. 2002, ApJ, 571, 779

Panaitescu, A., Kumar, P., & Narayan, R. 2001, ApJ, 561, L171

Peng, C. Y., Ho, L. C., Impey, C. D., & Rix, H. W. 2007, in Bulletin of the American Astronomical Society, Vol. 39, American Astronomical Society Meeting Abstracts, 804

Peng, F., Königl, A., & Granot, J. 2005, ApJ, 626, 966

Perley, D. A., Bloom, J. S., Modjaz, M., Miller, A. A., Shiode, J., Brewer, J., Starr, D., & Kennedy, R. 2008, GRB Coordinates Network, 7889, 1

Perley, D. A., Bloom, J. S., Modjaz, M., Poznanski, D., & Thoene, C. C. 2007a, GRB Coordinates Network, 7140, 1

Perley, D. A., Modjaz, M., Morgan, A. N., Cenko, S. B., Bloom, J. S., Butler, N. R., Filippenko, A. V., & Miller, A. A. 2012, ApJ, 758, 122

Perley, D. A., Thoene, C. C., & Bloom, J. S. 2007b, GRB Coordinates Network, 6774, 1

Perley, D. A., Thoene, C. C., Cooke, J., Bloom, J. S., & Barton, E. 2007c, GRB Coordinates Network, 6739, 1

—. 2007d, GRB Coordinates Network, 6739, 1

Perley, D. A., et al. 2009a, ApJ, 696, 1871

—. 2009b, AJ, 138, 1690

Perley, R. A., Chandler, C. J., Butler, B. J., & Wrobel, J. M. 2011, ApJ, 739, L1

Perna, R., & Belczynski, K. 2002, ApJ, 570, 252

Perri, M., Stratta, G., Fenimore, E., Schady, P., Barthelmy, S. D., Burrows, D. N., Roming, P., & Gehrels, N. 2007, GCN Report, 103, 1

Piranomonte, S., et al. 2008, A&A, 491, 183

Poli, F., et al. 2003, ApJ, 593, L1

Poole, T. S., et al. 2008, MNRAS, 383, 627

Popham, R., Woosley, S. E., & Fryer, C. 1999, ApJ, 518, 356

Predehl, P., & Schmitt, J. H. M. M. 1995, A&A, 293, 889

Price, P. A., Berger, E., Fox, D. B., Cenko, S. B., & Rau, A. 2006, GRB Coordinates Network, 5077, 1

Prieto, J. L., Stanek, K. Z., & Beacom, J. F. 2008, ApJ, 673, 999

Prochaska, J. X., et al. 2006, ApJ, 642, 989

Qin, B., Wu, X.-P., Chu, M.-C., Fang, L.-Z., & Hu, J.-Y. 1998, ApJ, 494, L57

Racusin, J., Barbier, L., & Landsman, W. 2007, GCN Report, 70, 1

Racusin, J. L., et al. 2008, Nature, 455, 183

—. 2009, ApJ, 698, 43

Ramos, B. H. F., et al. 2011, AJ, 142, 41

Rau, A., McBreen, S., & Kruehler, T. 2009, GRB Coordinates Network, 9353, 1

Reddy, N. A., & Steidel, C. C. 2009, ApJ, 692, 778

Rees, M. J. 1988, Nature, 333, 523

Rees, M. J., & Meszaros, P. 1998, ApJ, 496, L1

Rezzolla, L., Giacomazzo, B., Baiotti, L., Granot, J., Kouveliotou, C., & Aloy, M. A. 2011, ApJ, 732, L6

Rhoads, J. E. 1999, ApJ, 525, 737

Ricker, G. R., et al. 2003, in American Institute of Physics Conference Series, Vol. 662, Gamma-Ray Burst and Afterglow Astronomy 2001: A Workshop Celebrating the First Year of the HETE Mission, ed. G. R. Ricker & R. K. Vanderspek, 3–16

Roberts, L. F., Kasen, D., Lee, W. H., & Ramirez-Ruiz, E. 2011, ApJ, 736, L21

Roming, P. W. A., et al. 2005, Space Sci. Rev., 120, 95

—. 2006, ApJ, 651, 985

Rossi, A., Nardini, M., Klose, S., & Greiner, J. 2012, GRB Coordinates Network, 13335, 1

Rossi, E. M., & Begelman, M. C. 2009, MNRAS, 392, 1451

Rosswog, S. 2005, Nuovo Cimento C Geophysics Space Physics C, 28, 607

—. 2007, MNRAS, 376, L48

Rosswog, S., Korobkin, O., Arcones, A., & Thielemann, F.-K. 2013, ArXiv e-prints

Rosswog, S., Korobkin, O., Arcones, A., Thielemann, F.-K., & Piran, T. 2014, MNRAS, 439, 744

Rosswog, S., Liebendörfer, M., Thielemann, F.-K., Davies, M. B., Benz, W., & Piran, T. 1999, A&A, 341, 499

Rosswog, S., Ramirez-Ruiz, E., & Davies, M. B. 2003, MNRAS, 345, 1077

Rowlinson, A., O'Brien, P. T., Metzger, B. D., Tanvir, N. R., & Levan, A. J. 2013, MNRAS, 430, 1061

Rowlinson, A., et al. 2010a, MNRAS, 408, 383

—. 2010b, MNRAS, 409, 531

Ruffert, M., & Janka, H. 1999a, Progress of Theoretical Physics Supplement, 136, 287

Ruffert, M., & Janka, H.-T. 1999b, A&A, 344, 573

Sakamoto, T., Barthelmy, S. D., & Norris, J. 2011a, GRB Coordinates Network, 12477, 1

Sakamoto, T., Norris, J., Ukwatta, T., Barthelmy, S. D., Gehrels, N., & Stamatikos, M. 2007a, GRB Coordinates Network, 7156, 1

—. 2007b, GRB Coordinates Network, 7156, 1

Sakamoto, T., et al. 2011b, GRB Coordinates Network, 12464, 1

—. 2011c, GRB Coordinates Network, 12460, 1

—. 2013, ApJ, 766, 41

Salvaterra, R., Cerutti, A., Chincarini, G., Colpi, M., Guidorzi, C., & Romano, P. 2008, MNRAS, 388, L6

Salvaterra, R., Devecchi, B., Colpi, M., & D'Avanzo, P. 2010, MNRAS, 406, 1248

Saracco, P., et al. 2006, MNRAS, 367, 349

Sari, R., & Mészáros, P. 2000, ApJ, 535, L33

Sari, R., Piran, T., & Halpern, J. P. 1999, ApJ, 519, L17

Sari, R., Piran, T., & Narayan, R. 1998, ApJ, 497, L17

Sato, G., et al. 2005, GRB Coordinates Network, 3793, 1

—. 2006a, GRB Coordinates Network, 5064, 1

—. 2006b, GRB Coordinates Network, 5381, 1

—. 2007a, GRB Coordinates Network, 6681, 1

—. 2007b, GRB Coordinates Network, 7148, 1

Savaglio, S., Glazebrook, K., & Le Borgne, D. 2009, ApJ, 691, 182

Schady, P., et al. 2006, GCN Report, 6, 1

Scheck, L., Kifonidis, K., Janka, H.-T., & Müller, E. 2006, A&A, 457, 963

Schlafly, E. F., & Finkbeiner, D. P. 2011, ApJ, 737, 103

Schlegel, D. J., Finkbeiner, D. P., & Davis, M. 1998, ApJ, 500, 525

Schmidt, M. 2001, ApJ, 559, L79

Sheth, K., Frail, D. A., White, S., Das, M., Bertoldi, F., Walter, F., Kulkarni, S. R., & Berger, E. 2003, ApJ, 595, L33

Siegel, M. H., et al. 2010, GCN Report, 292, 1

Singer, L. P., Kasliwal, M. M., & Cenko, S. B. 2013a, GRB Coordinates Network, 15552, 1

—. 2013b, GRB Coordinates Network, 15572, 1

Soderberg, A. M., & Frail, D. A. 2006, GRB Coordinates Network, 4884, 1

Soderberg, A. M., Frail, D. A., & Chandra, P. 2006a, GRB Coordinates Network, 5388, 1

Soderberg, A. M., et al. 2006b, ApJ, 650, 261

Stamatikos, M., et al. 2011, GRB Coordinates Network, 11553, 1

Stanford, S. A., Dickinson, M., Postman, M., Ferguson, H. C., Lucas, R. A., Conselice, C. J., Budavári, T., & Somerville, R. 2004, AJ, 127, 131

Stefanon, M., & Marchesini, D. 2013, MNRAS, 429, 881

Stratta, G., et al. 2007, A&A, 474, 827

Sullivan, M., et al. 2006, ApJ, 648, 868

Suzuki, D., Hayashi, F., Kobara, S., Sako, T., Naito, H., & Omori, K. 2010, GRB Coordinates Network, 10885, 1

Svensson, K. M., Levan, A. J., Tanvir, N. R., Fruchter, A. S., & Strolger, L.-G. 2010, MNRAS, 405, 57

Tamura, N., & Ohta, K. 2004, MNRAS, 355, 617

Tanaka, M., & Hotokezaka, K. 2013, ArXiv e-prints

Tanga, M., Klose, S., Sudilovsky, V., Filgas, R., & Greiner, J. 2013, GRB Coordinates Network, 15214, 1

Tanvir, N. R., Levan, A. J., Fruchter, A. S., Hjorth, J., Hounsell, R. A., Wiersema, K., & Tunnicliffe, R. L. 2013a, Nature, 500, 547

Tanvir, N. R., Wiersema, K., & Levan, A. J. 2013b, GRB Coordinates Network, 15224, 1

Troja, E., Cummings, J. R., Palmer, D. M., Cucchiara, A., Barthelmy, S. D., Burrows, D. N., Roming, P., & Gehrels, N. 2008a, GCN Report, 118, 1

Troja, E., King, A. R., O'Brien, P. T., Lyons, N., & Cusumano, G. 2008b, MNRAS, 385, L10

Troja, E., et al. 2009, GCN Report, 248, 1

Trujillo, I., Erwin, P., Asensio Ramos, A., & Graham, A. W. 2004, AJ, 127, 1917

Tunnicliffe, R. L., et al. 2013, MNRAS

Uehara, T., et al. 2008, GRB Coordinates Network, 7223, 1

Ukwatta, T. N., et al. 2008, GCN Report, 111, 1

—. 2009, GRB Coordinates Network, 9337, 1

Updike, A. C., Bryngelson, G., & Milne, P. A. 2009, GRB Coordinates Network, 9361, 1

Urata, Y., et al. 2006, GRB Coordinates Network, 5717, 1

van den Bergh, S., Li, W., & Filippenko, A. V. 2005, PASP, 117, 773

van der Horst, A. J. 2005, GRB Coordinates Network, 4039, 1

—. 2006, GRB Coordinates Network, 5408, 1

van der Horst, A. J., Kouveliotou, C., Gehrels, N., Rol, E., Wijers, R. A. M. J., Cannizzo, J. K., Racusin, J., & Burrows, D. N. 2009, ApJ, 699, 1087

van der Horst, A. J., Wiersema, K., & Wijers, R. A. M. J. 2005, GRB Coordinates Network, 3405, 1

van Eerten, H., & MacFadyen, A. 2013, ApJ, 767, 141

van Eerten, H., Zhang, W., & MacFadyen, A. 2010, ApJ, 722, 235

van Eerten, H. J., & MacFadyen, A. I. 2011, ApJ, 733, L37

—. 2012, ApJ, 751, 155

van Paradijs, J., et al. 1997, Nature, 386, 686

Villasenor, J. S., et al. 2005, Nature, 437, 855

Virgili, F. J., Guidorzi, C., Melandri, A., & Mundell, C. G. 2012, GRB Coordinates Network, 13006, 1

Wainwright, C., Berger, E., & Penprase, B. E. 2007a, ApJ, 657, 367

—. 2007b, ApJ, 657, 367

Wakker, B. P., Lockman, F. J., & Brown, J. M. 2011, ApJ, 728, 159

Wang, C., Lai, D., & Han, J. L. 2006, ApJ, 639, 1007

Wang, X., Wang, L., Filippenko, A. V., Zhang, T., & Zhao, X. 2013, ArXiv e-prints

Watson, D. 2011, A&A, 533, A16

Watson, D., Hjorth, J., Jakobsson, P., Xu, D., Fynbo, J. P. U., Sollerman, J., Thöne, C. C., & Pedersen, K. 2006, A&A, 454, L123

Wieringa, M. H., Chandra, P., & Frail, D. A. 2007, GRB Coordinates Network, 7095, 1

Wijers, R. A. M. J., Rees, M. J., & Meszaros, P. 1997, MNRAS, 288, L51

Willmer, C. N. A., et al. 2006, ApJ, 647, 853

Wong, T.-W., Willems, B., & Kalogera, V. 2010, ApJ, 721, 1689

Wongwathanarat, A., Janka, H.-T., & Müller, E. 2013, A&A, 552, A126

Xin, L. P., Zhang, T. M., Qiu, Y. L., Wei, J. Y., Wang, J., Deng, J. S., Wu, C., & Han, X. H. 2011a, GRB Coordinates Network, 11554, 1

Xin, L.-P., et al. 2011b, MNRAS, 410, 27

Xu, D., Malesani, D., Hjorth, J., Jakobsson, P., Kruehler, T., Santiago, E., Groeneboom, N., & Hafreager, A. 2013, GRB Coordinates Network, 15304, 1

Xu, D., Smirnova, O., Purismo, T., Fynbo, J. P. U., & Jakobsson, P. 2012, GRB Coordinates Network, 14110, 1

Xue, X. X., et al. 2008, ApJ, 684, 1143

Yost, S. A., Harrison, F. A., Sari, R., & Frail, D. A. 2003, ApJ, 597, 459

Zaninoni, E., Bernardini, M. G., Margutti, R., Oates, S., & Chincarini, G. 2013, A&A, 557, A12

Zemp, M., Ramirez-Ruiz, E., & Diemand, J. 2009, ApJ, 705, L186

Zhang, B. 2013, ApJ, 763, L22

Zhang, B., Fan, Y. Z., Dyks, J., Kobayashi, S., Mészáros, P., Burrows, D. N., Nousek, J. A., & Gehrels, N. 2006, ApJ, 642, 354

Zhang, B., & Mészáros, P. 2001, ApJ, 552, L35

—. 2002, ApJ, 566, 712

Zheng, Z., & Ramirez-Ruiz, E. 2007, ApJ, 665, 1220

Ziaeepour, H., Barthelmy, S. D., Parsons, A., Page, K. L., de Pasquale, M., & Schady, P. 2007, GCN Report, 74, 2

Ziaeepour, H., et al. 2006, GCN Report, 21, 1

Zrake, J., & MacFadyen, A. I. 2013, ApJ, 769, L29